Springer Proceedings in Materials

Snehanshu Pal
Debdas Roy
Sudip Kumar Sinha *Editors*

Processing and Characterization of Materials

Select Proceedings of CPCM 2020

Springer

Springer Proceedings in Materials

Volume 13

Springer Proceedings in Materials publishes the latest research in Materials Science and Engineering presented at high standard academic conferences and scientific meetings. It provides a platform for researchers, professionals and students to present their scientific findings and stay up-to-date with the development in Materials Science and Engineering. The scope is multidisciplinary and ranges from fundamental to applied research, including, but not limited to:

- Structural Materials
- Metallic Materials
- Magnetic, Optical and Electronic Materials
- Ceramics, Glass, Composites, Natural Materials
- Biomaterials
- Nanotechnology
- Characterization and Evaluation of Materials
- Energy Materials
- Materials Processing

To submit a proposal or request further information, please contact one of our Springer Publishing Editors according to your affiliation:

European countries: **Mayra Castro** (mayra.castro@springer.com)
India, South Asia and Middle East: **Priya Vyas** (priya.vyas@springer.com)
South Korea: **Smith Chae** (smith.chae@springer.com)
Southeast Asia, Australia and New Zealand: **Ramesh Nath Premnath** (ramesh.premnath@springernature.com)
The Americas: **Michael Luby** (michael.luby@springer.com)
China and all the other countries or regions: **Mengchu Huang** (mengchu.huang@springer.com)

More information about this series at http://www.springer.com/series/16157

Snehanshu Pal · Debdas Roy · Sudip Kumar Sinha
Editors

Processing and Characterization of Materials

Select Proceedings of CPCM 2020

Springer

Editors
Snehanshu Pal
Metallurgical and Materials Engineering
National Institute of Technology Rourkela
Rourkela, India

Debdas Roy
Materials and Metallurgical Engineering
National Institute of Foundry and Forge
Ranchi, Jharkhand, India

Sudip Kumar Sinha
Metallurgical and Materials Engineering
National Institute of Technology Raipur
Raipur, India

ISSN 2662-3161 ISSN 2662-317X (electronic)
Springer Proceedings in Materials
ISBN 978-981-16-3936-4 ISBN 978-981-16-3937-1 (eBook)
https://doi.org/10.1007/978-981-16-3937-1

Contents

About the Editors

Dr. Snehanshu Pal is currently working as an assistant professor at the Department of Metallurgical and Materials Engineering, National Institute of Technology Rourkela. He has served as a postdoctoral fellow at the Department of Materials Science and Engineering, The Pennsylvania State University, USA. He has done Ph.D. in Metallurgical and Materials Engineering from the Indian Institute of Technology, Kharagpur, India. His research focuses on the study of deformation behavior of nanostructured material using MD simulation and modeling of metallurgical processes. He is leading the Computational Materials Engineering and Process Modeling Research Group at NIT, Rourkela, and a group dedicated to realizing the underlying physics behind the mechanical behavior of materials and simulating metallurgical processes. He has published 71 high-impact research articles in internationally reputed SCI indexed journals. He wrote two books, namely "Molecular Dynamics Simulation of Nanostructured Materials: An Understanding of Mechanical Behavior" and "Process Modelling for Steel Industry." He has supervised three doctoral theses and several master theses. He is an investigator of numerous sponsored research projects and industrial projects. He has active research collaborations with esteemed universities across the globe (such as the University of Florida, the University of Manitoba, Université Lille, and the National Academy of Science of Belarus). In addition, He is associated with various esteemed technical and scientific societies such as Indian Institute of Metals and Indian Institute of Engineers.

Dr. Debdas Roy is presently Associate Professor and Head at the Department of Materials and Metallurgical Engineering, National Institute of Foundry and Forge Technology, Hatia, Ranchi, Jharkhand, India. He obtained his Ph.D. (Metallurgical and Materials Engineering) from the Indian Institute of Technology, Kharagpur, India. His prime research interest comprises nanostructure material, nanomaterial, and biomaterial (synthesis, consolidation, and characterization). He has published 51 papers and a chapter in reputed international journal. He has also published a patent and awarded IEI Young Engineers Award in 2008 in the field of Metallurgical and Materials Engineering, Young Metallurgist of the Year in 2010.

Dr. Sudip Kumar Sinha is presently Assistant Professor at the Department of Metallurgical and Materials Engineering, National Institute of Technology Raipur, Chhattisgarh, India. He obtained his B.E. (Metallurgical and Materials Engineering) from Jadavpur University, Kolkata, M.Tech. (Materials Science and Engineering) from the Indian Institute of Technology, Kanpur, India, M.S. (Materials science and Engineering) from Washington State University, Pullman, USA, and Ph.D. (Metallurgical and Materials Engineering) from the Indian Institute of Technology, Kharagpur, India. His prime research interest comprises low-dimensional nanostructured materials, thin-film technology, chemical sensing of semiconductor metal oxides, and composite materials. He has published 29 papers and several chapters in reputed international journal and delivered several invited talks.

Induration of Indian Low Grade Iron Ore Pellets in a Pilot Heat Hardening System

G. M. Chowdhury, S. Sudhir, R. K. Ram, S. Dhara, and A. Mallick

Abstract Green pellet induration is generally conducted in travelling grate or grate kiln furnaces where drying, firing and cooling are performed by direct contact with hot gases with varying temperatures. Indian low grade goethite ore (FeO(OH)) usually contains a high amount of chemically bonded water (approx. 6%). This chemically bonded water gets suddenly released at a temperature between 350 and 450 ºC. Cracking and disintegration of some of the pellets are observed during induration. In the present investigation a suitable induration cycle has been developed for pelletization of the Indian low grade goethite ore to produce the commercial grade pellets. Green pellets with varying basicity of 0.1–0.6 were prepared in a laboratory disc pelletizer and thereafter, drying, pre-heating and firing were conducted in a tailor made laboratory scale horizontal zone furnace by varying the main process parameters such as temperature and duration of soaking. Thereafter, the experimental data were validated in a pilot pelletization system of capacity 60 kg per batch i.e. a straight grate simulator. Pellets obtained by optimizing the process parameters exhibit the properties like cold compressive strength, porosity, Reduction Degradation Index (RDI), Reducibility Index (RI) etc. in line with the commercial grade pellets.

Keywords Goethite ore · Pellet induration · Cold compressive strength

1 Introduction

General depletion of good quality iron ores and increased demands of the industry have motivated the researchers to utilize the low grade iron ore. The ore is pulverised and beneficiated to enrich the iron content as per requirement. The beneficiated micro-fines has the limited option to use in sintering process and pelletization is the effective route for the utilization of these fines. Pelletization process involves two steps, green ball preparation with the addition of binder followed by induration of green pellets to impart mechanical strength into the pellets and to obtain desired

G. M. Chowdhury (✉) · S. Sudhir · R. K. Ram · S. Dhara · A. Mallick
R&D Centre for Iron and Steel, Steel Authority of India Limited, Doranda Ranchi-834002, India
e-mail: golapmd@sail.in

S. Pal et al. (eds.), *Processing and Characterization of Materials*, Springer Proceedings in Materials 13, https://doi.org/10.1007/978-981-16-3937-1_1

metallurgical properties required for ironmaking processes. Indian low grade goethite ore (FeO(OH)) usually contains a high amount of chemically bonded water (approx. 6%). This chemically bonded water gets suddenly released at a temperature between 350 and 450 ºC. Cracking and disintegration of some of the pellets are observed during induration. This significantly hampers the strength of the indurated pellet and also the process yield. Pellet induration is generally conducted in travelling grate or grate kiln furnaces [1] where drying, firing and cooling stages are performed by direct contact with hot gases with varying temperatures. The mechanical strength of the pellets is influenced by the residence time and temperature profile within the firing zone. The residual moisture content also plays an important role when the pellets place in the firing zone as the induration process starts after completion of the drying stage. Therefore, drying of the green pellets is the main stage for the improvement of production rate as well as pellet quality; and this stage is also reported to be a major energy consumer [2, 3]. Patisson et al. [4, 5] reported that drying stage consumes about 25% of the total amount of energy required for pellet induration. Thus, minute development in the drying stage can result in substantial savings for the pellet producer for both capital and operating costs [2]. Several investigations [1–6] also investigated on the induration of iron ore green pellets. Influence of basicity and flux addition on the properties of iron ore pellets have also been reported by some investigators [7–9]. However, most of these studies are related on either with total induration process or modeling on the induration process. Comparatively few studies [6] have been investigated on the drying stage of the induration process. No study is reported on the pilot scale induration process of the green pellets. In the present study, an attempt has been made to show the effect of basicity on the properties of the roasted iron ore pellets in a pilot scale system.

2 Experimental

Iron ore concentrate of average size less than 100 μm was generated through beneficiation of goethite ore of Bolani iron ore mines. Green pellets of size 9–16 mm were produced in a laboratory disc pelletiser of 1 m diameter using the ore fines of minimum blaine value i.e. degree of fineness of the iron ore of 2000 cm^2/g with 0.6% bentonite as binder and with varying basicity (CaO/SiO_2) level of 0.1–0.6. Limestone and coke fines (0.8%) were used as additives. Chemical analyses of beneficiated iron ore, bentonite, limestone and coke fines are given in Table 1.

The thermo-gravimetric differential thermal analysis (TG–DTA) of the iron ore is shown in Fig. 1. It is observed that the mass loss i.e. LoI of the ore is 7.1%.

A schematic of the experimental setup used to study the induration of the green pellets is shown in Fig. 2. This is a tailor made horizontal zone furnace. The Furnace has different Heating Zones (isothermal zones) of 200, 1000 and 1400 °C designated as drying zone, pre-heating zone and firing zone, respectively. There is a separator between each zone. Separate control system as per required temperature zone with temperature and time variation has been maintained in the furnace. Furnace has

Table 1 Chemical analysis of beneficiated iron ore, bentonite, limestone and coke fines

Materials	Fe Total,%	SiO_2, %	Al_2O_3,%	Na_2O, %	K_2O %	$Ti0_2$, %	CaO, %	MgO, %	Lol, %
Iron ore	60.28	3.16	3.47	–	–	–	–	–	7.10
Bentoniite	6.87	40.39	16.23	3.84	0.79	1.79	0.92	2.31	20.82
Limestone	170	139	0.65	0.02	0.04	0.02	38.72	12.87	43.76
Coke fines	6.34	5.48	2.88	0.08	0.24	0.32	0.72	020	78.90

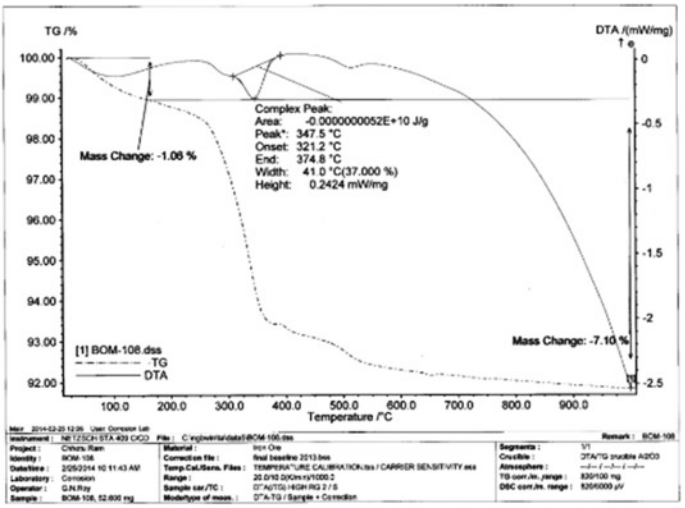

Fig. 1 TG–DTA analysis of beneficiated goethite ore

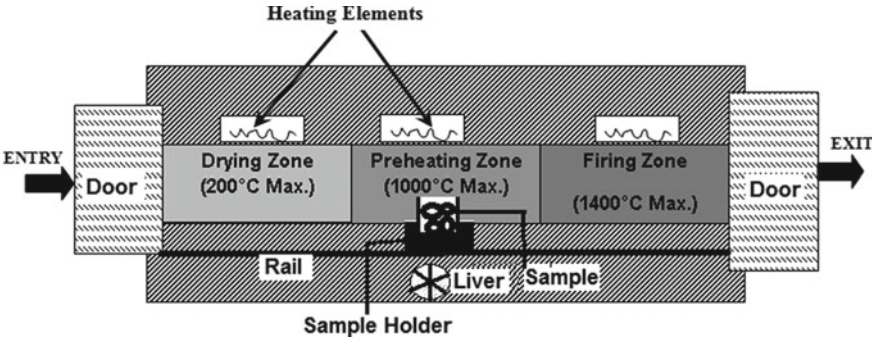

Fig. 2 Schematic representation of the horizontal zone furnace

rectangular c/s of 120 mm × 150 mm and a depth of 1600 mm. The temperature of the furnace can be varied at any temperature between 50 and 200 °C for drying zone, between 50 and 1000 °C for preheating zone, between 50 and 1400 °C for firing zone with ± 10 °C accuracy. In the present study the drying, preheating and firing were conducted at 120 °C, 900 °C and 1350 °C, respectively.

Thermocouples in different zones are placed at the centre of each zone. Heating element used as Kanthal Tubular for drying zone, Kanthal Globar SD elements (silicon carbide) for pre heating zone and Kanthal Super for firing zone. Kanthal is a heating element of Fe–Cr-Al alloy with Fe-73 wt%, Cr–2 wt% and Al–6 wt%. The doors are front opening type, insert-type, swing-aside, facing away from the operator in any position. There is an arrangement of pushing the trolley which moves on silicon carbide embossed rail by a lever. It carries and also transfers the special designed ceramic tray with materials between the different temperature zones. One scale type zone indicator is introduced to know the exact work zone of the material. The experimental data were validated in a pilot scale pellet heat hardening system of capacity 60 kg per batch. The schematic representation of the pilot heat hardening system is shown in Fig. 3.

The Cold Crushing Strength (CCS), Porosity, Reducibility Index (RI), Swelling Index (SI) and Tumbling Index (TI) of the roasted pellets were also measured in the laboratory. The porosity of the roasted pellets was conducted by mercury intrusion porosi-meter (Model: AMP-30 K-A-1, Make: Porous Materials Inc., USA).

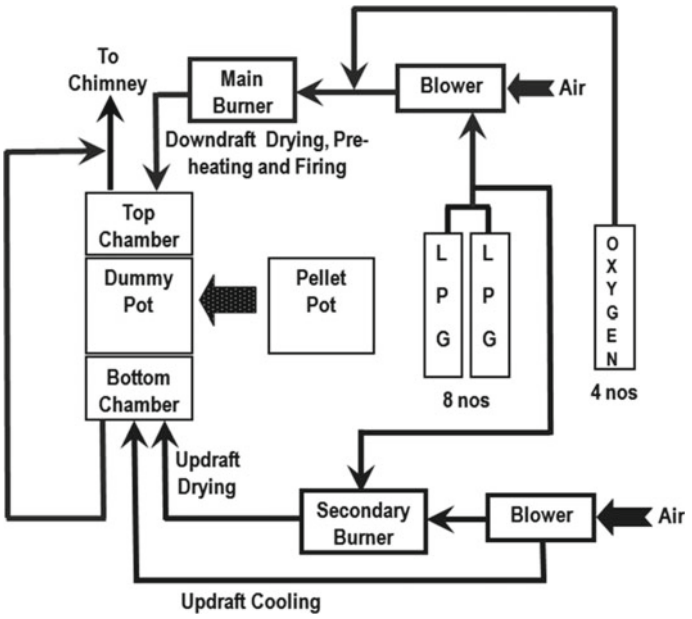

Fig. 3 Schematic representation of the pilot pelletization system

3 Results and Discussion

Figure 4 shows the variation of CCS values as function of basicity (CaO/SiO_2 ratio) of the heat hardened pellets. It is noticed that with increase in basicity the CCS values get improved and it becomes maximum at basicity level 0.3. An interesting result is found that on further increase in basicity level the CCS values get reduced. The silicate melt usually acts as a bonding phase in the fired pellets and the amount of this phase gets increased with increasing CaO content in the limestone fluxed pellets [8]. On the other hand, FeO content of the silicate melt is found to decrease with higher basicity of pellets [9]. In the later stages, low strength silicate melt phase is formed and reduction in CCS values is observed [9].

In Fig. 5, the results of Reducibility Index (RI) values have been plotted against different basicity values. The effect is likely same as noticed in Fig. 4 i.e. with increase in basicity the RI values get improved and it becomes maximum at basicity level 0.3. It is also found that on further increase in basicity level the RI values get reduced. Pellets with 0.3 basicity exhibits highest RI [appox.68%RDI]. This may

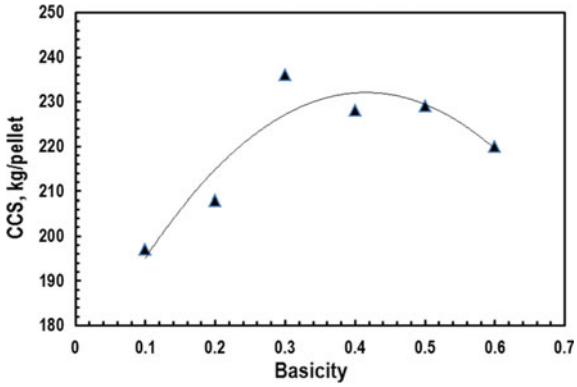

Fig. 4 Effect of basicity on CCS of hardened pellet

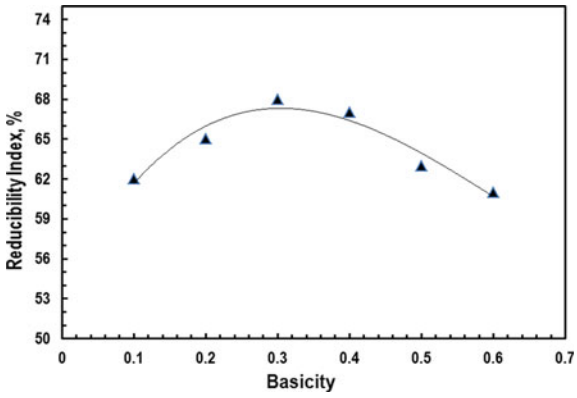

Fig. 5 Effect of basicity on reducibility of hardened pellet

be due to the formation of more hematite bonds and less silicate bonds. In the later stages i.e. with higher basicity values, amount of slag bond increases and hematite bond decreases [8]. It is reported that higher amount of stable bonding phases like silicates and its better distribution are accountable for the improved RI values of the fluxed iron ore pellets as the silicate phases are comparatively more stable than the oxide phases like hematite [9].

The variation of porosity as a function of basicity is shown in Fig. 6. It is observed that with increase in basicity the porosity values get improved and it achieves the highest level at basicity level 0.3. It is also found that on further increase in basicity level the amount of porosity gets reduced. Actual fact is that higher amount of recrystallization bonding resembles the formation of higher amount micro-pores.

At a basicity level of 0.3, the amount of slag bond and recrystallization bond get optimized and exhibits the good amount of porosity. On later cases i.e. with higher basicity values the slag bond predominates and porosity gets hampered.

The influence of basicity on tumbler index has been described in Fig. 7. It is noticed that the tumbler index increases initially with the increase in basicity; thereafter, it

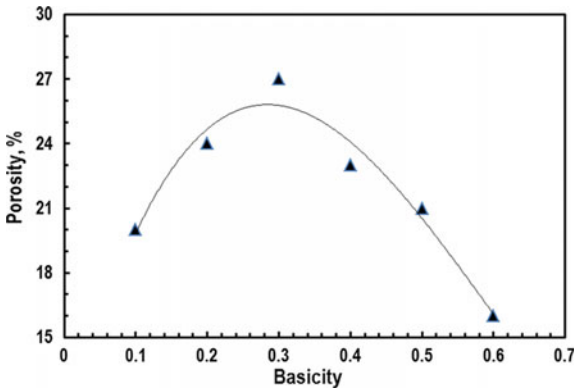

Fig. 6 Effect of basicity on porosity of hardened pellet

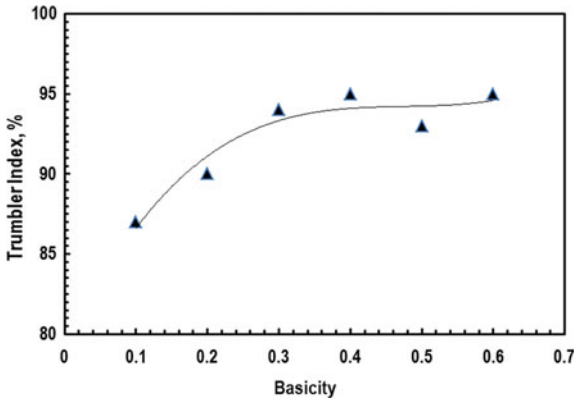

Fig. 7 Effect of basicity on tumbler index of hardened pellet

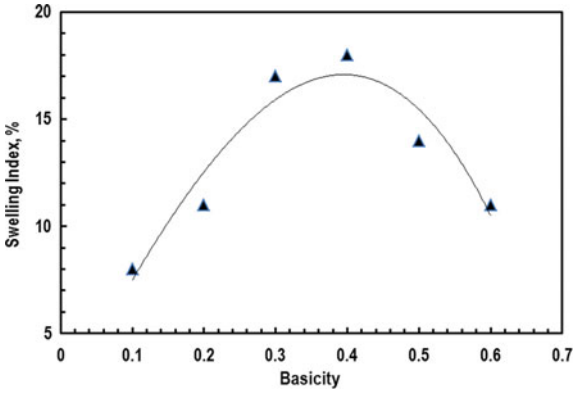

Fig. 8 Effect of basicity on swelling index of hardened pellet

becomes almost constant in the later stages. This may be due to slag bonding which affects the physical strength of the pellet. Higher basicity implies higher amount of slag bonding which imparts more strength to the pellet.

The effect of basicity on swelling index is shown in Fig. 8. It is noticed that the swelling index increases initially with the increase of basicity; thereafter, it gets reduced in the later stages. This may be due to the change in reducibility of the pellets which is explained in Fig. 5. Higher basicity implies higher amount of slag which hampers the swelling as well as the reducibility of the pellets.

The results of different tests conducted after hardening of the pellets i.e. CCS, Porosity, RDI, RI are highlighted in Table 2. The comparative study between bench scale and pilot scale has also been shown in Table 2. Pilot scale study results in higher CCS value and the pellets also exhibit better properties (porosity, tumbler, RI, etc.) compared to the laboratory scale study. This may be due to better rate of heat transfer from the pellet surface to interior which in turns results in superior properties of the roasted pellets. It is also revealed that pellets obtained in pilot study exhibit the properties in line with the commercial grade pellets.

Table 2 Salient properties of iron ore pellets

Pellet properties	Bench scale	Pilot scale	Commercial grade
CCS, kg/pellet	220	240	230–260
Porosity, %	24	27	25–30
Tumbler Index, %	93	35	>05
Reducibility Index, %	65	68	65–70
Swelling Index, %	15	18	15–20

4 Conclusions

The experiments have been carried out in a laboratory raising hearth furnace followed by validation in the Pilot Pellet Heat Hardening System.

Pilot scale study results better properties (CCS: 240 kg/p, Porosity: 27%, Tumbler Index: 95%, Reducibility Index: 68% and Swelling Index: 18%) compared to the laboratory scale study.

Pellets obtained in pilot study exhibit the properties in line with the commercial grade pellets.

References

1. Meyer K (1980) Pelletizing of iron ores. Springer., Berlin
2. Clark KN (1981) Iron ore pellet drying mechanisms under the heating conditions encountered in a straight-grate indurator. Trans Inst Min Metall C 90C:C66–C72
3. Thurlby JA, Batterham RJ (1980) Prediction of drying and spalling behaviour of hematite pellets. Trans Inst Min Metall C 89C:C125–C131
4. Patisson F, Bellot JP, Ablitzer D (1990) Study of moisture transfer during the strand sintering process,.Metall Trans B 21B:37–47
5. Patisson F, Bellot JP, Ablitzer D, Marli E, Dulcy C, Steiler JM (1991) Mathematical modeling of iron ore sintering process. Ironmaking Steelmaking 18(2):89–95
6. Ball DF, Dartnell J, Davison J, Grieve A, Wild R (1973) Agglomeration in iron ores. Heinemann Educational Books Ltd., London
7. Zhu D, Zhang F, Guo Z, Pan J, Yu W (2017) Grate-kiln pelletization of Indian hematite fines and its industrial practice. Int J. Min, Metall, Mater 24:473–485
8. Dwarapudi S, Sekhar C, Paul I, Prasad YGS, Modi K, Chakraborty U (2016) Effect of fluxing agents on reduction degradation behaviour of hematite pellets. Ironmaking Steelmaking 43:180–191
9. Dwarapudi S, Banerjee PK, Chaudhary P, Sinha S, Chakraborty U, Sekhar C, Venugopalan T, Venugopal R (2014) Effect of fluxing agents on the swelling behavior of hematite pellets. Int J Miner Process 126:76–89

On the Relationship Between Surface Microhardness and Roughness Produced by MAF Process

Shadab Ahmad, Rajneesh Kumar Singh, Ranganath M. Singari, and R. S. Mishra

Abstract Owing to the MAF process's capabilities for its efficient surface finishing, it is essential to understand the parallel quality of different response parameters and their interdependency. This paper focuses on identifying a relation between surface hardening and roughness induced by the MAF process. In this research work, the influence on micro-hardness from the value of surface roughness has been studied. The different experimental conditions are applied to Ti–6Al–4V specimens treated using a pulsating DC-MAF machining set-up, and Material removal was done using loosely bonded magnetic abrasive media. The surface roughness and microhardness share significant interdependency, represented by a graph showing the best relationship between surface microhardness and roughness.

Keywords Magnetic abrasive finishing · Surface roughness · Microhardness · Desirability function analysis · Genetic algorithm

1 Introduction

The magnetic abrasive finishing (MAF) process has proven to be extremely useful for the modification of surface integrity of advanced materials such as metal-composites, superalloys and ceramics [1]. In this, the magnetic field is used for controlling the flexible magnetic abrasive brush (FMAB), which removes material from the intended surface. FMAB is made of magnetic (ferrous) and abrasive (alumina) particles. To achieve finishing, these magneto-abrasive particles are positioned in the machining gap (between the magnetic poles and target surface) [2]. Beneath the influence of

S. Ahmad · R. M. Singari · R. S. Mishra
Department of Mechanical Engineering, Delhi Technological University, Delhi 110042, India

R. K. Singh (✉)
Department of Mechanical Engineering, Meerut Institute of Engineering and Technology, Meerut 250005, India
e-mail: rajneesh.singh@miet.ac.in

R. M. Singari
Department of Design, Delhi Technological University, Delhi 110042, India

S. Pal et al. (eds.), *Processing and Characterization of Materials*, Springer Proceedings in Materials 13, https://doi.org/10.1007/978-981-16-3937-1_2

a magnetic field, these particles are rearranged to form the FMAB, whose strength depends on the intensity of the magnetic field in the machining gap. The relative motion between the FMAB and the target surface results in the desired finishing [3, 4]. The FMAB behaves akin to a multi-point cutter and the material is removed from the finished surface in micro to nano-chips [5]. The heat generated during finishing is a result of the plastic deformation, fracture and frictional heat [6]. This heat, that's generated during MAF, acutely impacts the surface integrity, morphology and metallurgy of the target surface. Numerous attempts were made by researchers to accurately forecast the surface temperature and characterize its impact on the finished surface [7, 8].

Surface integrity also affects the hardness of the surface [9]. In MAF, this increase in temperature is responsible for a change in the hardness of the target surface and this, in turn, leads to an improvement in its tribological properties—hence, it is crucial for MAF to be done at optimal conditions to obtain the best possible result. It is impossible to avoid counter effects on hardness change along with roughness change, so the trade-off between minimizing roughness while improving surface hardness has been explored in this paper [10]. Yin et al. studied the effect of ultra-high-speed magnetic abrasive surface micro machining (UHSMAM) on the plastic strain and strain energy of the AISI machined surface [11]. Vahdati and Rasouli evaluated the effect of the various parameters of MAF on the surface finishing of Al-alloy and compared the RSM simulation of the same with the experimentally obtained results [12]. Singh et al. used a semi-empirical dimensional model vis-a-vis the Buckingham π-theorem for the evaluation of the impact of various process variables on the increase of surface temperature of the finished surface [13]. S. R. Bhagavatula and R. Komanduri found during chemomechanical polishing that, the solid-phase reaction takes place between the workpiece and abrasive because of elevated temperature and pressure produced primarily by frictional heat during the finishing of the surface [14]. To divulge the impact of the MAF process on the hardness of the target surface, M. Naif investigated the effect of using MAF for finishing on the hardness of the brass plate [15]. A regression analysis was done by him for the prediction of the most significant process variable affecting the response parameters. The hardness increased when the powder volume and coil current increased and decreased with an increment in working gap and rotational speed. Moreover, Shather et al. experimentally studied the effect of design and process factors on the mechanical properties of the MAF-finished surface [16]. Ahmad et al. used ANN-GA for the modelling and optimization of MAF of stainless steel SS302 and compared it with the Taguchi-ANOVA analysis of the same. The machining gap, voltage, abrasive size and rotational speed were considered as the input parameters for studying the response parameter of surface roughness [17]. Ali Tavoli et al. employed the 'group method of data handling' (GMDH)-type neural networks-GA and NSGA-II with Pareto-based optimization to construct a multi-objective optimization (MOO) model of abrasive flow finishing for brass and aluminum samples' material removal and surface finish. Such a combined application has led to the discovery of useful and interesting design relationships [18]. Recently, a hybrid MOO technique was developed by Singh et al. by using the Moth flame optimization on an ANN. Their key findings were that a better surface

finish and hardness could be obtained by minimizing the voltage and working gap [19].

The novelty of this paper lies in the exploitation of the benefits of surface finish improvement and parallel effects on microhardness change in the process. Taguchi analysis is used to discover the effect of process parameters on responses. The artificial neural network (ANN) is used to model the multi-response data, regression analysis also, ANN model is used to find the correlation between change in the microhardness and change surface roughness in during Magnetic Abrasive Finishing (MAF).

1.1 Magnetic Abrasive Finishing (MAF) Process

MAF is a finishing procedure used to boost the surface texture and quality of flat surface or cylindrical surface externally and internally [20]. MAF is a highly desirable process in the industry given its flexibility to work with a substrate irrespective of its physical and mechanical properties. Workpiece material may consist of alloys, composites and ceramics etc., [21, 22]. Traditionally, the MAF process consists of magnetic abrasive particles (MAPs) which, below the impact of a magnetic field, act as multi-faced cutting tools and erode the material from the surface of the materials (MAPs are made of ferromagnetic material and hence can be controlled using a magnetic field). The material removal depends heavily on the finishing pressure, which is under the impact of a magnetic field [23]. The schematics of the MAF process is demonstrated in Fig. 1, the equipotential lines representing that magnetic abrasives assembled on the work surface to abrade the material [6]. The rotational motion results in a cutting force parallel to the surface of the workpiece, and the penetration of the abrasives within the workpiece is reliant on the normal force created by the magnetic field intensity [24]. The MAPs are generally sintered or

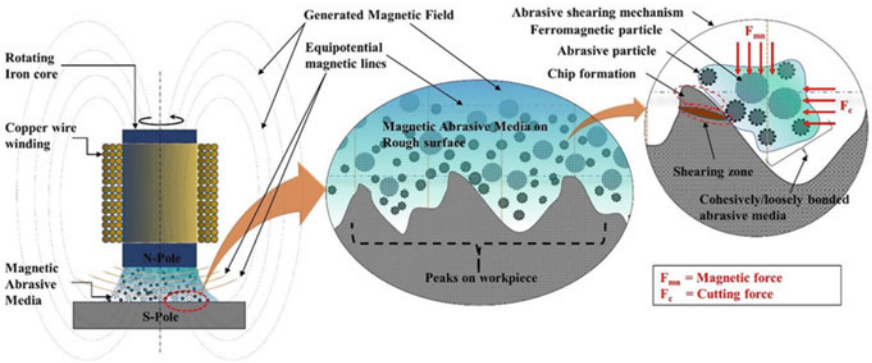

Fig. 1 Schematic diagram of the MAF process with loosely bonded magnetic abrasive media [6]

lubricant based [25]. The MAPs are magnetically arranged with each other along the line of the magnetic force [8].

2 Materials and Method

2.1 Material and Tools

Ti–6Al–4V/Titanium (Grade-5) (composition mentioned in Table 1) was the workpiece material for the analysis of MAF process. Magnetic abrasive media did the shearing operation for the removal of the material from the targeted surface as microchips [26]. The constituents of Magnetic abrasive media were Silicon carbide, and iron powder mixed together with lubricant oil in weight ratio as mentioned Table 2. An electromagnet attached to a lathe tool post—attached to a pulse DC controller ('pulse on time' = 60 ms, 'pulse off time' = 30 ms)—produces a pulsating magnetic field, as displayed in Fig. 2. Many individual control variables influence the func-

Table 1 The weight percent of material composition (Ti–6Al–4V)

Elements	Ti	V	Al	Fe	Mn	Zn	Mo
% weight composition	92.04	4.43	3.01	0.33	0.19	0.031	0.026

Table 2 Composition of magnetic abrasive media

Constituents	% weight concentration				Mesh size
Iron powder	60	50	40	30	300
Abrasive (SiC)	40	50	60	70	400
lubricant	10–20% of the total				–

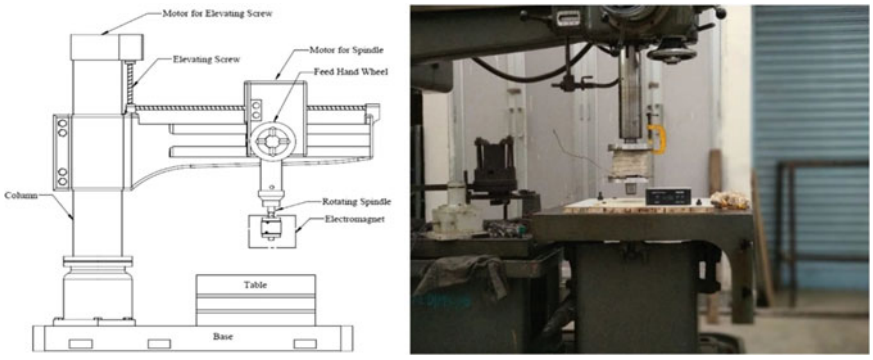

Fig. 2 Machining setup schematic and physical (electromagnet mounted on a radial drill)

tioning of the MAF process, including current, working gap, tool speed (rotational speed), abrasive composition.

3 Experimental Details

The Taguchi technique is a dominant instrument for the controlled design, arrangement, and collection of experimental data. It, further, informs us of the influence of process parameters on some basic variables for the design of successful systems and exposes the impact of unregulated variables at the same time [27]. The response parameter was, 'change in Surface Roughness' (ΔRa) in "μm" in 'change in the microhardness' (ΔHV) in Vickers hardness. Numerous researchers have used this approach successfully to explain the final results during the MAF process [15, 28, 29]. The control variables, their units, meanings, and levels are displayed in Table 3. The experimental data presented in Table 4 and observations were arranged according to the DOE of 'L_{16} orthogonal array'—with four inputs parameters and two outputs responses. The input parameters were current, working gap, and tool speed abrasive composition. Time of finishing for every experimental run was 15 min.

In the present research investigation, an electromagnet with a pole connected by a DC pulse source of power (30 ms off time and 60 ms on time) attached to the radial drill, the MAF set-up schematic and physical form is shown in Fig. 2. The electromagnet was provided a different current combination which generates a magnetic field with varying intensity at the pole end face. Slowly inserting the abrasive magnetic media in presence of the magnetic field in the machining gap, the FMAB was formed as shown in Fig. 3. First two images in Fig. 3 shows that in absence of lubricant oil and in the third image lubricant was mixed in the abrasive mixture to hold the abrasive and iron powder together. The Surface Roughness (Ra) in "μm" in the microhardness (ΔHV) in Vickers hardness was measured using "Taylor Hobson Precision Surtronic 3+ surface roughness tester" and "Fischer scope HM2000 S".

Table 3 Parameters, units, definition, and levels

Parameters	Units	Description	Levels			
			1	2	3	4
Current (x_1)	Amp	Current input to the electromagnet	0.8	1.2	1.6	2.0
Machining gap (x_2)	mm	Separation between tool and workpiece	1.5	2.0	2.5	3.0
Tool speed (x_3)	rpm	The relative motion of workpiece and tool	112	150	220	300
Abrasive composition (x_4)	wt. %	Magnetic abrasive media composition	40	50	60	70

Table 4 Experimental data, ANN predicted data, error, and SN ration results corresponding to L16 orthogonal array

S. No.	Input parameters and their values				Experimental		ANN predicted		Absolute error %		SN ratio for ΔRa (μm)	SN ratio for ΔHV
	×1	×2	×3	×4	ΔRa (μm)	ΔHV	ΔRa (μm)	ΔHV	ΔRa (μm)	ΔHV		
1	0.8	1.5	112	40	0.08	58.5	0.0800	58.4968	0.0800	0.0054	−21.9382	35.3431
2	0.8	2	150	50	0.066	51.63	0.0659	51.5892	0.0041	0.07883	−23.6091	34.2580
3	0.8	2.5	220	60	0.061	48.63	0.0610	48.2333	0.0022	0.81562	−24.2934	33.7380
4	0.8	3	300	70	0.062	45.6	0.0620	45.5698	0.0023	0.0661	−24.1522	33.1793
5	1.2	1.5	150	60	0.108	81.52	0.1080	94.8957	0.0015	16.4079	−19.3315	38.2252
6	1.2	2	112	70	0.073	49.56	0.0730	49.5443	0.0017	0.0316	−22.7335	33.9026
7	1.2	2.5	300	40	0.09	80.71	0.0899	80.7081	0.0006	0.0022	−20.9151	38.1385
8	1.2	3	220	50	0.054	41.5	0.0539	41.4823	0.1497	0.0426	−25.3521	32.3609
9	1.6	1.5	220	70	0.109	83.18	0.1089	63.1129	0.0023	24.1248	−19.2515	38.4003
10	1.6	2	300	60	0.089	82.18	0.0889	82.2021	0.0020	0.0269	−21.0122	38.2953
11	1.6	2.5	112	50	0.101	71.18	0.1010	54.1737	0.0007	23.8918	−19.9136	37.0471
12	1.6	3	150	40	0.081	67.24	0.0972	67.1971	20.0732	0.0636	−21.8303	36.5525
13	2	1.5	300	50	0.155	128.79	0.1550	128.8375	0.01788	0.0368	−16.1934	42.1976
14	2	2	220	40	0.147	121.53	0.1470	121.5438	0.0011	0.0113	−16.6537	41.6936
15	2	2.5	150	70	0.075	53.18	0.0750	53.1945	0.0030	0.0272	−22.4988	34.5149
16	2	3	112	60	0.073	51.05	0.0729	51.0267	0.0034	0.0454	−22.7335	34.1599

Fig. 3 FMAB and media on the workpiece without the magnetic field

This "Fischer scope HM2000 S" works as per the ISO 14577-1 and ASTM E 2546 standards. Furthermore, it measures the factors in micro and nanometer range.

4 Results and Discussion

The values of the output parameters obtained after each experiment in the design of the experiment table are given in Table 4. Taguchi analysis was done to decide rank wise effect of variables on outputs, regression done to understand trend between outputs. The ANN models developed were used to predict the output for various input sets.

4.1 Taguchi Analysis

In order to analyze the process quality and its properties, the S/N ratio (SNR) of the experimental data has been determined here. Based on the SNR, the control factors/variables have been ranked and shown in Table 5. From Table 5, clearly, the most influential factor that influenced the ΔRa is machining gap and followed by current, then by tool speed and abrasive composition, respectively. Also, the main effects plot (Fig. 4) shows the variations in the SNR, where the most influential

Table 5 Response table for S/N ratios-larger is better ΔR_a

Level	x_1	x_2	x_3	x_4
1	−23.5	−19.18	−21.83	−20.33
2	−22.08	−21	−21.82	−21.27
3	−20.5	−21.91	−21.39	−21.84
4	−19.52	−23.52	−20.57	−22.16
Delta	3.98	4.34	1.26	1.82
Rank	2	1	4	3

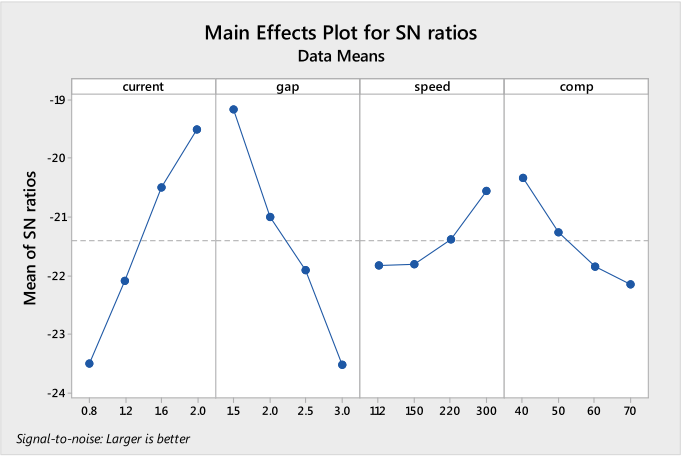

Fig. 4 Main effect plot for SN ration for ΔR_a (μm)

parameter is the machining gap and then current, abrasive composition and tool speed are 1.5 mm, 2 Amp, 40 wt% and 300 rpm respectively.

Also, it is seen that in the case of change in microhardness of the sample that the most influential parameter that affects the ΔHV is working gap and then current, followed by tool speed and abrasive composition, respectively. The changes in S/N ratio are displayed in 'main effects plot' (Fig. 5) where the most influential parameter is machining gap and then current, abrasive composition and tool speed are 1.5 mm, 2 Amp, 40 wt% and 300 rpm respectively. Based on S/N ratio, a rank of control factors is displayed in Table 6.

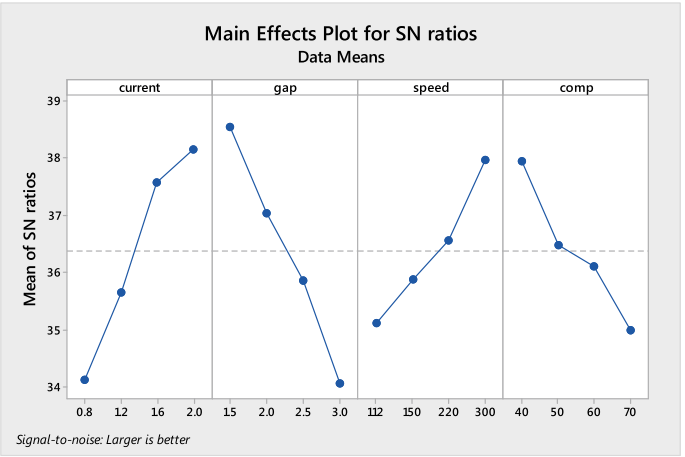

Fig. 5 Main effect plot for SN ration for ΔHV

Table 6 Response table for S/N ratios-larger is better ΔHV

Level	x_1	x_2	x_3	x_4
1	34.13	38.54	35.11	37.93
2	35.66	37.04	35.89	36.47
3	37.57	35.86	36.55	36.1
4	38.14	34.06	37.95	35
Delta	4.01	4.48	2.84	2.93
Rank	2	1	4	3

4.2 Regression Analysis and Linear Regression Model (ΔHV vs. ΔRa)

The linear regression equation was developed from set values of the machining gap and then current, abrasive composition and tool speed using MINITAB 17 software. To forecast ΔHV, however, a linear regression model was attained as Eq. 1. The developed model offers a linear dependency. Table 7 represents analysis of Variance between ΔHV versus ΔRa.

The linear dependence between the value of 'change in surface roughness' ΔRa and 'change in microhardness' ΔHV was obtained where ΔRa is in μm.

$$\Delta HV = -7.37 + 866.5\Delta R_a \tag{1}$$

Based on the above Eq. 1, a relation has been shown between ΔRa and ΔHV. Given the points on the 'normal probability plot' in Fig. 6, the model derived using Eq. 1 for the prediction of ΔHV were found to be satisfactory. Figure 6, indicates the estimated linear pattern with a slight disintegration of the normal distribution. In Fig. 6, a random pattern shows the plot of residuals versus fitted value, indicating that residuals have roughly constant variance, and 'residuals versus order plot' indicate that the collected information can be employed to detect the non-random error. In

Table 7 Analysis of variance

Source	DF	Adj SS	Adj MS	F-Value	P-Value
Regression	1	9570.5	9570.48	261.49	0
ΔRa (μm)	1	9570.5	9570.48	261.49	0
Error	14	512.4	36.6		
Lack-of-fit	13	511.3	39.33	35.43	0.131
Pure error	1	1.1	1.11		
Total	15	10082.9			

Model summary

S	R-sq	R-sq (adj)	R-sq (pred.)
6.0498	94.92%	94.56%	94.01%

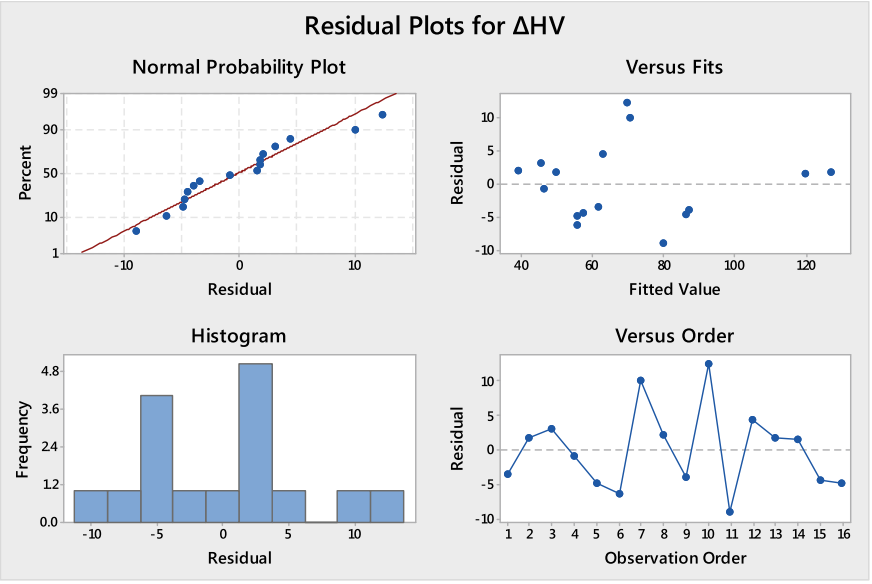

Fig. 6 Residual plot for ΔHV taking ΔRa as predicting factor

Fig. 6, the 'frequency versus residual plot' as there were slightly less outliers, supports the finer data variation; nevertheless, the histogram is negatively biased, indicating that the original findings have more weight on overall performance. Figure 7 shows scatterplot with trend line for ΔHV versus ΔRa.

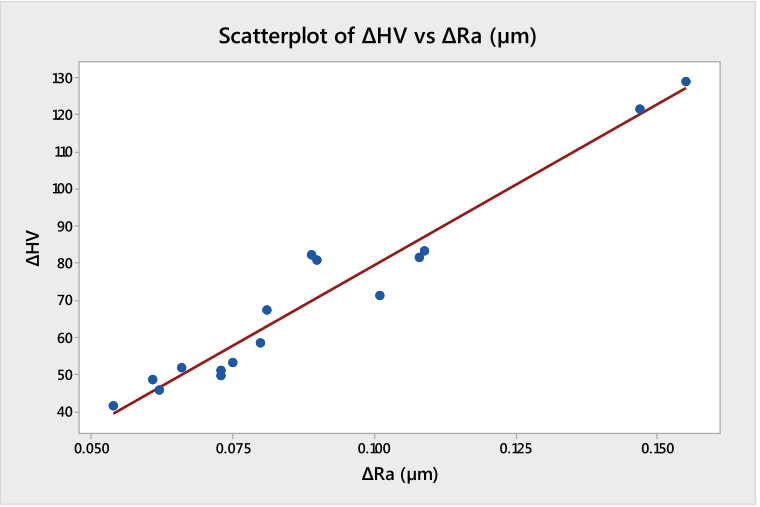

Fig. 7 Scatterplot with trend line for ΔHV versus ΔRa

4.3 Data Modelling with Artificial Neural Network

The 'change in Surface roughness' (ΔRa), 'change in the Microhardness' (ΔHV), values between the initial and final surfaces are modeled using artificial neural network. The ANN models are developed individually for modeling ΔRa, ΔHV.

In this section, modeling for the MAF process using ANN architecture with a backpropagation algorithm was used precisely its output concerning input parameters. Modeling the ANN works in stages: training, testing, and validation [17, 19]. The program codes were written for that purpose in MATLAB. Experimental data was trained in the ANN architecture, which is shown in Table 8. The neural network contains three different layers of neurons, out of which the first layer includes neurons corresponding to input parameters [30]. The 1st layer being the input layer, contains '5' neurons corresponding to each of the input variables; the 2nd layer is called the hidden layer. It has 10, 15 neurons, respectively, for (ΔRa) and (ΔHV) as shown in Table 8. The 3rd layer has '1' neuron corresponding to the single output value. For the present data outputs, the Levenberg–Marquardt training method was used for quick supervised learning is easy, safe, and computationally less expensive because of its adoptive learning and no-line search technique [31]. The transfer function selected for the hidden layer and output layer was Log-sigmoid and Tan-sigmoid, respectively, which were calculated as given by Eqs. (2) and (3) [32–34].

$$\tan sig\ (n) = \frac{2}{\left(1 + e^{-2n}\right)} - 1 \tag{2}$$

$$\log sig\ (n) = \frac{1}{(1 + e^{-n})} \tag{3}$$

where n is input for the function (Fig. 8).

The ANN predicted, and experimental values ΔRa, ΔHV, to a very high degree with one another, and it is visible from Fig. 11. The weight and bias of the developed network are stored after confirming with this high degree of maximum error. ANN architecture presented in Table 4 and the developed Neural Network architecture is shown in Fig. 5. Based on the network output after exhaustive trails, the number of the hidden layers and the number of neurons in each hidden layer were selected.

Table 8 ANN architecture for input to output modeling

Input	Output	ANN architecture
x_1, x_2, x_3, x_4, x_5	ΔR_a	5-10-1
x_1, x_2, x_3, x_4, x_5	ΔHV	5-15-1

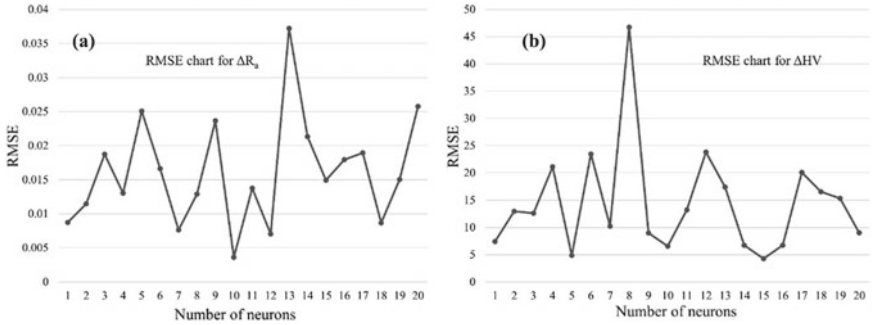

Fig. 8 RMSE chart for the selection of appropriate neurons used for the purpose of network training

Network efficiency was determined by percentage error [30, 35]. The percentage error was measured as Eq. (4) and the values determined are shown in Table 5. It is therefore guaranteed that the relationship between the values of input and output has been effectively learned by the developed ANN model. It can thus be used to optimize the operation (Figs. 9, 10 and 11).

$$Percentage\ error = \frac{(Experimental\ value - ANN\ predicted\ value) \times 100}{Experimental\ value} \tag{4}$$

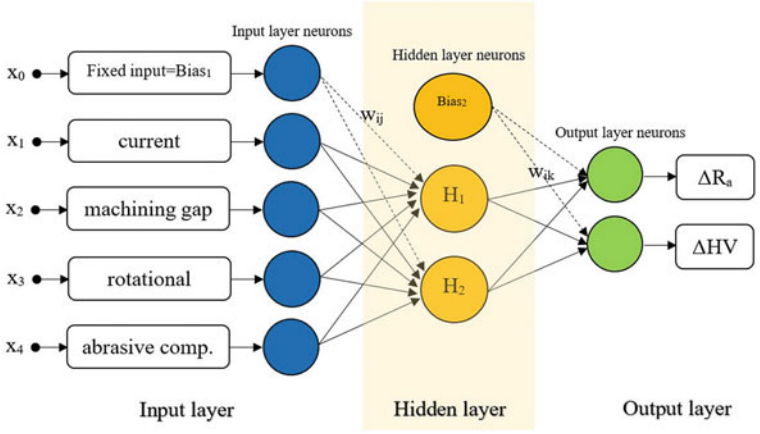

Fig. 9 ANN architecture

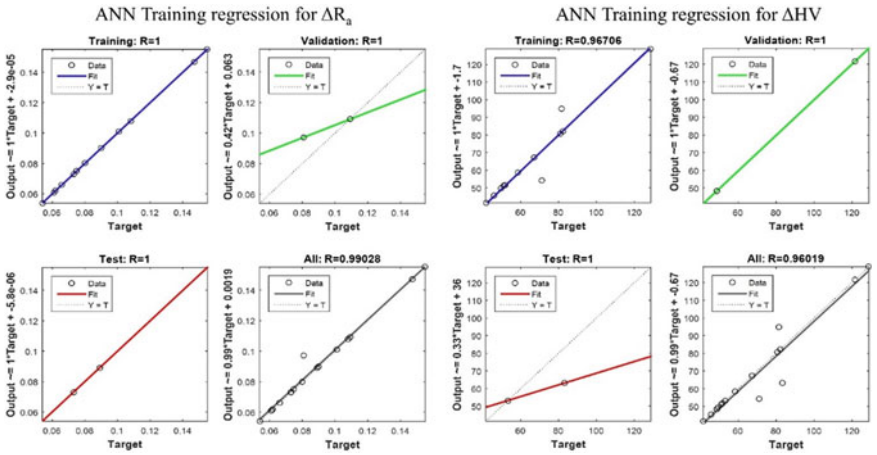

Fig. 10 Training plots of regression performance for trained ANN

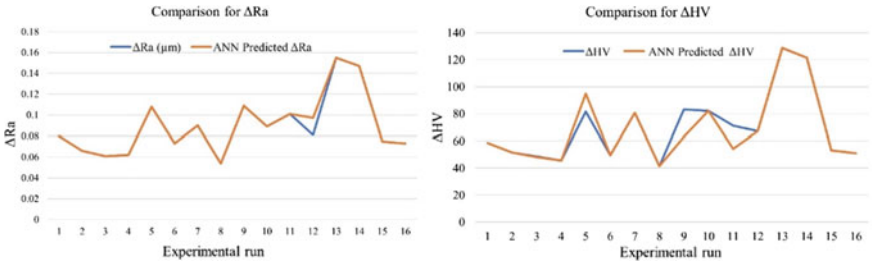

Fig. 11 Comparison of experimental and ANN predicted responses

4.4 Relationship Between Surface Microhardness and Roughness

The experimentally determined change in microhardness and change in roughness values are compared with predicted regression and ANN model values (Fig. 12). Comparison of ΔRa and ΔHV relationship, Fig. 12a shows regression scattered diagram based on experimental values and Fig. 12b shows ANN trained pattern between outputs. It is found, that given ANN model are within the range they were allowed to change, the ANN model is able to predict their values with a satisfactory efficiency. Compared to the regression model, the findings of the ANN model show it to be significantly more robust and reliable in estimating the values of change in microhardness; it can be used to model any production process. The proposed methods of prediction of results show how the use of this process can be expanded by changing variables for particular machining conditions within the constraints.

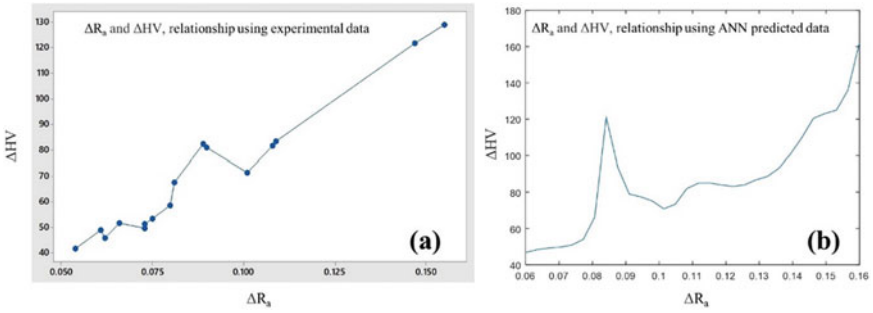

Fig. 12 **a, b** Comparison of ΔR_a and ΔHV relationship

5 Conclusions

The use of 'Design of Experiments' (DOE) to perform experiments has been outlined in this paper. The predicting ability of two revolutionary models—'regression and artificial neural network' (ANN) to predict the relationship b/w change in microhardness and change in roughness has been presented in this paper. Experiments were performed to determine microhardness and surface roughness effect in a MAF process for machining Ti–6Al–4V using SiC based magnetic abrasive media on the DOE technique. In order to build a 'regression model' and 'feed forward back propagation artificial neural network model' for the forecasting, the experimental values were used. Following conclusions can made.

(a) Taguchi analysis predicted the SN ratio and effect of variable factor rank wise.
(b) The ANN model, which has been developed, can predict ΔRa and ΔHV.
(c) Change in Microhardness increases with change in surface Roughness i.e. (level of finishing).
(d) Loosely bound magnetic abrasive media is a reasonable abrasive media for the finishing of Ti–6Al–4V by the MAF process. The composition of ferromagnetic material and abrasive particles in the media is determined to be critical for the desired finishing quality.
(e) The ANN model, which has been developed, can be used to optimize the MAF process concerning ΔRa and ΔHV.

References

1. Fox M, Agrawal K, Shinmura T, Komanduri R (1994) Magnetic abrasive finishing of rollers. CIRP Ann 43:181–184. https://doi.org/10.1016/S0007-8506(07)62191-X
2. Singh DK, Jain VK, Raghuram V, Komanduri R (2005) Analysis of surface texture generated by a flexible magnetic abrasive brush. Wear 259:1254–1261. https://doi.org/10.1016/j.wear.2005.02.030

3. Singh DK, Jain VK, Raghuram V (2004) Parametric study of magnetic abrasive finishing process. J Mater Process Technol 149:22–29. https://doi.org/10.1016/j.jmatprotec.2003.10.030
4. Ahmad S, Gangwar S, Yadav PC, Singh DK (2017) Optimization of process parameters affecting surface roughness in magnetic abrasive finishing process. Mater Manuf Process 32:1723–1729. https://doi.org/10.1080/10426914.2017.1279307
5. Yamaguchi H, Srivastava AK, Tan MA, Riveros RE, Hashimoto F (2012) Magnetic abrasive finishing of cutting tools for machining of titanium alloys. CIRP Ann 61:311–314. https://doi.org/10.1016/j.cirp.2012.03.066
6. Ahmad S, Singari RM, Mishra RS (2021) Tri-objective constrained optimization of pulsating DC sourced magnetic abrasive finishing process parameters using artificial neural network and genetic algorithm. Mater Manuf Process 1–15. https://doi.org/10.1080/10426914.2020.1866196
7. Kumar G, Yadav V (2009) Temperature distribution in the workpiece due to plane magnetic abrasive finishing using FEM. Int J Adv Manuf Technol 41:1051–1058. https://doi.org/10.1007/s00170-008-1557-7
8. Mulik RS, Srivastava V, Pandey PM (2012) Experimental investigations and modeling of temperature in the work-brush interface during ultrasonic assisted magnetic abrasive finishing process. Mater Manuf Process 27:1–9. https://doi.org/10.1080/10426914.2010.515647
9. Hashimoto F, Yamaguchi H, Krajnik P, Wegener K, Chaudhari R, Hoffmeister H-W, Kuster F (2016) Abrasive fine-finishing technology. CIRP Ann 65:597–620. https://doi.org/10.1016/j.cirp.2016.06.003
10. Levashov EA, Petrzhik MI, Tyurina MYa, Kiryukhantsev-Korneev FV, Tsygankov PA, Rogachev AS (2011) Multilayer nanostructured heat-generating coatings. Preparation and certification of mechanical and tribological properties. Metallurgist 54:623–634. https://doi.org/10.1007/s11015-011-9350-5
11. Yin C, Wang R, Kim J, Lee S, Mun S (2019) Ultra-high-speed magnetic abrasive surface micro-machining of AISI 304 cylindrical bar. Metals 9:489. https://doi.org/10.3390/met9050489
12. Vahdati M, Rasouli S (2016) Evaluation of parameters affecting magnetic abrasive finishing on concave freeform surface of Al alloy via RSM method. Adv Mater Sci Eng 2016:1–14. https://doi.org/10.1155/2016/5256347
13. Singh RK, Gangwar S, Singh DK (2019) Experimental investigation on temperature-affected magnetic abrasive finishing of aluminum 6060. Mater Manuf Process 34:1274–1285. https://doi.org/10.1080/10426914.2019.1628263
14. Bhagavatula SR, Komanduri R (1996) On chemomechanical polishing of Si_3N_4 with Cr_2O_3. Philos Mag A 74:1003–1017. https://doi.org/10.1080/01418619608242173
15. Naif NM (2012) Study on the parameter optimization in magnetic abrasive polishing for brass $CuZn_{33}$ plate using Taguchi method. Iraqi J Mech Mater Eng 12
16. Shather SK, Mousa SM (2015) The influence of design and technological parameters on the MAF process. Al-Khwarizmi Eng J 11:82–88
17. Ahmad S, Singari RM, Mishra RS (2020) Modelling and optimisation of magnetic abrasive finishing process based on a non-orthogonal array with ANN-GA approach. Trans IMF 98:186–198. https://doi.org/10.1080/00202967.2020.1776966
18. Ali-Tavoli M, Nariman-Zadeh N, Khakhali A, Mehran M (2006) Multi-objective optimization of abrasive flow machining processes using polynomial neural networks and genetic algorithms. Mach Sci Technol 10:491–510. https://doi.org/10.1080/10910340600996126
19. Singh RK, Gangwar S, Singh DK, Pathak VK (2019) A novel hybridization of artificial neural network and moth-flame optimization (ANN–MFO) for multi-objective optimization in magnetic abrasive finishing of aluminium 6060. J Braz Soc Mech Sci Eng 41:270. https://doi.org/10.1007/s40430-019-1778-8
20. Jain VK (2013) Advanced machining processes. Allied Publishers, New Delhi
21. Singh RK, Gangwar S, Singh DK (2020) On the temperature analysis of magnetic abrasive finishing of aluminum 6060 using finite element method. Mach Sci Technol 1–32. https://doi.org/10.1080/10910344.2020.1815036

22. Singh RK, Gangwar S, Singh DK (2020) Technological advances in magnetic abrasive finishing for surface treatment of alloys and ceramics. In: Inamuddin RB, Ahamed MI, Asiri AM (eds) Alloy materials and their allied applications. Wiley, pp 123–157. https://doi.org/10.1002/9781119654919.ch8
23. Singh DK, Jain VK, Raghuram V (2006) Experimental investigations into forces acting during a magnetic abrasive finishing process. Int J Adv Manuf Technol 30:652–662. https://doi.org/10.1007/s00170-005-0118-6
24. Mori T, Hirota K, Kawashima Y (2003) Clarification of magnetic abrasive finishing mechanism. J Mater Process Technol 143–144:682–686. https://doi.org/10.1016/S0924-0136(03)00410-2
25. Ahmad S, Singari RM, Mishra RS (2021) Development of Al_2O_3-SiO_2 based magnetic abrasive by sintering method and its performance on Ti-6Al-4V during magnetic abrasive finishing. Trans IMF 99:94–101. https://doi.org/10.1080/00202967.2021.1865644
26. Verma GC, Kala P, Pandey PM (2017) Experimental investigations into internal magnetic abrasive finishing of pipes. Int J Adv Manuf Technol 88:1657–1668. https://doi.org/10.1007/s00170-016-8881-0
27. De Souza HJ, Silva MB, Moyses CB, Alberto FL, Pontes FJ, Ferreira UR, Duarte RN, da Silva CE (2013) Robust design and Taguchi method application. In: Borges Silva M (ed) Design of experiments—applications. InTech. https://doi.org/10.5772/56580
28. Lin C-T, Yang L-D, Chow H-M (2007) Study of magnetic abrasive finishing in free-form surface operations using the Taguchi method. Int J Adv Manuf Technol 34:122–130. https://doi.org/10.1007/s00170-006-0573-8
29. Candan G, Yazgan HR (2015) Genetic algorithm parameter optimisation using Taguchi method for a flexible manufacturing system scheduling problem. Int J Prod Res 53:897–915. https://doi.org/10.1080/00207543.2014.939244
30. Yadav RN, Yadava V, Singh GK (2013) Multi-objective optimization of process parameters in electro-discharge diamond face grinding based on ANN-NSGA-II hybrid technique. Front Mech Eng 8:319–332. https://doi.org/10.1007/s11465-013-0269-3
31. Shanmuganathan S, Samarasinghe S (eds) (2016) Artificial neural network modelling. Springer International Publishing, Cham. https://doi.org/10.1007/978-3-319-28495-8
32. Bishop CM, Neural networks for pattern recognition, 251
33. Gluck MA, Myers CE (2001) Gateway to memory: an introduction to neural network modeling of the hippocampus and learning. MIT Press, Cambridge, MA
34. Rasmussen CE, Williams CKI (2006) Gaussian processes for machine learning. MIT Press, Cambridge, MA
35. Stojanović B, Vencl A, Bobić I, Miladinović S, Skerlić J (2018) Experimental optimisation of the tribological behaviour of Al/SiC/Gr hybrid composites based on Taguchi's method and artificial neural network. J Braz Soc Mech Sci Eng 40:311. https://doi.org/10.1007/s40430-018-1237-y

Heat Treatment Effect on the Corrosion Behaviour of Plasma Processed LM6 Alloy

Jagadish Parida, Subash Chandra Mishra, and Ajit Behera

Abstract Al-alloys are always used increasing in marine environments because of their better resistance, low density, good mechanical properties, excellent castability and fluidity. In this work, the study on the corrosion behaviour of LM6 alloy is prepared by the plasma melting method. Some of the alloy samples were heated at temperature 350 and 450 °C for 2 h then water quenched. All the alloy samples (both H.T and non-H.T) are exposed to seawater for 42 days, and then every 7 days measured the weight gain/loss. The microstructure, hardness and corrosion behaviour of the H.T and non-H.T corroded samples comparative study were carried out. The composition and morphology of corrosion products were examined with the help of an optical microscope, SEM and XRD. The results indicated that 450 °C H.T samples have lower corrosion rate values and higher hardness value than 350 °C H.T and non-H.T samples. Optical micrographs show that the size and number of isolated surface pits formed on H.T 450 °C alloy samples are less as compared to H.T at 350 °C and non-H.T alloy samples. 450 °C H.T samples exhibit more corrosion resistance than 350 °C H.T and non-H.T samples due to the heat treatment effect on the alloy samples. The pitting corrosion mechanism gets from the experimental investigation.

Keywords LM6 alloy · Weight gain/loss · Water quenching · Corrosion rate · Pitting corrosion · Plasma technique

Nomenclature

H.T	Heat-treated
non-H.T	Non-heat treated

J. Parida (✉) · S. C. Mishra · A. Behera
Metallurgical and Materials Engineering Department, NIT, Rourkela 769008, Odisha, India

S. Pal et al. (eds.), *Processing and Characterization of Materials*, Springer Proceedings in Materials 13, https://doi.org/10.1007/978-981-16-3937-1_3

1 Introduction

Mostly in marine environments, aluminium alloys are used due to their attractive properties like lightweight, high strengths, recyclability, good formability, heat and light reflectivity, electrical and thermal conductivity, corrosion resistance, non-magnetic behaviour etc. [1, 2]. Also, Al–Si alloy is used in this field because of its above specific properties. The properties of Al–Si alloys depend on the volume fraction, discrete physicochemical properties and main phase ingredient, i.e. Si crystals and α-Al solid solution and secondary phase's morphology. Very low solubility of Si than Al. So Si precipitates as pure Si in a coarse flake shape, due to this inhomogeneous chemical and mechanical properties [3]. The usage life of the engineering component depends on service temperature and environmental conditions factors etc. [4, 5]. Corrosion is a natural process in which a more chemically stable form, i.e. its oxide, chloride, hydroxide and sulfide formed from refined metal. During this process gradually materials destruction by electrochemical and chemical reaction with their environment [6]. Significantly corrosion behaviour is affected by the presence of the particle in the matrix of aluminium alloys [7]. Many factors like temperature, Oxygen, chemical salts, pollutants and humidity etc. that influence metal corrosion. The climate plays a crucial role among the different ingredients affecting the corrosion rate [8, 9]. Increasing temperature leads to change two variables such as: (1) the reaction rate and diffusion rate of oxygen form accelerate by increasing the molecular diffusion coefficient. (2) the oxygen solubility decreases [10]. Aluminium corrosion resistance means Al-oxide film that forms on its surface [11, 12]. When aluminium immersed in water usually passive film formed on the body [13]. Passive film naturally formed in seawater but due to the chloride ion, breaks down protection film and slowdown its repair. Generally, corrosion in aluminium metal/alloy, either pitting and crevice types or both in seawater. Localized corrosions depend on low values of weight loss and corrosion rate. Therefore according to aluminium, corrosion is determined based on pits depth measurement and crevice corrosion but not calculated corrosion rates from weight losses value [14]. Al-forms a protective film of oxide in the 4.0–8.5 pH order, but this depends on the substances present, type of oxide present and temperature that form insoluble salts or soluble combination with Al. it shows that the oxide film is soluble at pH values >8.5 and <4.0. However, it has declared the aluminium pitting potential in chloride solutions to be independent relatively of pH in the order 4–9 [15]. It recommend that corrosion mostly occurs in these areas due to silicon particles presence acting as a local cathode w.r.t the eutectic Al-phase due to proceed localized corrosion through the eutectic areas [16, 17]. Corrosion of Al-alloys in the marine atmospheric environment is not only affected by the high salt proportion but also by a mix of pollution factors and meteorological [18]. Nishimura et al. establish that in such environments, the high salinity and relative humidity are supporting; the higher humidity, the greater availability of Cl-1 to cause the Al-alloy corrosion [19].

LM6 (Al–12%Si) alloys can be prepared by different casting processes. Plasma casting technologies are advanced stir casting process which is the most efficient

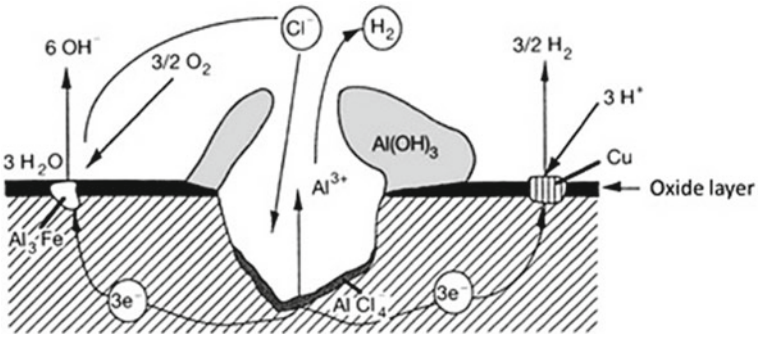

Fig. 1 Pitting corrosion mechanism of aluminium [20]. Copyright 2004, Elsevier

and economical process for the production of Al–Si alloy products. Advantage of this process over other is finer microstructures, better properties, high efficiency, short times and high cost. The objective of the research is to investigate the corrosion resistance of plasma processed LM6 alloys in seawater (it was collected directly 4 km away from the coastal sea shore of Puri, Odisha) and also focus on the characteristics, formation condition and morphology attack on alloy surface exposed to seawater. After every 7 days up to 42 days in seawater immersion of the sample and its corrosion data taken was used for weight gain/loss calculation, corrosion rate determination and hardness measurement. Also analysis SEM, XRD and optical microscopy of the corroded alloy samples which is kept 42 days in seawater (Fig. 1).

2 Experimental Work

In the present work, LM6 alloy was cast with the help of a plasma melting process in an induction heating furnace. The alloy chemical composition, which is used in research work, was shown in Table 1. Eighteen numbers sample cut having equal size and shape from LM6 alloy ingot. Six no's sample were H.T at a temperature of 350 °C and also six no's samples at a temperature of 450 °C for 2 h in a muffle

Table 1 Chemical composition of the LM6 alloy

Elements	Composition (wt. %)
Silicon	12
Manganese	0.5
Magnesium	0.1
Copper	0.1
Iron	0.6
Aluminium	86.7

furnace, then both were water quenched at room temperature. Before corrosion experiments, the sample was polished using SiC paper and subsequently polished using a sequence of emery paper (i.e. 1/0, 2/0, 3/0 and 4/0). Then fine polishing was carried out with the help of a velvet disc polisher (alumina slurry used) and finally after that clean the sample. The entire (both H.T at 350 and 450 °C and non-H.T) alloy sample is weighted (initial weight) in electronics weighing machine with an accuracy of 0.001 mg then kept in seawater for 42 days. Every 7 days, samples were taken from prepared closed vessels (glass containers) having 100 ml capacity then samples are drying (hot air) with the help of a hot dryer then weighed (final weight). After weighting, it compared with the initial weight, the difference indicating the weight gain/loss during that exposed period. Then the weight gain/loss and corrosion rates were calculated. The microstructures of all samples were characterized using scanning electron microscopy and optical microscopy. Measured Hardness value (average value taken for three different test places) using micro Vickers hardness testing machine having a load of 25 kg-f and time 10 s.

The corrosion rate in millimetres per year (mmpy) was calculated from the weight gain/loss using the formula:

$$\text{Weight gain/loss } (\Delta W) = W_{\text{Initial}} - W_{\text{Final}} \tag{1}$$

$$\text{Corrosion rate} = (K \times \Delta W)/(A \times D \times T) \tag{2}$$

where

W_{Initial} = Sample initial weight before immersion, W_{Final} = Sample final weight after exposure, ΔW = Weight gain/loss (gm), K = Constant = 87,600 mmpy, D = Alloy density (gm/cm^3) [non-H.T = 2.591 g/cc, 350 °C H.T = 2.61 g/cc and 450 °C H.T = 2.613 g/cc], A = Area (cm^2) and T = Exposure time (hrs).

3 Results and Discussion

3.1 Weight Gain/Loss and Corrosion Rate Determination

Figure 2a show weight gain/loss (ΔW) of alloy sample is evaluate using (1) as a function of times of immersion in days for LM6 alloy in seawater for non-H.T and H.T at 350 and 450 °C. It is notice that weight gain/loss was values higher non-H.T in comparison to 350 and 450 °C H.T samples. Results show that sample weight gain at the initial stage up to 21 days because weight gain due to the formation of the passive film on the surface top (i.e. compound formation takes place on the surface) of the samples. But from 21 to 28 days, weight losses takes place because of temporary corrosion attack in the sample so diffusion of corrosion compound from the surface of the sample. But then again weight gain occurs from 28 to 42 days

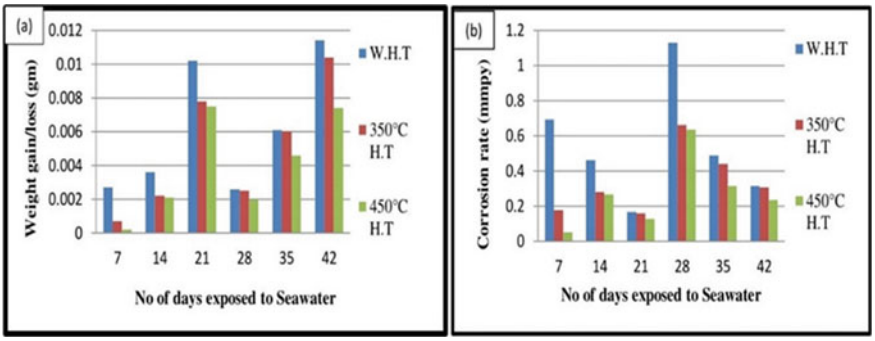

Fig. 2 Graph between **a** weight gain/loss of sample versus no of days exposed to seawater and **b** corrosion rate versus no of days exposed to seawater

because a chemical compound is again formed on a surface of a sample and the passive film became more thick layer (acts as a membrane), so weight gain result in all samples. The corrosion rate values are evaluate from weight gain/loss data using (2) for the alloy are plotted against no of days immersion are shown in Fig. 2b. It is seen that the corrosion rate values decrease from initially up to 21 days because of initial stage weight gain result, i.e. passive films formed on samples surface which act as a membrane so this happens. Then this value increases up to 28 days because due to the temporary breakdown of the passive films. So Corrosion attack result. This value again decreases from 28 days up to 42 days (i.e. corrosion rate decreases with increasing time) kept in seawater because the corrosion products layer is more compact and protective on the metal surface with time. When compare between three samples, corrosion rates are lower for 450 than 350 °C than non-H.T sample due to Corrosion was more prevalent, i.e. More Corrosion attack in 350 °C H.T and a non-H.T sample. Also maybe density value increases with heat treatment temperature i.e. 450 °C H.T sample high-density value than 350 °C H.T and a non-H.T sample so corrosion rate values decrease. Therefore 450 °C showed the corrosion resistance higher (low corrosion rate) at all times of immersion because due to the heat treatment effect.

3.2 Hardness Measurement

From this Fig. 3, It is clear that for all sample hardness value found to increases up to 21 days then decrease up to 28 days then again increases to 42 days because of a very thin passive film formation of Al oxide and hydroxide or compound form Al/Si with seawater element with on the surface top up to 21 days i.e. passive film act as a membrane. Hence, hardness value increases initially up to 21 days; then, formation compounds are removed from the surface i.e. chloride ion help for breakdown passive film [14], so hardness value decreases from 21 to 28 days. Again compound formed

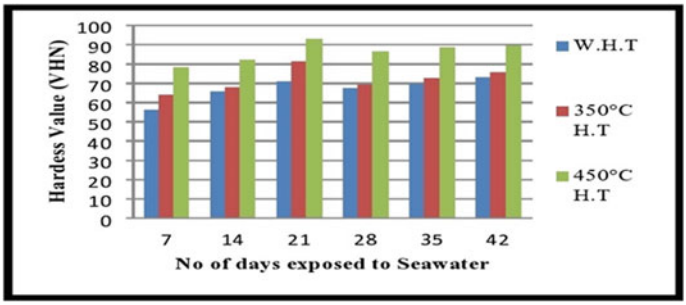

Fig. 3 Graph between hardness values samples versus no of days exposed to seawater

on sample surface so that passive film became thicker (i.e. more amount/number compound present) due to this reason hardness value also increases in all samples (450 and 350 °C H.T and non-H.T sample). Therefore 450 °C H.T samples are a higher hardness value than 350 °C H.T and non-H.T samples due to the heat treatment effect.

3.3 Microstructural Characterization

Figures 4, 5 and 6 show the optical micrograph of LM6 alloy in seawater for non-H.T, 350 °C H.T and 450 °C H.T corroded samples in 7, 14, 21, 28, 35 and 42 days respectively. Figure 4a–f show that microstructure of non-H.T corroded samples and

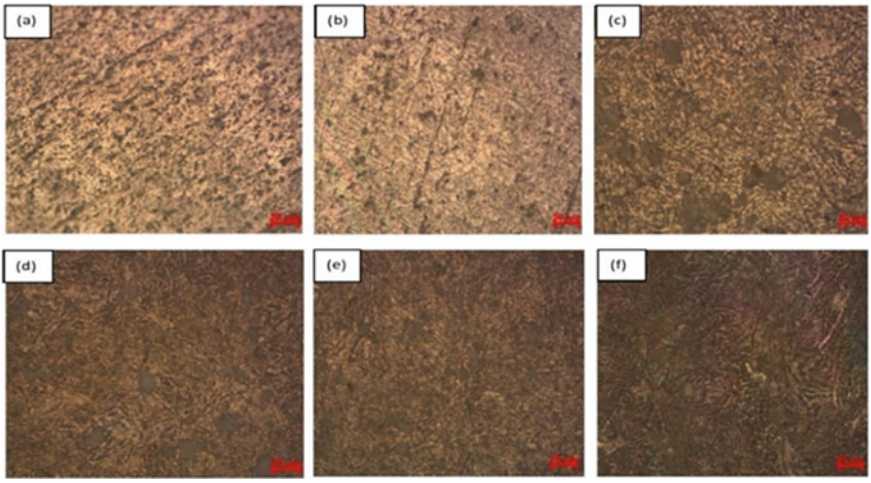

Fig. 4 Micrograph of non-H.T samples **a** 7 day, **b** 14 day, **c** 21 day, **d** 28 day, **e** 35 day and **f** 42 day

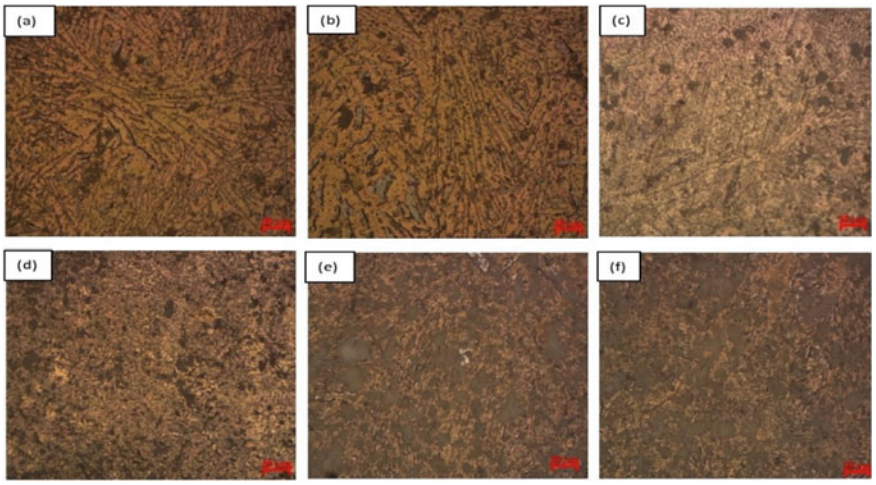

Fig. 5 Micrograph of 350 °C H.T samples **a** 7 day, **b** 14 day, **c** 21 day, **d** 28 day, **e** 35 day and **f** 42 day

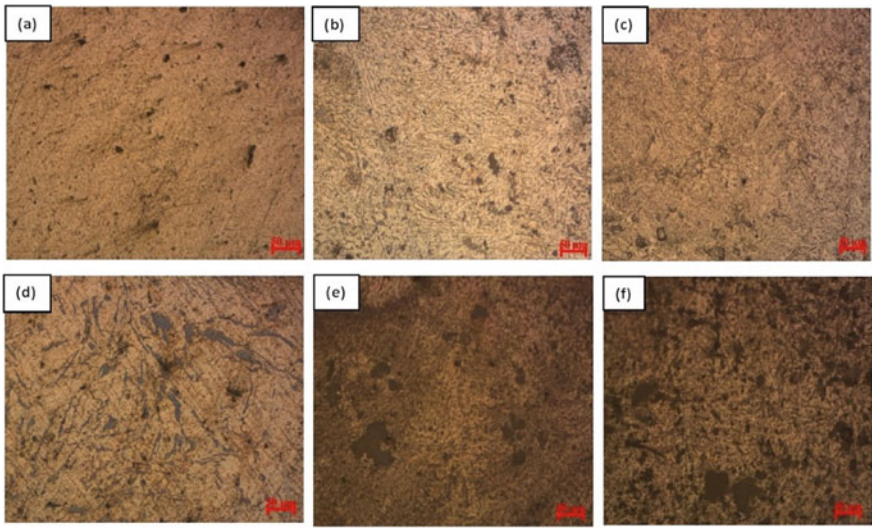

Fig. 6 Micrograph of 450 °C H.T samples **a** 7 day, **b** 14 day, **c** 21 day, **d** 28 day, **e** 35 day and **f** 42 day

Pits formed (non-uniform formation) on sample surface after formation corrosion product (intermetallic compounds) removed from the surface due to the surrounding matrix dissolution or breakdown of the passive film [21]. The number, size and depth of pits formed on the surface of the sample are increases when no. of immersion days increase from Fig. 4a–f and also maximum pit size can determine with the help of

pits depth and pits diameter. Similarly, from Fig. 5a–f and from Fig. 6a–f show the same behaviour occurs in the alloy sample.

When compare Figs. 4, 5 and 6, which shows number and size of pits and pit depth formed on surface 450 °C H.T sample (severe pits are not found) is less compared to 350 °C H.T samples and non-H.T samples. In other words, non-H.T samples are observed severe corrosion (more corrodent attack on the surface) compare to 450, and 350 °C H.T samples because due to inducing corrosion less in the 450, and 350 °C H.T samples and also microstructure change due to heat treatment. And also maybe more corrosion product formation in non-H.T sample surface so more washout corrosion products from the surface of samples than both H.T samples. 450 °C H.T alloy is more pitting corrosion resistance than the non-H.T and 350 °C H.T samples. So heat treatment affects corrosion attack on the surface of a sample.

3.4 SEM Observation

Figures 7 and 8 shows that many compounds formed on the surface by Si and Al reaction with the elements present in the seawater. Seawater contains O_2, Cl, Na etc., which are very reactive to Al and Si. Also, the compounds formed due to the corrosive attack on the sample surface. Large corroded portions of non-H.T samples compare to 450 and 350 °C H.T samples. From the analysis, higher heat treatment temperature shows that less composed corrosion products instead of non-H.T samples (observed higher intensity of corrosion).

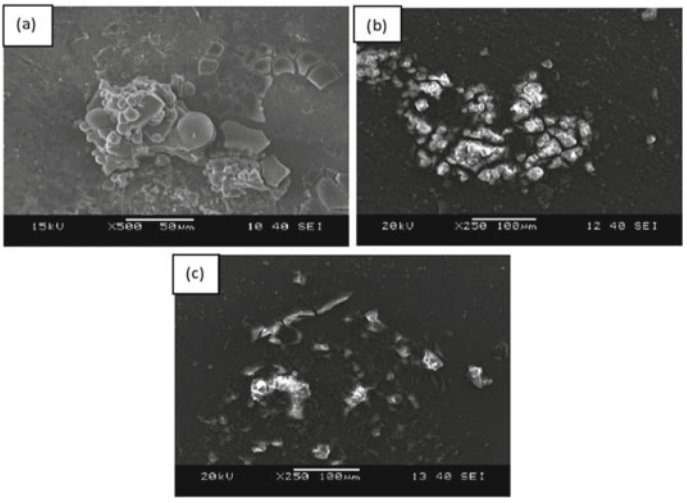

Fig. 7 SEM image of after 7 days corroded sample of **a** non-H.T, **b** H.T at 350 °C and **c** H.T at 450 °C

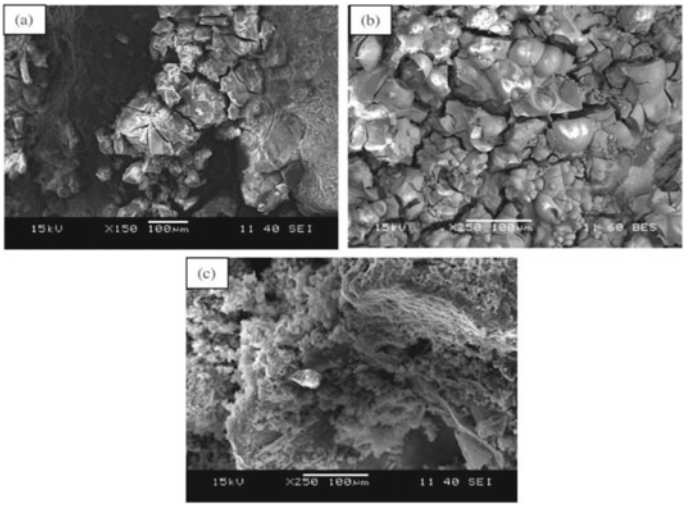

Fig. 8 SEM image of after 42 days corroded sample of **a** non-H.T, **b** H.T at 350 °C and **c** H.T at 450 °C

Figure 8a, b show that non-H.T and 350 °C H.T samples showed cracks form on the surface, but Fig. 8c show does not crack form. The formation of a cracked structure is due to corrosion products removal, which helps for cracking and also assist localized corrosion. When compare Fig. 8a, b and c, it shows that in non-H.T samples formation compound are more removed from the surface compared to 450 and 350 °C H.T samples due to this more crack formed on non-H.T than both H.T samples. Still, in 450 °C H.T samples passive film formation compound seen i.e. washout compound from the surface is less (no crack formed) in Fig. 8c. From [15] it knows that passive film formation depends on the substances present, type of oxide present and temperature, this may be a reason for the above. Therefore 450 °C H.T samples are more resistance to corrosion(less corroded) than 350 °C H.T and non-H.T samples.

3.5 XRD Analysis

Figure 9A, B shows the chemical composition of the corrosion product in the analysis by XRD. Al and Si peak along with Halite (Cl_1Na_1) and sodium tetra-chloro-aluminate ($Al_1Cl_4Na_1$) compound peak, are formed in all the samples. The compound is formed when seawater element (Na, Cl etc.) combine with Al and Si element present in alloy samples. But the only difference is the intensity of peak between all-alloy samples. That means $Al_1Cl_4Na_1$ and Cl_1Na1 compound peaks are of higher intensity and more number in a non-H.T sample than 350 and 450 °C H.T samples. The corrosion product ($Al_1Cl_4Na_1$ and Cl_1Na1) are more formed in the non-H.T

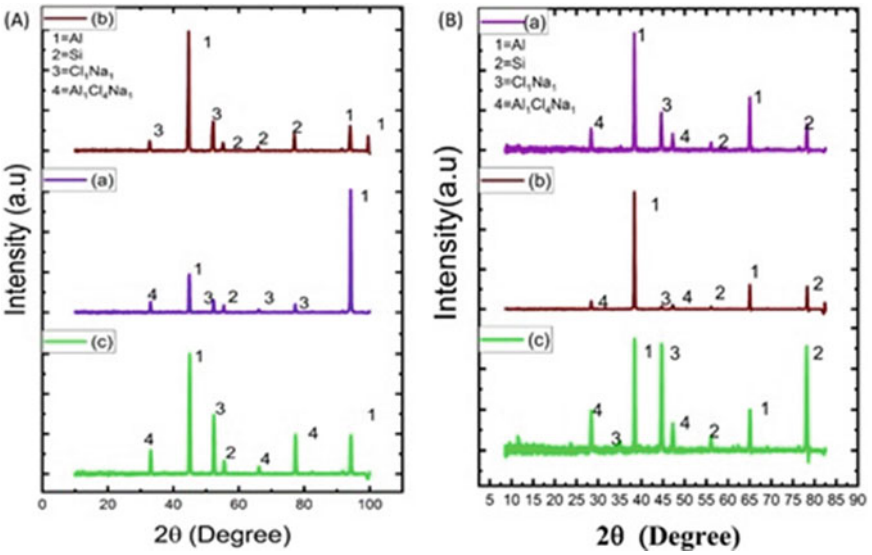

Fig. 9 XRD analysis of **A** after 7 days corroded sample of **a** 350 °C H.T, **b** 450 °C H.T and **c** non-H.T, **B** after 42 days corroded sample of **a** 350 °C H.T, **b** 450 °C H.T and **c** non-H.T

sample than 450 and 350 °C H.T samples. All Fig. 9a–c found that amount and number compound peak are more formed in the non-H.T sample (i.e. Observed higher intensity) than 450 and 350 °C H.T samples. Similarly, happen in Fig. 9B(a–c). But the difference between Fig. 9A, B is compound (corrosion product) formation less in 7 days corroded sample (thin passive layer) than 42 days corroded samples (thick passive layer). Due to this reason, more weight gain and high corrosion rate on non-H.T samples than both H.T samples. Hence heat treatment effect the corrosion behaviour of the alloy sample.

4 Conclusions

The following conclusions in this paper are

i. 450 and 350 °C H.T samples performed less weight gain from seawater compared to non-H.T samples. For all samples increase weight gain occurred concerning the number of days increases.
ii. 450 and 350 °C H.T samples have lower corrosion rate values and higher hardness value than non-H.T samples. So 450 and 350 °C H.T samples are higher corrosion resistance than non-H.T samples.
iii. 450 and 350 °C H.T samples show low values corrosion rate that means these alloys are used in marine environments.

iv. In seawater, pits are formed on a sample surface. Therefore pitting corrosion was obtained from the SEM and XRD analysis based on pits watching.

References

1. Melchers RE (2016) Principles of marine corrosion. In: Springer handbook of ocean engineering. Springer International Publishing, Cham, pp 111–126
2. Reboul MC, Baroux B (2011) Metallurgical aspects of corrosion resistance of aluminium alloys. Mater Corros 62(3):215–233. https://doi.org/10.1002/maco.201005650
3. Davis JR (ed) (1993) Aluminum and aluminum alloys
4. Middleton CJ, Timmins R, Townsend RD (1996) The integrity of materials in high temperature components; performance and life assessment. Int J Press Vessel Pip 66(1–3):33–57. https://doi.org/10.1016/0308-0161(95)00084-4
5. Krätschmer D, Roos E, Schuler X, Herter K-H (2012) Proof of fatigue strength of nuclear components part II: numerical fatigue analysis for transient stratification loading considering environmental effects. Int J Press Vessel Pip 92:1–10. https://doi.org/10.1016/j.ijpvp.2012.01.005
6. Syed S (2006) Atmospheric corrosion of materials. Emirates J Eng Res 11(1):1–24
7. Loto RT, Adeleke A (2016) Corrosion of aluminum alloy metal matrix composites in neutral chloride solutions. J Fail Anal Prev 16(5):874–885. https://doi.org/10.1007/s11668-016-0157-3
8. Malik MA, Hashim MA, Nabi F, AL-Thabaiti SA, Khan Z (2011) Anti-corrosion ability of surfactants: a review. Int J Electrochem Sci 6(6):1927–1948
9. Huang I-W, Buchheit R (2015) Uniform corrosion dependence on temperature and pH of aluminum alloys 2024–T3. ECS Trans 66(17):97–107. https://doi.org/10.1149/06617.0097ecst
10. Sherif ESM (2012) Corrosion behavior of magnesium in naturally aerated stagnant seawater and 3.5% sodium chloride solutions. Int J Electrochem Sci 7(5):4235–4249
11. Schütze M, Wieser D, Bender R (2010) Corrosion resistance of aluminium and aluminium alloys. Wiley
12. Revie, E, Winston R (2011) Uhlig's corrosion handbook, vol 51. Wiley
13. Hoeppner DW, Arriscorreta CA (2012) Exfoliation corrosion and pitting corrosion and their role in fatigue predictive modeling: state-of-the-art review. Int J Aerosp Eng 2012. https://doi.org/10.1155/2012/191879
14. Hyun K, Kim SJ (2017) Optimum corrosion protection potential for water cavitation peening-processed Al–Mg alloy in seawater. Surf Rev Lett 24(06):1850030. https://doi.org/10.1142/S0218625X18500300
15. Szklarska-Smialowska Z (1986) Pitting corrosion of metals. Natl Assoc Corros Eng Houston, Texas, EE 1
16. Tahamtan S, Fadavi Boostani A (2009) Quantitative analysis of pitting corrosion behavior of thixoformed A356 alloy in chloride medium using electrochemical techniques. Mater Des 30(7):2483–2489. https://doi.org/10.1016/j.matdes.2008.10.003
17. Tahamtan S, Fadavi Boostani A (2010) Evaluation of pitting corrosion of thixoformed A356 alloy using a simulation model. Trans Nonferrous Met Soc China 20(9):1702–1706. https://doi.org/10.1016/S1003-6326(09)60361-7
18. Natesan M, Venkatachari G, Palaniswamy N (2006) Kinetics of atmospheric corrosion of mild steel, zinc, galvanized iron and aluminium at 10 exposure stations in India. Corros Sci 48(11):3584–3608. https://doi.org/10.1016/j.corsci.2006.02.006
19. Nishimura T, Katayama H, Noda K, Kodama T (2000) Electrochemical behavior of rust formed on carbon steel in a wet/dry environment containing chloride ions. Corrosion 56(9):935–941. https://doi.org/10.5006/1.3280597

20. Christian V (2004) Corrosion of aluminium
21. Hossain A, Gulshan F, Engineering M (2016) Electrochemical corrosion behavior of Al-Si hypoeutectic alloy in simulated seawater environment, December, pp 21–23

Failures Investigation of Marine Propellers in Corrosive Environments

Vicky U. Mirashi, Sheron Johnson, Subray R. Hegde, Vijeesh Vijayan, and Sumanth Govindarajan

Abstract Marine corrosion failure of fishing boat propellers made of cast Nickel Aluminium Bronze were investigated. Specimens extracted from the corroded propellers were characterized by optical microscopy, scanning electron microscopy, and energy dispersive spectroscopy. The alloy comprises several Fe_3Al (κ_1, κ_2, κ_4), NiAl (κ_3) type intermetallic precipitates and β' martensite embedded in Cu-rich α-matrix. Transverse sections of the corroded region showed two distinct zones; a non-uniform top oxide layer and a partially corroded zone with selective corrosion of the β' martensite which run parallel to the κ_3 precipitates. From the microstructural analysis it is adjudged that the aggressive local corrosion of the matrix is preceded by cracking of the oxide by erosion, cavitation, etc., A slow growth of the oxide layer follows that reduces the corrosion rate. However, the corrosion cycle repeats on erosion or cracking of the oxide layer when the propeller is used in marine waters. Coupon specimens immersed in actual marine conditions is presented that supports the above theory.

Keywords Nickel aluminium bronze · Corrosion · Erosion · Cavitation · Cracking

1 Introduction

Copper alloys are known to have superior corrosion resistance and strength making them the preferred material choice for marine propellers. Failure of multicomponent alloy propellers used in real life applications occur due to variety of reasons like erosion, corrosion, cavitation, bio-corrosion [1, 2]. The material choice for propeller

V. U. Mirashi (✉) · S. R. Hegde · S. Govindarajan
Department of Metallurgical and Materials Engineering, National Institute of Technology Karnataka, Surathkal 575025, India

S. Johnson
S.R Propellers, Baikampady, Mangalore 575011, India

V. Vijayan
Department of Mechanical Engineering, NMAM Institute of Technology, Nitte, Karkala 574110, India

S. Pal et al. (eds.), *Processing and Characterization of Materials*, Springer Proceedings in Materials 13, https://doi.org/10.1007/978-981-16-3937-1_4

is made considering the cost, ease of casting, strength, erosion-corrosion resistance, amount of poisonous elements like lead and As [3]. The addition of Al to the Cu has shown substantial an increase in corrosion resistance [4]. Elements like Fe, Ni, Mn when added to Al containing Cu form intermetallic precipitates of the type Fe_3Al, NiAl etc [5]. which enhance the strength of the alloy, hence NiAl bronzes (NAB) have been widely used in the marine propellers especially is small and medium sized fishing boats. However, the NAB is very sensitive to processing owing to the complex solidification sequence, especially when employing casting techniques like carbon dioxide process which offers limited scope in altering the cooling rates of the alloy. SR propellers a local manufacturer experienced repetitive failure of the NAB propellers and wanted to understand the reason for failure of the propeller. This paper presents the findings from the investigation of a failed NAB propeller in the preview of what is already known from the literature available [6].

1.1 Phase Diagram

NAB have been widely studied and their equilibrium phase diagrams exist [7]. In the binary Cu–Al system, for up to 9% Al, single α phase field exist. Above 8% Al, β phase appears at high temperatures, which is both stronger and harder the α [8, 9]. However, on cooling below 565 °C, the β phase decomposes to a finely divided micro-structure containing α and another stronger, but less ductile, embrittling phase β' martensitic phase. The β' martensite is attacked preferentially in seawater and is not desirable [7, 10].

Nickel and iron additions suppress β' martensite when both iron and nickel are present nominally at 5%. The structure of 9–10% aluminium alloys is modified and, instead of the formation of β' martensite, a new phase κ (kappa) is created [7, 11, 12]. During the cooling process four different types of κ phases are formed i.e. κ_1, κ_2, κ_3, κ_4 phases (see Fig. 3a) [13, 14]. In terms of corrosion resistance, κ_1, κ_2 and κ_4 have little effect but κ_3 can have an influence, particularly if it forms a continuous network [7].

On non-equilibrium cooling rates, α phase, β' martensite, surrounded by lamellar eutectoid phases and a series of intermetallic κ-phases are formed [12]. The κ_1-phase is globular or rosette shaped and is reported to be iron-rich (based on Fe_3Al). The κ_2-phase (based on Fe_3Al) also takes the form of dendritic rosettes which are unevenly distributed at the α/β boundary and are smaller than the κ_1 rosette. The κ_3-phase appears lamellar shaped in the form of network throughout the microstructure. It grows normal to the α/β boundary, as well as forming at the boundary of the large κ_1-phase, and is described as being nickel-rich (NiAl). The κ_4-phase is a fine precipitate within the α-phase and is considered to be iron-rich (Fe_3Al) [14–16]. The corrosion of the NAB alloy is known to occur along the β' martensite which is present extensively under high cooling rates. Efforts has been made to modify and eliminate the β' phase using, laser reheating, shot peening, coatings. It is known that the partially oxidized surface during laser re-melting offers lower corrosion rates

which also provides superior erosion resistance due to the finer microstructure of the laser remelted microstructure.

Though the mechanism of corrosion is fairly known, there is no evidence on how erosion, corrosion and cavitation together will the failed propellers, the process of casting was critically observed, interacted with executives contribute in the real-life application. In this study we aim to identify qualitatively the mechanisms that are responsible for the failure of the marine propellers.

2 Experimental Method

Site visit was made by the team to visually inspect, collected operational history and relevant technical data. Following this discussion, manufacturer handed over the fractured samples along with the process details for investigation.

Standard failure investigation protocol that involved critical data collection, literature survey, visual inspection, chemical analysis, microstructural analysis was carried out. Samples extracted from failed propellers were cut using a hack saw and cross section specimens were prepared using low speed saw after sandwiching the surface with metal plates and glue to protect the oxide film. Metallographic sample preparation was carried out carefully to avoid spalling of the oxide film. Finally, disc polishing is carried out using slurry containing 0.5 μm alumina (see Fig. 2a, b). Microstructure study involving optical microscopy, scanning electron microscopy (SEM, JSM 6380, JEOL), energy dispersive spectroscopy (EDS, AMETEK).

Fresh coupons were used for conducting simulation experiment which were collected from the company along with the failed propellers. The coupons were immersed in Kanyakumari (Chinnamuttom harbor ship dockyard) for a period for 2½ months for simulation experiment. After the specific period the samples were seen visually and by optical microscopy for studying the surface changes happening.

3 Results and Discussion

3.1 Visual Inspection During Site Visit

It is observed that the propellers had signs of corrosion and erosion as shown in Fig. 1. The samples extracted from a failed propeller after operating in the coast of Kanyakumari was received from the manufacturer for investigation as shown in Fig. 2a. The outer edge of propellers showed loss of material, due to erosion and impact with rocks and sea-shells during operation in shallow waters However, the region which are well away from the edge showed severe corrosion and large dimples were observed on the surface. The specimens for inspection were obtain from thee dimpled region well away from the edge. Since the manufacturers provided the

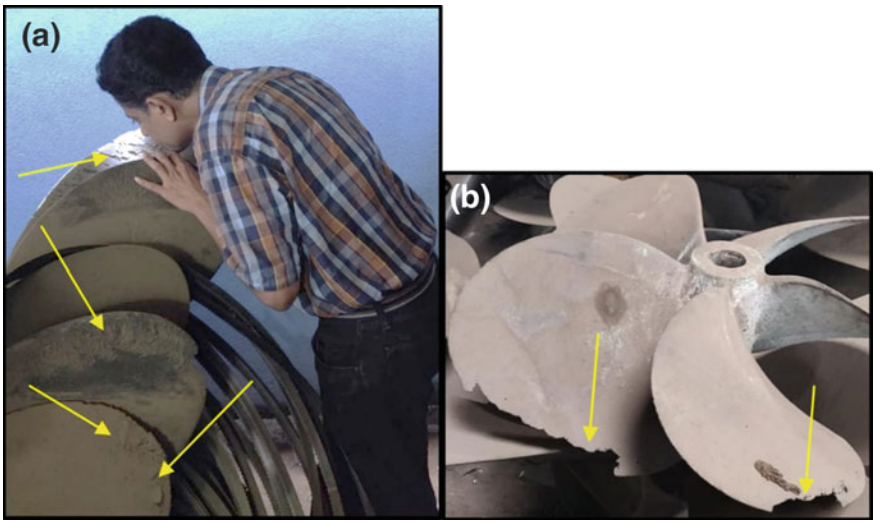

Fig. 1 **a** Photograph during site visit showing loss of material around the tip of the propeller (as shown in arrows). **b** Image showing failure propeller arm (as shown in arrows)

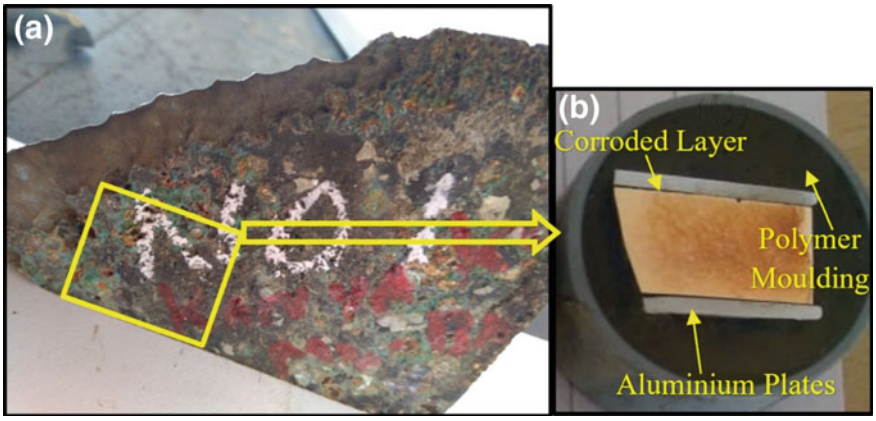

Fig. 2 **a** Photograph showing cut portion propeller tip of NAB, Kanyakumari. **b** Photograph showing the molded transverse section of propeller of the sample shown in this figure **a**. The sample was sandwiched between two metal plates to preserve the edge and to protect the corroded layer from spalling

propellers in a polished condition after the removing the material on the skin of the as-cast propeller surfaces. Hence, oxide scale and dimples has resulted from the usage of the propeller.

Table 1 Composition of different phases in NAB alloy

Microstructural phase (NAB)	Chemical composition in weight %				
	Cu	Al	Mn	Fe	Ni
Alpha	81–87	5–9	1–2	2–4	3–5
Kappa 1	7–15	9–11	2–3	67–73	5–8
Kappa 2	15–17	7–10	2–3	65–74	5–7
Kappa 3	45–54	14–18	1–2	6–9	15–18
Kappa 4	3–4	4–5	3–4	70–80	2–3

3.2 NAB Alloy Microstructure and Composition

NAB typically contained chemical composition of 77–82% Cu, 7–11% Al, 2–6% Fe, 0.5–4% Mn, 3–6% Ni, 0.1% Sn, 0.03% Pb, 1% Zn. NAB microstructure consisted of 5 phases, α, κ_1, κ_2, κ_3 and κ_4 could be identified from microstructure as shown in Fig. 3a, b which agree with the literature. Table 1 summarizes the compositions obtained for the different phases. The microstructure matches with the literature on the NAB alloys [7, 17].

3.3 Corrosion Layer

The corrosion layer consists of a thick oxide layer on top and inner partially corroded alloy layer as shown in Fig. 3c. The thickness of the corrosion layer is highly non-uniform which is about 30–300 μm. The oxide layer ranges from 10 to 60 μm in thickness. The partially corroded layer is also irregular and may be thicker than 200 μm in certain places. In the partially corroded region, it is observed that the corrosion is highly localized and follows the lamellar κ_3 phase with the α regions remain intact. It is known that the corrosion progresses along the embrittling phase β' which runs parallel to the κ_3 lamella. The Al rich β' is anodic to the dominant α phase and hence undergoes localized attack which is often observed as dark etched line between two α grains as shown in Fig. 3c. It can be perceived that this localized corrosion, though is very little in volume, can reduce the cohesion between the α grains and hence make the top subsurface structurally weak. The corrosion rate of α phase is slow which is responsible for top oxide layer. It can be observed that a passive oxide layer forms with time reducing both localized and bulk corrosion rates. However, it can be observed that the localized corrosion starts from the crack in the oxide scale as shown in Fig. 3d. This indicates that the localized corrosion progresses with damage to the oxide layer. This also explains why certain regions not exposed to erosion remain intact. The EDS line profile across the oxide layer is shown in Fig. 3e is presented in Fig. 3f. It reveals that the oxide layer shows wide fluctuation in the composition across the oxide probably due to non-participation of κ phases in

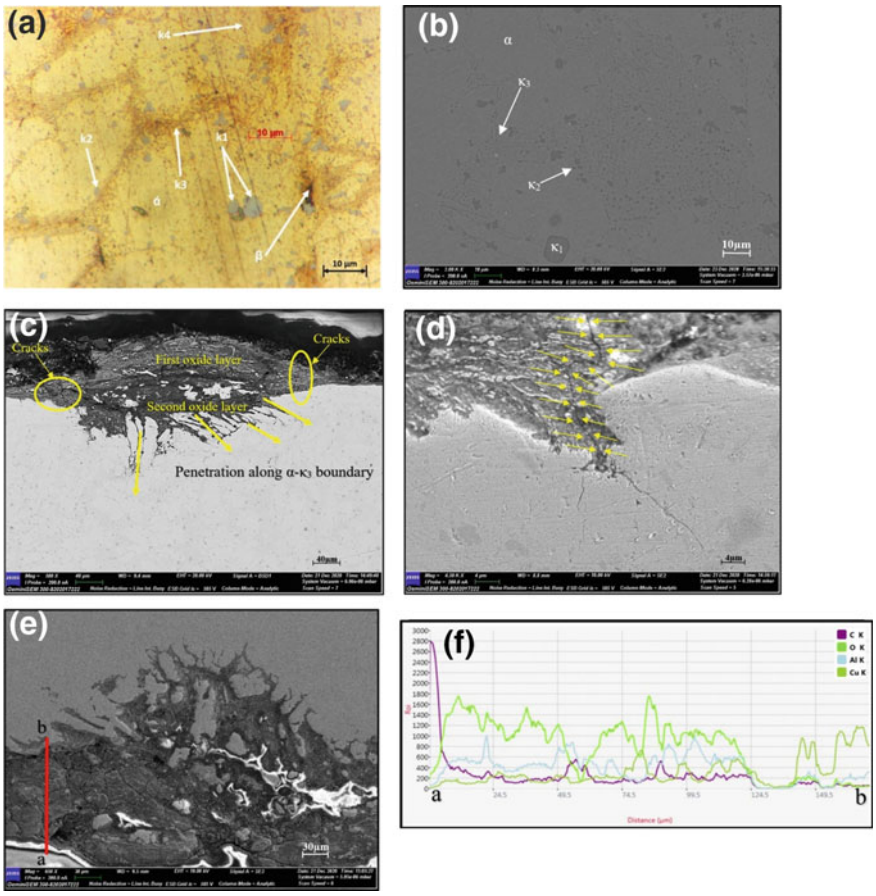

Fig. 3 **a** Optical microscopy showing different phases in NAB alloy. **b** SEM image showing different phases in NAB alloy. **c** Image showing second oxide layer formed and corrosion propagating along α-κ3 boundary. **d** Image showing crack propagation through oxide layer. **e** and **f** Plot for composition of oxide scale formation from surface to a certain depth

corrosion. However, it is possible that the excess Al from the crevices formed during localized corrosion of β' is transported to the metal oxide interface to form a barrier oxide. This barrier oxide protects the underlying metal from corrosion further. But the corrosion can restart of the one cracks are developed in the oxide layer due to erosion or impact of particles (as oxides are brittle in nature) (see Fig. 3d). Hence the corrosion (especially the localized corrosion) continues by a cyclic breaking and making of the oxide scale.

During solidification, the cooling rate decides the extent of β phase decomposition and the extent of β' which is rich in Al and hence it is more susceptible to localized corrosion as compared to α phase and lamellar shape gives more interfacial area for corrosion. Concentration gradient across the α-κ_3 boundary also may lead to

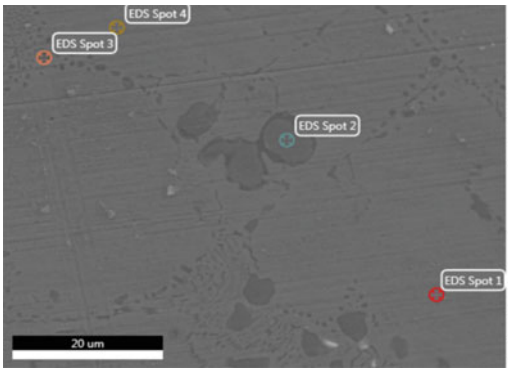

EDS Spot - 1

Element	Weight %	Atomic %
AlK	8.18	17.19
MnK	1.34	1.38
FeK	3.09	3.14
NiK	3.74	3.62
CuK	83.66	74.68

EDS Spot - 2

Element	Weight %	Atomic %
F K	2.14	5.78
AlK	6.24	11.90
CrK	0.63	0.63
MnK	2.53	2.36
FeK	66.42	61.15
NiK	5.24	4.59
CuK	16.80	13.60

EDS Spot - 3

Element	Weight %	Atomic %
AlK	17.37	31.70
MnK	2.30	2.06
FeK	24.50	21.60
NiK	21.56	18.08
CuK	34.27	26.55

EDS Spot - 4

Element	Weight %	Atomic %
AlK	7.97	16.80
MnK	1.35	1.40
FeK	2.87	2.92
NiK	3.80	3.68
CuK	84.01	75.20

Fig. 4 EDS result of the NAB microstructure

corrosion to initially begin along this boundary. From the NAB corroded propeller it is adjudged that the localized corrosion occurs parallel to the β' or α-κ_3 boundary. The thin lamellar network provides a path for Al and O diffusion. The κ-phase however are initially cathodic are not affected (due to rich Al content) which remain intact as shown by bright regions from the SEM result. Possible heat treatments to homogenize the Al content in the alloy, to transform residual β to α + κ and modify the κ_3 into a globular form may improve the corrosion resistance can be improved. The EDS spot analysis shown in Fig. 4 shows the large difference in the Al contents in the difference α formed at high temperatures and in the α-κ_3 eutectoid region.

3.4 Corrosion of NAB Coupons Dipped in Actual Environment

As mentioned in experimental procedure corrosion experiments were conducted for NAB coupons in actual condition as the failed propeller which were operated in Kanyakumari at Chinnamuttom harbor by immersing coupons for a period of 2½ months. Figure 5a is fresh coupon procured from the company to carry out simulation experiment. Figure 5b is coupon after a period of 2½ months in the sea water. Visually we can see that small pits have occurred on the surface of the coupons. This proves that corrosion initially starts in the form of pits on the surface and later penetrates deep into the metal along α-κ_3 boundary due to sudden decrease in Al content resulting in Interfacial corrosion. Figure 5c indicates occurrence of pits in NAB coupons. Since these coupons were stationery location for 2½ months, there is possibility of cavitation corrosion on the surface. The reason for pits may be because of attachment of marine organisms to the surface of the coupons causing biocorrosion.

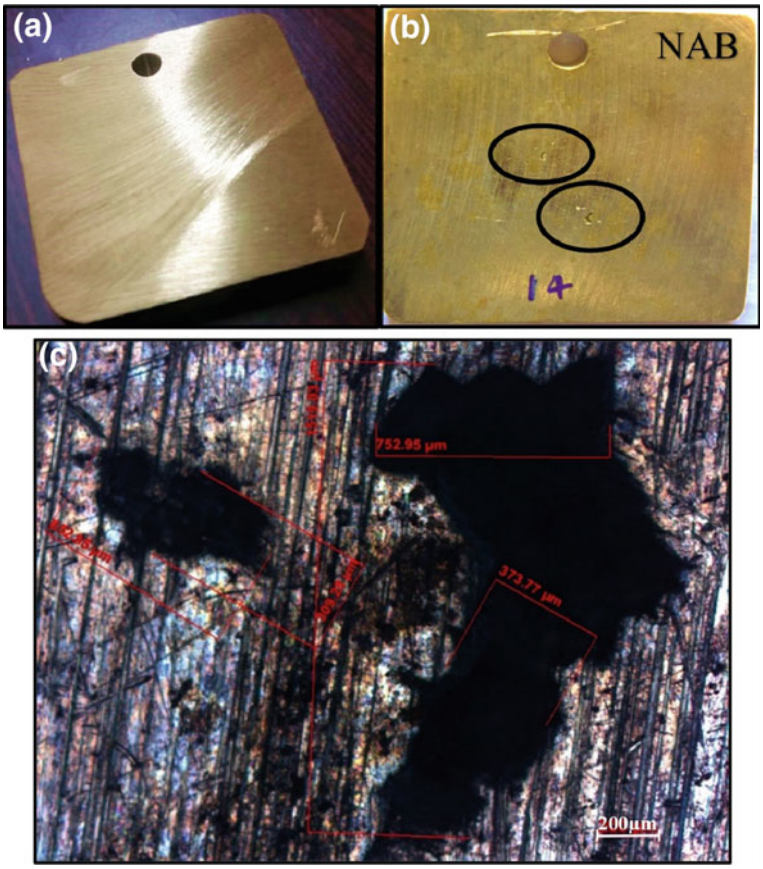

Fig. 5 **a** Fresh coupon before testing in real marine environments. **b** NAB coupon after testing in real marine environments showing pits, **c** Pitting corrosion occurrence in NAB

4 Conclusion

The overall corrosion process taking place in these alloys is due to combination of corrosion and erosion/cavitation. This indicates that the high erosion rates can influence the overall material removal rates. The slowest step in the process of corrosion is the corrosion of the large α grains occurring much slowly compared to the localized corrosion of the α-κ_3 This is indicated by the presence of large Cu rich α islands within the partially corroded layer beneath the oxide layer. However, the cohesion between the α grains is reduced greatly due the localized attack along the α-κ_3 region which surround the large α grains. An impact of right intensity from an erodent particles may remove large volumes of materials which is still largely metallic in nature. Such events may have been the cause of the dimpled appearance of the surface especially close to the edge. The top oxide layer shows alternate Al and

Cu rich oxides indicating that Al preferentially oxidizes by segregating to the surface drawing Al from Al rich α-κ_3/β' regions to the surface. Aluminium rich barrier oxide formation offers resistance to corrosion only if erosion does not affect the integrity of the formed oxide scale. Cracks allow oxygen/corrosive media to penetrate upto the metal inducing localized corrosion/pitting. As more and more cracks form, the corrosion penetrates deeper into the metal. Since the failure happened right after the yearly fishing break, it is expected that the micro-organisms in the local region might be responsible for the severe corrosion observed in Kanyakumari harbor. The same propellers used in the Malpe harbor in Karnataka, also having a fishing break during the same time did not show such failure.

Acknowledgements The authors would like to thank Central research facility for extending the use of its facilities.

References

1. Carvalho ML (2015) Corrosion of copper alloys in natural seawater: effects of hydrodynamics and pH. University Pierre et Marie Curie - Paris VI
2. Heiser JH, Soo P (1995) Corrosion of barrier materials in seawater environments
3. Claesson E, Rod O (2016) The effect of alloying elements on the corrosion resistance of brass
4. Pugachevaa NB, Pankratovb AA, Frolovac NYu, Kotlyarov IV (2005) Structural and phase transformations in $\alpha + \beta$ brasses
5. Zheng Y, Song Q, Ni DR, Ma ZY (2014) Characterization of the corrosion product films formed on the As-cast and friction-stir processed Ni–Al bronze in a 3.5 wt.% NaCl solution
6. Basumatary J, Wood RJK, Synergistic effects of cavitation erosion and corrosion for nickel aluminium bronze with oxide film in 3.5% NaCl solution
7. Richardson I, Powell C (2016) Guide to nickel aluminium bronze for engineers. Copper Development Association Publication No 222
8. Equilibrium diagrams selected copper alloy diagrams illustrating the major types of phase transformation. CDA (Copper Development Association) Publication No 94, 1992
9. Copper Development Association (CDA). http://copperalliance.org.uk/
10. Ding Y, Zhao R, Qin Z, Wu Z, Wang L, Liu L, Lu W (2019) Evolution of the corrosion product film on nickel-aluminium bronze and its corrosion behaviour in 3.5 wt % NaCl solution
11. Culpan EA, Rose G (1978) Microstructural characterization of nickel aluminium bronze. J Mater Sci
12. Jahanafrooz A, Hasan E, Lorimer GW, Ridley N (1983) Microstructural development in complex nickel-aluminium bronzes
13. Hasan F, Jahanafrooz A, Lorimer GW, Ridley N (1982) The morphology, crystallography, and chemistry of phases in As-cast nickel-aluminium bronze. Am Soc Metals Metallurg Soc AIME, 1338 13a
14. Cuevas AM (2002) Microstructure characterization of friction-stir processed nickel aluminium bronze through orientation imaging microscopy. Doctoral dissertation, Monterey, California. Naval Postgraduate School
15. Ahmad A (2017) Optimization parameters for cavitation erosion and corrosion using robotic FSP of NABs

16. Iqbal J, Hasany F, Ahmad F (2006) Characterization of phases in an As-cast copper-manganese-aluminium alloy
17. Scutelnicu E, Constantin E, Iordachescu M, Ocana JL (2008) Naval propellers reconditioning by friction stir welding—FSW. Dunarea de Jos University of Galati, Romania

Microstructural Evolution and Failure Behavior of Resistance Spot-Welded Dual Phase Steel

Gorti Janardhan, Goutam Mukhopadhyay, and Krishna Dutta

Abstract In present scenario the automobile manufacturers are thriving to reduce the mass of passenger cars, by improving fuel efficacy and minimizing the CO_2 emissions. Dual-phase steels are one of the most commonly used advanced high strength steel grades in the automotive industries. These steels have higher strength, good formability, and adequate weldability. The steel finds several applications in the fabrication of components such as chassis, suspensions, and body frame. Resistance spot welding (RSW) is one of the most widely used processes to join thin metal sheets. The current study aims to examine the microstructural and failure behaviour of spot-welded dual phase (DP) steel joints of 1.4 mm thickness. The findings show that the microstructure of fusion zone (FZ) of the joint mostly consisting of lath martensite, while the microstructure of heat affected zone (HAZ) manifests distinct characteristics viz. heat affected zone coarse grain (HAZ-CG) with coarser martensite, heat affected zone fine grain (HAZ-FG), and heat affected zone intercritical (HAZ-IC) with some ferrite and martensite packets at grain boundaries. The base metal (BM) predominately shows ferrite with martensite islands at grain boundaries. Under tensile-shear loading, crack initiated from the base metal. While the failure of coach-peel specimen takes place from HAZ-CG. The work concludes that the structural integrity of the joint is significantly controlled by microstructural variations, joint configuration, and location of the failure.

Keywords Spot-welds · Dual phase steel · Martensite · Load carrying ability · Location of failure

G. Janardhan (✉) · K. Dutta
Department of Metallurgical and Materials Engineering, National Institute of Technology, Rourkela, Rourkela 769008, India

G. Mukhopadhyay
R&D and Scientific Services, Tata Steel Limited, Jamshedpur 831001, India

S. Pal et al. (eds.), *Processing and Characterization of Materials*, Springer Proceedings in Materials 13, https://doi.org/10.1007/978-981-16-3937-1_5

1 Introduction

Today automakers and steelmakers are thriving towards maximizing the application of advanced high strength thinner steels in transport industry by meeting the requirements in terms of improving the fuel efficacy, lowering the carbon foot print and thereby reducing the weight of the passenger car. Dual phase (DP) steels are among the most widely used advanced high strength steel grades in the automobile industry [1]. DP steel constitutes of composite phases, which are ferrite as softer phase and martensite islands at grain boundaries as harder phase [2]. DP steels possess excellent combination of tensile strength as well as ductility. This steel is widely used in cross rails, bumper, body frames, chassis, pillars, and safety cage [3]. Resistance spot welding (RSW) is the most widely used process for joining several parts of a body in white assembled vehicle architecture. It is an efficient, economic and clean process as it does not involve any filler material [5]. Generally, an automotive body consists of 2000–5000 spot-welds [4]. Typically failure of spot-welds subjected to static loading occurs in two modes: interfacial propagation of crack through fusion zone and failure occurring by withdrawal of weld nugget from the sheet in pull out mode. The mode of failure has significant effect on the spot-welds integrity and its mechanical performance. They are critical as they directly influence the reliability of the vehicle. The effectiveness of resistance spot welds in automotive sectors is very well documented [8–10]. However, the joining of advanced high strength steels by RSW is a challenge as several problems arise mainly due to formation of complex microstructures in the Fusion Zone (FZ) and Heat Affected Zone (HAZ), vulnerability to shrinkage voids, porosity formation, tendency to occurrence of failure from fusion zone, as well as tendency for expulsion even at relatively lower heat inputs. All these factors directly influence the nugget size, microstructural evolution, load carrying ability and failure behaviour of the spot-welds [6, 7]. Limited works exist in open literature related to microstructural evolution and failure behaviour of DP steel resistance spot-welds. Henceforth, present work has been attempted to detailed examination of microstructural variations across different zones of the spot-welds and failure behaviour of the DP in both Tensile-Shear (TS) as well as Coach- Peel (CP) configurations.

2 Experimental Procedure

Dual phase steel sheets of thickness 1.4 mm were selected for the present investigation. The chemical composition of the steel was assessed by employing optical emission spectroscopy (OES) method; the results are summarized in Table 1. The details pertinent to the tensile properties of the steel sheets are presented in Table 2. The procedure adopted for welding experiments for joining of current material is elucidated in detailed manner in previous works of Janardhan et al. [6]. During spot welding experiments, the weld current and weld time were varied. The hold

Table 1 Chemical composition of as-received DP steel in weight percentage

Steel	C	Mn	Si	N	P	Ti	Cr	Al	Ni	S	Nb	Fe
DP	0.08	1.9	0.32	0.004	0.018	0.001	0.018	0.08	0.016	0.005	0.001	Bal

Table 2 Tensile characteristics of as-received DP steel

Steel	0.2% Yield strength (MPa)	Ultimate tensile strength (MPa)	% Uniform elongation	% Total elongation
DP	390 ± 4	645 ± 3	17 ± 2.5	22 ± 3.5

time as well as electrode force were kept constant at all process parameters (Table 3). Welded specimens were cut through the centre of the spot welds by slow speed cutter. Then these were mounted using phenolic resin and polished using different grades of emery papers followed by 0.25 μm diamond paste for obtaining mirror surface finish. 3% Nital was used as the etchant to reveal microstructures at different welding zones. The microstructural characterizations were carried out using optical and scanning electron microscopes. The micro-hardness distribution was measured with the help of Vickers micro-hardness tester using a load of 100 gmf with the dwell time of 15 s. The load carrying ability of the spot-welded joints in both TS as well as CP configurations (Fig. 1) were measured using Instron universal testing machine

Table 3 Resistance spot welding process variables

Welding current (kA)	Welding time (ms)	Hold time (ms)	Electrode force (kN)
6-7-8-9-10	150-225-300	200	3.8

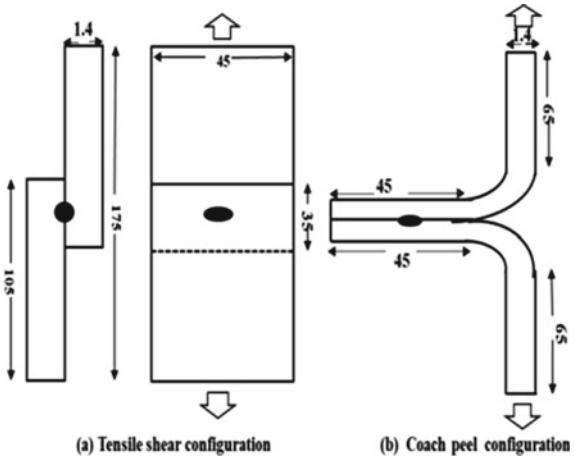

Fig. 1 Schematic of the joint configurations: **a** Tensile-shear, and **b** Coach-peel (all dimensions provided with the schematics in mm)

and the average readings of three samples were taken for each welding parameter. The specimens for failure investigations were prepared by following the standard metallography procedure followed by examining under Stereo microscope.

3 Results and Discussion

3.1 Macrostructure and Microstructure of the Joints

Typical cross-sectional view of the DP steel joint is exhibited in Fig. 2. It is observed that three distinct zones are existing viz., fusion zone, heat affected zone, as well as base metal (BM) respectively. The diameter (D) of weld nugget is labelled in Fig. 2a. The outer area just above periphery of weld nugget is referred as electrode indentation marked by an arrow mark. The notch at interfacial region of conjugated sheets is shown by an arrow. Figure 2b shows the overall macrograph of the distinct zones of spot-welded DP steel joint. It is observed that there is significant variation in the microstructural morphology of the FZ, HAZ while the BM experience no change. The weld thermal cycling of the joining process is responsible for such microstructural changes.

The region experiencing melting as well as solidification is the fusion zone as shown in Fig. 2b. The location with no melting, but underwent microstructural changes is the heat affected zone as shown in Fig. 2b. The HAZ is further subdivided into three types based on peak temperature attained as well as time spent namely, heat affected zone coarse grain (HAZ-CG) lying close to FZ, followed by heat affected zone fine grain (HAZ-FG) and the heat affected zone intercritical (HAZ-IC) is lying at interface. Typical SEM micrographs of distinct regions are exhibited in Fig. 3a–e. The SEM image of FZ shows clearly lath martensite as shown in Fig. 3. This is attributed to the achievement of highest temperature above melting point in this region. The SEM image of HAZ-CG shows coarse martensite as shown in Fig. 3b.

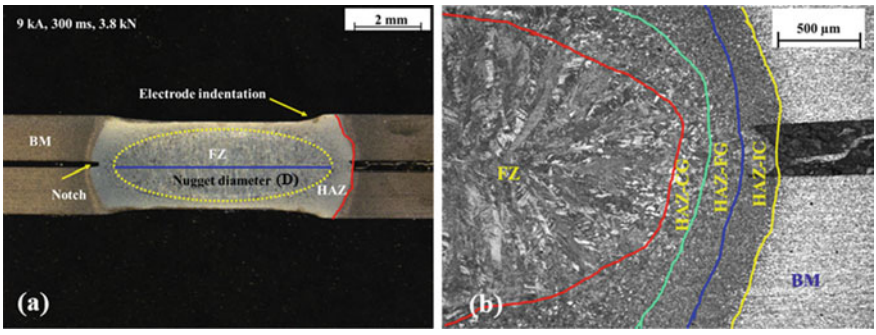

Fig. 2 **a** Macrostructure of the spot-welded DP steel, **b** Overall macrograph showing distinct zones of the DP joint

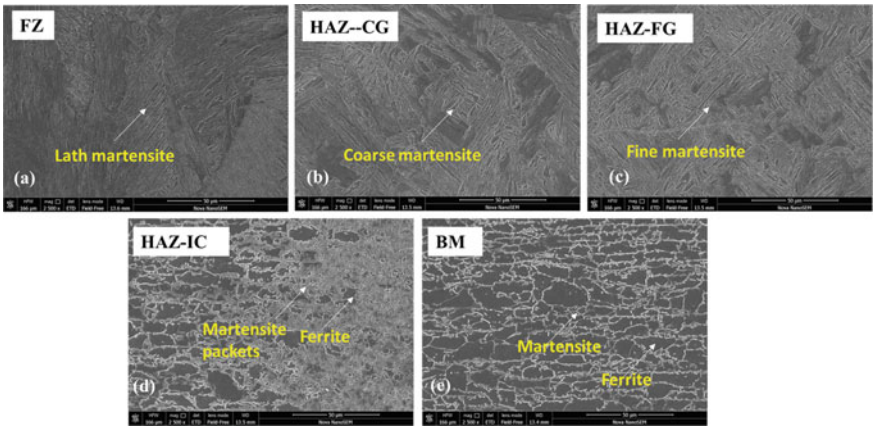

Fig. 3 Scanning electron micrographs of distinct regions of spot-welded DP steel joint: **a** FZ, **b** HAZ-CG, **c** HAZ-FG, **d** HAZ-IC, and **e** BM

The HAZ-FG illustrates finer martensite with some ferrite grains as exhibited in Fig. 3c. This is ascribed to greater peak temperature achieved beyond Ac_3 in HAZ-CG. The SEM image of HAZ-IC reveals martensite packets with ferrite grains as presented in Fig. 3d. This is due to the fact that temperature achieved in HAZ-IC lies among Ac_1 and Ac_3. The SEM image of the BM as illustrated in Fig. 3e consists of ferrite grains with martensite islands at grain boundaries. The microstructural variations may also be attributed to the higher cooling rates provided by RSW process because of employing of copper electrodes under water cooled condition rendering quenching effect and shorter welding cycle. These results are in good agreement with the existing results [7, 8].

The average micro-hardness values determined in distinct regions of the joints are summarized in Table 4. It is observed that micro-hardness is found to be maximum in the FZ due to formation of lath martensite, the micro-hardness is higher in HAZ-FG among different types of HAZ because of presence of finer martensite in this region, while it is lowest in the BM due to presence of mostly ferritic grains with martensite at grain boundaries.

Table 4 Average micro-hardness in various zones of spot-welded DP steel joints

Distinct zones of the joints	FZ	HAZ-CG	HAZ-FG	HAZ-IC	BM
Average micro-hardness (Hv)	425 ± 2.5	387 ± 3.6	405 ± 3.8	245 ± 4.5	220 ± 3

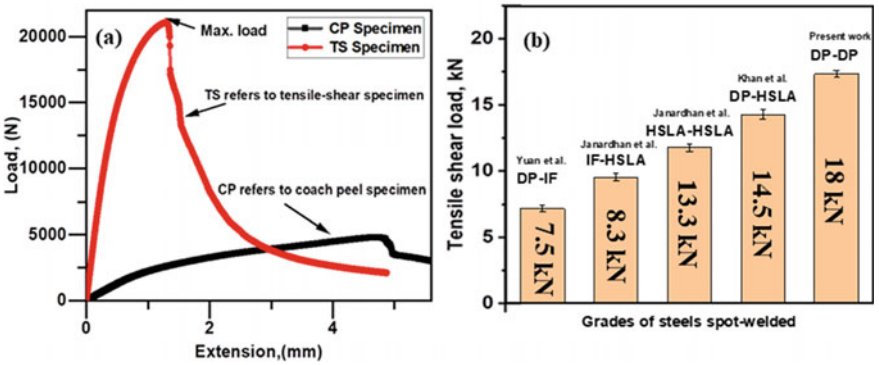

Fig. 4 **a** Typical load versus extension plots for DP steel joints, and **b** Comparison of load carrying ability for spot-welded joints on different steels

3.2 Load Carrying Ability of the Joints

Generally, TS and CP spot-welded joints are predominately used in automobile industries. Thus, in current study to determine load sustaining ability of the joints TS and CP joint configurations are considered. Typical load versus extension plots of spot-welded DP steel joints in both TS as well as CP specimens subjected to static loading is shown in Fig. 4a. The nature of plots is similar in the case of both TS as well as CP specimens. It is observed that the load increases conforming to extension values until maximum load is reached. As the crack initiates the load gradually reduces slowly unless tearing takes place in the base metal. The energy absorbed by the joint is area under the curve until the maximum load. The load carrying ability and energy absorbed by the TS specimen is lower than that of CP specimen. It is attributed to difference in mode of loading, nature of stress acting at interface of the sheets, and geometry of the specimens.

A comparison of the load carrying ability of the spot welded similar combination of DP-DP steel joint is carried out with that of the previously published works for IF-HSLA, HSLA-HSLA, and DP-IF spot-welded steel joints [6, 9–11]. Here IF stands for interstitial-free steel and HSLA stands for high strength low alloy steel. It is observed that load carrying ability of the DP-DP spot-welds is highest amongst all combinations of the joints (refer Fig. 4b). It is attributed to higher tensile strength of DP steel compared to that HSLA and IF steel.

3.3 Failure Behaviour of Spot-Weldments

The snapshots of the failed joints in pulling-out mode for both TS and CP specimens are shown in Fig. 5a. The failure behaviour of the spot-welds is influenced by nugget size, tensile strength of the BM, as well as stresses acting at the conjugated sheets. The

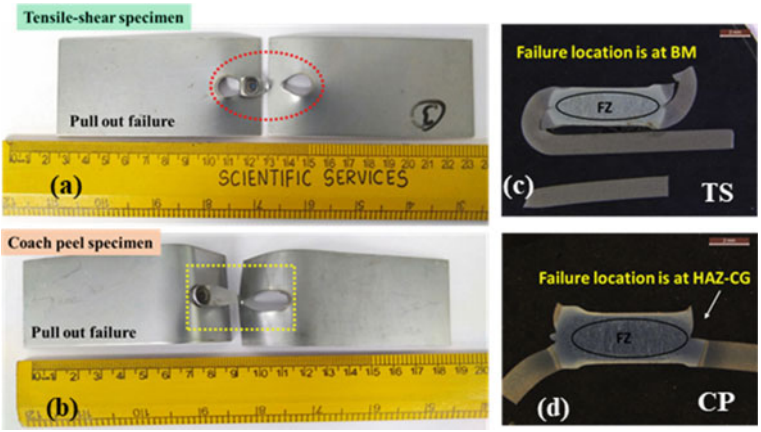

Fig. 5 **a, b** Visual views of failed TS and CP specimens in pull out mode and **c, d** Typical cross-sectional macro views of the TS and CP specimens

pulling out mode of failure for spot-welds refers to complete withdrawal of nugget from the BM under the applied tensile load [4]. This mode ensures sound quality of joint and provides sufficient integrity to vehicle architecture. The cross-sectional view of the failed TS specimen subjected to static loading is shown in Fig. 5c. It is observed that crack initiates at the BM. Additionally, during occurrence of failure, some plastic deformation and necking also take place until tearing. The failure of TS specimen is governed by the lowest hardness at location of failure. The failure of CP specimen subjected to static loading takes place from the HAZ-CG as shown in Fig. 5d. The crack initiation and propagation occur at the boundary of FZ and HAZ. This difference is attributed to the acting of bending stresses at interface of two sheets during failure at a single point over a smaller area.

4 Conclusions

In this work the suitability of DP steel spot-welds has been studied for their microstructure, hardness, load carrying ability, and failure behaviour. The obtained results and their relevant discussion lead to the following major inferences:

i. The load carrying ability and energy absorbed by the tensile-shear specimens is greater than that of coach peel specimens. It is attributed to variation in the mode of loading, geometric configuration, and stress acting at the interface of the two sheets.
ii. The micro-hardness profile of the spot-welded joints shows a continuous increase in hardness values from base metal to fusion zone through heat affected zone. The fusion zone shows the maximum hardness in the weld joint and the

lowest in the base metal. This is attributed to the morphological variations of the microstructures at different zones of welding.

iii. The microstructure of fusion zone of the joint mostly consisting of lath martensite, while the microstructure of heat affected zone manifests distinct characteristics viz. HAZ-CG with coarser martensite, HAZ-FG consisting of fine grains, and HAZ-IC with ferrite and some martensite packets at grain boundaries. The BM, on the other hand consists of mostly ferrite grains with martensite at boundaries.

iv. The spot-welds failed from the base metal in tensile-shear configuration, while in coach peel configuration failure occurred from HAZ-CG. The failure location is governed by lower hardness at the joint.

References

1. Matlock DK, Speer JG (2010) Processing opportunities for new advanced high-strength sheet steels. Mater Manuf Process 25:7–13. https://doi.org/10.1080/10426910903158272
2. Kwon OJ, Lee KY, Kim GS, Chin KG (2010) New trends in advanced high strength steel developments for automotive application. Mater Sci Forum 638–642:136–141. https://doi.org/10.4028/www.scientific.net/MSF.638-642.136
3. Jaber HL, Pouranvari M, Salim RK, Hashim FA, Marashi SPH (2017) Peak load and energy absorption of DP600 advanced steel resistance spot welds. Ironmak Steelmak 44:699–706. https://doi.org/10.1080/03019233.2016.1229880
4. Pouranvari M, Marashi SPH (2013) Critical review of automotive steels spot welding: process, structure and properties. Sci Technol Weld Join 18:361–403. https://doi.org/10.1179/1362171813Y.0000000120
5. Mukhopadhyay G, Bhattacharya S, Ray KK (2009) Strength assessment of spot-welded sheets of interstitial free steels. J Mater Process Technol 209:1995–2007. https://doi.org/10.1016/j.jmatprotec.2008.04.065
6. Janardhan G, Mukhopadhyay G, Kishore K, Dutta K (2020) Resistance spot welding of dissimilar interstitial-free and high-strength low-alloy steels. J Mater Eng Perform 29:3383–3394. https://doi.org/10.1007/s11665-020-04857-z
7. Park G, Kim K, Uhm S, Lee C (2019) Remarkable improvement in resistance spot weldability of medium-Mn TRIP steel by paint-baking heat treatment. Mater Sci Eng A 766:138401. https://doi.org/10.1016/j.msea.2019.138401
8. Wei ST, Lv D, Liu RD, Lin L, Xu RJ, Guo JY, Wang KQ (2014) Similar and dissimilar resistance spot welding of advanced high strength steels: welding and heat treatment procedures, structure and mechanical properties. Sci Technol Weld Join 19:427–435. https://doi.org/10.1179/1362171814Y.0000000211
9. Yuan X, Li C, Chen J, Li X, Liang X, Pan X (2017) Resistance spot welding of dissimilar DP600 and DC54D steels. J Mater Process Technol 239:31–41. https://doi.org/10.1016/j.jmatprotec.2016.08.012
10. Janardhan G, Kishore K, Dutta K, Mukhopadhyay G (2020) Tensile and fatigue behavior of resistance spot-welded HSLA steel sheets: effect of pre-strain in association with dislocation density. Mater Sci Eng A 793:139796. https://doi.org/10.1016/j.msea.2020.139796
11. Khan MS, Bhole SD, Chen DL, Biro E, Boudreau G, van Deventer J (2009) Welding behaviour, microstructure and mechanical properties of dissimilar resistance spot welds between galvannealed HSLA350 and DP600 steels. Sci Technol Weld Join 14:616–625. https://doi.org/10.1179/136217109X12464549883295

Impact of UV Illumination on the Mechanical, Optical and Thermal Properties of High Density Polyethylene-Nano TiO_2 and Polypropylene-Nano TiO_2 Composites

Pravash Ranjan Pradhan, Amit Kumar Mohanty, Lipsita Mohanty, and Shyama Prasad Mohanty

Abstract Photodegradation of organic molecule can be caused by the absorption of photon having appropriate energy. The process can be enhanced by addition of suitable catalysts which can absorb the photon depending on their band gap. In case of plastics, slow degradation of the products remains a major concern for environment. An approach has been made to examine the degradation of polymers using TiO_2 as photocatalyst. The present study focuses on photocatalytic degradation of polymers [high density polyethylene (HDPE) and polypropylene (PP)]-TiO_2 composites. Composites have been prepared by adding 1 wt% of TiO_2 nanoparticles to each polymer and processing using two roll mill followed by compression molding. Samples have been subjected to ultraviolet (UV) illumination and their mechanical, optical and thermal properties have been evaluated. Significant deterioration in mechanical properties has been observed in HDPE based composite as compared to PP based composite.

Keywords Photocatalytic degradation · HDPE · PP · TiO_2 · Tensile strength

1 Introduction

Plastics have become an integral part of human civilization. Plastics offer the advantages like light weight, chemical durability and ease of processing. The utilization of plastics is increasing day by day in the sector of domestic, medical, packaging, construction, automobiles, etc. However, there is parallel increase in the generation of plastic waste due to the slow degradation rate of plastics. Interaction of plastics with the environment leads to change in their chemical and physical properties. Absorption of photons by plastics leads to photodegradation of plastics involving the

P. R. Pradhan · A. K. Mohanty · L. Mohanty · S. P. Mohanty (✉)
Central Institute of Petrochemicals Engineering and Technology:Institute of Petrochemicals Technology (CIPET:IPT), B-25, C.N.I. Complex, Patia, Bhubaneswar 751024, Odisha, India

S. Pal et al. (eds.), *Processing and Characterization of Materials*, Springer Proceedings in Materials 13, https://doi.org/10.1007/978-981-16-3937-1_6

processes like chain scission and oxidation [1, 2]. Acceleration of the process can occur by suitable catalyst such as metal oxides like ZnO [3], TiO_2 [4], etc.

Ohtani et al. studied the photocatalytic degradation of polyethylene-TiO_2 composite films [4]. Whitening of the films was observed along with decrease in the mechanical properties. Preferential degradation occurs at the amorphous region surrounding the TiO_2 leading to creation of voids and hence, loss in transmittance of the samples. Garcia-Montelongo et al. prepared polypropylene (PP)-TiO_2 composite films by using twin screw extruder and hot press [5]. Upon subjecting the films to irradiation, whitening of the films were observed. With irradiation time, more increase in weight loss was observed in the composite films as compared to pristine films. TiO_2 promotes the photocatalytic degradation process by providing the free radicals for the reaction. Studies on photocatalytic degradation of several polymers also have been reported [6, 7]. In the present study, the photocatalytic degradation of high density polyethylene (HDPE) and PP based composites with TiO_2 nanoparticles as photocatalyst has been carried out. Both the polymers differ from each other mainly due to the pendant methyl group which is present in PP whereas absent in HDPE.

2 Experimental

HDPE (Grade-080M60, Indian Oil Corporation Limited), PP (Grade-1110MG, Indian Oil Corporation Limited) and TiO_2 (Aeroxide TiO_2 P25, Evonik) were used to prepare the samples.

First, the two roll mill was maintained at 180 °C, then the polymer granules were fed on to the heated roller and fluxing of the material was carried out. It was allowed to rotate until a homogeneous melt was achieved. For preparation of composites, 1 wt% of TiO_2 nanopowder based on the composite weight (200 g) was added to the homogeneous melt of polymer on the rollers and compounded. The machine was stopped when a uniform layer of polymer was formed on the rollers. Then the material was cooled and the layer formed on the rollers was removed. The films were made into small pieces and this was used for preparation of sheets by compression moulding. The dimension of the sheets prepared by compression moulding were ~16 × 16 cm^2 (Fig. 1). Each sheet prepared by compression was cut into two pieces. One piece of each sheet was subjected to UV illumination and the other piece was characterized for evaluating the samples without subjecting to UV illumination. The sheets were placed at a distance of 10 cm from the UV source and exposed for 100 h under ambient condition (27 ± 5 °C). After exposure, samples were stored in dark condition till characterization.

Tensile strength of the samples was evaluated using universal testing machine (Model-3382, Instron, US) according to ASTM D 638–08. Rectangular samples were cut and tested at a speed of 50 mm/minute. Impact strength of the samples was determined using Izod impact tester (Model-Impact 104, Tinius Olsen) following ASTM D 256–06. Samples of dimension 64.5 mm × 12.7 mm were prepared for testing. Specular gloss of the samples was measured using digital gloss meter (Model-

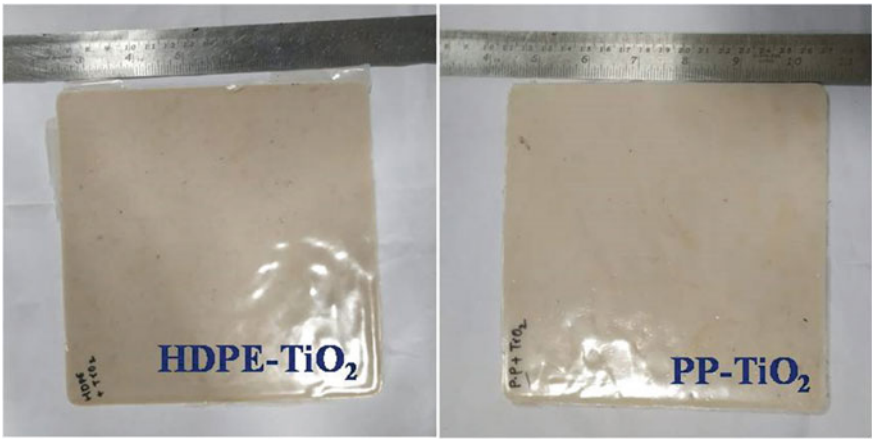

Fig. 1 Images of HDPE-TiO_2 and PP-TiO_2 samples prepared by compression moulding

SFM-115, S. C. Dey & Co., Kolkata) at an angle of 45°. All samples for mechanical and optical properties testing were conditioned at 25 °C and 55% relative humidity for 40 h before testing. Differential scanning calorimetry (DSC) was used to evaluate the thermal behaviour of the composites using differential scanning calorimeter (Model-DSC 8000, Perkin Elmer). Samples were heated from room temperature to 250 °C at a heating rate of 10 °C/minute in nitrogen atmosphere.

3 Results and Discussion

Mechanical properties of the composites were evaluated using tensile strength and impact strength measurements. As observed from Fig. 2, the tensile stress at break for HDPE-TiO_2 before and after 100 h of UV irradiation are 5.43 and 1.46 MPa, respectively. In case of PP-TiO_2, the tensile stress at break is 32.37 MPa which changed to 35.73 MPa after subjecting the samples to UV radiation for 100 h. The tensile stress at break decreases by 73.1% for HDPE-TiO_2 sample after UV light exposure whereas it increases by 10.3% for PP-TiO_2 sample. Shawaphun et al. have highlighted such observation in their study [8]. They have also used 1 wt% of TiO_2 and shown tensile strength retention for 96 h of illumination. According to them, in case of PP-TiO_2, the rate of chain scission is lower than the rate of crosslinking. This leads to increase in strength of samples post exposure. In the present study, exposure for 100 h shows better property in PP-TiO_2 than HDPE-TiO_2.

Apart from tensile strength, impact strength of composites before and after 100 h of UV light exposure was determined. Izod impact strength measurement method was used for such purpose. The impact strength for HDPE-TiO_2 before illumination was found to be 145.5 J/m which decreased by 47.7% to 76.1 J/m (Fig. 3). For

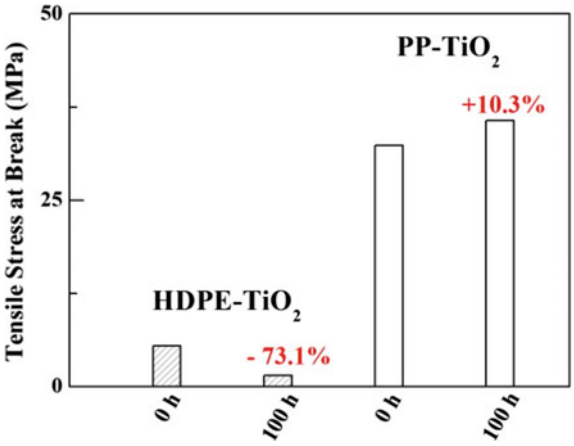

Fig. 2 Tensile stress at break for HDPE-TiO_2 and PP-TiO_2 specimens before (0 h) and after 100 h of exposure to UV light

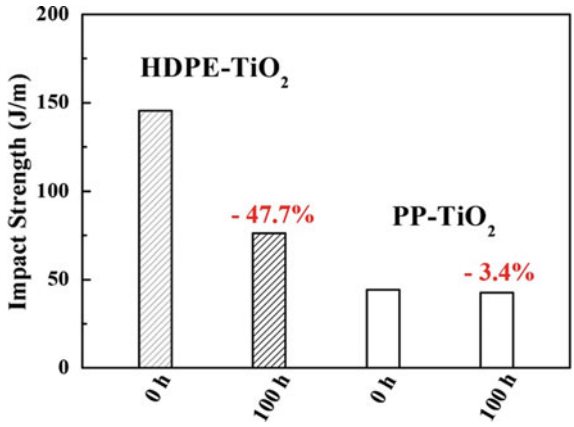

Fig. 3 Impact strength of HDPE-TiO_2 and PP-TiO_2 specimens before (0 h) and after 100 h of exposure to UV light

PP-TiO_2 sample impact strength of 44.2 and 42.7 J/m were obtained before and after 100 h of UV illumination, respectively. So, degradation due to illumination decreases the impact strength by 3.4%. From mechanical analysis of samples, it is inferred that HDPE-TiO_2 samples undergo drastic decrease in performance due to photodegradation whereas the PP-TiO_2 samples are marginally affected within the 100 h of exposure to UV light. It is speculated that in case of PP, pendant methyl groups get dissociated from the chain leaving the chain almost unaffected during the short exposure period. Hence, significant change in mechanical properties is not observed in PP-TiO_2 sample.

Figure 4 shows the specular gloss of specimens before and after 100 h of UV exposure in gloss units (GU). Gloss value increases by 14.3% and 22.7% for HDPE-TiO_2 and PP-TiO_2 samples, respectively after illumination. Under the UV light the surface of composites degrades leading to chain scission and formation of smaller molecules. The TiO_2 particles and degraded polymers might be increasing the gloss.

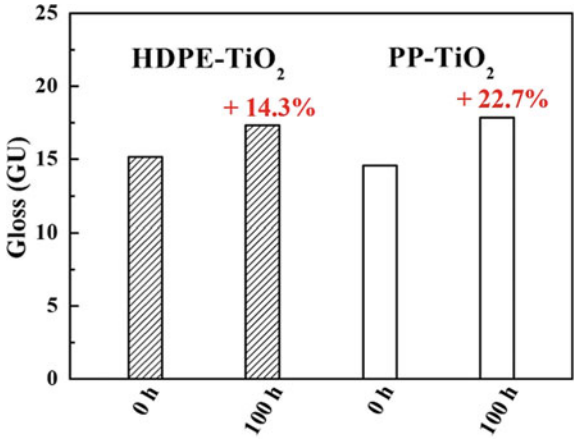

Fig. 4 Specular gloss of HDPE-TiO_2 and PP-TiO_2 specimens before (0 h) and after 100 h exposure to UV light

As observed from mechanical analysis of samples, the degradation of HDPE-TiO_2 sample is relatively higher than PP-TiO_2 sample. This is also reflected in the gloss measurements with HDPE-TiO_2 sample showing higher increase in gloss value post illumination. Under accelerated aging tests, initial increase or almost stable gloss values has been obtained for several polymeric samples [9, 10]. However, decrease in gloss values has been observed upon exposure for longer time. This is due to severe degradation of polymers leading to a chalky surface. In the present study since the exposure time has been 100 h so, the degradation of surface has been low.

Figure 5 shows the DSC curves for specimens before and after 100 h of exposure to UV light. Marginal shift in peak position to higher temperature (~1–1.5 °C) is observed in samples after being exposed to UV light. Crystallinity (X_C) can be determined using the enthalpy of fusion for the sample (ΔH_f) and for 100% crystalline polymer ($\Delta H°$) along with the weight fraction of nanoparticles using the following relation [11].

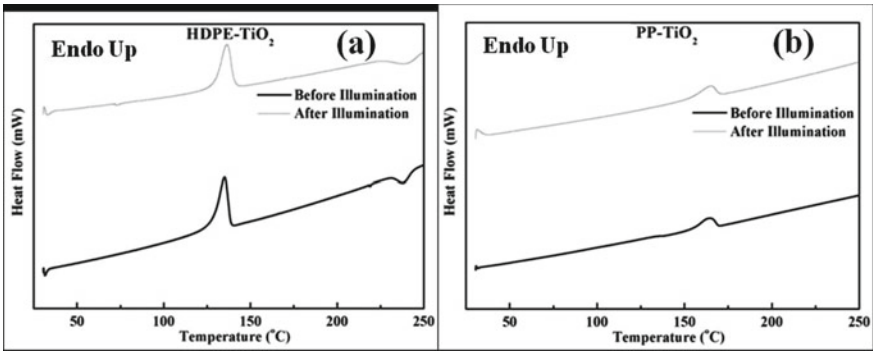

Fig. 5 DSC curves of specimens before and after (100 h) exposure to UV light **a** HDPE-TiO_2 and **b** PP-TiO_2

$$X_C(\%) = [\Delta H_f/(1 - \Phi_P)\Delta H^\circ] \times 100 \quad (1)$$

Melting enthalpy for crystalline PE and PP are 293 and 207 J/g, respectively [11, 12]. In case of HDPE based composites, the ΔH_f values were found to be 165.3 and 72.8 J/g before and after illumination, respectively. This corresponds to crystallinity of 57.0% in the former and 25.1% in the latter. For PP based samples, the ΔH_f values were found to be 51.0 and 29.8 J/g before and after illumination, respectively corresponding to crystallinity of 24.9% before illumination which changes to 14.5% post illumination. So, there occurs a decrease in crystallinity of 55.9% and 41.6% upon illumination for HDPE-TiO_2 and PP-TiO_2 samples, respectively.

4 Conclusions

HDPE-TiO_2 and PP-TiO_2 samples were prepared by compounding using two roll mill followed by compression moulding. Mechanical analysis shows drastic decrease in performance in the former. Gloss measurements indicated higher surface deterioration in HDPE-TiO_2 sample. Decrease in crystallinity was 55.9% for HDPE-TiO_2 sample as compared to 41.6% for PP-TiO_2 sample. So, under UV illumination for 100 h PP-TiO_2 sample was found to be more stable than HDPE-TiO_2.

Acknowledgements The authors acknowledge Evonik India Pvt. Ltd for providing the TiO_2 nanoparticles.

References

1. Wiles DM, Carlsson DJ (1980–81) Photostabilisation mechanisms in polymers: a review. Polym Degrad Stab 3:61–72
2. Yousif E, Haddad R (2013) Photodegradation and photostabilization of polymers, especially polystyrene: review. Springerplus 2:398
3. Bustos-Torres KA, Vazquez-Rodriguez S, Martínez-de la Cruz A, Sepulveda-Guzman S, Benavides R, Lopez-Gonzalez R, Torres-Martínez LM (2017) Influence of the morphology of ZnO nanomaterials on photooxidation of polypropylene/ZnO composites. Mater Sci Semicond Process 68:217–225
4. Ohtani B, Adzuma S, Nishimoto S, Kagiya T (1992) Photocatalytic degradation of polyethylene film by incorporated extra-fine particles of titanium dioxide. Polym Degrad Stab 35:53–60
5. García-Montelongo XL, Martínez-de la Cruz A Vázquez-Rodríguez S, Torres-Martínez LM (2014) Photo-oxidative degradation of TiO_2/polypropylene films. Mater Res Bull 51:56–62
6. Cho S, Choi W (2001) Solid-phase photocatalytic degradation of PVC–TiO_2 polymer composites. J Photochem Photobiol, A 143:221–228
7. Shang J, Chai M, Zhu Y (2003) Solid-phase photocatalytic degradation of polystyrene plastic with TiO_2 as photocatalyst. J Solid State Chem 174(1):104–110
8. Shawaphun S, Manangan T, Wacharawichanant S (2010) Thermo- and photo- degradation of LDPE and PP films using metal oxides as catalysts. Adv Mater Res 93–94:505–508

9. Zhao Q, Li X, Gao J (2007) Aging of ethylene-propylene-diene monomer (EPDM) in artificial weathering environment. Polym Degrad Stab 92:1841–1846
10. Rouillon C, Bussiere PO, Desnoux E, Collin S, Vial C, Therias S, Gardette JL (2016) Is Carbonyl index a quantitative probe to monitor polypropylene photodegradation? Polym Degrad Stab 128:200–208
11. Zhang G, Xiao Y, Yan J, Xie N, Liu R, Zhang Y (2019) Ultraviolet light-degradation behavior and antibacterial activity of polypropylene/ZnO nanoparticles fibers. Polymers 11:1841
12. Li D, Zhou L, Wang X, He L, Yang X (2019) Effect of crystallinity of polyethylene with different densities on breakdown strength and conductance property. Materials 12:1746

Effect of Steel Making Parameters on Nitrogen Level in Steel

Manish Kumar Singh, K. K. Keshari, A. Prasad, and A. Das

Abstract Various factors affecting the nitrogen pickup in liquid steel were studied. Nitrogen content is lowest at converter (average: 15 ppm) which further increases sharply from tapping to ladle Heating furnace (LHF) (average: 27 ppm). It continues to increase during treatment at LHF (average: 33 ppm). However there is slight increase in nitrogen pickup at caster (average: 41 ppm). Factors affecting nitrogen content at converter includes the ratio of scrap to hot metal charge, the quantity of fluxes, re-blows and tapping duration. Higher duration of arcing at LHF leads to higher nitrogen absorption. Sulphur and oxygen also contribute to nitrogen pickup. Results show that deoxidised steel has comparatively lower nitrogen pickup as compared to oxygen-bearing steel or partially killed steel. However, there is inverse relation between finished sulphur obtained at the end of LHF treatment and nitrogen pickup at caster. This study will give a basic guideline to steelmakers to produce stringent quality steel with lower nitrogen level.

Keywords Steel · Converter · Ladle refining · Nitrogen pickup · Sulphur · Factors affecting nitrogen

List of Symbols

BOF	Basic Oxygen Furnace
LHF	Ladle Heating Furnace
CC	Continuous Casting
CO	Carbon Monoxide
ppm	Parts per Million
SiMn	Ferroalloy Silico-Manganese

M. K. Singh (✉) · K. K. Keshari · A. Prasad
R&D Centre for Iron and Steel, Steel Authority of India Limited, Ranchi 834002, India
e-mail: manish1695@sail.in

A. Das
Rourkela Steel Plant, Steel Authority of India Limited, Rourkela 769011, India

S. Pal et al. (eds.), *Processing and Characterization of Materials*, Springer Proceedings in Materials 13, https://doi.org/10.1007/978-981-16-3937-1_7

LHF IN	Nitrogen analysis of steel just before LHF treatment
LHF OUT	Nitrogen analysis of steel just after LHF treatment
BOF TD	Nitrogen analysis of steel on First Turndown at Converter
Caster	Nitrogen analysis of steel taken from Tundish of Caster

1 Introduction

The quality requirement of the customers is becoming more stringent day by day thus limiting the especially concerning the gases and inclusions present in the steel. These gases and inclusions have considerable impact on the mechanical properties of final product of steel. Nitrogen is one of the most important gases which are normally present in small quantities in steel. It also forms carbonitride/nitride precipitates/inclusions in the presence of other alloying elements Niobium, Vanadium Carbon and Aluminium [1]. Although it is present in small quantities in steel, but its effects are often very significant both at steel making stage and on properties of finished product. The peritectic steels which as per their nature has tendency to contract during peritectic transformation and it may become brittle due to coarse γ-grain formation during solidification during process of slab casting by continuous caster. Peritectic steels containing Niobium and Vanadium, the fine nitride precipitates (a few tens of nm) are formed in combination with Carbon and Aluminium at the secondary cooling zone at the grain boundaries of the shell surface. These precipitates tend to make the strand surface embrittle at 700–900 °C, where unbending was usually practiced [2]. The presence of these precipitates reduces the hot ductility of steel and during the process of unbending at the straightener, they may lead to casting defects like transverse corner cracks [3]. In general, a lower level of nitrogen and oxide inclusions is desirable and considered to be good for steel quality. Often the internal quality of steel is judged by nitrogen content level which is an indirect indication of steel cleanliness and its quality issues associated with inclusions generated from re-oxidation in final product [4]. The present assignment has been taken keeping in view prime objective to study the effect of input material like hot metal, scrap, ferroalloys, and steel making process like re-blowing, tapping, arcing, and role of surface-active elements on nitrogen pickup. In the past, some studies have been attempted to find the possible source of nitrogen pickup in liquid steel, and accordingly, mathematical models were formed. But since, quantity or type of input or charged materials, grades, process parameters followed at each stage of steelmaking are different for different steel plants, so a study of nitrogen pickup needs to be done as per the existing condition of steelmaking of the shop. The shop steel making process is silicon aluminium killed. This study will help in controlling nitrogen at each stage of steelmaking via Converter (BOF)-Ladle Heating Furnace (LHF)-Continuous Caster (CC) route.

1.1 Nitrogen Pickup and Nitrogen Removal During Steel Making

In steelmaking, major sources of nitrogen include the input charge additions at the stage of oxygen steelmaking. The nitrogen bearing input charge materials are hot metal, scrap, impure blow oxygen and nitrogen in the stirring gas in case of bottom blowing [5]. So minimum purity of 99.5% oxygen is required to reduce nitrogen pickup in steel. Although nitrogen is present in the atmosphere at large quantity, but it does not become a source unless a reblow is done. During reblow, the converter fills up with air which entrains into the steel, resulting in a significant nitrogen pickup [6]. A small size of taphole can increase the tap time, resulting in nitrogen pickup in the ladle [7]. Other sources of the nitrogen pickup include ferroalloy additions during or after taping like low and medium-carbon ferrochromium, ferrotitanium, and ferrovanadium and petroleum coke used [6]. During secondary steelmaking at LHF, bottom purging of ladles with Argon decrease the dissolved gases like hydrogen and oxygen present in liquid steel by formation of low pressures. In case of nitrogen, it becomes difficult for the N atoms present in solution to form nitrogen molecules (N_2). During arcing at LHF, submerging of arc by ladle slag avoids exposure of arc to atmosphere, which avoids dissociation of nitrogen and getting dissolved in the steel. Surface active elements present in steel such as oxygen and sulphur influences the rate of nitrogen absorption. In case of electric arc furnace and oxygen converter, higher concentration of dissolved oxygen and/or sulphur lowers the nitrogen pickup [8, 9]. That's why it was found that the average nitrogen pickup during tap for deoxidized steels is significantly higher than for non-deoxidized steels. In case of vacuum degassing, the rate of nitrogen removal from the steel has been found increasing with decrease in sulphur content in steel [10–12]. Nitrogen is a diatomic gas and its solubility in liquid steel follows Sievert's law. Removal of nitrogen from liquid steel requires precipitation of dissolved nitrogen as gas from the steel. The equation for the precipitation of nitrogen as gas as per Sievert's law can be shown as below:

$$\mathrm{N} \leftrightarrow \frac{1}{2}\{\mathrm{N_2}\} \tag{1}$$

However, the precipitated nitrogen gas thus formed cannot itself get removed from the liquid steel. This is facilitated by some carrier gases like carbon monoxide and argon. These carrier gases adsorb the nitrogen gas and get flushed out from the liquid steel [13]. In case of BOF, carbon content in steel during refining forms carbon monoxide (CO) during decarburization. Formation of CO changes, the equilibrium in its neighbourhood. The partial pressure of nitrogen decreases in these local regions which favours, the Eq. 1 in forward direction. The nitrogen gas is further absorbed into the carbon monoxide gas bubbles. These gas bubbles are subsequently removed from the melt through metal-slag interface.

2 Experimentation

2.1 Study of Existing Steel Making Practice at Steel Melting Shop

The steel melting shop where this study was undergone is equipped with three basic oxygen furnaces (BOF) of 150 tons capacity each. BOF charge mainly consists of around 152–160 tons of hot metal and approx 15–20 tons of steel scrap depending on Si level of hot metal. Other fluxes used are calcined lime (10–15 tons) and calcined dolomite (4–6 tons). The blowing time ranges from 14 to 17 min and tapping duration under normal case ranges from 5 to 7 min. The average tapping temperatures ranges in between 1650 and 1680 °C. As per the grade requirement ferroalloys like silico-manganese (SiMn) are added in the ladle during tapping for alloying purpose. Rest additions are done at ladle furnace to meet the stringent chemistry range. After the arrival of heat at LHF, argon bottom purging is opened with the flow of 25–30 Nm^3/hr. Arcing is started along with purging for 3–5 min depending on input condition and final targeted grade. After arcing, aluminium wire is added to the tune of 200–400 m followed by temperature, sample and Celox for oxygen measurement. Arcing is continued to raise temperature coupled with small batches of lime (~200 kg) and aluminium wire is afterwards to reach Al level of ~0.02%. Based on sample analysis, trimming addition are done, the temperature is adjusted, soft purged for 2–3 min and sent to the caster. The shop is equipped with 3 single strand continuous casting machines.

2.2 Testing Procedure for Measurement of Nitrogen in Liquid Steel

Lollipop samples were collected from liquid steel at various stages of steel making viz BOF turndown, LHF initial (LHF IN), LHF final (LHF OUT) and at tundish/caster. The steel lollipop samples were first to cut into slices by saw machine. Out of these steel slices, only those samples were selected which are free from any visible blow-holes. Further, these samples were set on turning machine to get the samples finished into a pin sample of the dimension of nearly 10 mm length and 3 mm diameter Fig. 1.

These samples were further rubbed with emery paper just before testing in LECO TCH600 analyser. The principle of operation for nitrogen measurement in LECO TCH600 analyser is based on thermal conductivity of gases.

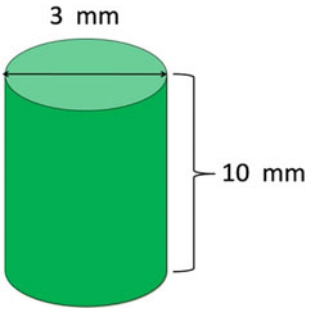

Fig. 1 Pin sample size of LECHO TCH600

3 Results and Discussions

3.1 Mapping of Nitrogen

Mapping of nitrogen was done at each of steel making via BOF-LHF-Caster. At BOF, nitrogen was measured after first turndown denoted as TD BOF. At LHF, nitrogen was measured twice. One sample was taken just before the treatment and another after treatment of steel which are denoted as LHF IN and LHF OUT respectively. And at last nitrogen was measured at caster which is simply denoted as Caster. Mapping of nitrogen at each stage of steelmaking has been shown in Fig. 2.

Nitrogen value measured at turndown has been denoted as BOF. Nitrogen analysis of steel just before LHF treatment has been denoted as LHF IN. Nitrogen analysis of steel just after LHF treatment has been denoted as LHF OUT. Nitrogen value measured at caster has been simply denoted as Caster. Mapping of nitrogen gave the range of nitrogen levels found at each stage of steelmaking. This mapping of nitrogen reveals that nitrogen content is minimum at BOF which further increases sharply from tapping to LHF, and lastly in tundish it increases slightly. Study of

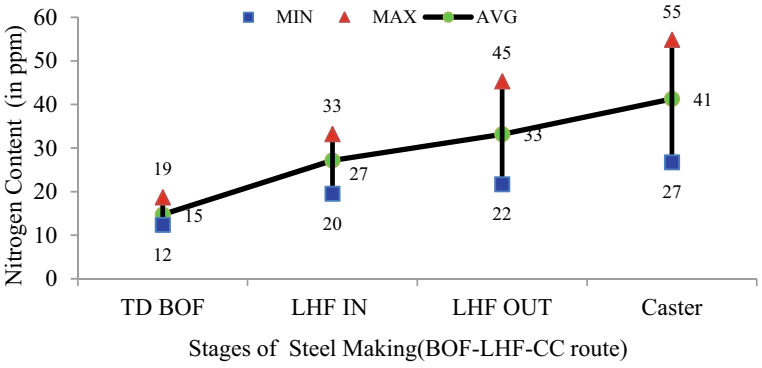

Fig. 2 Nitrogen mapping of steel melting shop

factors affecting nitrogen pickup is categorised according to stages of steel making process in steel melting shop: (A) Basic oxygen furnace (BOF), (B) Ladle Heating Furnace (LHF) and (C) Continuous Slab Caster/Tundish (CC).

(A) **Nitrogen Pickup at Basic Oxygen Furnace (BOF)**

3.1.1 Effect of Percent Hot Metal and Scrap Charge on Nitrogen Content in BOF

Steel scrap is supposed to be a good source of nitrogen. Thus increasing proportion of scrap in the charge may result in the rise of turndown nitrogen in the steel melt.

Steel scrap usually contains much lesser carbon content as compared to hot metal received from blast furnace. Higher percentage of scrap in charge leads to lesser generation of CO bubbles resulting in lesser removal of nitrogen by flushing action of CO bubbles. So, increasing hot metal to scrap ratio in BOF lead to decreased nitrogen content in the steel. It can be seen from Fig. 3 that nitrogen level is greatly affected by the hot metal to scrap ratio in (assuming same quality or grade of scrap). Increased percentage of scrap in charge leads to higher nitrogen on turndown.

3.2 Effect of Re-blows on Nitrogen Content in BOF

During refining of steel at BOF, reblowing of oxygen is done to achieve endpoint targets like carbon, phosphorus, turndown temperature etc. or in case of higher hot metal silicon leading to large slag volume. Before re-blows, converter vessels get

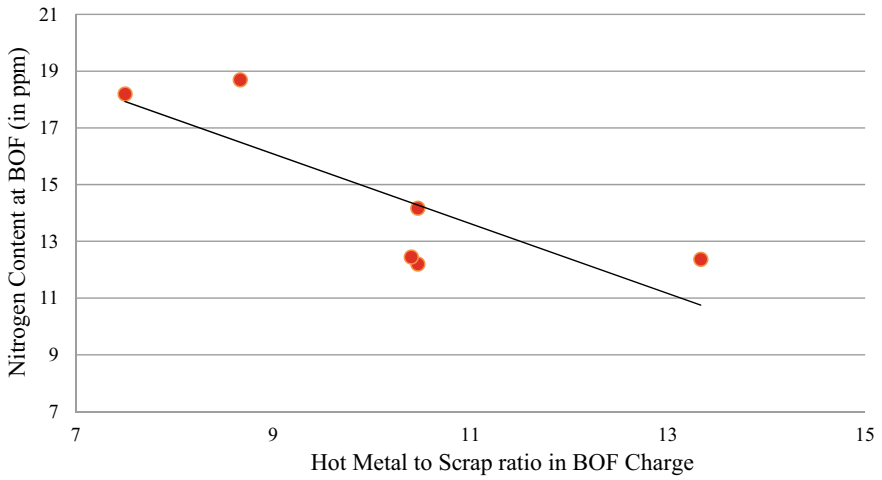

Fig. 3 Effect of hot metal to scrap ratio on nitrogen content in BOF

filled up with atmospheric air containing nitrogen. On re-blowing with oxygen, nitrogen got entrained into the steel. Also during re-blow, the concentration of carbon is lower while concentration of oxygen is higher. This leads to minimal carbon oxygen reaction resulting into lesser removal of nitrogen by flushing action of CO bubbles. Hence, re-blowing causes an increase in nitrogen content. Higher the duration of reblow, higher will be the probability of nitrogen pickup. From our current analysis of some heats found that after certain duration of reblow approximately 40 s in our case, nitrogen at turndown is ~12–18 ppm, very similar to heats with zero reblow. However, at higher re-blow duration above 90 s, there is an increase in nitrogen pickup up to 42 ppm.

3.3 Effect of Tapping Duration on Nitrogen Pickup in BOF

During tapping of steel from BOF to ladle, air bubbles with nitrogen present in atmosphere got absorbed into the liquid steel stream. Tapping duration of BOF is affected directly by size of taphole mouth at the time of tapping. Average tapping duration is 6–7 min with well-conditioned tap hole. However, if the taphole mouth gets chocked due to jamming and not round, tapping duration found to be increased with the scattered flow of steel stream, this increase the nitrogen absorption in molten steel. Higher tapping duration exposes steel stream to open atmosphere for larger time. This leads to higher pickup of nitrogen in steel. Similarly, if the tap hole gets enlarged due course of its life, most probably at the last stage, tapping duration found to be decreased and so the quantity of carryover slag with high FeO content may increase. Here in this case also nitrogen absorption in steel would be more. High FeO in ladle top slag resulted in relatively fluid slag which is less effective in protecting the top surface of the steel in ladle as compared to viscous slag which covers the steel in ladle more effectively. It can be seen from Fig. 4 that the nitrogen level is affected by tapping duration.

(B) **Nitrogen Pickup at Ladle Heating Furnace (LHF)**

3.3.1 Effect of Arcing Duration on Nitrogen Pickup in LHF

Nitrogen in the air gets absorbed into molten steel by being ionized into nitrogen ions in the arc region during arcing at LHF**.** As the surface of the molten steel in the arc area becomes bare due to the breakdown of the slag layer by the arc. It can be seen from the data analysis of heats in Fig. 5 that the nitrogen level is affected by arcing duration.

As arcing duration at LHF increases nitrogen pickup at LHF. Here nitrogen pickup is calculated by the difference of LHF IN and LHF OUT.

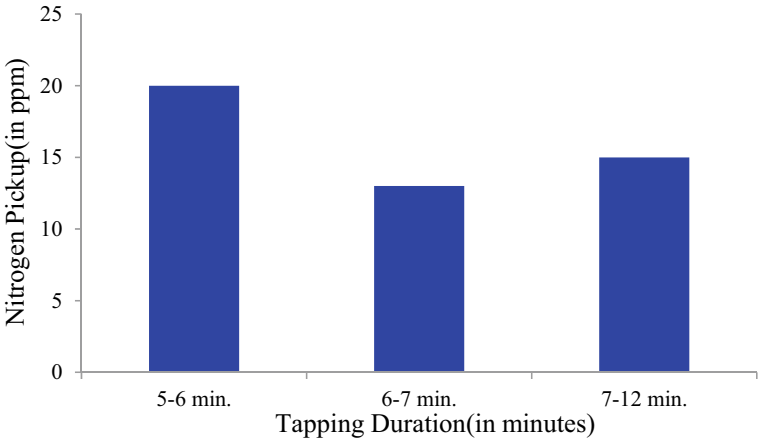

Fig. 4 Effect of tapping duration on nitrogen pickup in BOF

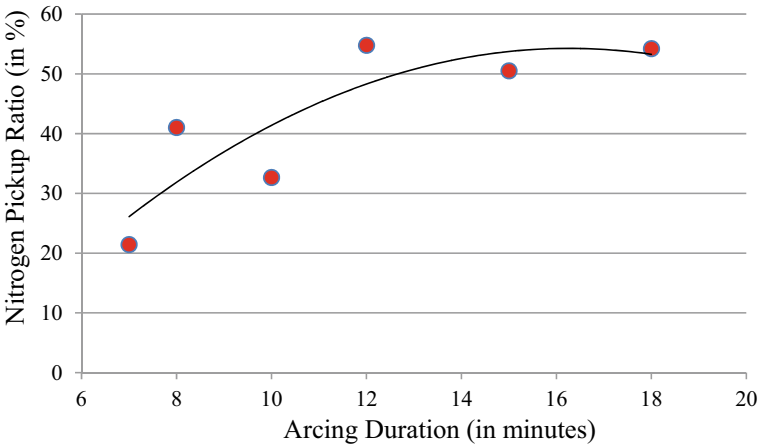

Fig. 5 Effect of arcing duration on nitrogen pickup in LHF

3.3.2 Effect on Nitrogen Pickup After Deoxidation of Steel

The rate of the nitrogen-liquid iron reaction is dependent on the concentration of surface-active elements. In steel surface active elements constitute oxygen and sulphur**.** Oxygen and sulphur present in liquid steel slow down both the rate of nitrogen pickup and desorption. Nitrogen absorption rate slows down in the presence of dissolved oxygen as adsorbed oxygen prefers to stay at the surface and act as a barrier. Therefore, nitrogen pickup is expected more in case of steel with low sulphur or oxygen.

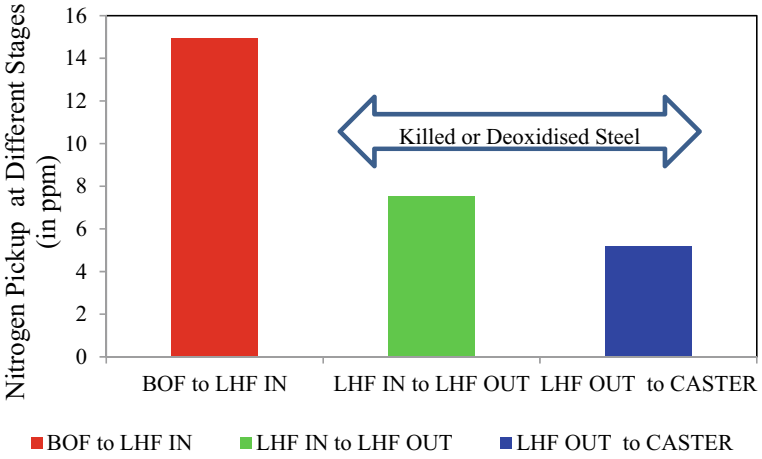

Fig. 6 Effect on nitrogen pickup after deoxidation of Steel

Higher sulphur or oxygen is present in the steel tapped from BOF. To tackle this problem calcined lime is added at LHF. Addition of lime forms basic slag which helps in desulphurisation and act as protective cover on ladle top to prevent nitrogen pickup. After treatment at LHF ladle top is also covered with rise husk. In our study as shown in Fig. 6, we found that nitrogen pickup is more from BOF to LHF IN as compared to the pickup of Nitrogen from LHF IN to LHF OUT or LHF OUT. This shows the importance of ladle slag and ladle top covering reagent at LHF in controlling nitrogen pickup in deoxidised steel which have comparatively higher tendency of nitrogen pickup.

(C) **Nitrogen Pickup at Continuous Caster**

3.3.3 Effect of Steel Sulphur on Nitrogen Pickup in Liquid Steel

Nitrogen desorption is more effective at lower oxygen and sulphur in steel. Harada and Janke [10] et al. concluded from different past experiments that the rate constant of nitrogen desorption in liquid steel decreases with an increase in oxygen and sulphur both at reduced and normal pressure. In other words, it means there will be more desorption and less nitrogen pickup with a decrease in sulphur content in the steel. Since both deoxidation and desulphurisation is mostly done at LHF, so both oxygen and sulphur are relatively lower in steel only after LHF treatment.

In the present study, it can be seen from Fig. 7 that lower nitrogen pickup in steel from LHF finishing to the caster is found in case of comparatively lower sulphur.

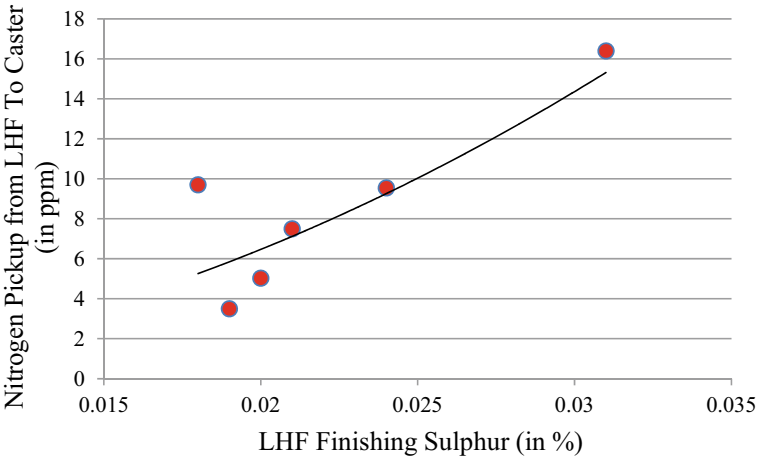

Fig. 7 Effect of surface active element sulphur on nitrogen pickup

4 Conclusions

(1) Steels produced through Converter (BOF)-Ladle Heating Furnace (LHF)-Continuous Caster (CC) route and killed by silicon-aluminium deoxidation process contain nitrogen in the range of 40–60 ppm.
(2) The nitrogen content in steel is minimum at BOF which further increases sharply from tapping to LHF, it continues to increase during the ladle furnace process, and lastly, in the tundish, it may increase slightly.
(3) The higher percentage of scrap and a lower percentage of hot metal BOF charge lead to higher nitrogen content at turndown.
(4) Nitrogen pickup occurs during tapping at BOF. Uneven or scattered stream of steel due to small and choked taphole during tapping or higher carryover slag due to large taphole lead to increased nitrogen content in the steel.
(5) Higher arcing duration at LHF leads to higher nitrogen absorption in steel. Lower sulphur content in deoxidised steel has lower nitrogen pickup in steel at the caster.
(6) Since there is an increase in nitrogen content at each stage of steelmaking. Therefore the strategy of producing steel with lower nitrogen steel should be to minimize nitrogen level at all stages of steel making process i.e. from BOF to Caster.

Acknowledgements I am very thankful to the management of RDCIS, SAIL and Rourkela Steel Plant, SAIL for their encouragement and constant support throughout the study.

References

1. Mintz B (1999) ISIJ Intl 39:833
2. Suzuki HG, Nishimura S, Nakamura Y (1984) Trans ISIJ 24(54):169
3. Thomas BG, Brimacomb JK, Samarasekera IV (1986) ISS Trans 7:7
4. Melville SD, Brinkmeyer L (1995) 78th steelmaking conference proceeding, ISS, Warrendale, PA, p 563
5. Goldstein DA, Fruehan RJ (1999) Metall Trans B 30B:945
6. Ghosh A (2001) Secondary steelmaking (principles and applications), Chapter 8, Section 8.5, CRC Press, Washington, p 241
7. Choh T, Iwata K, Inouye M (1983) Trans Iron Steel Inst Jpn 23:598
8. Pehlke RD, Elliott JF (1963) Trans Metall Soc AIME 227:844
9. Glaws PC, Kor GJW, Fryan RV (1989) 47th electric furnace conference proceedings, Warrendale, PA, ISS, p 383
10. Harada T, Janke D, Steel Res 60(8):337 (1989)
11. Bannenberg N, Bergmann B, Gaye H (1992) Steel Res 63:431
12. Steneholm K, Andersson M, Tilliander A, Jonsson PG (2013) Ironmak Steelmak 40(3):203
13. Fruehan R (1996) J ISIJ Int 36(Supplement):S58–S61

Influence of Crystallographic Orientation on the Mechanical Properties and Deformation Behavior of Ni Nanowire Using Large Scale Molecular Dynamics

Krishna Chaitanya Katakam, Sudhakar Rao Gorja, and Natraj Yedla

Abstract The influence of crystallographic orientation on nickel nanowire mechanical properties and deformation behavior has been studied using large-scale molecular dynamic simulations. In the model preparation, the embedded atomic method potential is used. The crystallographic orientations of Ni nanowire are [1–10], [20–1] [111] and [1–1–2]. All the tensile tests are carried at 10 K temperature and a deformation rate of 10^8 s^{-1}. The size of the Ni nanowire used for tensile studies is 100 Å (x-axis) × 1000 Å (y-axis) × 100 Å (z-axis) and comprises of ~ 925,000 atoms. The simulated results show that orientation has a significant effect on mechanical properties. Nanowire of various orientations yields by Shockley partial dislocation with intrinsic stacking faults followed by twinning partials. The yield stress of [1–20], [20–1], [111] and [1–1–2] orientations are 9.5 GPa, 11.7 GPa, 17.2 GPa and 10.5 GPa respectively.

Keywords Molecular dynamics · Nanowire · Orientation and mechanical properties

1 Introduction

In the last two decades, nanowires (NWs) importance in nanoscale electronic and mechanical systems is increasing drastically due to their application as interconnectors [1]. Nanowire one-dimensional structure and enthralling properties have made the researchers go much depth into their mechanical and physical properties for new findings during different loading conditions. Scientific interest among researchers on nanowires is mainly due to their unique performance in numerous applications [2]. Majorly in the modern functional systems like NW transistors of high mobility

K. C. Katakam (✉) · N. Yedla
Computational Materials Engineering Group, Department of Metallurgical and Materials Engineering, National Institute of Technology Rourkela, Rourkela 769008, India

S. R. Gorja
Corrosion Group, Materials Engineering Division, National Metallurgical Laboratory, Jamshedpur 831007, India

S. Pal et al. (eds.), *Processing and Characterization of Materials*, Springer Proceedings in Materials 13, https://doi.org/10.1007/978-981-16-3937-1_8

and strain-controlled logic gates, supercapacitors, conductors, and other magnetic field devices [3]. Nickel (Ni) NW is essential and widely used in electromagnetic systems, owing to its broad applications [4]. The NW applications in modern nanodevices are increasing gradually. For better functionality of these devices, it is necessary to understand the influence of crystallographic orientation, sample size, and shape on the NW deformation mechanisms and their mechanical properties.

In the last two decades, many researchers have worked experimentally and computationally in the investigation of understanding the deformation behavior of metal NWs. Many researchers have reported the size, shape, and orientation influence on the deformation mechanism of NWs [5–11]. The deformation mechanism in FCC metal NW is either by slip through partial dislocations or by twinning. NW crystallographic orientation and its loading direction mainly determine the deformation mechanism. Hence the crystallographic orientation plays a vital role, followed by loading direction in the deformation behavior of metal NWs. For instance, using molecular dynamics (MD) simulation, Park et al. [5] investigated the tensile and compressive behavior of FCC NWs (Copper, Nickel, and Gold) of <100> and <110> orientations. They said that the NW deformation mechanism depends on material intrinsic properties, crystallographic orientation, applied stress field, and exposed transverse surfaces. Wen et al. [6] studied NW orientation influence on Au NW mechanical properties under tensile and compressive loading. The studied crystallographic orientations of Au NWs are [100], [110], and [111] and reported that there is a strong influence of orientations on the NW mechanical properties. Sainath et al. [7], using MD simulations studied tensile and compressive behavior of BCC Fe NWs of <100>, <110>, <111>, <112> and <102> orientations. Later Rohit et al. [8] studied the NW orientation and loading direction effect on the deformation mechanism of Cu NW. They reported that under tensile loading, all the NWs deform by twinning. Under compression, the NW of orientation <100> deform by twinning, and NW with all other orientations deform by slip. In [9], the author studied the strain rate and orientation dependence on the single-crystal titanium NW under tensile loading. The studied orientations are [11–20], [−1100], [0001] and they reported on the influence of orientation in the deformation of titanium NW at various srain rates.

In the literature, it is noticed that there are no studies on the compressive and tensile studies of NW at different orientations on a large scale. To understand the orientation influence on the tensile deformation of Ni NW in a large scale, we considered a Ni NW of dimension 100 Å × 1000 Å × 100 Å. Hence in this study, we performed the uniaxial tensile test using MD simulations on NW of four different orientations. The considered crystallographic orientation are [1–10], [20–1], [111] and [1–1–2]. The deformation mechanism and the dislocations are responsible for yield and the generated dislocation during the plastic deformation are well analyzed.

2 Simulation Details

MD simulation is used to construct and test the Ni NW of four different orientations using EAM (embedded atomic method) potential [12]. Previously, many researchers have conducted the tensile test and observed metals deformation behavior using the EAM potential. For example, Pei et al. [13] investigated Ni ductile versus brittle fracture at different temperatures. Razaei et al. [14] used the above potential in the study of Ni graphene and reported a twinning behavior. Large scale atomic/molecular massively parallel simulator (LAMMPS) [15] is used in running the MD code for studying the tensile behavior of nanocrystalline materials [5, 16–18].

The NW is created by filling a simulation box with FCC crystalline Ni atoms (a_0 = 3.518 Å) with periodic boundary conditions along the y-axis [19]. In the other two directions (x and z) non-periodic boundary conditions are applied. All the NWs have a square cross-section with a box dimension of 100 Å (x-axis) × 1000 Å (y-axis) × 100 Å (z-axis). To study the orientation effect, four highly symmetry lattice orientated Ni NWs of [1–10], [20–1], [111], and [1–1–2] are constructed as shown in Fig. 1. After the NW preparation, it is relaxed by the conjugate gradient method [19, 20] and then equilibrated at 10 K temperature using the Nose–Hoover thermostat [21]. The equilibrated NW is then deformed along the y-axis at 10^8 s^{-1} strain rate and 10 K temperature. During the tensile test, the thermodynamic ensemble NVT is used. The tensile stress is calculated by using the virial stress at a time step of 1 fs [22]. During the tensile test of NW, the defect analysis is carried by using the centrosymmetric parameter (CSP) [23] and dislocation extraction algorithm (DXA) [24] of OVITO software [25].

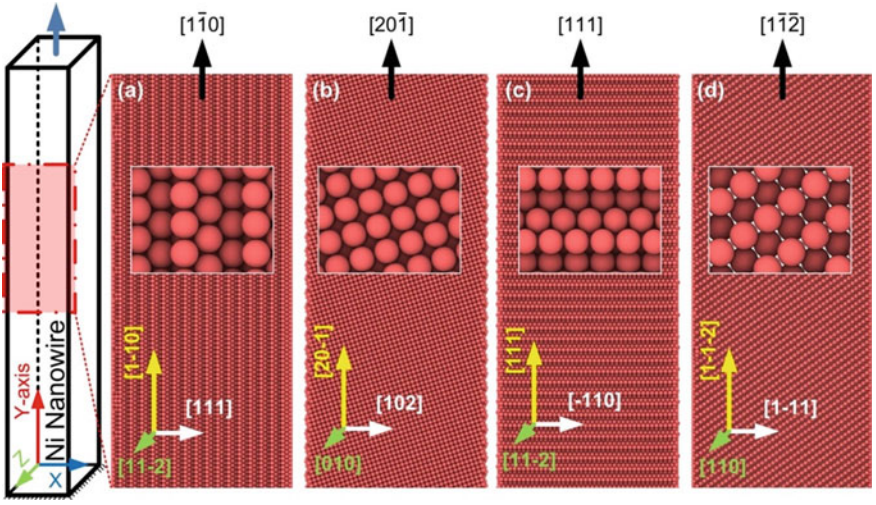

Fig. 1 Schematic view of Ni NW showing their orientations and surface structures and in the present investigation **a** [1–10], **b** [20–1], **c** [111] and **d** [1–1–2] orientations are considered

3 Results and Discussions

3.1 Stress–Strain Behavior

Figure 2 represents the true stress vs true strain curves of Ni NW of [1–10], [20–1], [111] and [1–1–2] orientations under tensile loading at 10^8 s^{-1} strain rate and 10 K temperature. All the NWs strained elastically up to yield load, followed by a sudden fall in stress. Straining the NW beyond the yield has caused plastic deformation followed by fracture at different NW regions based on their orientations. In the stress–strain curves, the slope of the initial linear region gives Young's modulus. All the mechanical properties, yield and fracture strain values are shown in Table 1. From the elastic region, it is noticed that FCC Ni NW has shown different stress–strain behavior depending on their orientation. A maximum elastic modulus of 232 GPa

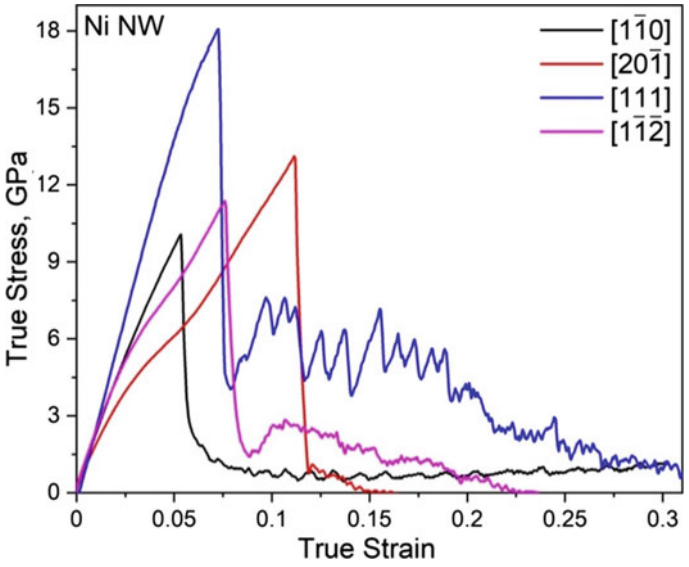

Fig. 2 True stress vs true strain curves of Ni NW of [1–10], [20–1], [111] and [1–1–2] orientations

Table 1 Mechanical properties of [1–10], [20–1], [111] and [1–1–2] Ni NW

Sl. no.	Nanowire orientation	Young's modulus GPa	Yield strength (GPa)	Yield strain	Fracture strain
1	[1–10]	172	9.5	0.053	–
2	[20–1]	90	11.7	0.112	0.152
3	[111]	232	17.2	0.075	0.352
4	[1–1–2]	120	10.5	0.076	0.225

is observed in [111] orientation followed by [1–10] (172 GPa), [1–1–2] (120 GPa) and [20–1] (90 GPa) orientations. The elastic modulus of [111] NW is more than that of nickel bulk sample ~199 GPa [26], but for [1–10] NW, it is almost close. From Fig. 2, it is noticed that the [111] orientation has recorded the highest stress ~17.2 GPa, and [1–10] orientation has the lowest stress (~9.5 GPa). The reported yield stress in [20–1] and [1–1–2] oriented NW are 11.7 and 10.5 GPa. The reported mechanical properties from the literature are based on the size, shape, temperature and at different loading conditions of NW [19, 27–29]. On a small scale, Park et al. [5] studied the tensile properties of Ni NW of <100> and <110> orientations and the reported yield stress is 8 GPa in <110> oriented NW.

3.2 Deformation Mechanisms

3.2.1 [1–10] and [20–1] oriented Ni NW

To observe the deformation mechanism during tensile loading, CSP analysis has been carried out on all NWs. In identifying the type of dislocation, we carried out DXA analysis and represented the dislocations in different colored lines. To identify the type of stacking faults, we deleted the fcc, bcc and other atoms from the sample and showed only the hcp atoms with dislocations along with stacking faults. Figure 3 represents the CSP (a) and DXA analysis (b) images at various strains during tensile loading of [1–10] (A) and [20–1] (B) oriented Ni NW. In the figure it can be observed that both the [1–10] (e = 0.053) and [20–1] (e = 0.112) NW yield by Shockley partial dislocation. The partial surrounds an intrinsic stacking fault with a burger vector of 1/6 <121>. In the process of nucleation and propagation of a Shockley partial in an FCC crystal structure, we can observe two adjacent close pack HCP atoms in-between the partials [6]. Straining the NW further, nucleation of twin partials forming twin boundaries can be observed in both [1–10] (e = 0.057) and [20–1] (e = 0.118) oriented NWs. After the yield strain (e = 0.057) the NW of [1–10] orientation has reoriented to [100] orientation due to twinning. At 14% strain, we can notice a second reorientation at the end of the [1–10] oriented NW. Straining the NW further, the twin region grows along the NW axis and hence there is an increase in the volume percentage of the reoriented region and no fracture is observed in [1–10] orientation up to 30% strain. Rohit et al. [8] have conducted tensile studies on FCC Cu NW using MD simulations and reported that there is a complete reorientation in <101>, <103>, <212>, and <214> oriented samples. In the present tensile studies, [20–1], [111] and [1–1–2] oriented NWs have been deformed up to their fracture strain but reorientation is not observed. This is due to the slip activation in more twin system which causes twin-twin interactions that results in the disruption of twin growth and reorientation [30].

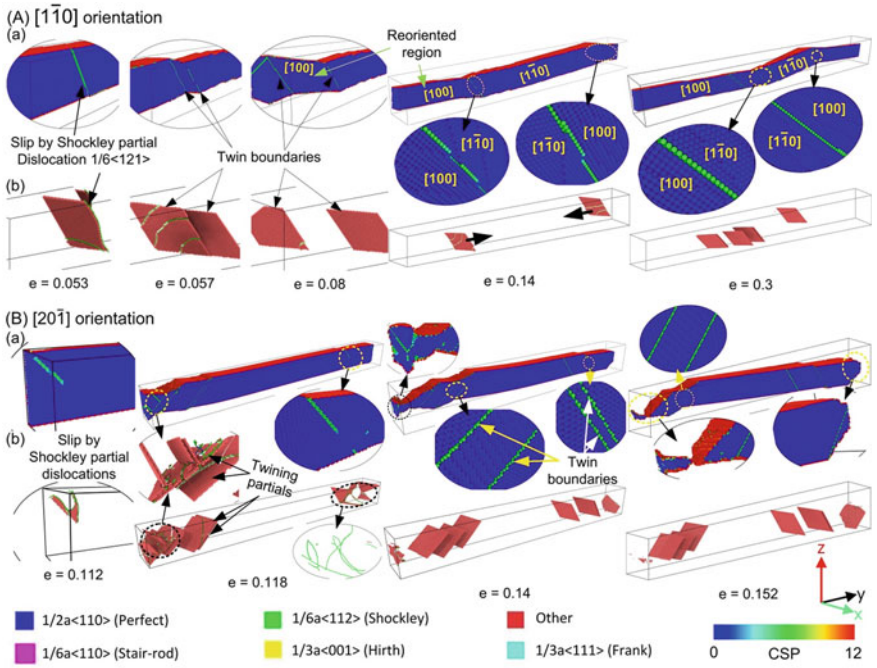

Fig. 3 Ni NW deformation behavior showing the CSP (**a**) and DXA analysis (**b**) at different strains during tensile loading in (**A**) [1–10] and (**B**) [20–1] orientations

3.2.2 [111] and [1–1–2] Oriented Ni NW

Figure 4 shows the CSP (a) and DXA analysis, (b) images at various strains during tensile loading of [111] (A) and [1–1–2] (B) oriented Ni NW. For [111] and [1–1–2] orientations, the plastic behavior is observed at the NW edge, corresponding to a strain, e = 0.075 and e = 0.076 with intrinsic stacking faults surrounded by Shockley partial dislocations. Similar deformation behavior is already shown by Zhan et al. [31] and Huang et al. [32] in their tensile deformation studies of Cu and Fe, Ni NWs using MD simulations. There is an increase in dislocation with strain in both [111] and [1–1–2] orientations after yield strain. This is because of slip activation on multiple slip systems and at strains e = 0.078 ([111]) and e = 0.08 ([1–1–2]), we can observe multiple intrinsic and extrinsic stacking faults. Dislocation densities of all oriented Ni NWs at yield strains is reported and explained in Sect. 3.3. The partials at the activated slip system start slipping on the close-packed {111} planes and their interaction results in the generation of Lomer-Cottrell (L-C) barriers [33] as shown in Fig. 4. Generally, these locks generate by the interaction of Shockley partials in different slip planes, which gives sessile stair rod dislocations as:

$$1/6\,[-21-1] + 1/6\,[1-21] \rightarrow 1/6\,[110] \tag{1}$$

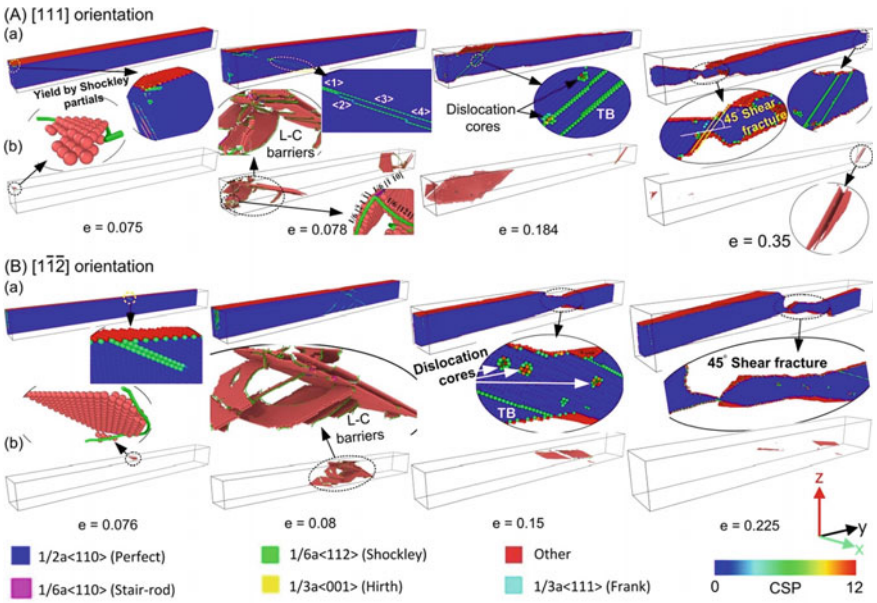

Fig. 4 Ni NW deformation behavior showing the CSP (**a**) and DXA analysis (**b**) at different strains during tensile loading in (**A**) [111] and (**B**) [1–1–2] orientations

The successive emission of partial dislocations after yield strain has transformed to a nano twin which is due to the twinning partial propagation along the initial stacking fault planes. The highlighted regions in the inset image (Fig. 4A(a) (e = 0.078)) are <1> intrinsic stacking fault; <2> extrinsic stacking fault; <3> twin formation and <4> widely separated twins. Straining the NW further, much wider twins can be observed in both [111] (e = 0.184) and [1–1–2] (e = 0.15) orientation and failed by 45° shear fracture.

3.3 Dislocation Density

Figure 5 display the dislocation densities (total and Shockley partial) of [1–10], [20–1], [111] and [1–1–2] orientated Ni NW at respective yield strains. Almost in all samples, the nucleated dislocations are Shockley partials, and they initiate the plastic deformation by slip followed by twinning. A minimum dislocation density (total) of 0.5×10^{15} m^{-2} observed in [111] and a maximum recorded in [1–10] orientation. In [34] the author studied the effect of void density on the dislocation and deformation behavior of a defective (voids) single crystal Ni of [100] orientation. The reported Shockley partial dislocation density is 50×10^{17} m^{-2} (single void), which is much higher than the present study is due to the different strain rate, orientation, sample defects, loading, and boundary conditions. In the present study dislocation density

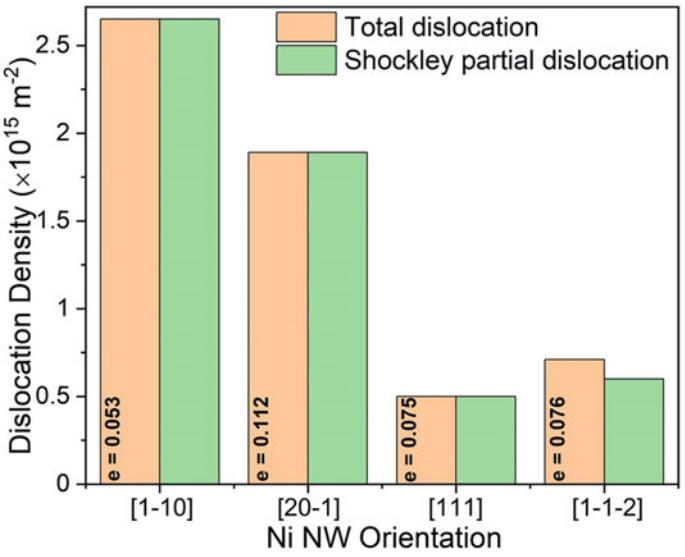

Fig. 5 Total and Shockley partial dislocation density of [1–10], [20–1], [111] and [1–1–2] oriented Ni NW at respective yield strains

increase with strain is observed in all NWs, with a significant percentage of Shockley partials.

4 Conclusions

The crystallographic orientation effect on the mechanical properties and deformation behavior of NW is studied. The tensile studies of Ni nanowires of [11–0], [20–1], [111], and [1–1–2] crystallographic orientations is carried out at 10 K temperature and deformation rate of 10^8 s^{-1}. The simulated results show that the orientation has a notable influence on NW deformation. It is noticed from the results that the NW of various orientations yields by Shockley partial dislocation with intrinsic stacking faults followed by twinning partials. The yield stress of [11–0], [20–1], [111], and [1–1–2] orientation are 9.5 GPa, 11.7 GPa, 17.2 GPa and 10.5 GPa respectively. During tensile loading, reorientation of Ni NW is noticed only in [1–10]. At yield strains, a minimum and maximum dislocation density (total) of 0.5×10^{15} m^{-2} and 2.65×10^{15} m^{-2} are observed in [111] and [1–10] oriented Ni NWs.

References

1. Peng C, Zhong Y, Lu Y, Narayanan S, Zhu T, Lou J (2013) Strain rate dependent mechanical properties in single crystal nickel nanowires. Appl Phys Lett 102:83102
2. Wang S, Shan Z, Huang H (2017) The mechanical properties of nanowires 1–24. https://doi.org/10.1002/advs.201600332
3. Sofiah AGN, Samykano M, Kadirgama K, Mohan RV, Lah NAC (2018) Metallic nanowires: mechanical properties–theory and experiment. Appl Mater Today 11:320–337. https://doi.org/10.1016/j.apmt.2018.03.004
4. Marson RL, Kuanr BK, Mishra SR, Camley RE, Celinski Z (2007) Nickel nanowires for planer microwave circuit applications and characterization. J Vac Sci Technol B Microelectron Nanom Struct 25:2619–2623. https://doi.org/10.1116/1.2801964
5. Park HS, Gall K, Zimmerman JA (2006) Deformation of FCC nanowires by twinning and slip. J Mech Phys Solids 54:1862–1881 (2006). https://doi.org/10.1016/j.jmps.2006.03.006.
6. Wen Y, Zhang Y, Wang Q, Zheng J, Zhu Z (2010) Orientation-dependent mechanical properties of Au nanowires under uniaxial loading 48:513–519. https://doi.org/10.1016/j.commatsci.2010.02.015
7. Sainath G, Choudhary BK (2016) Orientation dependent deformation behaviour of BCC iron nanowires. Comput Mater Sci 111:406–415. https://doi.org/10.1016/j.commatsci.2015.09.055
8. Rohith P, Sainath G, Choudhary BK (201) Computational condensed matter effect of orientation and mode of loading on deformation behaviour of Cu nanowires 17
9. Chang _18_Orientation and strain rate dependent tensile behavior of single crystal titanium NWs by MD.pdf, (n.d.)
10. Bin Ma_14_Effects of crystal orientation on tensile mech properties of single crystal tungsten NW.pdf, (n.d.)
11. Beretta_19_Orientation of Germanium NWs on Germanium and Silicon substrate for nanodevices.pdf, (n.d.)
12. Mendelev MI, Kramer MJ, Hao SG, Ho KM, Wang CZ (2012) Development of interatomic potentials appropriate for simulation of liquid and glass properties of nizr2 alloy. Philos Mag 92:4454–4469. https://doi.org/10.1080/14786435.2012.712220
13. Pei L, Lu C, Tieu K, Zhao X, Zhang L, Cheng K (2015) Ductile-to-brittle fracture transition in polycrystalline nickel under tensile hydrostatic stress. Comput Mater Sci 109:147–156. https://doi.org/10.1016/j.commatsci.2015.07.022
14. Rezaei R, Deng C, Tavakoli-Anbaran H, Shariati M (2016) Deformation twinning-mediated pseudoelasticity in metal–graphene nanolayered membrane. Philos Mag Lett 96:322–329. https://doi.org/10.1080/09500839.2016.1216195
15. Plimpton S (2011) LAMMPS: molecular dynamics simulator. http://lammps.sandia.gov/, Lammps. Sandia. Gov
16. Ruan Z, Wu W, Li N (2018) Effects of strain rate, temperature and grain size on the mechanical properties and microstructure evolutions of polycrystalline nickel nanowires: a molecular dynamics simulation. Wuhan Univ J Nat Sci 23:251–258. https://doi.org/10.1007/s11859-018-1318-x
17. Monk J, Farkas D (2007) Tension-compression asymmetry and size effects in nanocrystalline Ni nanowires. Philos Mag 87:2233–2244. https://doi.org/10.1080/14786430701361404
18. Zhang T, Zhou K, Chen ZQ (2015) Strain rate effect on plastic deformation of nanocrystalline copper investigated by molecular dynamics. Mater Sci Eng A 648:23–30. https://doi.org/10.1016/j.msea.2015.09.035
19. Wen YH, Zhu ZZ, Zhu RZ (2008) Molecular dynamics study of the mechanical behavior of nickel nanowire: Strain rate effects. Comput Mater Sci 41:553–560. https://doi.org/10.1016/j.commatsci.2007.05.012
20. Liu Y, Zhao J (2011) The size dependence of the mechanical properties and breaking behavior of metallic nanowires: a statistical description. Comput Mater Sci 50:1418–1424. https://doi.org/10.1016/j.commatsci.2010.11.026

21. Hoover WG (1985) Canonical dynamics: equilibrium phase-space distributions. Phys Rev A
22. Diao J, Gall K, Dunn ML, Zimmerman JA (2006) Atomistic simulations of the yielding of gold nanowires. Acta Mater 54:643–653. https://doi.org/10.1016/j.actamat.2005.10.008
23. Kelchner CL, Plimpton SJ, Hamilton JC (1998) Dislocation nucleation and defect structure during surface indentation. Phys Rev B 58:11085
24. Stukowski A, Bulatov VV, Arsenlis A (2012) Automated identification and indexing of dislocations in crystal interfaces. Model Simul Mater Sci Eng 20. https://doi.org/10.1088/0965-0393/20/8/085007
25. Stukowski A (2010) Visualization and analysis of atomistic simulation data with OVITO-the open visualization tool. Model Simul Mater Sci Eng 18. https://doi.org/10.1088/0965-0393/18/1/015012
26. Hertzberg RW (1983) Deformation and fracture mechanics of engineering materials. Wiley 1983:697
27. Setoodeh AR, Attariani H, Khosrownejad M (2008) Nickel nanowires under uniaxial loads: a molecular dynamics simulation study. Comput Mater Sci 44:378–384. https://doi.org/10.1016/j.commatsci.2008.03.035
28. Wen YH, Zhu ZZ, Shao GF, Zhu RZ (2005) The uniaxial tensile deformation of Ni nanowire: atomic-scale computer simulations. Phys E Low-Dimensional Syst Nanostruct 27:113–120. https://doi.org/10.1016/j.physe.2004.10.009
29. Wang WD, Yi CL, Fan KQ (2013) Molecular dynamics study on temperature and strain rate dependences of mechanical tensile properties of ultrathin nickel nanowires. Trans Nonferrous Met Soc China 23: 3353–3361. https://doi.org/10.1016/S1003-6326(13)62875-7
30. Sainath G, Choudhary BK, Jayakumar T (2015) Molecular dynamics simulation studies on the size dependent tensile deformation and fracture behaviour of body centred cubic iron nanowires. Comput Mater Sci 104:76–83. https://doi.org/10.1016/j.commatsci.2015.03.053
31. Zhan HF, Gu YT, Yan C, Feng XQ, Yarlagadda PKDV (2011) Numerical exploration of plastic deformation mechanisms of copper nanowires with surface defects. Comput Mater Sci 50:3425–3430. https://doi.org/10.1016/j.commatsci.2011.07.004
32. Huang D, Zhang Q, Guo Y (2006) Molecular dynamics simulation for axial tension process of α-Fe and Ni nano wires. Ordnance Mater Sci Eng 5:4
33. Zhang Y, Jiang S, Zhu X, Zhao Y (2016) A molecular dynamics study of intercrystalline crack propagation in nano-nickel bicrystal films with (0 1 0) twist boundary. Eng Fract Mech 168:147–159. https://doi.org/10.1016/j.engfracmech.2016.10.008
34. Yanqiu Zhang YZ, Jiang S, Zhu X (2017) Influence of void density on dislocation mechanisms of void shrinkage in nickel single crystal based on molecular dynamics simulation. Phys E 90:90–97

Biomass Derived Carbon for the Reduction of Iron Ore Pellets

Swapan Suman and Anand Mohan Yadav

Abstract In traditional iron making, coke acts as the reductant as well as source of energy for the reduction of iron ores to metallic iron. The coal that is used for making coke are of superior class and has low reserves, therefore an effort has been made to reduce the needs of coking coal with bio-char derived from biomass waste. Biochars can become a better option for replacing the premium quality of coking coal for reduction purpose in iron-steel industry. This study presented here comprises the comparative study for reduction of Iron ore pellets using different bio-char reductants i.e. Saw Dust Char (SDC), Eucalyptus Shell Char (ESC), Sugarcane Waste Char (SWC). Iron ore were subjected to thermal reduction with the help of biochars reductants and the iron ore was efficaciously abridged to metallic-iron stage. Reduction commenced at approximately 900 °C and was almost completed at 1050 °C. The obtained result shows the highest reduction percentage in Saw Dust Char (SDC). Along with Saw Dust Char, Eucalyptus Shell Char and Sugarcane Waste Char can also be used for iron ore reduction processes with a higher calorific value and lower activation energy.

Keywords Biomass · Saw dust char · Reduction · Iron-ore pellets

1 Introduction

Iron and steel making industry plays a vital role in any country's growth and economy. According to the WCA (World Coal Association), 60–70% of steel production in the world is dependent on metallurgical coal based process [1]. Global steel production

S. Suman (✉)
Department of Mechanical Engineering, Meerut Institute of Engineering and Technology, Meerut 250005, Uttar Pradesh, India
e-mail: swapan.suman@miet.ac.in

Department of Fuel and Mineral Engineering, IIT (ISM), Dhanbad 826004, Jharkhand, India

A. M. Yadav
Department of Chemical Engineering, Meerut Institute of Engineering and Technology, Meerut 250005, Uttar Pradesh, India

S. Pal et al. (eds.), *Processing and Characterization of Materials*, Springer Proceedings in Materials 13, https://doi.org/10.1007/978-981-16-3937-1_9

has sharply improved above 1869 million tons in the year 2018–19 [2]. As per Working Group of Coal and Lignite, the steel production in 2016–17 was 100–110 MT, and about 65–70 MT of coking coal was required for DRI process [3–4]. Of this, coking coal is approx. 33 billion tons and remaining coals, comprising of low grade coals including poor coking and non-coking coals (NCC), account for 252.40 billion tons [5]. Low volatile poor coking coals (LVCC) have sizeable share in the total content of low grade coals [6]. Thus continuous depletion of the coking coal reserves forces us to exploit the abundantly available poor quality coals in place of coking coal using appropriate technologies [7–8] or utilizing other alternative source of energy, preferably with the potential to replace fully or partially the coal and having relatively less concern of environmental contaminants and climate change.

In present scenario, the practice to meet the complete demand of scarce coking coal is through the import of coking coal and utilizing available low-grade non-coking-coal using suitable technologies. The production of direct reduced iron (DRI) can be considered as potential option for utilization of low-grade coal in the area of iron and steel making [7]. This is because the availability of natural gas, among the various flexible reductants (like low-grade non-coking coal, charcoal, natural gas, etc.), is very limited. India is the leading producer of direct reduced iron in the world [9]. But, due to the limitation imposed by Indian Government, search for the alternatives began, and direct reduction of iron ore using a reluctant resulted as an alternative to the steel scuffle.

In the context of alternative renewable sources of energy, biomass and its wastes can be a potential option [10, 11]. Beside, biomass and its wastes are considered to be cost effective and competitive with fossil fuel [12, 13], and have less content of N, S & NOx [10, 13, 14]. Biomass energy is expected to be a sustainable option to meet 50% demand of world's energy throughout the next century [12]. Bio-char known as a solid carbonaceous by-product of thermal conversion of biomass [15], and comparable with coal [16, 17] and has been established as CO_2 neutral as well [11].

In 2014, India produced nearly 350 million tons of biomass wastes [18], a potential source of renewable energy. Several studies have been made on the pyrolysis of different biomass wastes [19–20]**,** but these wastes could not secure their access into the iron-making process due to their non-plasticity behavior and lower calorific value. However, biomass wastes are adequate for energy conversion and can be improved, if it carbonized to char [21, 22]. Keeping the above in view, the aim of the present study was to evaluate the potential of utilization of different biomass reductants for metallurgical purposes.

2 Materials and Methods

2.1 Sample Collection and Preparation

Saw Dust of Gamhar tree (*Gmelinaarborea*), Eucalyptus Shell (ES) and Sugarcane Waste (SW) was collected from Meerut, Uttar Pradesh, India, which was further reduced to $-0.85 + 0.425$ mm size for carrying out conventional pyrolysis at 700 °C for one hour @10–12 °C/min heating rate. The resultant wood dust char (SDC), Eucalyptus Shell Char (ESC) and Sugarcane Waste Char (SWC) was taken for further study. Iron ore was collected from Chhattisgarh iron-mines, India. After analyzing the iron ore, it contains (54–58)% Fe, 1.46% Al_2O_3 and 0.58% SiO_2.

2.2 Methodology

Proximate and ultimate analyses and gross calorific/heating value (GCV). The 'proximate analysis' and 'ultimate analysis' of samples were conducted following standard procedures. For proximate analysis (ash, moisture, volatile matter and fixed carbon) of SD, ES and EW and corresponding chars SDC, ESC, and SWC, determined by ASTM (D1762-84) method [23, 24] and for ultimate analysis (C, H, N, S and O), ASTM E777, 778 and 775' standard process was followed using the C-H-N-S analyzer. The heating values of the studied samples were calculated using bomb calorimeter by following 'ASTM D4809-00' method [25, 26].

Pellet preparation. Disc pelletizer was used to prepare the iron ore pellet by adding 8–10% moisture in drop-wise manner without any binder. The size of the iron ore pellet was approximately 12–15 mm kept. Than the prepared pellets was dried in an oven at 108 °C for 4–5 h. These dried iron-ore pellets were fired at 1200 °C for 6 h using a high temperature muffle furnace. Finally, fired pellets were kept in desiccators for further reduction tests.

3 Results and Discussion

3.1 Proximate and Ultimate Analyses and Gross Calorific Value (GCV)

The values of proximate and ultimate analyses, calorific value and plastic properties of the samples SD, ES, SW, SDC, ESC and SWC are shown in Table 1.

The proximate and ultimate analysis of selected samples are carried out on as recieved (ar) basis. The content of VM in SD, ES and SW are 71.63, 66.54 and 72.37% respectively.

Table 1 Proximate, ultimate, gross calorific value and plastic properties of the samples

Characterization	Samples					
	SD	SDC	ES	ESC	SW	SWC
M%	6.10	2.90	8.59	4.22	4.59	7.34
Ash%	4.02	10.08	10.04	21.65	4.73	14.44
VM%	71.63	15.96	66.54	6.67	72.37	5.63
FC%	18.27	71.14	14.83	68.00	18.31	72.59
N%	0.50	0.57	0.31	0.87	0.50	0.89
C%	58.92	78.40	39.17	71.05	58.93	79.85
H%	7.38	1.36	4.73	1.10	5.34	3.17
O%	31.79	19.45	55.65	28.10	35.07	16.02
S%	0.05	0.22	0.14	0.12	0.16	0.07
GCV(MJ/Kg)	18.33	20.80	15.24	19.16	18.43	20.94

* All parameters are on as received basis

From ultimate analysis it can be perceived that the high carbon contents were found in SD, ES and SW (58.92, 39.17 and 58.93%, respectively) with less content of nitrogen (0.50, 0.31 and 0.50%, respectively), Hydrogen (7.38, 4.73 and 5.34%) and sulphur (0.05, 0.14 and 0.16%). The value of GCV in SD, ES and SW are 18.33, 15.24 and 18.43 MJ/kg respectively.

Table 1 also demonstrate the proximate and ultimate analysis of obtained biochars from SD, ES and SW. It can be perceived from the values presented in Table 1 that the volatile matter content diminishes. Although, the nitrogen and sulphur content were low in the studied samples. The carbon contents of SDC, ESC and SWC are 78.40, 71.05 and 79.85%. The presence of carbon, hydrogen and oxygen in biomass participate in char formation and it cause for higher heating value of the samples [27, 28]. Heating values of all the obtained biochar are 20.80, 19.16 and 20.94 MJ/Kg.

Hence, an attempt can be made to find out the potential of these wastes for iron ore reduction or for metallurgical purposes using appropriate technologies (like coke making after pre-treatments or DRI) [3, 29, 8, 28–30]. The proximate and ultimate analyses and GCV of SDC, ESC and SWC are comparable with the coals [12, 13, 16, 17] and rather with relatively less content of N, S, and NOx [14].

3.2 Reduction Study

In the current investigation, an effort has been made to study the coordinated effects of the reduction time, temperature, and ash content of the reductants on the rate of reduction of iron-ore pellets. The present work goal is to compare the reduction potential of SDC, ESC and SWC for reduction of iron ore pellets. The experiments were conceded out at reduction temperatures of 1173 K, 1223 K, 1273 K and 1323 K

at a heating rate of 15–30 °C/min for a varying reduction time period of 15, 30, 45, 60, and 75 min. Natures of the curves for all the reductants are shown in Fig. 1. The rate of reduction of reduced pellets is calculated using the formula:

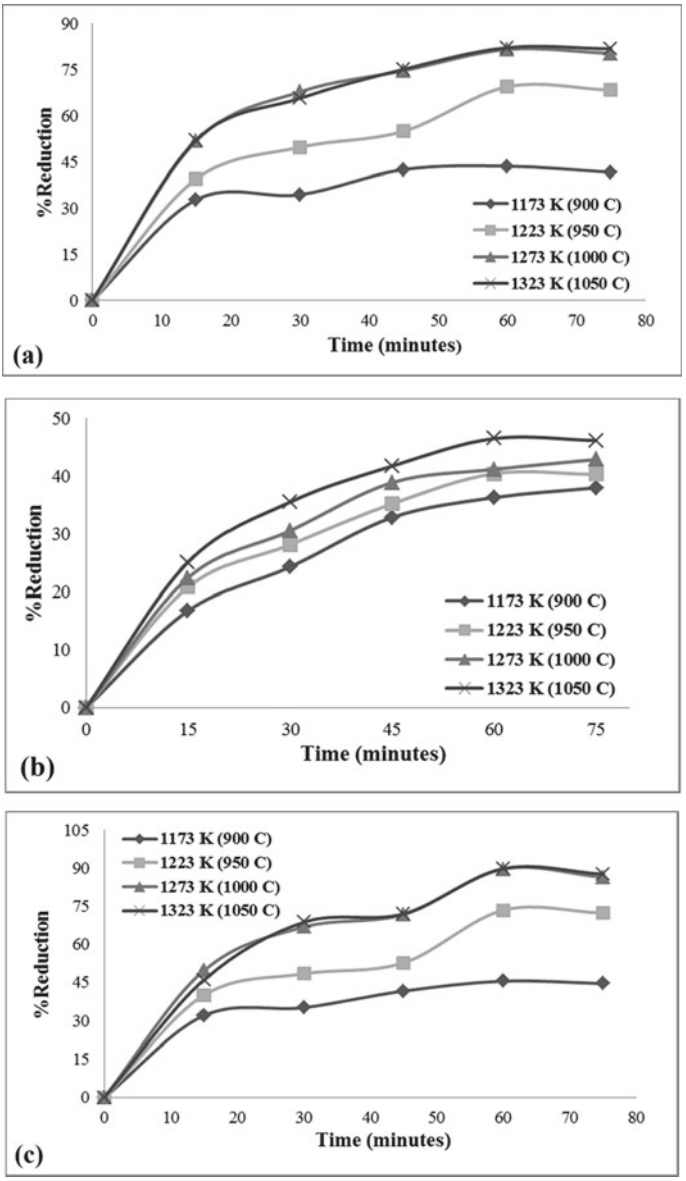

Fig. 1 **a** Plot between Reduction % and time for iron ore pellets using SDC. **b** Plot between Reduction % and time for iron ore pellets using ESC. **c** Plot between Reduction % and time for iron ore pellets using SWC

$$\text{Degree of reduction} = \frac{\text{Weight loss}}{\text{Total weight of removable oxygen in iron oxide}} \times 100 \quad (1)$$

From the Fig. 1a–c, it can be seen that the nature of the curves is almost similar at all the four reduction temperatures for all the reductants, and it can be perceived that the rate of reduction increases with the increase in time and temperature. Extreme reduction reached to the level of 89% at 1323 K in 60 min in case of SDC whereas in case of ESC and SWC, corresponding figures were about 45%and 85%, respectively in the same condition of reduction process.

3.3 Kinetics Study

The kinetic analysis is essential for the estimation and better understanding of thermal conversion. The diffusion control model was used to determine the reduction performance of iron-ore pellets with different reducing agent. According to Szekely [31], the diffusion control model is expressed as: $1–2/3R–(1–R)^{2/2} = K_p t$. where, R is the degree of reduction, K_p is the reaction rate constant, and t is time (minutes).

In each reductant case, the value of K_p at each studied temperature was determined by plotting graph between $1–2/3R–(1–R)^{2/3}$ and time t which is shown in Fig. 2a–c. Arrhenius equation was used to calculate the activation energy which is expressed as $\ln K_p = \ln A - E/RT$ which is shown in Fig. 3a–c,

where, A = Arrhenius constant;

E = Activation energy;

R = Universal gas constant;

T = Temperature.

From the values of activation energy obtained (Table 2), it can be seen that SWC is having lowest activation energy followed by ESC and SWC. This may be because of low volatility and low carbon content in SWC which starts quick reaction to promote reduction of iron ore pellets even at lower time (15 min) and temperature (1173 K).

Overall SDC, ESC and SWC are having less activation energy; this may be because of its high calorific value, high carbon content and lower ash content. In this way these biochars can play an imperative role as a reductant for iron ore and can be equally used as a reductant with a less activation energy.

4 Conclusions

The studied bio-char samples were efficaciously employed for the reduction of iron ore pellets. The time and temperature using in reduction process have given a momentous influence on the reduction%. The process at high temperature reduction is controlled by using diffusion reaction mechanism. Because of occurrence of

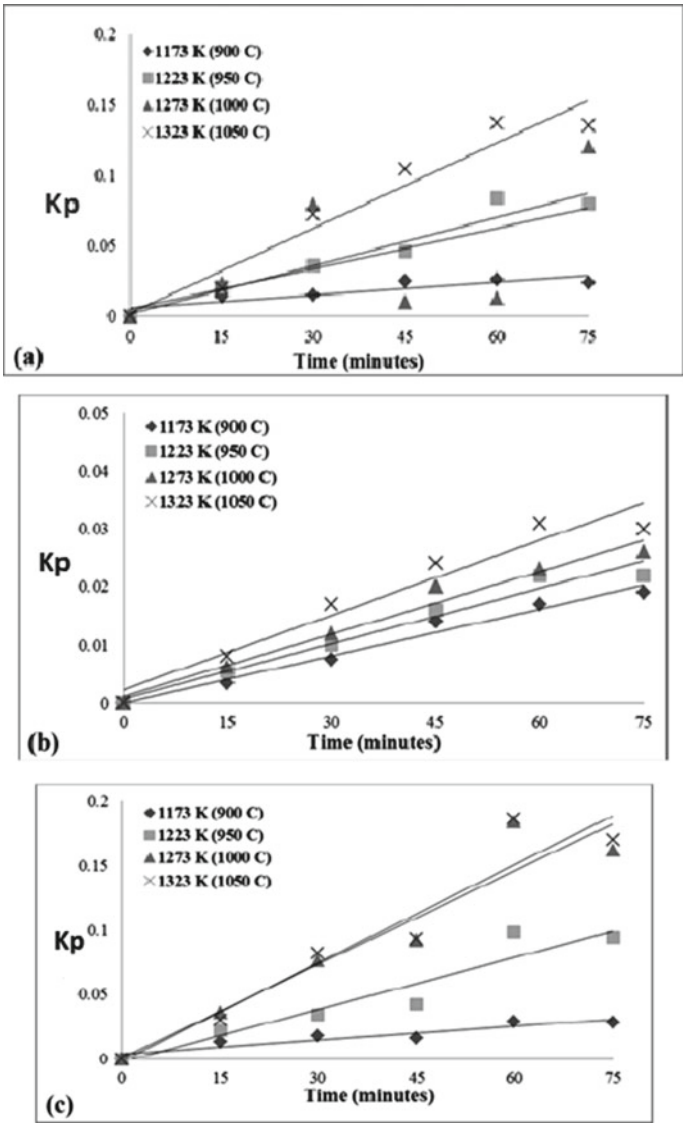

Fig. 2 **a** Plot of Kp against time t for each reductant SDC. **b** Plot of Kp against time t for each reductant ESC. **c** Plot of Kp against time t for each reductant SWC

adequate quantity of biochar and also as carbon monoxide, that is main source of reducing agent and it is steady at 1273 K.

Proper utilization of other biomass wastes can also be done in this way; instead of calling them as wastes we can designate them as biomass by product. Finally they can be used for Iron-Steel industries.

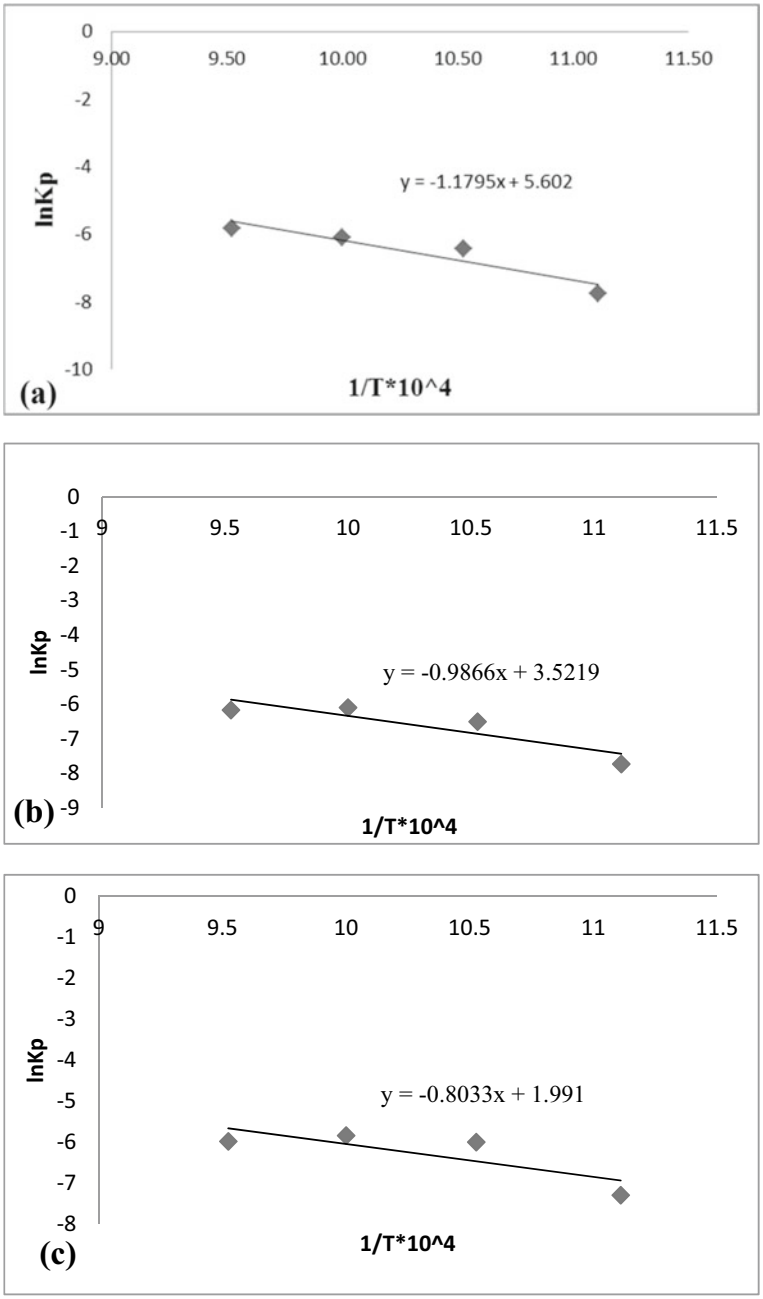

Fig. 3 Plot of Kp against 1/T for each reductant **a** SDC, **b** ESC and **c** SWC

Table 2 Activation energy of SDC, ESC and SWC

Reductants	Activation energy (KJ/mole)
SDC	98.02
ESC	82.02
SWC	66.78

References

1. http://www.worldcoal.org/sites/default/files/coal_facts_2013(11_09_2019).pdf
2. World Steel Association (2019) World steel in figures © World Steel Association. https://www.worldsteel.org/en/dam/jcr:96d7a585-e6b2-4d63-b9434cd9ab621a91/World%2520Steel%2520in%2520Figures%25202019.pdf.
3. Mousa E, Wang C, Riesbeck J, Larsson M (2016) Biomass applications in iron and steel industry: an overview of challenges and opportunities. Renew Sustain Energy Rev 65:1247–1266
4. http://www.genrl-trading.com/Industrycoal.html
5. www.coal.nic.in/sites/upload_files/coal/files/coalupload/wp101014.pdf
6. Sengupta S (2015) Raw material for steel industry. Steel World 42–52
7. Prasad HN, Singh BK, Dhillon AS (2011) Ironmaking Steelmaking 28:312–332
8. Gautam S (2015) Assessment of low volatile poor caking Indian coal for coke making. Int J Coal Preparation Utilization. https://doi.org/10.1080/19392699.2015.1123697
9. Gautam S (2016) Effect of washing and stamping on coke making of a low grade Indian coal: correlation between various properties. Ironmaking Steelmaking. https://doi.org/10.1080/03019233.2016.1217115
10. Patnaik NK (2011) Future of DRI industry and availability of coal. SIMA, DRI 8–11
11. Brassard P, Palacios JH, Godbout S, Bussieres D, Lagace R, Larouche JP, Pelletier P (2014) Comparison of the gaseous and particulate matter emissions from the combustion of agricultural and forest biomasses. Biores Technol 155:300–306
12. Tinwala F, Mohanty P, Parmar S, Patel A, Pant KK (2015) Intermediate pyrolysis of agro-industrial biomasses in bench-scale pyrolyser: product yields and its characterization. Biores Technol 188:258–264
13. Energy for cooking in developing countries (2006) World energy outlook. Int Energy Agency (IEA) 419–445. https://www.iea.org/publications/freepublications/publication/cooking.pdf. Accessed 23 May 16
14. McKendry P (2002) Energy production from biomass (part1): overview of biomass. Biores Technol 83(1):37–46
15. Gonzalez JF, Gonzalez- CM, Ramiro A, Gonzalez J, Sabio E, Ganan J, Rodrıgguez M (2004) Combustion optimization of biomass residue pellets for domestic heating with a mural boiler. Biomass Bioenerg 27(2):145–154
16. Masek O, Budarin V, Gronnow M, Crombie K, Brownsort P, Fitzpatrick E, Hurst P (2013) Microwave and slow pyrolysis biochar—comparison of physical and functional properties. J Anal Appl Pyrolysis 100:41–48
17. Fu P, Hu S, Xiang J, Sun L, Su S, Wang J (2012) Evaluation of the porous structure development of chars from pyrolysis of rice straw: effects of pyrolysis temperature and heating rate. J Anal Appl Pyrolysis 98:177–183
18. Mohanty P, Pant KK, Naik SN, Parikh J, Hornung A, Sahu JN (2014) Synthesis of green fuels from biogenic waste through thermochemical route—the role of heterogeneous catalyst: a review. Renew Sustain Energy Rev 38:131–153
19. Pallavi HV, Srikanta SS, Kiran BM, Vyshnavi DR, Ashwin CA (2013). J Eng Sci Comp Sci Eng Tech 2:160–172
20. Yargicoglu EN, Sadasivam BY, Reddy KR, Spokas K (2014) Physical and chemical characterization of waste wood derived biochars. Waste Manage 36:256–268

21. Lee Y, Park J, Ryu C, Gang KS, Yang W, Park YK, Jung J, Hyun S (2013) Comparison of biochar properties from biomass residues produced by slow pyrolysis at 500 °C. Bioreso Techno 148:196–201
22. Saidur R, Abdelaziz AE, Demirbas A, Hossain MS, Mekhilef S (2011) A review on biomass as a fuel for boilers. Renew Sustain Energy Rev 15:2262–2289
23. Vladimir S (2006) Iron ore reduction using sawdust: experimental analysis and kinetic modelling. Renew Energy 31:1892–1905
24. Demirbas A (2004) J Anal Appl Pyrol 72:243–248
25. Gupta OP (1990) Fuels, furnaces and refractory, 1st edn. Khanna Publication, Delhi
26. Gautam S, Yadav RS, Suresh N (2015) Evaluation of the characteristics of as-received and washed low grade Indian coals for their industrial applications. Energy Sources Part A Recov Utilization, Environ Effects 37(19):2138–2149. https://doi.org/10.1080/15567036.2010.53151
27. Das S, Sharma S, Choudhury R (2002) Energy 27:405–414
28. Kumar V, Saxena VK (2014) Int J Comput Eng Res 04:39–57
29. Gautam S (2010) Ph.D thesis. Entitled "Studies on Low/Medium Volatile Coking Coals for their suitability in Iron and Steel Industries". Indian School of Mines Dhanbad, Jharkhand
30. Kuyumcu HZ (2014) Sven Sander, Stamped and pressed coal cakes for carbonisation in by-product and heat-recovery coke ovens. Fuel 121:48–56
31. Szekely J, Sohn HY, Evens JW (1967) Gas-solid reactions. Academic Press, New York
32. Gautam S (2010) Assessment of low-volatile poor caking Indian coal for coke making. Int J Coal Prep Util. https://doi.org/10.1080/19392699.2015.1123697
33. Mohanty P, Nanda S, Pant KK, Naik S, Kozinski J, Dalai AK (2013) Evaluation of the physio-chemical development of biochars obtained from pyrolysis of wheat straw, timothy grass and pinewood: effects of heating rate. J Anal Appl Pyrolysis 104:485–493
34. Prasad AN, Rao PVT, Poddar NN, Charterjee A (1992) Selection of coals for coke making by classical top charging and stamp charging. Coke making Congress 2:231–235
35. Chatterjee A, Prasad HN (1994) Response of high ash Indian Coals to pre-carbonization techniques. Fuel 88(67):1417–1427
36. TISCO (Tata Iron and Steel Company) (1995) Evaluation of coking characteristics of coal blends used at Durgapur Steel Plant by stamp charging and conventional top charging. Report of R&D Division, TISCO, May
37. CFRI (Central Fuel Research Institute) (1996) Golden jubilee monograph. In: Basu TK, Mitra PK, Chowdhury SG, Roy J, Chowdhury A (eds) Coal carbonization
38. Krishnan SH, Dash PS, Guha M, Kumar D, Deshpande DP (2004) Application of binder in stamp charge coke making. ISIJ Int 44:1150
39. Dash PS, Krishnan SH, Sharma R, Banerjee PK, Haldar SK (2005) Laboratory scale investigation to improve the productivity of stamp charge coke oven through optimization of bulk density of coal cake. ISIJ Int 45:1577–1586
40. Tiwary HP, Banerjee PK, Saxena VK, Haldar SK (2014) Effect of Indian coking coal on coal quality in non-recovery Stamp charged coke oven. J Iron Steel Res Int 21:673–678

Extraction of Eu (III) in Presence of Lactic Acid Using D2EHPA as Organic Phase Extractant

Gouri Sankar Mohapatra, Nilam Swain, Badrinarayan Rout, Sanghamitra Pradhan, and Sujata Mishra

Abstract Europium is a valuable lanthanide element which is mainly recognised for its use in making fluorescent lamps and TV screens. Efforts are going on to recover Eu effectively from waste where liquid–liquid extraction appears as crucial separation technique to separate an element from waste. In this paper, solvent extraction of Eu (III) from aqueous HCl medium with acidic extractant D2EHPA in kerosene has been studied. Lactic acid has been added to act as a complexant for Eu(III) in the process. The effect of variation of experimental parameters like lactic acid concentration, D2EHPA molarity on extraction of Eu(III) as well as thermodynamics has been analyzed. The percent extraction of Eu (III) decreases from 75 to 60% when concentration of lactic acid is increased from 1.2 to 2 M. By increasing the concentration of D2EHPA, percent extraction increased. The change in enthalpy was found to be positive which indicates the system is endothermic in nature. Under the influence of temperature variation, highest 78.46% of Eu (III) was extracted at 325 K using 0.1 M D2EHPA. Extraction of 0.001 M Eu (III) in 0.1 M lactic acid with variation of D2EHPA concentration gives cent percent results. The optimum condition was obtained with maximum 91.42% extraction of 0.01 M Eu (III) in 1 M lactic acid using 0.2 M DEHPA in kerosene.

Keywords Eu (III) · Lactic acid · D2EHPA

1 Introduction

Rare earth elements (REEs) include fifteen lanthanides and two transition elements which are present in their ores in a dispersed manner due to their geochemical properties. This makes their mining expensive. Economically operable mines of these elements are limited which is the main reason of these are being called as rare earth elements [1, 2]. REEs do not occur as individual element as gold (Au), copper (Cu) and silver (Ag). They occur together in various ores as minor or major constituents.

G. S. Mohapatra · N. Swain · B. Rout · S. Pradhan · S. Mishra (✉)
Department of Chemistry, Institute of Technical Education and Research (FET), Siksha 'O' Anusandhan Deemed to be University, Khandagiri Square, Bhubaneswar, Odisha 751030, India
e-mail: sujatamishra@soa.ac.in

S. Pal et al. (eds.), *Processing and Characterization of Materials*, Springer Proceedings in Materials 13, https://doi.org/10.1007/978-981-16-3937-1_10

Some main sources of rare earths are bastnaesite, monazite, loparite and lateritic ion adsorption clays [3, 4]. REEs are widely used in lot of devices which are used in daily life. Rare earths are used in computer memory, DVDs, rechargeable batteries, cell phone, magnets, head or ear phones, catalytic converters, fluorescent lightings, cameras, various military weapons, armoured vehicles etc. REE are also used as catalysts, phosphors, and polishing compounds [5].

Europium is a lanthanide rare earth element which has significant use as a doping agent in red phosphor in television screens and in fluorescent lamps. It has two isotopes ^{151}Eu, ^{153}Eu and the most common oxidation states are +2, +3. The reactivity of Eu is maximum among all rare earths. The crustal abundance of europium is 0.3 ppm. Eu does not occur free in nature. Along with other lanthanides, it is found in the minerals like monazite and bastnaesite. Pure europium can be obtained from these minerals. Top three countries produce europium are China, Russia and Malaysia [6]. Pramanik et al., in their research paper showed the elemental composition of the phosphor powder resulted from fluorescent lamp waste. The analysis shows that the fluorescent lamps contains 1.6 wt% of europium. The worldwide need for REEs is increasing at a rate of 3.7–8.6% per annum [8]. According to a report produced by Indian Ministry of Mines, nearly 486 million units of fluorescent lamps were manufactured in the year 2010. The amount of rare earth oxides used in those fluorescent lamps was estimated to be 2000 t [7]. All these fluorescent lamps are dumped in garbage when their life cycle is complete. This leads to the permanent dissipation of India's mineral resources. The skillful recycling and reuse of these dumped rare earth oxides can help in decreasing the exploitation of primary rare earth resources and fulfilling the demand of the market up to large extent.

Several separation techniques are used to separate the rare earth elements from their ores as well as from the wastes e.g., electronic wastes, lamp phosphor, permanent magnets, hard disk drives, used batteries etc. which contain rare earth elements. Solvent extraction technique is recognized as an excellent separation technique because of its ease, simplicity, cost effectiveness and wide scope. D2EHPA or di-(2-ethylhexyl) phosphoric acid) is a colourless acidic extracting agent. It shows high percent extraction in low acid medium This can be explained using law of mass action. DEHPA is majorly in dimer form when reacts with rare earths [9–11]. Mishra et al., carried out extraction of Eu (III) using two extractants D2EHPA and Cyphos IL 104 (trihexyl(tetradecyl) phosphonium bis (2,4,4-trimethylpentyl) phosphinate). It has been found that separation of Y(III)/Eu (III) is better with D2EHPA than that using Cyphos IL 104 [12]. Mishra et al. stated that separation factor was 60.6 using 0.1 M D2EHPA at pH 2.56 [13]. Awwad et al. reported that percentage extraction of Eu (III) employing extractant CYANEX 921 (93% 0f tri-n-octylphosphine oxide).Percent extraction of Eu was nearly same for diluents like toluene, n-hexane, cyclohexane and kerosene. The extraction of Eu (III) increased with increase in pH.Percentage of extraction was maximum after 5 min at pH 3.0 [14]. Pradhan et al. investigated the solvent extraction of Eu (III) with variation of contact time, extractant, nitrate concentrations and temperature [15].

The present study focused on the solvent extraction of Eu (III) from hydrochloric acid medium using D2EHPA diluted with kerosene. The effect of variation of experimental variables like shaking time, lactic acid concentration, pH variation,D2EHPA concentration, temperature on percent extraction has been studied. Various conditions were optimised in order to recover maximum Eu (III).

2 Experimental

2.1 Materials

Europium oxide [Eu_2O_3] powder supplied by Loba Chemie Pvt. Ltd., Mumbai, India, 99.9% AR was used. D2EHPA or di-(2-ethylhexyl) phosphoric acid procured from Merck Specialities Pvt. Ltd., Mumbai, India was used as extractant. Kerosene was used as organic phase diluent. Lactic acid, 90% extra pure used in this present investigation as complexing agent was supplied by Merck Specialities Private Limited. All are of AR grade chemicals. Xylene, toluene and benzene were acquired from Merck.

Instruments used in this study. Citizen (CY320C) digital balance with accuracy ±0.001 g was used for weighing chemicals. Organic phase and aqueous phase were mixed properly with the help of magnetic stirrer (Spinot model MC- 02). In raffinate, Eu (III) content was measured by Systronics UV–Visible spectrophotometer (Model no. 2202).

2.2 Methods

The aqueous metal solution of Eu (III) was made on dissolution of requisite amount of its oxide in concentrated HCl followed by dilution to 50 mL using distilled water. Then, an aqueous phase solution was prepared by mixing europium solution and lactic acid and then diluting to the desired concentration. Organic phase solution was prepared from D2EHPA in kerosene of desired concentration. Experiments were performed in separating funnel by mixing equal volumes of aqueous phase and organic phase for five minutes. This was enough to reach the equilibrium.The raffinate was analysed to estimate Eu (III) content spectrophotometrically using chromophoric reagent Arsenazo III.

2.3 Data Analysis

Solvent extraction is the separation technique which deals with the measurement of equilibrium concentration of Eu (III) in the aqueous phase and the organic phase. The extent of extraction has been estimated by various terms are discussed briefly. Distribution ratio (D) is given as

$$D = {}^{[Eu(III)]_{org}}\!/_{[Eu(III)]_{aq}} \tag{1}$$

where $[Eu(III)]_{organic}$ represents equilibrium concentration of Eu(III) after extraction and $[Eu(III)]_{aqueous}$ represents equilibrium Eu(III) concentration in the raffinate after extraction.

The percentage of extraction (%E) measures how much metal ions are transferred to the organic extract from the aqueous feed. The percent extraction is given as,

$$\%E = {}^{100D}\!\Big/\!\left[D + \tfrac{V_{aq}}{V_{org}}\right] \tag{2}$$

where, V_{aq} and V_{org} are the volumes of the aqueous and organic phases, respectively. In this case, $V_{aq} = V_{org.}$, therefore,

$$\%E = {}^{100D}\!/_{[D+1]} \tag{3}$$

3 Results and Discussion

3.1 Influence of Shaking Time

The shaking time variation was done by agitating equal volumes of aqueous feed containing 0.001M Eu (III) in 0.1M lactic acid and organic phase with 0.1M D2EHPA in kerosene at pH 3. This has been examined to know the minimum time period needed for establishment of equilibrium in this case.Cent percent extraction was resulted in each case when variation in the shaking time was from 5 to 20 min.After five minutes further increase in time had no pronounced impact on the extraction percentage. This may be owing to the strong affinity of Eu(III) for the organophosphorous extractant, D2EHPA and very short period of time was adequate to attain equilibrium extraction condition.For subsequent experiments five minutes shaking time was maintained.

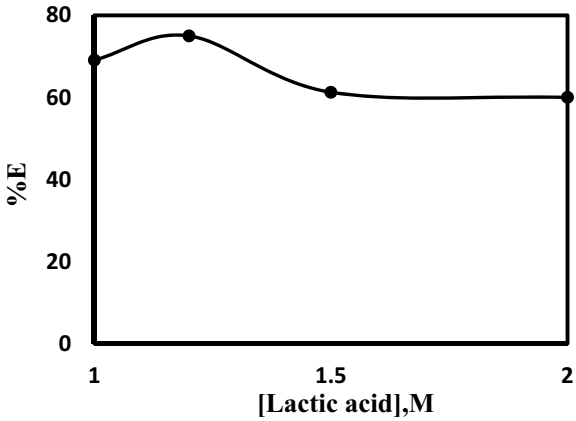

Fig. 1 Plot of %E versus [Lactic acid], M; Aqueous phase: 0.01 M Eu (III) and [Hlac];1 /1.2 / 1.5 / 2M at pH 2; Organic phase: 0.1 M D2EHPA in kerosene, 298 K

3.2 Variation of Lactic Acid and Hydrogen Ion Concentration

As lactic acid has been utilized as a complexing agent in the aqueous feed, the effect of alteration of lactic acid concentration has been undertaken. The extraction of Eu (III) (0.01 M) at pH 2 by 0.1 M D2EHPA in kerosene has been carried out. The pH of the raffinate with lactic acid concentration 1, 1.2, 1.5, and 2 M was found to be 1.9, 1.98, 1.98, and 2 respectively.

This shows the drop-off in percentage of extraction of Eu(III) with rise in the lactic acid molarity (see Fig. 1). The drop-off in percent extraction is because of the constitution of strong Eu- lactate bond at high concentration of lactic acid, due to which the Eu could not go to the extractant phase. The pH data shows that pH of the raffinate is less than aqueous feed pH ensuring the hydrogen ion exchange process with the metal ion.

The extraction of 0.01 M Eu(IIII) was carried out from 0.1 M lactic acid solution,varying aqueous pH from 2 to 3 using 0.1 M D2EHPA as extractant. It was seen that with increase in initial aqueous phase pH from 2 to 3, the %E of Eu(III) enhances from 51.4 to 75.2 indicating release of hydrogen ion in the process of extraction.

3.3 Variation of D2EHPA Concentration

The concentration of an extractant plays an important role in the extraction process since it makes bond with the metal ion and separates it from the aqueous phase. In this context, D2EHPA molarity has been varied from 0.05 to 0.2 M. The extraction of 0.01 M Eu (III) in 1.5 M lactic acid at pH 2 using three different concentration of D2EHPA has been carried out.

Figure 2 shows that with rise in concentration of D2EHPA, percentage extraction increases. Thus, at pH 2 of aqueous phase, the extraction of Eu(III) gets enhanced with

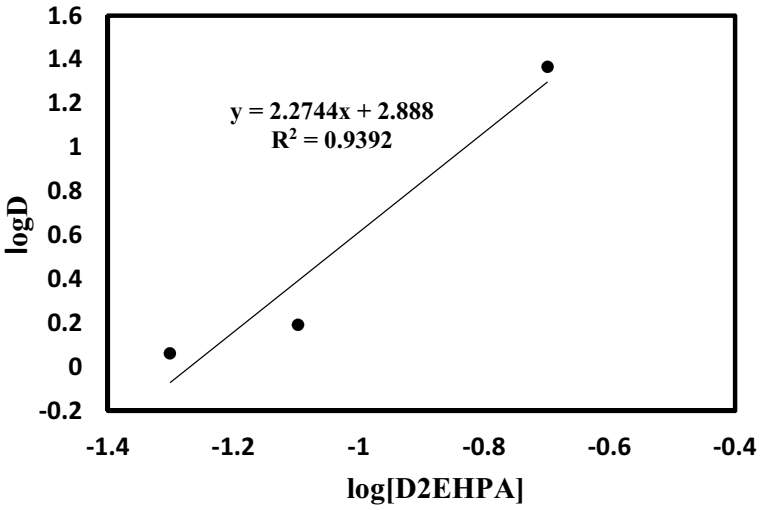

Fig. 2 Variation of log D with log[D2EHPA]: Aqueous Feed: 0.01 M Eu (III) + 1.5 M [Hlac]M, pH 2; Organic extract: 0.05 / 0.08 / 0.2 M DEHPA in kerosene, 298 K

increase in molarity of the extractant. Based on slope analysis, it is confirmed that two moieties of D2EHPA are complexed with Eu (III) in the extraction process. The involvement of two D2EHPA in extraction process is evident from the value of slope (2.2) in Fig. 2. Dimerisation of D2EHPA in organic phase depends on the polarity of solvent [16, 17].The association between D2EHPA molecules to form dimer gets enhanced in non polar diluent such as kerosene.In case of D2EHPA diluted with polar solvents,the probability of dimer formation decreases due to high dielectric constant of polar solvent. The mechanism of formation of dimer has been illustrated in Fig. 3. Eu(III) is extracted by D2EHPA through cation exchange mechanism[18, 19].

The probable mechanism of extraction as evident from above slope value is represented as

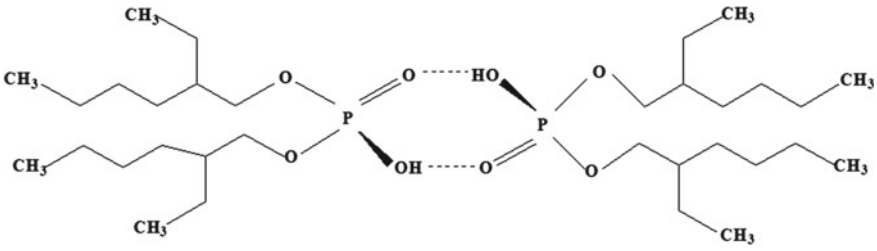

Fig. 3 Representation of dimer of D2EHPA

Table 1 Percentage of extraction of Eu (III) in 0.1 M lactic acid using different D2EHPA concentration

[D2EHPA], M	%E
0.02	100
0.04	100
0.05	100
0.06	100

Table 2 Percent extraction of Eu (III) in 1 M lactic acid using different D2EHPA concentration

[D2EHPA], M	D	%E
0.1	3.038	75.23
0.2	10.66	91.42

$$Eu^{3+}(aq) + 2H_2R_2(org) \rightarrow EuR_3.RH(org) + 3H^+(aq) \quad (4)$$

The extraction of 0.001 M Eu (III) in 0.1 M lactic acid using 4 different concentrations of D2EHPA in kerosene has been carried out. After the analysis 100% extraction was observed in each case. The pH of the aqueous phase was maintained at 3 initially. In each case, cent percent extraction was achieved (Table 1).

The extraction of 0.01 M Eu (III) at pH 3 in 1 M lactic acid using 2 different concentrations of D2EHPA in kerosene has been carried out. The shaking time was 5 min. After equilibration the pH of the raffinate was 2.97. From the data (Table 2), this is clear that percentage of extraction rises with enhancement in D2EHPA concentration. High extractant concentration favours higher percent extraction.

3.4 Variation of Temperature

The study of thermodynamics has a great significance in liquid–liquid extraction technique.Solvent extraction systems furnish understanding about the metal ion complexation in the aqueous solution.The solvation is stronger in aqueous solution as compared to that in the organic phase. Interaction of metal ions with the extractants are associated with enthalpy and entropy changes. The influence of temperature variation on the %E of Eu(III) has been analyzed. The extraction of 0.01 M Eu (III) in 1.5 M lactic acid at pH 2 using 0.1 M D2EHPA in kerosene has been carried out. Four different experiments were done by varying the temperature of the system at 298, 305, 320, and 325 K, respectively. The pH of the raffinate was found to be 1.98, 1.98, 1.99, and 1.99 when temperature of the system was maintained at 298, 305, 320, and 325 K, respectively.It has been observed that temperature increases, percent extraction increases. The standard enthalpy change, ΔH° estimated from the slope of of the linear plot of logD against 1000/T (Fig. 4) and standard entropy change,ΔS° determined from the intercept on the basis of van't Hoff relation (Eq. 5) [12] and found as $\Delta H^\circ = 18.725$ kJ mol^{-1} and $\Delta S^\circ = 67.237$ JK^{-1} mol^{-1},respectively.

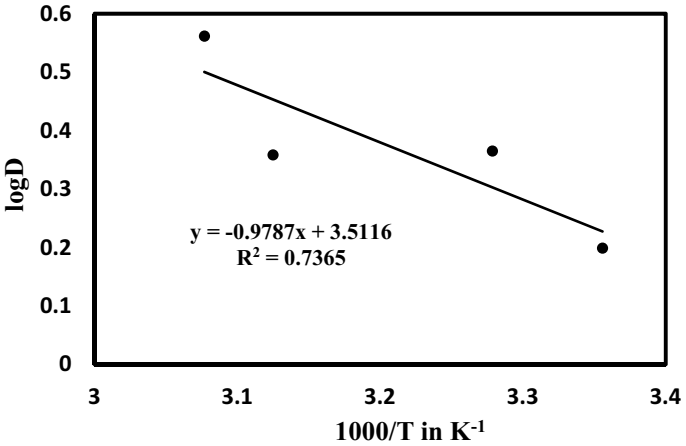

Fig. 4 Variation of log D with 1000/T in $K^{-1;}$ Aqueous phase: 0.01 M Eu (III) + [Hlac] M = 1.5 M, pH 2;Organic phase: 0.1 M D2EHPA in kerosene, T = 298 / 305 / 320 / 325 K

Positive enthalpy change indicates that the system is endothermic in nature and positive entropy change indicated formation of Eu (III)-D2EHPA inner sphere complex releasing some molecules of water from hydration sphere of metal.

$$\log D = -\frac{(\Delta H^{\circ})}{2.303RT} + \frac{(\Delta S^{\circ})}{2.303\ R} \tag{5}$$

4 Conclusions

From the experiments, it is concluded that percentage of extraction of Eu (III) enhances with rise in D2EHPA molarity. With increase in temperature, the percent extraction of the system increases. In lactic acid concentration variation, it was detected that the percent extraction increases up to 1.2 M lactic acid concentration and then reduced with further rise in lactic acid molarity. In temperature variation experiment with 0.1 M D2EHPA, highest 78.46% of Eu (III) was extracted at 52 °C. Extraction of 0.001 M Eu (III) from aqueous phase comprise of 0.1 M lactic acid, using different D2EHPA concentration gives cent percent results. The change in standard enthalpy (ΔH°) of the system is positive, so the system is endothermic in nature. The optimum condition was obtained with maximum 91.42% extraction of 0.01 M Eu (III) in 1 M lactic acid using 0.2 M DEHPA in kerosene.This could be instrumental if applicable to recover Eu from phosphor waste.

Acknowledgements The authors are grateful to the Siksha 'O' Anusandhan Deemed to be University authorities for providing the facilities and support to undertake this investigation.

References

1. Ismail NA, Aziz MAA, Yunus MYM, Hisyam A (2019) Selection of extractant in rare earth solvent extraction system: a review. Int J Rec Technol Eng 8(1):728–743
2. Castor SB, Hendrik JB, Kogel JE, Trivedi NC, Barker JM, Krukowski ST (2006) Industrial minerals and rocks: commodities, markets and uses. Soc Min Mineral United States 7:769–792
3. Dostal J (2017) Rare earth element deposits of alkaline igneous rocks. Resources 6(34):1–2
4. Wyoming's rare earth elements homepage. https://www.wsgs.wyo.gov/minerals/rare-earths.aspx
5. King HM REE–Rare Earth Elements and their Uses. https://geology.com/articles/rare-earth-elements/
6. RSC homepage. https://www.rsc.org/periodic-table/element/63/europium
7. Pramanik S, Sinha MK, Kumari A, Jha MK, Sahu SK (2016) Recovery of rare earth oxide from phosphor powder of spent fluorescent lamp. In: Hydrometallurgy conference 2016: sustainable hydrometallurgical extraction of metals. Southern African Institute of Mining and Metallurgy, Cape Town, pp 1–3
8. Tan Q, Li J, Zeng X (2015) Rare earth elements recovery from waste fluorescent lamps: a review. Environ Sci Technol 45(7):749–776
9. Peppard DF, Mason GW, Maier JL, Driscoll WJ (1957) Fractional extraction of the lanthanides as their di-alkyl orthophosphates. J Inorg Nucl Chem 4(5–6):334–343
10. Peppard DF, Ferraro JR, Mason GW (1958) Hydrogen bonding in organophosphoric acids. J Inorg Nucl Chem 7(3):231–244
11. Peppard DF, Mason GW, Driscoll WJ, Sironen RJ (1958) Acidic esters of orthophosphoric acid as selective extractants for metallic cations–traces studies. J Inorg Nucl Chem 7(3):276–285
12. Mishra BB, Devi NB (2018) Solvent extraction and separation of Eu (III) using a phosphonium ionic liquid and an organophosphorus extractant–A comparative study. J Mol Liq 271:389–396
13. Mishra BB, Devi NB, Sarangi K (2019) Yttrium and europium recycling from phosphor powder of waste tube light by combined route of hydrometallurgy and chemical reduction. Miner Eng 136(1):43–49
14. Nasser S, Awwad HM, Gad H, Aly HF (2008) Extraction of Eu (III) from nitrate medium by Cyanex 921using solvent extraction technique. Int J Phys Sci 3(1):022–027
15. Pradhan S, Swain N, Sarangi B, Mishra S (2019) Demonstration of extraction performance of Aliquat 336 for Eu (III) from nitrate medium. Mater Int 1(1):0001–0005
16. Hirashima Y, Kodera H, Shiokawa J (1982) Extraction of lanthanoids with bis(2-ethylhexyl) hydrogenphosphate equilibria in the region of high loading. Nippon Kagakukaishi 1982(4):627–631
17. Morais CA, Ciminelli VST (2004) Process development for the recovery of high-grade lanthanum by solvent extractant. Hydrometallurgy 73:237–244
18. Vera YM, Braga FD (2020)Separation of gadolinium and europium from chloride media by the solvent extraction technique. REM Int Eng J 73(1)
19. Gomes RC, Seruff LA, Scal MLW, Vera YM (2018) The influence of lactic acid concentration on the separation of light rare earth elements by continuous liquid-liquid extraction with 2-ethylhexyl phosphonic acid mono-2-ethylhexylester. J Metall Mater Trans B 49(1):460–465

Trialkyl Phosphine Oxide as an Extracting Agent for Solvent Extraction of Nd(III) from HNO_3/$NaNO_3$ Solution

Suchitra Behera, Susmita Prusty, Nilam Swain, Sanghamitra Pradhan, and Sujata Mishra

Abstract Neodymium, one of the critical rare earth metals is in demand nowadays due to enormous technological applications and its limited supply has enforced the metallurgists to search resources for its efficient recovery. Solvent extraction is widely used as a separation technique for rare earth extraction and separation. The present investigation represents detailed investigation on solvent extraction of Nd(III) from acidic nitrate solution utilising trialkyl phosphine oxide (TAPO) in kerosene. The effects of operating variables like shaking time, TAPO molarity, HNO_3 and nitrate ion concentration, nature of diluents and influence of temperature on the extraction of Nd(III) were analysed. With rise in HNO_3 molarity from 0.01 M to 0.1 M, increased extraction percentage has been exhibited but extraction trend tends to decrease when the concentration of acid increased to 1 M. Using 0.2 M TAPO in kerosene, 96% Nd(III) has been extracted. Thermodynamic studies showed negative value of enthalpy change indicating exothermic extraction and negative value of change in entropy confirming the constitution of Nd(III)-TAPO complex. Maximum extraction of Nd(III) has been achieved on using kerosene as diluent due to its lower dielectric constant value compared to other diluents under consideration.

Keywords Solvent extraction · Nd(III) · TAPO

1 Introduction

Rare earth elements (REEs) are group of seventeen elements which are employed in wide range of green technical usage such as Ni-MH batteries, permanent magnets electric vehicles and many house hold equipments [1]. Due to increase in green energy sources and new technologies, the role of REEs have become dominant in modern societies [2]. REEs are the most demanding elements and are widely used in magnetic materials, catalyst and several other fields [3]. World's 95% REEs have been supplied by China leading to high price and risk due to limited supply due

S. Behera · S. Prusty · N. Swain · S. Pradhan · S. Mishra (✉)
Department of Chemistry, Institute of Technical Education and Research (FET), Siksha 'O' Anusandhan Deemed to be University, Khandagiri Square, Bhubaneswar, Odisha 751030, India
e-mail: sujatamishra@soa.ac.in

S. Pal et al. (eds.), *Processing and Characterization of Materials*, Springer Proceedings in Materials 13, https://doi.org/10.1007/978-981-16-3937-1_11

to the worldwide financial situation during 2011 [4]. Neodymium is a rare earth element which is found in the form of ore like bastnasite and monazite i.e., 40 ppm by weight [5]. In these minerals, neodymium is rarely dominant, with cerium being the most abundant lanthanide; some exception includes kozoite-(Nd) and monazite-(Nd) [6]. Due to huge applications in high technology devices, there is supply risk of this element. Nowadays neodymium is widely applied in permanent magnets those are used in microphones, loudspeakers, hard disks of computers, wind turbines and electric motors [7].

Solvent extraction as a hydro metallurgical method commonly applied in industries for the recovery and separation of metals at tracer level as well as at micro level. In this process the amount of solute which is extracted from one liquid phase to the other phase is measured. By using suitable extracting agent with high ability, this process can reach selective separation o r group separation of trace elements. The main attraction of solvent extraction process is high distribution ratio between the two liquid phases of the solute. Pavon et al., performed investigations on of recovery of neodymium using Cyanex 572 (A mixture of phosphinic and phosphonic acids) in chloride medium from waste NdFeB magnet through solvent extraction. It has been reported that 99.99% Nd(III) in chloride medium has been recovered with a purity of 99.7% of Dy/Nd/Tb [8]. Panda et al., investigated the extraction behaviour of Nd(III) with Cyanex 921 (93% of tri-*n*-octylphosphine oxide) diluted in kerosene from acidic nitrate medium They reported that with increment in HNO_3 molarity from 0.001 to 0.008 M, the extraction gradually increases. With 0.01 M HNO_3, the extraction of Nd(III) decreased and temperature had a negative influence in the extraction process [9].

Gergoric et al., employed TODGA (N, N, N′, N′-tetraoctyl-3-oxapentane-1,5-diamide) to recover Pr, Nd and Dy from NdFeB magnet waste through liquid–liquid extraction. They reported the influence of diluting agents like hexane,solvent 70, toluene, cyclohexane, and 1-octanol on the extraction process and for solvent 70, highest separation factor was achieved with 0.01 M TODGA [3]. Suresh et-al., studied the extraction and separation of Nd(III) with CMPO (Octyl (phenyl)-*N*, *N*-diisobutyl carbamoyl methyl phosphine oxide) using tri-n-amyl phosphate (TAP) and TBP (tri-*n*-butyl phosphate) as modifiers. It was reported that by using TAP/n-dodecane, Nd(III) was extracted [10]. Mokili et al., employed TBP as extractant in dodecane and the extraction isotherm of water and lanthanide was predicted by using Mikulin-Sergievskii- Dannus model [11]. Preston et al., recovered Pr and Nd from waste calcium sulphate sludge using TBP [12]. Fox et al., have studied on the Pr(III) and Nd(III) complex formation with TBP in supercritical carbon dioxide medium. From the spectral data, equilibrium constants were calculated using hard-equilibrium models and least squares regression [13].

The present study aims to determine the extraction percentage of Nd(III) from aqueous HNO_3/$NaNO_3$ solution using TAPO (trialkyl phosphine oxide) in kerosene. The extraction has been analysed with reference to variation in shaking time, concentration of HNO_3, TAPO and $NaNO_3$. The effect of temperature and variation of diluents have also been monitored.

2 Experimental

2.1 Materials

Trialkyl phosphine oxide (TAPO) purchased from HWB, Talcher was used as extractant. Nd_2O_3, $NaNO_3$, HNO_3 of AR grade were utilized and these were procured from Merck India Ltd. Kerosene (Sd. fine chemicals Ltd) was employed as diluent in the organic phase. Xylene, toluene, benzene, MIBK used in diluent variation experiment were procured from Merck.

2.2 Methods

The Nd(III) stock solution was prepared by dissolving an appropriate quantity of Nd_2O_3 in concentrated HNO_3 followed by dilution with desired amount of double distilled water. Extractant solution of desired molarity was prepared by taking required quantity of TAPO in kerosene [8]. The aqueous phase contains Nd(III), $NaNO_3$ and HNO_3. Both phases, 10 mL each were shaken for a period in order to achieve equilibrium. The contents were kept for some time to separate the two phases. The Nd(III) content in the initial aqueous feed as well as in the raffinate was analysed with the help of Arsenazo (III) using spectrophotometer. All the experiments are done in triplicate to avoid any kind of error.

2.3 Instrument Used in This Study

Citizen (CY320C) digital balance with accuracy $\pm$ 0.001 g was utilized for weighing chemicals**.** Aqueous phase and organic phases and were mixed properly with the help of magnetic stirrer (Spinot model MC-02). In raffinate, Nd (III) content was measured by Systronics UV-Visible spectrophotometer (Model no. 2202).

2.4 Data Analysis

Among the various methods, solvent extraction is considered as a versatile and popular method of separation. The following terms are used to measure the extent of extraction of metal ion of interest.The ratio between concentrations of Nd(III) ion after extraction in organic phase to that after extraction in the aqueous phase is known as D (distribution ratio).

$$D = [Nd]_{org}/[Nd]_{aq} \quad (1)$$

where, D represents distribution ratio. $[Nd]_{org}$ is the concentration of Nd(III) in the organic phase and $[Nd]_{aq}$ represents Nd(III) concentration in the raffinate. The extent to which a Nd (III) is extracted is known as the %E (percentage of extraction).

$$\%E = 100D/[D + (\frac{V_{aq}}{V_{org}}) \tag{2}$$

where V_{aq} and V_{org} are the volumes of aqueous phase and organic phase, respectively. If the phase volume ratio becomes unity, i.e. ($V_{aq} = V_{org}$) then the above equation can be written as:

$$\%E = 100D/[D + 1] \tag{3}$$

3 Results and Discussion

3.1 Variation of Shaking Time

The solvent extraction of Nd(III) (0.01 M) from 0.1 M HNO_3 and 1 M $NaNO_3$ using 0.1 M TAPO in kerosene has been examined by varying the shaking time from 10 to 30 min. After analysis, it has been observed that there is a slow and gradual decline in the extraction from 59.23% to 50.47% with variation of shaking time from 10 to 30 min (Fig. 1). Hence, shaking time of 10 min was kept for all experimental studies.

3.2 Influence of HNO_3 Concentration

The extractant behaviour of Nd(III) by TAPO using varying HNO3 molarity from 0.01 M to 1 M has been studied. Sodium nitrate concentration was kept fixed at 1 M.The extraction was seen to increase from 54.95% to 59.23% with increase in molarity from 0.01 M to 0.1 M but when HNO_3 molarity increased from 0.1 M to 1 M, the extraction of metal decreased since nitric acid was extracted by extractant TAPO forming TAPO.HNO_3 at higher acid molarity (Fig. 2).

3.3 Influence of Concentration of $NaNO_3$

The effect of $NaNO_3$ on the Nd(III) (0.01 M) from HNO_3 (0.1 M) with use of 0.1 M TAPO in kerosene has been investigated by varying its concentrations from 0.5 M to 2 M,.The extraction percentage of Nd(III) decreases from 79.36% to 51.96% with

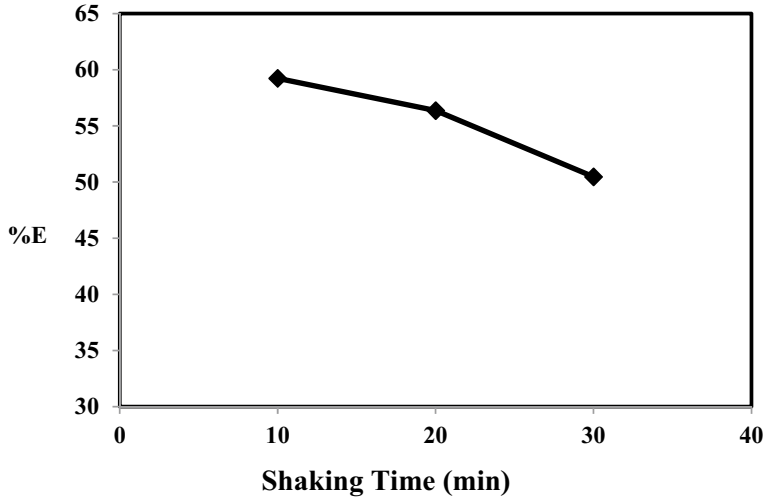

Fig. 1 Graph showing %E of Nd(III) against shaking time [Aqueous phase: [Nd(III)] = 0.01 M, $NaNO_3$ = 1 M, HNO_3 = 0.1 M, Temperature = 298 K, Organic phase: 0.1 M TAPO in kerosene (O/A = 1:1)]

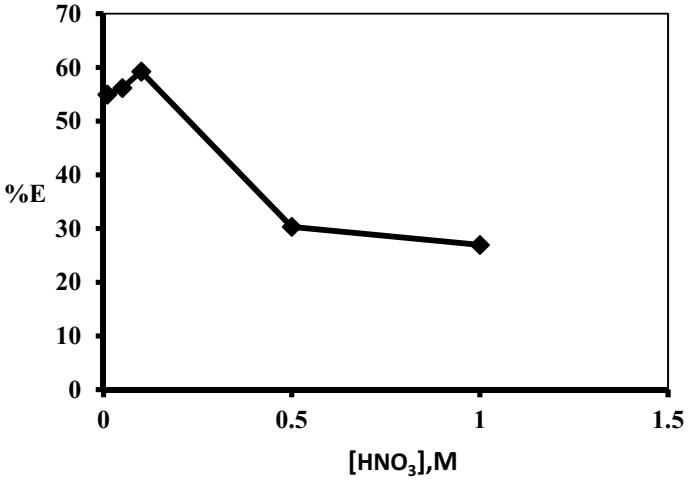

Fig. 2 Plot of %E of Nd(III) against [HNO_3], M. Aqueous phase: [Nd(III)] = 0.01 M, $NaNO_3$ = 1 M, Temperature = 298 K, Organic phase: 0.1 M TAPO in kerosene, Shaking time = 10 min, O/A ratio = 1:1

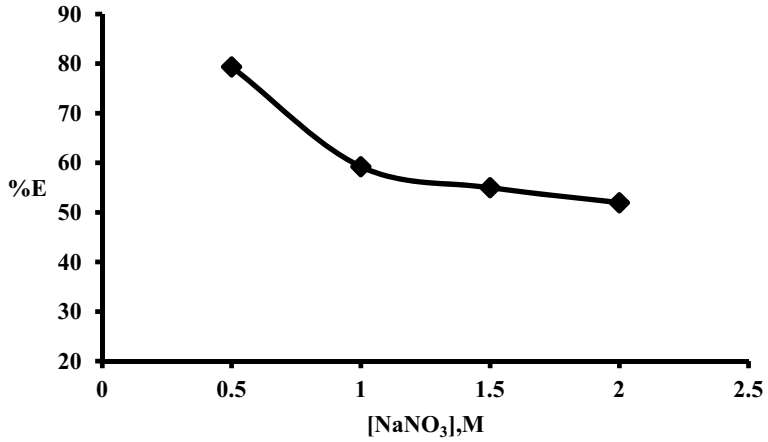

Fig. 3 Plot of %E of Nd(III) against [$NaNO_3$], M. Aqueous phase: [Nd(III)] = 0.01 M, [HNO_3] = 0.1 M, Temperature = 298 K, Organic phase: 0.1 M TAPO in kerosene, Shaking time = 10 min, O/A ratio = 1:1

rise in nitrate molarity, which may be because of the salting in effect (Fig. 3). The salting in effect increases the formation of more Nd-nitrate species.

3.4 Influence of TAPO Concentration

The variation in concentration of the extractant influences the extraction process in a positive manner because the extractant extracts the metal ion through complex formation. The concentration of TAPO was varied from 0.05 M to 0.5 M for 0.01 M Nd(III) extraction from aqueous solution with 1 M $NaNO_3$ and 0.1 M HNO_3. Th extraction of Nd(III) was observed to increase from 54.09% to 96% with rise in TAPO molarity from 0.05 M to 0.2 M (Fig. 4). This enhancement is attributed to the inclusion of TAPO in the coordination sphere of Nd(III) forming extractable complex.

3.5 Influence of Temperature

Thermodynamic study throws light on the extraction mechanism of solvent extraction. Extraction of 0.01 M Nd(III) from aqueous phase containing 0.1 M HNO_3 and 1 M $NaNO_3$ using 0.1 M TAPO in kerosene was carried at temperature range from 298 to 318 K. After extraction, it was found that the extraction percentage decreased from 59.23% to 36.02% with hike in temperature (Fig. 5). The standard enthalpy and entropy changes have been estimated from the plot of logD versus 1000/T (Fig. 5)

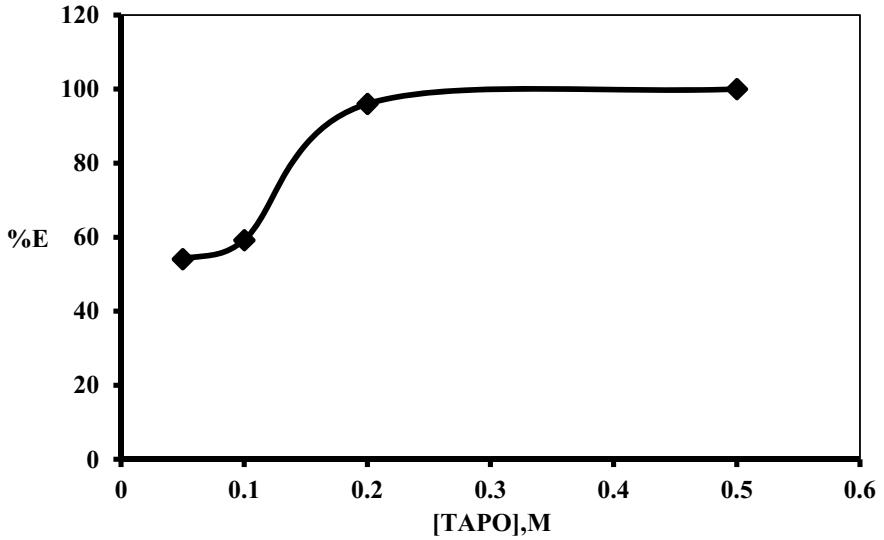

Fig. 4 Plot of %E of Nd(III) against [TAPO], M. Aqueous phase: [Nd(III)] = 0.01 M, [$NaNO_3$] = 1 M, [HNO_3] = 0.1 M, Temperature = 298 K, Shaking time = 10 min and O/A ratio: 1:1

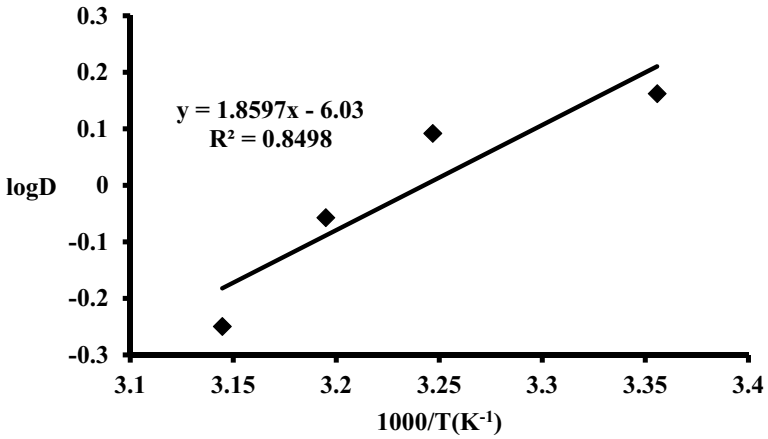

Fig. 5 Plot showing log D against 1000/T in case of Nd(III) extraction. Aqueous phase: [Nd(III)] = 0.01 M, [$NaNO_3$] = 1 M, [HNO_3] = 0.1 M and Organic phase: 0.1 M TAPO in kerosene, Shaking time = 10 min, O/A ratio = 1:1

using Van't Hoff equation [14].

$$logD = -\frac{\Delta H^{\circ}}{2.303RT} + \frac{\Delta S^{\circ}}{2.303R} \tag{4}$$

Table 1 Influence of diluents on Nd(III) extraction.Aqueous phase: [Nd(III)] = 0.01 M, [$NaNO_3$] = 1 M, [HNO_3] = 0.1 M, T = 298 K and organic phase: 0.1 M TAPO, Shaking time = 10 min, O/A ratio = 1:1

Diluent	Dielectric constant	D	%E
Kerosene	1.82	1.453	59.23
Benzene	2.27	0.758	43.11
Toluene	2.38	0.127	11.26
Xylene	2.57	0.01	0.99
MIBK	13.11	0.128	11.34

From Fig. 5, ΔH^o and ΔS^o have been calculated from slope and intercept and equal to -35.607 kJ mol^{-1} and -115.46JK^{-1} mol^{-1}, respectively. The negative ΔH^o value shows extraction process is exothermic and negative ΔS^o value reveals the constitution of Nd (III)-TAPO complex in the organic extract.

3.6 Influence of Diluents

Diluents play an important role in determining solvent characteristics and transport properties. Its polarity also influences the complexation process. Diluent variation effect on the extraction of Nd (III) was studied using TAPO in various organic diluents like kerosene, xylene, benzene, MIBK and toluene.Highest extraction was accomplished on employing kerosene as diluting agent (Table 1). This is due to the low dielectric constant value of kerosene as compared to other diluents under consideration. Kerosene is non polar, less toxic, and cheaply available.

4 Conclusions

In this investigation the concentration of TAPO and nitric acid exhibited optimistic influence in case of extraction studies of Nd (III). Enhanced nitrate ion concentration in the aqueous phase led to decrease in extraction percentage of the metal whereas enhancement in temperature had a positive effect on the Nd(III) extraction. The changes in enthalpy and entropy are found as negative confirming about the extraction reaction as exothermic with the formation of Nd(III)-TAPO complex.

Acknowledgements The authors are indebted to Siksha 'O' Anusandhan Deemed to be University authorities for the support to perform this research work.

References

1. Alonso E (2012) Evaluating rare earth element availability: a case with revolutionary demand from clean technologies. Environ Sci Technol 46:3406–3414
2. Gergoric M, Barrier A, Retegan T (2019) Recovery of rare earth elements from neodymium magnet waste using glycolic, maleic and ascorbic acids followed by solvent extraction. J Sustain Metallurgy 5:85–96
3. Gergoric M, Ekberg C, Foreman, Mark R, St J, Steenari B, Retegan T (2017) Characterization and leaching of neodymium magnet waste and solvent of the rare earth elements using TODGA. J Sustain Metallurgy 3:638–645
4. Binnemans K, Jones P, Blanpain B, Gerven T, Yang Y, Watlon A, Buchert M (2013) Recycle of rare earths: a critical review. J Clean Prod 51:1–22
5. Lee JD (1991) Concise inorganic chemistry, 4th edn, p 862
6. Hudson Institute of Mineralogy (1993–2018) "Mindat.org"
7. Zepf V (2013) Rare earth elements a new approach to the nexus of supply, demand and use: exemplified along the use of neodymium in permanent magnets. Springer
8. Pavon S, Fortuny A, Coll MT, Sastre AM (2018) Neodymium recovery from NdFeB magnet wastes using Primene 81R. Cyanex 572 IL by solvent extraction. J Environ Manage 222:359–367
9. Panda N, Devi NB, Mishra S (2012) Solvent extraction of neodymium(III) from acidic nitrate medium using Cyanex 921 in kerosene. J Rare Earth 30:794
10. Suresh A, Rao C, Sabharwal K, Srinivasan T, Rao P (1999) Third phase formation in the extraction of Nd(III) by octyl (phenyl)-*N*, *N*-diisobutyl carbamoyl methyl phosphine oxide (OΦDCMPO). Solvent Extr Ion Exch 17:73–86
11. Mokili B, Poitrenaud C (1996) Modelling of the extraction of neodymium and praseodymium nitrates from aqueous solutions containing a salting out agent or nitric acid by tri-*n*-butyl phosphate. Solvent Extr Ion Exch 14:617–634
12. Pestron J, Preez C (2008) The recovery of a mixed rare earth oxide and the preparation of cerium, europium and neodymium oxide from a south African phosphoric acid sludge by solvent extraction. Mineral Process Extractive Metallurgy Rev Int J 18:175–200
13. Fox R, Ball R, Harrington P, Rollins H, Jolley J, Wai C (2004) Praseodymium nitrate and neodymium nitrate complexation with organophosphorous reagents in supercritical carbon dioxide solvent. J Supercrit Fluids 31:273–286
14. Kreyszig E (1979) Advance engineering mathematics. Wiley

Impact of Brick Powder on Tensile and Flexural Properties of a Hemp Fiber

V. V. N. Sarath, D. Charan Sai, and B. Aditya

Abstract Natural fibers, it was the word attracted by the entire world and replaces most of the materials because of their properties improvement, ease of availability, low cost, and renewable nature. By using these fibers along with matrix and reinforcements, advanced fiber-reinforced composite materials were developed. These properties may vary due to the conditions like type and size of the fiber, place of growth and their environmental conditions, chemical method and their time period, water absorption nature, fiber orientation and type of filler material, and their particle size. Now a day's most researchers focused on composite materials prepared by using the various powders as a filler material. As a part of it for the first time, this paper focused to study the impact of different percentages of brick powder on properties of a natural hemp fiber. While among them10wt% and 40wt% of brick powder composite materials were received the highest ultimate tensile strength and flexural strength properties than the remaining materials.

Keywords Brick powder · Filler material · Hemp fiber

1 Introduction

Technological improvement associated with consumer requests and desires keeps on expanding the requests in worldwide assets and prompting significant issues of material accessibility and ecological maintainability. From the most recent couple of many years, biofiber composites have been going through a momentous change [1]. Most of the researchers still working on natural fibers discovery, it is not only due to the ease of availability, low cost, and renewable nature but also has a predominant character in fiber properties. In a field of the automotive sector where weight plays a prominent role in the reduction of fuel, usage was possible by utilizing these materials will make it possible [2], natural fibers are broadly categorized into three types: Plant-based, Animal-based, and Minerals. Among them, as bast, seed, leaf, fruit, stalk, cane grass, and reed fibers, wood are plant-based fibers. Most of the researchers still

V. V. N. Sarath (✉) · D. C. Sai · B. Aditya
Pragati Engineering College, Surampalem, Peddapuram, India

S. Pal et al. (eds.), *Processing and Characterization of Materials*, Springer Proceedings in Materials 13, https://doi.org/10.1007/978-981-16-3937-1_12

looking for an alternate way to developing the fibers physical, chemical, mechanical, and thermal properties of these materials. Because these were highly depending some of the conditions like type and size of the fiber, place of growth and their environmental conditions, chemical method and their time period, water absorption nature, fiber orientation and type of filler material, and their particle size [1–13]. Apart from this, a hybrid type of natural fiber composite materials was also been developed in a stacking sequence by different layers of materials, it was also equally established and creates a history in the improvement of properties than the natural fibers. In the bast fibers family, hemp fiber is the strongest and stiffest available plant fiber in cannabis species according to its potential consideration, utilization of these fibers as reinforcement in composite materials have rapidly increased. It's noticed that these various aspects of characteristics not only made as a good replacement for glass fibers at a lower price but also resulted mostly in more applications, especially in the fields of automotive and construction products. Elasticity, ease of processing, and recycling were also the reasons for the recognition of hemp fiber along with its high strength. Mainly there is a requirement of consumer education as far as the benefits of hemp are concerned, and numerous business sectors are anticipating the utilization of this fiber as it gradually advances into turning into another choice for makers [14]. Accordingly, in Non-wood bio-based materials category a detailed explanation, morphology, and the applications of various natural fibers were discussed, Figs. 1 and 2 shows the mature field and stem of hemp fiber [15] and as a part of it for the first time, this paper focused to study the impact of different percentages of brick powder on tensile and flexural properties of natural hemp fiber.

By varying the acorn powder at different percentages with a thermoplastic resin, composites were prepared and its mechanical properties evaluation was done. Similarly, by varying the walnut and SiO_2 contents composite material was prepared, its physical and mechanical properties were studied. Among which improvement in tensile and flexural properties was finally observed due to 50% added of walnut shell flour [16, 17]. A sisal fiber filled with coconut shell powder, polymer composite material was prepared and performed drilling operation on it [18].

Fig. 1 Hemp field with mature hemp plants

Fig. 2 Hemp stem

In addition to this cow dung powder [19], wood powder [20, 21] correspondingly a biosynthesized Nanopowder was used to improve the mechanical and thermal properties of sisal, coir, and banana hybrid composites [22].

2 Materials

The materials used for the fabrication of composite was a hemp fiber mat, a polished wax box usually applied to finished wooden furniture's was procured from the local suppliers of Vijayawada, and a thin plastic film which was usually available in stationery shops. The LY556 and HY951 epoxy resin and hardener were purchased from Hyderabad. These epoxy and hardener were mixed in a ratio of 1:10 and stirred 10 to 15 min manually in a beaker, during the process no air bubbles should be entrapped into it.

2.1 Sieve Analysis

It is a standard procedure to assess the granular material particle size distribution movement through a series of sieves in a staking sequence. These particles allow to travel among each size of a sieve mesh either horizontally or vertically, then the amount of material stopped from each of them was measured and considered as a fraction of the whole mass. Different methods of sieving techniques are available, according to the usage and material it may vary. It is a suitable process for the utilization of both organic and inorganic materials which consists of sand, stones, granite, coal, seeds, etc. each sieve has an assigned number with fixed particle size. The stacked sequence of sieve analysis should be arranged in ascending order i.e., the

Table 1 Observation table for sieve analysis of Brick Powder

S. no	Sieve designation	Mass of sieve (g)	Sieve wt. + soil wt. (g)	Soil retained (g)	Cumulative retained (g)	Cumulative retained (%)	% Fine
1	4.75 mm	420	460	40	40	10	90
2	2.0 mm	280	340	60	100	25	75
3	1.0 mm	300	320	20	120	30	70
4	600 microns	280	320	40	160	40	60
5	425 microns	300	460	160	320	80	20
6	300 microns	320	340	20	340	85	15
7	150 microns	320	360	40	380	95	5
8	75 microns	360	380	20	400	100	0

fine-sized sieve is placed below the bottom of the stack and the remaining sieves will be lies over it according to the increasing order of sieve size. Among the available processes, the manual sieving method was used for producing a fine powder size of the brick powder. Methods of sieves, sieve number and particle size, their procedure and arrangement, the importance of particle size, and their impact on mechanical properties were presented [23–28]. Because of which fine particle size of powder was adopted in this project not only because of its importance but also for a proper mixing into the solution.

Table 1 shows the sieve analysis of the brick powder ranging from 75 microns to 4.75 mm, along with it the maximum and minimum percentage of fineness was also reported to the same sieve designations with a value of 90 and 0%.

2.2 Model Calculations

For 4.75 mm sieve:

Cumulative retained = 40 g.

Cumulative % retained = $\frac{40}{400} \times 100$

= 10%

Percentage of passing = 100 − (Cumulative % retained)

100–10 = 90%

For 150 microns sieve:

Cumulative retained = 380 g

Cumulative % retained = $\frac{380}{400} \times 100$

= 95%

Percentage of passing = 100 − (Cumulative % retained)
= 5%.

3 Fabrication Process

The composite material was fabricated by using a hand-layup method, initially a thin layer of 0.5 mm thick plastic film was placed and apply the wax into it. This film resists the heat, and the applied wax on the film helps to remove these laminates easily. The powder form of red brick material with a sieve size of 75 microns was added to the epoxy and hardener mixture at weight percentages of 10 wt%, 20 wt%, 30 wt%, and 40 wt%, now the solution was stirred manually until it's completely mixed into it, then epoxy and hardener mixture was applied with the brush. A layer of 0.80 mm thick and 250 × 250 mm size of hemp fiber mat was placed and apply the paste into it. A roller was used for leveling and uniform distribution of the material, during this process air bubbles formed while mixing of resins may also be removed. Then again, another layer was placed and repeats the same procedure until the desired thickness of the laminate sheet was obtained for testing. Finally, on top of it again plastic film was placed and applying pressure with roller for removing the excess amount of solution from it and the following Fig. 3a–d shows the various stages of the fabrication process.

3.1 Mechanical Testing

After a stipulated period from the different weight percentages of fabricated brick powder polymer composite laminates, Tensile and Flexural test samples were prepared according to ASTM D 3039 and D 790 standards and performed testing on the universal testing machine.

3.2 Tensile Test

The hemp fiber polymer composites were prepared by varying a brick powder composition of 10 wt%, 20 wt%, 30 wt%, and 40 wt%. A comparison was made between them with a 0 wt% of composition i.e., pure hemp fiber, three samples were prepared for each percentage of composition, and tests were performed on it and an average value was taken. While among which 10 wt% of brick powder polymer composite material recorded the highest ultimate tensile strength than the remaining compositions of materials, along with comparison was made between the yield load and elongation, these were represented in the following graphs Fig. 4(1 and 2). Various properties like ultimate load, ultimate tensile strength, percentage of elongation, yield

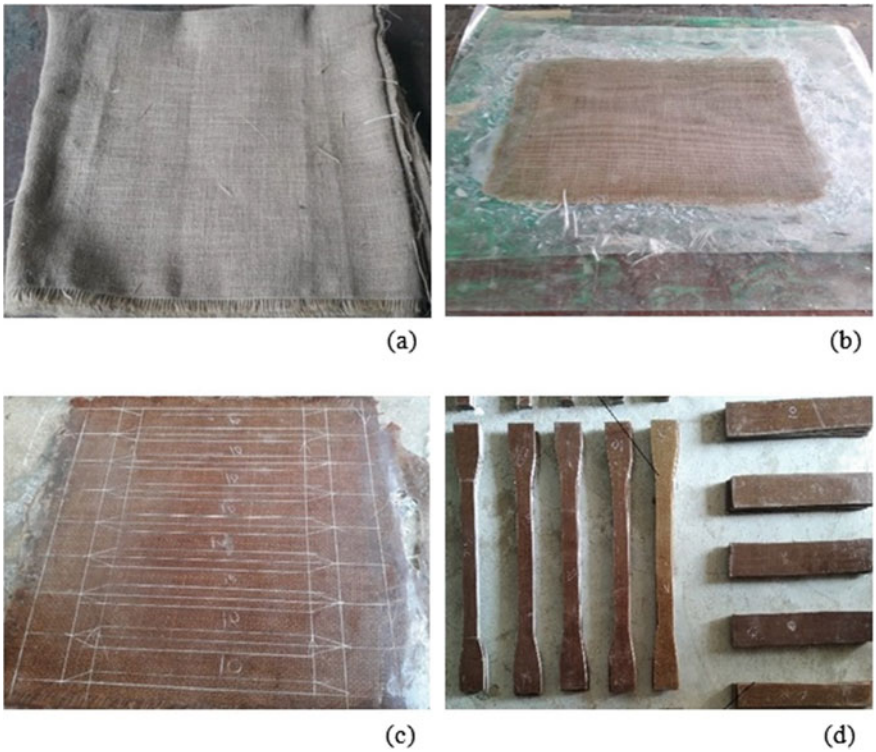

Fig. 3 **a–d** Shows the various stages of fabrication process. **a** Pure Hemp fiber. **b** Brick powder mixed epoxy resin on fiber mat. **c** Fabricated 10 wt% brick powder composition sample. **d** Tensile and flexural samples

load, and yield stress are obtained from each composition of samples and their values were represented in the above Table 2.

3.3 Flexural Test

Similarly, by supporting both ends and a load are applied gradually in a center flexural test was performed on five compositions and three samples of each, the average value was taken and comparisons were made between them. The properties of ultimate load and flexural strength values were also represented in the same Table 2.

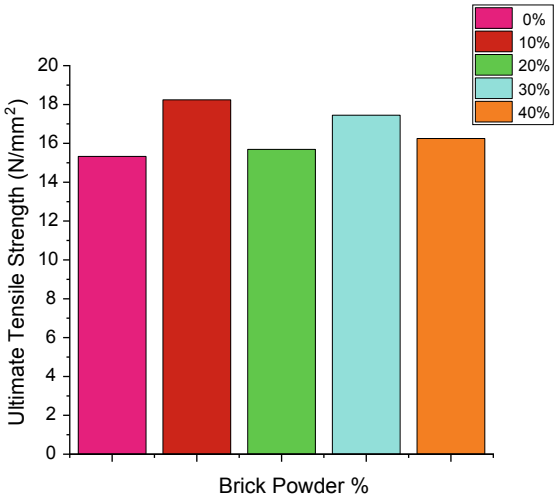

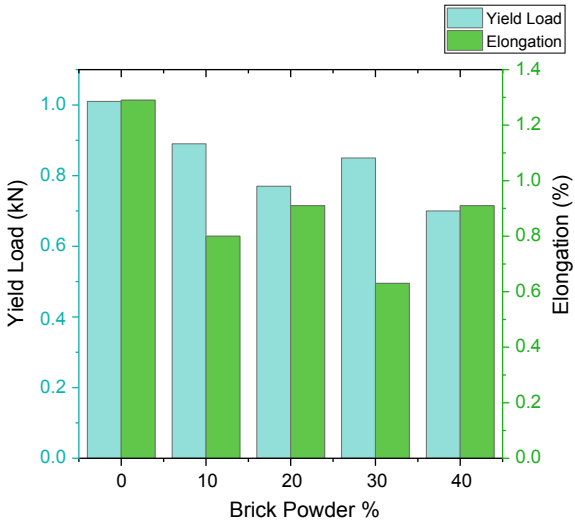

Fig. 4 (**1** and **2**) Shows the comparative values of different compositions of tensile properties. (**3**) Shows the comparative values of different compositions of flexural properties

4 Conclusion

A comparison was made between them with a 0wt% of composition i.e., pure hemp fiber, with the remaining composite materials. Three samples were prepared for each percentage of composition, and tests were performed on it and an average value was taken.

- In tensile test 10 wt% of brick powder polymer composite material recorded the highest ultimate tensile strength than the remaining compositions of materials.

Fig. 4 (continued)

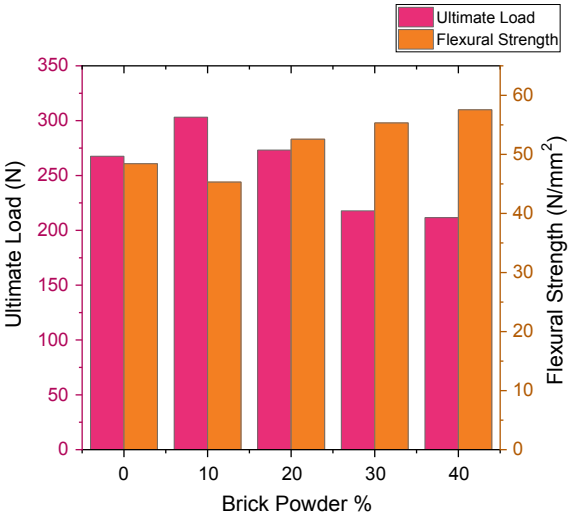

Table 2 Tensile and flexural properties of polymer composite materials

Brick powder (%)	Ultimate load (kN)	Ultimate tensile strength (N/mm^2)	Elongation (%)	Yield load (kN)	Yield stress (N/mm^2)	Ultimate load (N)	Flexural strength (N/mm^2)
0%	1.22	15.34	1.29	1.01	13.33	267.58	48.43
10%	1.29	18.24	0.80	0.89	12.54	303.17	45.32
20%	1.07	15.70	0.91	0.77	11.19	273.25	52.57
30%	1.02	17.45	0.63	0.85	14.48	217.80	55.33
40%	0.91	16.26	0.91	0.70	12.35	211.55	57.56

- Apart from that comparison was made between the yield load and elongation of different composite materials. Then it observed that composition of 0 wt%, i.e., pure hemp fiber has an equal highest value of yield load and elongation than the remaining.
- Similarly, in flexural test 40 wt% of brick powder composite material was received the highest flexural strength properties than the remaining composites.

Future scope:
The impact of brick powder on material properties may also be studied by:

- Carrying out not only by changing the various natural and synthetic fibers but also along with the different epoxy resins and hardeners.
- Varying the particle sizes of brick powder on fibers or by changing the weight portion of different fibers with a constant percentage of brick powder.

References

1. Faruk O, Bledzki AK, Fink H-P, Sain M (2012) Biocomposites reinforced with natural fibers: 2000–2010. Prog Polym Sci 37(11):1552–1596. https://doi.org/10.1016/j.progpolymsci.2012.04.003
2. Latif A, Abrar M, Manaf MA, Maslamany L, Hussain MS, Mohamad N (2015) Mechanical properties of short fiber and non-Woven Kenaf reinforced polypropylene composites: effects of oil palm shell powder addition. Appl Mech Mater 815:111–115. https://doi.org/10.4028/www.scientific.net/AMM.815.111
3. Goud V, Alagirusamy R, Das A, Kalyanasundaram D (2019) Influence of various forms of polypropylene matrix (fiber, powder and film states) on the flexural strength of carbon-polypropylene composites. Compos B Eng 166:56–64. https://doi.org/10.1016/j.compositesb.2018.11.135
4. Chavooshi A, Madhoushi M (2013) Mechanical and physical properties of aluminum powder/MDF dust/polypropylene composites. Construct Build Mater 44:214–220. https://doi.org/10.1016/j.conbuildmat.2013.02.079
5. Duan J, Obi Reddy K, Ashok B, Cai J, Zhang L, VaradaRajulu A (2016) Effects of spent tea leaf powder on the properties and functions of cellulose green composite films. J Environ Chem Eng 4(1):440–448. https://doi.org/10.1016/j.jece.2015.11.029
6. Aigbodion VS, Edok RO (2018) Chemical treatment of natural fibers for polymer composites production 6
7. de Farias MA, Farina MZ, Pezzin APT, Silva DAK (2009) Unsaturated polyester composites reinforced with fiber and powder of peach palm: mechanical characterization and water absorption profile. Mater Sci Eng C 29(2):510–513. https://doi.org/10.1016/j.msec.2008.09.020
8. Singha AS, Thakur VK (n.d) Study of mechanical properties of urea-formaldehyde thermosets reinforced by pine needle powder 18
9. Santiagoo R, Ismail H, Hussin K (n.d.) Mechanical properties, water absorption, and swelling behaviour of rice husk powder filled polypropylene/recycled acrylonitrile butadiene rubber (pp/nbrr/rhp) biocomposites using silane as a coupling agent 14
10. Abdul-Hussein AB (2015) Effect of nature materials powders on mechanical and physical properties of glass fiber/epoxy composite 23
11. Haldar P, Modak N, Sutradhar G (2017) Comparative evaluation of mechanical properties of sisal-epoxy composites with and without addition of aluminium powder. Mater Today: Proc 4(2):3397–3406. https://doi.org/10.1016/j.matpr.2017.02.228
12. Kamardin NK, Taib YM, Kalam A (2013) Impact toughness of Kenaf powder, polypropylene and Kevlar. Appl Mech Mater 393:152–155.https://doi.org/10.4028/www.scientific.net/AMM.393.152
13. Sumesh KR, Kanthavel K, Vivek S (2019) Mechanical/thermal/vibrational properties of sisal, banana and coir hybrid natural composites by the addition of biosynthesized aluminium oxide nano powder. Mater Res Express. https://doi.org/10.1088/2053-1591/aaff1a
14. Bhat G, Rong H (2005) 10-biodegradable nonwovens. In: Blackburn RS (ed) Biodegradable and sustainable fibres. Woodhead Publishing Series in Textiles. Woodhead Publishing, pp 310–342. https://doi.org/10.1533/9781845690991.310
15. Jones D, Brischke C (eds) (2017) 3-nonwood bio-based materials. In: Performance of bio-based building materials. Woodhead Publishing, pp 97–186. https://doi.org/10.1016/B978-0-08-100982-6.00003-3
16. Li S, Wang C, Zhuang X, Yong Hu, Chu F (2011) Renewable Resource-based composites of acorn powder and polylactide bio-plastic: preparation and properties evaluation. J Polym Environ 19(1):301–311. https://doi.org/10.1007/s10924-010-0280-2
17. MohseniTabar M, Tabarsa T, Mashkour M, Khazaeian A (2015) Using silicon dioxide (SiO_2) nano-powder as reinforcement for walnut shell flour/HDPE composite materials. J Indian Acad Wood Sci 12(1):15–21. https://doi.org/10.1007/s13196-015-0139-1

18. Navaneethakrishnan S, Athijayamani A (2016) Measurement and analysis of thrust force and torque in drilling of sisal fiber polymer composites filled with coconut shell powder. Int J Plastics Technol 20(1):42–56. https://doi.org/10.1007/s12588-016-9139-2
19. Reddy RK, Subba Rao TT, Padma Suvarna R (2014) Studies on thermal characteristics of cow dung powder filled glass–polyester hybrid composites. Compos Part B Eng 56: 670–672. https://doi.org/10.1016/j.compositesb.2013.08.059
20. Salemane MG, Luyt AS (2006) Thermal and Mechanical properties of polypropylene–wood powder composites. J Appl Polymer Sci 100(5): 4173–4180. https://doi.org/10.1002/app.23521
21. Sombatsompop N, Yotinwattanakumtorn C, Thongpin C (2005) Influence of type and concentration of maleic anhydride grafted polypropylene and impact modifiers on mechanical properties of PP/wood sawdust composites. J Appl Polym Sci 97(2):475–484. https://doi.org/10.1002/app.21765
22. Sumesh KR, Kanthavel K, Ajithram A, Nandhini P (2019) Bioalumina nano powder extraction and its applications for sisal, coir and banana hybrid fiber composites: mechanical and thermal properties. J Polym Environ 27(9):2068–2077. https://doi.org/10.1007/s10924-019-01496-x
23. Editor (2017) Sieve analysis—particle size analysis procedure. Basic Civil Engineering (blog). https://basiccivilengineering.com/2017/06/sieve-analysis-test.html
24. Igwe NN (2019) Preparation, characterization, and study of effect of particle sizes on different loading of polymer matrix composites using sugar-cane bark fiber. Int J Eng Sci Invent (IJESI) 08(12):71–84
25. Ameh AO, Isa MT, Sanusi I (2015) Effect of particle size and concentration on the mechanical properties of polyester/date palm seed particulate composites. Leonardo Electron J Pract Technol 26:65–78
26. Vinayagamoorthy R (2020) Effect of particle sizes on the mechanical behaviour of limestone-reinforced hybrid plastics. Polym Polym Compos 28(6):410–420. https://doi.org/10.1177/0967391119883163
27. Lintang Edi Wahyuni N, Soeswanto B (2019) The effects of particle size and content on morphology and mechanical properties of rice straw and coal fly ash filled-polypropylene composites. J Phys Conf Ser 1175:012282. https://doi.org/10.1088/1742-6596/1175/1/012282
28. Fu S-Y, Feng X-Q, Lauke B, Mai Y-W (2008) Effects of particle size, particle/matrix interface adhesion and particle loading on mechanical properties of particulate-polymer composites. Compos B Eng 39(6):933–961. https://doi.org/10.1016/j.compositesb.2008.01.002

Low Cycle Fatigue Behavior of a Microalloyed Steel

Md Abu Bakkar, Bishal Kanrar, and Debdulal Das

Abstract Low cycle fatigue (LCF) tests of a low-carbon microallyed steel have been performed to assess its response under cyclic loading for automobile application. Material exhibits significant initial cyclic hardening afterward prolong cyclic softening until failure at higher strain ranges ($\geq$1.50%); however, sustained cyclic softening from second cycle onwards is observed at lower strain amplitudes ($\leq$1.00%). The selected steel is found to follow non-Masing behavior but its fatigue life can well be described by strain-life relationship. Various monotonic and cyclic properties are determined and discussed together with mechanism of fatigue failure.

Keywords Strain life · Microalloyed steel · Low cycle fatigue · Failure mechanism

1 Introduction

Weight reduction of vehicle parts is one of the primary focuses of research in the few decades in order to lessen the fuel consumption and greenhouse gas emissions. Therefore, the use of high strength structural steels in automotive application is increasing day-by-day by replacing low strength steels like mild steel. In this regard, high strength low alloy (HSLA) steels is of great importance owing to the advantage of less weight and cost savings [1]. HSLA steels are commonly produced by controlled thermo-mechanical treatment. These steels content microalloying elements like Nb, Ti and V. The generation of fine carbides and carbo-nitrides of microalloying elements not only reduces grain coarsening but also enhances strength via grain boundary strengthening and precipitation strengthening [2]. HSLA steels are used for manufacturing of automotive components like bumpers, chassis members and door-intrusion beams with the sole purpose to combine adequate formability with enhanced weldability as well as reduce weight without loss in strength.

Fatigue property plays an important role in quality control of any automotive component since it experiences dynamic loading during service [3]. Components in a vehicle are often operated under adverse conditions and in many cases; these

Md A. Bakkar · B. Kanrar (✉) · D. Das
Indian Institute of Engineering Science and Technology, Shibpur, Howrah 711103, India

S. Pal et al. (eds.), *Processing and Characterization of Materials*, Springer Proceedings in Materials 13, https://doi.org/10.1007/978-981-16-3937-1_13

are required to last the lifetime of the vehicle without any form of inspection [4]. Failure of some components can result in accidents and loss of lives. Cyclic loading is defined as the application of repeated load i.e., fluctuating stresses, strains, forces etc. that causes fatigue failure of a material or structural component [5]. Under cyclic loading, materials fail frequently at lower loads due to fatigue which is the progressive structural damage [6]. The design of any automobile components to resist fatigue failure is still a difficult task for engineers. It is a subject that has been receiving a considerably amount of interest to set protocols with extensive applications in different areas. During fatigue failure, slip bands appear in some grain indicating the beginning of fatigue failure and with increase in number of cycles, the slip bands broaden consistently causing damage localization simultaneously [7]. As a consequence, intragranular microcracks are formed. Fatigue failure of the mechanical component is occurred in three stages i.e., at first crack initiation, then propagation of cracks and final fracture [10].

The primary aim of the present study is to investigate the low cycle fatigue (LCF) performance of a low carbon microalloyed steel, commonly referred to as BSK46 steel, to assess its suitable for manufacturing of wheel disc and other car components. Cyclic as well as monotonic properties are determined. In addition, applicability of strain-life approach to describe the fatigue behavior of the selected steel is verified and the mechanisms of its fatigue failure are identified.

2 Experimental Procedures

The material selected for this exploration was a hot rolled BSK 46 automobile grade steel produced by thermomechanical treatment. The nominal composition of the selected steel is C-0.07 Mn-0.86 S-0.007 P-0.018 Si-0.04 Cr-0.02 Ni-0.02 Mo-0.002 Cu-0.005 Al-0.042 Ti-0.03 V-0.002 Nb-0.029 (all in wt.%). For the microstructural study, the specimens were examined by following steps i.e., sectioning, mounting, grinding and mechanical polishing down to 0.5 μm diamond paste. The etching was done using 2 ml HNO_3 in 98 ml C_2H_6O solution. Digital images were captured by inspecting the etched specimens under optical microscope (Axiovert 40 MAT, Carl Zeiss). Tensile tests were performed using INSTRON 8801 machine maintaining a fixed strain rate (10^{-3} s^{-1}) at room temperature (300 K).

The specimens generally used for LCF property assessment, is typically machined to get very high polished surface in the reduced section. For fatigue testing, the specimens were placed precisely between two wedge shaped grips. The LCF tests at ambient temperature were performed with the help of Instron 8862 machine under completely reversed ($R_\varepsilon = -1$) total strain controlled mode. These were done at four total strain amplitude values ($\Delta\varepsilon_t/2 = 0.25$, 0.50, 0.75 and 1.00%) by means of triangular waveform keeping a fixed strain rate of 2×10^{-1} s^{-1}. All the tests were done until the specimens completely breakdown. A computer was used to store the experimental data by an automatic acquisition system @200 data per hysteresis

loop. Tensile and fatigue fractured surfaces were examined under SEM to identify the mechanisms of failure.

3 Results and Discussion

3.1 Microstructure and Static Mechanical Properties

Optical microstructure of the selected steel is depicted in Fig. 1a. It reveals uniform distribution of fine pearlite in the ferritic matrix. The tensile curve of BSK46 steel reveals yield point elongation (Fig. 1b), which is a common phenomenon for low carbon hot rolled steels. The calculated values of yield and ultimate tensile strength are 345 and 570 MPa, respectively. The uniform elongation value is 15.1%, while 57% is the total elongation. Using true stress–strain data and employing the power law relationship, the strain hardening exponent (n) is determined as 0.154 by linear regression analysis [8, 9]. Analyses of the tensile fracture surface validate ductile failure mode of the material owing to the coalition of dimples created from the inclusions or precipitates. It corroborates well with the higher elongation to fracture of the selected micro-alloyed steel (Fig. 1b).

3.2 Low Cycle Fatigue Behaviour

Cyclic Stress Strain Response. During cyclic plastic deformation, different kinds of behaviour are observed in the material like cyclic hardening or softening [11, 12]. Increase of stress range with cycle numbers represents cyclic hardening. In case of cyclic softening, the stress range reduces with number of cycle. Figure 2 depicts the

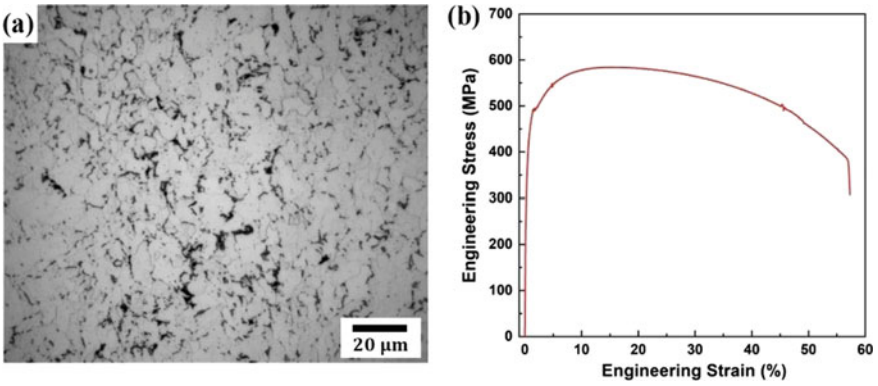

Fig. 1 **a** Representative optical microstructure and **b** tensile stress–strain curve of BSK 46 steel

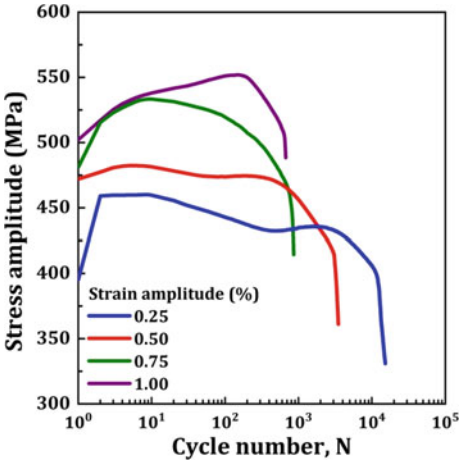

Fig. 2 Stress amplitude variation with the cycle number

effects of cycle number on stress amplitude at different total strain ranges ($\Delta\varepsilon_t$). The results in Fig. 2 reveal that the selected steel experiences considerable amount of initial cyclic hardening followed by prolong cyclic softening until failure when strain ranges is $\geq$1.50%. However, at lower strain lower strain ranges ($\leq$1.00%), it undergoes sustained cyclic softening from second cycle onwards.

The cyclic stress–strain diagram of the material is represented by joining the peaks at half-life of the hysteresis loops ($N_f/2$) evaluated at distinct strain ranges. The cyclic characteristics of a material can be expressed by power law equation as [11, 13]:

$$\frac{\Delta\sigma}{2} = K'\left(\frac{\Delta\varepsilon_p}{2}\right)^{n'} \tag{1}$$

where, the cyclic strength coefficients is denoted by K' and cyclic strain hardening exponent is presented by n'. The $\Delta\sigma$ is the stress amplitude, and $\Delta\varepsilon_p$represents change in plastic strain amplitude. The magnitude of n' is derived as 0.141 by the least square method [11, 13].

Masing Behaviour. Masing behaviour of material can be verified via construction of the master curve [14]. In this present study, the hysteresis loops are moved precisely to construct the master curve via overlapping the loading branches for all applied strain ranges (Fig. 3). The master curve is generally defined by the creation of uphill branch which can be expressed as [15]:

$$\Delta\varepsilon^* = \frac{\Delta\sigma^*}{E} + 2\left(\frac{\Delta\sigma^*}{2K^*}\right)^{\frac{1}{n^*}} \tag{2}$$

where,

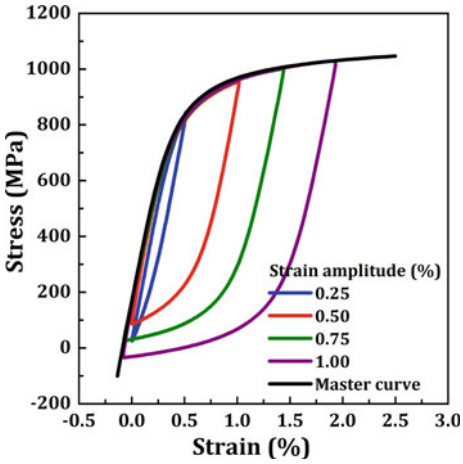

Fig. 3 Master curve showing the Masing deviation

$$\Delta\sigma^* = \Delta\sigma - \delta\sigma_0 \tag{3}$$

$$\Delta\varepsilon^* = \Delta\varepsilon - \left(\frac{\delta\sigma_0}{E}\right) \tag{4}$$

Here, the K^* and n^* can be estimated by fitting the master curve (Fig. 3). The value of $\delta\sigma_0$ can also be quantified directly from the Fig. 3. For a material that exhibits ideal Masing behaviour, the magnitude of $\delta\sigma_0$ should be zero for all strain ranges [8]. The results in Fig. 3 demonstrate that the $\delta\sigma_0$ values are non zero at several strain ranges; therefore, it can be inferred that BSK46 steel acts as non-masing material under cyclic loading.

Fatigue Life Prediction. The strain life approach is considered to anticipate the fatigue life of BSK46 steel. It is formulated from well-established power law equations, the Basquin relation and the Coffin–Manson (C–M) equation [16]. The C–M relation is expressed as [17]:

$$\frac{\Delta\varepsilon_p}{2} = \varepsilon_f'(2N_f)^c \tag{5}$$

where, the plastic strain range is expressed by $\Delta\varepsilon_p$. The ε_f' is commonly identified as the fatigue ductility coefficient, and c is referred to as the ductility exponent. $2N_f$ denotes the cycle reversals to failure. The Basquin equation can be written as [17]:

$$\frac{\Delta\varepsilon_e}{2} = \frac{\sigma_f}{E}(2N_f)^b \tag{6}$$

where, $\Delta\varepsilon_e$ indicates elastic strain range, the mean stress amplitude is expressed by σ_f'. The empirical constant called elastic fatigue ductility exponent is exhibited by

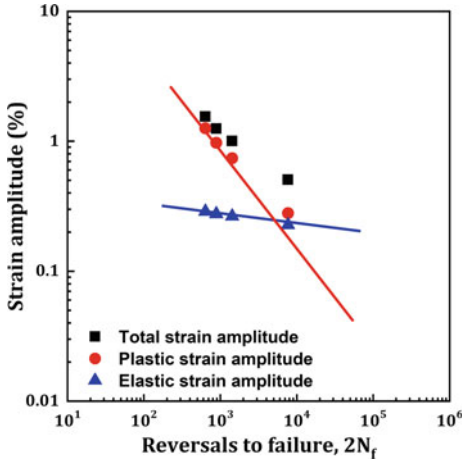

Fig. 4 Coffin-Manson and Basquin curve

b. The total strain amplitude ($\Delta\varepsilon_t/2$) is the summation of plastic ($\Delta\varepsilon_p/2$) and elastic strain amplitude ($\Delta\varepsilon_e/2$):

$$\frac{\Delta\varepsilon_t}{2} = \frac{\Delta\varepsilon_e}{2} + \frac{\Delta\varepsilon_p}{2} \tag{7}$$

$$\frac{\Delta\varepsilon_t}{2} = \frac{\sigma_f}{E}(2N_f)^b + \varepsilon'_f(2N_f)^c \tag{8}$$

The exponents and coefficients of these equations are represented by respective slopes and the intercepts which are calculated from linearly fitted plastic and elastic data points on a logarithmic-logarithmic coordinate system (Fig. 4). Parameters related to the strain-life relationship are compiled in Table 1.

For medium carbon microalloyed steel, Sarma et al. [18] have reported the *b* and *c* values as −0.09 and −0.64, respectively; whereas, n' value of 0.14. Sankaran et al. [19] have reported n' of 0.16 and *c* value of −0.67 for other microalloyed steel. The values *b*, *c* and n' are reported to vary from −0.067 to −0.086, −0.40 to −0.53 and 0.13 to 0.21 for Mo, V and Ti microalloyed steels [20]. In the present study, n′ is calculated as 0.14 whereas, the magnitudes of *b* and *c* are found to be −0.1 and −0.74, respectively. Therefore, the cyclic parameters of the studied steel correlate well with similar parameters reported earlier for varying microalloyed steels [18–20].

The fatigue life transition point ($2N_T$) is expressed by a common junction where two linear fitting lines meet as shown in Fig. 4. This point can be indicated as $2N_T$ [21]:

$$2N_T = \left[\frac{(\varepsilon'_f E)}{(\sigma'_f)}\right]^{\frac{1}{(b-c)}} \tag{9}$$

Table 1 Static and dynamic properties

Static properties	
True fracture stress, σ_f (MPa)	670
True yield stress, $\sigma_{0.002}$(MPa)	345
True fracture ductility, ε_f	0.45
Strain hardening exponent, n	0.154
Strength coefficient, K (MPa)	914
Reduction in cross-section area (%)	74.5
Dynamic properties	
True yield stress, $\sigma'_{0:002}$ (MPa)	483
Strain hardening exponent, n'	0.141
$b = n'/(1 + 5n')$ [Morrow] (–)	0.083
Fatigue strength exponent, b (–)	0.105
Fatigue ductility coefficient, ε'_f	1.980
$c = 1'/(1 + 5n')$ [Morrow] (–)	0.586
Fatigue ductility exponent, c (–)	0.744
$b = n'/(1 + 2\ n')$ [Tomkins]	0.110
Fatigue transition life in reversals, $2N_T$	2856

Above the $2N_T$, Basquin equation is significant, whereas below this point the Coffin-Manson equation is prevailing. The intersection is approximately 2856 cycles for the investigated material.

Failure Mechanism

To understand the mechanisms of fatigue failure, the failed specimen tested at 0.5% strain amplitude is examined under SEM and images have been captured at different places. A set of representation images is presented in Fig. 5. Macro view of the fracture surface in Fig. 5a shows three distinct zones. Two semi-circular zones roughly outlined by black lines are fatigue fractured areas developed by nucleation of fatigue cracks at two different locations. Multiple crack initiation sites have been previously reported in many steels [18]. The initiation of cracks at multiple locations accelerates the fatigue decay resulting in early failure. The other zone in Fig. 5a corresponds to fast fracture occurred due to tensile overloading. Magnified view of one of the fatigue fracture zones is shown in Fig. 5b. The crack initiation sites are located at the surface of the specimen as the fatigue fracture is a surface phenomenon [7]. The primary direction of fatigue crack propagation is indicated in Fig. 5a, b. On magnifying a portion close to crack initiation point, transverse micro-cracks are observed (Fig. 5c). Zoomed view of Fig. 5c shows beach marks (Fig. 5d) which are a typical signature of fatigue failure [22].

Figure 5e shows magnified view of the fast fracture zone which is evidenced the ductile mode of fracture. On further magnification, well-developed dimples are

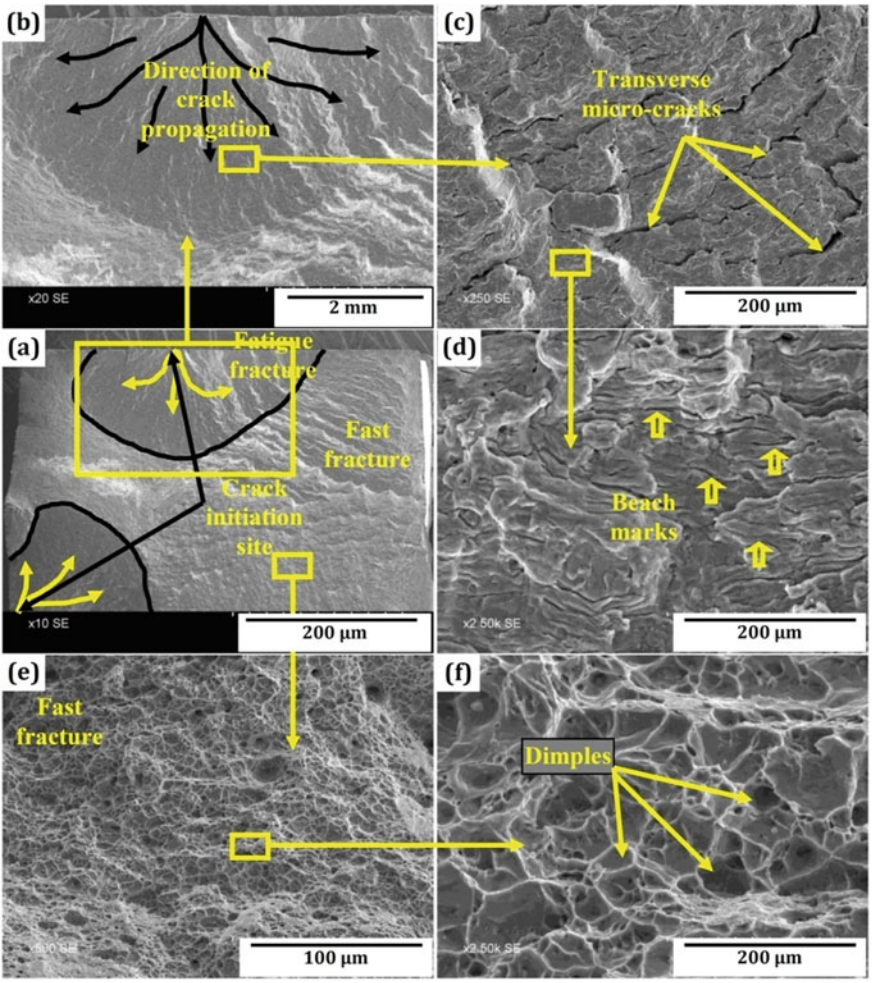

Fig. 5 Fracture surface of failed specimen strained at 0.5% strain amplitude

observed (Fig. 5f) which confirms the ductile mode of fracture in the fast fracture zone due to the tensile failure [23].

4 Conclusions

Apart from the evaluation of LCF response, microstructure examinations with tensile tests were also performed considering BSK46 steel. Following conclusions may be drawn:

- The selected microalloyed steel undergoes significant initial cyclic hardening afterward prolong cyclic softening till failure at higher strain ranges ($\geq$1.50%); however, sustained cyclic softening from second cycle onwards is observed at lower strain ranges ($\leq$1.00%).
- The constructed master curve reveals that the material does not obey Masing behaviour as Masing deviations are noticed at the compressive tips of the hysteresis loops.
- BSK46 steel follows strain life relationship. The associated parameters are determined which will be helpful for the design of the structure concerning this material.
- Fracture surface examinations infers that the fatigue cracks initiated at multiple locations while the fast fracture due to tensile over loading occurs via coalescence of micro voids.

References

1. Patel J, Klinkenberg C, Hulka K (2001) Hot rolled HSLA strip steels for automotive and construction applications. In: Proceedings of the international symposium Niobium, pp 647–674 (2001)
2. Lee WB, Hong SG, Park CG, Park SH (2002) Carbide precipitation and high-temperature strength of hot-rolled high-strength, low-alloy steels containing Nb and Mo. Metall Mater Trans A 33(6):1689–1698
3. Godefroid LB, Faria GL, Candido LC, Araujo SC (2014) Fatigue failure of a welded automotive component. In: Zhang Z (ed) 20th European conference on fracture 2014, Procedia Mater. Sci. vol. 3. Elsevier, Amsterdam, pp 1902–1907
4. Heyes AM (1998) Automotive component failures. Eng Fail Anal 4(1):129–141
5. Corrosionpedia Homepage, https://www.corrosionpedia.com/definition/6333/cyclic-loading. Last accessed 01 Dec 2020
6. Lee YL, Barkey ME, Kang HT (2011) Metal fatigue analysis handbook: practical problem-solving techniques for computer-aided engineering, 1st edn. Elsevier, USA
7. Suresh S (1998) Fatigue of materials, 2nd edn. Cambridge University Press, United Kingdom
8. Bakkar MA, Saha R, Das D (2020) low cycle fatigue performance and failure analysis of reinforcing bar. Met Mater Int 1–15
9. Bakkar MA, Kanrar B, Saha R, Das D (2020) High-strain low-cycle fatigue behavior of thermomechanically treated rebar. J Fail Anal Prev 20:1029–1037
10. Dieter JE, Bacon D (2010) Mechanical metallurgy, 3rd edn. Cornell University, USA
11. Polak J, Klesnil M, Lukas P (1977) On the cyclic stress-strain curve evaluation in low cycle fatigue. Mater Sci Eng A 28(1):109–117
12. Laughlin DE, Hono K (2014) Physical metallurgy, 5th edn. Elsevier, Amsterdam
13. Das B, Singh A (2019) understanding strain controlled low cycle fatigue response of P91 Steel through experiment and cyclic plasticity modeling. Fusion Eng Des 138:125–137
14. Roy SC, Goyal S, Sandhya R, Ray SK (2012) Low cycle fatigue life prediction of 316 l(n) stainless steel based on cyclic elasto-plastic response. Nucl Eng Des 253:219–225
15. Narendra PVR, Prasad K, Krishna EH, Kumar V, Singh KD (2019) Low cycle fatigue (LCF) behavior and cyclic plasticity modeling of E250A mild steel. Structures 20:594–606
16. Coffin LF (1953) A study of the effects of cyclic thermal stresses on a ductile metal. Knolls Atomic power laboratory, University of Michigan, Michigan

17. Zhang Y, Hu CL, Zhao Z, Li AP, Xu XL, Shi WB (2013) Low cycle fatigue behaviour of a Cr–Mo–V matrix-type high-speed steel used for cold forging. Mater Des 44:612–621
18. Sarma VS, Padmanabhan KA (1997) Low cycle fatigue behaviour of a medium carbon microalloyed steel. Int J Fatigue 19:135–140
19. Sankaran S, Sarma VS, Padmanabhan KA (2003) low cycle fatigue behavior of a multiphase microalloyed medium carbon steel: comparision between ferrite- pearlite and quenched and tempered microstructures. Mater Sci Eng A 345:328–335
20. Johnson JA, George K, David KM (2000) Fatigue of microalloyed bar steels. SAE Technical Paper
21. Chakraborti PC, Mitra MK (2006) Microstructural response on the room temperature low cycle fatigue behaviour of two high strength duplex ferrite–martensite steels and a normalised ferrite–pearlite steel. Int J Fatigue 28(3):194–202
22. Zheng H, Abel AA (1999) Fatigue properties of reinforcing steel produced by TEMPCORE process. J Mater Civ Eng 11(2):158–165
23. Das B, Bakkar A, Khutia N, Das D (2017) Low cycle fatigue performance evaluation of TMT rebar. Mater Today: Proc 4(2):2554–2563

Seismic Performance Assessment of a TMT Rebar

Md Abu Bakkar, Rajib Saha, and Debdulal Das

Abstract In this study, the behavior of thermomechanically treated Fe 500S rebar under cyclic loading in a completely reversed triangular waveform at ambient room temperature and strain amplitudes ranging from 0.3 to 1.0% has been examined to understand its behavior under seismic conditions. Low cycle fatigue behavior has been studied following the plastic strain energy approach while focusing on the failure mechanisms through critical examinations of the fracture surfaces. These have been supplemented with measurement of tensile property and characterization of microstructure. It has been observed that selected rebar undergoes severe cyclic softening until fracture at all strain amplitudes suggesting reduction of its seismic resistance. The studied material follows a near Masing behavior. The energy life equation is formulated which can be used for structural design purposes. Fatigue cracks always initiate at the rib roots and propagate adjacent to the rim section weakening the core for fast fracture.

Keywords Low cycle fatigue · Cyclic softening · Energy life · Failure mechanism · TMT rebar

1 Introduction

Rebar along with concrete forms essential reinforcement for the structures like dams, bridges, industrial and commercial structures, flyovers etc. The concrete carries the entire compressive load while the rebars bears the tensile counterpart. In a seismic event, the concrete rapidly breaks into small pieces due to its brittle nature, and transfers the full load on the rebars [1–4]. Under dynamic loading, the rebars eventually fail and result in a huge economical loss with a lot of casualties. Therefore, it is very important to study and understand the behaviors of rebars under dynamic conditions before their applications to ensure the longevity of the structure to be formed. For

M. A. Bakkar (✉) · D. Das
Indian Institute of Engineering Science and Technology, Shibpur, Howrah 711103, India

R. Saha
Research and Development Division, TATA Steel, Jamshedpur, Jharkhand 831001, India

S. Pal et al. (eds.), *Processing and Characterization of Materials*, Springer Proceedings in Materials 13, https://doi.org/10.1007/978-981-16-3937-1_14

a prolonged existence of the structure, the rebars must have the ability of absorption and dissipation of the load by the means of strain energy along with extensive deformation before final fracture. Hence, it is of utmost importance to understand the fatigue behavior of rebars.

Thermomechanically treated (TMT) rebars, in general, have a hard rim of tempered martensitic over a relatively soft core of ferrite-pearlite. It is worthy to mention that micro-alloyed rebars having uniform ferrite pearlite structure throughout the cross-section tends to have higher cyclic toughness and fatigue life [5]. Even though, buckling and corrosion induces severe structural damage particularly in the coastal areas, fatigue remains the main cause of failure in any seismic event [6, 7]. For seismic prone areas, rebars with relatively low yield strength are ideal as an energy dissipating material. However, the enhancement of tensile strength to yield strength ratio does not significantly increase the low cycle fatigue (LCF) performance [8]. Coffin–Manson relationship is the classical approach for predicting fatigue life of wide range of structural materials; however, the energy based approach has proven to be more effective with better accuracy in predicting fatigue life of rebars [9].

The presence of ribs in the rebars plays a major role in diminishing fatigue as these ribs act as the stress risers and facilitate the early initiation of the crack [10]. But these ribs on the surface can't be removed as these ribs hugely contribute to the bonding of the rebars with the concrete. The fatigue properties of rebars are governed by the rib geometry [11]. Hence rib geometry is an important aspect to study while understanding fatigue failure of rebars. Earlier, attempts have been made to optimize the rib design to minimize its adverse effects on fatigue performance [12].

Understanding the fatigue behavior under LCF regime of rebars is, therefore, a very essential aspect for the construction field considering the losses caused in any seismic events. In this study, an attempt has been made to understand the LCF behavior of Fe 500S grade TMT. Emphasis has been made on the energy-based approach to envisage the fatigue life of rebar and the mechanism of fatigue failure through fracture surface study.

2 Experimental Procedures

A commercially available Fe 500S grade TMT rebars with 12 mm diameter was used in the present study. The microstructure was examined following the standard metallographic procedures. The cross-section of the rebar was cut and grinded for the mechanical polishing by emery paper down to 0.5 μm diamond paste. The etching of the polished sample was carried out using 2% HNO_3 in 98% C_2H_6O solution. Carl Zeiss made Axiovert 40 MAT optical microscope was employed to take the digital images of the rebar at its various zones. Tensile tests were carried out using Instron made 8801 servo-hydraulic universal testing machine at a fixed strain rate (10^{-3} s^{-1}). At least three samples were tested using a gauge length of 170 mm to estimate the average tensile properties.

In the ASTM:E606-12 standard for LCF tests, it is stated that the samples should have a highly polished surface. But as for rebars are concerned, due to the importance of the ribs in the rebar, surface finishing was not possible as the results would not reflect the actual behavior of the rebars [13]. Therefore, as-received rebars with no surface alteration were used to carry out the LCF tests in an electromechanical actuator controlled Instron made 8862 machine. Rebars of 120 mm length were cut for LCF tests where the gauge length is 20 mm. An external extensometer of 12.5 mm gauge length was used to control the applied strain. A constant strain rate of 10^{-3} s^{-1} in a triangular waveform with strain ratio (R) of −1 was maintained during the LCF tests. All tests were done till the entire partition of specimens or when the peak stress is reduced by 30% while recording 200 data points for each hysteresis loop. The fracture surfaces of failed rebars were examined using Jeol made JSM 5510 SEM to reveal the failure mechanism.

3 Results and Discussion

3.1 Microstructure

The microstructures at different zones along with a macro image of the chosen rebar are depicted in Fig. 1. The macro view in Fig. 1a reveals two distinct zones namely rim and core. The rim region is not uniform and the mean thickness of the rim is approximately 0.8 mm. The microstructure reveals tempered martensite in the rim region while the core region shows ferrite and pearlite. The TMT rebars are manufactured in the process called tempcore in which three consecutive stages of heat treatment are done [14]. In the first stage, hot rolled steel bars are passed through quenching chambers where pressurized water jets quench the surface of the bars to transform the austenite into martensite layer in the surface. The bars then comes out of the quenching chambers in the second stage where the heat in the core region of the bars transfers to the cold surface resulting in the auto-tempering of martensite. Finally, the bars are then allowed to cool normally in the air in the cooling bed to achieve the room temperature. During cooling, the austenite present in core region of the bars are transformed into ferrite-pearlite structure [15].

3.2 Tensile

The stress–strain curve of the selected rebar is presented in Fig. 2. Discontinuous yielding is observed as can be expected from low carbon TMT rebars [15]. The estimated yield strength is 536 MPa whereas the ultimate tensile strength is 681 MPa. The uniform and total elongation values are 15.4% and 20.4%, respectively. The magnitudes of the strength coefficient (K) as well as the strain hardening exponent

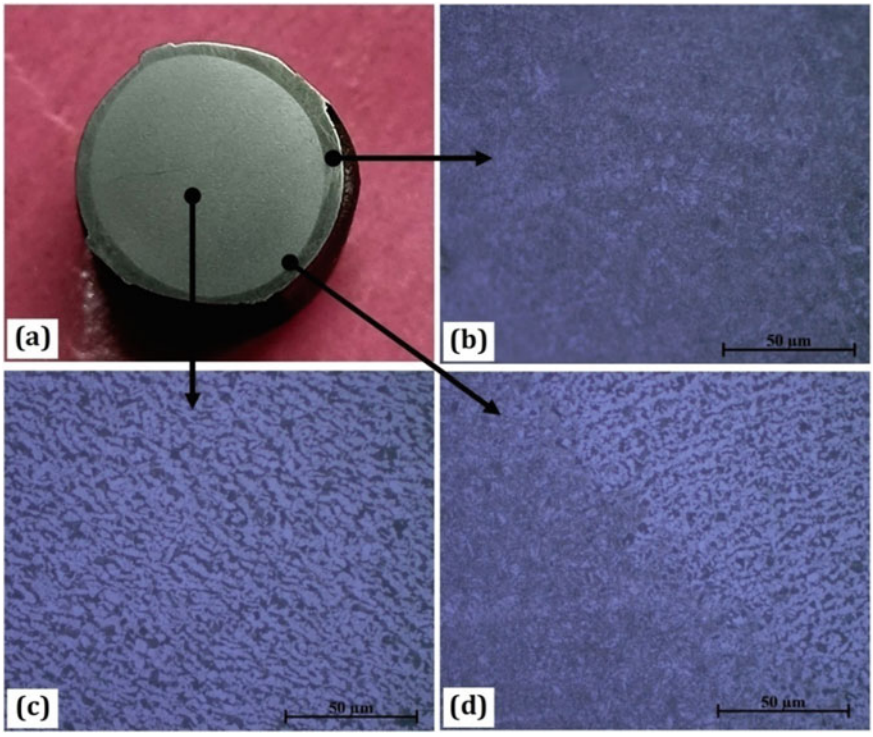

Fig. 1 Microstructure of Fe 500S TMT rebar. **a** Macrostructure of the cross section, and microstructure corresponding to the **b** rim, **c** core and **d** transition regions

Fig. 2 Uniaxial stress strain tensile curve

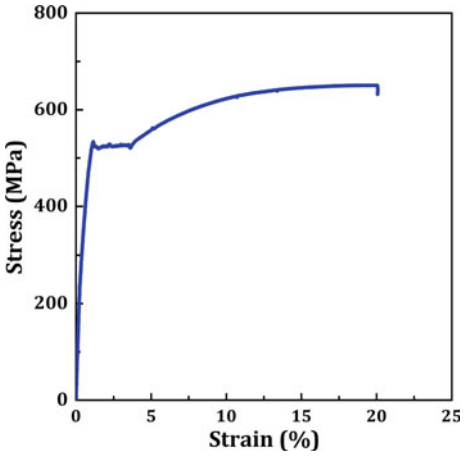

(n) obtained through linear regression method are 445 and 0.144, respectively. The reported yield and ultimate tensile strength values of Fe 500D rebar are 544 and 630 MPa [16]. Similarly, yield strength of Fe 500SD rebar is reported as 580 MPa and its tensile strength is 677 MPa [4]. These results suggest that the Fe 500S rebar like Fe 500D rebar is of superior quality according to Indian standard BIS 1786:2008.

3.3 Low Cycle Fatigue Response

The variations of stress amplitude with cycle number of the selected rebar are presented in Fig. 3. It can be noticed clearly that stress amplitude continuously decreases until fracture with increasing cycle number. This observation reveals that the material undergoes severe cyclic softening throughout the cyclic loading irrespective of the applied strain amplitude [17]. A material with tensile to yield strength ratio more than 1.4 experiences cyclic hardening, otherwise cyclic softening is commonly observed [4, 18]. The tensile to yield strength ratio of Fe 550S rebar is 1.27; therefore, the cyclic softening response is expected.

The cyclic softening behavior is associated with the microstructural changes in the material during cyclic loading. The rebars have a hard martensitic outer layer called the rim containing high dislocation density. These dislocations during the course of cyclic loading, rearrange themselves with the result in the generation of dislocation cell structures and annihilation of dislocations which leads to the higher mobility of dislocations resulting the rebar to show cyclic softening characteristic [19, 20].

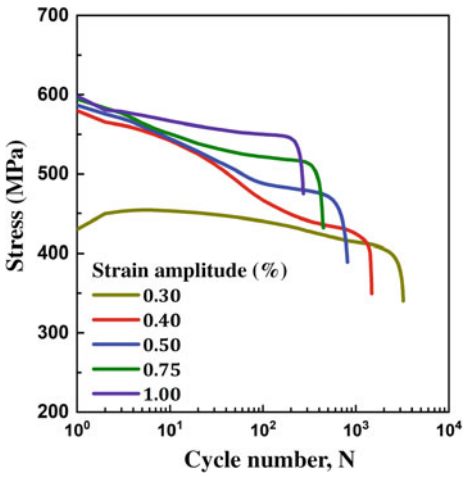

Fig. 3 Variation of stress amplitude with number of cycle at different strain amplitudes

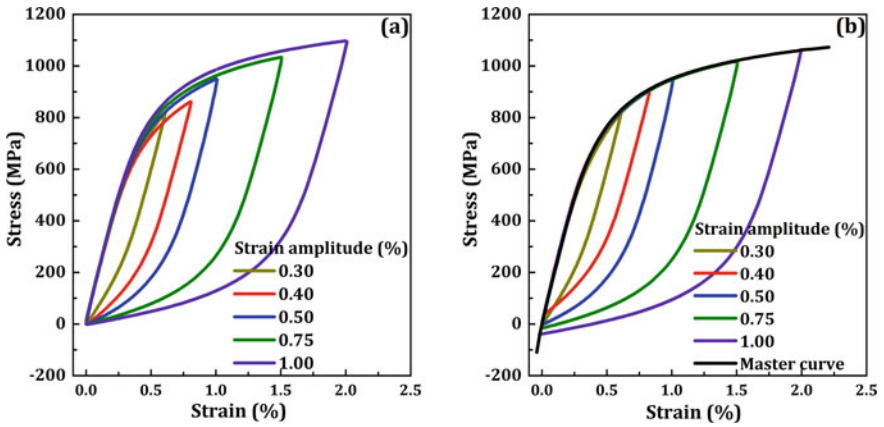

Fig. 4 **a** Stable hysteresis loops translated at a common compressive tip, and **b** Master curve showing Masing deviation

3.4 Hysteresis Loop Analysis

The stable hysteresis loops are considered for the analysis of LCF behavior. In conditions where the stability is absent, the hysteresis loop for the half life of the material is considered to analyze the fatigue behavior [21]. Hence, the hysteresis loops at half of the fatigue lives are considered in the present study. For a material that obeys Masing behavior, the incremental branches of these loops should make a common envelope [22]. The compressive tips for all the stable hysteresis loops are translated to a common origin. The generated curve in Fig. 4a does not show a common envelope but the deviations are very little and can be considered as a near-Masing material [16].

The hysteresis loops at half life in Fig. 4a are translated such that the forward tensile branches for these loop forms a common loading curve known as master curve. The constructed master curve is shown in Fig. 4a. The deviation in the compressive tip of the hysteresis loop is called Masing deviation and denoted by $\delta\sigma_0$. For an ideal Masing material, $\delta\sigma_0$ [23] is zero; however, this value is within $\pm$ 40 MPa for the investigated rebar. Therefore, it could be considered to be a near Masing material [24].

3.5 Plastic Strain Energy Analysis

During the cyclic loading, there is continuous absorption and dissipation of strain energy. In case of concrete reinforced structure, the total cyclic load is handled by the rebars in any seismic event since brittle concrete fails easily. The fatigue damage or the material's fatigue resistance is called the plastic strain energy [25]. The amount

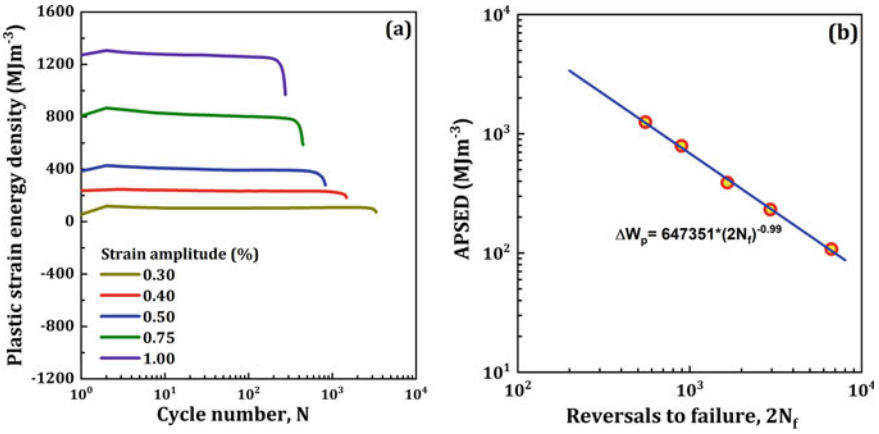

Fig. 5 **a** Plastic strain energy density (PSED) variation with cycle number, **b** Average PSED (APSED) variation with failure reversals

of energy absorbed in a particular cycle is the area of that particular hysteresis loop. The variation of hysteresis energy or the plastic strain energy density (PSED) with cycle number is shown in Fig. 5a. It can be noticed that there is an increment in PSED in the first cycle thereafter the value remains constant until a few cycles before failure where it decreases rapidly. The most part of fatigue life deals with crack initiation which is the nucleation and stable growth of micro-cracks [16]. During this time the PSED remains constant till the formation of macro-cracks by the coalescence of the micro-cracks after which there is a rapid decrease in the PSED as the load bearing capacity of the material gets reduced [25].

The PSED at half-life is commonly referred to as the average plastic strain energy density (APSED). The change of APSED with reversals to failure is shown in Fig. 5b in a double logarithmic graph. Morrow [26], and Golos and Ellyin [22] have correlated $\Delta W_p{}^{Ave}$ with failure reversal number ($2N_f$) by a power law equation as:

$$\Delta W_P^{Ave} = A(2N_f)^{\alpha} \tag{1}$$

where, A and α are the coefficient and exponent of plastic strain energy, respectively. A is also known as the coefficient of fatigue toughness which represents the capability of a material to absorb strain energy. Regression analysis of the data in Fig. 5b assist to find the values of A and α of the selected Fe 500S as 647.4 GJ/m^3 and -0.99, respectively. These parameters could be useful for the design and selection of rebars for concrete reinforced structure in the seismic prone areas.

3.6 Failure Mechanism

With the fatigue failure being surface phenomenon, the presence of notches in the surface deteriorates the fatigue life [27]. As for the rebars are concerned, the presence of ribs on the surface have an adverse effect on fatigue life. These ribs act as high-stress concentration areas. Therefore, these zones act as the potential sites for fatigue crack initiation sites. Though having an adverse effect on the fatigue life, the ribs cannot be removed owing to their significance in the perception of civil engineering. Hence as received specimens were tested and analyzed. A large number of SEM images of fracture surface had been recorded for a failed specimen tested at 1.0% strain amplitude. Among these, a few selected images is presented in Fig. 6.

Two distinct zones can be noticed in Fig. 6a which is demarked by black line. The area inside the black line is zone of fast fracture or tensile fracture, and the outer zone is the fatigue fracture. Two sites are marked as the crack initiation sites where the macro-cracks are generated [28, 29]. The fatigue cracks are started at the rib roots (Fig. 6a) which are the regions of higher stress concentration. Magnified view of the crack initiation zone is shown in Fig. 6b where the direction of fatigue crack propagation is also indicated. Fatigue cracks are found to propagate along the rim region. In case of TMT rebar, rim region contents tempered martensite which is hardened compared to ferrite-pearlite core (Fig. 1). Therefore, fatigue cracks propagate following rim region as it requires less energy [30].

A further magnified vision of the site near to the site of crack initiation reveals transverse micro-cracks as shown in Fig. 6c. On increasing the magnification further, fine striation marks are noticed as presented in Fig. 6d. Striations are caused by the repeated closer and opening of the cracks due to cyclic loading [5]. Zoomed view of the area corresponding to fast fracture has a dull appearance (Fig. 6e). Further magnified view in Fig. 6f reveals the presence of well developed dimples which is the signature of ductile fracture caused by tensile overloading in the last or final loading cycle. The macro-cracks propagate and become large enough making the material weak and at some point, the material becomes so weak that it cannot sustain the load and fails suddenly in the final cycle. It is worthy to mention that with raise in strain amplitude, the fatigue crack initiation and propagation processes take place at faster rates because of the increase in the rate of dislocation accumulation [31]. Hence, the number cycle to failure reduces with increasing strain amplitude. The area associated with fatigue failure diminishes with raise in the strain amplitude.

4 Conclusions

The fatigue properties under low cycle regime of Fe 500S TMT steel rebar which has been investigated over wide total strain amplitudes (0.3–1.0%). The investigation also included microstructure and tensile. The major conclusions are:

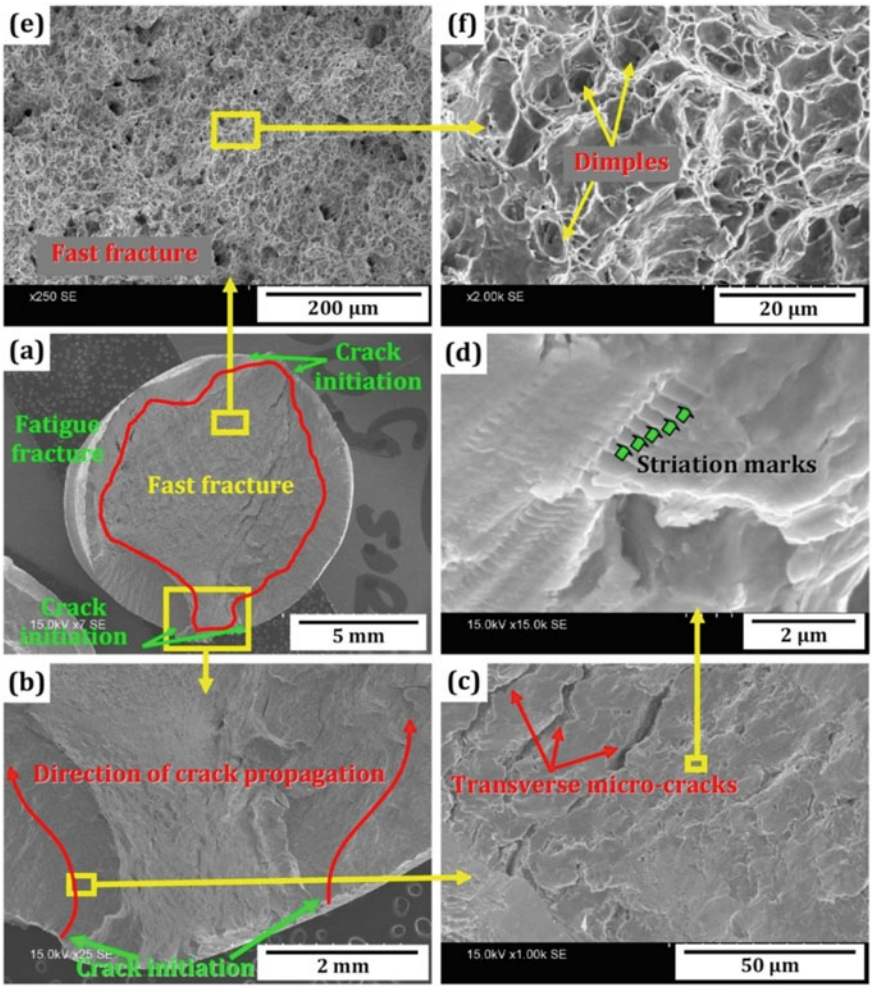

Fig. 6 Scanning electron microscope images showing the fracture behavior of Fe 500S TMT rebar of a failed specimen tested at 1.0% strain amplitude

- Fe 500S rebar experiences pronounced cyclic softening suggesting the worsening in the resistance to fatigue failure during any seismic events.
- Analyses of hysteresis loops and master curve establish that the investigated material follows near Masing behavior.
- The energy life equation is formulated for the material and using this equation the failure cycle can be calculated based on the applied energy which can be very useful for the design purpose of any structure for the selected rebar.

- The crack initiation sites are the rib roots owing to the higher stress concentration and cracks propagate in the rim region as less energy is required in hard tempered martensite in comparison to the soft ferrite-pearlite core.

References

1. Kumar R, Gardoni P (2012) Modeling structural degradation of RC bridge columns subjected to earthquakes and their fragility estimates. J Struct Eng 138:42–51
2. Tilly GP (1979) Fatigue of steel reinforcement bars in concrete: a review. Fatigue Fract Eng Mater Struct 2:251–268
3. MacGregor JG, Jhamb IC, Nuttall N (1971) Fatigue strength of hot rolled deformed reinforcing bars. Journal Proceedings 68:169–179
4. Bakkar MA, Kanrar B, Saha R, Das D (2020) High-strain low-cycle fatigue behavior of thermomechanically treated rebar. J Fail Anal Prev 20:1029–1037
5. Paul SK, Rana PK, Das D, Chandra S, Kundu S (2014) High and low cycle fatigue performance comparison between micro-alloyed and TMT rebar. Constr Build Mater 54:170–179
6. Apostolopoulos CA (2007) Mechanical behavior of corroded reinforcing steel bars S500s tempcore under low cycle fatigue. Constr Build Mater 21:1447–1456
7. Kashani MM, Alagheband P, Khan R, Davis S (2015) Impact of corrosion on low-cycle fatigue degradation of reinforcing bars with the effect of inelastic buckling. Int J Fatigue 77:174–185
8. Bar HN (2013) Low cycle and ratchetting fatigue behavior of high UTS/YS ratio reinforcing steel bars. J Mater Eng Perform 22:1701–1707
9. Abdalla JA, Hawileh RA, Oudah F, Abdelrahman K (2009) Energy-based prediction of low-cycle fatigue life of BS 460B and BS B500B steel bars. Mater Des 30:4405–4413
10. Paul SK, Majumdar S, Kundu S (2014) Low cycle fatigue behavior of thermo-mechanically treated rebar. Mater Des 58:402–411
11. Zheng H, Abel A (1998) Stress concentration and fatigue of profiled reinforcing steels. Int J Fatigue 20:767–773
12. Majumdar S, Ali R, Kumar A, Deb A (2018) Optimum rib design in TMT rebars to enhance fatigue life while retaining bond strength. J Mater Civ Eng 30:4017313
13. Mander JB, Panthaki FD, Kasalanati A (1994) Low-cycle fatigue behavior of reinforcing steel. J Mater Civ Eng 6:453–468
14. Park CS (2019) Tempcore process simulator to analyze microstructural evolution of quenched and tempered rebar. Appl Sci 9:2938
15. Panigrahi BK, Jain SK (2002) Impact toughness of high strength low alloy TMT reinforcement ribbed bar. Bull Mater Sci 25:319–324
16. Bakkar MA, Saha R, Das D (2020) Low cycle fatigue performance and failure analysis of reinforcing bar. Met Mater Int 1–15
17. Nandy S, Sekhar AP, Das D, Hossain SJ, Ray KK (2016) Influence of dynamic precipitation during low cycle fatigue of under-aged AA6063 alloy. Trans Indian Inst Met 69:319–324
18. Hertzberg RW, Vinci RP, Hertzberg (1989) Deformation and fracture mechanics of engineering materials. Wiley (1989)
19. Hussain K, De Los Rios ER (1993) Monotonic and cyclic stress-strain behaviour of high strength steel. Metall Sci Tecnol 11
20. Maier H, Gabor P, Gupta N, Karaman I, Haouaoui M (2006) Cyclic stress–strain response of ultrafine grained copper. Int J Fatigue 28:243–250
21. Chakraborti PC, Mitra MK (2005) Room temperature low cycle fatigue behaviour of two high strength lamellar duplex ferrite-martensite (DFM) steels. Int J Fatigue 27:511–518
22. Gołoś K, Ellyin F (1988) A total strain energy theory for cumulative fatigue damage. Trans ASME J Press Vessel Technol 110:35–41

23. Guguloth K, Sivaprasad S, Chakrabarti D, Tarafder S (2014) Low-cyclic fatigue behavior of modified 9Cr–1Mo steel at elevated temperature. Mater Sci Eng A 604:196–206
24. Das B, Bakkar A, Khutia N, Das D (2017) Low cycle fatigue performance evaluation of TMT rebar. Mater Today Proc 4:2554–2563
25. Sarkar PP, De PS, Chakraborti PC (2017) Strain energy based low cycle fatigue damage analysis in a plain C-Mn rail steel. Mater Sci Eng A 707:125–135
26. Morrow JD (1965) Internal friction, damping and cyclic plasticity. ASTM STP 378:45
27. Rocha M, Bruehwiler E, Nussbaumer A (2015) Microstructural influence on the scatter in the fatigue life of steel reinforcement bars. Int J Fatigue 75:205–212
28. Pantazopoulos G, Pressas I, Vazdirvanidis A (2019) Fatigue failure analysis of a Ø14 B500C steel rebar: Metallurgical evaluation and numerical simulation. Eng Fail Anal 101:180–192
29. Suresh S (1998) Fatigue of materials. Cambridge university press
30. Zheng H, Abel AA (1999) Fatigue properties of reinforcing steel produced by TEMPCORE process. J Mater Civ Eng 11:158–165
31. Dutta K, Sivaprasad S, Tarafdar S, Ray KK (2010) Influence of asymmetric cyclic loading on substructure formation and ratcheting fatigue behavior of AISI 304LN stainless steel. Mater Sci Eng A 527:7571–7579

An Assessment of Wettability of Glass/Epoxy Composites Modified with CNT and MLG

Shiny Lohani, Srinivasu Dasari, Soumya Sumit Dash, Rajesh Kumar Prusty, and Bankim Chandra Ray

Abstract As the commercialization of fiber-reinforced polymer (FRP) composites is gaining momentum and new investigations for understanding their behavior are constantly being undertaken by researchers worldwide. Exhaustive studies are being conducted to interpret the behavior of FRP composites modified with nanoparticles like multi-walled carbon nanotubes (MWCNTs) and multi-layered graphene (MLG). The effect of environmental factors determines the feasible use of these composites in commercially viable applications. This study aims to interpret the surface properties of FRP composites modified by nanoparticles in terms of contact angle measurement using water at room temperature. In this study, nanofillers were incorporated into epoxy and this modified polymer was used for fabricating the laminated glass fiber reinforced polymer (GFRP) composites. Six types of laminates were prepared having different concentration of MWCNT (0.2, 0.4 and 0.6 wt%) and MLG (0.2, 0.4 and 0.6 wt%)., Samples from each of these laminates were used for measuring the water contact angle. The values obtained for different nanoparticle concentrations in the GFRP composite were compared and analysed with neat GFRP composite. 0.6 wt% MLG-GE samples showed the highest contact angle among all samples suggesting the role of nanoparticles in decreasing hydrophilicity of composites, thereby increasing their durability.

Keywords GFRP composite · Contact angle · Multi-walled carbon nanotubes · Multi-layered graphene

1 Introduction

Fiber-reinforced polymer (FRP) composites are being extensively commercialized, owing to the various benefits they offer in terms of high strength-to-weight ratio, good corrosion resistance, flexibility in design, and excellent structural properties [1]. Intending to further improvise their properties, incorporation of nanomaterials,

S. Lohani · S. Dasari (✉) · S. S. Dash · R. K. Prusty · B. C. Ray
FRP Composite Lab, Department of Metallurgical and Materials Engineering, National Institute of Technology, Rourkela 769008, India

S. Pal et al. (eds.), *Processing and Characterization of Materials*, Springer Proceedings in Materials 13, https://doi.org/10.1007/978-981-16-3937-1_15

most popularly, carbon nanotubes and graphene, into the laminated composites via different techniques is becoming the point of interest for researchers. Researchers globally are carrying out experiments and investigations to understand the behavior of this modified epoxy with nanofillers composites under specific environmental conditions and for more commercial applications. The surface of material plays a crucial role in determining its compatibility with the environment; it is important to interpret how the environment can affect the surface properties of FRP composites so that they can be put to real-world applications [2].

To improve the mechanical performance of FRP composites, modification by adding nanofillers has become an active research interest. Nanofillers like 1-D carbon nanotubes and 2-D graphene are being explored for their high elastic modulus, tensile strength, high aspect ratio, low density, and thermal conductivity, to mitigate the drawbacks of various materials. When nano-sized particles are incorporated into a material, their physical interaction with the matrix facilitates good interfacial adhesion. This is the primary reason for the improvement of mechanical properties of composites modified with nano-fillers [3, 4]. Interfacial properties are related to the surface characteristics of the nanofillers and can be correlated to wettability. Effective estimation of surface properties can be done by measuring the contact angle of a liquid on the solid surface. Using water as the liquid and measuring its contact angle on polymeric specimens can help in deciding their use for various applications. The composite which is better than others in allowing water to drain off from its surface promises more durability and increased life span. Understanding the flow and wettability performance of glass/epoxy modified with nanomaterials will assist in producing void-free parts and successful designing of components using composites [5, 6].

Researchers in the past have conducted evaluations of the contact angle of liquids on polymeric samples. Hameed et al. [7] studied the wettability behavior of epoxy resin blends modified with thermoplastics and GFRP composites using various liquids. They observed a decrease in wettability and hydrophilicity with increasing concentration of thermoplastic poly styrene-co-acrylonitrile (SAN) in the matrix. Song et al. [8] evaluated the water contact angle of Basalt fiber reinforced polyamide composites and made important conclusions regarding the surface roughness, surface energy, and hydrophilicity characteristics of the composites. A study conducted by Park et al. [9] inferred an increase in surface energy and surface roughness due to the addition of CNTs and hence a reduction in hydrophilic behavior was observed. They investigated the static contact angle of CNT-epoxy nanocomposites and concluded hydrophobic behavior by wettability tests. The characterization of surface properties of nanofillers, nanofilms, as well as composites containing nanofillers as reinforcements has become an interesting research area. Such studies are being actively taken up by various research professionals as important research topics [2, 4, 10]. The scientific community is taking a keen interest in assessing the wettability behavior which is evident from various research works as mentioned above. The Young-Dupre Equation is the combination of the Young equation, which relates surface energy to contact angle, and the Dupre equation, which relates surface energy to work of adhesion. Work of adhesion is an important parameter which is a measure of how strong

the contact between two phases. The Young-Dupre equation relates work of adhesion with contact angle [11].

The current investigation deals with measuring the water contact angle of GFRP composites modified by different concentrations of multi-walled carbon nanotubes (MWCNT) and multi-layer graphene (MLG). The Young-Dupre Equation was used to calculate the strength of contact between the drop of water and the sample surface.

2 Experimentation

2.1 Materials

For fabricating the laminated composites, 3 K plain woven E-glass fiber was used as reinforcement. This fiber, with each filament 15 μm in diameter, was supplied by Owens Corning, India. The matrix used was epoxy resin, bearing the chemical name diglycidyl ether of Bisphenol A (DGEBA) and trade name Lapox L-12, along with the curing agent Triethylene tetra amine (TETA) with trade name K-6, both procured from Atul Industries Ltd. India. The two types of nanofillers used in the experiment, MWCNT and MLG were supplied by Platonic Nanotech Ltd. India.

2.2 Matrix Modification

The incorporation of nanofillers into the epoxy resin involves several steps described as follows. The measured amount of MWCNT (0.2, 0.4 and 0.6 wt% of epoxy) was added to 250 mL of acetone taken in a conical flask. The mouth of the flask was closed to avoid the evaporation of acetone. It was magnetically stirred at room temperature at 1000 rpm for 30 min. Then it was sonicated in an ultrasonicator for 30 min. Meanwhile, epoxy resin was taken into another conical flask and magnetically stirred at 120 °C and 400 rpm for 30 min. The acetone solution with MWCNT was poured into epoxy resin and this flask was placed on the magnetic stirrer at 120 °C and 1000 rpm. After all the acetone evaporated, the flask was degassed under vacuum for 18 h. The same procedure was followed to prepare MLG modified epoxy of concentrations (0.2, 0.4 and 0.6 wt% of epoxy).

2.3 Fabrication

The modified matrix was used for the fabrication of laminates by hand lay-up technique. This involved spreading modified epoxy with the help of a brush on a glass fiber sheet, placing another sheet on top of it, and then rolling a hand roller over it.

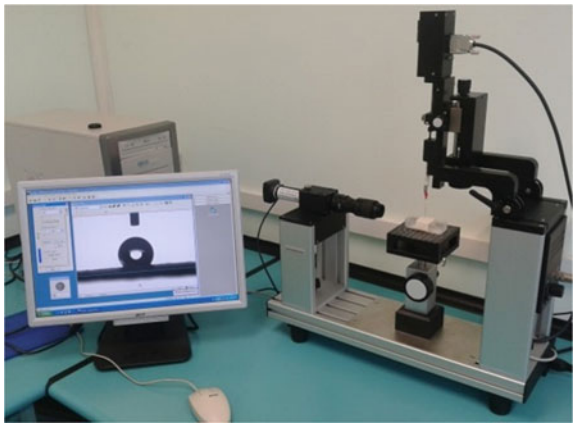

Fig. 1 Contact angle meter

10-layered laminates were prepared and hot pressed for 20 min at 60 °C ensuring a thickness of 3 mm. Samples of dimension 25 mm × 25 mm × 3 mm were cut and polished, and then cured at 140 °C for 6 h.

2.4 Water Contact Angle Measurement

Contact Angle Meter (Data Physics OCA 30, Germany) is the instrument which was used for measuring the static contact angle at room temperature. This video-based instrument is equipped with a nano dosing system and uses Wilhelmy plate and sessile drop techniques. A liquid droplet of 500nL volume can be placed on the surface of a sample at 1.2 bar pressure. The equipment contains a video-based system that enables careful observation of the liquid drop and ensures precise measurement of the contact angle. The measurement involves drawing a tangent at the point of contact of the drop with the substrate (explained in Sect. 3). Tangents are drawn on both the left and right ends of the liquid drop with the substrate as the base. Those observations are considered in which the contact angle obtained at the left end and the right end show the minimum difference. The difference in contact angle values may vary at the left and right end of the same drop due to surface roughness and distortions in the sample. Figure 1 shows the contact angle meter used for the measurement.

3 Results and Discussion

Wettability is an important characteristic which determines the suitability of a material for specific applications. Wettability determination is based on the material surface contact angle. Contact angle is the main parameter that characterizes the drop

shape on the solid surface and is also a property of the interface that can be directly measured. Wettability depends on the surface roughness and chemical composition. A change in these parameters can affect the contact and, therefore, wettability [12]. The contact angle of a liquid on a particular substrate determines how well it can wet the substrate. A contact angle of 0° signifies perfect wetting of the substrate by the liquid and that of 180° shows complete non-wetting. For contact angles less than 90°, the attractive forces between the liquid and the substrate dominate the surface tension of the substrate and the substrate has good wettability. If the contact angles are greater than 90°, the substrate has lower wettability for the liquid and the surface tension is dominant over the attractive forces between the liquid and the substrate (shown in Fig. 2).

Figure 3 shows the water contact angle values of glass/epoxy samples containing different concentrations of nanofillers (MWCNT and MLG). For glass/epoxy composites modified with MWCNT, the contact angle increases as the concentration of the nanofillers in the composite is increased. A steep increase in contact angle occurs by the addition of 0.2 wt% MWCNT in the epoxy matrix, as shown in Fig. 1.

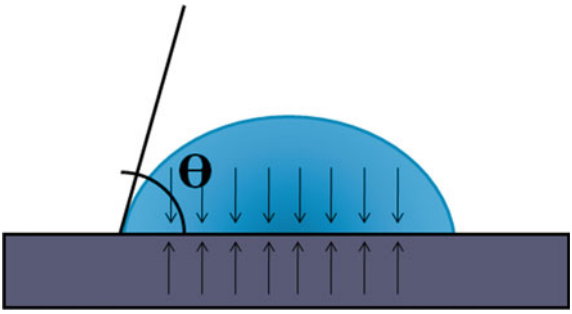

Fig. 2 The contact angle of a water drop with the substrate

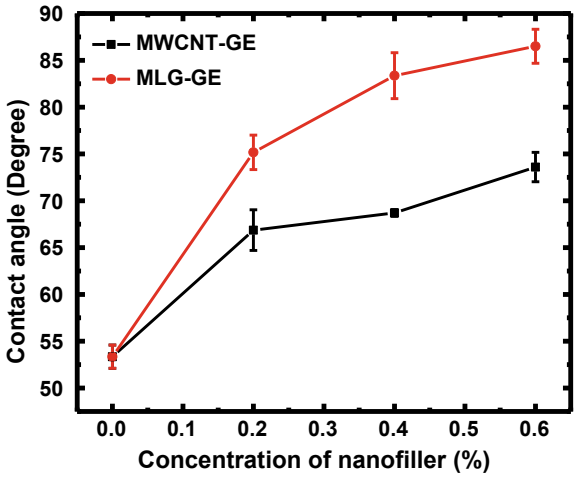

Fig. 3 The water contact angle for MWCNT-GE and MLG-GE with 0.2, 0.4, and 0.6 wt% nanofillers

On increasing MWCNT content, 0.4% MWCNT-GE shows a slight increment in contact angle value. The slope of the increment curve is not as steep as the previous case. By adding 0.6 wt% MWCNT, the contact angle has increased 39.5% than neat GE composite. This depicts that matrix modification with MWCNTs increases contact angle and reduces wettability. Reduction in wettability after the addition of carbon nanotubes may be due to increased surface roughness along with heterogeneity effects. The surface roughness of a solid sample can amplify the hydrophobic behavior of materials [10, 13]. Another reason is the decrement of the number of hydrogen bonds with increasing CNT concentration in composites [14]. Likewise, in MLG-GE samples, contact angle increases with the increasing concentration of MLG in the matrix. The increase in the value of water contact angle is higher for the same concentrations of MLG than for MWCNT nanofillers embedded in GE samples, the highest value being 86.5°, shown by 0.6 wt.% MLG-GE. This suggests that MLG provides higher hydrophobicity to GFRP composite than MWCNT. The primary reason for this could be the 2-D nature and flaky morphology of MLG in contrast to the 1-D tube-like structure of MWCNTs. Studies done on specific surface area (SSA) of CNTs and graphene have concluded that graphene has much higher SSA than nanotubes [15, 16]. As already established, both these nano-fillers are hydrophobic; the one with higher SSA will provide more repulsion to the liquid droplet, thereby having higher contact angle. Since graphene has higher SSA, so this might be the reason for higher contact angle values obtained for MLG-GE samples. With much steeper curves, MLG addition in GFRP has shown a remarkable increment in water contact angle than all other configurations considered in the study. Modified epoxy with 0.6 wt% of MLG in GE composite shows a 68.4% increase in contact angle than neat GE. Large water contact angles were obtained for graphene sheets in literature as well, which supports the results obtained in the current study. Further, thicker graphene sheets, i.e. those with more layers show higher hydrophobicity [17].

Figure 4 shows optical images of the water drop on the sample surface. On careful observation, the changes in the wetting behavior can be understood. Figure 4a shows the water drop shape on neat GE substrate. The spread in the drop shape subsequently reduces in Fig. 4b–d as the concentration of MWCNT in the composite increases. The decrease in the spreading of the water drop is much more evident when Fig. 4a is compared to Fig. 4e–g with increasing concentrations of MLG in the composite.

When the contact angle is acute (i.e., less than 90°), it indicates that the composite substrate is hydrophilic in nature. As the contact angle increases and approaches values closer to 90°, there is a reduction in hydrophilicity and the substrate becomes less wettable by water. For the same concentration, MLG-GE specimens show a higher contact angle than MWCNT-GE samples. This shows that, for the same concentration, MLG is more effective in reducing the hydrophilicity of the composite than MWCNT. A reduction in hydrophilic behavior means that the composite is less wettable than water which reduces the chances of water adsorption and increases the service life of the composite.

The discussions about the wettability behavior of these composites can be analyzed further using the concept of “work of adhesion”. Denoted by W_{ls}, it is the work done to separate two phases. When a liquid wets the substrate, the interface

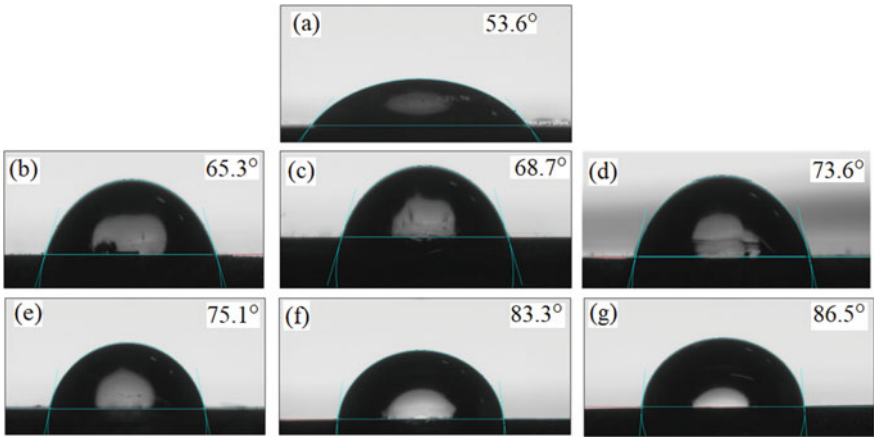

Fig. 4 Optical images of water drop on **a** neat GE, **b** 0.2% MWCNT-GE, **c** 0.4% MWCNT-GE, **d** 0.6% MWCNT-GE, **e** 0.2% MLG-GE, **f** 0.4%-MLG-GE, **g** 0.6% MLG-GE

is formed which is accompanied by the release of energy in correspondence to the surface tension of the solid and liquid [2, 7].

The contact angle is related to the surface free energy of the solid, liquid and their interface by the Young's equation as follows:

$$\gamma_s = \gamma_{sl} + \gamma_l \cos\theta \tag{1}$$

where γ_s, represents the surface free energy of the surface of the solid, γ_l is the surface free energy of the liquid, γ_{sl} is the surface free energy of the solid–liquid interface, and θ is the contact angle made by the liquid on the solid substrate.

Dupre's equation relates work of adhesion with the surface energies as follows:

$$W_{sl} = \gamma_s + \gamma_l - \gamma_{sl} \tag{2}$$

On combining Eqs. (1) and (2), we arrive at the following relationship for a solid–liquid interface, called the Young-Dupre's Equation.

$$W_{sl} = \gamma_l(1 + \cos\theta) \tag{3}$$

This means that W_{sl} can be calculated from the surface tension of the liquid and the contact angle. Table 1 shows the W_{sl} values calculated for all the samples considered in this study.

W_{ls} is a measure of the strength of contact between two phases. A high W_{ls} value signifies that there is strong contact between two phases. From the values presented in Table 1, it can be deduced that as the concentration of nano-filler increases, W_{ls} decreases. This means that the adherence of the liquid phase, i.e., water, with the

Table 1 W_{sl} calculated using Eq. (3) for all samples

Sample	W_{ls} (mJ/m^2)	Sample	W_{ls} (mJ/m^2)
Neat GE	114.7		
0.2% MWCNT-GE	102.04	0.2% MLG-GE	90.48
0.4% MWCNT-GE	98.11	0.4% MLG-GE	80.37
0.6% MWCNT-GE	92.29	0.6% MLG-GE	76.36

sample surface decreases with increasing nano-filler content. Therefore, the surface wettability and hydrophilicity reduce with an increase in the concentration of nano-fillers, which makes the substrate less wettable by water.

4 Conclusions

In the presented work, the water contact angle of glass/epoxy composites modified with different concentrations of MWCNT and MLG were measured and compared with neat glass/epoxy composite. The following conclusions can be drawn based on the analysis done.

- The addition of nanofillers increases the water contact angle. The values increase with an increase in concentration, both in MWCNT-GE and MLG-GE. By adding 0.6 wt% MWCNT, the contact angle has increased 39.5% than neat GE composite. The highest value of θ, 86.5° was shown by 0.6 wt% MLG-GE.
- The increment in water contact angle observed for the same concentration is higher for MLG incorporated GE composites than those modified with MWCNT.
- Work of adhesion, a measure of the strength of contact between the solid and liquid, decreases with an increase in the concentration of nanofillers, suggesting a decrement in hydrophilicity of the composites. Increase in hydrophobic nature will enable the composites to have better durability by draining off water easily from the surface.
- Analysis of the results reveals applications of FRPs modified with nanofillers in environments suffering from frequent rain showers, high humidity, and certain marine applications as well.

Acknowledgements The authors are profoundly grateful to the National Institute of Technology Rourkela and Science and Engineering Research Board (DST) (ECR/2018/001241) for dispensing financial support for continuing the research work. The technical support from Mr. Rajesh Patnaik is highly thankful.

References

1. Alberto M (2013) Introduction of fibre-reinforced polymers—polymers and composites: concepts, properties and processes. Fiber Reinf. Polym. - Technol. Appl. Concr. Repair. InTech. https://doi.org/10.5772/54629.
2. Wang S, Zhang Y, Abidi N, Cabrales L (2009) Wettability and surface free energy of graphene films. 25:11078–11081. https://doi.org/10.1021/la901402f
3. Raj R, Maroo SC, Wang EN (2013) Wettability of graphene. https://doi.org/10.1021/nl304647t
4. Zhang L, Wang J, Fuentes CA, Zhang D, Van Vuure AW, Seo JW et al (2017) Wettability of carbon nanotube fibers. Carbon N Y 122:128–140. https://doi.org/10.1016/j.carbon.2017.06.027
5. Oskouei AV, Bazli M, Ashrafi H, Imani M (2018) Flexural and web crippling properties of GFRP pultruded profiles subjected to wetting and drying cycles in different sea water conditions. Polym Test 69:417–430. https://doi.org/10.1016/j.polymertesting.2018.05.038
6. Benzarti K, Colin X (2013) Understanding the durability of advanced fibre-reinforced polymer (FRP) composites for structural applications. https://doi.org/10.1533/9780857098641.3.361
7. Hameed N, Thomas SP, Abraham R, Thomas S (2007) Morphology and contact angle studies of poly (styrene-co-acrylonitrile) modified epoxy resin blends and their glass fibre reinforced composites. 1:345–355. https://doi.org/10.3144/expresspolymlett.2007.49
8. Song J, Liu J, Zhang Y, Chen L (2015) Basalt fibre-reinforced PA1012 composites : morphology, mechanical properties, crystallization behaviours, structure and water contact angle. https://doi.org/10.1177/0021998313519484.
9. Park J, Wang Z, Jang J, Renaud J, Gnidakoung N, Lee W et al (2009) Composites: part A interfacial and hydrophobic evaluation of glass fiber/CNT – epoxy nanocomposites using electro-micromechanical technique and wettability test. Compos Part A 40:1722–1731. https://doi.org/10.1016/j.compositesa.2009.08.006
10. Park JM, Wang ZJ, Jang JH, Gnidakoung JRN, Lee W Il, Park JK et al (2009) Interfacial and hydrophobic evaluation of glass fiber/CNT-epoxy nanocomposites using electro-micromechanical technique and wettability test. Compos Part A Appl Sci Manuf 40:1722–1731. https://doi.org/10.1016/j.compositesa.2009.08.006.
11. Schrader ME (1995) Young-Dupre revisited. Langmuir 11:3585–3589. https://doi.org/10.1021/la00009a049
12. Slepickova Kasalkova N, Slepicka P, Kolska Z, Svorcik V (2015) Wettability and other surface properties of modified polymers. Wetting and wettability. InTech. https://doi.org/10.5772/60824
13. Kim SH (2008) Fabrication of superhydrophobic surfaces. J Adhes Sci Technol 22:235–250. https://doi.org/10.1163/156856108X305156
14. Werder T, Walther JH, Jaffe RL, Halicioglu T, Noca F, Koumoutsakos P (2001) Molecular dynamics simulation of contact angles of water droplets in carbon nanotubes. Nano Lett 1:697–702. https://doi.org/10.1021/nl015640u
15. Peigney A, Laurent C, Flahaut E, Bacsa RR, Rousset A (2001) Specific surface area of carbon nanotubes and bundles of carbon nanotubes. Carbon N Y 39:507–514. https://doi.org/10.1016/S0008-6223(00)00155-X
16. Sur UK (2012) Graphene: a rising star on the horizon of materials science. Int J Electrochem 2012:1–12. https://doi.org/10.1155/2012/237689
17. Melios C, Giusca CE, Panchal V, Kazakova O (n.d.) Water on graphene: review of recent progress

Preparation and Optical Characterization of $LaMnO_3$ Thin Films by Sol–Gel Technique

Apurba Mahapatra, Somnath Mahapatra, Rashmirekha Sahu, and Pawan Kumar

Abstract Searching for a chemically stable solar-absorbing layer having earth-rich elements is the key factor for next-generation photovoltaic techniques. Many theoretical studies proposed that Mott insulators have potential as photovoltaic materials. In this study, we report the systemic resuls of structural, microstructural, and optical properties of Mott insulator $LaMnO_3$ (LMO) thin films. Structural characterization was performed by X-ray diffraction (XRD), and microstructural properties was studied by FESEM. The crystallite size and particle size of the LMO thin film are ~17.8 nm and in 30–50 nm range with uniform grain distribution. EDX spectrum of LMO thin films confirmed the maintenance of the stoichiometric ratio of $LaMnO_3$. The optical property of LMO thin films was studied and analyzed by a UV–Vis spectrometer. LMO thin films show an indirect bandgap of ~1.27 eV with a strong electron correlation. LMO is another promising material as a light absorber for next-generation solar cells due to its absorption onset at ~1.2 eV and then two subsequent peaks at ~2.2 and ~3.1 eV with strong light absorption over a wide wavelength range in the solar spectrum.

Keywords Mott insulators · Photovoltaic · Bandgap

1 Introduction

Among next-generation photovoltaic techniques, inorganic–organic lead halide perovskites received a special attention due to their good power conversion efficiency (PCE) with their easy and low-cost fabrication [1, 2]. The PCE of the hybrid inorganic–organic perovskite solar cells (PSCs) has improved from 3.3 to 25.2% within a decade [1, 3]. Despite the progress, low long-term stability [4] and lead toxicity are the main constraints in the way of commercialization. Recently, single-crystalline based lead halide perovskites are used for optoelectronic application due

A. Mahapatra · S. Mahapatra · R. Sahu · P. Kumar (✉)
Department of Physics & Astronomy, National Institute of Technology, Rourkela, India
e-mail: pawankumar@nitrkl.ac.in

S. Pal et al. (eds.), *Processing and Characterization of Materials*, Springer Proceedings in Materials 13, https://doi.org/10.1007/978-981-16-3937-1_16

to higher stability than their polyaniline counterparts and thin films [5–7]. Chemically stabile solar-absorbing materials having earth-rich elements is the key factor for next-generation photovoltaic techniques. According to the Schockley-Queisser limit, the performance of the photovoltaic will be maximized for ~1.34 eV bandgap solar cells. Oxide materials are chemically non-toxic, cheap, and stable, but it is tough to find proper oxide materials for photovoltaic applications due to higher bandgap and lower conductivity. In the last few years, Mott insulators resolve this problem due to their wide-bandgaps [8]. Many theoretical studies proposed that Mott insulators have potential as photovoltaic materials [9–11]. Manousakis et al. predicted that the solid Coulombic interaction may prompt the carrier multiplication process in Mott insulators, increasing the quantum efficiency [12]. Perovskite Mott insulators have general formula of ABO_3, where A and B cations are in coordinates with 12 oxygen (anions) such as $SrTiO_3$, $LaVO_3$, $LaMnO_3$ (LMO), etc. When an electrical insulator material converts to an electrical conductor under several factors, like stress, electric field, temperature, composition, oxidation, etc., then this process is known as Mott transition. The conductivity increases due to the Mott transition (electron–electron transition). The electron–electron correlation inside Perovskite Mott insulators can be increased by oxidizing or adding some impurities like n or p type doping, metal doping, carbone composite etc. [13] Oxide-based Mott insulators have unique characteristics, same as inorganic–organic lead halide perovskites. They are soluble in the organic solvent, environmental friendly (lead-free), low-temperature solution-based processing and strong light absorption (104–105 cm^{-1}), which makes them promising as a solar-absorbing material [8]. Lingfei Wang et al. explored Mott insulator $LaVO_3$ as a solar-absorbing layer and showed its strong light absorption over a wide wavelength range with an indirect bandgap of ~1.08 eV [14]. According to Hubbard model, oxide Mott insulator $LaVO_3$ shows strong electron–electron repulsion within partly filled vanadium (V) 3d band at the Fermi level. It breaks the half-filled valance band (VB) to the filled lower Hubbard band (LHB) and unfilled upper Hubbard band (UBH). Moreover, the Mott insulators with similar perovskite structures and appropriate bandgap (theoretically 1.34 eV) can offer strong light absorption in the solar spectrum and can be used as solar-absorbing material. On the other hand lanthanum manganite (LMO) is mainly used as a magnetic field sensor and other electronic devices, due to colossal magnetoresistance (CMR) effect and complex magnetic behavior. Mott insulator LMO has $LaVO_3$ like perovskite structure which may have a potential for next-generation solar cell absorber materials.

In this study, we fabricate LMO thin film on a glass substrate by sol–gel technique and directly analyzed its structural and optical behaviors, and discussed it in detail. Our results reveal that LMO is another promising material for the solar-absorbing layer due to its absorption onset at ~1.2 eV followed by two subsequent peaks at ~2.2 and ~3.1 eV with an indirect bandgap of ~1.27 eV.

2 Experimental Procedure

2.1 Synthesis of LMO Thin Films

The processing steps of LMO thin film by the sol–gel technique are summarized in Fig. 1. Equimolar amounts of Lanthanum(III) acetylacetonate and Manganese(III) acetylacetonate ware dissolved separately in 5 ml methanol and 5 ml propanoic acid at 80 °C in a fume hood. After 10 min, Lanthanum(III) acetylacetonate was mixed drop by drop in Manganese(III) acetylacetonate solution at 100 °C. Next, equimolar amount of Ethylene glycol was used as a stabilizer and heated for 30 min. Next, the transparent LMO solution was cooled to room temperature and sealed. Glass slides and FTO (Fluorine doped tin oxide) coated glass were used as a substrate for thin film deposition. After one day, the glass and FTO coated substrates were washed and then dried and heated up to 500 °C and then cooled. Next, the glass substrates and FTO coated glass are placed for 20 min under UV-rays. Next, the thin film deposition substracts are heated up to 120 °C on a hot plate and put on the spin-coating unit. LMO solution was dropped on glass and FTO coated substrates and rotated with 1000 rpm for 30 s. Next, the films were dried at 200 °C and cooled down. This deposition process was repeated six times, and the final LMO films were annealed at 570 °C for 3 h.

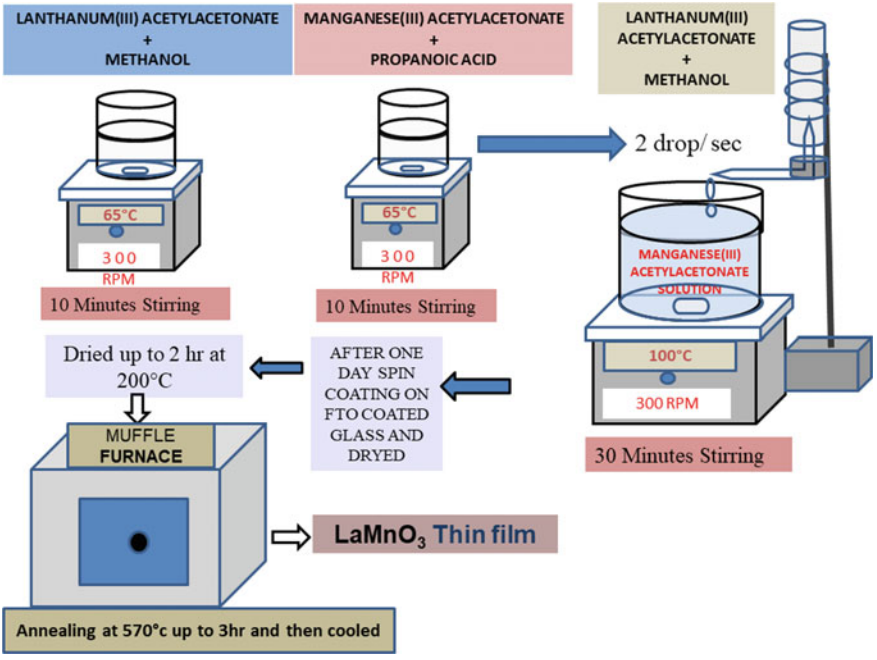

Fig. 1 Summary steps of LMO thin-film preparation by sol–gel technique

2.2 Characterization of LMO Thin Films

The X-ray diffraction (XRD) patterns of LMO thin films were recorded with a Rigaku Ultima IV diffractometer equipped with copper 1.5406 Å Kα radiation over a 2θ range of 20–70° without rotating the samples at room temperature. The morphology, energy-dispersive X-ray analysis (EDX), and average particle size of LMO thin films were observed by a compact NOVA Nano-SEM (field emission scanning electron microscopy (FESEM)) unit. The optical properties of LMO thin films have been studied by SHIMADZU UV-200 UV-V is spectrometer (SHIMADZU UV-200).

3 Results and Discussion

3.1 X-Ray Diffraction Analysis

The XRD diffraction patterns of LMO thin films, taken after annealed at 570 °C confirmed the single-phase perovskite-type $LaMnO_3$ structure matched with JCPDS No. 75–0440 (Fig. 2b). The XRD patterns of LMO films annealed at 550 °C have secondary phases with peak shift (Fig. 2a). The average crystallite size (D) of LMO films was calculated by using the Debye–Scherrer formula [15]:

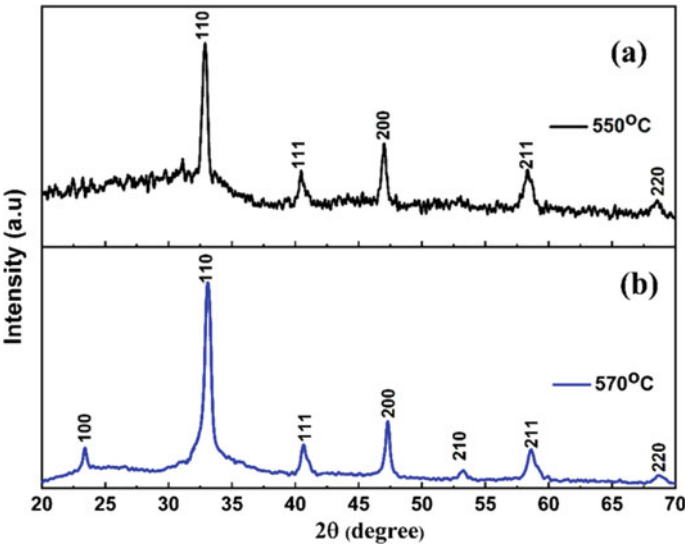

Fig. 2 XRD patterns of LMO films deposited on glass subtract and annealed at **a** 550 °C and **b** 570 °C

$$D = (k * \lambda)/(\beta * \cos(\theta)) \quad (1)$$

where, β, λ, θ, k are the full width at half maximum (FWHM), X-ray radiation wavelength, the Bragg angle, respectively, and the dimensionless shape factor (=0.94). Optimized processing temperature for LMO thin films using this method is lower compared to traditional solid-state reaction, reverse micellar route using Tergitol and atomic layer deposition (ALD) technique, [16, 17] and also cost-effective. The calculated average crystallite size using this formula is found to be ~17.8 nm.

3.2 FESEM and EDX Spectra Study

FESEM micrograph and EDX spectrum of optimized LMO films are shown in Fig. 3a, b, respectively. FESEM image shows LMO thin-films have spherical particles with an average particle size between 30 and 50 nm. No specific impurity was noticed from EDX spectrum of LMO films. Through EDX spectrum analysis, the stoichiometric ratio of LMO films was calculated, which is summarized in Table 1. The EDX results give the stoichiometric ratio of La:Mn:O as 1:1.03:3.35, which is relatively similar to the theoretical ratio of $LaMnO_3$. The LMO film growth on glass substrate is homogeneous and uniform.

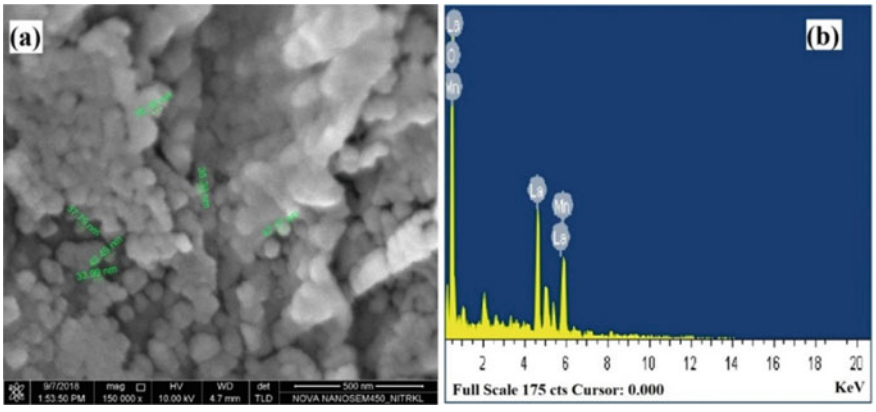

Fig. 3 **a** Surface morphology and **b** EDX pattern of LMO thin films deposited on glass subtract and annealed at 570 °C

Table 1 Element composition of LMO thin films

Elemental	Weight%	Atom%	Calculated ratio of elements
O, K	21.6	62.25	3.35
Mn, K	22.78	19.19	1.03
La, L	55.62	18.56	1

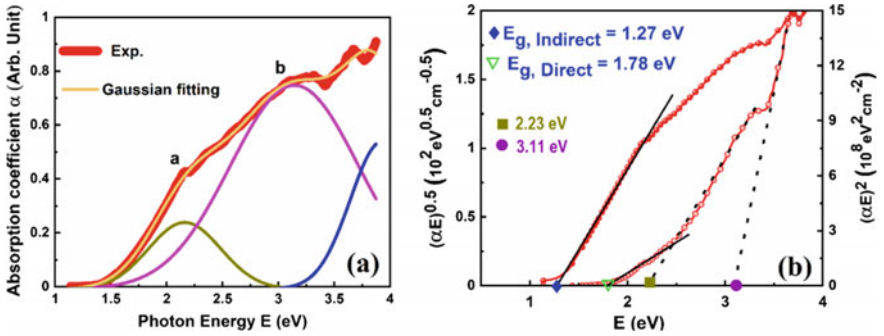

Fig. 4 **a** Absorption spectrum of LMO thin films and fitting curves with three Gaussian peaks. **b** Tauc plot of absorption spectrum (for direct and indirect bandgap calculation) of LMO thin films

3.3 UV–Vis Spectra Analysis

UV–visible absorbance spectra of the LMO films (Fig. 4a) are systematically measured and evaluated at room temperature. The absorption spectrum displays two subsequent peaks at ~2.2 and ~3.1 eV with an absorption onset at ~1.2 eV. The absorption onset and ~2.2 eV peak overlay with the solar spectrum in the visible range. These results indicate that, like $LaVO_3$, LMO is another promising material for solar-absorbing material in solar cells [8, 14]. After a small decrease at ~2.3 eV, absorption rapidly enhances in the UV range. Three Gaussian peaks can fit this absorption spectrum of LMO [14, 18]. Tauc plots of thin films using Tauc equation are shown in Fig. 4b [15].

$$\alpha h\nu = B\left(h\nu - E_g\right)^n \tag{2}$$

where B is a constant and α, h, ν, E_g are the absorption coefficient, Planck constant, frequency of the incident electromagnetic radiation, and bandgap energy, respectively. In this equation, the value of 'n' becomes two and half for indirect and direct bandgap of the film, respectively. For indirect bandgap, the Tauc equation can be express as,

$$(\alpha E)^{(1/2)} = B\left(h\nu - E_g\right) \tag{3}$$

For dirct bandgap, this equation becomes,

$$(\alpha E)^2 = B\left(h\nu - E_g\right) \tag{4}$$

Figure 4b shows both Tauc plots for direct and indirect bandgap of LMO thin films. Like LVO films, $(\alpha E)^2$ versus E plot of LMO thin films shows complex behavior [14]. In Fig. 4b, the linear fitting at absorption edge and higher-energy range respectively

gives a direct bandgap of ~1.78 eV and two direct bandgaps at ~2.23 and ~3.11 eV, which hints towards a hierarchical like band-gap behaviour [19]. Above the absorption edge, $(\alpha E)^{(1/2)}$ versus E plot shows a sharp rise with indirect bandgap of ~1.27 eV. These study suggest that LMO films has an indirect band gap, with the sharp rise at the absorption edge. On the other hand, direct bandgaps at higher energy suggest that the strong electron correlation in LMO. This strong electronic correlation may enable an indirect transition from LHB to UHB. This results revels widerange absorption with several interband-intraband excitations in LMO films.

4 Conclusions

LMO thin films were successfully prepared and optimized at a relatively lower temperature compared to other synthesis processes. The crystallite size and particle size of the LMO thin film are ~17.8 and 30–50 nm. The particle size of films is in the nanometer range, and there is a uniform distribution of grains. EDX spectrum of LMO thin films confirmed the maintenance of stoichiometric ratio in the thin films. UV–visible absorbance spectra of the LMO films indicating that, like $LaVO_3$, LMO is another promising material for solar-absorbing material due to its absorption onset at ~1.2 eV with two subsequent peaks at ~2.2 and ~3.1 eV. These bandgap studies suggest that LMO film has an indirect bandgap of ~1.27 eV with gradual enhancement at the absorption edge with strong electron correlation. These results reveal that the LMO films can be used in solar cells and other photo-sensing devices.

References

1. Mahapatra A, Prochowicz D, Tavakoli MM, Trivedi S, Kumar P, Yadav P (2020) A review of aspects of additive engineering in perovskite solar cells. J Mater Chem A 8:27–54
2. Kalam A, Al-Sehemi AG, Mahapatra A, Verma D, Trivedi S, Pandey MK (2019) Identification of defects and defect energy distribution in the perovskite layer of MAPbI3-xClx perovskite solar cell. Mater Res Express 6:105510
3. Best Research-Cell Efficiency Chart (2021) Photovoltaic Research. NREL. https://www.nrel.gov/pv/cell-efficiency.html. Accessed 21 Jan 2021
4. Mahapatra A, Parikh N, Kumar P, Kumar M, Prochowicz D, Kalam A, Tavakoli MM, Yadav P (2020) Changes in the electrical characteristics of Perovskite solar cells with aging time. Molecules 25:2299
5. Kalam A, Runjhun R, Mahapatra A, Tavakoli MM, Trivedi S, Tavakoli Dastjerdi H, Kumar P, Lewiński J, Pandey M, Prochowicz D, Yadav P (2020) Interpretation of resistance, capacitance, defect density, and activation energy levels in single-crystalline MAPbI3. J Phys Chem C 124:3496–3502
6. Mahapatra A, Parikh N, Kumari H, Pandey MK, Kumar M, Prochowicz D, Kalam A, Tavakoli MM, Yadav P (2020) Reducing ion migration in methylammonium lead tri-bromide single crystal via lead sulfate passivation. J Appl Phys 127:185501
7. Song Y, Bi W, Wang A, Liu X, Kang Y, Dong Q (2020) Efficient lateral-structure perovskite single crystal solar cells with high operational stability. Nat Commun 11

8. Dixit H, Punetha D, Pandey SK (2019) Performance investigation of Mott-insulator LaVO3 as a photovoltaic absorber material. J Electron Mater 48:7696–7703
9. Scafetta MD, Cordi AM, Rondinelli JM, May SJ (2014) Band structure and optical transitions in LaFeO3: theory and experiment. J Phys Condens Matter 26
10. Nakamura M, Sawa A, Fujioka J, Kawasaki M, Tokura Y (2010) Interface band profiles of Mott-insulator/Nb: SrTiO3 heterojunctions as investigated by optical spectroscopy. Phys Rev B Condens Matter Phys 82:201101
11. Arima T, Tokura Y, Torrance JB (1993) Variation of optical gaps in perovskite-type 3d transition-metal oxides. Phys Rev B 48:17006–17009
12. Coulter JE, Manousakis E, Gali A (2014) Optoelectronic excitations and photovoltaic effect in strongly correlated materials. Phys Rev B Condens Matter Mater Phys 90:165142
13. Subudhi S, Mahapatra A, Mandal M, Das S, Sa K, Alam I, Subramanyam BVRS, Raiguru J, Mahanandia P (2020) Effect of Co doping in tuning the band gap of LaFeO3. Integr Ferroelectr 205:61–65
14. Wang L, Li Y, Bera A, Ma C, Jin F, Yuan K, Yin W, David A, Chen W, Wu W, Prellier W, Wei S, Wu T (2015) Device performance of the Mott insulator LaVO3 as a photovoltaic material. Phys Rev Appl 3:064015
15. Mahapatra A, Subudhi S, Swain S, Sahu R, Negi RR, Samanta B, Kumar P (2019) Electrical and optical properties of yttrium titanate thin films synthesized by Sol-Gel technique. Integr Ferroelectr 203:43–51
16. Ahmad T, Ramanujachary KV, Lofland SE, Ganguli AK (2006) Reverse micellar synthesis and properties of nanocrystalline GMR materials (LaMnO3, La0·67 Sr0·33 MnO3 and La0·67 Ca0·33 MnO3): ramifications of size considerations (2006)
17. Khanduri H, Chandra Dimri M, Vasala S, Leinberg S, Lõhmus R, Ashworth TV, Mere A, Krustok J, Karppinen M, Stern R (2013) Magnetic and structural studies of LaMnO3 thin films prepared by atomic layer deposition. J Phys D Appl Phys 46:175003
18. Sushko PV, Qiao L, Bowden M, Varga T, Exarhos GJ, Urban FK, Barton D, Chambers SA (2013) Multiband optical absorption controlled by lattice strain in thin-film LaCrO3. Phys Rev Lett 110
19. Sun Q-C, Sims H, Mazumdar D, Ma JX, Holinsworth BS, O'neal KR, Kim G, Butler WH, Gupta A, Musfeldt JL (2012) Optical band gap hierarchy in a magnetic oxide: electronic structure of NiFe2O4. Phys Rev B 86:205106

Influence of TiO_2 Particle on the Friction Stir Welding of 7075 Al Alloy

Gautam Behera, Subhadra Sahoo, Nigamananda Ratha, Abhijit Rout, and Manila Mallik

Abstract The effect of TiO_2 particles on the mechanical and corrosion properties of the friction stirred welded 7075 aluminium alloys were studied. Surface topography of the welded samples was carried out with a scanning electron microscope (SEM). Energy dispersive spectroscopy (EDS) was performed to analyze the presence of TiO_2 particles in the weld. The tensile strength of the base 7075 Al alloy was compared with the reinforced and unreinforced weld. The tensile strength of the base alloy is high as compared to weld alloy. The drastic decrease in tensile strength of the welded sample may be ascribed to the dynamic recrystallization followed by grain growth which is the consequence of heat generated due to the friction between the tool and weld material. Residual stresses generated due to welding also affect the strength of the weld. However, the tensile strength of the reinforced alloy is found to be more in contrast to the unreinforced 7075 aluminium alloy. It can be interrelated to the existence of TiO_2 particles which is incorporated in the matrix. The fracture surface was examined through SEM. Overall it shows the ductile mode of fracture. However, in the presence of TiO_2 particle, there is evidence of both intergranular and transgranular fracture. The corrosion behavior was studied by conducting potentiodynamic polarization test with 3.5 wt% NaCl solution. The base alloy shows more corrosion resistance than the unreinforced and reinforced weld.

Keywords Friction stir welding · Stir zone · Nugget · Dimple · Transgranular fracture · Intergranular fracture

1 Introduction

High strength to weight ratio and high fracture toughness of 7075 Al alloy makes it suitable for various applications which include automotive, aerospace, defense, and marine industries [1, 2]. Depending on the area of application, this alloy is joined with the same or different Al alloy. For joining purpose, solid state joining

G. Behera · S. Sahoo · N. Ratha · A. Rout · M. Mallik (✉)
Department of Metallurgical and Materials Engineering, Veer Surendra Sai University of Technology, Burla 768018, Odisha, India

S. Pal et al. (eds.), *Processing and Characterization of Materials*, Springer Proceedings in Materials 13, https://doi.org/10.1007/978-981-16-3937-1_17

especially solid-state welding has gained a lot of attention. Friction stir welding (FSW) comes under solid state joining which is vastly suggested for Al alloys [3, 4]. It is a hot deformation process where the tool rotates and generates heat by the friction between the tool and the base metal [5]. Welding defects are inevitable, but FSW is confronted with less welding defects. Not only fewer welding defects but the weld portion imparts high mechanical strength also. The joining is possible without the temperature exceeding 0.8 T_m (K) and typically, the welding temperature for aluminum 7075 alloy lies between 425 and 480 °C [5]. Many researchers have worked on FSW of 7075 aluminum alloy [4, 5]. In addition to this, some work has also been carried out on friction stir welding of heat treated 7075 alloys to the other grades of aluminium alloy [6]. The change in properties of weld metal is related to the change in microstructure which is associated with structure–property co-relation. Tool geometry, rotating speed of the tool, welding speed, and the prior condition of weld metal are the measure factors that affect the property of the weld metal during FSW. Composite preparation through the addition of reinforcement to the matrix by the process of friction stir welding has gained a lot of attention. Aluminium metal matrix composite has been synthesized successfully by FSW with improved properties and homogeneous distribution of reinforcement. The effect of reinforcement like SiC, TiC, carbon nanotubes (CNT), and TiO_2 has already been studied on different properties of friction stir welding of aluminium alloys [7–12]. Bahrami et al. have studied the effect of SiC on the properties of FSW of 7075 alloy. Both the tensile strength and the toughness are increased due to the amalgamation of SiC nanoparticles in 7075 Al alloy [13]. Lim et al. have used multi-walled carbon nanotube (MWCNT) as a reinforcement in the matrix of Al alloy [12]. It is observed that the factors like the rotation of the tool speed and the penetration of the probe are going to affect the distribution of MWCNT. Homogeneous distribution is achieved when the rotation of the tool is increased from 1500 to 2500 rpm. Micron size SiC particles have also been used as a reinforcement for Al 6351 alloy where the grain growth is restricted due to SiC particles [14]. Mechanical behavior is studied for Al 2618 metal matrix composite reinforced with 20% Al_2O_3 where the tensile test is conducted for the nugget zone at different strain rates and high temperature i.e. in the range of 400–500 °C [15]. Above 10^{-2} s^{-1} strain rate, it shows higher ductility and strain rate sensitivity. Hybrid composite is also synthesized by FSW where SiC and graphite particulate are used as reinforcement in 6063 Al alloy. Surface composite using graphite and graphite + SiC are also synthesized at different volume fractions. SiC particulate reinforced composite shows improved property as compared to graphite and graphite + SiC reinforced composite [8]. Palanivel et al. have worked on the synthesis of Aluminum metal matrix hybrid composite where TiB_2 and BN are used as reinforcement [16]. It is noticed that the wear mode in case of sliding wear is changed from adhesive wear to abrasive wear. As per available literature, no researcher has studied the influence of TiO_2 powder on the mechanical and corrosion properties of FSW of 7075 aluminium alloy.

2 Experimental Procedure

For this study, plates of aluminium 7075 alloy were taken whose dimension was of (12 × 10 × 6) mm^3. Welds were produced with and without TiO_2. The average particle size of TiO_2 was in the range of 2–5 μm with a purity of 99%. A groove of 2 mm depth and 1 mm width was prepared along the weld line to accommodate TiO_2 powder in both the plates, which is represented in Fig. 1 (left).

FSW was conducted at a spindle speed of 750 rpm under a load of 100 kg. It was done at a feed rate of 35 mm/min. The FSW was attached with a hot worked tool steel (H13) with a hardness of 52 HRC and the shoulder dia. was 18 mm. The pin dia. and height were 6 and 5.8 mm, respectively. The experimental setup is shown in Fig. 1 (right). The transverse section was polished and etched with Keller's reagent. Then the polished surface was examined with a scanning electron microscope (SU3500 HITACHI SEM). Compositional characterization was done with energy dispersive spectroscopy (Oxford EDS) attached to SEM. The tensile test was done in a universal testing machine (UTE-HGFL-TS-20) and the test sample was prepared according to ASTM E8M-04 standard. The test was done at a rate of 0.003 s^{-1}. The fracture surface of the tensile sample was studied through SEM. The corrosion test was done in POTENTIOSTAT 302 N attached with NOVA 2.1 software. 3.5 wt% NaCl solution was prepared for the test. Platinum and saturated Ag/AgCl were used as counter and reference electrode, respectively. The potential sweep range was from −1 to +1 V. The sample to be corroded was used as a working electrode. The scan rate was 0.05 mV/sec. Optical micrographs of the corroded surface were captured by an optical microscope (Leica DM 1705M).

Fig. 1 The groove along the weld line of 7075 aluminium alloy (left) and the tool set up of for FSW of 7075 aluminium alloy (right)

3 Results and Discussion

3.1 Microstructural Characterization

Different zones are created during FSW which comprises of nugget or stir zone (SZ), thermomechanical affected zone (TMAZ), and heat affected zone (HAZ) [17]. Different zones of the unreinforced and reinforced weld are shown in Figs. 2 and 3, respectively. Figure 4 shows the high magnification image of the stir zone with smooth onion rings which symbolize a good weld quality. Onion rings are the characteristic features of the FSW that are formed due to both rotational and translational movement of the probe [18]. In certain cases, onion rings get disappear due to high tool rotational speed, as a result of the easy flowability of the material [19]. Hasan et al. have revealed that there is no deleterious effect of the onion rings on the weld behavior [20]. The distribution of TiO_2 particles is seen in Fig. 5b. It is also verified through EDS (Fig. 5d) where well defined peaks of Ti are present.

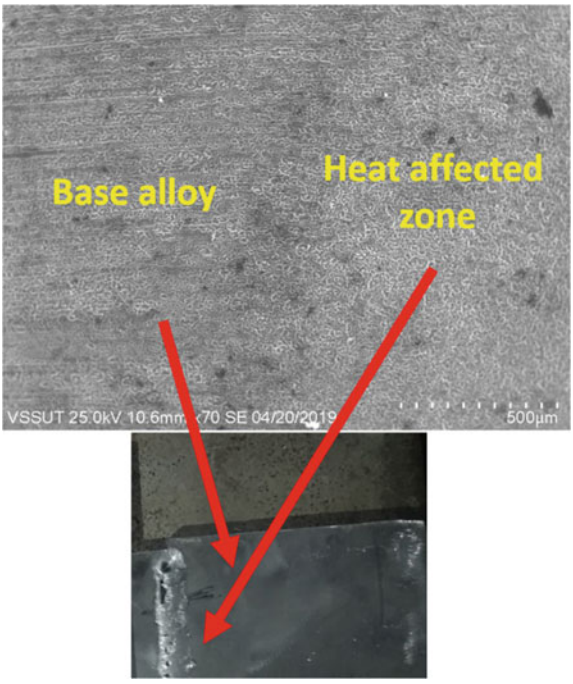

Fig. 2 SEM microstructure of base alloy and heat affected zone of FSWed uneinforced 7075 aluminium alloy

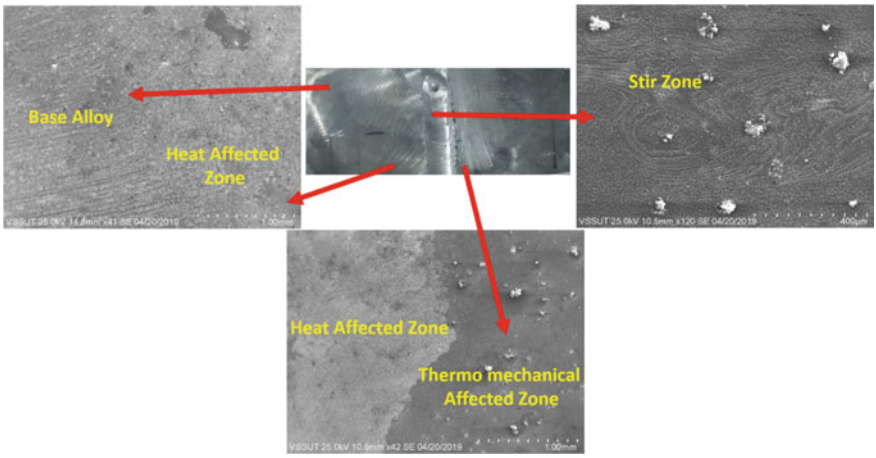

Fig. 3 SEM microstructure of different zones of FSWed 7075 aluminium alloy reinforced with TiO_2 powder

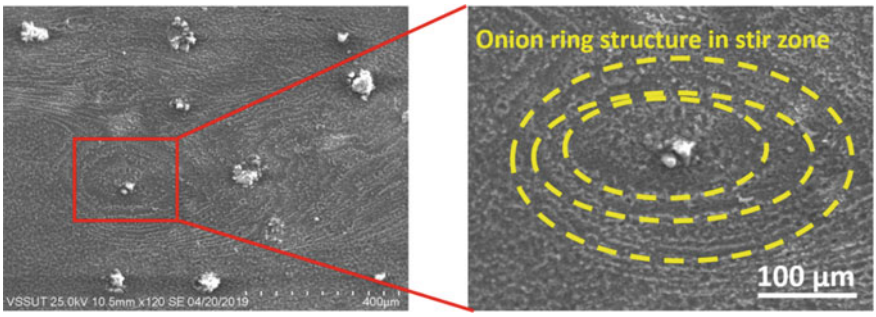

Fig. 4 The presence of onion rings in the SEM image of nugget or stir zone for 7075 aluminium alloy reinforced with TiO_2 powder

3.2 Tensile Test Analysis

The tensile test data is shown in Table 1. This shows that the tensile strength of the base alloy is high as compared to weld alloy. The drastic decrease in tensile strength of the welded sample may be attributed to the dynamic recrystallization followed by grain growth which is the aftermath of heat generated due to the friction between the tool and weld material. Residual stresses generated during welding also affect the strength of the weld. However, the tensile strength of the reinforced alloy is found to be more in contrast to the unreinforced 7075 aluminium alloy. It can be interrelated to the presence of TiO_2 particles in the matrix. Dislocation density is increased due to the thermal mismatch between the reinforced particle and the matrix alloy which in succession increases the strength of the reinforced FSWed sample [21].

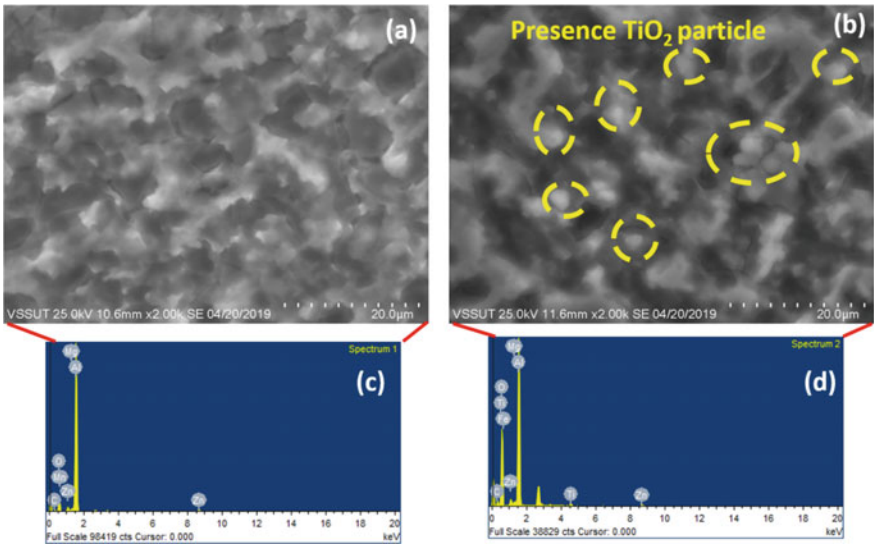

Fig. 5 SEM micrographs of stir zone present in the weld sample: **a** unreinforced and **b** reinforced, and bulk EDS of the weld **c** unreinforced and **d** reinforced

Table 1 Ultimate tensile strength (UTS) of base and FSWed 7075 Al alloy

	Base 7075 Al alloy	FSW without reinforcement	FSW with reinforcement
UTS (MPA)	430.19	132.68	140.42

3.3 Fractography

It is observed from Fig. 6a, b that the mode of fracture is ductile and which is confirmed through the dimple like features present in the SEM micrographs.

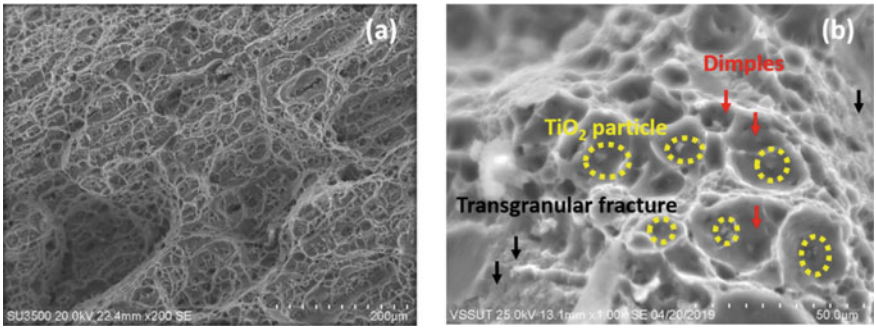

Fig. 6 Fracture surface of the weld 7075 aluminium alloy: **a** unreinforced and **b** reinforced with TiO_2

In the case of a reinforced FSWed sample, TiO_2 particles are partially bulged out from the center of the dimples present in the fractograph. It indicates that the interface between the TiO_2 particle and the matrix acts as the nucleation site for the fracture and the decohesion finally terminates with ductile fracture. Dimples are shown as red arrow marks in Fig. 6b. However, some evidence of transgranular fracture (black arrow mark present in Fig. 6b is also perceived in some regions of the fracture surface of the reinforced weld.

3.4 Corrosion Plot Analysis

It is observed from the corrosion plot (Fig. 7) and Table 2 that the base 7075 Al alloy shows higher corrosion resistance than the reinforced as well as unreinforced weld. The diminution of corrosion resistance in the weld is due to the welding defect and residual stress generated during welding. It has already been revealed that 7075 alloy is a precipitation strengthened alloy. The precipitate gets coarsen as the

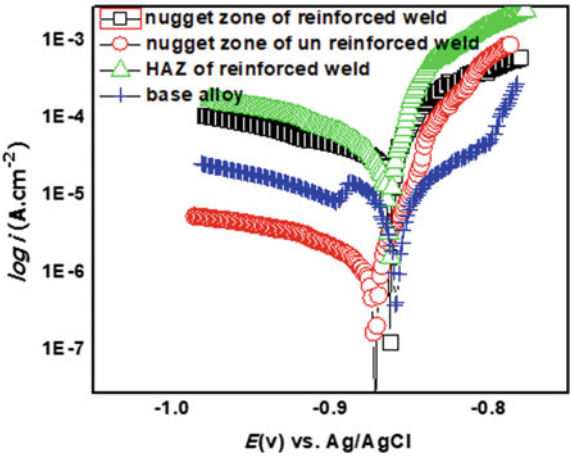

Fig. 7 The potentiodynamic polarization curve for base alloy, unreinforced and reinforced weld, and HAZ of reinforced weld

Table 2 The parameters for potentiodynamic curves

Different regions of sample	I_{corr} (mA/cm^2)	$-E_{corr}$ (mV vs. SCE)
Unreinforced weld (Stir zone)	1.077E−02	862.97
Reinforced weld (Stir zone)	4.302E−04	871.24
Reinforced weld (HAZ)	4.0304E−02	848.3
Base alloy	3.7005E−04	858.26

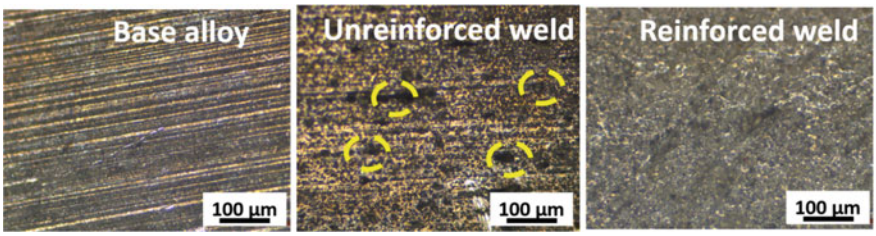

Fig. 8 Optical micrographs of pits formed due to corrosion in base alloy, unreinforced and reinforced weld

welding temperature reaches the mushy state temperature. A galvanic cell is developed between the precipitate and the matrix where the precipitates formed in grain boundary acts as a cathode and the rest area behaves as an anode [22]. However, the corrosion is a pitting type of corrosion which is visible in Fig. 8. The pitting corrosion mainly depends on the chloride ion concentration [23]. The improvement in corrosion resistance of reinforced weld is because of the passivation provided by uniformly distributed TiO_2 particles in an aluminium alloy matrix. Uniform distribution of TiO_2 particles also prevents the formation of a galvanic cell.

4 Conclusions

i. Reinforced particle i.e., TiO_2 was successfully incorporated into 7075 aluminium alloy through friction stir welding. These are uniformly distributed in the matrix.
ii. The tensile strength of TiO_2 reinforced weld is more than the unreinforced weld sample. The reduction in tensile strength of the weld sample in comparison to the base alloy sample is due to dynamic recrystallization followed by grain growth. The increase in tensile strength of the reinforced weld is due to the addition of TiO_2 particles.
iii. Ductile fracture is observed in both unreinforced and reinforced TiO_2 weld. There was some sign of transgranular type brittle fracture in the reinforced weld.
iv. The base alloy shows higher corrosion resistance than the weld. The incorporation of the reinforced particle increases the corrosion resistance of the weld alloy. Pitting type of corrosion is observed in weld alloy and the improvement in corrosion resistance of reinforced weld is because of the passivation provided by uniformly distributed TiO_2 particles in an aluminium alloy matrix.

References

1. Su JQ, Nelson TW, Mishra R, Mahoney M (2003) Microstructural investigation of friction stir welded 7050–T651 aluminium. Acta Mater 51(3):713–729
2. Shen Z, Yang X, Zhang Z, Cui L, Li T (2013) Microstructure and failure mechanisms of refill friction stir spot welded 7075–T6 aluminum alloy joints. Mater Des 44:476–486
3. Gerlich A, Avramovic-Cingara G, North TH (2006) Stir zone microstructure and strain rate during Al 7075-T6 friction stir spot welding. Metall Mater Trans A 37(A):2773–2786
4. Israr JJP, Israr M (2017) Experimental investigation of friction stir welding of aluminium alloy AA7075 for various process parameters. Int J Mech Solids 12(2):169–177
5. Kumar PV, Reddy GM, Rao KS (2015) Microstructure, mechanical and corrosion behavior of high strength AA7075 aluminium alloy friction stir welds—effect of post weld heat treatment. Def Technol 11(4):362–369
6. Kumar SK, Kumar P (2016) Study the effect of parameters of friction stir welding on the impact strength of aluminium 6063. Int J Curr Eng Technol 6(3):993–998
7. Tabasi M, Farahani M, Besharati Givi MK, Farzami M, Moharami A (2015) Dissimilar friction stir welding of 7075 aluminum alloy to AZ31 magnesium alloy using SiC nanoparticles. Int J Adv Manuf Technol
8. Dhayalan R, Kalaiselvan K, Sathiskumar R (2014) Characterization of AA6063/SiC-Gr surface composites produced by FSP technique. Procedia Eng 97:625–631
9. Bahrami M, Helmi N, Dehghani K, Kazem M, Givic B (2014) Exploring the effects of SiC reinforcement incorporation on mechanical properties of friction stir welded 7075 aluminum alloy: fatigue life, impact energy, tensile strength. Mater Sci Eng A 595:173–178
10. Uzun H (2007) Friction stir welding of SiC particulate reinforced AA2124 aluminium alloy matrix composite. Mater Des Mater Des 28:1440–1446
11. Mirjavadi SS, Alipour M, Emamian S, Kord S, Hamouda AMS, Koppad PG, Keshavamurthy R (2017) Influence of TiO2 nanoparticles incorporation to friction stir welded 5083 aluminum alloy on the microstructure, mechanical properties and wear resistance. J Alloy Compd 712:795–803
12. Lim DK, Shibayanagi T, Gerlich AP (2009) Synthesis of multi-walled CNT reinforced aluminium alloy composite via friction stir processing. Mater Sci Eng A 507(1):194–199
13. Bahrami M, Helmi N, Dehghani K, Givi MKB (2014) Exploring the effects of SiC reinforcement incorporation on mechanical properties of friction stir welded 7075 aluminum alloy: Fatigue life, impact energy, tensile strength. Mater Sci Eng A 595:173–178
14. Karthikeyan P, Mahadevan K (2015) Investigation on the effects of SiC particle addition in the weld zone during friction stir welding of Al 6351 alloy. Int J Adv Manuf Technol 80(9):1919–1926
15. Cavaliere P (2005) Mechanical properties of friction stir processed 2618/Al2O3/20p metal matrix composite. Compos A Appl Sci Manuf 36(12):1657–1665
16. Palanivel R, Dinaharan I, Laubscher RF, Davim JP (2016) Influence of boron nitride nanoparticles on microstructure and wear behavior of AA6082/TiB2 hybrid aluminum composites synthesized by friction stir processing. Mater Des 106:195–204
17. Thota V, Rao K, Kalvala P (2004) Studies on friction stir welded AA 7075 aluminum alloy. Trans Indian Inst Met 57:659–663
18. Krishnan KN (2002) On the formation of onion rings in friction stir welds. Mater Sci Eng A 327(2):246–251
19. Weng F, Liu Y, Chew Y, Lee BY, Ng FL, Bi G (2020) Double-side friction stir welding of thick magnesium alloy: microstructure and mechanical properties. Sci Technol Weld Joining 25(5):359–368
20. Hasan MM, Ishak M, Rejab MRM (2017) Effect of pin tool design on the material flow of dissimilar {AA}7075-{AA}6061 friction stir welds. IOP Conf Ser Mater Sci Eng 257:12022
21. Akbari MK, Baharvandi HR, Shirvanimoghaddam K (2015) Tensile and fracture behavior of nano/micro TiB2 particle reinforced casting A356 aluminum alloy composites. Mater Des 1980–2015(66):150–161

22. Gharavi F, Matori K, Yunus R, Othman NK, Fadaeifard F (2015) Corrosion behavior of Al6061 alloy weldment produced by friction stir welding process. J Mater Res Technol 31
23. Corral J, Trillo E, Li Y, Murr L (2000) Corrosion of friction-stir welded aluminum alloys 2024 and 2195. J Mater Sci Lett 19:2117–2122

Correlation of Corrosion Resistance of Hot Rolled UHSS with Its Microstructure

Pradip K. Patra and Ashok Kumar Srivastava

Abstract Usage of Ultra High Strength Steel (UHSS) is found to be increasing in automobile application for enabling vehicle weight reduction with higher safety. This steel is mostly used for long and cross member of vehicle and exposed to contact of corrosive material while vehicle is running. Corrosion test of Hot rolled UHSS coil conforming to EN 10149-2-S700MC and S650MC are done by Potentiodynamics Polarization Test Method in Potentiometer with 3.5% aqueous NaCl solution as electrolyte. Although both the coils are rolled from same heat (Chemistry), but exhibited significantly different corrosion rate, such as 1.427 mm/year for S700MC and 0.287 mm/year for S650MC. Detail microstructure study under optical microscope, SEM, and EBSD shows that S700MC is having much higher dislocation density, grain boundary area, precipitate interface than that of S650MC. Hence strengthening mechanisms such as precipitation, dislocation, grain refinement—which have contributed to higher strength in S700MC, are the reason for higher corrosion rate also.

Keywords UHSS · Steel · S700MC · S650MC · Corrosion · Microstructure

1 Introduction

1.1 Air Pollution and Vehicle Emission

For containment and reduction of air pollution, Government of India (GOI) is taking lot of initiatives over last few decades. India participated in United Nations conference on Human Environment in Stockholm, Sweden in 1972 to boost this international initiative. Subsequently GOI enacted The Air (Prevention and Control of Pollution) Act'1981 as follow up action. Latest initiative is National Clean Air Programme (NCAP)'2019 [1] under Ministry of Environment, Forest and Climate Change (MoEFCC). The impact of air pollution is not only limited to human health, but extends to entire flora and fauna. As it is air borne, its impact is felt far away from

P. K. Patra (✉) · A. K. Srivastava
Department of Metallurgical Engineering, SOE, OP Jindal University, Raigarh 496109, India

S. Pal et al. (eds.), *Processing and Characterization of Materials*, Springer Proceedings in Materials 13, https://doi.org/10.1007/978-981-16-3937-1_18

source. Incidences of episodic air pollution in winter in Delhi and its negative impact on human health is known to all due to huge media coverage. Although different source adds different constituents of air pollution, contribution of vehicle in overall air pollution is very significant.

In the vehicle/transport sector, GOI has taken following key actions for improvement of energy efficiency and control of air pollution:

(i) Advanced vehicle emission and fuel quality standards: BS-IV from 2017 and BS-VI from 2020. *(BS-VI, which is equivalent to Euro-VI emission norm, is very strictly implemented for new vehicle registration in India w.e.f. 01.04.2020 in spite of COVID-19 pandemic and lot of representation for crumbling automobile industry to extend the deadline).*
(ii) Plan to introduce a voluntary fleet modernization and an old-vehicle scrappage programme in India.
(iii) Introducing a National Electric Mobility Mission Plan 2020.
(iv) Introducing gas as an automotive fuel in many cities.

While signing MOU with Finland's Environment Minister Krista Mikkonen through virtual summit on 26.11.20 on biodiversity conservation, India's Environment Minister Prakash Javaedkar stated that voluntary target of reducing emissions intensity of India's GDP by 21 per cent over 2005 levels by 2020 had been already achieved. India is also confident to reduce by 35 per cent much ahead of the target year of 2030 [2]. Corporate Average Fuel Efficiency norms is also implemented in India. Automobile manufacturers need to improve fuel efficiency by 10% by 2021 over that in 2017 and 30% or more by 2022 [3]. For improving fuel efficiency of transport vehicle along with reduction of emission of pollutants, lighter vehicle is the major solution. But lighter vehicle may compromise safety.

1.2 Vehicle Safety

As per the WHO Global Report on Road Safety 2018, India ranks at the top of world (11 death per 1 lac population—4th highest) for automotive fatalities accounting almost 11% of Road accidents across the world [4]. In calendar year of 2018, about 4.7 lacs of road accidents happened leading to 1.5 lacs death in India. Road accidents and death are higher over previous year by 0.5% and 2.3% respectively. In line with adaptation of world standard emission norms, GOI is also developing Bharat New Vehicle Safety Assessment Program (BNVSAP) [5, 6] similar to Global New Car Assessment Programme (NCAP) [7] for voluntary safety star rating. MoRTH-GOI has notified on 28.04.15 [8] making crash test mandatory for models of vehicles manufactured from 1st October'2019 onwards. Car buyers have started comparing safety features also in addition to price, fuel economy and look of the car for selection. For protection of occupants of vehicle in case of a crash/accident, vehicle structure has to be strong. Structure made of thicker steel can make it stronger, but vehicle will be heavier.

1.3 Smart Stronger Steel for Lighter But Safer Vehicle

Automakers started looking for much stronger steel with good formability, weldability, fatigue strength, which can replace mild/high strength steel in vehicle structure with lower thickness (*minimum 20% savings on steel weight*) to get lighter vehicle with higher rating in crash test. Advanced High Strength Steel (AHSS) with ultimate tensile strength (UTS) > 780 MPa, is usually called Ultra High Strength Steel (UHSS) [9, 10]. UHSS meets such requirement of automakers. Position of UHSS steel – EN 10149-2-S650MC/S700MC is shown within famous Steel Strength Ductility Diagram, published by World Auto Steel (Fig. 1). As per specification of S650MC and S700MC, minimum YS (MPa) and range of UTS (MPa) are 650/700–880 and 700/750–950 respectively. This UHSS is manufactured by different steel makers with different composition and different process. In this research project, EN 10149-2-S650MC/S700MC is produced in JSW Steel, Dolvi works. Alloy design is done to select Low Carbon High Strength Low Alloy (HSLA) with Nb-Ti microalloy combination at optimum Fe-alloy cost with judicial use of Thermo-Mechanical-Controlled-Process (TMCP) of hot rolling in Compact Strip Process (CSP). Usually such steel contains ferrite phase (soft) steel with combination of bainite, martensite, retained austenite and fine precipitates (hard phases) to produce favourable combination of strength, formability and fracture toughness [11, 12]. UHSS is mostly used for making long and cross members of cars and heavy vehicles and body of dumpers, which is exposed to contact of corrosive materials/atmosphere while in use.

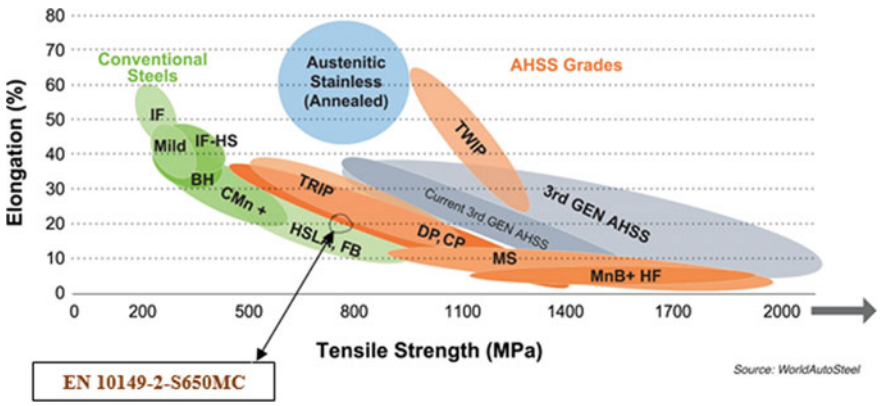

Fig. 1 Steel strength ductility diagram [9]

1.4 Corrosion Resistance of UHSS

Availability of research paper of corrosion test of bare UHSS is very limited. In actual use, all structural components of vehicle are coated to protect from corrosion. Even then corrosion resistance of base steel remains important for its life cycle. Hunsu Gerengi et al. have studied corrosion resistance of Docol 1200 and Docol 1400. They have used electrochemical corrosion test in 3.5 wt% NaCl solution [13]. Docol 1200 is cold rolled complex phase (CP) steel with UTS about 1200 MPa. Docol 1400 is cold rolled martensitic steel with UTS about 1400 MPa. Corrosion resistance of Docol 1200 is found to be better than Docol 1400 contrary to comparison of their strength. Usually as the strength of steel increases (other than stainless and other corrosion resistant steel), its corrosion resistance decreases. The metal atoms with the highest free energy are more susceptible to corrosion [14]. Atoms at surface or interphase are of higher free energy in comparison to atoms lying in bulk of material. Interphases are boundaries among different phases, grains, precipitates, impurities, voids, dislocations etc. Hence atoms in surface or interfaces are more likely to be corroded. The more is the interphases, the more is the corrosion rate. Same factors are also main contributing factor to strength of steel. It appears that stronger steel will be less corrosion resistant.

In the present work, Corrosion test of Hot rolled UHSS coil conforming to EN 10149-2-S700MC and S650MC are done by Potentiodynamics Polarization Test Method in Potentiometer with 3.5% aqueous NaCl solution as electrolyte. The corrosion test results are analysed w.r.t. respective microstructures and EBSD reports for metallurgical explanation.

2 Experimental Method

Industrial trial production of this UHSS is done in the integrated steel plant of India—JSW Steel Limited, Dolvi works (erstwhile ISPAT Industries Limited) through (BF + SIP) – CONARC – LF – CSP (TSC + TF + HSM). Compact Strip Process (CSP) is combination of Thin Slab Caster (TSC) + Tunnel Furnace (TF) + 6-hi tandem Hot Strip Mill (HSM). Slab thickness is 50–65 mm.

Primary steel making is done in CONARC, which is equipped with arcing + oxygen blowing from top as well as sides for flexibility of charge mix as well as high productivity. It is also having bottom purging facility of inert gas and eccentric bottom tapping (EBT). Charge consists mainly of DRI and Hot Metal. Ladle Furnace (LF) is having latest metallurgical facilities like Level-2 automation, bottom argon purging, wire injection, oxygen measurement, Fe-alloy and flux of required quantity (load cell) is added through conveyer and chute. There is automated precise addition control to produce steel within a very narrow range of chemistry, superheat and high degree of cleanliness [15–17]. Liquid steel ladle moves from LF to TSC for slab casting. Each slab moves to HSM within 8 to 10 min through TF and gets hot rolled

to coil. High level of automation, quality control and monitoring mechanism at every stage [17, 18] ensures desired surface and internal quality of slab and coil free of harmful inclusion.

The coil is processed in cut to length line as per customer order. For research purpose 2 full width sample is cut—each of 1 m length after cutting of first packet (approximately 120 m from tail end) and brought to R&D after proper identification marking with sticker. Leaving 50 mm at center and 50 mm from both edges across width, from remaining portion at random 15 pieces of parent sample of 300 × 300 mm are cut with marking of coil no. and rolling direction. Samples for chemical, mechanical, bend, impact test are cut and prepared as per requirement of EN10149-part2-2013, EN10149-part1-2013 and ISO 6892–1-2016. Such samples are cut from both of coil no. 7C21-S650MC and 7C31-S700MC, hot rolled to 6.0 mm thick coil from same heat no. AD7 one after another, but with different cooling parameters in mill. Table 1 shows Product chemistry and cooling parameters. Table 2 shows Mechanical properties.

Samples for corrosion test are mechanically dry polished. Various grades of SiC paper (60, 100, 220, 320, 400, 600, 1/0, 2/0, 3/0 and 4/0) are used progressively, followed by wet polishing with 0.3 μm diamond paste to mirror finish and rinsed thoroughly with deionized water to ensure its cleanliness. A set of 6 samples are prepared from each coil with dimension of 6 × 12 × 12 mm. Top and bottom surface diagonal is reduced to 15.5 mm by grinding each corner. Thickness is reduced from 6 to 4 mm by grinding as shown in Fig. 2a. Corrosion test is conducted by Potentiodynamics Polarization Test Method in Potentiometer (Autolab PGSTAT302N) in Corrosion Lab (Fig. 2b) of Department of Metallurgy, OPJU, Raigad. It is performed in a set up with 3.5% aqueous NaCl solution as electrolyte, mirror polished sample disc as working electrode (WE), saturated Calomel as reference electrode (RE) and a counter electrode (CE) made of SS316. Corrosion test set up is shown in Figs. 5 and 6. Cathodic and anodic reactions happen on surface after dipping a metal in corrosive liquid-electrolyte. Metal gets oxidised by releasing electrons. The electrolyte gets reduced. Ecorr is Corrosion Potential, which is developed in the metal (WE) relative to the RE. Both cathodic and anodic currents are present on WE at Ecorr. Rate of reduction must equal to rate of oxidation, which means these currents are exactly equal in magnitude. Linear relationship exits in between metal oxidation (corrosion) rate and corrosion current Icorr as per Faraday's law. By using bultler–volumer equation, this corrosion current and corrosion density can be calculated [19]. A potential is applied between WE and RE and the current is measured by the potentiostat between WE and CE. With control of potential difference in between WE and CE, the same between RE and WE is gets automatically controlled. The tafel pots are obtained by plotting logarithm current versus applied potential. The tafel slopes, Ecorr, Icorr, corrosion rate, polarisation resistance etc. are determined with the help of in-built software. The potential is controlled at sweep rate of 10 mV/s. It is recorded from −535.48 to −524.9 mV for 7C21 and from −570.98 to 547.49 mV for 7C31.

Samples for metallography from both the coils are prepared by conventional process followed by examination under Olympus make (model-PME3) optical microscope and JEOL make (model-JSM6390) Scanning Electron Microscope (SEM) in

Table 1 Product chemistry and cooling parameters in hot rolling mill

Coil no.	C	Mn	Si	P	S	Cr	Mo	Nb	V	Ti	N	Al	FT (°C)	CT (°C)	CR (°C/s)
7C21	0.047	1.67	0.28	0.011	0.005	0.02		0.063	0.006	0.123	0.0065	0.029	890	517	30.9
7C31	0.046	1.65	0.26	0.012	0.005	0.01		0.061	0.005	0.123	0.0067	0.026	889	579	25.4

Table 2 Mechanical properties of hot rolled coil

Coil no.	Avg YS (Mpa)	Avg UTS (Mpa)	% EL	Grade	Charpy impact (J)	
					−20 °C	−40 °C
7C21	673.4	746.3	18	S650MC	175	116
7C31	725.7	774.3	20	S700MC	205	144

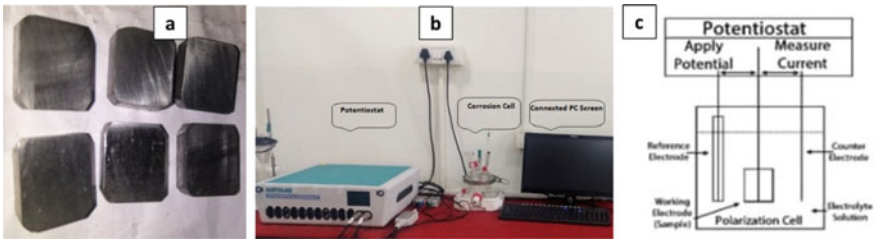

Fig. 2 **a** Dry polished samples of 7C21 for corrosion test. **b** Corrosion test set up (Potentiometer—Auto lab PGSTAT302N). **c** Schematic diagram of the corrosion test set up

NABL accredited laboratory of JSW Steels, Dolvi Works. Electron back scattered diffraction (EBSD) study is done under SEM of Hitachi make (model-3400 N) in R&D of JSW Steel, Vijaynagar Works to compare grain size distribution, grain mis-orientation, texture and dislocation density.

3 Results and Discussion

3.1 Corrosion Test Results

First 2 tests are to be abandoned due to noise in output. This test is very sensitive to condition of the apparatus and the preparation of the set up. Samples and corrosion setup are prepared again with extra precautions taking help of video article on 'Potentiodynamic Corrosion Testing' by Selin et al. [20]. Corrosion test results calculated by in built NOVA 1.10 software are shown in Fig. 3. Corrosion rate of 7C31 (S700MC) is 1.427 mm/year, which is much higher in comparison to 0.287 mm/year corrosion rate of 7C21 (S650MC). Polarisation resistance of 7C31 is also lower than that of 7C21. Polarisation resistance is nothing but resistance to oxidise or to corrode. Corrosion Potential (Ecorr) and Corrosion Current (Icorr) have linear relationship with corrosion rate. These 2 values of 7C31 are also higher than 7C21. It shows that although 7C31-S700MC is superior to 7C21-S650MC in terms of mechanical properties, but it is inferior in terms of corrosion resistance. Hunsu Gerengi et al. have also made similar observation while studying corrosion resistance of Docol 1200

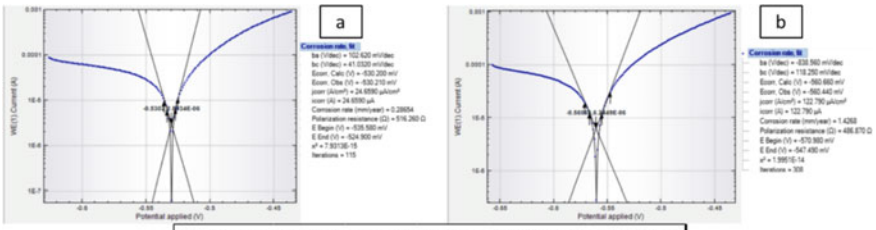

Comparison of Corrsion test result of 7C21 (a) vs 7C31 (b) sample

SAMPLE	Ecorr, Calc (mV)	Ecorr, Obs (mV)	jcorr (μA/cm²)	Corrosion rate (mm/year)	Polarization resistance (Ω)
7C21-S650MC	-530.2	-530.21	24.659	0.28654	516.26
7C31-S700MC	-560.66	-560.44	122.790	1.4268	486.87

Fig. 3 Potentiodynamic polarization curve. **a** 7C21-S650MC, **b** 7C31-S700MC

and Docol 1400. Although the latter is superior in terms of mechanical properties, but inferior in terms of corrosion resistance [13].

However in 2 earlier studies of the author it is found that by proper alloying and microstructural development, corrosion resistance can be improved along with mechanical strength. In similar comparative corrosion test of hot rolled weathering steel versus mild steel, it is found that weathering steel is superior to mild steel both in terms of mechanical strength and corrosion resistance [21, 22]. YS - UTS (MPa) values are 466–530 versus 411–470. Corrosion rate (mm/yr) values are 0.1216 versus 0.1226. This is due to passivation effect of alloying elements like 'P', 'Cu' and 'Cr' in weathering steel. Comparison of DP780 versus DP600 also shows that the former is superior both in terms of tensile strength and corrosion resistance [23]. Average UTS (MPa) values are 800 versus 600. Polarisation resistance (kΩ) values are 1.9121 versus 1.1878. The only difference in between these 2 steels is boron (B) alloying in DP780 versus no 'B' in DP600. 'B' contributes in strength by increasing hardenability and other metallurgical reaction. It improves corrosion resistance by reducing grain boundary energy with precipitation of boron-carbides.

3.2 Optical and SEM Results

Microstructure consists of mainly fine grain quasi polygonal ferrite (about 90%) with traces of granular bainite (about 10%). Very fine and uniform grain size of ferrite with presence of bainite, finer and greater no of precipitates are main contributor to ultra high strength of this steel. Comparison of grain size of these 2 coils is shown in Table 3 and Fig. 4. Average grain size of S650MC and S700MC is 4.14 and 3.68 micron respectively. It is evident that finer grain size has contributed to higher strength in S700MC, but reduces its corrosion resistance due to more grain boundary areas. In S700MC precipitates are finer and higher in nos leading to more interface area and faster corrosion rate (Fig. 5).

Table 3 Grain size comparison

Grain size comparison within UHSS grade								
		Unit of grain size	Sample location w.r.t. top/bottom surface of rolling					
Sample ID	Grade		Top	Top −2 mm	Center	Bottom +2 mm	Bottom	Average
7C21	S650MC	ASTM no	13.09	12.71	12.65	12.82	13.13	12.88
		Area (sq-micron)	14.51	19.4	20.32	17.58	13.92	17.15
		Calculated grain size in micron						4.14
7C31	S700MC	ASTM no	13.36	13.18	13.09	13.08	13.4	13.22
		Area (sq-micron)	12.28	13.95	14.76	14.89	11.97	13.57
		Calculated grain size in micron						3.68

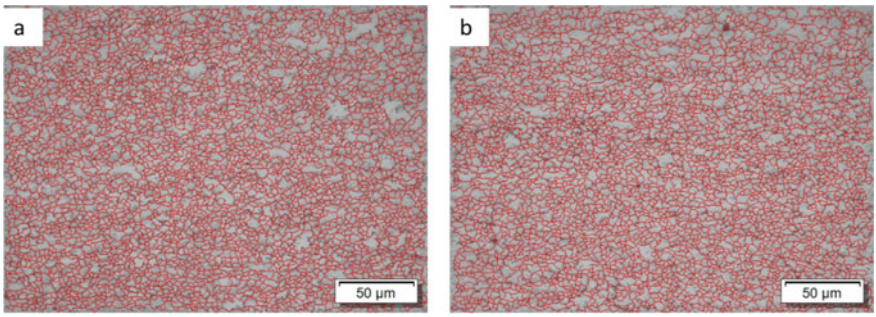

Fig. 4 Grain boundary marking in optical microscope (mag × 500) for measurement of grain size by image analysis. **a** 7C21/S650MC, **b** 7C31/S700MC

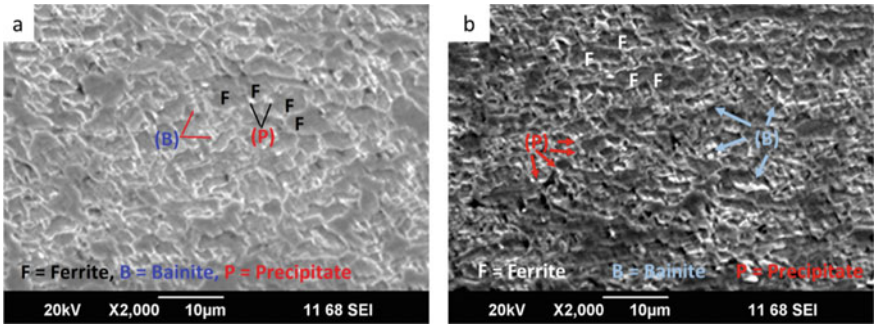

Fig. 5 Microstructure-SEM (mag × 2000). **a** 7C21-S650MC, **b** 7C31-S700MC

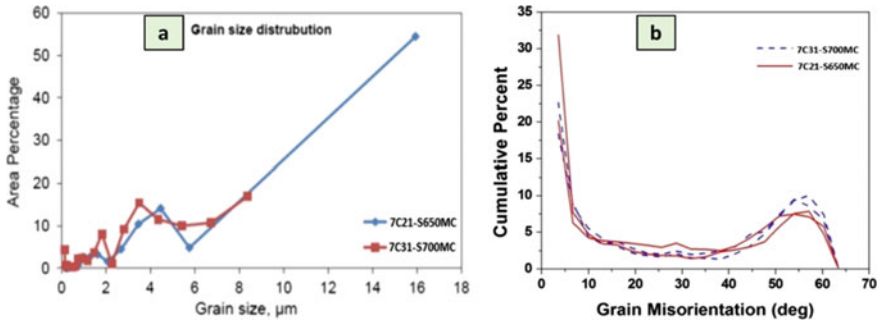

Fig. 6 Comparison of **a** grain size distribution, **b** grain misorientation

3.3 EBSD Results

Grain Size distribution and Grain Misorientation: 7C21-S650MC consists 55% of grains with grain size (diameter) 16 μm and 41% of grains have size (diameter) range 1–6 μm. 7C31-S700MC consists 90% of grains with grain size range 1–9 μm with maximum grain size 8.37 μm (Fig. 6a). Finer grain size is mostly due to larger no of precipitaes pinning grain boundaries. High Angle Grain Boundary (HAGB) fraction is more and Low Angle Grain Boundary (LAGB) fraction is less for 7C31-S700MC than that in 7C21-S650MC (Fig. 6b). It is well known that HAGB is stronger barrier than LAGB for dislocation movement leading to more dislocation pile up at grain boundary for HAGB. Li et al. [24] claim in their study on effect of Ti in High Strength Automotive Beam steel that addition of Ti decreases LAGB and increases HAGB. Decrease of LAGB may be due to pinning effect of TiN precipitate on dislocation motion and increase of HAGB may be for refining of bainite by Ti.

Comparison of Inverse Pole Figure (IPF) (Fig. 7) of both sample reveals that in 7C31-S700MC, {111} grain orientation parallel to rolling plane is much more in comparison to that in 7C21-S650MC. Better {111} texture formation in 7C31 contributes to its higher formability [25] as evident from its higher elongation values in spite of higher tensile strength (Table 2).

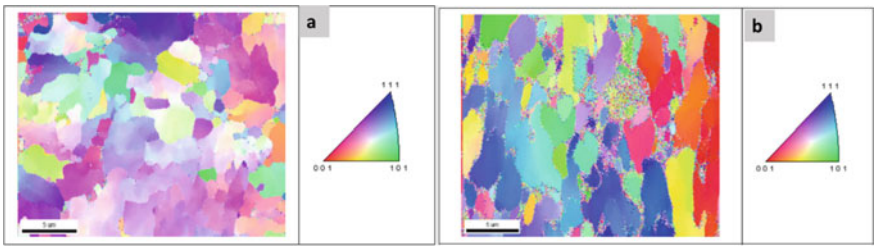

Fig. 7 Comparison of EBSD pole figures. **a** 7C21-S650MC, **b** 7C31-S700MC

Comparison of IPF grain orientation map (Fig. 7) reveals pile up of dislocations at grain boundary (appearing as dots), which contributes to finer GS by pinning effect and high YS. Where as in 7C21-S650MC, dislocation pile up at grain boundary is much less. Reason for difference of dislocation pile up at grain boundaries of these 2 coils are already described. Higher grain boundary area and higher dislocation density contribute to higher interface area. Higher interface area leads to higher corrosion rate for 7C31-S700MC in comparison to that of 7C21-S650MC.

4 Conclusion

Although UHSS coil no. 7C31 is superior to coil no. 7C21 of same heat in terms of strength, but it is inferior in terms of corrosion resistance.

The factors which contribute to superior strength of UHSS like finer grain size, finer and larger nos of precipitates, higher dislocation density etc. also attributes to higher corrosion rate due to higher interface area.

However by proper alloy and process design both mechanical strength and corrosion resistance can be improved simultaneously.

Acknowledgements The authors are grateful to the management of JSW Steel & OPJU for necessary support and motivation for conducting this research work, use their facilities and giving permission to submit this paper for publication.

References

1. NCAP document published by MoEFCC, GOI. In: Sundaray NK, Bhardwaj SR (eds) (2019). http://moef.gov.in/wp-content/uploads/2019/05/NCAP_Report.pdf. Accessed 27 Nov 2020
2. https://technovuus.araiindia.com/blogs/blogDetails/Mjg2. Accessed 30 Nov 2020
3. Gupta S, Huddar N, Iyer B et al (2018) The future of mobility in India's passenger-vehicle market. McKinsey & Company Insight
4. Road Accidents in India 2018, MoRTH, Government of India (2019)
5. https://www.bankbazaar.com/insurance/motor-insurance-guide/bharat-new-vehicle-safety-assessment-program-for-cars.html. Accessed on 30 Nov 2020
6. https://en.wikipedia.org/wiki/Bharat_New_Vehicle_Safety_Assessment_Program. Accessed 30 Nov 2020
7. https://www.business-standard.com/article/automobile/indian-carmakers-improve-car-safety-but-yet-to-reach-international-levels-120110500061_1.html. Accessed 30 Nov 2020
8. Notification of MoRTH-Govt of India, The Gazette of India no. 884, dated 2015/04/30
9. Killer S, Kimchi M, Mooney PJ (2017) Introduction to advanced high-strength steels (AHSS). AHSS—application guidelines—world auto steel. Version 6.0, pp 10–13
10. https://www.automotivemanufacturingsolutions.com/manufacturing-with-uhss/31444.article. Accessed 03 Oct 2020
11. Wang R et al (2006) Micro structure and precipitation behavior of Nb Ti complex micro alloyed steel produced by compact strip processing. ISIJ Int 46(9):1345–1353
12. Béjar-Gómez L, Medina-Flores A, Carréon H (2009) Production and characterization of niobium and titanium micro alloyed steels. Revista Mexicana de F´Isica S 55(1):110–113

13. Gerengi H, Şen N, Uygur I, Solomon M (2019) Corrosion response of ultra-high strength steels used for automotive applications. Mater Res Express 6(8). IOP Publishing Ltd
14. Noel JJ (2003) Effects of metallurgical variables on aqueous corrosion. Corrosion: fundamentals, testing, and protection. ASM handbook, vol 13A. ASM International, pp 258–265
15. Jadhav S, Patra PK, Khandekar AV, Sam S, Pradhan M (2016) Operating experience of CONARC and development of triple lance in CONARC at JSW Steel Ltd. Dolvi Works. Steel Tech 10(3)
16. Patra PK, Chakraborty S, Sam S (2014) Close control of chemistry process parameters and mechanical properties of Nb micro-alloyed steel at JSW Steel Dolvi. In: Annual conference of NMD. Indian Institute of Metals. Pune, India
17. Singhai M, Sharma HV, Patra PK, Chandra A (2015) Overview of technological breakthrough & in house innovations in JSW Steel Dolvi. In: International Conclave on Iron & Steel Making: QCFI, Bhilai, India
18. Singhai M, Kumar DS, Sam S, Patra PK (2016) Optimization of process parameters of Boron microalloyed steel in thin slab caster to avoid transverse corner cracks. SIMPRO. Ranchi, India
19. Kumar N, Manoj MK, Haldar R (2016) Effect of re-aging on strength, corrosion and dry sliding wear behavior of 7075 aluminum alloy. J Mater Sci Nanotechnol 4(2)
20. Munir S, Pelletier MH, Walsh WR (2016) Potentiodynamic corrosion testing. J Vis Exp (115)
21. Patra PK, Singhai M, Sam S, Kumar S (2014) Improvement of total life cycle performance and aesthetic look of various structures using higher corrosion resistant steel. CCIPRA. IIEST, Shibpur (Kolkata)
22. Patra PK, Singhai M, Sam S, Kumar S (2014) Use of weathering steel in construction. Seminar on steel. The preferred choice of material for construction. INSDAG-FICCI, Mumbai
23. Kumar S, Singhai M, Deai R, Sam S, Patra PK (2016) Development of AHSS for improved vehicle safety, fuel efficiency and CO_2 emission. J IIE (India) Ser D 2(97):153–158
24. Yongliang L, Fuming W, Changrong L, Zhangbing Y, Yutian H, Ruifang C (2016) Effect of titanium on continuous cooling transformation and mechanical properties of high-strength automobile beam steel. In: AISTech 2016 proceedings, Pittsburgh, USA, pp 2747–2757
25. Ghosh P, Ghosh C, Ray RK, Bhattacharjee D (2008) Precipitation behaviour and texture formation at different stages of processing in an interstitial free high strength steel. Scripta Mater 59:276–278

Influence of Nb^{5+} Doping on Microstructure and Electrical Properties of NBT Ceramics

Rashmirekha Sahu, A. Mahapatra, S. Swain, and P. Kumar

Abstract $Na_{0.5}Bi_{0.5}TiO_3$ (NBT), Nb^{5+} doped $(Na_{0.5}Bi_{0.5})_{1-x/2}$ $Ti_{1-x}Nb_xO_3$ and $Na_{0.5}Bi_{0.5}Ti_{1-x}Nb_xO_3$ ceramics for $x = 0.01$ were synthesized by microwave-assisted conventional solid-state reaction route. Microwave processing technique is chosen for sintering of ceramics, as it is a powerful method, which enables sintering in a short time and its fast heating rate avoid grain growth in the ceramics. XRD pattern showed the evolution of single-phase perovskite structure with rhombohedral symmetry of pure and doped NBT ceramics, sintered at 1000 °C for 30 min in a microwave furnace matches with JCPDS No. 36-0340. Microstructure of all the ceramics was investigated by FESEM and observed that grain size decreases with doping. Dielectric study reveals that all ceramics showed diffused phase transition around temperature T_m with diffusivity in the range of 1.5–2 and Nb doping shifted T_m toward the lower temperature side. Polarization-electric field (P~E) hysteresis loops at room temperature confirmed the ferroelectric behavior of the ceramics.

Keywords Perovskite · Microwave · Hysteresis loop · Rhombohedral symmetry · Diffusivity

1 Introduction

Since the discovery of ferroelectric materials, lead-based materials remain the technologically important and extensively investigated class of ferroelectric oxides [1]. However, the presence of lead and its toxicity demand for advancement of environmentally safe lead-free materials [2]. Sodium bismuth titanate (NBT) is an alternative lead-free material to replace lead-based materials like PZT. NBT is a relaxor ferroelectric having a perovskite structure with A-site complexity. It is rhombohedral in structure at room temperature and transforms into tetragonal and then into cubic structures with increasing temperature. It exhibits strong ferroelectricity with high

R. Sahu · A. Mahapatra · S. Swain · P. Kumar (✉)
Department of Physics & Astronomy, National Institute of Technology, Rourkela 769008, Odisha, India
e-mail: pawankumar@nitrkl.ac.in

S. Pal et al. (eds.), *Processing and Characterization of Materials*, Springer Proceedings in Materials 13, https://doi.org/10.1007/978-981-16-3937-1_19

remnant polarization which is associated with lone pair effect of Bi^{3+} ions, somewhat similar to Pb^{2+} ions in lead-based ferroelectric systems [3]. However, its high coercive field and conductivity make it difficult to pole, which can be improved by modification or doping. Attempts were made with many aliovalent doping either by higher valence-donor or lower valence-acceptor dopants. Several studies reported that A-site or B-site doping with donor dopant enhances the properties of ferroelectric materials. Usually, it was observed that low-level donor doping in titanate-based perovskites can significantly tailor the material properties [4]. Niobium doping in PZT shows enhancement in electrical resistivity, fatigue behavior, and hysteresis squareness [1, 5]. Niobium doped PZT films were investigated by Haccart et al. [6] and it was observed that introduction of Nb enhances dielectric, piezoelectric, and ferroelectric properties especially by increasing remnant polarization and decreasing coercive field for lower doping concentration (2 at.%). Kumar et al. [2] reported that a higher value of dielectric constant and Curie temperature was obtained by doping Nb into BNKT ceramics, and also the higher value of remnant polarization was observed for 0.4% of Nb doping. Enhanced piezoelectric and ferroelectric properties were observed in partially substituted Nb^{5+} in $Bi_{0.5}Na_{0.5}TiO_3$-$0.03BaZrO_3$ (BNT-BZ3) ceramics by Rahman et al. [7]. Zuo et al. [8] addressed that at solubility limit of niobium in BNT lattice is limited to 3% and piezoelectric and ferroelectric properties get enhanced at low doping level of Nb, due to formation of cation vacancies. However, there were no reports on niobium doped NBT ceramics synthesized via microwave processing technique. In this work, effect of microwave-assisted B-site doping with donor dopant Nb^{5+} in NBT ceramics was studied from a defect structure viewpoint. Here, microwave heating is chosen as it provides significant advantages like rapid heating rate, lower processing temperature and time, higher density, etc. over conventional heating [9].

2 Experimental Details

$Na_{0.5}Bi_{0.5}TiO_3$ (NBT), Nb^{5+} doped $(Na_{0.5}Bi_{0.5})_{1-x/2}Ti_{1-x}Nb_xO_3$ (abbreviated as NBTN-A) and $Na_{0.5}Bi_{0.5}Ti_{1-x}Nb_xO_3$ (abbreviated as NBTN-B) ceramics for $x = 0.01$ were synthesized by microwave-assisted conventional solid-state reaction route. Samples were prepared using Na_2O_3, Bi_2O_3, TiO_2, and Nb_2O_5 raw powders with a purity of more than 98%. A stoichiometric amount of powders were uniformly mixed through ball milling. Powders were calcined at 800 °C for 15 min in microwave furnace. Calcined powders were pressed uniaxially to form green pellets and then the pellets were sintered at 1000 °C for 30 min in microwave furnace. Sintered pellets were electroded using silver paste for electrical measurements. Phase formation and lattice parameters were determined using an X-Ray diffractometer (RigakuUltima IV, Japan). Microstructural characterization was performed using field emission scanning electron microscope (NOVA Nano SEM). Dielectric properties were measured at room temperature and elevated temperature (up to 450 °C) at different frequencies by LCR meter (HIOKI LCR-HiTESTER). Ferroelectric property i.e., P~E hysteresis

loops were measured using Radiant Precision Premier II, where the samples are immersed in insulating silicone oil to prevent arcing during high voltage testing.

3 Results and Discussion

Figure 1 presents the XRD patterns of calcined and sintered NBT and Nb-doped NBT ceramics at room temperature. All the reflections correspond to a single perovskite structure, which matches with the JCPDS No. 0336-0340, for different compositions. Single-phase of NBTN-A and NBTN-B indicates the diffusion of Nb into NBT lattice.

From FESEM, as shown in Fig. 2, it is observed that with the increase of Nb doping content grain size decreases. Average grain sizes for NBT, NBTN-A, and NBTN-B are found to be 0.56 μm, 0.44 μm and 0.25 μm respectively. This is due to the addition of higher valence dopants, which results in the formation of cation vacancies

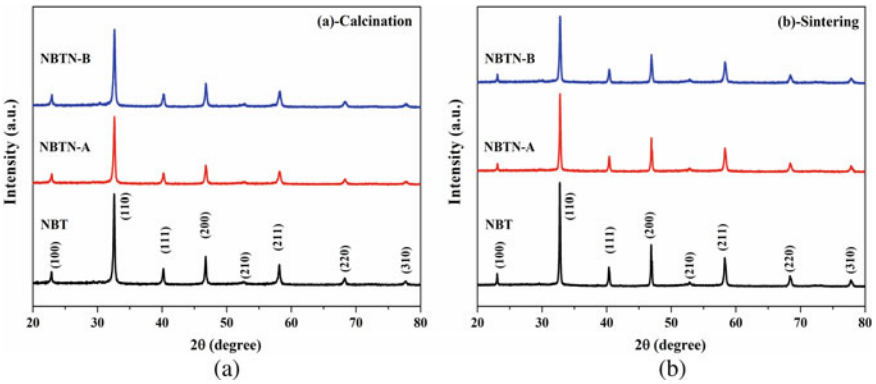

Fig. 1 Room temperature XRD pattern of **a** calcined NBT and Nb-doped powders, **b** sintered NBT and Nb-doped ceramics

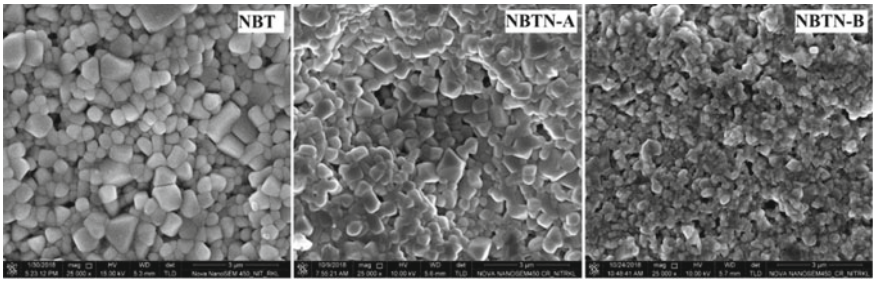

Fig. 2 FESEM of NBT and Nb-doped ceramics

to compensate for the charge. These vacancies concentrate near grain boundaries, weaken the mass transportation and hence grain growth inhibited [10].

Room temperature dielectric constant (ε_r) and loss (tanδ) as a function of frequency of NBT based ceramics is shown in Fig. 3a. It is observed that with an increase of frequency, ε_r decreases. At low frequency, all four polarizations (electronic, ionic, orientational, and space charge) are present and with increasing frequency contribution of individual contribution toward total polarization decreases as a result ε_r decreases. For all the ceramics, the initial value of tanδ decreases and then increases at a higher frequency which suggests the presence of dielectric relaxation process [11]. The tanδ shows lower value for Nb-doped ceramics compared to that of the parent NBT ceramics. Figure 3b shows temperature dependence of ε_r at four different frequencies (1, 10, 100 kHz and 1 MHz) for NBT and Nb-doped NBT ceramics. It is observed that from room temperature to 450 °C, two dielectric anomalies are present. One at higher temperature corresponds to transition temperature (T_m) at which ε_r attains maximum value and the other at lower temperature corresponds to depolarization temperature (T_d) at which anti-ferroelectric to ferroelectric transition takes place. It is also observed that plots of pure NBT ceramics show more dispersion than the doped one. For Nb-doped system shifting of T_m to lower temperature side can be related to change in ionic radii. As Nb^{5+} (0.64 Å) has higher ionic radius than Ti^{4+} (0.605 Å), it weakens the B-O bond and hence T_m is reduced [12].

Relaxor behavior of ceramics was characterized by calculating diffusivity parameter (γ) using modified Curie-Weiss law given by,

$$\frac{1}{\varepsilon_r} - \frac{1}{\varepsilon_m} = \frac{(T - T_m)^\gamma}{C}$$

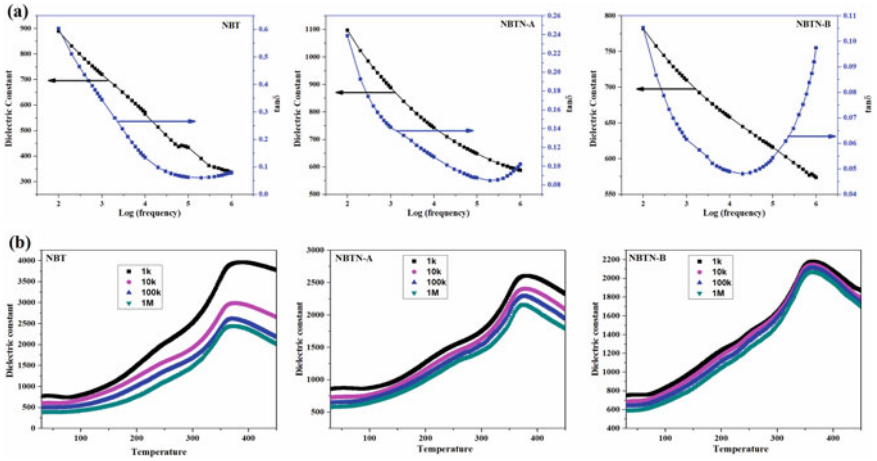

Fig. 3 Variation of **a** dielectric constant and loss w.r.t. frequency at room temperature **b** dielectric constant w.r.t. temperature for NBT and Nb-doped ceramics

where 'C' is Curie-Weiss constant and 'γ' is diffusivity factor. Plot of $\ln(1/\varepsilon_r - 1/\varepsilon_m)$ versus $\ln(T - T_m)$ at 1 kHz frequency of NBT and Nb-doped NBT ceramics are shown in Fig. 4. Value of γ for NBT, NBTN-A, and NBTN-B ceramics was found to be ~1.92, ~1.91 and ~1.78, suggests the diffused phase transition behavior. Diffusivity property matches with the relaxor properties, observed in temperature-dependent dielectric curve. Diffused phase transition is observed in the ceramics due to compositional fluctuations as more than one cation tries to occupy the same crystallographic A (Na and Bi at A-site) and B (Ti and Nb at B-site) sites of NBT based ceramics [13].

Ferroelectricity of the ceramics is characterized by polarization (P) versus electric field (E) hysteresis loops, shown in Fig. 5. Ceramics do not show well-developed

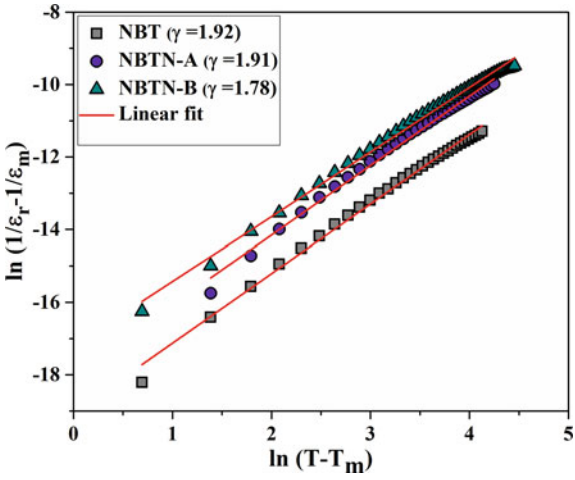

Fig. 4 Plot of $\ln(1/\varepsilon_r - 1/\varepsilon_m)$ as a function of $\ln(T - T_m)$ at 1 kHz for NBT and Nb-doped ceramics

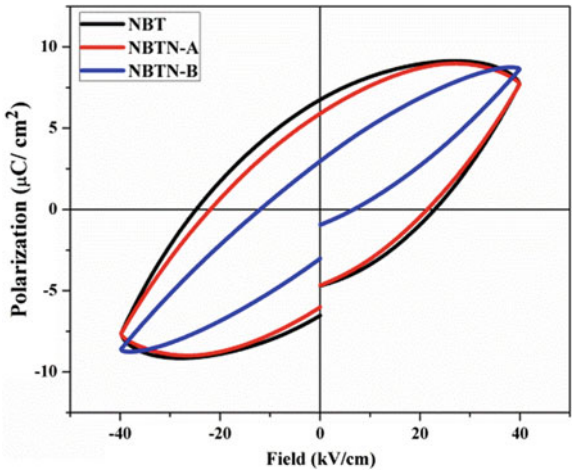

Fig. 5 Room temperature P-E hysteresis loops of NBT and Nb-doped ceramics

saturated P~E loops for an applied field of ~40 kV/cm. It is observed that both remnant polarization (P_r) and coercive field (E_c) decrease with the increase of Nb doping. Decrease in P_r can be related to decrease in grain size. Grain boundary has low permittivity and with decreasing grain size, grain boundary density increases [14]. As a consequence, P_r decreases as the grain size decreases. Comparing three ceramics, NBT has larger grain size than NBTN-A and NBTN-B has smaller grain size compared to rest of the ceramics. In the same way, NBT has higher P_r value than NBTN-A ceramics and NBTN-B ceramics have smaller P_r value. Decrease in E_c can be associated with Nb-donor doping. With donor doping, cation vacancies are created to compensate for the charge imbalance and suppress the formation of oxygen vacancy, which decreases pinning of domain wall and hence E_c.

4 Conclusion

With of help of microwave-assisted solid-state reaction technique, pure NBT and Nb-doped NBT ceramics prepared successfully. Absence of secondary peaks confirms the single-phase formation of all the ceramics from the XRD study. With Nb-doping, grain size decreases, and T_m shifts to lower temperature side. Diffusivity (γ) value confirms the diffusive nature of all the ceramics. Decrease in P_r is associated with decrease in grain size and decrease in E_c is associated with donor-doping effect.

References

1. Pereira M, Peixoto AG, Gomes MJM (2001) Effect of Nb doping on the microstructural and electrical properties of the PZT ceramics. J Eur Ceram Soc 21:1353–1356. https://doi.org/10.1016/S0955-2219(01)00017-6
2. Kumar K, Kumar B (2012) Effect of Nb-doping on dielectric, ferroelectric and conduction behaviour of lead free Bi 0.5(Na 0.5K 0.5) 0.5TiO 3 ceramic. Ceram Int 38:1157–1165. https://doi.org/10.1016/j.ceramint.2011.08.045
3. Rödel J, Jo W, Seifert KTP, Anton EM, Granzow T, Damjanovic D (2009) Perspective on the development of lead-free piezoceramics. J Am Ceram Soc 92:1153–1177. https://doi.org/10.1111/j.1551-2916.2009.03061.x
4. Li M, Li L, Zang J, Sinclair DC (2015) Donor-doping and reduced leakage current in Nb-doped Na0.5Bi0.5TiO3. Appl Phys Lett 106:0–5. https://doi.org/10.1063/1.4914509
5. Griswold EM, Sayer M, Amm DT, Calder ID (1991) The influence of niobium-doping on lead zirconate titanate ferroelectric thin films. Can J Phys 69:260–264. https://doi.org/10.1139/p91-043
6. Haccart T, Remiens D, Cattan E (2003) Substitution of Nb doping on the structural, microstructural and electrical properties in PZT films. Thin Solid Films 423:235–242. https://doi.org/10.1016/S0040-6090(02)01045-3
7. Rahman JU, Hussain A, Maqbool A, Malik RA, Song TK, Kim MH, Lee S, Kim WJ (2015) Effect of donor doping on the ferroelectric and the piezoelectric properties of lead-free 0.97(Bi0.5Na0.5Ti1−xNbx)O3–0.03BaZrO3 ceramics. J Korean Phys Soc 67:1240–1245. https://doi.org/10.3938/jkps.67.1240

8. Zuo R, Wang H, Ma B, Li L (2009) Effects of Nb^{5+} doping on sintering and electrical properties of lead-free (Bi 0.5Na 0.5)TiO 3 ceramics. J Mater Sci Mater Electron 20:1140–1143. https://doi.org/10.1007/s10854-008-9840-9
9. Oghbaei M, Mirzaee O (2010) Microwave versus conventional sintering: a review of fundamentals, advantages and applications. J Alloys Compd 494:175–189. https://doi.org/10.1016/j.jallcom.2010.01.068
10. Pal V, Dwivedi RK, Thakur OP (2014) Effect of neodymium substitution on structural and ferroelectric properties of BNT ceramics. Mater Res Bull 51:189–196. https://doi.org/10.1016/j.materresbull.2013.11.060
11. Negi RR, Chandrasekhar M, Kumar P (2019) Structural, microstructural, dielectric and ferroelectric properties of BaTiO 3-based ceramics. Process Appl Ceram 13:164–172. https://doi.org/10.2298/PAC1902164N
12. Kuang SJ, Tang XG, Li LY, Jiang YP, Liu QX (2009) Influence of Zr dopant on the dielectric properties and Curie temperatures of Ba(ZrxTi1-x)O3 ($0 \leq x \leq 0.12$) ceramics. Scr Mater 61:68–71. https://doi.org/10.1016/j.scriptamat.2009.03.016
13. Raddaoui Z, El Kossi S, Dhahri J, Abdelmoula N, Taibi K (2019) Study of diff use phase transition and relaxor ferroelectric behavior of Ba0.97Bi0.02Ti0.9Zr0.05Nb0.04O3 ceramic. RSC Adv 9:2412–2425. https://doi.org/10.1039/c8ra08910h
14. Zhang Q, Su Y (2018) Thickness and grain-size dependence of ferroelectric properties in columnar-grained BaTiO3 thin films. J Appl Phys 124:0–9. https://doi.org/10.1063/1.5041893

Comparative Study of Hydroxyapatite Synthesized by High Energy Ball Milling in Wet and Dry Conditions

Sujata Swain, P. Kumar, and Sonia

Abstract Mechanochemical method was used to obtain nano-size hydroxyapatite/HA powder, both in wet and dry conditions, by using $CaCO_3$ and $(NH_4)H_2(PO_4)$ as starting materials. Nano-particles of HA were obtained by high energy ball milling in wet conditions having rotation speed of 600 rpm/10 h by taking ethanol as grinding liquid and zirconia balls as grinding media. From EDS analysis, an additional peak of aluminium/Al was observed in wet milled HA powders, whereas no such additional peak was observed in dry milled HA powders. Dry milling was carried out at 300 rpm with 5 h milling time. Average particle size of HA from FESEM analysis was found to be in 27–80 nm range dry milled powders. XRD study shows evolution of the pure HA phase. Optimized calcination and sintering temperature of the HA system were at 800 °C and 1000 °C, respectively, synthesized using microwave-assisted high energy ball milling technique.

Keywords HA · High energy ball milling · EDS · XRD

1 Introduction

In recent years, interest in the research field of biomaterials and bio-ceramics is increasing. For biomedical applications, depending on the requirement, both densified and porous ceramics are being widely used [1, 2]. Nowadays, biomaterials are getting special attention due to their possibility of replacing human bone, etc., without harming the natural environment of the body [3]. From the application point of view, biomaterials have been used to replace many body parts like teeth, ankle, hip, knee, elbow, and other joint damages. HA, with micron size grains, have poor mechanical properties. In contrast, higher surface area to volume ratio of nanoscale HA accounts

S. Swain · P. Kumar (✉)
Department of Physics & Astronomy, National Institute of Technology, Rourkela 769008, Odisha, India
e-mail: pawankumar@nitrkl.ac.in

Sonia
Department of Chemistry, Govt. Autonomous College, Rourkela, Odisha, India

S. Pal et al. (eds.), *Processing and Characterization of Materials*, Springer Proceedings in Materials 13, https://doi.org/10.1007/978-981-16-3937-1_20

its better mechanical properties, making it suitable for load-bearing applications [4]. Nano roughness, nanoporosity, and high surface energy properties of nano-HA system favor adsorption of proteins, required for better cell adhesion, proliferation, differentiation [5, 6]. Sintering of processed system depends on particle size, shape and agglomeration of starting precursors. Particle size is also a major criterion as it determines the activation energy and hence the grain growth of ceramics [7]. Several methods have been applied for the processing of nano crystalline HA system like hydrothermal, wet chemical, sol-gel, co-precipitation, emulsion, mechanochemical etc. [8–11]. Recently, mechanochemical technique is receiving attention to produce nano size HA due to its low processing cost, and high reproducibility [7, 12, 13]. In mechanochemical mixing chemical phenomena occurs during mechanical activation of solids [14, 15]. Further, to maintain nano size in the final sintered body, microwave heating plays a dynamic role compared to conventional heating. In microwave sintering, nano grain size is maintained due to its very high heating rate compared to conventional sintering [16]. Microwave processing has many advantages over conventional processing of materials like lower processing temperature, lower processing time, higher density, better microstructure, volumetric heating, etc., make microwave heating process a quite effective method rather than conventional heating process [17].

2 Experimental Details

Calcium carbonate/$CaCO_3$(Merck) and ammonium dihydrogen phosphate/$(NH_4)H_2(PO_4)$ (Merck) were taken as starting precursors with 1.67 molar ratio and mixed well by using alumina vials and balls as milling media?. For mechanochemical milling powder to ball weight ratio was taken as 1/3 (see Fig. 1). To avoid excessive heating, milling was performed for 15 min run, followed by 30 min gap. Ethanol was used as the grinding media for wet milling. 600 rpm for 10 h was used for wet milling, whereas 300 rpm for 5 h was used for dry milling. After mechanochemical milling, for particle size analysis, FESEM analysis of the milled powder was carried out. Calcination and sintering were carried out in a microwave furnace with heating rate of 20 °C per min. Poly vinyl alcohol/PVA solution of 3wt% of the calcined powder was added to make green pellets. Calcined powder was pressed into pellets of 10 mm diameter with thickness ~1.5 mm using steel die by applying hydraulic pressure of ~80 MPa with a loading time of 4 min. X-ray Diffractometer/XRD study of calcined powder and sintered compacts was carried out in the 2θ range of 20–70° using a scan rate of 10°/min with a step size of 0.02. Crystallite size/D was determined by using the Debye Scherrer formula [18] in Eq. (1), where value of K is 0.94, λ is the wavelength of the source used in XRD, and β stands for FWHM (radian).

$$D = \frac{K\lambda}{\beta \cos\theta} \tag{1}$$

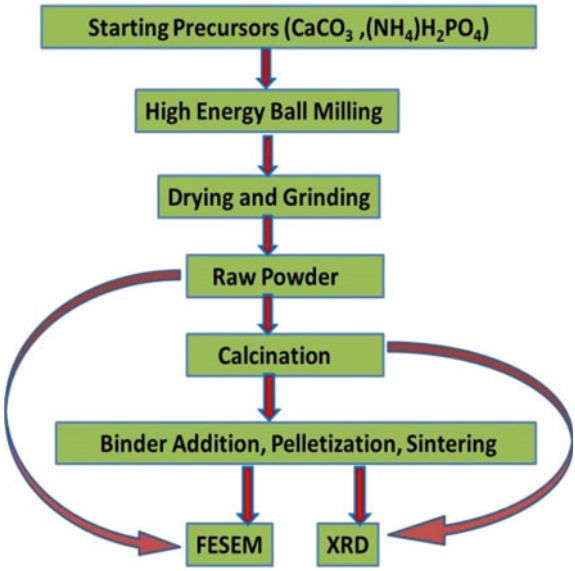

Fig. 1 Flow chart for synthesis and characterization of HA

3 Results and Discussion

Figure 2 displays FESEM microstructures of HA powder after wet milling and dry milling. Particle size in 27–60 nm and 27–80 nm ranges were obtained in wet milled and dry milled powders, respectively. With decreasing milling time and rpm, particle size, obtained in dry milling, of HA system has slightly increased. Particles with spherical shapes and irregular shapes are obtained for dry milled and wet milled powders. Spherical shapes of wet milled particles may be because of higher rpm and

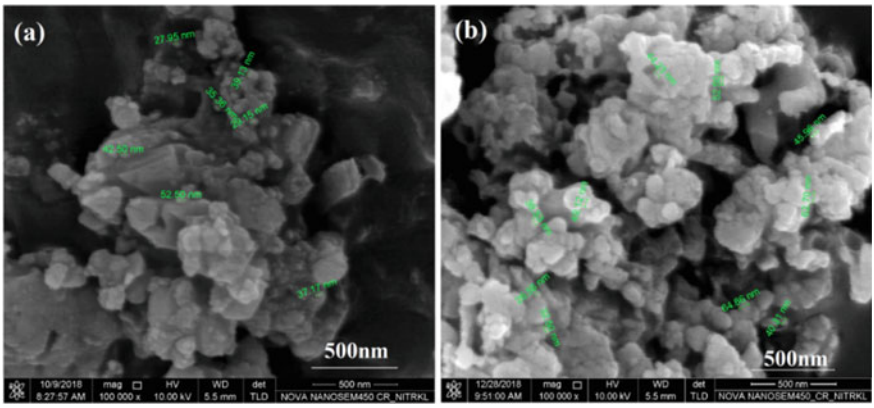

Fig. 2 FESEM micrographs of **a** wet and **b** dry milled HA powders

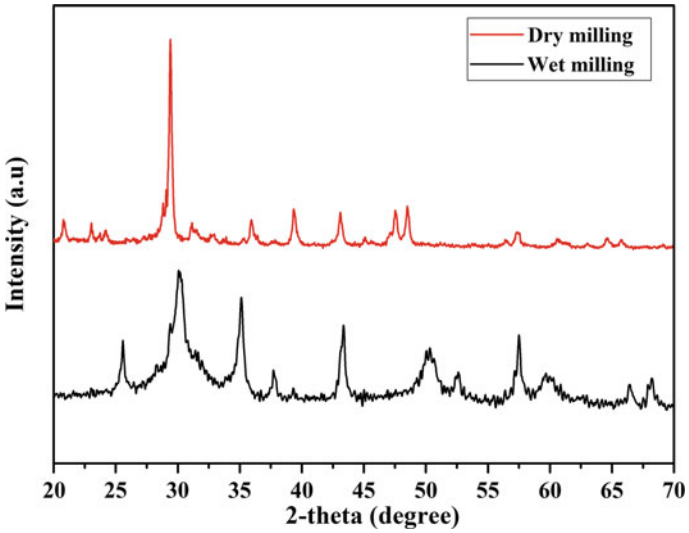

Fig. 3 XRD patterns of raw HA powder in wet and dry milling

higher milling time than the dry milled powders. Movement of milling balls increases with the increase of their kinetic energy, which leads to increased collision between the balls and wall of the vial [19]. This high kinetic energy is transferred to powder particles, which breaks them by reducing their size into nanoscale range [20].

Figure 3 suggests that size of the particle that obtained from wet milling was less than compared to dry milled raw HA powder. Sharp peak of XRD for dry milling showed more crystallinity than wet milled raw powder. XRD patterns of calcined and sintered samples of HA system was shown in Fig. 4. XRD patterns of calcined HA powder show broad peaks with pure phase, identified by JCPDS card no. 76-0694. No secondary phases were observed in sintered HA samples and the crystallite size was obtained ~29 nm for sintered HA samples, calculated by using Debye Scherer formula. XRD study shows that high energy ball milling followed by microwave heating process is an effective technique in lowering the processing temperatures. Lowering of calcination temperature by high energy ball milling method can be due to obtained nano particles possess more surface area and high reactivity [18]. Also, microwave heating plays an important role for lowering processing temperature, as, microwaves interact directly with the sample rather being conducted into the sample from external source, which provide rapid volumetric heating and shorten processing temperature [17]. From Fig. 4, it was observed that for sintered HA, XRD peak has been shifted slightly to higher angle with respect to calcined HA. This shifting of peak can be attributed to rearrangement of atom periodicity when transformation occurred from amorphous to crystalline HA [21].

Figure 5 shows XRD patterns of calcined and sintered dry milled HA samples. Due to increase in average particle size in dry milling, calcination temperature increased

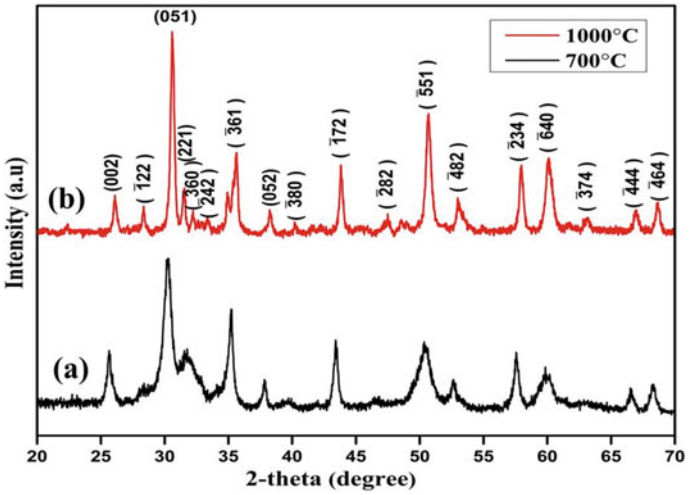

Fig. 4 XRD patterns of wet milled **a** calcined **b** sintered HA system

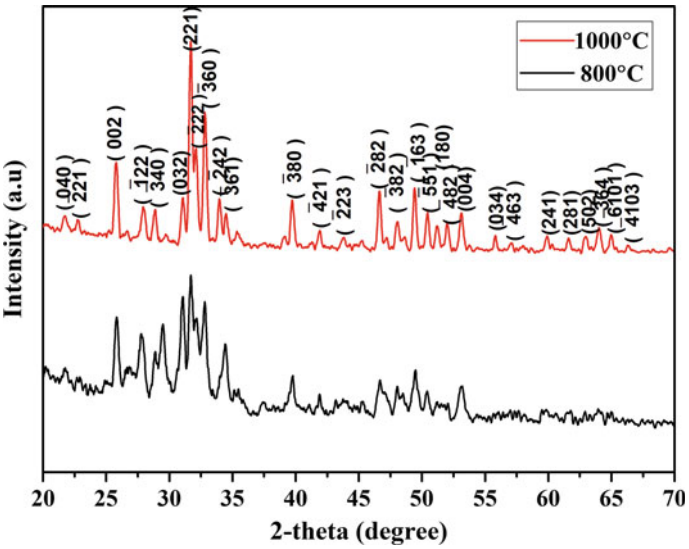

Fig. 5 XRD patterns of dry milled **a** calcined **b** sintered HA system

from 700–800 °C. Here also, pure HA phase is identified by JCPDS card no. 76-0694. Crystallite size of sintered compact is ~25 nm, calculated by using the Debye Scherer formula. Figure 6a displays EDS (Energy dispersive X-Ray spectroscopy) spectra of wet milled sintered HA samples. In sintered HA compacts, an extra peak of aluminium is obtained. Al contamination may be related to inner wall of the vial, which is made of alumina. Also, various factors like grinding liquid, high rotation

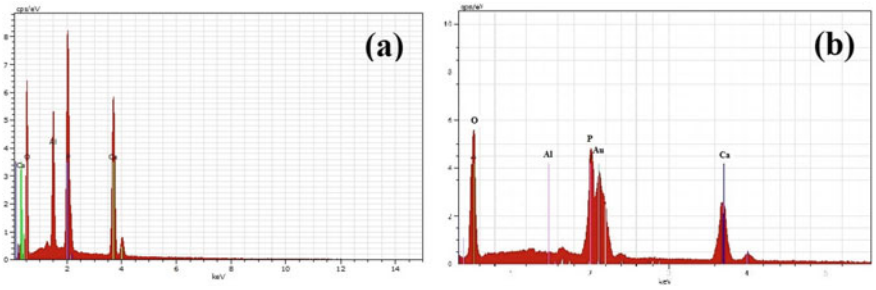

Fig. 6 EDS spectra of **a** wet milled and **b** dry milled HA sample

Table 1 Atomic percentage of HA

Milling condition	Ca	P	O	Al
Wet	14.83	8.94	70.16	6.07
Dry	19.87	14.48	65.65	0.01

speed, and more milling time can also cause the contamination. Due to high rotation speed of grinding balls, impact of collision, between the walls of vial and balls increases, and in liquid medium, this can increase the contamination. Higher the milling time, higher the contamination is observed [22]. To avoid Al contamination, dry milling with reduced rotation speed and reduced milling time is used. Figure 6b shows EDS spectra of dry milled HA sintered samples, which show no aluminium peak. Table 1 depicts atomic percentage of HA analyzed by EDS.

4 Conclusion

High energy ball milling followed by microwave heating process was found to be an effective in lowering the calcination temperature and also maintain nano size. Average particle size of HA from FESEM analysis was found to be in 27–80 nm range dry milled powders. XRD study displays the evolution of the pure HA phase. Optimized calcination and sintering temperature of the HA system were at 800 °C and 1000 °C respectively, synthesized using microwave-assisted high energy ball milling technique. Al contamination occurred in wet milling, whereas no Al contamination was observed in dry milling. Dry milling process combined with microwave heating process accounts nano size HA powders with low processing cost, high yield, and no risk of contaminations.

References

1. Muralithran G, Ramesh S (2000) The effects of sintering temperature on the properties of hydroxyapatite. Ceram Int 26:221–230. https://doi.org/10.1016/S0272-8842(99)00046-2
2. Prakasam M, Locs J, Ancane KS, Loca D, Largeteau A, Berzina-Cimdina L (2015) Fabrication, properties and applications of dense hydroxyapatite: a review. J Funct Biomater 6:1099–1140. https://doi.org/10.3390/jfb6041099
3. Szcześ A, Hołysz L, Chibowski E (2017) Synthesis of hydroxyapatite for biomedical applications. Adv Colloid Interface Sci 249:321–330. https://doi.org/10.1016/j.cis.2017.04.007
4. Feng P, Niu M, Gao C, Peng S, Shuai C (2014) A novel two-step sintering for nano-hydroxyapatite scaffolds for bone tissue engineering, 1–10. https://doi.org/10.1038/srep05599
5. Poinern GEJ, Brundavanam RK, Le XT, Fawcett D (2013) The mechanical properties of a porous ceramic derived from a 30 nm sized particle based powder of hydroxyapatite for potential hard tissue engineering applications. Am J Biomed Eng 2:278–286. https://doi.org/10.5923/j.ajbe.20120206.07
6. Elfalaky A, Hashem H, Mohamed T (2014) Bone-like material, synthesis, optimization and characterization. Nanosci Nanoeng 2:10–16. https://doi.org/10.13189/nn.2014.020102
7. Sharifah A, Iis S, Mohd H, Singh R (2011) Mechanochemical synthesis of nanosized hydroxyapatite powder and its conversion to dense bodies. Mater Sci Forum 694:118–122. https://doi.org/10.4028/www.scientific.net/MSF.694.118
8. Tan CY, Ramesh S, Tolouei R, Sopyan I, Teng WD (2011) Synthesis of high fracture toughness of hydroxyapatite bioceramics. Adv Mater Res 264–265, 1849–1855. https://doi.org/10.4028/www.scientific.net/AMR.264-265.1849
9. Thangamani N, Chinnakali K, Gnanam FD (2002) The effect of powder processing on densification, microstructure and mechanical properties of hydroxyapatite. Ceram Int 28:355–362. https://doi.org/10.1016/S0272-8842(01)00102-X
10. Orlovskii VP, Komlev VS, Barinov SM (2002) Hydroxyapatite and hydroxyapatite-based ceramics. Inorg Mater 38:973–984. https://doi.org/10.1023/A:1020585800572
11. Chaikina MV, Bulina NV, Ishchenko AV, Prosanov IY (2014) Mechanochemical synthesis of hydroxyapatite and its modifications: Composition, structure, and properties. Russ Phys J 56:1176–1182. https://doi.org/10.1007/s11182-014-0159-0
12. Silva CC, Graça MPF, Valente MA, Sombra ASB (2007) Crystallite size study of nanocrystalline hydroxyapatite and ceramic system with titanium oxide obtained by dry ball milling. J Mater Sci 42:3851–3855. https://doi.org/10.1007/s10853-006-0474-0
13. Chetty A, Wepener I, Marei MK, Kamary, Y. E1, Moussa RM, Ydroxyapatite H, Ynthesis S (2018) Polym Compos Mater Sci Manuf 1–57
14. Pandya HM, Anitha P (2014) Comprehensive review of preparation methodologies of nano hydroxyapatite. J Environ Nanotechnol 3:101–121. https://doi.org/10.13074/jent.2013.12.132058
15. Toriyama M, Ravaglioli A, Krajewski A, Celotti G, Piancastelli A (1996) Synthesis of hydroxyapatite-based powders by mechano-chemical method and their sintering. J Eur Ceram Soc 16:429–436. https://doi.org/10.1016/0955-2219(95)00123-9
16. Fang Y, Agrawal DK, Roy DM, Roy R (1994) Microwave sintering of hydroxyapatite ceramics. J Mater Res 9:180–187. https://doi.org/10.1557/JMR.1994.0180
17. Oghbaei M, Mirzaee O (2010) Microwave versus conventional sintering: A review of fundamentals, advantages and applications. J Alloys Compd 494:175–189. https://doi.org/10.1016/j.jallcom.2010.01.068
18. Swain S, Muneer AS, Sahu R, Mahapatra A, Negi RR, Samanta B, Nanda D, Kumar P, Dasgupta S, Sonia (2020) Structural, mechanical and dielectric properties of microwave-assisted high-energy ball milling synthesis of hydroxyapatite. Integr Ferroelectr 205:186–193. https://doi.org/10.1080/10584587.2019.1675014
19. Dinda S, Bhagavatam A, HA, Guru PD, Orc ID (2020) Mechanochemical synthesis of nanocrystalline hydroxyapatite from Ca(H2PO4)2.H2O, CaO, Ca(OH)2, and P2O5 Mixtures. Nanomaterials 10:2232

20. Adzila S, Sopyan I, Yong TC, Singh R, Hoong WY, Purbolaksono J, Hamdi M (2013) Mechanochemical synthesis of nanohydroxyapatite bioceramics. Indian J Chem Inorg Phys Theor Anal Chem 52:1570–1575
21. Lopez HF, Mendoza H (2013) Temperature effects on the crystallization and coarsening of nano-CeO 2 powders. ISRN Nanomater 2013:1–7. https://doi.org/10.1155/2013/208614
22. Rhee SH (2002) Synthesis of hydroxyapatite via mechanochemical treatment. Biomaterials 23:1147–1152. https://doi.org/10.1016/S0142-9612(01)00229-0

Investigation of Elastic Properties of Rutile Titanium Dioxide from First Principles

Supreet Mohanty, Shubham, Rajesh Kumar Prusty, and Bankim Chandra Ray

Abstract Titanium Dioxide (TiO_2) has played a significant role in the materials science world and technology due to its elastic properties and extensive use in a vast-ranging sphere of applications. Previously, there have been significant studies experimentally for the calculation of elastic properties of TiO_2. In this study, the main aim is to find and explain the procedure to calculate the elastic properties of the rutile TiO_2. To do so, we have used the first principle calculation with the support of Quantum Espresso software and a further processing package, ElaStic. The ElaStic tool can compute the full stiffness tensor of second-order elastic constant (SOEC) for any crystal structure. For this, it does the first principle calculation of total-energy or stress evaluation and thus estimates the crystal structure's elastic properties. The obtained elastic moduli using the Voigt theory in this work were validated with the experimental outcomes already available, and it showed a good agreement with it.

Keywords Titanium Dioxide · Rutile · Elastic properties · First principles · Ab initio · Density functional theory · Second-order elastic constant

1 Introduction

TiO_2, due to its remarking catalytic properties and exceptional semiconducting and elastic nature, has been a material of significance. It shows chemical stability, less hazardous nature and nature-friendly material. TiO_2 in nanoscale is found to be a strong oxidizing agent with a greater surface area and, hence, is often used as a filler to be embedded in the polymers to enhance the polymer's mechanical property. There have been studies based on the influence of fillers like graphene, nano-silica, TiO_2 on polymers such as epoxy and vinyl ester, with an aim to improve the matrix's mechanical property. With the minimal cost of production and a higher dielectric constant, it is a relatively inexpensive material. It can be synthesized by various procedures involving gas and solution phases [1–3].

S. Mohanty · Shubham (✉) · R. K. Prusty · B. C. Ray
FRP Composites Laboratory, Department of Metallurgical and Materials Engineering, National Institute of Technology, Rourkela 769008, India

S. Pal et al. (eds.), *Processing and Characterization of Materials*, Springer Proceedings in Materials 13, https://doi.org/10.1007/978-981-16-3937-1_21

TiO_2 is signified as extended-bandgap semiconductors and, due to its particulate nature, it is one of the significantly used semiconductor materials in the industry. Even though it was found more than two centuries ago and was processed commercially for about 100 years, presently, TiO_2 is ideally studied for its dynamic properties like magnetic, electric, photocatalytic, catalytic, electrochemical, and others. Considering the polymorphs of TiO_2, it exists in three forms in nature, i.e., rutile, anatase, and brookite. Commercial aspects of rutile and anatase are feasible. The structure of rutile & anatase are tetragonal unit cells, and there also exists octahedra structures for TiO_6, but their space groups are different. $P4_2/mnm$ (136) is the rutile space group with formula units of two TiO_2 in one unit cell, and the space group of anatase with formula units of four TiO_2 in one unit cell has the space group I41/amd (141). Of the three polymorphs that occur in nature, the most famous of all is Rutile TiO_2. Rutile, in its bulk shape, is known to be stable. At NTP, it is considered to be thermodynamically stable, ranging up to 1830 K its melting point, due to its large crystallite size. Contrary to findings by Mammone et al. [4], it has been emphasized that by applying the Raman spectroscopy method, rutile TiO_2 above 10 GPa, can be converted into a columbite structure [5].

In the field of materials science and technology engineering, the study of SOECs is currently a topic of considerable importance as they monitor the elastic properties of a material. Due to this, there is a pressing requirement for the calculation and measurement of these constants. Apart from these, SOECs are related to physical factors such as phonon spectra, inter-atomic potentials, phase transitions and structural stability, primarily the equation of state. Apart from these, they also cater to the thermodynamic properties like melting point, thermal expansion, specific heat, Debye temperature, and Grüneisen parameters. Higher accuracy, systematic calculations of the material based on density functional theory (DFT) are new approaches for providing a determined alternate experimental procedure for efficiently finding the elastic constants of complicated crystal structures. In the present analysis, we implemented ElaStic [6] to calculate the elastic properties of rutile TiO_2. ElaStic is a method that does ab initio measurement of SOECs, using physical stress or the total energy resulting from the strain applied, based on their numerical distinction of a crystal. The latest ElaStic implementation interfaces with the Quantum ESPRESSO for performing calculations based on DFT [7, 8].

2 Modelling Method

2.1 Quantum Espresso (QE) Software

The Quantum Espresso is a software suite emphasizing first principle calculation to get the material's electronic structure intended for modelling. It is open-source software established on ab initio quantum chemistry approaches and performs the density functional theory (DFT) calculations. Parameters such as total energies are

estimated for TiO_2 using Quantum Espresso. Thus using the total energies, the elastic properties for TiO_2 are evaluated using the processing package ElaStic. We used Quantum Espresso tools in this study to perform ground state measurements of the overall usage of energy and explore the material properties of different structures. Using QE, different models can be computed and analyzed to explain nanoscale and scale-up material behavior. For each constituent element, the input is given to the software, such as the pseudopotentials (PPs) along with atomic number of individual constituent elements. In addition, QE also includes structural feedback to measure the system's material properties. The structural information of the unit cell is taken as an input. The unit cell is then assumed to be replicated in both directions in such a manner that it can simulate the macroscopic system. For the unit cell, in the case of lower-dimensional applications, vacuum spaces such as wire or film or a quantum dot are filled. For QE, the periodic boundary conditions that scale the model to infinitely large crystalline structures are also supported in all three directions.

2.2 SOEC Methodology

We used the ElaStic suite for rutile TiO_2 in stiffness matrix generation for the analysis. The second/third-order elastic constants for the substance can be computed using this ElaStic package. These constants can also be used to calculate the Voigt & Reuss averaged moduli like Young's, bulk, and shear as well as the Poisson ratio. In Fig. 1, the flowsheet for the tool ElaStic can be seen. The input is supplied by the crystal

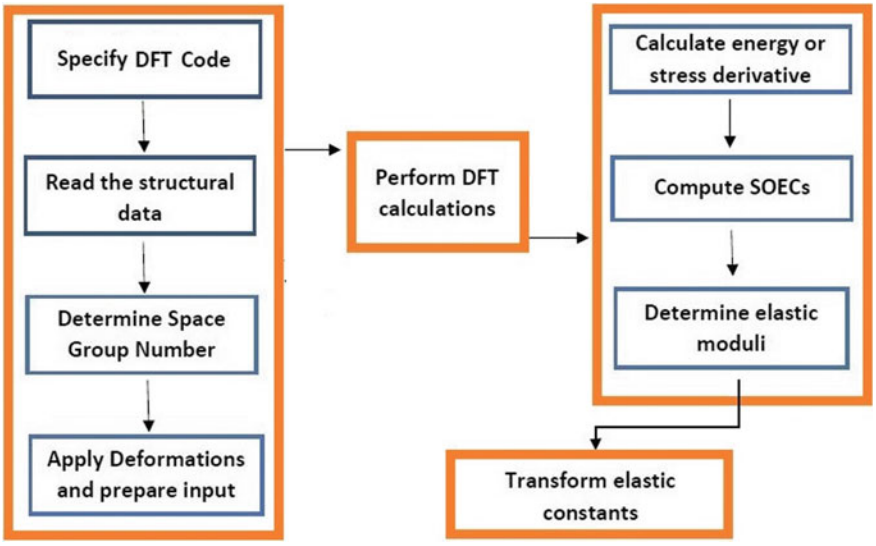

Fig. 1 Algorithm flowchart used for calculating SOEC using ElaStic tool [6]

structure for the substance to be analyzed. Optimisation of the material's crystal structure for cell parameters and atomic positions to acquire the required precision and to achieve equilibrium configuration is a very critical operation. For this, as the reference structure, the optimal configuration of the studied material is used. For a chosen strain stage, the crystal structure is further calibrated for a deformed state to achieve the equilibrium conditions.

3 TiO_2 Modelling

In this, we performed total energy calculations for the distorted structures of TiO_2, and all the calculations were simulated using the Quantum-Espresso package [9] and ultrasoft pseudopotentials(USSP) [10]. Then for these calculations, the basis of a plane wave (PW) with cutoff energy determined using energy optimisation was used in the input. Then the exchange and correlation factors in the Perdew-Burkee-Ernzerhof's (PBE) form are treated by generalized gradient approximation (GGA) [11]. Considering the QUANTUM ESPRESSO package, we created the crystals' input and periodic arrangement of crystals in three dimensional. The bond distance (equilibrium) was studied through constraint relaxing by conformal mapping and total energy minimization was done with Quantum Espresso package's help [12]. From this, we got the equilibrium cell dimension to be about, a = b = 4.651 A^o and c = 2.969 A^o. Figure 2 shows the ball and stick model depiction of the crystal structure of rutile TiO_2.

Table 1 shows some of the parameters taken for the calculation. For calculation of the derivative (second/first) of the energy (stress) at the point of equilibrium with

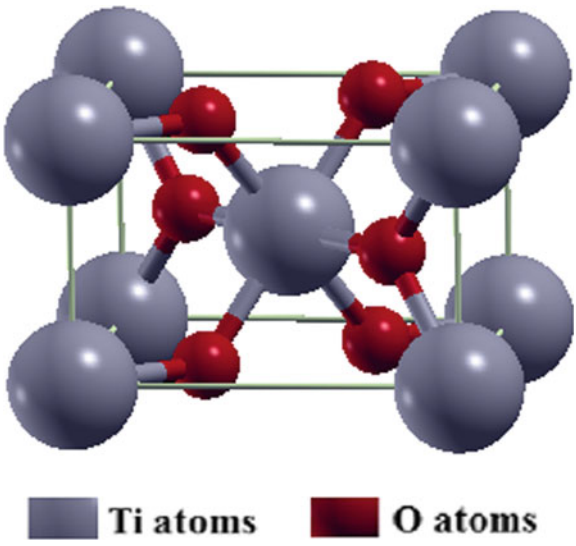

Fig. 2 Ball and stick model depiction of the crystal structure of rutile, one of the polymorphs of TiO_2

Table 1 Parameters and values selected in the ElaStic tool

Parameters	Values
Order of elastic constants	2
Method of calculation	Energy
Space-group number	136
Maximum Lagrangian strain	0.05
Number of distorted structures	41

respect to the Lagrangian strain, a procedure for polynomial fitting is implemented. It is found that the values of SOECs can be influenced by order of polynomial fit and the range of distortion.

3.1 Calculating Elastic Moduli

Reasonable averaging techniques are used to evaluate further elastic constants dependent on isotropic parameters such as elastic moduli (Young's, shear and bulk). There are three commonly used average implementation methods that occur in the ElaStic software. In the case of the Voigt [13] rule, a strain of uniform measure is assumed; in the instance of uniform stress, the Reuss [14] method is true. The Voigt, Reuss moduli findings are stated in terms of constants of rigidity (cij) and compliance (sij), respectively.

$$\begin{bmatrix} C_{11} & C_{12} & C_{13} & 0 & 0 & 0 \\ C_{12} & C_{11} & C_{13} & 0 & 0 & 0 \\ C_{13} & C_{13} & C_{33} & 0 & 0 & 0 \\ 0 & 0 & 0 & C_{44} & 0 & 0 \\ 0 & 0 & 0 & 0 & C_{44} & 0 \\ 0 & 0 & 0 & 0 & 0 & C_{66} \end{bmatrix}$$

The shear and bulk modulus in the Voigt method is, in particular,

$$G_V = \frac{1}{15}[(c_{11} + c_{22} + c_{33}) - (c_{12} + c_{13} + c_{23}) + 3(c_{44} + c_{55} + c_{66})] \quad (1)$$

$$B_V = \frac{1}{9}[(c_{11} + c_{22} + c_{33}) + 2(c_{12} + c_{13} + c_{23})] \quad (2)$$

For the Reuss procedure, the corresponding expressions are.

$$G_R = 15[4(s_{11} + s_{22} + s_{33}) - (s_{12} + s_{13} + s_{23}) + 3(s_{44} + s_{55} + s_{66})]^{-1} \quad (3)$$

$$B_R = [(s_{11} + s_{22} + s_{33}) + 2(s_{12} + s_{13} + s_{23})]^{-1} \tag{4}$$

Hill [15, 16] finds that it is strict upper and lower bounds when Voigt's and Reuss' elastic moduli are applied, respectively. Therefore, Hill gave an average bulk and shear moduli evaluated from these upper and lower limits and was expressed as:

$$B_H = \frac{1}{2}(B_V + B_R) \tag{5}$$

$$G_H = \frac{1}{2}(G_V + G_R) \tag{6}$$

The Poisson ratio (v) and the Young modulus (E) are obtained as a relationship between the shear modulus (G) and the bulk modulus (B) in all the factors considered for the average procedures discussed here, as,

$$v = \frac{3B - 2G}{2(3B + G)} \tag{7}$$

$$E = \frac{9BG}{3B + G} \tag{8}$$

4 Results

As mentioned in the previous sections, we obtain the results for the SOECs computed by the ElaStic code from the input values. From this simulation, our primary focus includes explaining some of the basic ab initio concepts, showing the procedures used and the results' accuracy. Considering such interpretation, computed data obtained using DFT should be regarded as for T = 0 K values; in contrast, most of the experimental procedures are performed at room temperature (T = 298 K). While performing first-principle calculations of the SOECs, it is essential to optimise ionic positions and lattice parameters. Thus the optimisation of various parameters has been performed for the crystal system we have taken into consideration.

Table 2 shows elastic moduli, as well as Poisson's ratio, obtained using the Voigt method in this work and a comparative representation of elastic moduli with the experimental data available in the literature. Deviations between the theoretical and experimental results may be related to temperature or any other environmental effects.

Table 2 Comparison of elastic properties obtained using the Voigt method in this study with the experimental values present in the available literature

	Our work	Experimental results [17]	Percentage difference
Young's modulus (GPa)	294.87	311.6	5.36
Poisson's ratio	0.25	–	–
Bulk modulus (GPa)	193.71	210.3	7.88
Shear modulus (GPa)	118.30	124.4	4.9

5 Conclusions

The elastic properties of TiO_2 (rutile) are systematically studied by means of the first principle calculation by Quantum Espresso in addition to the ElaStic tool. Here in this study, the elastic moduli (Young's, bulk and shear) found using the Voigt method was 294.87 GPa, 193.71 GPa, and 118.30 GPa respectively. The Poisson ratio, calculated using the Voigt method, was found to be 0.25. The percentage difference of Young's modulus, bulk modulus, and shear modulus estimated using the DFT in this work compared to experimental values present in literature was found to be 5.36, 7.88, and 4.9, respectively.

Acknowledgements The authors of this study want to express their sincere gratitude to the NIT Rourkela, India, and also to SERB (ECR/2018/001241) for making available the requisite facilities and financial support to carry out this work. The writers would also like to acknowledge the technical assistance provided by Mr. Rajesh Patnaik for this research.

References

1. Caravaca MA, Miño JC, Pérez VJ, Casali RA, Ponce CA (2008) Ab initiostudy of the elastic properties of single and polycrystal TiO_2, ZrO_2 and HfO_2 in the cotunnite structure. J Phys Condens Matter 21(1). https://doi.org/10.1088/0953-8984/21/1/015501
2. Nayak RK, Mahato KK, Routara BC, Ray BC (2016) Evaluation of mechanical properties of Al_2O_3 and TiO_2 nano filled enhanced glass fiber reinforced polymer composites. J Appl Polym Sci 133(47). https://doi.org/10.1002/app.44274
3. Jena A, Prusty SRK, Ray BC (2020) Mechanical and thermal behaviour of multi-layer graphene and nanosilica reinforced glass Fiber/Epoxy composites. Mater Today Proc 33, 5184–5189. https://doi.org/10.1016/j.matpr.2020.02.879
4. Mammone JF, Nicol M, Sharma SK (1981) Raman spectra of TiO_2-II, TiO_2-III, SnO_2, and GeO_2 at high pressure. J Phys Chem Solids 42(5):379–384. https://doi.org/10.1016/0022-3697(81)90045-7
5. Jun Z, Jing-Xin Y, Yan-Ju W, Xiang-Rong C, Fu-Qian J (2008) First-principles calculations for elastic properties of rutile TiO_2 under pressure. Chin Phys B 17(6):2216–2221. https://doi.org/10.1088/1674-1056/17/6/046

6. Golesorkhtabar R, Pavone P, Spitaler J, Puschnig P, Draxl C (2013) ElaStic: a tool for calculating second-order elastic constants from first principles. Comput Phys Commun 184(8):1861–1873. https://doi.org/10.1016/j.cpc.2013.03.010
7. Hohenberg P, Kohn W (1964) Inhomogeneous electron gas. Phys Rev 136(3B):B864–B871. https://doi.org/10.1103/PhysRev.136.B864
8. Mermin ND (1965) Thermal properties of the inhomogeneous electron gas. Phys Rev 137(5A):A1441–A1443. https://doi.org/10.1103/PhysRev.137.A1441
9. Giannozzi P et al (2009) Quantum Espresso: a modular and open-source software project for quantum simulations of materials. J Phys Condens Matter 21(39). https://doi.org/10.1088/0953-8984/21/39/395502
10. Vanderbilt D (1990) Soft self-consistent pseudopotentials in a generalized eigenvalue formalism. Phys Rev B 41(11):7892–7895. https://doi.org/10.1103/PhysRevB.41.7892
11. Perdew JP, Burke K, Wang Y (1996) Generalized gradient approximation for the exchange-correlation hole of a many-electron system. Phys Rev B 54(23):16533–16539. https://doi.org/10.1103/PhysRevB.54.16533
12. Fakhrabad DV, Shahtahmassebi N (2013) First-principles calculations of the young's modulus of double wall boron-nitride nanotubes. Mater Chem Phys 138(2):963–966. https://doi.org/10.1016/j.matchemphys.2013.01.004
13. Voigt W (1966) Lehrbuch der Kristallphysik (mit Ausschluss der Kristalloptik). Vieweg+Teubner Verlag
14. Reuss A (1929) Berechnung der Fließgrenze von Mischkristallen auf Grund der Plastizitätsbedingung für Einkristalle. ZAMM—J Appl Math Mech Z Für Angew Math Mech 9(1):49–58. https://doi.org/10.1002/zamm.19290090104
15. Hill R (1952) The elastic behaviour of a crystalline aggregate. Proc Phys Soc Sect A 65(5):349–354. https://doi.org/10.1088/0370-1298/65/5/307
16. Hill R (1963) Elastic properties of reinforced solids: Some theoretical principles. J Mech Phys Solids 11(5):357–372. https://doi.org/10.1016/0022-5096(63)90036-X
17. Wachtman JB, Tefft WE, Lam DG (1962) Elastic constants of rutile (TiO_2). J Res Natl Bur Stand Sect Phys Chem 66A(6):465. https://doi.org/10.6028/jres.066A.047

Molecular Dynamics Simulation-Based Investigation of Mechanical Behavior of CNT Embedded Nanocrystalline Al at Cryogenic Temperature

Pokula Narendra Babu and Snehanshu Pal

Abstract A molecular dynamics simulation based study has been carried out to examine the mechanical performance of nanocrystalline (NC) aluminum and NC Al embedded with Carbon nanotube (CNT) composite under uniaxial tensile loading for cryogenic temperature (77 K) through hybrid potentials for interatomic interactions of Al-CNT at 10^{10} s^{-1} strain rate. Armchair type CNTs ((5, 5), (15, 15), and (30, 30)) are preferred as reinforcing material in this study. The structural variation and defect evolution are also examined during the tensile deformation. NC Al embedded with CNT composite has exhibited higher ultimate tensile strengths in contrast to NC Al without CNT. It has been found that the matrix (NC Al) has fractured first through grain boundaries, then CNT has fractured through Stone–Wales defect. Shockley partial dislocations are the driving factor for the crack initiation leading to fracture of NC Al and CNT embedded NC Al composites.

Keywords Nanocrystalline material · Aluminum · Carbon nanotube · Dislocation · Molecular dynamics

1 Introduction

With extra-ordinary physical characteristics and mechanical properties such as high elastic modulus (~1 TPa), low density (~1.5 g/cm^3), higher tensile strength, high aspect ratio, electrical and heat conductivity; CNTs are taken as reinforcing material in metal matrix composites (MMCs) for structural applications [1–4]. Moreover, CNTs are successfully implemented in biomedical applications, electrical industry, additive sectors, energy applications, sporting equipment, molecular electronics industry, etc., [5–10]. On the other hand, Nanocrystalline materials have grabbed a lot of attention because of their increasing significance in the present scenario for

P. N. Babu (✉) · S. Pal
Department of Metallurgical and Materials Engineering, National Institute of Technology Rourkela, Rourkela 769008, India

S. Pal
Centre of Nanomaterials, National Institute of Technology Rourkela, Rourkela 769008, India

S. Pal et al. (eds.), *Processing and Characterization of Materials*, Springer Proceedings in Materials 13, https://doi.org/10.1007/978-981-16-3937-1_22

all industrial applications [11–14]. The grain size of nanocrystalline materials has less than 100 nm. They exhibited superior mechanical properties to polycrystalline materials due to their triple or quadruple grain boundary junctions and a high percentage of grain boundaries [15–18]. In the earlier phase, single-crystal aluminum materials are chosen as matrix material in conjunction with nanofillers (such as CNTs, carbon nanofibers, nanodiamond, graphene, etc.) as reinforcing materials [19–21]. As per the literature survey of Chen et al. CNTs reinforced Al matrix composites exhibited simultaneous improvement in tensile strength and fracture strain due to its advance in bonding conditions among the CNT and Al. They have also presented that the composite's loading bearing capacity increases due to CNT bearing external loads [22]. For example, Choi et al. have performed molecular dynamics analysis on CNT embedded aluminum composites under uniaxial tensile loading and found that overall mechanical properties are improved as an increase in CNTs volume fraction. They have revealed that CNTs withstand excessive load-bearing capacity, leading to improved fracture strain of the composite [23]. For instance, Junfeng et al. have predicted that stiffness and elasticity are enhanced proportionally to the CNT diameter by performing molecular dynamics simulations on aluminum composites aligned with CNTs. They also revealed that armchair type CNTs had exhibited higher growth in Al matrix composites' mechanical behavior than zigzag type CNTs. The characteristics of CNTs govern the fracture performance of CNT embedded Al composite [24]. To meet industrial applications' requirements and improve the mechanical performance of CNT embedded MMCs, nanocrystalline materials are chosen as matrix materials. Nanocrystalline aluminum is considered a matrix material in metal matrix composites in aggregation with CNT as a reinforcement material to enhance mechanical properties and bonding characteristics [25–27]. As per Choi et al. analysis, they have performed uniaxial tensile loading on the CNT embedded nanocrystalline composite (i.e., aluminum with single walled CNTs), and they have determined that composites strength is enhanced by two factors: (1) Grain size decrement and (2) Intensifying in CNTs volume fraction (CNTs enhances the ductility and toughness by effectively blocking the voids and cracks propagation) [28]. For instance, Pal et al. have done the uniaxial tensile performance of CNT-NC Al at diverse temperatures. They determined that the highest strength and vacancy concentration are obtained for high CNT diameters at the interface due to its higher surface area [29]. Beyond all the above studies, the mechanical deformation behavior and fracture mechanism of CNTs inserted in NC Al composite are not studied yet at cryogenic temperature. However, experimentally is difficult to carry out this process due to cost, machine availability, and time constraints. So, MD simulation is one of the preeminent tools to analyze all these simulations at necessary constraints such as strain rate, temperature, different loading conditions, etc., [30–35]. In this paper, the fracture mechanism and deformation behavior of NC Al and CNT-NC Al composite at cryogenic temperature have been investigated through a uniaxial tensile process through molecular dynamics simulations. The CNTs influence on the mechanical behavior and fracture processes of NC Al has also been studied. The structural changes that occur during uniaxial tensile loading have been analyzed through OVITO software parameters such as Centrosymmetry parameter, Atomic strain, and Dislocation analysis.

2 Simulation Details

LAMMPS software is preferred to carry out the MD simulations on NC Al followed by CNT incorporated NC Al composite [36]. NC Al specimen is created through the Voronoi method [37] using Atomsk software [38] with dimensions of 20 nm^3. Armchair type CNTs ((5,5), (15,15), (30,30)) are created with the aid of TubeASP and incorporated in NC Al specimens. The volume fraction of CNTs used in this study are (5,5)CNT: 0.075%, (15,15)CNT: 0.224%, and (30,30)CNT: 0.448%. Figure 1 depicts the matrix material (nanocrystalline aluminum), reinforcement material (CNT), and CNT embedded NC Al composite. Periodic boundary conditions are implemented in 3 directions. The time step of 1 fs is considered to perform uniaxial tensile loading.

EAM potential is used for interatomic interactions of Al-Al [39], AIREBO potential is preferred for C–C interatomic interactions [40]. The LJ (Lennard–Jones) potential is chosen for Al-C interactions [41]. The cut-off distance is considered as 10.2 Å. LJ (Lennard–Jones) 12–6 is computed as per Eq. (1)

$$E = 4\epsilon \left[\left(\frac{\sigma}{r} \right)^{12} - \left(\frac{\sigma}{r} \right)^{6} \right] \tag{1}$$

where E means the intermolecular potential of Al-C atoms, σ means distance where the interatomic potential is zero, r means distance among two atoms, and ϵ means potential depth. The Conjugate gradient method has been used to carry out the energy minimization. Equilibration has been performed at cryogenic temperature with NPT ensemble for 20,000 time steps. The 10^{10} s^{-1} strain rate is selected to perform uniaxial tensile testing along Z direction [001] with the NVT ensemble. OVITO software is used for the post-processing work of the MD simulations [42]. Common

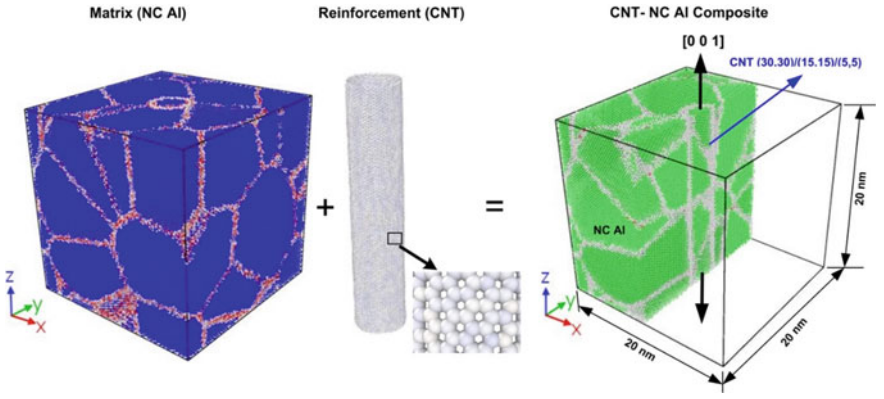

Fig. 1 Centro-symmetry parameter snapshot illustrates the NC Al (Matrix) and CNT (reinforcement), and whereas Common neighbor analysis shows the CNTs embedded with NC Al composite

neighbor analysis (CNA) is preferred to recognize the defects such as stacking faults and twinning etc. [43]. The overall dislocation density and dislocation types are investigated through dislocation analysis (DXA) [44]. Local shear strain distribution is analyzed with Atomic strain (AS) [45, 46].

3 Results and Discussion

The mechanical behavior, CNT fracture process, and deformation behavior of composite are elucidated in detail in this section. Figure 2a depicts the stress–strain plots for CNT incorporated NC Al composites for three armchair type-CNTs ((5,5), (15,15), and (30,30)) and NC Al specimen. NC Al embedded with (30,30) CNT composite has exhibited higher ultimate tensile strength in contrast to NC Al without CNT and other CNTs. The tensile strength drops continuously in NC Al without CNT specimen (i.e., black line in Fig. 2a) compared to the CNTs embedded in NC Al composite specimens. On the other hand, the fracture strain of the CNTs incorporated in NC Al is enhanced with increasing CNTs volume fraction [47, 48]. The NC Al exhibits a more significant fracture strain contrary to CNTs embedded NC

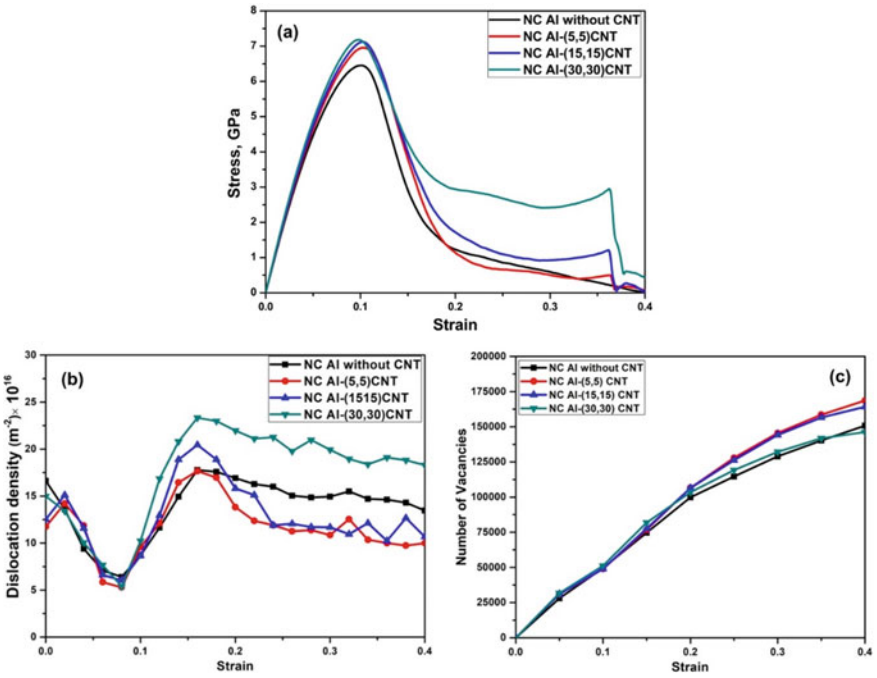

Fig. 2 Illustrates the **a** Stress–strain curves, **b** Overall dislocation density and strain plots, and **c** Number of vacancies-strain of specimens during tensile testing at cryogenic temperature

Al composite specimens. The plots of CNTs embedded NC Al composite specimens show rise and fall between the strain range of 0.35–0.4, which indicates that CNTs withstand the external loads through the matrix during loading.

The composite specimens' mechanical behavior is illustrated through the dislocation density analysis as per Fig. 2b. Figure 2b depicts the overall dislocation density plots for the composite specimens. Dislocations exist in the grain boundaries before loading, and loading causes dislocations movement in the specimen. Initially, the dislocation density decreases upto a strain of 0.09 and then increases rapidly upto the strain of 0.16; finally, it reaches a steady-state through the rise and fall manner upto the fracture point. In which (30,30) CNT incorporated NC Al specimen exhibits higher dislocation density owing to higher CNT diameter compared to other CNTs. However, it is noticed that the CNTs hinder dislocation movement due to a mismatch among the CNTs and matrix at the interface, as reported in the literature [49]. The vacancy population to strain are depicted in Fig. 2c. Dislocations movement causes vacancies generation in both cases (NC Al and followed by CNT-NC Al composite) of specimens. The vacancy population is increasing for 4 cases (NC Al and three armchair-CNTs embedded NC Al composite) as the deformation progresses upto a strain of 0.2; later on, NC Al specimen exhibits lower population vacancy in contrast to CNTs-NC Al composite specimens. There is no significant effect by CNTs on vacancy concentration. However, the vacancy concentration has greater at the CNT-Al interface in CNT incorporated NC Al composites.

Figure 3 illustrates the dislocation density analysis of dislocation types for the NC Al, CNT-NC Al specimens by uniaxial tensile testing at cryogenic temperature. Four dislocations (they are: Perfect, Stair-rod partial, Shockley partial, and Frank partial dislocations) have been considered to carry out this analysis because the fracture mechanism of the composite is mainly affected by these dislocations. The trend of the dislocation density path (diminishes at initial stages upto 0.1 strain and then rises upto a 0.16–0.18 strain range, later reaches to stable stage until the final deformation) is similar in four cases (a) NC Al, (b-d) CNTs embedded NC Al composite specimens. Shockley partial dislocations have exhibited higher dislocation density with respect to strain compared to the other three dislocations and are so high for (d) CNT (30,30) embedded NC Al composite specimen. Whereas, in the case of Perfect dislocations, Stair-rod, and frank partial dislocations, there is no much variation in dislocation density throughout the tensile deformation process as per Fig. 3(a-d). The Shockley partial dislocation density is increasing, corresponding to CNT diameter. The characteristics (size and diameter) of CNT affect the dislocations generation and annihilation at the matrix and CNT interface. The Shockley dislocations are majorly contributed to dislocation for the driving tensile deformation process.

Figure 4 shows the NC Al specimen's deformation process through atomic snapshots of various features (such as AS, CNA, CSP, and DXA) during uniaxial tensile loading at cryogenic temperature. The NC Al specimen's fracture is initiated with void formation at a strain of 0.12 at the triple grain boundary junction as per Fig. 4a. Initially, dislocations exist in grain boundaries of NC Al because grain boundaries are sources for the dislocations. However, loading on NC Al specimen leads to dislocations motion and which causes vacancies generation. Stacking faults formation and

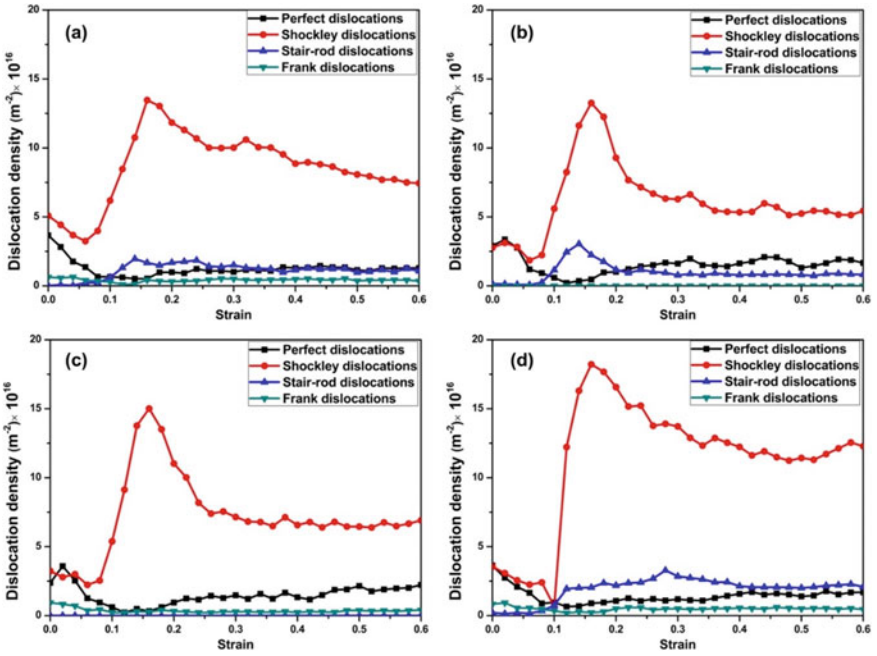

Fig. 3 Plots of dislocation types of dislocation densities for **a** NC Al, **b** (5,5), **c** (15,15), and **d** (30,30) CNTs embedded NC Al composite specimens at 77 K

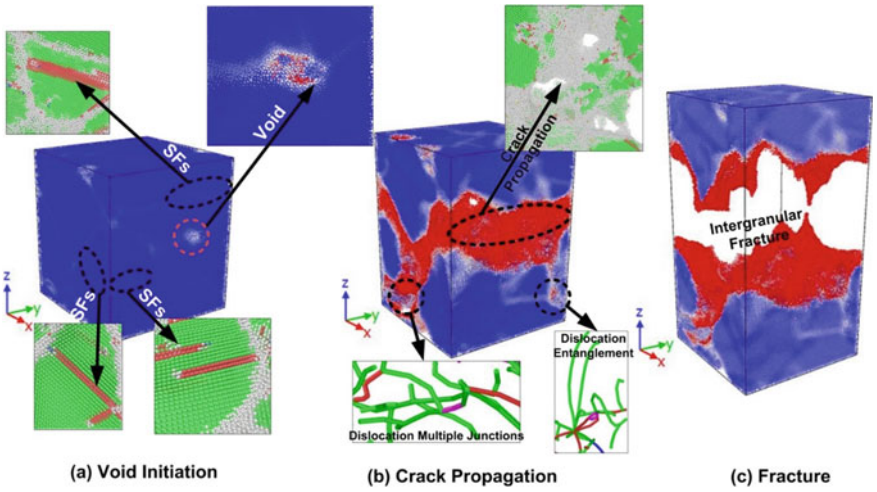

Fig. 4 Tensile deformation process of NC Al through atomic strain snapshots: **a** void initiation, **b** crack propagation, and **c** complete fracture during tensile deformation at cryogenic temperature. (Inset shows Common neighbor analysis and dislocation analysis)

propagation are shown by Common Neighbor Analysis during the void generation in NC Al. The cracks are developed in specimens owing to voids accumulation at the intersection of grain boundaries. The crack is propagated along the grain boundaries (i.e., intergranular crack propagation) at 0.35 strain as per Fig. 4b. During the crack propagation period, the dislocation entanglements and dislocation multiple junctions are depicted in inset figures of dislocation analysis at crack zones. The dislocation density and vacancy population are diminished at the end of the tensile deformation. Finally, the intergranular fracture occurs in NC Al at strain as per Fig. 4c.

Figure 5 depicts the atomic snapshots of (30,30) CNT-NC Al composite at cryogenic temperature during uniaxial tensile testing through atomic strain analysis. Figure 5a displays the void inception at the CNT-Al grain boundary interface due to vacancies accumulation at a strain of 0.13, which causes failure initiation to the composite. Stacking faults formation and propagation are shown in zoom vision with Common Neighbour Analysis. The distribution of shear strain is uniform in both materials of NC Al and CNT. As the loading progresses, the void becomes a crack, and it propagates along the grain boundaries in the matrix material. Simultaneously, CNT bears the external loads acting on the composite at a strain of 0.21, as shown in Fig. 5b. Dislocation analysis depicts the dislocation types, dislocation

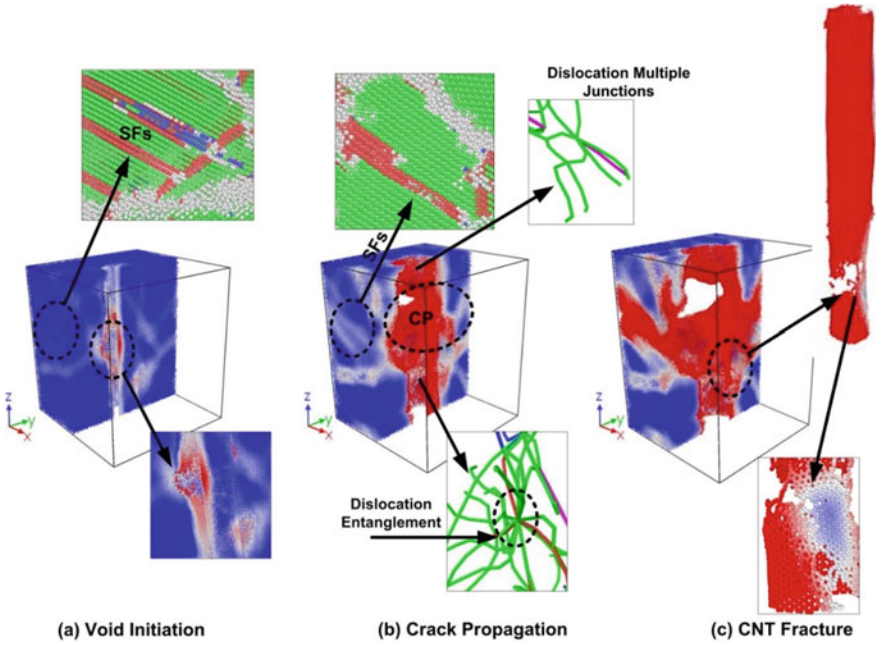

Fig. 5 Tensile deformation process of (30,30) CNT incorporated NC Al composite through atomic strain snapshots in slice visualization: **a** void initiation, **b** crack propagation, and **c** CNT fracture during tensile deformation at cryogenic temperature. (Inset shows common neighbor analysis and dislocation analysis)

entanglements, and dislocation junctions in Fig. 5b. Shockley dislocations are higher in number and which supports the tensile deformation. Initially, the dislocations are the highest upto 0.2 strain, then it decreases gradually and later reaches a steady-state upon loading on the composite specimen as per Fig. 2b. At a strain of 0.37, the CNT is fractured due to shear strain inhomogeneity and which is shown clearly in the zoom view of Fig. 5c, where the CNT is fractured at the bottom portion. Matrix (NC Al) cracking is the mechanism of composite failure for all the CNTs embedded in NC Al composites at the cryogenic temperature because of no cracks in CNTs as per Fig. 5. The metals exhibit extremely low ductility at very low temperatures like cryogenic temperature. The deformation process (i.e., fracture mechanism) is similar for (5,5) and (15,15) CNTs embedded in NC Al composites. The stages involved in the CNT embedded NC Al composite specimens are void generation, crack initiation and propagation at the CNT-Al interface, and CNT rupture in the tensile deformation.

Figure 6 illustrates the fracture behavior process of (30,30) CNT through atomic strain snapshots in a step-by-step manner at cryogenic temperature. The CNT's failure is initiated by disordered atoms arrangement as per Fig. 6d. CNT rupture occurs in the specimen through shear failure at the same strain of voids inception in the specimen during loading. Another mechanism is Stone–Wales defect formation, and it causes to CNTs failure by reducing its strength [23]. The carbon atoms in hexagonal shape of CNTs are distorted into rings of five, seven, and eight carbon atoms (inset figure shows these distortions known as Stone–Wales defects) are shown in Fig. 6e. These defects induce distortion in CNTs and which causes failure initiation, rapid propagation, and finally leading to fracture of CNT as per Fig. 6f. The fracture mechanism is similar for (5,5) and (15,15) CNTs embedded in NC Al composite specimens.

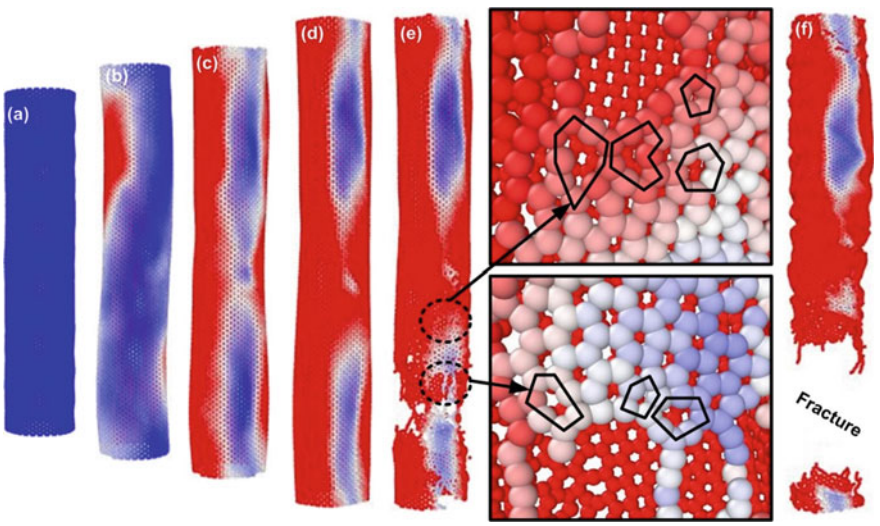

Fig. 6 Atomic strain snapshots illustrate the (30,30) CNT fracture process during tensile loading (Inset Figures show the Stone–Wales defect)

Overall, the set of events involved in the deformation mechanism of NC Al, CNT embedded NC Al composite during tensile testing are void initiation (in triple grain boundary intersections in NC Al, and whereas, at the interface of CNT-NC Al in CNT-NC Al composite), crack initiation and propagation in matrix (NC Al) material through the grain boundary and then fracture of the whole specimen. The CNT is fractured through the shear failure (bonds broken by atoms disruption) and Stone–Wales defect. The dislocation density is high for CNT embedded NC Al composite than NC Al due to CNT addition. The Shockley dislocations are higher than other dislocations, the driving factor for the tensile deformation.

4 Conclusions

The mechanical behavior of NC Al and CNT incorporated NC Al composite specimens has been examined during uniaxial tensile testing in Z-direction through MD simulations with hybrid potentials at cryogenic temperature. CNT (30,30) incorporated NC Al specimen has exhibited the highest ultimate tensile strength than the NC Al. We have also noticed that an intensify in CNT diameter leads to rise in dislocation density of composites. CNTs embedded NC Al composites have shown the highest dislocation density compared to NC Al. It is found that the intergranular fracture (i.e., fracture along the grain boundaries) takes place in both NC Al and CNT embedded NC Al composites. The fracture of CNT happens through rupture and Stone–Wales defect processes during tensile loading. Matrix fails first, and then CNT fractures in the CNT incorporated NC Al composite at cryogenic temperature. Shockley partial dislocations are key driving factors for the tensile deformation at cryogenic temperature. This study's upshots provide a well sympathetic of the CNT fracture mechanism incorporated NC Al composite at an atomic scale. Such knowledge will benefit to outspread the enrichment in mechanical behavior and specimen life.

References

1. Bakshi SR, Lahiri D, Agarwal A (2010) Carbon nanotube reinforced metal matrix composites-a review. Int Mater Rev 55(1):41–64
2. Radhamani AV, Lau HC, Ramakrishna S (2018) CNT-reinforced metal and steel nanocomposites: a comprehensive assessment of progress and future directions. Compos A Appl Sci Manuf 114:170–187
3. Guo B, Zhang X, Cen X, Chen B, Wang X, Song M, Du Y (2018) Enhanced mechanical properties of aluminum based composites reinforced by chemically oxidized carbon nanotubes. Carbon 139:459–471
4. Chen B, Li S, Imai H, Jia L, Umeda J, Takahashi M, Kondoh K (2015) Load transfer strengthening in carbon nanotubes reinforced metal matrix composites via in-situ tensile tests. Compos Sci Technol 113:1–8

5. Raphey VR, Henna TK, Nivitha KP, Mufeedha P, Sabu C, Pramod K (2019) Advanced biomedical applications of carbon nanotube. Mater Sci Eng, C 100:616–630
6. Bulusheva LG, Sysoev VI, Lobiak EV, Fedoseeva YV, Makarova AA, Dubois M, Okotrub AV (2019) Chlorinated holey double-walled carbon nanotubes for relative humidity sensors. Carbon 148:413–420
7. Muhulet A, Miculescu F, Voicu SI, Schütt F, Thakur VK, Mishra YK (2018) Fundamentals and scopes of doped carbon nanotubes towards energy and biosensing applications. Mater Today Energy 9:154–186
8. Jang YT, Moon SI, Ahn JH, Lee YH, Ju BK (2004) A simple approach in fabricating chemical sensor using laterally grown multi-walled carbon nanotubes. Sens Actuat B Chem 99(1):118–122
9. De Volder MF, Tawfick SH, Baughman RH, Hart AJ (2013) Carbon nanotubes: present and future commercial applications. Science 339(6119), 535–539
10. Choi WB, Chung DS, Kang JH, Kim HY, Jin YW, Han IT, Kim JM (1999) Fully sealed, high-brightness carbon-nanotube field-emission display. Appl Phys Lett 75(20):3129–3131
11. Pal S, Mishra S, Meraj M, Mondal AK, Ray BC (2018) On the comparison of interrupted and continuous creep behaviour of nanocrystalline copper: a molecular dynamics approach. Mater Lett 229:256–260
12. Kumar KS, Van Swygenhoven H, Suresh S (2003) Mechanical behavior of nanocrystalline metals and alloys. Acta Mater 51(19):5743–5774
13. Suryanarayana C, Koch CC (2000) Nanocrystalline materials–current research and future directions. Hyperfine Interact 130(1–4):5
14. Pal S, Gururaj K, Meraj M, Bharadwaj RG (2019) Molecular dynamics simulation study of uniaxial ratcheting behaviors for ultrafine-grained nanocrystalline nickel. J Mater Eng Perform 28(8):4918–4930
15. Ovid'ko IA, & Sheinerman AG (2004) Triple junction nanocracks in deformed nanocrystalline materials. Acta Mater 52(5):1201–1209
16. Schiøtz J, Jacobsen KW (2003) A maximum in the strength of nanocrystalline copper. Science 301(5638):1357–1359
17. Kelsall RW, Hamley IW, Geoghegan M (eds) (2005) Nanoscale science and technology. Wiley, Chichester, p 108
18. Gleiter H (2000) Nanostructured materials: basic concepts and microstructure. Acta Mater 48(1):1–29
19. Zhai W, Srikanth N, Kong LB, Zhou K (2017) Carbon nanomaterials in tribology. Carbon 119:150–171
20. Bartolucci SF, Paras J, Rafiee MA, Rafiee J, Lee S, Kapoor D, Koratkar N (2011) Graphene–aluminum nanocomposites. Mater Sci Eng A 528(27):7933–7937
21. Curtin WA, Sheldon BW (2004) CNT-reinforced ceramics and metals. Mater Today 7(11):44–49
22. Chen B, Kondoh K, Imai H, Umeda J, Takahashi M (2016) Simultaneously enhancing strength and ductility of carbon nanotube/aluminum composites by improving bonding conditions. Scripta Mater 113:158–162
23. Choi BK, Yoon GH, Lee S (2016) Molecular dynamics studies of CNT-reinforced aluminum composites under uniaxial tensile loading. Compos B Eng 91:119–125
24. Xiang J, Xie L, Meguid SA, Pang S, Yi J, Zhang Y, Liang R (2017) An atomic-level understanding of the strengthening mechanism of aluminum matrix composites reinforced by aligned carbon nanotubes. Comput Mater Sci 128:359–372
25. Zhang H, Maljkovic N, Mitchell BS (2002) Structure and interfacial properties of nanocrystalline aluminum/mullite composites. Mater Sci Eng, A 326(2):317–323
26. Babu PN, Gargeya BSK, Ray BC, Pal S (2020) Atomistic investigation of mechanical behavior for CNT reinforced nanocrystalline aluminum under biaxial tensile loading. Mater Today Proc 33:4942–4950
27. Shi Y, Zhao L, Li Z, Li Z, Xiong DB, Su Y, Guo Q (2019) Strengthening and deformation mechanisms in nanolaminated single-walled carbon nanotube-aluminum composites. Mater Sci Eng A 764:138273

28. Choi HJ, Bae D (2011) Strengthening and toughening of aluminum by single-walled carbon nanotubes. Mater Sci Eng A 528(6):2412–2417
29. Pal S, Babu PN, Gargeya BSK, Becquart CS (2020) Molecular Dynamics simulation based investigation of possible enhancement in strength and ductility of nanocrystalline aluminum by CNT reinforcement. Mater Chem Phys 243:122593
30. Reddy KV, Pal S (2019) Atomistic study of fracture behavior of metallic glass fiber reinforced metal-matrix nanocomposite during bending creep deformation process. Int J Mater Res 110(12):1142–1149
31. Xue ZW, Wang LD, Zhao PT, Xu SC, Qi JL, Fei WD (2012) Microstructures and tensile behavior of carbon nanotubes reinforced Cu matrix composites with molecular-level dispersion. Mater Des 34:298–301
32. Reddy KV, Pal S (2020) Accumulative roll bonding of Cu–Zr nanolaminate: Atomistic-scale investigation of structural evolution and grain orientation scatter dependence on rolling parameters. J Appl Phys 127(15):154305
33. Silvestre N, Faria B, Lopes JNC (2014) Compressive behavior of CNT-reinforced aluminum composites using molecular dynamics. Compos Sci Technol 90:16–24
34. Meraj M, Deng C, & Pal S (2018) Stress-induced solid-state amorphization of nanocrystalline Ni and NiZr investigated by atomistic simulations. J Appl Phys 123(4):044306
35. Babu PN, Becquart CS, Pal S (2020) Molecular dynamics simulation-based study of creep–ratcheting behavior of nanocrystalline aluminum. Appl Nanosci 1–17
36. Plimpton S (1995) Fast parallel algorithms for short-range molecular dynamics. J Comput Phys 117(1):1–19
37. Chen D (1995) Structural modeling of nanocrystalline materials. Comput Mater Sci 3(3):327–333
38. Hirel P (2015) Atomsk: a tool for manipulating and converting atomic data files. Comput Phys Commun 197:212–219
39. Mishin Y, Farkas D, Mehl MJ, Papaconstantopoulos DA (1999) Interatomic potentials for monoatomic metals from experimental data and ab initio calculations. Phys Rev B 59(5):3393
40. Stuart SJ, Tutein AB, Harrison JA (2000) A reactive potential for hydrocarbons with intermolecular interactions. J Chem Phys 112(14):6472–6486
41. Dandekar CR, Shin YC (2011) Molecular dynamics based cohesive zone law for describing Al–SiC interface mechanics. Compos A Appl Sci Manuf 42(4):355–363
42. Stukowski A (2009) Visualization and analysis of atomistic simulation data with OVITO–the open visualization tool. Model Simul Mater Sci Eng 18(1):015012
43. Honeycutt JD, Andersen HC (1987) Molecular dynamics study of melting and freezing of small Lennard-Jones clusters. J Phys Chem 91(19):4950–4963
44. Stukowski A, Bulatov VV, Arsenlis A (2012) Automated identification and indexing of dislocations in crystal interfaces. Model Simul Mater Sci Eng 20(8):085007
45. Shimizu F, Ogata S, Li J (2007) Theory of shear banding in metallic glasses and molecular dynamics calculations. Mater Trans 0710160231
46. Falk ML, Langer JS (1998) Dynamics of viscoplastic deformation in amorphous solids. Phys Rev E 57(6):7192
47. Chunfeng D, Zhang X, Yanxia MA, Dezun W (2007) Fabrication of aluminum matrix composite reinforced with carbon nanotubes. Rare Met 26(5):P450 455
48. Liu ZY, Xiao BL, Wang WG, Ma ZY (2014) Tensile strength and electrical conductivity of carbon nanotube reinforced aluminum matrix composites fabricated by powder metallurgy combined with friction stir processing. J Mater Sci Technol 30(7):649–655
49. Lu YB, Yang QS, He XQ, Liew KM (2016) Modeling the interfacial behavior of carbon nanotube fiber/polyethylene composites by molecular dynamics approach. Comput Mater Sci 114:189–198

Parametric Investigation on Drilling Behavior of 3D Printed CFRP Composites

Anshuman Das, G. Surya Rao, K. Debnath, and R. N. Mahapatra

Abstract CFRP (Carbon fiber reinforced polymer) composites are widely used in manufacturing industries since it offers attractive mechanical and physical properties like high strength, high modulus, and low density. Conventional drilling is an inevitable machining operation which is mostly performed for making hole in composites. In this study, CFRP composite was fabricated as a plate structure of 4 mm in thickness to investigate its drilling behavior. The drilling behavior was experimentally investigated through different drilling parameters. The effect of different drilling parameters namely axial feed (45, 63, and 90 mm/min), rotational speed for the spindle (250, 710, 2000 RPM), and three various geometries of the drill bits are analyzed on two machining characteristics one is torque other one is radial force and the last one is highest temperature during drilling of CFRP composites. The drilling parameters were also optimized through Taguchi technique. The relative significance of the drilling parameters was obtained by analysis of variance (ANOVA).

Keywords 3D Printing · CFRP · Drilling · Thrust force · Torque · Temperature

1 Introduction

In comparison to conventional materials, the specific strength and specific modulus of the Carbon fiber reinforced polymer composite are superior. For the assembly operations, it is often necessary for the Carbon fiber reinforced polymer composite structure to achieve final dimensions. To attain neat geometry machining operations like milling are the secondary operating process. Drilling is the most preferable machining operation for achieving a better assembly, especially for the fiber-reinforced composites. Even though fiber-reinforced composites are better in achieving overall geometry, it still requires performing machining operations to meet specific engineering

A. Das (✉)
Department of Mechanical Engineering, DIT University, Dehradun, Uttarakhand 248009, India

G. S. Rao · K. Debnath · R. N. Mahapatra
Department of Mechanical Engineering, National Institute of Technology Meghalaya Shillong, Shillong 793003, India

S. Pal et al. (eds.), *Processing and Characterization of Materials*, Springer Proceedings in Materials 13, https://doi.org/10.1007/978-981-16-3937-1_23

requirements. Due to the high strength, lightweight and load-bearing capacity the advanced composite materials are widely using in structural applications. In the modern researches of the manufacturing field, machining of Carbon fiber reinforced polymer composite materials are very much important in the development of different industrial applications. The presence of reinforcing carbon fibers in the composite employing difficulties in the machining process due to anisotropic, high abrasiveness, and non-homogeneous. It is necessary to understand the potential of the applications and the issues associated with the machining of the fiber-reinforced composite plays an important role. Madhavan et al. [1] investigated the effect of different drills on Carbon fiber reinforced polymer composite. The effect of feed rate, cutting speed, and geometry on various responses was observed. Poor surface finish and lower delamination were observed on the composite under high spindle speed and low feed rate. The author also concluded that the hardness of drill material influencing the cutting forces. Barik et al. [2] examined the relationship between the hole quality and process parameters of the Carbon fiber reinforced polymer composite, by monitoring the radial force and drilling torque. Author concluded that thrust force, torque, and hole roundness are increased by increasing the speed of cutting and feeding rate. By increasing the speed of spindle and feeding rate the delamination rate was decreasing. Chen et al. [3] studied the cutting force variations and the effect of drilling parameters, tool geometry on the CFRP composite. The experimental results proved that by the choice of legitimate tool geometry and drilling parameters no delamination was observed. Koklu and Morkavur [4] preferred a cryogenic machining approach for drilling of CFRP composite. Various machining characteristics were compared with dry condition. The authors concluded that the overall results of the cryogenic machining approach improved the machinability of CFRP composite. Harris et al. [5] investigated the performance of coated tools while machining the CFRP composite and compared them with high-speed steel tools. At specific machining parameters, the hole quality and the tool life was improved significantly by the coated tools. Xu et al. [6] analyzed the impact of specialized drills on the high-strength CFRP composite. By varying the drilling parameters the forces, hole morphology, hole accuracy, tool wear, and damage on the composite were examined. Desai et al. [7] performed a full factorial design on the CFRP composite by varying different machining parameters. The quality of hole and circularity was analyzed by performing the experimental investigation using a coated carbide tool. Roberto et al. [8] investigated CFRP/CFRP laminated for aircraft fuselage panels. An artificial neural network is utilized to implement quick decisions for changing the tool on a time basis. Cong et al. [9] studied different machining characteristics in rotary ultrasonic machining on CFRP composite. The impact of various coolants on the output was examined, and it was found the feasible results were attained under cold air instead of cutting fluid. Reddy et al. [10] discussed the influence of cutting parameters in the drilling of CFRP composite. The effect of various machining parameters on the material removal rate was discussed. Vaibhav et al. [11] compared the conventional drilling and ultrasonically assisted drilling of CFRP composite. Better results are achieved in the ultrasonic-assisted drilling. Shahabaz et al. [12] examined coated and uncoated drills on the CFRP composite by varying the drilling parameters. The drill diameter is one

the most influencing parameter followed by the spindle speed and feed rate. Coated drill outperformed uncoated drill. Zheng et al. [13] investigated a CFRP composite by developing a theoretical model for rotary ultrasonic drilling. Rathod et al. [14] optimized the cutting parameters during machining the CFRP composite. ANOVA was used to determine the significant parameters and their contribution on the responses. Won et al. [15] investigated the drilling behavior of CFRP composite by varying the machining parameters. Nagaraja et al. [16] studied the behavior of CFRP-G926 composite in drilling to examine the effect of feed rate and cutting speed. The author concluded that the overall experimentation helped to find out the proper combination of different input parameters to reduce the delamination. Micheal et al. [17] examined the impact of machining parameters upon various machining characteristics of the CFRP composite. Sobri et al. [18] examined 25.4 mm thick CFRP composite by mechanical drilling and laser machining. Based on the hole and cut quality the relation between the drilling parameters was defined. Yasar et al. [19] investigated the surface damages and delamination on the CFRP composite while performing drilling. The author mainly focused on the effect of cutting parameters and drill geometry on the hole diameter and surface roughness. The author concluded that the feed rate was one of the most important factors according to the analysis of variance. Jaafar et al. [20] examined different drilling attributes by varying input parameters on unidirectional CFRP laminates. Thrust force measurement was affected by the variation of the point angle. The delamination of the minor right-hand side helix drill was less compared to the straight fluted drill. Ameur et al. [21] examined the optimum combinations of the input parameters in drilling to attain a better hole quality while performing drilling of CFRP composite. The tool material and the feed rate influenced the thrust force highly. While increasing the spindle speed cylindricity errors were observed on the holes.

It is quite clear from the above literature that most of the researchers focused on evaluating the drilling characteristics of CFRP by using different fabrication processes on composite manufacturing. Negligible literature is available focusing on the 3D printed CFRP composite drilling behavior. So In the current investigation, impact of drilling parameters on 3D printed CFRP composite was studied and the drilling parameters are optimized.

2 Materials and Methods

2.1 Fabrication of Workpiece Material

With the help of 3D printing or additive manufacturing, three dimensional solid objects can be easily framed from a digital file. The main mechanism used in this process is addition of layers one by one. Complex or intricate shapes can be easily produced from 3D *printing* using less material compared to conventional manufacturing methods. The Carbon fiber reinforced composite was fabricated by using a 3D

Fig. 1 3D printing machine

printing machine (Mark Forged Company X7) shown in Fig. 1. In the 3D printing machine, two spools can be used at a time one is for matrix material and another for fiber material. Carbon fiber is incorporated with the onyx thermoplastic matrix material of layer thickness of 0.125 microns. The matrix material is kept inside an isolated dry box to free from moisture content. The composite plate of 100 × 100 × 3 mm specimen was modeled by using PTC Creo software. The model was exported to the Eiger.io site which is interlinked with the 3D printing machine. Initially, on the workbench of the 3D printing machine, a washable gum was applied to stick the specimen steadily. In the layer wise, the 3D printer will fabricate the composite plate according to the modeled specimen dimensions.

2.2 Measurements

The performance of drilling of the composite plate was researched by utilizing a knee type vertical milling machine (Make: Batliboi Ltd., Model: BFV5). The readied CFRP composite plate was mounted on an apparatus that was fixed on a dynamometer. The dynamometer is connected with a multi-channel charge amplifier (Make: Kistler, 5070A) and with a connection of a DAQ system (Make: Kistler, 5697A1). The range of the dynamometer in Z-direction is −5 to +100KN with an affectability of −3, 7pC/N. Around 3–5 kHz is the natural frequency range for the

Table 1 Drilling parameters

Factors	Level-1	Level-2	Level-3
A: Spindle speed (RPM)	250	710	2000
B: Feed (mm/min)	45	63	90
C: Types of milling cutter	8-facet	Dagger	Slot

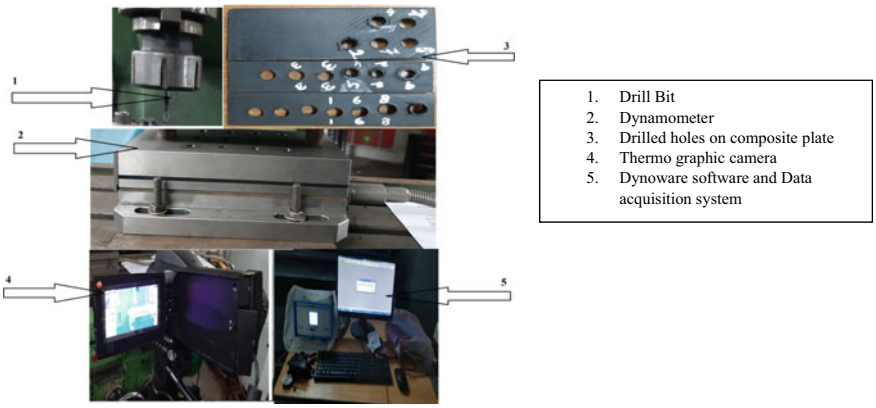

Fig. 2 Drilling set-up and response measurement system

dynamometer. Minor variations in the amplitude will be detected by keeping the high sampling rate as 1000 Hz. For the present study, different drilling parameters were considered as shown in Table 1. The induced maximum temperature while machining the CFRP composite was obtained by the thermo graphic camera (Make: Testo, Model: 885–2 SET). The infrared camera resolution of 320 × 240 pixels, thermal responsiveness < 30 mK at +30 °C. The precision of the estimations ±2 °C. The drilling on the composite plate was performed with the feed rate of 45, 63, 90 mm/min and spindle speed of 250,710 and 2000 rpm using 8-facet, dagger and slot drill bit, shown in Fig. 3. All the drill bits are made of solid carbide with a diameter of 8 mm. In Fig. 2 the whole experimental set-up was shown. To check the flawlessness of the outcomes, three readings are considered for each exploratory run and their mean is taken as final reading.

2.3 Design of Experiments

The machining characteristics of CFRP composite in drilling activity have been investigated by Taguchi analysis. The machining parameters such as spindle speed, feed rate, and type of drill bit selected with different levels. All the drilling parameters are considered at three levels. Orthogonal array L_9 was considered to carry out the experiments on different levels. The optimized process parameters were defined by

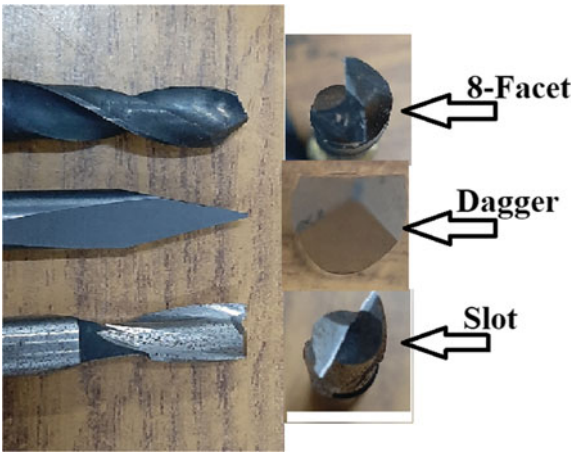

Fig. 3 Drill bits (Different types)

the signal to noise ratio. The output responses are thrust force, torque, and maximum temperature while machining. The ultimate goal in present experimental investigation is to improve the drilling characteristics of CFRP composite. The relative significance of the machining parameters affecting the responses is defined by the analysis of variance. Each process parameter contribution was determined percentage-wise by the ANOVA. These outcomes are broken down with the assistance of analysis of variance (ANOVA), main effect plot, and multiple regression analysis got utilizing the MINITAB-16 programming. The significance of info factors on reactions is dictated by ANOVA. The results of drilling experiments have been graphically analyzed through main effect plot.

3 Results and Discussions

3.1 ANOVA Analysis

To find out the significant drilling variables ANOVA analysis was implemented on the results of the experiments. The results of ANOVA completed at 5% significance level are shown in Tables 1, 2 and 3. For different responses such as cutting force, drilling torque and machining temperature.

The ANOVA analysis of cutting force is shown in Table 3. It was observed that all the three contributing parameters are found to be significant for cutting force. Speed was discovered to be the main significant parameter followed by drill type and feed. Anova analysis of drilling torque is shown in Table 4. All the parameters are found to be notable one for the drilling torque. Speed and drill type are most significant followed by feed. Analysis of variance of machining temperature is shown in Table

Table 2 Machining responses

Speed (rpm)	Feed (mm/min)	Drill type	F_z (N)	M_z (Nm)	Temperature (°C)
250	45	8-Facet	125.000	0.57	90.0
250	63	Dagger	123.000	0.89	87.0
250	90	Slot	151.129	0.70	85.0
710	45	Dagger	90.449	0.85	95.0
710	63	Slot	93.746	0.92	80.0
710	90	8-Facet	78.076	0.60	104.2
2000	45	Slot	90.926	0.28	120.3
2000	63	8-Facet	51.849	0.23	127.0
2000	90	Dagger	76.236	0.29	145.0

Table 3 ANOVA analysis of cutting force

Source	DF	Seq SS	Adj SS P	Adj MS	F	p
Speed (rpm)	2	5893.84	5893.84	2946.92	3979.79	0.000
Feed (mm/min)	2	309.53	309.53	154.77	209.00	0.005
Drill type	2	1097.31	1097.31	548.65	740.93	0.001
Residual error	2	1.48	1.48	0.74		
Total	8	7302.16				

Table 4 ANOVA analysis of drilling torque

Source	DF	Seq SS	Adj SS P	Adj MS	F	p
Speed (rpm)	2	0.484289	0.484289	0.242144	21,793	0.000
Feed (mm/min)	2	0.036689	0.036689	0.018344	1651.00	0.001
Drill type	2	0.073756	0.073756	0.036878	3319.00	0.00
Residual error	2	0.000022	0.000022	0.000011		
Total	8	7302.16				

Table 5 ANOVA analysis of machining temperature

Source	DF	Seq SS	Adj SS P	Adj MS	F	p
Speed (rpm)	2	3340.62	3340.62	1670.31	311.56	0.003
Feed (mm/min)	2	286.55	286.55	143.27	26.72	0.036
Drill type	2	340.15	340.15	170.07	31.72	0.031
Residual error	2	10.72	10.72	5.36		
Total	8	3978.04				

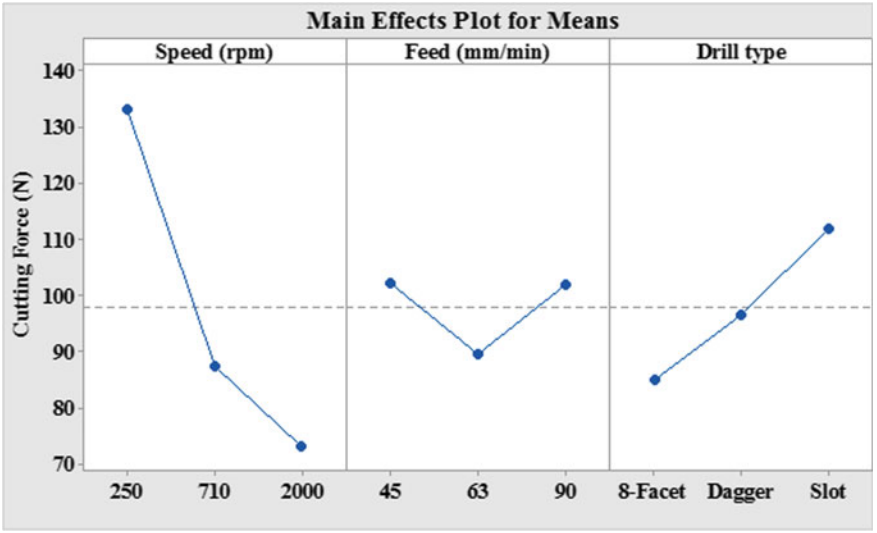

Fig. 4 Main effects plot for cutting force

5. All the parameters are found to be significant for machining temperature. Speed was again found to be the most significant followed by drill type and feed.

3.2 Analysis with Main Effects Plot

Different responses such as cutting force, drilling torque and machining temperature are analyzed with the help of main effects plots shown in Figs. 4, 5 and 6.

The standard deviation of the plot is 30.21209.

The standard deviation of the plot is 0.57.

The standard deviation of the plot is 90.

Graphical analysis for cutting force is shown in Fig. 4. It was delineated from the figure that with speed increment, cutting force was reduced this might be due to increment in machining temperature. This can be seen from the Fig. 6. From Fig. 6, it was found that with speed temperature was increased. It was found that with feed, mix trend was observed for cutting force. Cutting force was found to be increased with drill type. Machining force was observed to be highest for slot type drill. Temperature increased linearly with speed, because as speed increased very less time might be available for heat transfer to the surroundings.

In the Fig. 5, the mixed trend was found for drilling torque with all the machining parameters. With initial value of machining parameters, drilling torque was increased up to intermediate value, but when value was increased to highest level for machining parameters, decrement in drilling torque was there.

Fig. 5 Main effects plot for drilling torque

Fig. 6 Main effects plot for machining temperature

In Fig. 6, Machining temperature was analyzed with three machining parameters. With speed, machining temperature was increased linearly. And with feed and drill type, mixed trend was observed. With feed, temperature was initially reduced but then enhanced but with drill type just opposite trend was observed.

Some interesting trend was observed with slot type drill bit, both temperature and torque reduced but force increased. With feed same trend was observed for cutting force and temperature but just opposite trend was found for drilling torque. With speed, force and torque reduced drastically but temperature increased enormously. 8 facet drills produced less machining force compared to dagger drill. This happened because of longer chisel edge and flutes with spiral shape.

4 Conclusion

The thrust force, torque, and the maximum temperature while machining the composite were observed to define the performance of the drilling. Analysis of variance (ANOVA) is performed to define the relative significance of each varying parameter. From ANOVA analysis, it was delineated that speed was the most dominating parameter for all the three responses compared to feed and drill type. Slot type drill performed better compared to other two types of geometries in terms of temperature and torque. Compared to other two parameters like speed and drill type, feed was not found to be more prominent for the responses. With speed, linear increment of temperature was noticed because at high speed, there might be chance of less heat transfer to the surroundings due to less time. 8 facet drill performed better in terms of cutting force and torque due to better chip removal and contact. The slot type drill performed better in terms of cutting temperature because of better heat removal to the surroundings. Torque was found to be less in slot type drill compared to dagger type because of non clogging of chips with smooth removal. Similar nature of curve was found in force and temperature with feed. This was mainly observed due to chip clogging at higher feed rate.

References

1. Madhavan S, Prabu SB (2012) An experimental study of influence of drill geometry on drilling of carbon fiber reinforced plastic composites
2. Barik T, Parimita S, Pal K (2017) Parametric study and process monitoring on drilling of CFRP composites. In Proceedings of the 10th international conference on precision, pp 953–957
3. Chen WC (1997) Some experimental investigations in the drilling of (CFRP) composite laminates. Int J Mach Tools Manuf 37(8):1097–1108
4. Koklu U, Morkavuk S (2019) Cryogenic drilling of (CFRP). Surf Rev Lett 26(09):1950060
5. Harris M, Qureshi MAM, Saleem MQ, Khan SA, Bhutta MMA (2017) Carbon fiber-reinforced polymer composite drilling via aluminium chromium nitride-coated tools: Hole quality and tool wear assessment. J Reinf Plast Compos 36(19):1403–1420
6. Xu J, Li C, Chen M, El Mansori M, Ren F (2019) An investigation of drilling high-strength CFRP composites using specialized drills. Int J Adv Manuf Technol 103(9–12):3425–3442
7. Desai B, Rana J, Gajera H Study of hole quality parameters in drilling of (CFRP) Using design of experiments 2, 461–465
8. Segreto T, Caggiano A, Nele L (2020) Smart multi-sensor monitoring in drilling of CFRP/CFRP composite material stacks for aerospace assembly applications. Appl Sci 10(3):758
9. Cong WL, Feng Q, Pei ZJ, Deines TW, Treadwell C (2012) Rotary ultrasonic machining of carbon fiber-reinforced plastic composites: using cutting fluid versus cold air as coolant. J Compos Mater 46(14):1745–1753
10. Reddy GS, Kumar R Experimental investigation to optimize process parameters in drilling operation for composite materials. Int J Eng Adv Res Technol (IJEART). ISSN, 2454–9290
11. Phadnis VA, Makhdum F, Roy A, Silberschmidt VV (2012) Experimental and numerical investigations in conventional and ultrasonically assisted drilling of CFRP laminate. Procedia Cirp 1:455–459
12. Shahabaz SM, Shetty N, Shetty SD, Sharma SS (2020) Surface roughness analysis in the drilling of carbon fiber/epoxy composite laminates using hybrid Taguchi-Response experimental design. Mater Res Express 7(1):015322
13. Zheng K, Dong S, Liao W (2019) Investigation on thrust force in rotary ultrasonic drilling of CFRP using brad drill. Mach Sci Technol 23(6):971–984
14. Rathod CM, Chudasama M, Darji S (2015) An investigation of hole size, circularity and delamination during drilling operation of carbon fiber rein forced polymer with using ANOVA. IJSTE 2, 53–59
15. Won MS, Dharan CKH (2002) Drilling of aramid and carbon fiber polymer composites. J Manuf Sci Eng 124(4):778–783
16. Nagaraja R, Rangaswamy T (2018) Drilling of CFRP and GFRP composite laminates using one shot solid carbide step drill K44. In: AIP conference proceedings, vol 1943, no 1, p 020025. AIP Publishing LLC
17. Michael G (2017) Optimization of drilling parameters on CFRP composites. Int J Sci Dev Res IJSDR 2(8):33–43
18. Ahmad Sobri S, Robert H, David W, Shuaib NA (2018) Drilling strategy for thick (CFRP): a preliminary assessment. J Eng Technol Sci 50(1):21–39
19. Yaşar N, Korkmaz ME, Günay M (2017) Investigation on hole quality of cutting conditions in drilling of CFRP composite. In: MATEC web of conferences, vol 112, p 01013. EDP sciences
20. Jaafar MF, Salleh MS, Izamshah R, Hassan MH, Sundi SA, Hafiz MSA, Kasim MS Influence on thrust force and delamination for one shot drilling of (CFRP)
21. Ameur MF, Habak M, Kenane M, Aouici H, Cheikh M (2017) Machinability analysis of dry drilling of carbon/epoxy composites: cases of exit delamination and cylindricity error. Int J Adv Manuf Technol 88(9–12):2557–2571

Prediction of Fatigue Life of Glass-Vinyl-Ester-Polyurethane Sandwich Structure Using Mathematical Model

Akhtar Khan, Anshuman Das, and Akula Siva Bhaskar

Abstract Predicting the fatigue life of a Polymer Composite Sandwich Structures (PCSS) is always a great deal of challenge to composite design engineers. Various factors like fundamental constituting elements and their properties, type of manufacturing process, working conditions such as type of loading, maximum or minimum loading and frequency of application of load as well as the environmental surroundings influence the fatigue life of PCSS. For the present experimental study, GVE-PU (Glass-Vinyl-Ester-Polyurethane) a polymer composite sandwich structure is selected. It is widely used in manufacturing components like wind turbine blades, ship casings and surfing planks which are majorly subjected to cyclic loadings. Initially GVE-PU composite laminates having foam density ranging from 100 to 300 kg/m^3 were developed through hand-lay-up process. These sandwich laminated were subjected to flexural and fatigue testing under 60–80% of ultimate flexural loading with 6–9 Hz frequency. Furthermore, the test results were analyzed in the form of 2D & 3D surface plots to compare GVE-PU with GVE (Glass- Vinyl-Ester) composite. Both laminate results were compared and S–N curves were drawn to identify the distinctive stress dominated and cycle dominated zones to draw conclusions. Finally a mathematical expression was developed to predict the fatigue life of PCSS laminate.

Keywords Fatigue life · PCSS · GVE-PU sandwich

1 Introduction

Polymer Composite Sandwich Structures (PCSS) are the material of choice for many structural applications. It has numerous advantages over metals such as low density, low dielectric loss, high specific strength, and designed an-isotropic properties with

A. Khan (✉) · A. S. Bhaskar
Indian Institute of Information Technology, Design and Manufacturing, Kurnool, AP 518007, India

A. Das
DIT University, Dehradun, Uttarakhand 248009, India

S. Pal et al. (eds.), *Processing and Characterization of Materials*, Springer Proceedings in Materials 13, https://doi.org/10.1007/978-981-16-3937-1_24

dimensional stability for complex contours; corrosion resistant and high fatigue life. These PCSS are subjected to different types of fatigue loading, such as tension-tension, tension–compression, compression-compression, with different ramp rates, depending on the application. The fatigue loads on the wind turbine blades are different from that of an aircraft stabilizer or a radar dome or a boat hull. The application defines the targeted fatigue properties for PCSS, and the targeted properties are achieved by choosing suitable matrix and reinforcement material. The matrix material could be an ester, epoxy or bismalemide; the fiber reinforcement could be glass, carbon, aramide, or a combination of these materials, the sandwich material could be polyurethane foam (PUF), metallic, fiber or polymer honeycomb. Vinyl-Ester with glass fiber and PUF would be the material of choice for small and large wind turbine blades, because it has better moisture resistance compared to other resins, processing temperatures are lower compared to epoxy resins, and is easy on fabrication due to low viscosity. Glass fibers have significant cost advantage over equivalent carbon fiber composites, and are therefore preferred. Conformal profile and density of PUF can be easily controlled to produce PCSS with the desired performance characteristics [1–5]. The most preferred materials used in constructing spacecrafts and aircrafts are FRPC (Fiber- Reinforced Polymer Composite) materials. Specifically, in aerospace vehicles FRPCs are used as fundamental skeletal materials. The following paper discusses the challenges associated with current generation composite materials and brings forth the scope for future advancement as structure materials. The safety and reliability of an aircraft majorly depends on constructing prediction models, damage impact and tolerance [6]. Fiber fractions have a great deal of influence on thermal degradation of Glass and Carbon fiber reinforced epoxy composites [7]. The effect of debonding of interphase results in weight changes in hydrothermally aged fiber reinforced plastics. The main reason for gaining weight and debonding at interphase is due to penetration of water. This was experimentally evaluated and concluded by comparing results of FRP and plain resin [8]. The fatigue life cycle of PCSS are affected by surface finish, internal defects, operating environment, temperature and stress cycles [9–12]. Fatigue life cycle tests are broadly classified into low cycle and high cycle fatigue. In high cycle fatigue tests, the peak loads are considerably lower than the ultimate load of the PCSS, hence the failure is high. However during low cycle fatigue, the peak fatigue loads are high with loading frequency in the range of 0.1–10 Hz. The focus of this study is on low cycle fatigue behavior of glass-vinyl ester-PUF sandwich composite.

2 Experimental Details

Glass-Vinyl Ester (GVE) polymer composite laminates was prepared using the wet-hand lay-up technique. Vinyl Ester Resin, Ecmalon 9911 (2% cobalt (accelerator), 50% Methyl Ethyl Ketone Peroxide (MEKP) (catalyst) in 10% DMA solution, with ratio of resin: accelerator: catalyst: promoter 100:2:2:2) was used as the matrix material and glass fiber with balance plain weave 0/90 fiber orientation and 360 gsm was

used as the reinforcement in the weight ratio of 35:65 respectively. The GVE laminates were post cured at 50 °C for 30 min followed by heating up to 70 °C and soaking for 60 min and finally heating to 85 °C and soaking for 120 min. The glass-transition temperature after curing was 85 °C, measured using Mettler DSC 823. The laminates were cut, to test specimen size of 127 × 12.7 × 6 mm for further testing. Polymer composite sandwich structures with different density polyurethane foams (100, 200 and 300 kg/m^3) were prepared by mixing equal ratio of isocynate and polyol and casting under different pressures with 3 mm GVE face sheets on either sides. The flexural and fatigue tests on GVE composite laminates were conducted as per ASTM D 790 and for GVE-PUF sandwich composites, as per ASTM C 393. The test specimen dimensions were length 200 mm, width 30 mm, PU core thickness 24 mm and GVE laminate face sheets on either side with a thickness of 3 mm The flexural and fatigue tests were conducted using a Kalpak make, 5 Ton, three-point bend test setup, as shown in Fig. 1a & b. To determine fatigue behavior of PCSS, first determine the behavior of polymer composites face sheets that make up the two load bearing surfaces of the sandwich structure. Therefore as part of this study, flexural tests were first conducted on glass-vinylester (GVE) composites and then on the polyurethane foam sandwich structure with GVE face sheets. The ultimate flexural load is used to determine the maximum fatigue load that can be applied on the test specimen. Figure 1c shows the type of fatigue cycle tension—tension mode, which was applied to the polymer composites and sandwich composite test specimen as part of this work. For the purposes of the present study, 60% and 80% of flexural ultimate

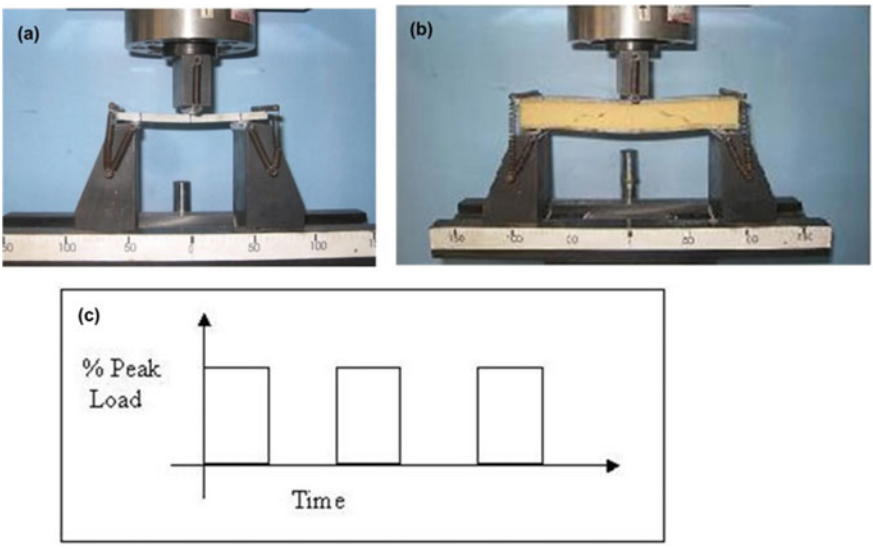

Fig. 1 Three point bend test setup used for flexural and fatigue tests on glass-vinyl ester (GVE) composite and glass vinyl ester poly urethane (GVE-PU) sandwich composites & schematic of fatigue cycle (tension-tension mode)

loads were applied at frequencies of 6 and 9 Hz with corresponding amplitude of 2 and 1.25 mm respectively.

3 Results and Discussion

Figure 2a shows the flexural stress–strain graph of Glass-Vinyl-Ester (GVE) composite before and after post curing. Post curing results in the improvement of flexural strength by 16% from 300 to 350 MPa. This increase in tensile strength is associated to the amorphous to crystalline transition of the resin and to improved attachment bonding among fiber phase and resin matrix. The computed modulus of elasticity is 12455 MPa. Figure 2b compares the load verses deflection behavior of GVE composite and GVE-PU sandwich composites. The load bearing capacity of GVE-PU composite is 2000 N, with 300 kg/m^3 foam (thickness of 24 mm), sandwiched between two GVE face-sheets of 3 mm, which is twice that of GVE laminate for a deflection of 5 mm. The plot clearly shows that with increase in PU density the load carrying capacity increases. A careful analysis of the test results and repeated experiments revealed that ultimate load (L in Newton) carrying capacity of GVE-PU is a polynomial function of foam density (D in Kg/m^3), as given by the following equation (See Eq. 1):

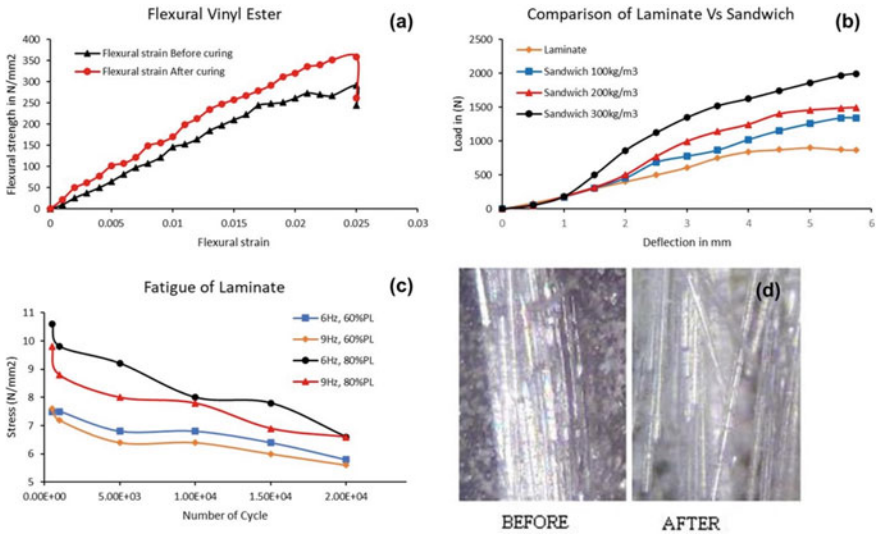

Fig. 2 **a** Flexural stress versus strain plots of GVE composite laminates; **b** Load versus deflection plots of GVE laminates and GVE -PUF-sandwich composites **c** S–N curve for GVE composite laminates **d** microscopic images of glass-vinyl ester (GVE) composite test specimen before and after fatigue test

$$L = 0.005D^2 + 1.7D + 920 \quad (1)$$

Figure 2c shows the (Stress versus Number of Cycles) S–N response of GVE composite as a function of frequency and percentage of ultimate load (%PL). The slope of zone 1 is determined by the percentage of ultimate load (80%PL corresponds to 252 N and 60%PL corresponds to 188 N). The load carrying capacity drops drastically because of the cumulative effect of the inherent defects. The duration of Zone 2 is approximately 5000 fatigue cycles, during this low cycle fatigue, cracks and delamination gets initiated in the laminates. The next transition is Zone 3 with a noticeable slope arising as a result of the accumulated defects caused during fatigue loading in Zone 2. This is followed by a gradually drop in stress as a function of number of fatigue cycles that is zone 4. Figure 2d shows the infinitesimal pictures of the GVE composite subjected to fatigue tests. The micrographs unmistakably displays the rupture of glass fibers, matrix cracking and debonding between inter laminates. However, rupture of fiber is major mode of failure. The root causes for such failures are higher fatigue loading and entrapped dissolved gases during Hand-layup process, which ultimately affects the fragile matrix and fiber interface. Under ordinary working conditions, GVE composites are exposed to 10 to 20% of fatigue loading where as in the current test the composite structure is exposed to extreme loading conditions (60 to 80% of ultimate load).

Statistical analysis was carried out on test results according to Taguchi's Design of Experiments (DOE), L4 orthogonal array was adopted to conduct experimental trails to calculate affect of ultimate load and frequency of failure. The response function was the number of cycles to failure, which was obtained by fitting a polynomial curve to the results obtained after 20,000 = 2E + 04 cycles. Based on the analysis, the effect of frequency on fatigue life was 47% and that of percentage ultimate load was 53%.

In comparison to plot 3(A), plot 3(C) has distinct fatigue curves, as a function of percentage of ultimate load. Higher fatigue loads, results in higher stresses, with the top two curves for 80% of ultimate load at 6 and 9 Hz. The overlapping curves in 3(A) indicate collapsing of the pores in the foam, at different loads and frequencies, the number of cycles to failure is difficult to predict or model in such cases. The most notable features of all the fatigue curves, laminate and the sandwich structures, is the existence of distinct zones. Figure 3d shows the formulated S–N = Stress verses Number of cycles curve. The slope of the curve during Zone 1 largely depends of the fatigue load and inherent defects in the composite. Zone 2 depends on the defect initiation and propagation within the composite as a function of fatigue loading. The rate at which these defects propagate will determine the width of the Zone 2. Once a critical number of defects are generated as a result of fatigue loading, Zone 3 will set in. The slope of Zone 3 is determined by rate of propagation of these defects across the sample. Once these defect lines get terminated Zone 4 will begin, and continues till the formation of the next set of critical defects. It is also definitely possible that there could be more than two transitions (zone 1, 3) and two plateau (zone 2, 4) for a given PMC subjected to fatigue loading. Based on these experimental results, a mathematic model was developed to relate the effect of frequency and density of

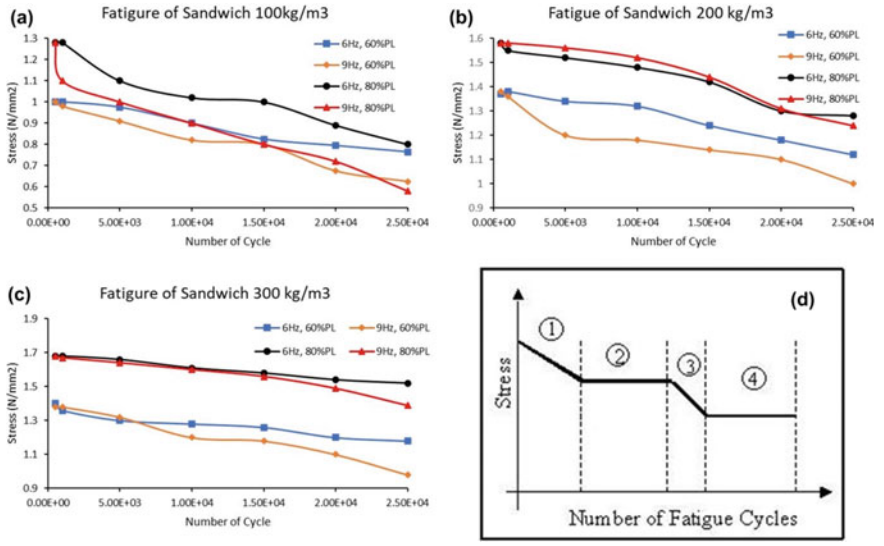

Fig. 3 **a**–**c** S–N cure of GVE-PU sandwich composite with PU density of 100; 200; 300 kg/m^3 Fig. 3d formulated S–N curves for polymer composites and sandwich structure

PUF, to the fatigue life of GVE-PU composites. Figure 4 show the 2D contour plots and 3D surface plots of this model. The graphs indicate that at low frequency and low fatigue loads the fatigue life is high with an extended zone 1 & 3. The slopes are gradual and the crack propagation rate is slow. However with increase in fatigue load and frequency the fatigue life will reach saturation within 10^5 cycles, beyond which the load carrying capacity drops significantly, which means Zone 4 is broad. The relationship between PUF density, load and fatigue life (Fig. 5) is much more complex. Higher the PUF density, higher is the load carrying capacity and therefore higher fatigue life, but this relation is non-linear and has interaction effects.

Figure 3a–c shows the fatigue behavior of GVE-PUF sandwich composite. Higher the density of the foam, the pores are finer, and therefore the cells become rigid, this impedes the propagation of cracks within the sample under fatigue load. In comparison to plot 3(A), plot 3(C) has distinct fatigue curves, as a function of percentage of ultimate load. Higher fatigue loads, results in higher stresses, with the top two curves for 80% of ultimate load at 6 and 9 Hz. The overlapping curves in 3(A) indicate collapsing of the pores in the foam, at different loads and frequencies, the number of cycles to failure is difficult to predict or model in such cases. The most notable features of all the fatigue curves, laminate and the sandwich structures, is the existence of distinct zones. Figure 3d shows the formulated S–N = Stress verses Number of cycles curve. The slope of the curve during Zone 1 largely depends of the fatigue load and inherent defects in the composite. Zone 2 depends on the defect initiation and propagation within the composite as a function of fatigue loading. The rate at which these defects propagate will determine the width of the Zone 2. Once a

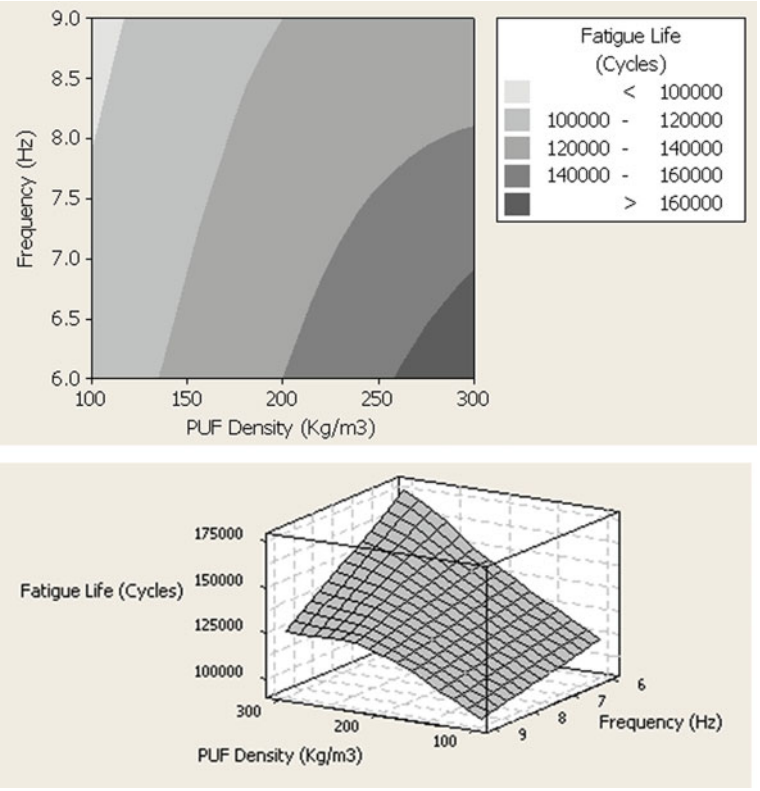

Fig. 4 Models to predict the fatigue life of GVE-PUF sandwich composites as a function of frequency and PUF density

critical number of defects are generated as a result of fatigue loading, Zone 3 will set in. The slope of Zone 3 is determined by rate of propagation of these defects across the sample. Once these defect lines get terminated Zone 4 will begin, and continues till the formation of the next set of critical defects. It is also definitely possible that there could be more than two transitions (zone 1, 3) and two plateau (zone 2, 4) for a given PMC subjected to fatigue loading. Based on these experimental results, a mathematic model was developed to relate the effect of frequency and density of PUF, to the fatigue life of GVE-PU composites. Figure 4 show the 2D contour plots and 3D surface plots of this model. The graphs indicate that at low frequency and low fatigue loads the fatigue life is high with an extended zone 1 & 3. The slopes are gradual and the crack propagation rate is slow. However with increase in fatigue load and frequency the fatigue life will reach saturation within 10^5 cycles, beyond which the load carrying capacity drops significantly, which means Zone 4 is broad. The relationship between PUF density, load and fatigue life (Fig. 5) is much more complex. Higher the PUF density, higher is the load carrying capacity and therefore higher fatigue life, but this relation is non-linear and has interaction effects.

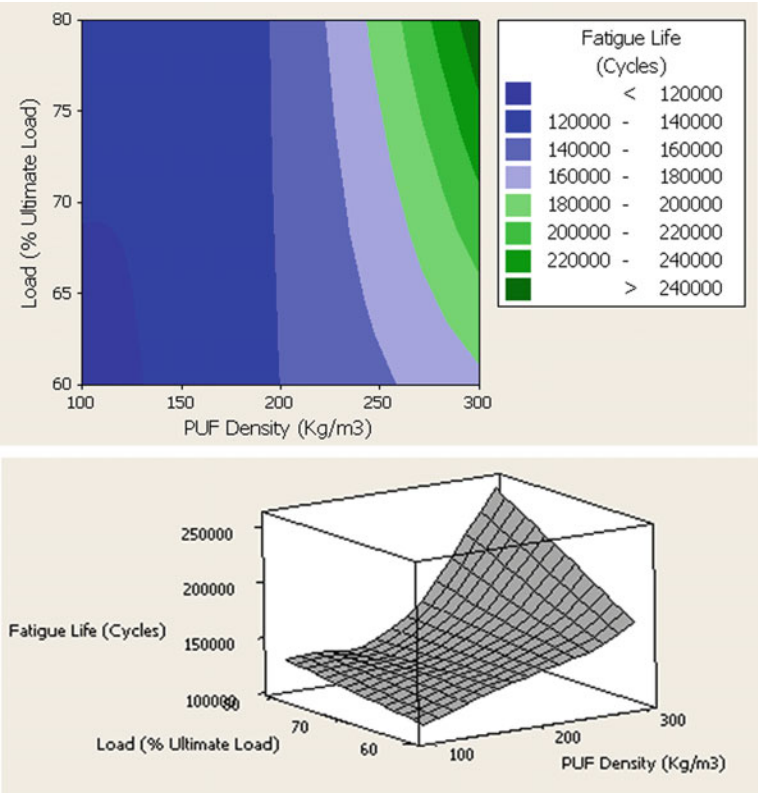

Fig. 5 Models to predict the fatigue life of GVE-PUF sandwich composites as a function of load and PUF density

4 Conclusions

The load carrying capacity of polyurethane foam sandwich structures with a foam density of 300 kg/m^3 with 3 mm glass-vinyl-ester face sheet is twice that of glass-vinyl-ester composite. Higher the density of the foam sandwiched between the face sheets, higher is the load carrying capacity and the fatigue life. The fatigue load has a dominant effect on the fatigue life of the sandwich composite than frequency. Both the GVE laminate and GVE-PU sandwich composite show distinct zones in the S–N cures, The slope, width of these zones, and the fatigue life of GVE-PU composites can be predicted by adopting mathematical models, proposed in this work.

References

1. Kanny K, Mahfuz H (2005) Flexural fatigue characteristics of sandwich structures at different loading frequencies. Compos Struct 67:403–410
2. Kulkarni N, Mahfuz H et al (2003) Fatigue crack growth and life prediction of foam core sandwich composites under fatigue loading. Compos Struct 59:499–505
3. El Mahi A, Bezazi A (2004) Modelling the flexural behavior of sandwich composite materials under cyclic fatigue. Mater Des 25, 199–208
4. Johnson AF, Smith GD (1986) Mechanical properties and design of sandwich materials. Composites 17, 321–28
5. Belingardi G, Martella P, Peroni L (2007) Fatigue analysis of honeycomb composite sandwich beams. Composites: Part A, 38, 1183–1191
6. Mangalgiri PD (1999) Composite materials for aerospace applications aeronautical development agency, vimanapura po, Bangalore, India 22(3):657–664
7. Mukherjee C, Case ED (2004) Silica coatings on bismaleimide (BMI) polymeric substrates" A. Lee materials science and mechanics department, Michigan state university, East lansing, MI, 48824, USA. Vol 35, pp 1389–1396
8. Malkapuram R, Kumar V, Yuvraj SN (2008) Recent development in natural fibre reinforced polypropylene composites. J Reinf Plast Compos 28:1169–1189
9. Ramesh M, Sudharsan P (2018) Experimental investigation of mechanical and morphological properties of flax-glass fiber reinforced hybrid composite using finite element analysis. SILICON 3:747–757
10. Ramnath BV, Elanchezhian C, Nirmal PV, Prem Kumar G, Santhosh Kumar V, Karthick S, Rajesh S, Suresh K (2014) Experimental investigation of mechanical behavior of jute-flax based glass Fiber reinforced composite. J Fibers Polym 15:1251–1262
11. Athijayamani A, Thiruchitrambalam M, Manikandan V, Pazhanivel B (2010) Mechanical properties of natural fibers reinforced polyester hybrid composite. Int J Plast Technol 11:104–116
12. Soudmand BH, Nezhad SK (2016) Experimental investigation on the mechanical properties of co-polypropylene/GF/CaCO3 hybrid nanocomposites. J Polym Sci Ser A 58:454–463

Improving Health and Productivity of Calcining Kiln Through Several Innovations in Refractory Maintenance Practices at Rourkela Steel Plant

S. Roy, P. R. Padhee, A. Bhattacharyya, and R. K. Singh

Abstract Calcined Lime is one of the most important ingredients in both primary and secondary steel making for removal of impurities to make clean steel. Lime quality depends on limestone characteristics, calcination process and kiln health. Refractory performance of lime kilns plays crucial role in enhancing the productivity and product quality of lime kilns. After the capacity expansion of hot metal production from 1.9 to 4.2MT in RSP, 2 new vertical twin shaft lime kilns, supplied by M/s. Cimprogetti, Italy, were introduced in 2012–13. However, maintaining quantity and quality of produced lime remained a challenge due to frequent refractory failure in these kilns. RSP employed several innovative repair methodologies and introduced design changes and applied superior materials to substantially improve the life of these kilns. These interventions resulted in reducing overall down time of kilns, thereby improving calcined lime quality and productivity for steel making. Frequent thermal imaging along with design modification helped to prevent sudden pre matured failure in kilns. As a result, consistent better life of more than two years could be achieved. Good recative lime with LOI less than 5.2 and Reactivity more than 320 could be produced in line with enhanced steel production of SMS-II.

Keywords Steel · Lime · Calcination · Lime Kiln · Refractory

1 Introduction

Calcined Lime is an essential and critical ingredient for steel making process. Calcined lime is used as a fluxing agent for removal of impurities, maintaining slag chemistry and basicity (CaO/SiO_2) by facilitating desulphurization, de-phosphorization, preventing over-oxidation of steel in BOF and secondary metallurgy treatment. The time, efficiency, and effectiveness of lime reactions depend on

S. Roy · P. R. Padhee
Rourkela Steel Plant (RSP), Steel Authority of India Limited, Rourkela, India

A. Bhattacharyya · R. K. Singh (✉)
R & D Centre for Iron and Steel (RDCIS), Steel Authority of India Limited, Ranchi, India
e-mail: rksingh@sail.in

S. Pal et al. (eds.), *Processing and Characterization of Materials*, Springer Proceedings in Materials 13, https://doi.org/10.1007/978-981-16-3937-1_25

its quality, quantity and size [1]. Soft burnt lime with good reactivity, high CaO and lower fines is required to facilitate desulphurization, de-phosphorization, refractory protection and less lime consumption. Generally, quality of lime is influenced by limestone characteristics, calcination process, kiln health (refractory and structural condition) and fuel quality [2, 3]. Calcination of limestone is an endothermic chemical reaction in solid state and hence requires considerable input of energy. The limestone is charged into the kiln and, while progressing through the kiln, is being decomposed or calcined. Theoretically 56 kg of CaO is produced from 100 kg of $CaCO_3$ during complete calcination. The calcination, a simple single stage firing process, is carried out in either rotary or vertical shaft kiln. Earlier there were single shaft counter current kilns, but eventually parallel-flow regenerative dual shaft kilns came into existence to reduce energy costs and to increase productivity. These kilns are made up of two side-by-side vertical shafts which are connected in the middle, allowing gases to flow from one shaft to the other through connecting channel or cross over channel area. Each shaft functions in alternate manner. If one shaft is acting as the calcining shaft, the other serves as the preheating shaft. Limestone is charged in shafts from the top. Hot combustion gases are fired down the first shaft calcining the lime. The exhaust then flows across the connecting channel or cross over channel and flows up through the second shaft preheating the lime. The flow is reversed in every 12–14 min. The lime is cooled in the bottom section of each shaft with a countercurrent flow of air. Calcined lime exits from the bottom of each shaft. Parallel flow kilns can be fired with natural gas or oil. They are energy-efficient and produce high quality lime [4]. The shaft reversal produces a long burning zone with constant low temperature (within 950 °C) which is ideal for the production of high quality soft burned reactive lime. The heat loss of the regenerative kiln is minimal with lower exhaust gas temperatures and low lime temperature at discharge end [5].

These vertical dual shaft kilns are divided into four zones by imaginary horizontal planes as depicted in Fig. 1. From the top to bottom in sequence are: (a). Stone storage zone, (b). Preheating zone, where stones are heated near dissociation temperature. (c). Calcining zone where combustion takes place and (d). Cooling and discharge zone where the lime is cooled with the help of cooling air discharged in to the discharge table. Arches are installed over pillars to support the weight of the entire flue chamber relined by refractory bricks through with the hot flue gas passes from one shaft to the next preheating the limestone thus creating regenerative heat transfer. Connecting channel or crossover channel connects the two shafts allowing flow of hot gas between the shafts. Failure of arches will lead to the collapse of flue chamber wall and roof causing passage of limestone to the flue chamber leading to blockage of flue chamber. This will not allow the smooth passage of flue gases subsequently increasing pressure and temperature of the kiln and ultimately stoppage of kiln operation.

The calcining zone of shaft kiln has the highest operating temperature that necessitates the selection of higher quality basic brick to optimize the refractory campaign life. Refractories of arch and connecting channel areas are most failure prone due to the load on the arches which support the entire flue chamber of the kilns and high temperature at the connecting channel area to the tune of 1150 °C to 1250 °C. Therefore, special attention is required for the refractory selection of arches which should

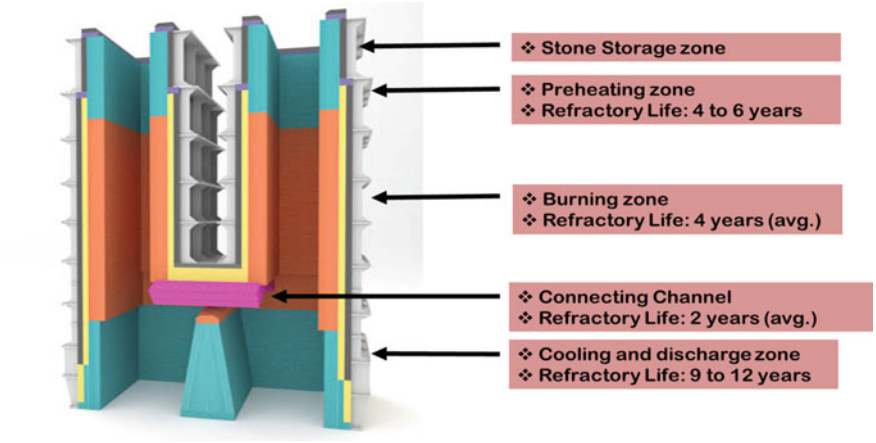

Fig. 1 Operating principle and temperature profile of twin shaft kiln

not lower or loosen itself after multiple heating or cooling cycles. Entire kiln is lined with dual lining consisting of a high temperature brick at the inner hot surface backed by fireclay brick and insulating brick next to the steel shell. The intent of the dual lining is to minimize shell heat losses. 40–60% Al_2O_3 based high alumina bricks are used in preheating and cooling zone whereas, 85–87% MgO based Magnesia bricks are used in the calcining zone to extend the working life of the refractory lining for heavily loaded kilns.

Kiln health is one of the determining factors for kiln productivity, good calcination of raw stone as well as the calcined product quality. Refractory performance of lime kilns plays crucial role in enhancing the reliability and availability of lime kilns. Optimizing the performance of the refractory lining is an ongoing process. Care must the taken in (a) installation (type of refractory and location), (b) inspection (wear patterns and thickness measurements) and (c) schedule maintenance (avoid patchwork of odds and ends). Besides, the refractory brick linings in all kilns must be replaced periodically, because heat, abrasion, and temperature changes cause them to disintegrate. Plants try to avoid cooling and reheating lime kilns as much as possible because this hastens disintegration [5].

In RSP, there are three different types of double shaft kilns of different production capacities designed by M/s. Mearz and M/s. Cimprogetti. The existing kiln details at RSP are given in Table 1. Circular and rectangular dual shaft kilns of 150 and 250 tons per day capacity are designed by M/s. Mearz. These are comparatively older kilns where mixed gas is used as fuel. D-shaped dual shaft kilns of 350 tons per day capacity are designed by M/s. Cimprogetti and commissioned in 2013. Heavy furnace oil is used as fuel in these kilns.

Table 1 Kiln details at RSP

Type/technology provider	Height (mts.)			Fuel	Channel temp	Lances/ shaft	Refractory used		
	Preheating	Burning	Cooling				Preheating	Burning	Cooling
Rectangular twin shaft/Maerz	4.5	6.0	4.2	Mixed gas	800–900	18	39% Al_2O_3	Mag-chrome	39% Al_2O_3
Circular twin shaft/Maerz	4.1	6.0	5.4	Mixed gas	850–950	18	42% Al_2O_3	85% MgO	42% Al_2O_3
D-Shape twin shaft/Cimprogetti	2.34	7.8	2.73	HFO	850–950	30	62% Al_2O_3	87% MgO	42% Al_2O_3

2 Problems in Lime Kiln

Consistent productivity and product quality have been remained as a challenge for the new kilns since inception due to the occurrence of frequent pre matured failures. Regular occurrence of hot spots at connecting channel area was a major drawback. Repeated failure of brick retainer plate, partition plate and thermocouple protection cylinder were also causes of concern. The damage in the metallic protection cylinder and in the surrounding castable was resulting in faulty temperature readings by thermocouple due to its frequent damage in prolonged high temperature exposure. Repeated failures of arches increased the kiln down time deteriorating kiln productivity and product quality. Besides during capital repair, de-bricking of the stack area was a matter of concern as construction of scaffolding platform up to the cross over channel area was the only possible approach. It was not only affecting the workmanship but also enforcing unsafe practices. This paper reports the detailed analysis of the problems and suggests solutions to minimize them.

3 Experimental

To improve the health, productivity, reliability and product quality of 350 TPD oil fired D-shaped dual shaft kilns several innovative repair methodologies have been adopted, modification in original design and upgradation of refractory specification has been carried out. Initially six most failure prone areas of kiln have been identified for modifications. These are connecting channel area, arch area, poking hole sleeves, thermocouple surroundings, retainer and bifurcation plate. Preventive maintenance practices have been stressed upon to nullify any surprising failures. The critical areas such as poking door, thermocouples have been protected from repetitive sudden failures for better kiln handling. Design modifications have been carried out to improve refractory performance along with better safety and workmanship.

3.1 Design Modification

To protect the retainer plate in cross over channel L shape brick has been introduced instead of castable lining to cover the retainer plate (Fig. 2). To protect the thermocouple from frequent damage SS anchors have been welded on the metallic protection jacket of thermocouple for better holding of castable lining for the first time. Two man-holes have been constructed just above the crossover channel as shown in Fig. 3 for easy and safe de-bricking of stack area during capital repair.

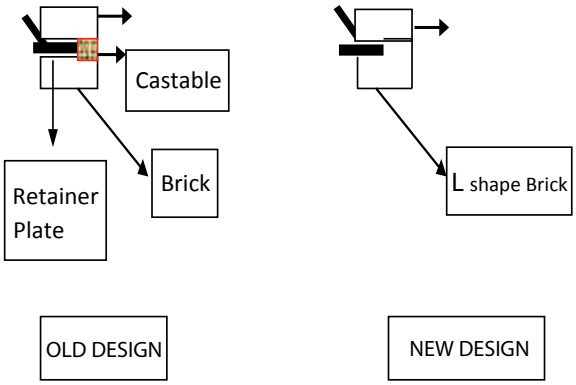

Fig. 2 Designing L shape brick replacing castable to protect the retainer plate of D-shape twin shaft kiln

Fig. 3 Designing man-hole at the connecting channel area of D-shape twin shaft kiln

3.2 Application of Superior Materials

To minimize the hotspot generations at cross over channel, improved quality insulating castable with maximum operating temperature 1300 C has been introduced in place of the original low quality castable. The material of retainer plate and bifurcation plate has been changed to SS quality for longer life. The entire thermocouple jacket has also been changed to SS quality. In place of earlier conventional castable, 90% high alumina self-flow castable has been applied in 2 layers on the metallic thermocouple protection jacket with anchors. Superior quality Magnesia bricks of 92–96% MgO with 2–4% ZrO2 has been used in arch area in place of earlier 85% MgO based bricks.

3.3 *Improvement in Regular Maintenance and Inspection Practices*

Pressure grouting has been introduced with bubble alumina based materials to stop hot spot generations at connecting channel area. As a Proactive preventive maintenance of kilns shell temperature measurement has been enforced at every shift to detect vulnerable area of the kilns. Table 2 depicts the shell temperature measurement data. Apart from shell temperature measurement, thermal imaging of the kilns is being carried out once in every 3 months for better preventive maintenance. FLIR P640, Sweden make infrared thermo vision camera was used for thermal imaging. The equipment can measure temperature from –40 C to 2000 C, with resolution of 0.1 C. The thermal imaging has been done at around pilot burner and above cross over channel in the new kilns. The images were taken at emissivity of 0.85. Images are taken from the platform or floor levels where proper approach is available. As per Fig. 4 thermal imaging data clearly shows the high temperature zones those need regular attention.

Table 2 Shell temperature measurement data

Kiln no	Quality	Rate	T-1	T-2	Shaft-1	Shaft-2
1	Lime	250	800	797	215	185
2	Lime	250	850	835	195	210
3	Dolo	270	765	795	175	190
4	Lime	220	780	810	219	227
5	Lime	350	1025	980	198	218
6	Lime	320	950	898	214	219

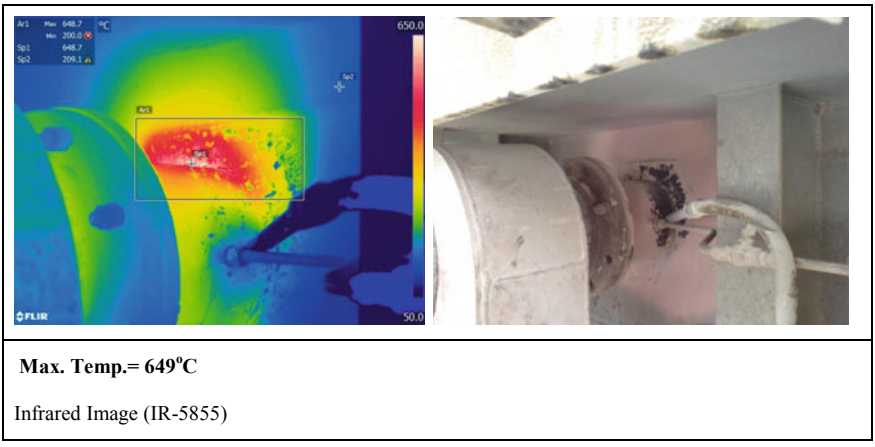

Fig. 4 Thermal image of right hand side pilot burner of D-shape twin shaft kiln

3.4 Modification in Operational Practices

- All traps are being checked at the first week of every month to detect any gas/air leakage.
- Regular poking of the connecting channel and flue channel for smooth passage of flue gas is practiced.
- Lance cleaning is done weekly once in every kiln for uniform distribution of gas and to keep the mixed gas pressure below 2 kg.
- Non-return valve of gas lances is cleaned weekly once.
- 100% availability of booster to maximize the production of gas fired kilns has been ensured.
- One additional gas line of 800 mm diameter has been provided for uninterrupted supply of gas and regular maintenance of gas lines without affecting production.

4 Results and Discussion

Frequent and sudden failure of six identified areas caused poor kiln availability, increased specific consumption of refractory, mechanical spares and also negatively influenced kiln productivity and product quality. The above measures have been implemented and resulted in substantial improvements towards better kiln availability, productivity and product quality. Table 3 depicts the kiln productivity and availability. Previously low quality insulation castable with maximum operating temperature 950 C was used at the crossover channel area where the temperature often exceeds 1100 ± 100 C during operation. Due to formation of low melting phases there was shrinkage in the castable causing hot air exposure to the shell. It increased the occurrences of hot spots at cross over channel area and eventually resulted in shell meltdown. Superior quality insulating castable with maximum operating temperature 1300 C could ensure the sealing of all inside passages of hot gas at connecting channel area preventing hot spot generation and shell puncture. The shell temperature at this area has been reduced to 150–180 C from earlier 250–300 C after the modification.

Previously MS quality or SS-304 plates were used as brick retainer plates in the crossover channel area causing frequent plate damage, brick dislodgement and eventually shut down of the kiln. After this work, improved quality SS plates have

Table 3 Kiln availability and productivity

Year	15–16	16–17	17–18	18–19	19–20
Productivity (Tons)	228,118	235,994	263,787	303,652	312,538
Kiln availability (%)	94.14	94.30	94.38	94.38	94.36

been used for longer life. The bifurcation plate between the two shafts has also been changed to SS quality. Earlier conventional castable was used at the retainer plate area in between two brick layers for preventing hot gas exposure to the plates. But due to poor high temperature properties the castable got crumbled exposing the low quality plates to hot gas. Using 90% high alumina self-flow castable improved the refractory life. As a result, 100% life improvement of retainer and bifurcation plates and seamless performance throughout the campaign life could be achieved.

There are two thermocouples at the crossover channel area, one in each shaft which record the temperature and act as the eyes of the kiln operator to check the temperature inside the kiln. The faulty temperature reading by thermocouples could be minimized by changing the quality of protection jacket, surrounding castable and by welding anchors during casting. The thermocouple was initially inserted into a cylindrical metal jacket which was welded to the channel roof. The Jacket was made of both low quality steel and surrounded by bricks with a 40–60 mm layer of conventional castable in between brick and jacket. But the castable was eroded very fast due to absence of anchors and eventually the metallic jacket got melted within few days of kiln operation due to high temperature exposure. Now the entire jacket has been changed to SS quality. 90% High alumina self-flow castable in 2 layers has been applied for the first time with SS anchors which has ensured proper holding of the castable. With this, the chance of air leakage from the thermocouple area or burning out of the metal protective jacket could have been eliminated resulting proper temperature recording by the thermocouples. Metal jacket life has been increased by more than 200%. Accurate temperature measurement could be made possible for longer duration (more than 6 months) as compared to earlier condition (2 months).

Earlier frequent damage and failure of arch areas resulted increase in the number of major shutdowns of kilns. Improved quality refractory bricks at arch area reduced the number of major repairs of the kiln due to arch failure by 100% by enhancing the life of arch. In this superior quality bricks, formation of low melting phases like Monticellite, Merwinite and Di-calcium ferrite is very low due to the presence of Calcia Stabilized Zirconia (CSZ) and calcium zirconate which leads to improved thermo-mechanical properties.

Construction of two man-holes above the crossover channel has provided better approach to the stack area. Earlier constructing scaffolding platform up to the cross over channel area was the only way to reach there. Now limestone can be charged just below the man hole level that acts as the platform without any chance of collapse. Workmanship has been improved manifold, safety could have been ensured and cleaning of debris has become much faster through the man-hole saving downtime. It reduced total capital repair time by 40%.

In regular maintenance practice, pressure grouting with bubble alumina based insulating refractory castable has been used to seal the air passage inside the kiln at connecting channel area. It helped to stop hot spot generations and reduce the shell temperature. Bubble alumina provides low density high insulation refractory castable with low thermal conductivity for high temperature application.

In addition to these, frequent thermal imaging and daily shell temperature monitoring were also carried out to detect potential threat areas in kilns. It was aimed

to detect the vulnerable areas well before hotspot or shell puncture. It gave an idea regarding thermal regime of kilns which helped early detection of boulder formation inside the kiln too.

These interventions have resulted in reducing overall down time of kilns and played crucial role to achieve consistently better life of around two years, to improve the kiln productivity and product quality and ensuring increasing demand for good quality lime for steel making.

5 Conclusions

The design modification, structural modification, using superior quality materials in capital repairs and regular maintenance has improved the kiln campaign life from 1 to 2 years. The downtime for capital repair of the kilns has been brought down from 40 to 30 days. Kiln productivity and availability has been increased consistently. Specific consumption and cost for refractory for regular maintenance (related to minor repairs) has been substantially reduced after these interventions.

After substantial benefit derived, few more modifications are in pipeline for further improvement of kiln health. Using pre-fabricated monolithic components in pillar, applying corundum bricks in arches, S type or R type thermocouple (platinum rhodium) instead of K type thermocouple (nickel chromium) and up gradation of Oil fired kilns to dual fired kilns where both HFO and natural gas can be used will be attempted in near future.

Acknowledgements The authors extend their sincere gratitude to the management of Rourkela Steel Plant and Research and Develpment Centre for Iron and Steel units of Steel Authority of India Limited for valuable support and guidance during this work.

References

1. Manocha S, Ponchon F (2018) Management of lime in steel. Metals 8:686. https://doi.org/10.3390/met8090686
2. Gallo G (1915) Sulla strutura dei calcari per calce grassa. Ann Chim Appl 214 ± 225
3. Boynton RS (1980) The chemistry and technology of lime and limestone, 2nd edn. Wiley, New York
4. Robert HB, Michelle AB, Heller KH, Domanico JL, Muth MK, O'Connor AC, Spooner RB (2000) Lime production: industry profile, Final report, Research triangle institute, Center for economics research, Research triangle park, NC 27709
5. Comparison of lime kiln types, Blitzco GmbH Stuttgart Germany, www.blitzco.de

Fly-Ash Derived Zeolite as a Versatile Novel Material in Civil Engineering: An Overview

Manisha Maharana and Sujit Sen

Abstract Increasing energy demand and dependence on coal as a fuel to satisfy demand of energy sector in many countries resulted in increasing production of Fly ash (FA). Most part of the fly ash has been utilized for construction. Nearly 30% of fly ash is discarded on landfill spots, which poses a great threat to the environment. To achieve a goal of 100% utilization of fly ash in sustainable way, alternative technology is very much required to convert fly ash to useful materials. Synthesis of zeolites from fly ash is an emerging approach to utilize fly ash. Numerous experimental researches confirms that zeolite has superb mechanical properties and thermal stability which can be used in building materials. Also due to its superior molecular sieving and ion-exchange capabilities, zeolites have a wide range of applications in civil engineering. This paper delivers an overview on various zeolite synthesis approaches from fly ash, and a detailed description of application of zeolite in the field of construction. The analysis of the data presented by different researchers shows that one of the useful properties of zeolite in the field of construction is improving concrete strength by the addition of zeolite.

Keywords Fly ash · Zeolite · Construction

1 Introduction

Amount of fly ash produced from thermal power plants is increasing very fast throughout the world. In India, nearly 90 million tons of coal fly ash is produced per year. Disposal of such large amount of fly ash is very difficult. Due to having uniform particle size, synthetic zeolite is more preferably used than natural zeolite. But the common problem faced by researchers in the process of zeolite synthesis is the cost of raw materials. There are many cheap natural silicon and aluminium sources which can be utilised for zeolite synthesis such as coal fly ash, red mud, clay which are normally industrial by products or waste. Coal fly ash is one such source

M. Maharana (✉) · S. Sen
Department of Chemical Engineering, National Institute of Technology Rourkela, Rourkela, Odisha 769008, India

S. Pal et al. (eds.), *Processing and Characterization of Materials*, Springer Proceedings in Materials 13, https://doi.org/10.1007/978-981-16-3937-1_26

which is abundantly available. It is generally formed as by product from combustion of coal. Zeolite synthesized from fly ash has many environment related applications. Researchers have been developing advanced techniques for zeolite synthesis from fly ash such as hydrothermal treatment process, fusion process, and microwave irradiation techniques. These synthesis methods depend on many fly ash factors such as Si/Al ratio, pH, temperature, reaction time, nature of reactants [1].

Zeolites have larger external surface area which is a very important factor in improving catalysis and adsorption processes. In addition to this, zeolite also acts as excellent building blocks for construction of structured materials. One important application of zeolites is applying nanoscale zeolite for the synthesis of zeolite membranes and films. Zeolites offers high homogeneity, high intactness between zeolite layers and decreases cracks formation in films.

There are different applications of zeolite as adsorbent or catalyst in different fields. This paper focuses on applications of zeolite in construction and wastewater treatment. In the field of construction, zeolite has been used as an anti-bacterial agent, helps in inhibition of concrete cracking, improves concrete strength, maintains humidity, acts as carrier fluidising agent [2]. Similarly, zeolite has also played significant role in the field of wastewater treatment such as removal of dye, heavy metals, organic and inorganic contaminants [3]. Other than wastewater treatment, zeolites synthesized from fly ash have also been applied for carbon dioxide capture [4].

2 Zeolite Synthesis Techniques from CFA

2.1 Hydrothermal Synthesis

In this method, CFA is treated with alkali solution and heated up to a particular temperature. Many studies have been done using this conventional method for synthesis of zeolite. Williams and Roberts [5] stated that the best result for zeolite synthesis from fly ash achieved by using NaOH rather than KOH. After a period, crystalline zeolite nuclei starts growing which finally results in the conversion of all amorphous fly ash into crystalline zeolite. Among others, this method is the simplest one which can be done in either open or closed surrounding. There are many mechanisms suggested for hydrothermal treatment of zeolite but mainly all involves dissolution of ionic species, and arrangement of silicon and aluminium around structure directing agent (SDA) which results in zeolite framework. Pa et al. [6] synthesized crystalline boggsite zeolite from coal fly ash by hydrothermal method using 2M NaOH solution at 80–85 °C for 6–9 h. Kotova et al. [7] reported synthesis of many types of zeolites such as zeolite X, zeolite P from coal fly ash by hydrothermal reaction with NaOH at 90–100 °C and also found that reaction temperature affects the most in the process of zeolite synthesis. Researchers have stated this method as an energy efficient and eco-friendly.

2.2 Fusion Followed by a Hydrothermal Method

In this method, alkali mainly NaOH is fused with fly ash at a temperature ranging from 30 to 750 °C which results in dissolution of crystalline substance present in raw material to amorphous phase. Then hydrothermal treatment is done which results in higher yield of zeolite in comparison with conventional hydrothermal treatment method. Many studies have been done in the synthesis of zeolite from fly ash which showed very good yield. And this method shows better result compared to simple hydrothermal treatment method. Highly crystalline zeolite X produced from coal fly ash by conventional fusion followed by hydrothermal method at a fusion temperature of 550 °C and hydrothermal treatment at 90 °C with an aging time of 18 h [8]. Zhang et al. [9] synthesized zeolite from fly ash by the same method at a fusion temperature of 600 °C for 90 min and hydrothermal treatment at 100 °C for 9 h in a stainless alloy autoclave. The synthesized zeolite showed efficient adsorption of phosphate from aqueous solution. Similarly Santosa et al. [10] stated synthesis of A type zeolite from CFA at 600 °C fusion temperature for 1 h and hydrothermal crystallisation carried out at 90–100 °C for 4 h in an autoclave kept inside oven. The authors have also stated that fly ash with low Si/Al ratio results in synthesis of zeolite with low Si/Al ratio. Zeolite synthesized by this method have been successfully applied in various construction sectors.

2.3 Microwave Irradiation Technique

Microwave assisted hydrothermal treatment of fly ash for crystalline mesoporous zeolite synthesis is a faster technique compared to conventional hydrothermal treatment method as fly ash contains microwave absorption material which can be applied as catalyst to stimulate synthesis of zeolite. Other advantages of this technique are: cheap, high yield and purity. It is also economical as it uses microwave whose wavelength ranges from 1 mm to 1 m and frequency between 300 MHz and 300 GHz. This method takes less time in nucleation of homogenous and crystallisation of zeolite. This method is best for industries producing zeolite as it is easier to achieve zeolite production in large quantity in a short period of time. Microwave irradiation process accelerates the traditional hydrothermal treatment process by heating raw materials by microwave radiation and further subjects the sample to hydrothermal treatment. Querol et al. [11] first synthesized zeolite (NaP1, KM philipsite, F linde) from fly ash by using microwave assisted hydrothermal treatment method using both NaOH and KOH. Both conventional as well as microwave irradiation method results into similar type of zeolite but microwave assisted method takes less activation time (30 min) than conventional method (24–48 h). Cui et al. [12] studied on zeolite production from coal fly ash and its application in wastewater treatment such as removal of Cu^{+2}, Fe^{+2}, NH^{+4}, Mn^{+2} with better adsorption performance by following cation exchange principle.

Table 1 Zeolite synthesis from coal fly ash by various synthesis methods

Zeolite types	Synthesis methods	References
Zeolite X, zeolite P	Hydrothermal treatment	[11]
Zeolite A	Hydrothermal treatment	[14]
Zeolite P	Hydrothermal treatment	[15]
Zeolite A	Fusion followed by hydrothermal treatment	[16]
Zeolite NaP	Fusion followed by hydrothermal treatment	[17]
Zeolite NaA	Fusion followed by hydrothermal treatment	[18]
Zeolite NaP1	Microwave irradiation technique	[19]
Zeolite NaA	Microwave irradiation technique	[20]
Zeolite LTA	Microwave irradiation technique	[21]
Sodalite, cancrinite	Molten salt method	[22]
Zeolite A	Ultrasonic method	[23]
Zeolite X	Fusion followed by sonication	[24]
Nanozeolite X	Sonication-assisted hydrothermal method	[25]

2.4 Ultrasonic Method

In this method, fly ash or other mineral source containing aluminosilicates such as red mud, clay is subjected to ultrasonication with an alkali. Ultrasonication helps in dissociation of fly ash particles which results in higher zeolite yield. This method does not require additional hydrothermal treatment as heat (up to 75 °C) is generated in a short time span (10 min) during the process.

Ultrasound affects both physical and chemical phenomena related to nucleation process and growth of crystal [2]. The chances of getting zeolite becomes high if fly ash is treated by ultrasonic irradiation along with hydrothermal treatment [13]. Table 1 shows work done on fly ash based zeolite by different methods.

3 Application of Zeolite in Construction

3.1 Zeolite as Anti-bacterial Agent

Zeolite, a crystalline aluminosilicate has a 3 dimensional structure made of Al–O and Si–O tetrahedroids. The micropores present inside the structure tends to bond positively charged ions to balance the unbalance valence of Al–O tetrahedroids. The ions bonded can be exchanged with other cation, which makes zeolite an excellent ion-exchange material. This property of zeolite is used as an anti-bacteria agent by bonding Ag^+ ions into zeolite framework by ion-exchange mechanism as Ag^+ ions has good anti-bacterial effect. The anti- bacterial effect is achieved by discharge

of Ag^+ ions or by generation of active oxygen. Zeolite anti-bacterial agent can be utilised in various fields such as in making floor brick, wall brick.

3.2 Inhibition of Cracking of Concrete

Alkali present in cement undergoes alkali aggregate reaction in the presence of moisture which leads to expansion and then cracking of concrete. To overcome this problem, commercial zeolite or natural zeolite powder can be applied to replace cement partially. Zeolite exhibits an excellent effect in inhibition of mortar expansion caused by alkali aggregate reaction [26]. The mechanism behind this is due to the ion exchange property of zeolite. Zeolite bonds with the base material present in cement by ion exchange and reduces K^+ and Na^+ concentration which further inhibits the alkali aggregate reaction [2].

3.3 Enhancement of Concrete Strength

Higher the amount of alkali present in concrete, lower is the compressive strength [27]. Replacing cement partially by fine zeolite powder and carbonate lowers the alkali content as well as increases the compressive strength of concrete.

3.4 Non-alkali Accelerating and Anti-freeze Admixture

The anti-freeze agent (sodium nitrite) and accelerating agent (sodium sulphate) used in concrete has high Na^+ content which stimulates alkali aggregation reaction in concrete. Fine zeolite powder can be applied as carrier to absorb Na^+ by ion-exchange process which finally results into a non-alkali, accelerating and anti-freeze admixture. It also increases the compressive strength of concrete due to pozzolanic reaction in zeolite powder [28].

3.5 Zeolite as Gas Carrier for Volume Expansion

Natural zeolite after calcination acts as gas carrier called as natural zeolite gas carrier (NZGC). NZGC helps in expansion of volume when equal amount of NZGC is mixed with cement and water. The volume expands about 1.6 times than the original volume. The concrete formed by addition of NZGC is of light weight due to the presence of gas bubbles. Thus equal addition of NZGC with cement paste results into a light weighted, large volume, high strength concrete [29].

3.6 As Carrier Fluidising Agent

Natural zeolite can be used as carrier fluidising agent (CFA) in concrete making. CFA is made by mixing water reducing agent (plasticizer) and fine zeolite powder in equal ratio. The water reducing agent in liquid form getsinto fine zeolite powder which converts zeolite into carrier fluidising agent. CFA can be applied for controlling the increase or decrease in concrete slump. High slump results in decrease in compressive strength of concrete as cement to water ratio decreases and low slump concrete causes more struggle to spread as it is thicker and is also not appropriate for many applications. Low slump forms trapped air pockets inside concrete structure which decreases the compressive strength of concrete. Therefore to balance the slump value CFA can be used.

3.7 Maintenance of Humidity

The adsorption and desorption property of zeolite can be effectively utilised in maintaining the humidity in mortar. At low humidity environment, zeolite desorbs water and at high humidity environment, it re-adsorbs moisture. Thus offers a protective environment to buildings and museums from damage.

4 Conclusion

Zeolites are efficient material in improving the concrete strength. Furthermore, fly ash based zeolite is a new source in construction and building applications. It can be used for the production of concretes and mortars. Partial replacement of cement with zeolite increases concrete compressive strength, reduces slump value of fresh concrete, protects from sulphate attack, inhibits chlorine diffusion into the concrete mixture. A series of new products can be produced by taking advantage of the unique properties of zeolite to solve the problems arising in the field of construction as per various practical requirements.

References

1. Georgiev D, Bogdanov B, Angelova K, Markovska I, Hristov Y (2009) Synthetic zeolites—structure, classification, current trends in zeolite synthesis. In Economics and society development on the base of knowledge: international scientific conference
2. Roy P, Das N (2017) Ultrasonic assisted synthesis of Bikitaite zeolite: a potential material for hydrogen storage application. Ultrason Sonochem 36:466–473
3. Shi J, Yang Z, Dai H, Lu X, Peng L, Tan X, Shi L, Fahim R (2018) Preparation and application of modified zeolites as adsorbents in wastewater treatment. Water Sci Technol 621–635

4. Majchrzak-Kucęba I, Nowak W (2005) A thermogravimetric study of the adsorption of CO_2 on zeolites synthesized from fly ash. Thermochim Acta 437:67–74
5. Williams CD, Roberts CL (2009) A comparative study of two methods for the synthesis of fly ash-based sodium and potassium type zeolites. Fuel 88:1403–1416
6. Pa FC, Kasmuin MZ, Ismail S, Baharun N (2007) Hydrothermal synthesis of zeolites from fly ash
7. Kotova O, Shabalin I, Shushkov D, Kocheva L (2016) Hydrothermal synthesis of zeolites from coal fly ash. Adv Appl Ceram 115:152–157
8. Ojha K, Pradhan NC, Samanta AN (2004) Zeolite from fly ash: synthesis and characterization. Bull Mater Sci 27:555–564
9. Zhang M, Zhang H, Xu D, Han L, Zhang J, Zhang L, Wu W, Tian B (2011) Removal of phosphate from aqueous solution using zeolite synthesized from fly ash by alkaline fusion followed by hydrothermal treatment. Sep Sci Technol 46:2260–2274
10. Santosa SJ, Kunarti ES (2014) Synthesis of zeolite A from coal fly ash by alkali fusion and hydrothermal. Adv Mater Res Trans Tech Publ 198–203
11. Querol X, Alastuey A, López-Soler A, Plana F, Andrés JM, Juan R, Ferrer P, Ruiz CR (1997) A fast method for recycling fly ash: microwave-assisted zeolite synthesis. Environ Sci Technol 31:2527–2533
12. Cui HM, Ke LF, Li F, Kang T (2012) Microwave-assisted zeolite hydrothermal synthesis from coal fly ash and its application. Appl Mech Mater Trans Tech Publ 380–384
13. Wakihara T, Tatami J (2013) Top-down tuning of nanosized zeolites by bead-milling and recrystallization. J Jpn Petrol Inst 56:206–213
14. Behin J, Bukhari SS, Dehnavi V, Kazemian H, Rohani S (2014) Using coal fly ash and wastewater for microwave synthesis of LTA zeolite. Chem Eng Technol 37:1532–1540
15. Ojumu TV, Du Plessis PW, Petrik LF (2016) Synthesis of zeolite A from coal fly ash using ultrasonic treatment—a replacement for fusion step. Ultrason Sonochem 31:342–349
16. Deng H, Ge Y (2015) Formation of NaP zeolite from fused fly ash for the removal of Cu(II) by an improved hydrothermal method. RSC Adv 5:9180–9188
17. Barrer RM (1982) Hydrothermal chemistry of zeolites. Academic Press
18. Breck DW (1984) Zeolite molecular sieves: structure, chemistry and use. Krieger
19. Park M, Komarneni S (1997) Occlusion of KNO_3 and NH_4NO_3 in natural zeolites. Zeolites 18:171–175
20. Sivalingam S, Sen S (2019) Valorization of coal fly ash into nanozeolite by sonication-assisted hydrothermal method. J Environ Manage 235:145–151
21. Wakihara T, Ichikawa R, Tatami J, Endo A, Yoshida K, Sasaki Y, Komeya K, Meguro T (2011) Bead-milling and postmilling recrystallization: an organic template-free methodology for the production of nano-zeolites. Cryst Growth Des 11:955–958
22. Park M, Choi CL, Lim WT, Kim MC, Choi J, Heo NH (2000) Molten-salt method for the synthesis of zeolitic materials: I. Zeolite formation in alkaline molten-salt system. Microporous and Mesoporous Mater 37:81–89
23. Ghrear TMA, Rigolet S, Daou TJ, Mintova S, Ling TC, Tan SH, Ng EP (2019) Synthesis of Cs-ABW nanozeolite in organotemplate-free system. Microporous Mesoporous Mater 277:78–83
24. Murayama N, Yamamoto H, Shibata J (2002) Zeolite synthesis from coal fly ash by hydrothermal reaction using various alkali sources. J Chem Technol Biotechnol Int Res Process Environ Clean Technol 77:280–286
25. Mastropietroa TF, Molinaria R, Argurioa P, Curcioa E, Poerio EDT (2015) Synthesis of Nay-type nanozeolites and their assembling into microporous membranes. Chem Eng 43
26. Razmgar K, Hosseini ZBM (2016) Removal of As(V), Cr(VI) and Pb(II) from aqueous solution using surfactant-modified Sabzevar nanozeolite. Adv Environ Technol 2:105–109
27. Yurekli Y (2016) Removal of heavy metals in wastewater by using zeolite nano-particles impregnated polysulfone membranes. J Hazard Mater 309:53–64

28. Abdollahi B, Shakeri A, Aber S, Bonab MS (2018) Simultaneous photodegradation of acid orange 7 and removal of Pb2+ from polluted water using reusable clinoptilolite–TiO_2 nanocomposite. Res Chem Intermed 44:1505–1521
29. Hassaninejad-Darzi SK, Kavyani S, Torkamanzadeh M, Tilaki RD (2017) Applicability of ZSM-5 nanozeolite to removal of ternary basic dyes: an adsorption study using high-accuracy UV/Vis-chemometric methods. Monatshefte für Chemie-Chemical Monthly 148:2037–2049

Investigation on the Stress Distribution During Hard Turning of AISI 52100 Steel Using Al_2O_3/TiCN Cutting Tool Coated with Mono-layered AlCrN and Multi-layered AlTiN/TiN Coating

Ch Sateesh Kumar, Pawan Kumar, Kamlesh Kumar, Filipe Fernandes, Himadri Majumder, Akhtar Khan, and Saroj Kumar Patel

Abstract The stress distribution in the tool and workpiece materials play a substantial part in describing the usability of the machining process that can be of serious concern during hard turning operation. Thus, the present work focuses on studying the stress distribution in the hardened workpiece of AISI 52100 steel (63 HRC) and the cutting tool (Al_2O_3/TiCN) numerically. The thin-films of mono-layered AlCrN and multi-layered AlTiN were deposited on to the mixed-ceramic cutting tools using cathodic arc evaporation (CAE) process. Later, the coated tools were subjected to continuous turning tests under dry cutting environment. The experimental data has been used to validate the numerical model so that the stress distribution can be predicted. The finite element analysis apparently indicated the reduction of stress in the workpiece material while machining with coated cutting tools with AlTiN coating exhibiting superior performance at the highest feed rate and AlCrN coating outperforming at the highest cutting speed. This peculiar behaviour is closely associated with the oxidation resistance and thermal stability of AlCrN and AlTiN coatings. Further, the stress distribution in the cutting tools at adverse cutting conditions clearly specify superiority of CAE coated tools over uncoated ceramic cutting tool.

C. S. Kumar (✉) · P. Kumar · K. Kumar
Department of Mechanical Engineering, Madanapalle Institute of Technology and Science, Madanapalle, Andhra Pradesh 517325, India
e-mail: drsateeshkumarch@mits.ac.in

F. Fernandes
Advanced Materials Group, Department of Control Engineering, Czech Technical University in Prague, Technická 2, Prague 6 16000, Czech Republic

H. Majumder
Department of Mechanical Engineering, G. H. Raisoni College of Engineering of Management, Pune, Maharashtra 412207, India

A. Khan
Department of Mechanical Engineering, Indian Institute of Information Technology, Design and Manufacturing, Kurnool 518007, India

S. K. Patel
Department of Mechanical Engineering, National Institute of Technology, Rourkela, Odisha 769008, India

S. Pal et al. (eds.), *Processing and Characterization of Materials*, Springer Proceedings in Materials 13, https://doi.org/10.1007/978-981-16-3937-1_27

Keywords Hard machining · Coated tool · Stress distribution

1 Introduction

Materials with hardness above 45 HRC come under difficult-to-cut category and their machining demands sufficient thermal stability and strength for the cutting tools. High hardness of the workpiece material would make it difficult to remove material from the surface that leads to generation of high cutting forces and temperatures during the cutting operation [1]. In this regard, the mixed-ceramic cutting tools based on alumina exhibit satisfactory suitability for adverse machining conditions that involve high temperatures and machining forces. Also, their economical nature has made them an imperative alternative to costly cubic-boron-nitride and polycrystalline cubic-boron-nitride cutting tools. Further, coating deposition on cutting tools have illustrated remarkable capability in refining the performance of alumina-based tools during metal cutting operations [2]. Additionally, the structure of the coating is quite significant and considerably affects the cutting performance of tools having thin-film depositions [3]. The coating/substrate adhesion strength and other coating properties like oxidation resistance, hardness and surface morphology also have noticeable impact on the usability and performance of thin films. The superior coating/substrate adhesion would prevent coating removal when loaded whereas the superior oxidation resistance provides thermal stability under adverse cutting conditions [3–7]. Further, it has been observed that the numerical techniques have proved very efficient in determining the performance of cutting tools during various machining operations with different thin-film depositions. The numerical techniques could lead to proper estimation of stresses and temperature distribution in the cutting zone which are very difficult to explore during experimental tests [8]. The literature also suggests that the performance analysis of thin-film coated cutting tools during machining has remained mostly restricted to analysing tool wear and temperature generation [9–11]. On the contrary, stress distribution in the tool and workpiece material can be used to predict the machining performance of coated tools effectively [12, 13] which can prove quite prolific during hard turning where the associated stresses and temperature is quite high [14]. However, a limited amount of work can be seen that investigates the stress distribution in the tool and workpiece material numerically. Thus, the present work emphasizes on investigating the stress distribution in the cutting tool (Al_2O_3/TiCN) with AlCrN and AlTiN/TiN based thin-film coatings that will be predicted using a finite element model. Further, the stresses in the hardened AISI 52100 steel taken as the workpiece material will also be studied and analysed.

2 Experimental Methodology

The thin-flim depositions of AlCrN having mono-layered and AlTiN/TiN having multi-layered structures on to the alumina-based mixed-ceramic cutting tools (Al_2O_3/TiCN, designation: SNGA120408) were carried out by means of cathodic arc evaporation (CAE) process. The CAE process is a physical vapour deposition (PVD) technique which utilizes a cathode electrode for vaporization of target material. The coating deposition takes place inside a vacuum chamber. Nitrogen is used as the reactive gas for the deposition of nitride based thin-films. The target materials and the other deposition parameters have been described in Table 1. The deposited thin-films had different structures with AlCrN coating having a mono-layer deposition whereas the AlTiN coating had a multi-layered structure with alternate AlTiN and TiN layers of thin-films. The measured coating thickness for the AlCrN coating was approximately 3 μm and for AlTiN/TiN coating was nearly 4 μm. After the coating deposition, the cutting tests were performed as per the scheme mentioned in Table 2. The depth of cut for all the turning tests was kept constant at 0.5 mm. The turning operation on the hardened AISI 52100 steel (63 HRC) was carried out under dry cutting environment. The purpose of using dry cutting environment is to study the effect of thin-film depositions on the cutting tools more precisely. Further, the dry environment would facilitate adequate exploration of the cutting zone.

Table 1 Parameters for thin-film deposition

Parameter	Value
Power	3.5 kW
Pressure inside chamber	0.3 Pa
Gas pressure (nitrogen)	2 Pa
Coating environment	Nitrogen gas (N_2)
Bias voltage (substrate)	−50 to −150 V
Targets for deposition	$Al_{67}Ti_{33}$ (Ti), $Al_{70}Cr_{30}$
Temperature during deposition	400–600 °C

Table 2 Turning test scheme for experiments

Run	Feed rate in mm/rev	Cutting speed in m/min
1	0.12	180
2	0.12	145
3	0.12	110
4	0.16	110
5	0.20	110

2.1 Numerical Analysis

In the present work for finite element (FE) analysis of machining operation, Deform 3D software package has been utilized. The flow stress model for workpiece material and hybrid friction model that considers the sticking and sliding zones of friction has been adopted for the present work which has been successfully utilized by Kumar and Patel [15]. However, as defining chip morphology is not the main purpose of the present investigation, damage model has not been implemented. The elimination of the damage model during numerical analysis would save considerable computational time and also provide simplicity to the numerical analysis by eradicating numerical errors caused due to material damage. The cutting tool has been assumed to have a rigid structure whereas a visco-plastic material structure was considered for the workpiece. A definition of finer mesh at the cutting zone ensured elimination of meshing errors. This is a necessary step to get more precise and accurate results from the adopted numerical models. Also, the efficiency of the numerical models can be evaluated with properly performed mesh convergence analysis. Later, the tool-stress has been determined by die-stress analysis. The die-stress analysis process facilitates the consideration of the tool as a rigid material and reduces significant computational time. Further, the numerical results were compared with the experimental machining forces for validation of the employed numerical model. The validation of predicted machining forces is extremely necessary to know the accuracy of the equations employed in the finite element analysis process.

3 Results and Discussion

3.1 FE Model Validation

Before predicting the stress distribution in the cutting tool and the workpiece materials, the adopted numerical model has been checked for accuracy. The model validation has been carried out by comparing the experimental and numerical cutting forces corresponding to different levels of cutting velocities as per the experimental scheme. It has been observed that the adopted finite element numerical model resulted in 3–6% of error in cutting forces when compared to the experimentally measured forces. The error reduced with the increase of cutting speed which may be due to the decline in tool wear with the rise of cutting speed. However, the trend of forces remained the same in both numerical and experimental results. Thus, the obtained machining forces from the present FE model showed close agreement with the experimental results. This agreement can also be seen in Fig. 1.

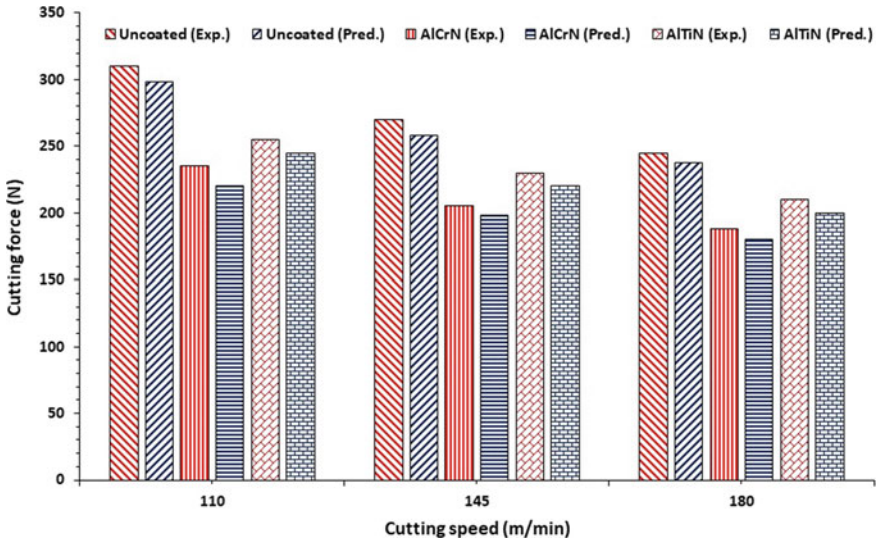

Fig. 1 Variation of experimental and predicted cutting force with cutting speed

3.2 Cutting Tool-Stress Distribution

Figure 2a illustrates the variation of predicted maximum stress with cutting speed for the cutting tools with and without thin-film deposition. The evaluated results clearly indicate a reduction of tool-stress with cutting speed which is mainly attributed to the decrease in machining forces due to the thermal softening of the workpiece material. Further, the machining with coated tools accounted to significant tool-stress reduction owing to the lower associated friction and superior wear resistance [15]. Also, it has been perceived that the AlCrN coated cutting tool corresponded to lower tool-stress when compared to the AlTiN coated tool at higher cutting speeds which shows superior thermal stability of AlCrN coating at higher temperatures [16]

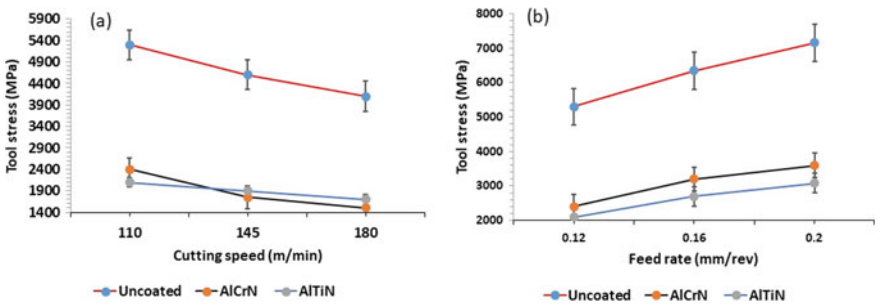

Fig. 2 Variation of maximum tool-stress with **a** cutting speed and **b** feed rate for uncoated and coated cutting tools

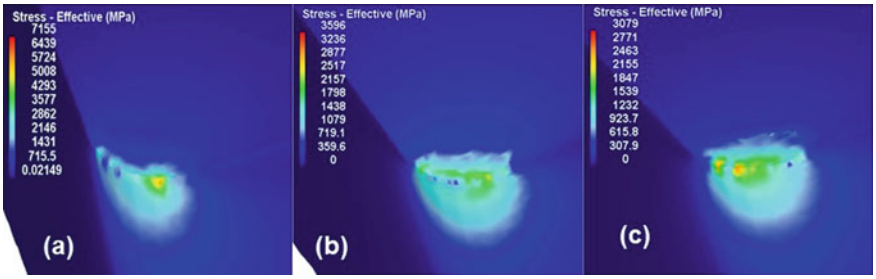

Fig. 3 Predicted stress distribution at 0.2 mm/rev feed rate for **a** uncoated **b** AlCrN coated and **c** AlTiN/TiN coated cutting tool

and reduced machining forces. On the contrary, when the feed rate is increased, the maximum tool-stress increased (see Fig. 2b) which is because of the rise of machining forces with the increase of feed rate. The application of coatings again resulted in lowering of tool-stresses. However, the multi-layered thin-film structure of AlTiN/TiN coating was more suitable for adverse cutting conditions i.e. at higher feed rates. The stress distribution at the most adverse cutting condition (0.2 mm/rev feed rate and 115 m/min cutting speed) in Fig. 3 clearly specifies superiority of AlTiN based multi-layered coating.

3.3 Workpiece-Stress Distribution

Figure 4 illustrates the variation of maximum stress generated in the workpiece material with the increase of cutting speed and feed rate respectively. The application of coatings results in reduction of stress in the workpiece material. The phenomenon remains the same even if the cutting speed increases. However, this reduction is not very significant as compared to the variation that is observed with the growing cutting

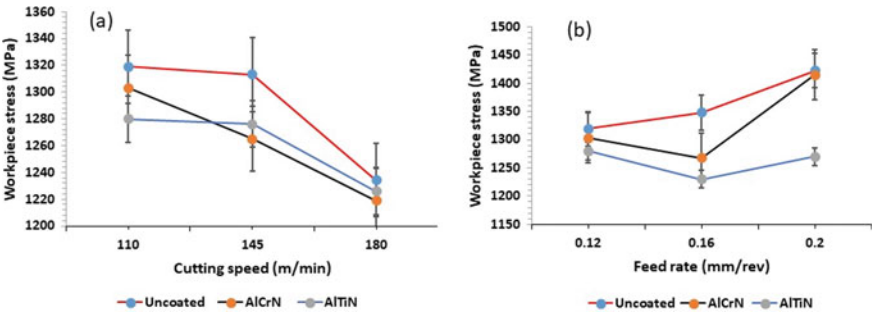

Fig. 4 Variation of maximum predicted stress in the workpiece material (AISI 52100 steel) with **a** cutting speed and **b** feed rate

speed. Contrarily, the maximum workpiece-stress corresponding to AlCrN coating increases and matches the stress corresponding to uncoated tool at a feed rate of 0.2 mm/rev which is the identified most adverse machining condition in the present investigation. From this observation it is apparent that the multi-layered AlTiN coating would outperform mono-layered AlCrN coating under adverse machining conditions.

4 Conclusions

The present work involves investigation on the stresses developed in uncoated and coated Al_2O_3/TiCN mixed-ceramic cutting tool and AISI 52100 steel (63 HRC hardness) during dry turning operation. The conclusions that can be drawn are listed below:

1. The deposition of thin-film coatings on the mixed-ceramic tools resulted in reduction of tool-stresses which would directly influence the tool life for coated cutting tools.
2. There was no significant reduction in workpiece-stress while machining with coated cutting tools. However, at adverse machining conditions the AlCrN coated tool accounted to approximately the same workpiece-stress distribution as that corresponding to uncoated cutting tool.
3. The AlCrN coated tool showed better performance when compared to the tool coated with AlTiN/TiN coating at higher cutting speeds due to the lower corresponding machining forces. However, AlTiN/TiN based multi-layer coating illustrated superior performance under adverse machining conditions indicating better resistance of multi-layered coating structure at elevated machining forces and temperature.

References

1. Chinchanikar S, Choudhury SK (2013) Effect of work material hardness and cutting parameters on performance of coated carbide tool when turning hardened steel: an optimization approach. Measurement 46:1572–1584. https://doi.org/10.1016/j.measurement.2012.11.032
2. Kumar CS, Patel SK (2019) Effect of duplex nanostructured TiAlSiN/TiSiN/TiAlN-TiAlN and TiAlN-TiAlSiN/TiSiN/TiAlN coatings on the hard turning performance of Al_2O_3-TiCN ceramic cutting tools. Wear 418–419:226–240. https://doi.org/10.1016/j.wear.2018.11.013
3. Prengel HG, Jindal PC, Wendt KH, Santhanam AT, Hegde PL, Penich RM (2001) A new class of high performance PVD coatings for carbide cutting tools. Surf Coat Technol 139:25–34. https://doi.org/10.1016/S0257-8972(00)01080-X
4. Martan J, Beneš P (2012) Thermal properties of cutting tool coatings at high temperatures. Thermochim Acta 539:51–55. https://doi.org/10.1016/j.tca.2012.03.029
5. Das P, Anwar S, Bajpai S, Anwar S (2016) Structural and mechanical evolution of TiAlSiN nanocomposite coating under influence of Si3N4 power. Surf Coat Technol 307:676–682. https://doi.org/10.1016/j.surfcoat.2016.09.065

6. Yang W, Xiong J, Guo Z, Du H, Yang T, Tang J et al (2016) Structure and properties of PVD TiAlN and TiAlN/CrAlN coated Ti(C, N)-based cermets. Ceram Int 43:1911–1915. https://doi.org/10.1016/j.ceramint.2016.10.151
7. Kumar CS, Patel SK (2017) Hard machining performance of PVD AlCrN coated Al_2O_3/TiCN ceramic inserts as a function of thin film thickness. Ceram Int 43:13314–13329. https://doi.org/10.1016/j.ceramint.2017.07.030
8. Kumar CS, Zeman P, Polcar T (2020) A 2D finite element approach for predicting the machining performance of nanolayered TiAlCrN coating on WC-Co cutting tool during dry turning of AISI 1045 steel. Ceram Int 46:25073–25088. https://doi.org/10.1016/j.ceramint.2020.06.294
9. Noordin MY, Venkatesh VC, Sharif S (2007) Dry turning of tempered martensitic stainless tool steel using coated cermet and coated carbide tools. J Mater Process Technol 185:83–90. https://doi.org/10.1016/j.jmatprotec.2006.03.137
10. M'Saoubi R, Johansson MP, Andersson JM (2013) Wear mechanisms of PVD-coated PCBN cutting tools. Wear 302:1219–1229. https://doi.org/10.1016/j.wear.2013.01.074
11. Okada M, Yoshida A, Furumoto T, Watanabe H, Asakawa N, Otsu M (2016) Mechanisms and characteristics of direct cutting of tungsten carbide using a diamond-coated carbide end mill. Int J Adv Manuf Technol 86:1827–1839. https://doi.org/10.1007/s00170-015-8324-3
12. Yen YC, Jain A, Altan T (2004) A finite element analysis of orthogonal machining using different tool edge geometries. J Mater Process Technol 146:72–81. https://doi.org/10.1016/S0924-0136(03)00846-X
13. Nemetz AW, Daves W, Klünsner T, Ecker W, Teppernegg T, Czettl C et al (2018) FE temperature- and residual stress prediction in milling inserts and correlation with experimentally observed damage mechanisms. J Mater Process Technol 256:98–108. https://doi.org/10.1016/j.jmatprotec.2018.01.039
14. Tönshoff HK, Arendt C, Amor RB (2000) Cutting of hardened steel. CIRP Ann Manuf Technol 49:547–566. https://doi.org/10.1016/S0007-8506(07)63455-6
15. Kumar CS, Patel SK (2017) Effect of chip sliding velocity and temperature on the wear behaviour of PVD AlCrN and AlTiN coated mixed alumina cutting tools during turning of hardened steel. Surf Coat Technol 334:509–525. https://doi.org/10.1016/j.surfcoat.2017.12.013
16. Endrino JL, Fox-Rabinovich GS, Gey C (2006) Hard AlTiN, AlCrN PVD coatings for machining of austenitic stainless steel. Surf Coat Technol 200:6840–6845. https://doi.org/10.1016/j.surfcoat.2005.10.030

Increase in Productivity of Old Continuous Slab Caster Through Enhancement of Sequence Size by Preventing Rise in Mould Water Inlet Temperature Above 42 °C, in CCM-I:SMS-I of Rourkela Steel Plant

Prabodh Ranjan Padhee

Abstract Copper mould is an important and integral component of any Conventional Slab Caster for steel to take care of the initial solidification. In case of SMS-I, Rourkela Steel Plant, the slab caster was a "Brown field project" and was commissioned in 1996. This project was having severe space constraints, as it was built in the old SMS which was commissioned during late fifties. In this slab caster the copper mould is a "Constant cooling water volume" design and water flow could not be altered, as per the casting speed. Therefore, the strand shell formed in the mould is thicker in case of lower casting speed and thinner in case of higher casting speed. As per the DPR, the designed sequence size of slab casting was only 2 (Two), with a total production capacity of 0.305 MT per annum. Further, Ladle Heating Furnace was not envisaged during commissioning of slab caster. Though, several attempts were made to cast more than 2 heats in the caster, it was not possible, primarily due to logistic issues, in absence of LHF. Subsequently, the Ladle Heating Furnace (LHF) was commissioned, adjacent to the slab caster in 1998. However, even after LHF was commissioned, the maximum sequence that could be cast was only 5 (Five), with a heat size of 66 Tons. Due to higher production demand, for increasing the sequence size, it was found that the major constraint was "Inlet water temperature to the Copper Mould", which was crossing the threshold limit of 42 °C. In the present study, an in depth analysis of mould inlet water temperature was carried out and the problem was eradicated, so as to cast more than 5 (Five) heat sequence to increase the productivity.

Keywords Steel · Continuous slab caster · Copper mould · Mould inlet water · Water temperature

P. R. Padhee (✉)
Steel Authority of India Limited, Rourkela Steel Plant, Rourkela, India

S. Pal et al. (eds.), *Processing and Characterization of Materials*, Springer Proceedings in Materials 13, https://doi.org/10.1007/978-981-16-3937-1_28

1 Introduction

Slab Caster of Steel Melting Shop-I was commissioned in 1996 with a production capacity of 0.305 MT per annum of steel [1]. As envisaged in DPR, the sequence size was only 2 and initially no Cold Rolled Non Oriented (CRNO) steelmaking was included to be cast in the slab caster. The conventional ingot route was being continued, in addition to slab caster. Such decision was taken, because of logistic issues of Secondary Metallurgy Area with De-gassing facilities having Vacuum Arc Refining (VAR) and Vacuum Oxygen Refining (VOR) unit, but without Ladle Heating Furnace (LHF). Further, due to space constraints, the slab caster was constructed in a different geographical location, farther from the Secondary Metallurgy Area. However, several attempts were made to cast CRNO steel through Slab caster route, as the De-gassing facilities were brought in Secondary Metallurgy area in early Nineteen Eighties, to produce Silicon Steel.

Subsequently, necessity was felt to have one Ladle Heating Furnace (LHF) and after 2 years, LHF was newly erected and commissioned in November 1998, keeping in view, the production demand of special steel including CRNO steel, through Continuous Casting route. After commissioning of LHF adjacent to the slab caster, the problem of logistic issue was eliminated to a great extent and after stabilization of production of CRNO through slab caster route, Ingot route was completely stopped from December'2001. The production demand at SMS-I, subsequently went on rising with a CRNO percentage of more than 30% of total production. Mostly, special quality steel was made in SMS-I like SAILMA, IS-3589, Medium Carbon, SAILCOR etc. in addition to CRNO steel. However, the greatest challenge was to make longer sequence, particularly in summer months and early rains, when the ambient temperature was high and the moisture content in the atmosphere was high, respectively [1]. As explained earlier, since the caster was designed for 2 heat sequence as per DPR, it was not possible to go beyond 5 heat sequence, even after commissioning LHF, as the primary constraint being the mould inlet temperature crossing the threshold limit of 42 °C [2, 3].

Further, there was no scope to increase the cooling water volume, as the original design of copper mould was of "Constant cooling water volume". Therefore, the strand shell leaving the mould was thicker in case of lower casting speed than at higher casting speed [4, 5]. As, there was demand for higher productivity, thereby higher throughput from caster with longer sequence, the following analysis was done and subsequently, several modifications were carried out, for improvement, with minimum cost.

1.1 Analysis and Diagnosis of Problem

The Copper Mould of SMS-I is a curved mould design with Non-variable (Constant cooling water volume) as per the original design and installation (Fig. 1). Since, this

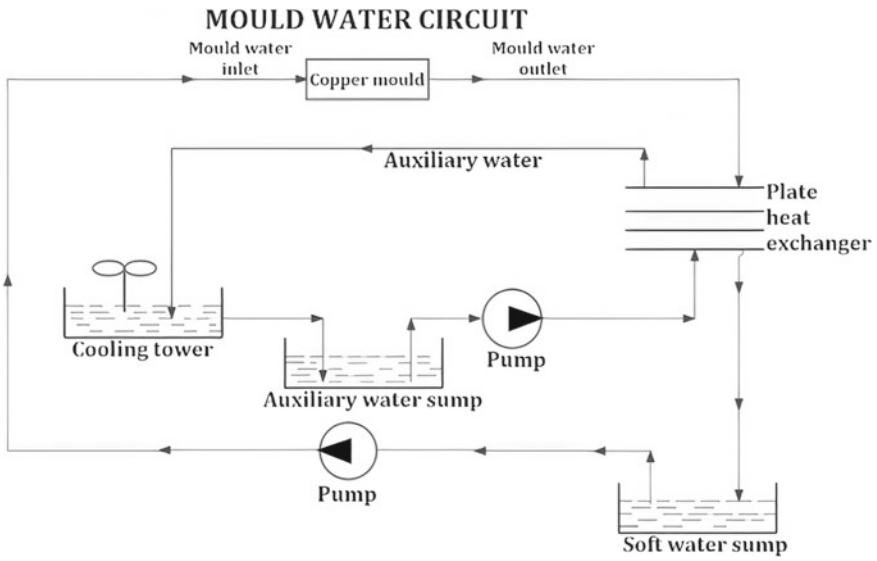

Fig. 1 Mould water circuit diagram

was a design parameter and accordingly the Soft water pump capacity was 320 m^3/h and 6 kg/cm^2. There was no alternative scope in the mould for taking out the heat flux from the liquid steel, in different casting speed, as the flow of water could not be altered in the copper mould. Therefore, the strand shell leaving the mould was thicker in case of lower casting speed than at higher casting speed.

There was only one plate heat exchanger in the mould cooling circuit, which was not adequate to bring down the temperature below 42 °C in summer days and early rains, for longer sequence. The cooling water supplied to the heat exchanger (Auxiliary water) for cooling the soft water of the mould through Vertical turbine pump having a pumping capacity of 800 m^3/h became inadequate, for longer sequence. There were only 2 (Two) Vertical turbine pumps for the auxiliary water, with one running and one standby philosophy. There were severe space constraints in the pump house and installing additional pump was not possible. The existing pump could not be replaced/altered because of the design of the pump foundation and mounting dimension of the frame for the motor.

The auxiliary cooling tower was having 3 cells meant for cooling soft water of the mould, passing through heat exchanger. As per design philosophy, 2 cooling tower cells could run at a time with one stand by. The possibility of running all 3 cooling towers was not possible because of its maintainability. The major problem of maintenance area, was the failure of worm gear box of the cooling tower fan. Further, there was no scope to add one more cell in the cooling tower, because of severe space constraint and high capital expenditure.

All the problems explained above, were critically analysed and the following actions were taken to achieve the desired result, by containing the mould inlet temperature below 42 °C for higher sequence size:

2 Experiment and Modifications

One additional heat exchanger (PHE) having 205 no. of plates was procured and installed in October'2012, as per the specification of the existing original design of PHE. This was kept as a stand by during the chockage of the other heat exchanger. The alternate heat exchanger was run during the demand and the other one was kept as standby after cleaning. This process also involved 2–3 h' production down time. Hence, geared type butterfly valves were incorporated in each PHE for isolation, instead of closing the main gate valve, to avoid production shutdown. By this modification, 2–3 h' total production loss could be eliminated.

The normal cleaning time for PHE was taking around 3 days by taking out each and every plate and cleaning it outside and then fixing it back. This practice was stopped in February, 2013 and the plates were cleaned in situ by just closing the geared butterfly valve and making an arrangement for high pressure water jet. After such arrangement, the job was completed within 12 h. After achieving 12 h cleaning time, it gave a big boost for operating both the heat exchangers simultaneously (Parallel heat exchangers) and the threat of down time for cleaning of chockage for about 3 days was eliminated.

After doing this modification, the temperature could be contained to certain extent, but it was not adequate. As the production demand was gradually going up for sustainability of SMS-I., further analysis was done with regard to heat exchangers. It could be ascertained that surface area of heat exchangers can be increased and accordingly, the OEM of the heat exchangers was consulted and calculation was done. Accordingly, 40 no. of additional plates were fixed in both the heat exchangers in April'2013 and the heat exchangers were run simultaneously in parallel, as per the demand. It resulted in a substantial drop in temperature with some effect on the pressure drop across the heat exchangers. (As shown in Fig. 2).

There were 2 (Two) Auxiliary cooling water pumps having capacity, Flow of 800 m^3/h and Pressure 10 kg/cm^2. with one running and one stand by philosophy. Since the number of plates were increased from 205 to 245 and because of chokage of heat exchangers over a period of running, there was a slight pressure drop of the auxiliary cooling water to the tune of 1–2 kg/cm^2, which affected the cooling performance/efficiency of the heat exchangers. Further, while running both the heat exchangers in parallel, the flow also got affected. Hence, several discussions were held with Vertical Turbine pump companies, to increase the flow of water by about 20% since 20% plates were increased in each heat exchanger and taking the pressure drop into consideration. As complete replacement of base frame and motor along with pump was not possible for space and financial constraints, the challenge was to mount the pump on the same base frame and use the same motor having 90 kW rating

Fig. 2 Modified heat exchangers

and frame size 280 M4. Finally, M/s WPIL supplied the pump, having a capacity of 920 m^3/h. which is 15% additional capacity with respect to the existing pump (As shown in Fig. 3). The photograph of new pump has been shown in Fig. 4 which is in the knock down condition and that was assembled for making one vertical turbine pump and was installed. This pump was assembled and fitted in December, 2014 and performance was assessed. The result of the heat exchangers was very encouraging, after changing the pump. The duration of interval of chokage increased and the pressure drop was maximum to the tune of 0.8 to 1 kg/cm^2.

It was some time necessary to run 3 cooling towers in place of 2, during summer days to contain the temperature below 42 °C. It, means, no standby cell was kept for any emergency. However, the primary problem with the cooling tower, was the gear box of the cooling fan. The gear box is a Worm reduction gear box and the lubrication was splash lubrication. Because of inadequate oil splashing, the worm wheel made up of bronze was getting worn out very fast and the cooling tower fan

Fig. 3 Existing pump

Fig. 4 New pump

Fig. 5 Oil tank above gear box

was having frequent breakdown. Further, there was inadequate space and design constraints to replace the Gear box and Motor. Therefore, a modification was done by providing an oil tank above the level of gear box (As shown in the Fig. 5) to ensure proper lubrication in the gear box by drip lubrication. This modification was done completely in-house, with minimum cost. After doing the modification in the month of April/May, 2013, all the 3 cooling tower could be run, as per the demand, without any breakdown.

3 Result and Discussion

After implementing the above innovation and modifications, the normal sequence size could be increased from 5 to 8 for all grades, depending upon the order size. Attempt was made to make heat in multiple of 8, which could fetch better productivity from the same old caster.

The annual average sequence size in 2001–2002 was only 2.46. After commissioning and stabilisation of Ladle Heating Furnace (LHF), it could be continuously increased and finally the highest annual sequence size achieved in 2011–2012 was 5.4. However, that was not adequate, as per the requirement of SMS-I and the problem of rise in Mould water inlet temperature in summer days still persisted. Only after installing the parallel heat exchanger (PHE) in October'2012, the annual average sequence size could be increased and in 2012–2013, average annual sequence of 5.98 could be achieved.

Thereafter, in June'2013, the capacity of Vertical Turbine pump for Auxiliary water for heat exchanger was replaced with a higher capacity pump as explained above and all the water related problem of PHE was eradicated.

After completing all the Plate heat exchanger (PHE) related job, the only problematic area left was the cooling tower, as all the 3 cells were required to run during summer days. That problem was also addressed by modifying the lubrication system from "Splash lubrication" to "Drip lubrication "of the Cooling Fan Worm Gear box, as explained at point no. 3 in "Modification done" above.

All the above innovation and modifications could finally resulted in containing the mould water inlet temperature, below 42 °C, irrespective of climate and sequence size. Tundish fly could be made possible only after the above modification was done. Table 1 indicates the number of heat cast with "Tundish fly" on the following days.

The production target of SMS-I for FY 2013–2014 was 4,21,000 Tons. Till end of June'2013, SMS-I was starving for hot metal. After the commissioning of new BF# 5, SMS-I started getting hot metal from August, 2013. Therefore, from August'2013 till March'2014 i.e. in 8 months, the production was 2,89,000 Tons, with average monthly rate of 36,122 Tons. Considering the rate of production, after modification, the rate of increase was around 2.9% more than the APP. This was made possible primarily, because of longer sequence, due to above modification.

The above achievement gave a confidence to start Total tundish management (TTM) of 8 heat sequence in place of 5 heat sequence. TTM of 8 heat sequence was started in the first week of October, 2014 and was stabilized (Tables 2 and 3).

The above modification and thereby, higher sequence casting resulted in substantial direct benefit with respect to generating: (a) Longer sequence, (b) less tundish skull, (c) less crop end. The achievement of increasing the sequence size, resulted

Table 1 Number of heat cast with "Tundish fly" on the following days

Sl. No.	Date	No. of heats and grade per sequence
1	20-7-2013	10 Non-CRNO
2	25-8-2013	14 Non-CRNO
3	27-8-2013	14 CRNO
4	29-8-2013	13 Non-CRNO
5	18-9-2013	23 Non-CRNO
6	28-9-2013	16 Non-CRNO
7	29-10-2013	16 Non-CRNO

Table 2 TTM of 8 heat sequences

Year	No. of sequence of more than 8 (eight) heats	Total no of heat sequences	% Sequences with more than 8 heats
2013–2014	37	232	15.9
2014–2015	58	213	27.2
2015–2016	80	232	34.4

Table 3 Average sequence size and annual production

Financial year	Annual production target in tons	Actual production in tons	Longest sequence size of financial year	Average sequence size of financial year
2014–2015	445,000	412,100	11	6.49
2015–2016	400,000	326,239	12	6.90
2016–2017	242,000	232,364	11	6.43
2017–2018	500,000	343,598	11	6.96
2018–2019	400,000	378,003	10	6.41
2019–2020	430,000	349,477	10	6.42

in higher caster yield and reducing the cost of production per ton of steel at SMS-I. (As shown in Table 4).

However, there was a perpetual problem, which was faced in the slab caster was “Strand struck up”. To investigate the problem, after the above modification in the mould water circuit, more than hundred data were taken in different grades of steel, with different slab width and further research and analysis was conducted. Accordingly, a relationship with Tundish temperature and Slab exit temperature could be established. It was evident from the result that, liquid metal pool length in the mould, strand shell thickness and mushy zone thickness during solidification depends on the primary cooling intensity and to some extent on casing powder.

Since the cooling water volume was constant to the Copper mould in case of SMS-I, it was found during the investigation that the impact of mould inlet water temperature had, some effect on the slab exit temperature from the strand, which caused “Strand struck up”. Modifications were also done further in the secondary cooling and the Pinch roll drive. However, with the research, the monitoring of Tundish temperature was strictly followed. It further, improved the productivity of caster, as “Strand struck up” phenomenon was eliminated in the slab caster of SMS-I.

As, mostly special steel is made in SMS-I, the hot metal supply was decided as per the order position and hence it was not consistent every month or for every financial year. It can be seen from Table 2, that, irrespective of overall production, the highest sequence that could be achieved in several occasion, was above 10 and the annual average sequence was always more than 6.4. The higher sequence size, resulted in higher productivity and lower cost of production.

Table 4 Caster yield before and after modification

2009–2010 (before	2010–2011 (before	2011–2012	2012–2013 (after)	2013–2014	2014–2015	2015–2016	2016–2017	2017–2018	2018–2019	2019–2020
98.64	98.76	98.5	98.91	98.95	98.94	99.06	99.07	99.15	99.05	99.03

4 Conclusions

After executing the modifications in the mould water circuit, substantial improvement was observed in the mould water inlet temperature and even in summer days, irrespective of higher sequence size above 5 (Five), the mould inlet water temperature could be contained below 42 °C. "Tundish Fly "also could be started in slab caster, thereby increasing the productivity. Subsequent to the positive result obtained from the modifications, more research was conducted to predict the slab exit temperature from the strand, so as to monitor and maintain the liquid steel temperature in the tundish, for different grades of steel. That could further eradicate the "Strand struck up "phenomenon in slab caster. After eliminating the "Strand struck up" phenomenon, not only productivity could be increased but also, improvement in quality could be achieved. Therefore, the compendium of above research and modifications can be replicated in any Old slab caster having copper mould with "Constant cooling water volume "along with severe space constraint to increase productivity and better quality, with minimum revenue expenditure, without any capital cost.

Acknowledgements I extend my sincere gratitude to Shri R. K. Patra, Chief General Manager, SMS-I, Shri A. V. Pradeep, General Manager, SMS-I and their team for facilitating the above modifications and research at Slab caster of Steel Melting Shop-I, Rourkela Steel Plant.

References

1. Pal S, Behera KK, Padhee PR, Sarkar S, Halder C (2019) Optimization between Tundish temperature and slab exit temperature to eliminate "Strand Stuck-Up" phenomenon in continuous casting process of steel by implementation of multi-objective evolutionary and genetic algorithm. https://doi.org/10.1002/srin.201800506
2. Peng Y, Bao P, Mei N, Yang LK (2015) First Influence of inlet cooling water temperature and velocity on billet mould heat transfer. https://doi.org/10.13374/j.issn2095-9389
3. Mazumdar S, Ray SK (2001) Solidification control in continuous casting of steel. R&D Centre for Iron and Steel, Steel Authority of India Ltd (SAIL), Ranchi, India
4. Kromhout A, Dekker Kawamoto ER, Boom R (2013) Challenge to control mould heat transfer during thin slab casting. 206–215. https://doi.org/10.1179/1743281212Y.0000000030
5. Miłkowska-Piszczek K, Dziarmagowski M, Buczek A, Pióro J (2012) The methods of calculating the solidifying strand shell thickness in a continuous casting machine. A Faculty of Metals Engineering and Industrial Computer Science, AGH-University of Science and Technology. Al. Mickiewicz 30, 30-059 Krakow, Poland, Aiatan & Ketrab, ul. Galicyjska 25/2, 32-087 Zielonki, Poland

Microstructural and Spectroscopic Studies of Aluminium/Graphene Nanocomposites Synthesized by Solid State Reaction

Tapan Dash and Binod Bihari Palei

Abstract Super nanocomposites of aluminium/graphene (0.7 and 1 wt%) have been successfully synthesized by solid state reaction technique. For developing homogenous mixture of compositions an innovatively designed planetary ball mill was employed. 8 h of ball milling under argon atmosphere was carried out to prevent oxidation of composites. Sintering of well compacted pellets were carried out at 580 °C. XRD, FESEM, micro Raman, electrical conductivity and microhardness analysis of composites were carried out to produce an optimized product. Pure aluminium shows electrical conductivity and microhardness values of 38.9×10^6 S/m and 392 ± 39 MPa respectively. The sintered aluminium-graphene (1 wt%) composite shows significantly higher electrical conductivity (120.2×10^6 S/m) and microhardness (1746 ± 58 MPa) values than that of pure aluminium.

Keywords Nanocomposite · XRD · Graphene · Aluminium

1 Introduction

Aluminium (Al) is a very popular metal for various industrial applications. It shows remarkable mechanical and physical properties such as density low, high resistance towards corrosion and good ductility [1–6]. These superior properties of aluminium make it as one of the fittest candidate material for various industrial applications including aerospace industry, automobile sector, marine engineering, and architectural fields [1–6]. It's tribological properties has found to be poor. Because of having poor strength, it is hardly used in its original pure metallic form. In this backdrop, alternate material in form of alloy or composite with aluminium is continuously being addressed by the material research community. Since last two decades aluminium

T. Dash (✉)
Centurion University of Technology and Management, Bhubaneswar, Odisha, India
e-mail: tapan.dash@cutm.ac.in

B. B. Palei
CSIR-Institute of Minerals and Materials Technology, Bhubaneswar, Odisha, India

S. Pal et al. (eds.), *Processing and Characterization of Materials*, Springer Proceedings in Materials 13, https://doi.org/10.1007/978-981-16-3937-1_29

has been drawn special attention as a metal matrix for developing various composites or alloys. For special industrial application, normally various required secondary components or elements are added to it to improve its application. To improve its mechanical strength, different ceramic additives such as Al_2O_3, SiC, BN, and B_4C are reinforced with it [7, 8]. From recent times an outstanding materials such as graphene is in focus for using as a reinforcing material for enhancing the aluminium properties. Graphene can be considered as one of the most promising nanomaterials because of its unique combination of super properties. It has unique properties such as "high mechanical strength, current density, high electron mobility, ballistic transport, chemical inertness, high thermal conductivity, electrical conductivity, biosensor, energy field, display field super hydrophobicity" [9–20]. Hence it is supposed that by reinforcing graphene in aluminium, a super metal matrix nano composite can be developed which has great industrial applications. Literature reports both increasing and decreasing of microhardness value of aluminium matrix after graphene reinforcement. Li et al. [21] reports that 1 wt% graphene addition increases microhardness upto 794 MPa whereas Garg et al. reports graphene addition (0.1–0.5 wt%) shows lower microhardness (270.7–278.5 MPa) in comparison to pure aluminium [22]. 8.9% improvement of electrical conductivity for Al-graphene (0.5 wt%) composite in comparison to pure Al reported by Chyada et al. [23]. But the work done by Xu et al. [24] shown 30.6% less electrical conductivity for composite of Al-graphene (1 wt%) in comparison to pure Al.

The work presents successful aluminium-graphene composite (0.7 and 1 wt%) synthesized by 8 h of ball milling followed by 580 °C sintering for 6 h. Properties of as prepared materials were studied by using "characterization analytical techniques such as such as X-ray diffraction (XRD), field emission scanning electron microscopy (FESEM), micro Raman, electrical and microhardness". Al-graphene composites (0.7 and 1 wt%) prepared by 8 h of milling show high electrical and microhardness values than that of pure Al.

1.1 Experimental

Aluminium of 99.7% purity was taken from Sigma-Aldrich. Our self-prepared graphene of 99.9% purity was used in this study. The details about the synthesis of graphene reported in our earlier reported work [11]. The aluminium and graphene materials were used as starting materials for the synthesis of aluminium-graphene composite. The powder composite of aluminium and graphene was prepared by dry ball milling technique. During the ball milling powder-to-ball ratio was kept as 1:9. No solvents, additives, and chemicals were used in ball milling jars. The jars (two) were kept inside glove bags. Stainless steel ball of dia. 8 mm was used for ball milling purpose. These balls were used as a medium of grinding. The frequency of 26 Hz was maintained for period of 8 h during rotate of jars. The 8 h of ball milling was chosen because in our earlier reported work [11], we found that after 8 h of milling the crystallinity of graphene layers became disordered and more defects start generating on

basal plane of graphene layers. After successful complete of milling, samples were being allowed to be cooled down by placing them in a refrigerator and these sample derivatives can be used for different sintering thereafter. The sintering of composites were carried out under 580 °C for 6 h. After sintering successfully completed, samples were taken for different characterizations. "X-ray diffraction (XRD) was carried by PANalytical X'Pert Pro diffractometer. Microstructural behavior of the samples was taken by field emission scanning electron microscopy (FESEM), ZEISS SUPRA (55). Renishaw inVia Reflex (UK) spectrometer was used for micro Raman analysis. Microhardness of composites were done by LECO (load 0.5 kg, 20 s dwell time). Multimeter, Keithley 6221 with four probes was used for electrical conductivity study of composites".

2 Results and Discussion

Crystallographic behaviour of aluminium-graphene composites were studied by XRD. The results and interpretation are shown in the Fig. 1. XRD pattern were evaluated within the 2θ range of 5°–80°. XRD analysis report confirms the composite formation between aluminium and graphene. The XRD analysis of pure ball milled aluminium sample infers the peaks due to only Al. Peaks of (111), (200) and (311) are found in the ball milled pure Al sample. The Al with graphene 0.7 and 1 wt% interestingly show additional peak of graphene as C(002) along with different peaks of Al. So, XRD result confirms the Al-graphene composite formation. Two theta and FWHM of the corresponding peaks of the different planes correspond to different phases were found and compared to their standard values with JCPDS files. The XRD indicates well-ordered and better crystalline behaviour of the composites.

FESEM analysis of typical sintered Al-graphene (1 wt%) composite was carried out (Fig. 2). It exhibits the presence of graphene flakes in the matrix of aluminium. The

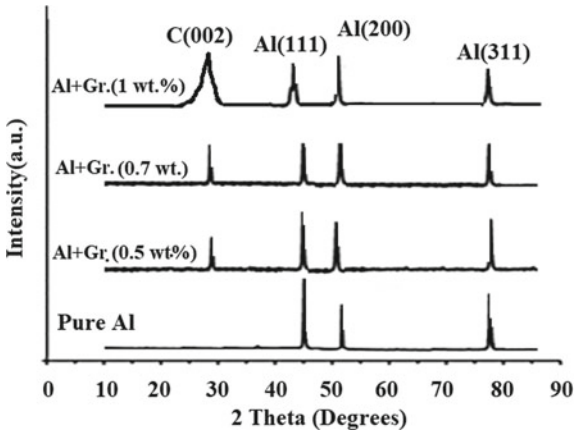

Fig. 1 XRD spectra of pure aluminium and aluminium-graphene composites

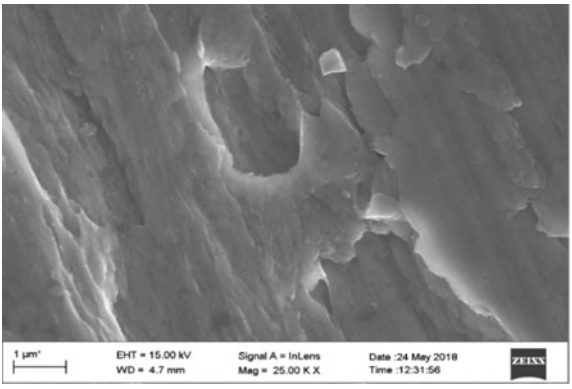

Fig. 2 FESEM result of typical aluminium-graphene (1 wt%) composite

distribution of grains of graphene were found to be irregular. But surface defect and porous network structure were found to be absent in the FESEM analysis. This result indicates about the quality of composite prepared by optimized sintering condition.

The microhardness of sintered Al-graphene composites were determined. It was found that microhardness value increases by reinforcing graphene in aluminium matrix. Pure Al shows hardness value of 392 ± 39 MPa. But the typical 0.7 and 1 wt% graphene reinforced aluminium composites exhibit microhardness of 1530 ± 78 MPa and 1746 ± 58 MPa respectively. In comparison to the literature data the microharness and electrical conductivity were significantly improved. In this work the microhardness of 1 wt% graphene reinforced Al was found to be more than two times than the literature reported value of 794 MPa [21]. As per the "microstructural and hardness results are concerned, it is observed that graphene addition improves structural and mechanical property of composite". Al is known for good electrical applications. The electrical conductivity of pure aluminium was found to be 38.9×10^6 S/m. 0.7 and 1 wt% graphene reinforced aluminium composites show significant improvement of electrical conductivity value i.e. 87×10^6 and 120.2×10^6 S/m respectively. The improved microhardness and electrical conductivity values observed in this work are attributed to the well dispersion of graphene in the composite.

Spectroscopic behavior of typical aluminium-graphene composites having 0.7 and 1 wt% graphene were evaluated by micro Raman spectroscopy and presented in Figs. 3 and 4 respectively. Raman spectra give three peaks. These peaks are belong to carbon (graphene). The peaks at 1349–1350, 1581–1585 and 2753–2790 cm^{-1} are attributed to D (1st order disorder peak in graphite lattice), G (graphite lattice peak) and 2D (2nd order disorder peak in graphite lattice). The peak intensity of 2D is same as that of G which confirms bilayer nature of graphene in composite in case of 1 wt% reinforced graphene. But multilayer graphene observed in case of 0.7 wt% reinforced graphene to Al.

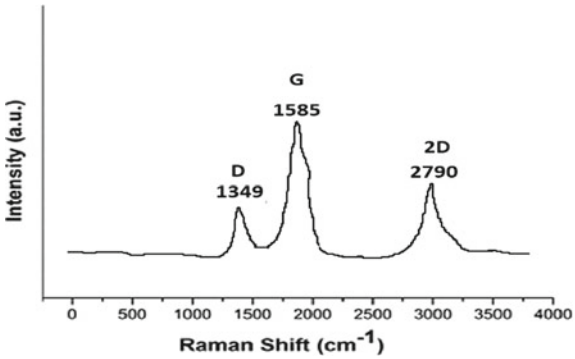

Fig. 3 Micro Raman result of typical aluminium-graphene (0.7 wt%) composite

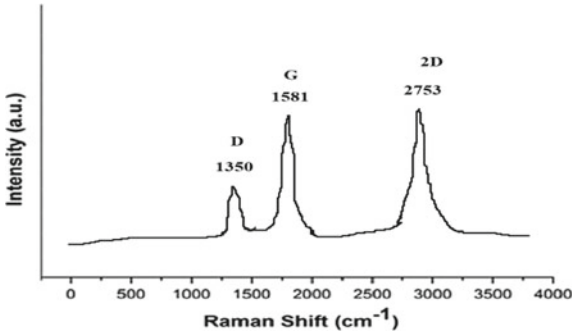

Fig. 4 Micro Raman result of typical aluminium-graphene (1 wt%) composite

3 Conclusion

Al-graphene (0.7 and 1 wt%) composites were successfully synthesized by "8 h of dry planetary ball milling followed by sintering at 580 °C (for 6 h)". XRD of pure aluminium shows peaks of Al only. Aluminium-graphene composites (0.7 and 1 wt%) show peaks due to both Al and graphene. Oxidation of Al was not detected in the composites. Micro Raman result shows three peaks such as D, G and 2D. The composite microstructure of typical Al-graphene (1 wt%) was seen from FESEM analysis. It shows irregular distribution of graphene grains in the matrix of Al. Al with 1 wt% shows improved hardness (1746 ± 58 MPa) and electrical conductivity (120.2×10^6 S/m) values in comparison to that of pure Al.

References

1. Miracle DB (2005) Metal matrix composites—from science to technological significance. Compos Sci Technol 65:2526–2540
2. Shabani MO, Mazahery A (2012) Optimization of process conditions in casting aluminum matrix composites via interconnection of artificial neurons and progressive solutions. Ceram Int 38:4541–4547
3. Kurapova OY, Novik NN, Archakov IY (2014) Synthesis of the precursor for aluminium-graphene composite. Rev Adv Mater Sci 39:41–47
4. Wang J, Li Z, Fan G, Pan H, Chen Z, Zhang D (2012) Reinforcement with graphene nanosheets in aluminum matrix composites. Scripta Mater 66:594–597
5. Kim BJ, Kim JP, Park JS (2014) Effects of Al interlayer coating and thermal treatment on electron emission characteristics of carbon nanotubes deposited by electrophoretic method . Nanoscale Res Lett 9:1–6
6. Pierard N, Fonseca A, Colomer JF, Bossuot C, Benoit JM, Van Tendeloo G, Pirard JP, Nagy JB (2004) Ball milling effect on the structure of single-wall carbon nanotubes. Carbon 4:1691–1697
7. Sun C, Song M, Wang Z, He Y (2011) Effect of particle size on the microstructures and mechanical properties of SiC-reinforced pure aluminum composites. J Mater Eng Perform 20:1606–1612
8. Garg P, Gupta P, Kumar D, Parkash O (2016) Structural and mechanical properties of graphene reinforced aluminum matrix composites. J Mater Environ Sci 7:1461–1473
9. Dash T, Rout TK, Palei BB, Bajpai S, Kundu S, Bhagat AN, Satpathy BK, Biswal SK, Rajput A, Sahu AK, Biswal SK (2020) Synthesis of α Al_2O_3–graphene composite: a novel product to provide multi functionalities on steel strip surface. SN Appl Sci 2:1–9
10. Geim AK, Novoselov KS (2007) The rise of graphene. Nat Mater 6:183–191
11. Dash P, Dash T, Rout TK, Sahu AK, Das S, Biswal SK, Mishra BK (2016) Preparation of graphene oxide by dry planetary ball milling process from natural graphite. RSC Adv 6:12657–12668
12. Gunasekaran RK, Jayasankar K, Dash T, Dash A, Jena BK, Mishra BK (2016) Shear-force-dominated dual-drive planetary ball milling for scalable production of graphene and its electrocatalytic application with Pd nanostructures. RSC Adv 6:20067–20073
13. Böhm S (2014) Graphene against corrosion. Nat Nanotechnol 9:741–742
14. Allen MJ, Tung VC, Kaner RB (2010) Honeycomb carbon: a review of graphene. Chem Rev 110:132–145
15. Aneja KS, Bohm S, Khannaa AS, Bohm HLM (2015) Graphene based anticorrosive coatings for Cr(VI) replacement. Nanoscale 7:17879–17888
16. Ovidko IA (2014) Metal-graphene nanocomposites with enhanced mechanical properties: a review. Rev Adv Mater Sci 38:190–200
17. Dash S, Dash T, Rout TK (2020) Preparation of graphene oxide by dry planetary ball milling technique under oxygen atmosphere. IOP Conf Ser Mater Sci Eng 872(012180):1–6
18. Palei BB, Dash T, Biswal SK (2020) Reduced graphene oxide synthesis by dry planetary ball milling technique under hydrogen atmosphere. IOP Conf Ser Mater Sci Eng 872(012158):1–6
19. Palei BB, Dash T, Biswal SK (2020) Successful synthesis of graphene-aluminum composite with improved microhardness. Int J Eng Adv Technol 9:2218–2221
20. Dhar S, Dash T, Palei BB, Rout TK, Biswal SK, Mitra A, Sahu AK (2020) Silicon-graphene composite synthesis: microstructural, spectroscopic and electrical conductivity characterizations. Mater Today Proc 33:5136–5142
21. Li G, Xiong B (2017) Effects of graphene content on microstructures and tensile property of graphene-nanosheets/aluminum composites. J Alloys Compd 697:31–36
22. Garg P, Gupta P, Kumar D, Parkash O (2016) Structural and mechanical properties of graphene reinforced aluminum matrix composites. J Mater Environ Sci 7(5):1461–1473

23. Chyada FA, Jabur AR, Alwan HA (2017) Effect addition of graphene on electrical conductivity and tensile strength for recycled electric power transmission wires. Energy Procedia 119:121–130
24. Xu CL, Wei BQ, Ma RZ, Liang J, Ma XK, Wu DH (1999) Fabrication of aluminum–carbon nanotube composites and their electrical properties. Carbon 37:855–858

Characterization of AA7075 Alloy Foam Using Calcium and Magnesium Carbonate as Foaming Agent

Ram Krishna Rathore, Nitish Kumar Singh, and J. Francis Xavier

Abstract In this work new composite aluminum foam AA7075 with 3% silicon carbide (SiC) reinforcement was fabricated by stir casting method using calcium carbonate ($CaCO_3$) and magnesium carbonate as a foaming agent. To examine the compressive deformation, deflection, hardness experiments were tested. Quasi-static compression behavior universal testing machine for aluminum metal foam (AA7075 foam) with aluminum casted panel. The thickness of the panel was 1 and 1.5 mm. As the result of the experiment, the compressive strength and stiffness were measured maximum at 1.5 mm thickness panel. The metal panel thickness is also a significant function in the compressive strength and the deformation of the metal foam.

Keywords Aluminium foam · Compressive strength · Powder metallurgy · Stir casting

1 Introduction

Aluminium metal foams (AMFs) are made with different procedures such as Stir casting, powder metallurgy, Liquid Diffusion Welding Method, sintering, foaming compact blowing agents, injection of gas in melt metals using a foam generator. In such methods properties of combined materials are used as parameters for optimization in literature, to develop foams at a cheaper cost [1, 2]. The metal foam gives the better potential for lightweight structures for absorption of energy with thermal management [1]. Metal foams show a mixture of mechanical and physical characteristics such as lighter in weight, better explicit stiffness, good strength to weight proportions, and incredibly expanded energy absorption properties make it use inside the car and aviation fields. It furthermore reduces the fatigue to decrease inertia developed in tension applications and compression cases [2]. Aluminium metal Foam behaves strongly under low pressure and in high pressure, its behaviour

R. K. Rathore (✉)
Department of Mechanical Engineering, RCET, Bhilai, Chhattisgarh, India

N. K. Singh · J. F. Xavier
School of Mechanical Engineering, VIT Bhopal University, Bhopal, India

S. Pal et al. (eds.), *Processing and Characterization of Materials*, Springer Proceedings in Materials 13, https://doi.org/10.1007/978-981-16-3937-1_30

is like wood. There's a specific change of strain over that froths are flexible in nature and their change in shape recoverable [3]. AMFs are having a unique blend of the property of low thickness, low weight-related mechanical characteristics and better absorption of energy. Metal foams fabricating through powder metallurgy method by heat treatment a compacted blend of an alloy of aluminium and a foaming agent TiH_2 to keep maintain the temperature above the melting point of aluminium. The foaming agent TiH_2 discharges hydrogen gas into the liquefied aluminium and generate the aluminium foam. The PM foaming technique is quick expansion happening during a couple of moments useable cellular structure of foam will be obtained [4]. Stir casting is the best appropriate foam creation techniques for the generation of AMFs so that this will give a better outcome over the investigation on mechanical application [5].

Banhart [2] studied the variation in inclination angle for the temperature of the heat-treated surface on metallic foam in case of heat transfer experimentally. The experiment carried out on an aluminium plate in different inclination angle at horizontal direction using an electrical resistor. By using this experiment, we got the temperature varies linearly to inclination angle (up to 45° and 60°). The thermal efficiency (maximum) of aluminium foam is nearly 17% in the vertical direction. Sahu et al. [6] investigated quasi-static compression behaviour and characterization of 2014 aluminium alloys and 25% volume fraction of chemosphere particles foam which has been manufactured through stir casting method. The microstructure of the metallic foam is tested by scanning electron microscope. The strain rate of 0.001/s on the stress–strain curve was calculated experimentally. Sowmiya et al. [7] visually investigated the image of foams created by different trials, Macrostructure (optical microscope), FEM Simulation by LS DYNA was done for pure closed-cell Aluminium foams, which was manufactured by Direct-foaming with the foaming agent as calcium carbonate ($CaCO_3$) with and without foam. Mahadev et al. [8] studied the different methods for aluminium foam and different cellulose metallic structures. It has been observed from the literature the different manufacturing processes for aluminium foam are categorised as solid, liquid and gaseous. AMF shave some special property such as reduced mass with less specific weight, better compressive strength, better energy absorption quality, and high stiffness. It has been also observed that from the literature review AMFs mainly created by the stir casting method. Ramasamy and Dennison [9] investigated tensile strength, Hardness, microstructure (SEM) of aluminium (LM0) foam which was created by the Melt route method and Stir Casting method by using dolomite as a foaming agent in a proportion of 10:1. This paper explored that preheated dolomite-aluminium foam has great mechanical properties and better porosity. Birla et al. [5] studied Microstructural (SEM), Compression testing, Relative density of foams of Aluminium alloy (LM13)-chemosphere foam which was manufactured by Stir casting method using CaH_2 (0.6 wt% of alloy) was used as a foaming agent. A closed-cell HFs with varying relative density was made in this research. Ertürk and Aydin [10] investigated the quantity of sodium chloride (NaCl) required to manufacture the aluminum foam by using the gravity die casting method, which allows manufacturing of open-cell A365-aluminum foam as an absorbent material, by adding NaCl will increase the porosity and decrease the density of the foam.

2 Experimental Details

2.1 Material

In this research, aluminum AA7075 alloy (the composition and mechanical characteristics of AA70705 are shown in Tables 1 and 2 respectively) with zinc as the primary alloying element and magnesium as the secondary alloying element was used as the raw material. AA7075 has good mechanical strength and excellent resistance to corrosion high fatigue strength, creep resistance, high formability compares to aluminum. This material is generally used in various mechanical applications aerospace, the automobile also used in thin section and intricate castings like switch boxes, structural panel.

2.2 Production of Aluminum Alloys AA7075 +3% by Weight of SiC Composite Foam

Stir casting process was used to fabricate two different types of foams (Fig. 1), two charges of aluminum AA7075 (1455 g weight of composite) +3% of SiC by weight (45 g) were melted in the crucible (graphite) shown in Fig. 2b in stir casting electric

Table 1 Chemical composition of AA7075 aluminum alloy

S. No.	Element	Weight in %
1	Zinc (Zn)	5.62
2	Magnesium (mg)	2.52
3	Copper (Cu)	1.63
4	Chromium (Cr)	0.22
5	Silicon (Si)	0.06
6	Iron (Fe)	0.18
7	Aluminum (Al)	89.77

Table 2 Mechanical properties of AA7075 aluminium alloy

S. No.	Property	Value
1	Density	2810 kg/m^3 (2.8 g/cc)
2	Melting point	6350 C
3	Modulus of elasticity	70–80 Gpa
4	Poisons ratio	0.35
5	Specific heat capacity	960 kg-K
6	Tensile strength	230 Mpa
7	Yield strength	105 a

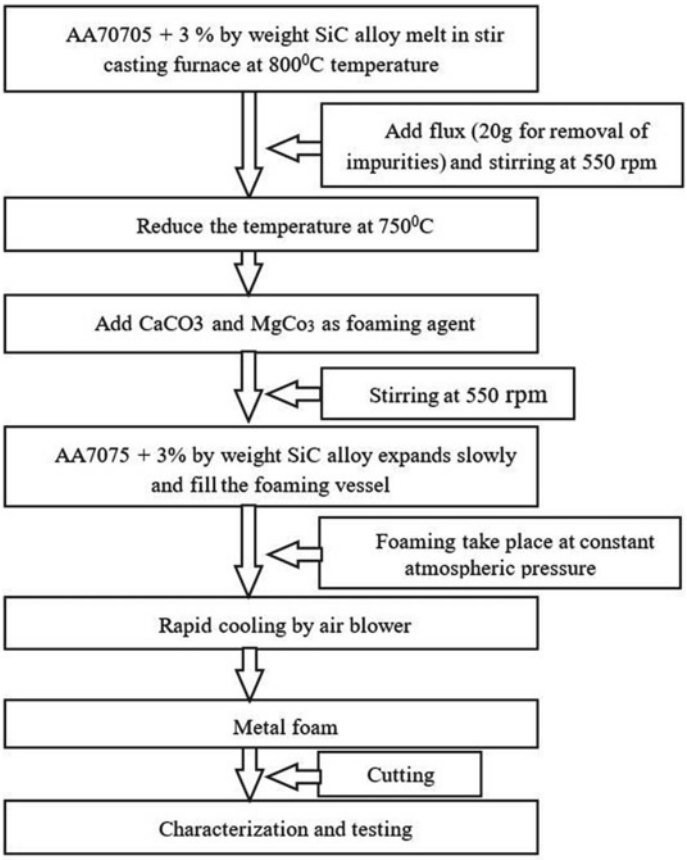

Fig. 1 Stir casting method of foam synthesis

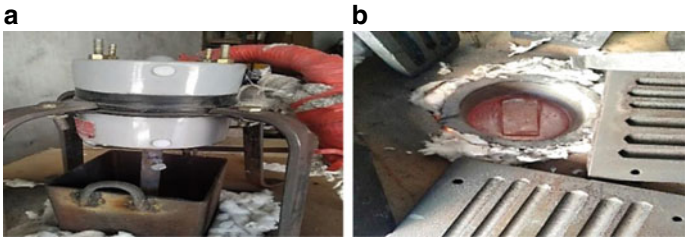

Fig. 2 Illustrates the **a** Stir casting setup **b** Graphite crucible

arc furnace as shown in Fig. 2a at 8000 C, 20 g flux was added in the molten alloy and stir for 5 min at 550 RPM for removal of impurities and then temperature decreases at 7500 C, 1.5% $CaCO_3$ and 1.5% $MgCO_3$ two types of foaming agent added in charges and stirred for 10 min for proper homogeneous mixing of the foaming agent then the liquid metal was taken out from the oven and cooled by the blower to create solid metal foam. The solid foam is taken out from the crucible and make a sample by machining process for characterization and testing.

3 Characterization

The composite foam created using the stir casting method are shown in Fig. 3a, b. The shown samples were tested to evaluate mechanical characteristics such as compressive strength, and hardness tests conducted at different conditions at the Universal Testing Machine and Digital Rockwell hardness machine correspondingly.

3.1 Compression Test

Compressive tests of aluminium alloy AA7075 +3% by weight of SiC, Hybrid composite foam with $CaCO_3$ and $MgCO_3$ as foaming agent shows in Fig. 3a, b were

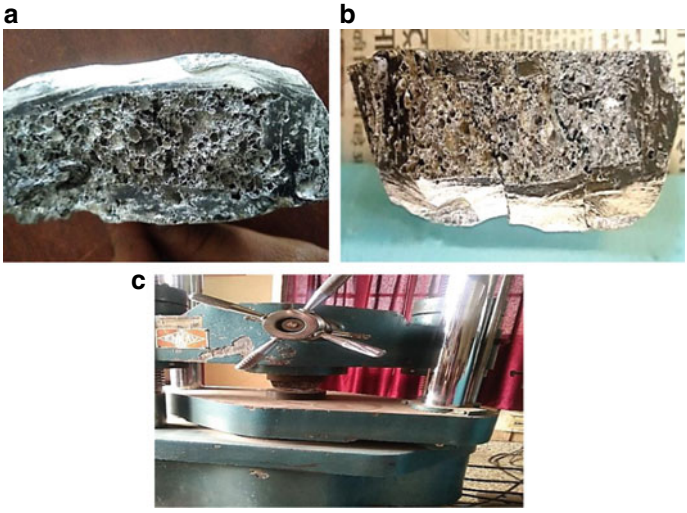

Fig. 3 Image of **a** Compression test sample of 1 mm panel **b** 1.5 mm panel with compressive failure **c** Sample being tested on UTM

performed on the Universal testing machine (UTM) shown in Fig. 3c. For compression test Specimen with approximately 60 mm × 60 mm × 30 mm dimensions were prepared with an EDM wire cutting machine.

$$\text{Compressive strength} = \frac{\text{Load}}{\text{Crossection area}} \tag{1}$$

3.2 Energy Absorption Characteristics

The AMFs exhibit the three regions during compression test linear region, plateau region and densification region. The plateau region is the reason where the stress will be nearly constant during the compression test. Energy absorption characteristics of foam can be estimated by using the following formula:

$$E_{\text{foam}} = \int_0^{\varepsilon D} \sigma \, d\varepsilon \tag{2}$$

where εD—densification strain,
σ—stress,
ε—strain.

3.3 Hardness Test

To determine the hardness properties of prepared foam samples, a hardness test was conducted using a Rockwell hardness machine (FIE make Model TRSB-D) at 200 N force. The indentation hardness is identified as resilient to perpetual or plastic deformation in static or dynamic loading conditions. The diamond-type indenter used in current research of surface hardness measurement of the composite sample.

4 Results and Discussion

4.1 Load Deflection Behavior

The load–deflection curve of both samples (1.5 and 1 mm thickness) is shown in Fig. 4. It is observed from Fig. 4 that 1.5 mm single side panel foam sample the maximum peak load and deflection during the compressive test is 156 KN and

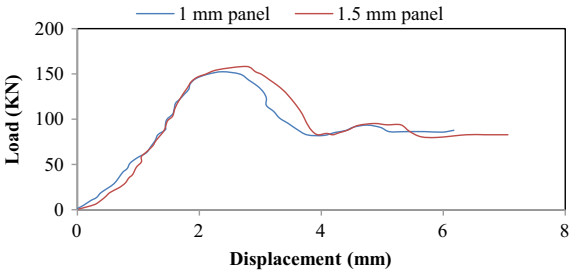

Fig. 4 Load–deflection curve

6.6 mm, which is higher as compared to 1 mm single side panel foam sample having maximum peak load and maximum deflection is 152 KN and 6.1 mm.

It is seen that load is strongly correlated with the thickness of the sandwich panel. It can be seen that under the same core material, the load-bearing capability increases with the increased thickness of the sandwich panel. The reason is that the framework of the foamed aluminum alloy is stronger with a higher thickness of the sandwich panel.

4.2 Compressive Strength

The compressive strength of the samples was calculated by using Eq. (1) and it is observed from Fig. 5 that for 1 mm panel foam maximum compressive strength of foam is 84.44 N/mm^2, which is slightly lower as compared to sample 1.5 mm panel having compressive strength is 86.667 N/mm^2, which is evident that increase in the thickness of panel in the prepared foam increases the compressive strength.

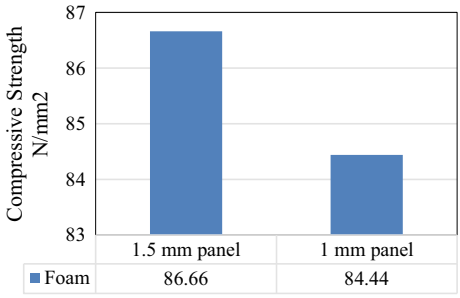

Fig. 5 comparative charts for maximum compressive strength (N/mm^2)

Table 3 Compressive properties of prepared foams

Foams samples (using different type of foaming agent)	Maximum compressive strength (N/mm^2)	Average plateau stress (N/mm^2)	Energy absorption capacity (MJ/m^3)
1.5 mm panel foam	86.667	61.11	6.72
1 mm panel foam	84.44	58.88	6.064

Table 4 Rockwell hardness of the samples

S. No.	Thickness of panel	Rockwell hardness (HRB)
1	Zinc (Zn)	5.62
2	Aluminum (Al)	89.77

4.3 Energy Absorption Characteristics

The Energy absorption characteristics of the specimen were estimated by using Eq. (2) and the in Table 3. The energy absorption characteristics for 1.5 mm panel foam is approximately 1.1 times more than that of 1 mm panel foam due to more values of the plateau stress.

4.4 Hardness Test

The hardness (indentation hardness) of both samples was determined by using the Rockwell hardness test is presented in Table 4.

The Rockwell hardness of both the specimens of hybrid composites was evaluated as given in Table 4. It was seen that the hardness of 1.5 mm panel foam is less than the hardness of 1 mm foam. The hardness of sample 1 (1.5 mm panel), and sample 2 (1 mm panel) is 30.67 and 34.232 HRB respectively.

5 Conclusion

The 1.5 mm single-sided panel foam showed superior compressive properties than 1 mm single-sided panel foam. The compressive load carrying capacity, deflection, maximum compressive strength and plateau stress of the AA7075 foam with calcium carbonate and magnesium carbonate as a foaming agent with 1.5 mm single-sided panel increases as compared to 1 mm single-sided panel foam. The energy absorption capacity for a 1.5 mm single-sided panel is approximately 1.1 times more than compared to a 1 mm single-sided panel. From the Rockwell hardness test, it was observed that the 1 mm single-sided panel is 1.12 times harder than as compared to 1.5 mm single-sided panel. Due to its lightweight and good compressive strength

compare to the bare foam, this material will be used in the window frame, flooring of heavy vehicle.

References

1. Banhart J (2013) Light-metal foams - History of innovation and technological challenges. Adv Eng Mater 15(3):82–111. https://doi.org/10.1002/adem.201200217
2. Banhart J (2001) Manufacture, characterisation and application of cellular metals and metal foams. Prog Mater Sci 46(6):559–632. https://doi.org/10.1016/S0079-6425(00)00002-5
3. A. Pandey, D. Muchhala, R. Kumar, S. S, A. N. C. Venkat, and D. P. Mondal, "Flexural deformation behavior of carbon fiber reinforced aluminium hybrid foam sandwich structure," *Compos. Part B Eng.*, vol. 183, p. 107729, 2020, doi: https://doi.org/10.1016/j.compositesb.2019.107729.
4. Mondal DP, Goel MD, Upadhyay V, Das S, Singh M, Barnwal AK (2018) Comparative Study on Microstructural Characteristics and Compression Deformation Behaviour of Alumina and Cenosphere Reinforced Aluminum Syntactic Foam Made Through Stir Casting Technique. Trans Indian Inst Met 71(3):567–577. https://doi.org/10.1007/s12666-017-1211-x
5. S. Birla, D. P. Mondal, S. Das, D. K. Kashyap, and V. A. N. Ch, "Effect of cenosphere content on the compressive deformation behaviour of aluminum-cenosphere hybrid foam," *Mater. Sci. Eng. A*, vol. 685, no. October 2016, pp. 213–226, 2017, doi: https://doi.org/10.1016/j.msea.2016.12.131.
6. S. Sahu, M. Z. Ansari, and D. P. Mondai, "Microstructure and compressive deformation behavior of 2014 aluminium cenosphere syntactic foam made through stircasting technique," *Mater. Today Proc.*, vol. 25, no. xxxx, pp. 785–788, 2019, doi: https://doi.org/10.1016/j.matpr.2019.09.019.
7. Sowmiya S, Nallanukala P, Anburaj J, Simhachalam B (2018) Development of Metallic Aluminium Foam Casting Using Calcium Carbonate Precursors for Side Impact Beam Application. Mater. Today Proc. 5(9):20362–20370. https://doi.org/10.1016/j.matpr.2018.06.411
8. Mahadev, C. G. Sreenivasa, and K. M. Shivakumar, "A Review on Prodution of Aluminium Metal Foams," *IOP Conf. Ser. Mater. Sci. Eng.*, vol. 376, no. 1, 2018, doi: https://doi.org/10.1088/1757-899X/376/1/012081.
9. Ramasamy Karuppasamy and M. P. Milon Selvam Dennison, "Preparation and Characterization of Aluminium Foam Prepared Through Melt Route Method," *Int. Res. J. Eng. Technol.*, vol. 5, no. 3, pp. 190–195, 2018, [Online]. Available: www.irjet.net.
10. Ertürk AT, Aydin I (2017) Enhanced mechanical performance of aluminum glass fiber reinforced foam material by Cu modification. Acta Phys Pol A 131(3):470–473. https://doi.org/10.12693/APhysPolA.131.470.r45t

Fused Tungsten Carbide Synthesis by Thermal Arc Plasma Melt Cast Method

Ranjan Kumar Moharana and Tapan Dash

Abstract Fused tungsten carbide (WC–W_2C) was synthesized successfully form WC+W (0, 5 and 10 wt%) by arc plasma melt-cast method within only 10 min. of plasma reaction. The products were found having high density. X-ray diffraction and field emission scanning electron microscopy show clear evidence of formation of fused tungsten carbide. Fused tungsten carbide with 10 wt% shows improved microhardness and Young's modulus values in comparison to that of pure tungsten carbide.

Keywords Fused tungsten carbide · Thermal arc plasma method · X-ray diffraction · Microstructure

1 Introduction

Tungsten and carbon react together to form two stable compounds such as tungsten carbide (WC) and tungsten semicarbide (W_2C). Recent literature addresses that W_2C has higher hardness than WC [1]. Tungsten mono carbide (WC) exhibits very high melting point (~2700 °C) and high microhardness (~23 GPa) [1–12]. When WC and W_2C phase formed together in a composite it is called fused tungsten carbide. It show better mechanical properties than WC. Tungsten carbide generally used in developing "rock drill buttons, pressing dies, cutting tools for hard materials, and other abrasion-resistant components". The above uses of tungsten carbide is possible because of it is having considerable toughness, high strength, and high wear resistance behaviour. Generally graphite and induction furnaces were used for preparing WC–W_2C composites [8]. But in these methods huge energy is used for synthesis of WC–W_2C composite. To reduce the energy consumption an alternate method is needed to prepare such composite. Plasma method is considered as an alternate technique to prepare such composite with consumption of less energy. Also time can be significantly saved by processing WC–W_2C composite by plasma route.

R. K. Moharana · T. Dash (✉)
Centurion University of Technology and Management, Bhubaneswar, Odisha, India
e-mail: tapan.dash@cutm.ac.in

S. Pal et al. (eds.), *Processing and Characterization of Materials*, Springer Proceedings in Materials 13, https://doi.org/10.1007/978-981-16-3937-1_31

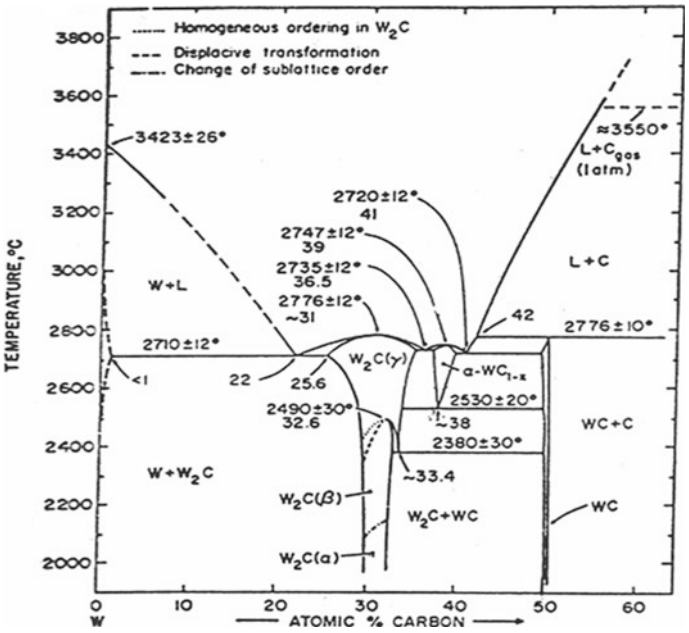

Fig. 1 W–C system phase diagram [8, 13, 14]

In this case thermal plasma was used in transferred arc mode. The main objective of the work is to prepare a very hard and tough composite of WC–W_2C. From phase diagram it is observed that melt of W and C after a pseudo-eutectic reaction at around 2500 °C, WC and W_2C (Fig. 1) [8, 13, 14] composites were produced. The above advantage has been taken to synthesize novel composites of WC–W_2C. The paper presents evaluation of microstructural and mechanical properties of composites by using techniques such as "X-ray diffraction, Fourier transform infra-red (FTIR), Brunauer–Emmett–Teller (BET) and micro hardness".

2 Experimental

Pellets of W and WC powder was prepared by applying 7 T load for 30 s. Poly vinyl alcohol (PVA) was used as binder during pellet preparation. The "specifications of the powder samples are as follows: WC powder: grain size 10 μm; W powder: grain size 7 μm; C wt% in WC was 6.12–6.17 (bound C), 0.052 max (free C)".

Around 10 plasma experiments were carried out to prepare suitable WC–W_2C composites. W (0, 5 and 10 wt%) was varied in WC to prepare such composites. Voltage 50–60 V and Current: 260–310 A were employed for preparing such composites of WC–W_2C. As plasmagen gas argon was used. Semi open type plasma reactor of 30 kW was employed for melt and casting of such composite. Melting of samples

was conducted for 5–10 min followed by cooling of 6 h. Graphite vessel was used as crucible. "X-ray diffraction (XRD) was carried out by PANalytical X'Pert Pro diffractometer (CuKα, λ = 0.15406 nm). Fourier transform infra-red (FTIR) spectra were done in the range of 400–4000 cm^{-1} (Spectrum GX, PerkinElmer). The pore volume was calculated by Brunauer–Emmett–Teller (BET) method (ASAP 2020). Vickers microhardness values of composites were evaluated at a load of 0.5 kg (LECO micro hardness tester). Density composites were determined by Archimedes' principle".

3 Results and Discussion

Thermal arc plasma melt-cast method was employed to prepare composites of WC–W_2C from WC + W (0, 5 and 10 wt%) compositions within 10 min. of plasma reaction. Yield of product was found above 88% with corresponding power consumption recorded around 110 kWh per kg. Composite samples show the presence of phases: WC, W_2C and C (graphite) (Fig. 2). As per the W–C phase diagram (Fig. 1), there exists eutectoid decomposition at 1250–1300 °C: $W_2C \Leftrightarrow (W) + WC$ [13, 15]. Due to increase of W % in WC, more amount of formation of W_2C phase cannot be ruled out and which is also proved from the XRD result. The intensity of W_2C phase was found to be increased with increasing wt.% of W in WC and which generally helps in developing a hard and tough fused tungsten carbide composites [8, 9].

These phases were found in hexagonal structures. The XRD confirms the composite formation of WC and W_2C. Melt-cast WC shows peak of C(002). As wt% of W increases in WC increases, the intensity of W_2C phase increases. But WC–W_2C composites with 5 and 10 wt% W shows absence of C(002) peak. FTIR

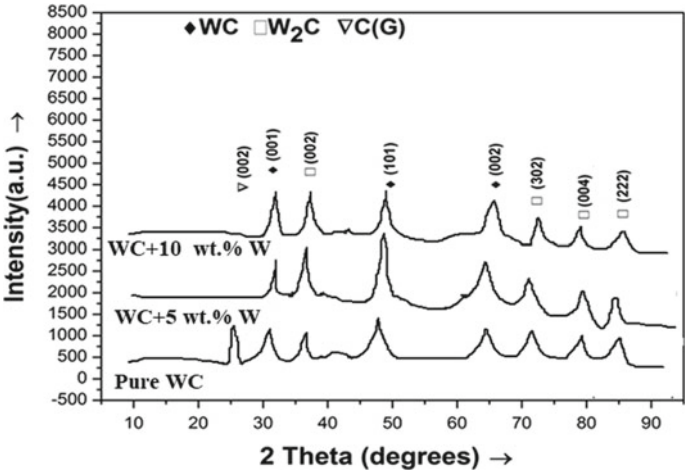

Fig. 2 XRD results for arc plasma melt-cast tungsten carbide composite samples, C(G) graphite

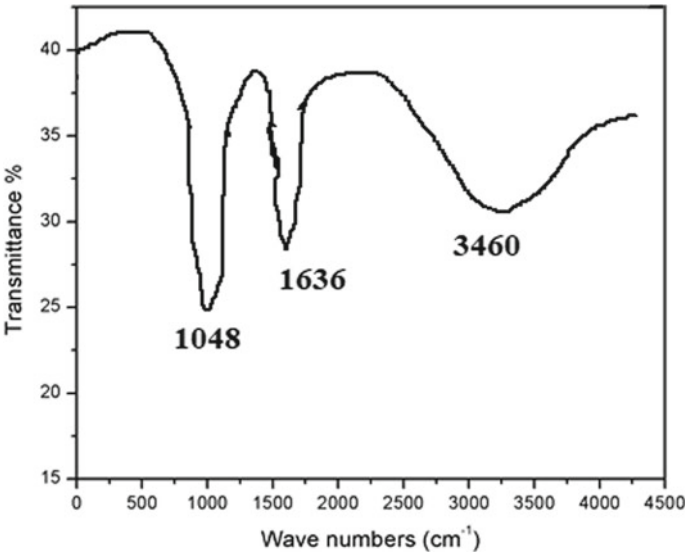

Fig. 3 FTIR result of arc plasma melt-cast WC–W_2C composite sample with 10 wt% W

result of melt-cast WC–W_2C composite with 10 wt% W sample (Fig. 3) exhibits peaks of "vibrational stretching of W–C in hexagonal crystal structure (1048 cm^{-1}), C=C (aromatic) stretching (1636 cm^{-1}) and O–H stretching (3440 cm^{-1})". Density of composites was determined by Archimedes principle. It was found that the melt cast pure WC, WC + 5 wt% W and WC + 10 wt% W composites exhibit density 15.2, 16.7 and 16.9 g/cm^3 respectively. Pore volume of the melt-cast products was calculated by BET method and it was found that pore volume were obtained in 0.0075–0.0092 cm^3/g range. Micro structure of composite was taken by FESEM for typical WC–W_2C composite with 10 wt% W sample (Fig. 4). It shows white, grey and black phases in the composites. The major phase is due to white grains. Black region may be due to pores or due to contribution of carbon graphite phase. The composites were polished and tested for evaluation of microhardness. While melt-cast pure WC showed micro hardness at 1620–1598 $VHN_{0.5}$; 5 and 10 wt% W added WC plasma treated samples exhibit hardness of 2450 $VHN_{0.5}$ and 2620 $VHN_{0.5}$ respectively.

4 Conclusion

Composites of WC–W_2C successfully synthesized by arc plasma melt-cast method within only 10 min. of reaction. XRD and FTIR studies confirm composite formation. From BET and microhardness characterizations, it is observed that arc plasma melt-cast WC–W_2C (with 10 wt%) composites exhibit significantly higher hardness (than

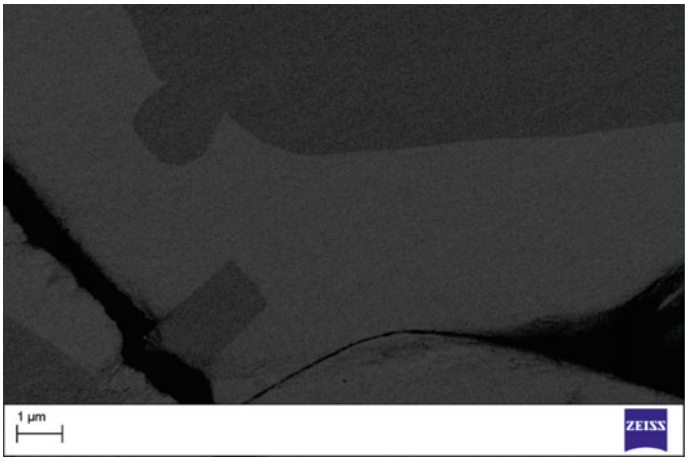

Fig. 4 FESEM analysis of WC–W_2C composite sample with 10 wt% W

pure WC) with minimal porosity. Three type of phases were observed in FESEM result of typical WC–W_2C composite with 10 wt% W sample.

References

1. Mukhopadhyay A, Basu B (2011) Recent developments on WC-based bulk composites. J Mater Sci 46:571–589
2. Sun JL, Zhao J, Gong F, Ni XY, Li ZL (2019) Development and application of WC-based alloys bonded with alternative binder phase. Crit Rev Solid State Mater Sci 44:211–238
3. Poetschke J, Richter V, Gestrich T (2012) Sintering behaviour of binderless tungsten carbide. In: Euro PM2012 congress an exhibition, Basel, pp 7–12.
4. Ma DJ, Kou ZL, Liu YJ, Wang YK, Gao SP et al (2016) Submicron binderless tungsten carbide sintering behavior under high pressure and high temperature. Int J Refract Metal Hard Mater 54:427–432
5. Tsai KM, Hsieh CY, Lu HH (2010) Sintering of binderless tungsten carbide. Ceram Int 36:689–692
6. Demirskyi D, Ragulya A, Agrawal D (2011) Initial stage sintering of binderless tungsten carbide powder under microwave radiation. Ceram Int 37:505–512
7. Li SK, Li JQ, Li Y, Liu FS, Ao WQ (2015) Dense pure binderless WC bulk material prepared by spark plasma sintering. Mater Sci Technol 31:1749–1756
8. Dash T, Nayak BB (2013) Preparation of WC-W_2C composites by arc plasma melting and their characterisation. Ceram Int 39:3279–3292
9. Dash T, Nayak BB (2016) Preparation of multi-phase composite of tungsten carbide, tungsten boride and carbon by arc plasma melting: characterization of melt-cast product. Ceram Int 42:445–459
10. Dash T, Nayak BB, Abhangi M, Makwana R, Vala S, Jakhar S, Rao CVS, Basu TK (2014) Preparation and neutronic studies of tungsten carbide composite. Fusion Sci Technol 65:241–247
11. Dash S, Dash T, Debasish D, Palei BB, Rout TK (2020) Microstructural and mechanical studies of thermal arc plasma treated tungsten carbide. Indian J Nat Sci 10:24339–24343

12. Nayak BB, Dash T, Pradhan SK (2020) Spectroscopic evaluation of tungsten carbide-titanium carbide composite prepared by arc plasma melting. J Electron Spectrosc Relat Phenom 245(146993):1–8
13. Kublii VZ, Velikanova TY (2004) Structural studies of materials-ordering in the carbide W_2C and phase equilibria in the tungsten-carbon system in the region of its existence. Powder Metall Met Ceram 43:630–644
14. Rudy E (1970) Technical report AFML-TR-69-117, part V, The phase diagram of W-B-C. Wright-Patterson Air Force Base, Ohio, USA, p 6
15. Kublii VZ, Velikanova TY, Gnitetskii OA, Makhovitskaya SI (2000) Structural parameters of the low-temperature matastable form of the carbide W_2C. Powder Metall Met Ceram 39:151–156

Study of Physico-Mechanical Behaviour of Alkali Treated Date Palm Petiole Fiber/Epoxy Composites

Janaki Dehury and Jyotiranjan Mohanty

Abstract Various industries like construction, automotive and packaging show their keen interest for development of new natural fiber composites (NFC) by considering different parts of natural fiber such as leaf, fruit, stem, trunk etc. Hence, the current research was planned to fabricated five numbers of new composites with varying the fiber concentrations (0, 8, 16, 24 and 32%) and evaluate the significance of fiber concentration on physical characteristics such as absorption of water, density, void content as well as mechanical characteristics like tensile strength, impact energy, compressive strength and flexural strength of alkali treated date-palm petiole reinforced in epoxy matrix. The outcome depicted that the composite with fiber concentration (16%) have better mechanical properties than the other alternatives. The maximum tensile strength, and impact energy is acquired with the composite having 16 wt% fiber content was found to be 46.40 MPa and of 5.1 J. However, the compressive strength and flexural strength of composite goes on increasing as the fiber loading increases upto 24 wt% fiber content and was found to be 70.38 and 52.26 MPa respectively. Analysis of failure of fractured surface is carried out using SEM as a result of matrix cracking, void content and fiber pullout.

Keywords Date palm · Petiole · Rachis · Epoxy · Surface modification · NaOH · SEM

1 Introduction

Recently, there has been a speedy expansion in research and modernization of natural fiber reinforced composites (NFC). Major importance is given to NFC than synthetic fiber composites (SFC) because of its various plus points such as easy availability, lower cost, bio-degradable, environmental friendly, non-hazardous, non-toxic with acceptable specific mechanical properties. Various researchers explained that utilization of green material in polymer composites not only replacing the harmful synthetic

J. Dehury (✉) · J. Mohanty
Department of Mechanical Engineering, Veer Surendra Sai University of Technology (VSSUT), Burla, India

S. Pal et al. (eds.), *Processing and Characterization of Materials*, Springer Proceedings in Materials 13, https://doi.org/10.1007/978-981-16-3937-1_32

fiber but also control the pollution, and gave better mechanical properties. This growing demand for various materials applicable for different types of applications directed towards expansion and development of polymeric composites with different parts of natural fibers as reinforcing agents. Therefore, researchers are showing their strong interest on developing natural fibers by considering different parts of natural fiber such as leaf, stem, trunk, branches, fruits etc. Srinivasa and Bharath [1, 2] studied about treatment of alkali and impact on polymer composites with areca fiber. They concluded that KOH treatment gives better surface bonding of matrix and fiber. Kabir et al. [3] in their review paper they have specified that alkali, stearic acid, silane, acetylation, coupling agents, peroxide, permanganate, sodium chlorite, triazine, isocynate, fatty acid derivate (oleoyl chloride), benzoylation, fungal, acrylation and acrylonitrile grafting treatments improve thermo-mechanical properties as well as dimensional stability of resultant composites. Tripathy et al. [4] analysed the matrix compatibility of fiber for improvement of the characteristics of composite overally by carrying out treatment through chemicals on the surface of the fibers. Chemical treatment of fiber is not only improves dimensional stability but also enhances the mechanical properties [5, 6]. Boynard et al. [7] studied that alkaline treatment changes the mechanical characteristics of Luffa-fiber reinforced polyester resin. They showed that mechanical as well as flexural properties increased with alkali treatment which they explained in relation to contact area and surface roughness. Oushabi et al. [8] studied about thermal, mechanical as well micro-structure of date palm fibers (DPFs) and interface of DPF-Polyurethane composite. They concluded that treating with alkali can eliminate cellulose materials which are not required increase the strength of the fibers. Sulaiman [9] studied the Date palm fibre as a material which can be used for insulation and found that the type of resin, pressure during curing and the fibre-resin ratio are important factors that affecting the thermal conductivity. However, the size and orientation of fibre is negligible effect on thermal conductivity.

2 Materials and Methods

In the present research, a series of composites were fabricated using conventional hand layup technique by varying the wt% of fiber from 0 to 32 with an interval of 8 (see Table 1). Here alkali treated petiole part of date palm fiber were consider as a reinforcing material and Epoxy resin LY556 and corresponding harder as a binder. Epoxy with hardener for 10:1 proportion is mixed together as per wt% and recommendation of mixing ratio, and then cured at room temperature to examine the significance of fiber concentration on physical characteristics such as absorption of water, density, fraction of voids and mechanical characteristics of the composites like compressive and tensile strength, impact energy and flexural strength.

Table 1 Composite composition

Composites	Fiber content (wt%)	Matrix content (wt%)
DPP0	0	100
DPP1	8	92
DPP2	16	84
DPP3	24	76
DPP4	32	68

2.1 Testing of Physical Properties

Theoretical density of composites specimens has been measured according Agrawal and Broutman Equation [10] and the experimental density of composites specimens has been measured using the water displacement method. A Square specimen with size 10 mm × 10 mm was cut and the weights was measured using digital balance with a 10–3 g resolution. Then it was allowed to be absorbed in distilled water at room temperature. The mean density has been calculated by taking average of five specimens of each group. A critical problem in the application of natural fibers is moisture absorption. Therefore, water absorption test was done (ASTM D 570-98 standard). We weighted specimens at a regular interval of 24 h. The mathematical equations are given below for calculating void percentage, density and water absorption properties.

$$\rho_{\text{th}} = \frac{1}{\frac{\text{wf}}{\rho\text{f}} + \frac{\text{w}_\text{m}}{\rho_\text{m}}} \tag{1}$$

$$Void(\%) = \frac{\rho_{\text{th}} - \rho_{\text{exp}}}{\rho_{\text{th}}} \times 100 \tag{2}$$

$$Wa\ \% = \frac{\text{Wt} - \text{Wo}}{\text{Wo}} \times 100 \tag{3}$$

w_f = weight % of fibre, w_m = weight % of matrix, ρ_f = theoretical density of fibre, ρ_m = theoretical density of matrix, w_t = weight of specimen after t hours of immersion and w_o = initial weight.

2.2 Testing of Mechanical Properties

The tensile test of composite specimen has been measured according to ASTM 638 standard. The test has been done using a Servo hydraulic static testing (INSTRON 3382) machine. Composites of fiber loading of five different samples (0, 8, 16, 24 and 32%) are recorded for the average values for analysis. 2 mm/min of cross-head speed was used for tests maintaining the required temperature. Flexural tests were also carried out in the same machine by using three-point bending attachment at the

same speed as per ASTM 790 standard. Compressive test was also performed in INSTRON 3382 and average data has been note down for examine. The compressive strength of composite specimen has been measured by using same machine with replacement of only the attachment and recorded the results for analysis. Impact test was conducted to get information about how the material withstands fracture during impact loads. All the specimens were prepared/cut as per ASTM 256 (1989) standard and tested on Charpy Impact testing machine. Notches of the specimen were kept at the middle and fixed as simply supported. Then the specimen was hit with high impact by dropping it from a height with the velocity of 3.4 m/s. For each loading condition, samples tested were five and the average of all was recorded for analysis.

2.3 Micro-structural Analysis

The micro-strucure of composites was observed with HITACHI SU350 Scanning Electron Microscope (SEM). The surface and interface of matrix were observed for analysis of the composites.

3 Results and Discussion

3.1 Physical Properties

Density plays a significant role in other properties of the composites as well. It depends upon amount of fiber and matrix materials and their individual proportions. There is some percentage variation between theoretical and experimental densities, due to presence of voids inside the fabricated samples of the composites as illustrated in the Table 2.

From Table 2 and Fig. 1 it was observed that due to increase in fiber concentration, the percentage of voids also increases. This is because of the presence of maximum amount of cellulose in natural fiber.

Table 2 Theoretical density, experimental density and void percentage of composites

Composites	Theoretical density (g/cc)	Experimental density (g/cc)	Void fraction (%)
DPP0	1.20	1.197	0.250
DPP1	1.146	1.138	0.654
DPP2	1.098	1.089	0.819
DPP3	1.053	1.042	1.044
DPP4	1.012	0.985	2.667

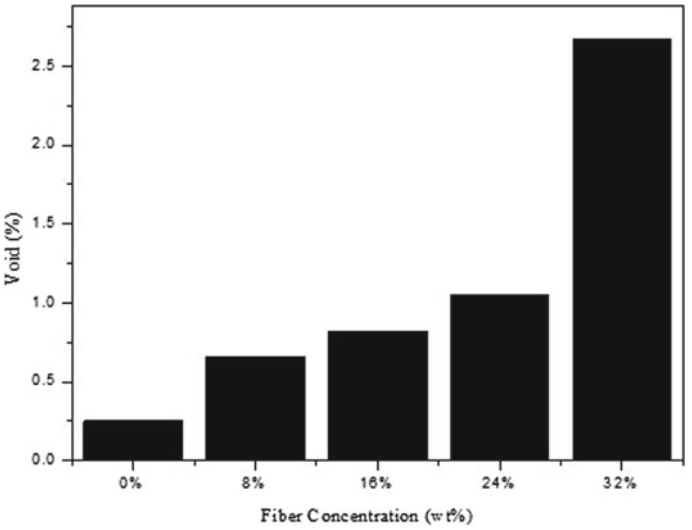

Fig. 1 Void (%) of DatePalm petiole/epoxy composites at different fiber loading

Figure 2 shows that as the reinforcement of fiber goes on increasing, the rate absorption of water increases almost linearly. The composite with 32% fiber loading shows maximum water carrying capacity. The similar behaviour was also observed by previous researchers [2]. This is because natural fiber contents maximum amount of cellulose.

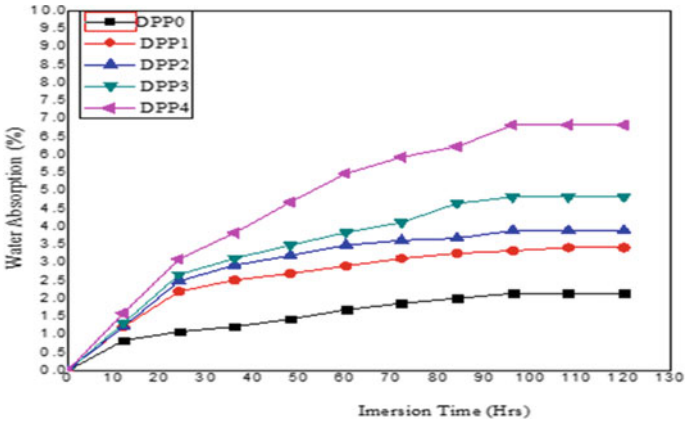

Fig. 2 Water absorption (%) of DatePalm petiole/epoxy composites at different fiber loading

3.2 Mechanical Properties

Figure 3 shows that as the fiber loading increases, the tensile strength also increases, up to 16 wt% and then decreases. The 16 wt% DPP composite shows a very appreciable increase in tensile strength whereas at 24–32 wt% it loses its ductility. Hence there is decrease in tensile strength. Figure 4 however revealed that the tensile modulus shows an increasing trend in a linear pattern with the increase in fiber concentration. The maximum tensile modulus was found at 32 wt% fiber loading.

Flexural strength is the resistance of bending force before failure. Figure 5 shows that flexural strength raises up to 24 wt% of fiber and decreases when loading of fiber decreases. Initially, rise in flexural strength up to 24 wt% fiber loading is mainly due to reinforcing effect by the fibers. This resulted into an uniform stress distribution from continuous matrix phase to dispersed fiber phase. When fiber content is above 24 wt%, then there is a decrease in flexural strength. The decline in flexural strength at high fiber content is on the account of poor fiber-matrix adhesion, which encouraged the formation of micro-crack at interface and also loses its bending nature. The trend of increased flexural strength with increased fiber content is similar to the result from tensile strength. In case of higher fiber content the resistance to shearing decreases due to poor interfacial adhesion and the failure takes place due to shear. The decrement in flexural strength at 32 wt% fiber content is a result of shear failure.

Variation in impact strength of the composites according to fiber loading is depicted in Fig. 6. It is observed that with increase in fiber loading from 0 to 16 wt%, the Impact Energy increase. However with the further rise in fiber loading, it goes on decreases. Composite with 16 wt% fiber loading absorb more energy than the others,

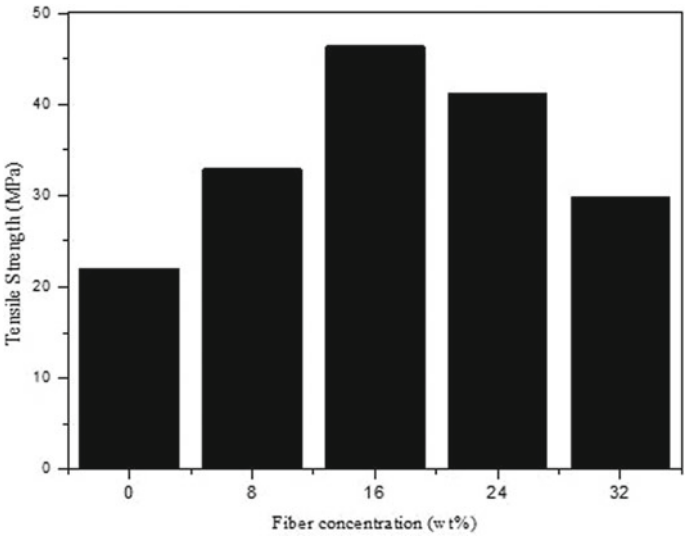

Fig. 3 Tensile strength of DatePalm petiole/epoxy composites at different fiber loading

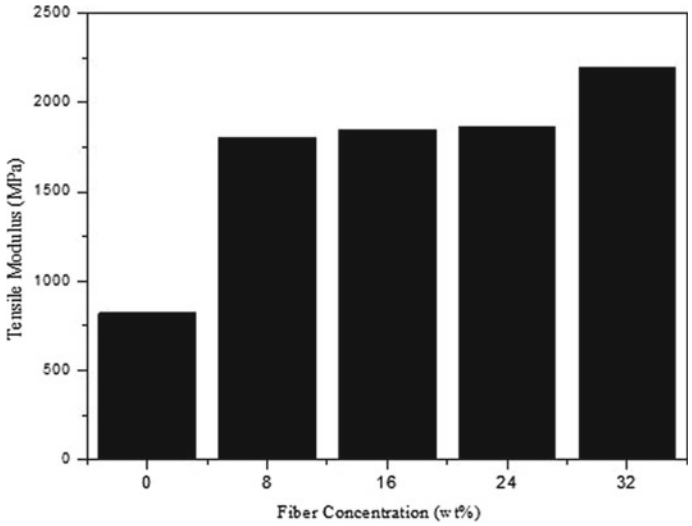

Fig. 4 Tensile modulus of DatePalm petiole/epoxy composites at different fiber loading

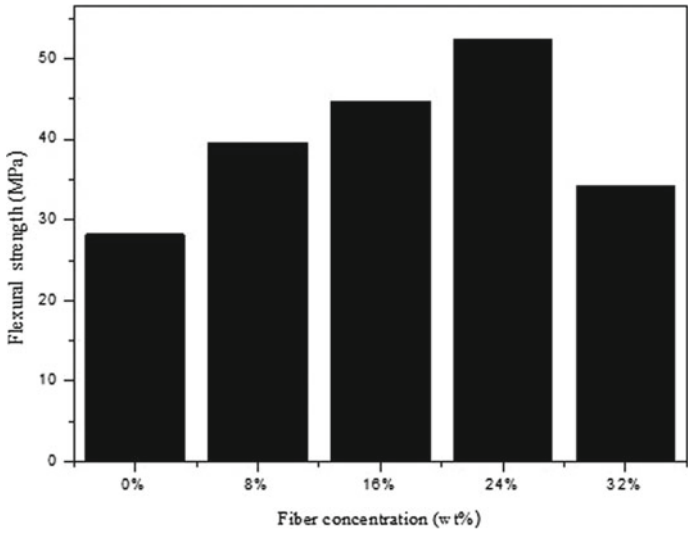

Fig. 5 Flexural strength of DatePalm petiole/epoxy composites at different fiber loading

the reason for the higher impact strength is proper fiber arrangement on composite result in difficult in propagation of crack with further increase in fiber concentration crack formation occurs this may be due to the presence of voids.

The fluctuation in compressive strength with respect to fiber loading is presented in Fig. 7. It reveals that initially the compressive strength increases with increase

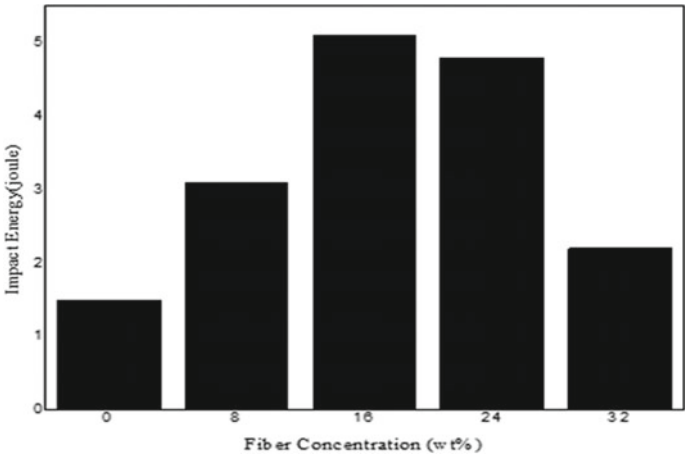

Fig. 6 Impact energy of DatePalm petiole/epoxy composites at different fiber loading

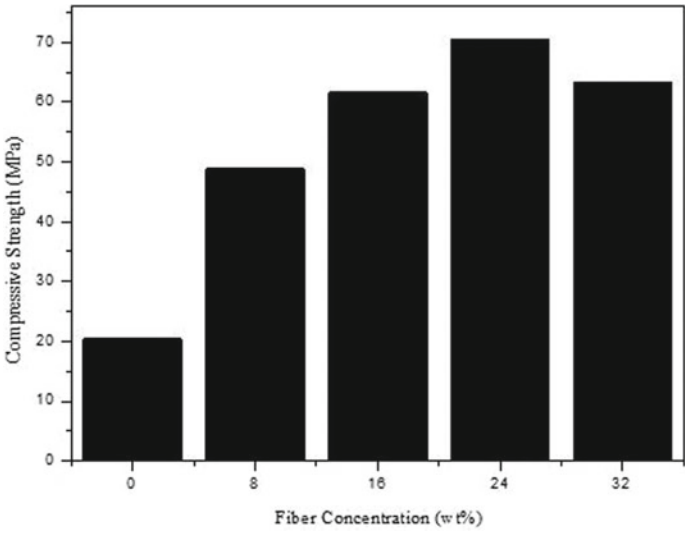

Fig. 7 Compressive strength of DatePalm petiole/epoxy composites at different fiber loading

in fiber loading from 0 to 24 wt%. Further increases in fiber loading, compressive strength decreases because loses its ductility and hence a moderate ductile fracture occur.

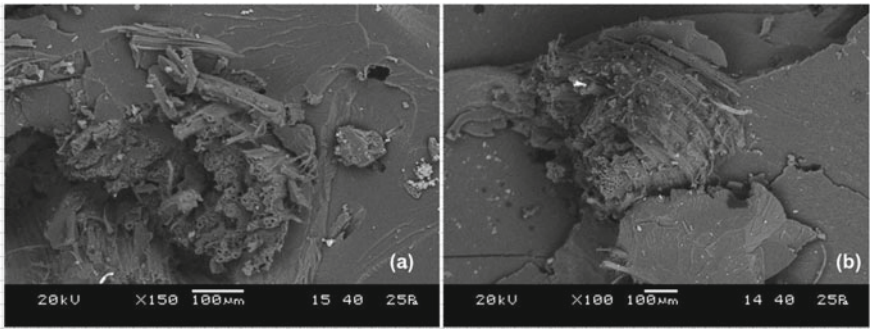

Fig. 8 Fracture analysis of DatePalm petiole/epoxy composites at different fiber loading

3.3 Surface Morphology of Fracture Surface

The microstructure of the broken samples after flexural tests of the DPP composite was performed using Scanning Electron Microscope. Figure 8a, b illustrate the SEM image of fractured surface of composite specimen with 16 and 24 wt% fiber loading respectively. It was found that the fibers were not so good in adhesion from the resin surface because of poor interfacial bonding. Also it was observed that amuser of void and matrix cracking was there.

4 Conclusions

In this study an investigation was made to know how the fiber alteration and the reinforcement composition influence the physio-mechanical behaviours of alkali treated date palm petiole-Epoxy composite. The experiment was conducted for comparison of variation properties like mechanical and physical characteristics of various fiber loading for the date palm petiole-fiber composite. From the above results and discussion it is concluded that (i) A set of new date palm petiole-Epoxy composites were successfully prepared by using conventional hand lay-up technique. (ii) The maximum void content and water absorption were found in case of maximum fiber loading composites, but the minimum value was obtained in case of only epoxy composite. This is due to the presence maximum amount of hydroxyl group in natural fiber. (iii) The mechanical characteristics such as tensile strength, impact energy, flexural strength and the compressive strength of composites were increases directly with fiber loading up to certain extend and then decreases negatively. This is on the account of improper adhesion between fiber–matrix interfaces. The maximum impact energy and tensile strength were obtained 5.1 J and 46.40 MPa respectively for the composites with 16 wt% fiber content. However the maximum compressive strength and flexural strength of composite is found 70.38 and 52.26 MPa respectively for the composites with 24 wt% fiber loading. (iv) It was observed from the

SEM images that the fibre pull-out, cracks, void content and matrix cracking are main reasons behind the tensile failure.

References

1. Srinivasa CV, Bharath KN (2013) Effect of alkali treatment on impact behaviour of areca fibers reinforced polymer composites. World Acad Sci Eng Technol Int J Chem Nuclear Metall Mater Eng 7(4)
2. Medina L, Schledjewski R, Schlarb AK (2009) Process related mechanical properties of press molded natural fiber reinforced polymers. Compos Sci Technol 69(9):1404–1411
3. Kabir M, Wang H, Lau KT, Cardona F (2012) Chemical treatments on plant-based natural fibre reinforced polymer composites: an overview. Compos Part B 43:2883–2892
4. Tripathy S, Dehury J, Mishra D (2016) A study on the effect of surface treatment on the physical and mechanical properties of date palm stem fiber embedded epoxy composites. Mater Sci Eng 115(1)
5. Bledzki AK, Gassan J (1999) Composites reinforced with cellulose based fibres. Prog Polym Sci 24(2):221–274
6. Das M, Chakraborty D (2006) Influence of alkali treatment on the fine structure and morphology of bamboo fibers. J Appl Polym Sci 102(5):5050–5056
7. Boynard CA, Monteiro SN, D'Almeida JRM (2003) Aspects of alkali treatment of sponge gourd (LuffaCylindrica) fibers on the flexural properties of polyester matrix composites. J Appl Polym Sci 87(12):1927–1932
8. Oushabi A, Sair S, Oudrhiri Hassani F, Abboud Y, Tanane O, El BA (2017) The effect of alkali treatment on mechanical, morphological and thermal properties of date palm fibers (DPFs): study of the interface of DPF-polyurethane composite. S Afr J Chem Eng 23:116–123
9. Al-Sulaiman FA (2003) Date palm fibre reinforced composite as a new insulating material. Int J Energy Res 27:1293–1297
10. Agrawal BD, Broutman LJ (1990) Analysis and performance of fiber composites, 2nd edn. John Wiley & Sons, Inc, pp 2–6

Crack Orientation Effects on Vibration Characteristics of Bi-directional Linearly Varying Thickness Partially Cracked Isotropic Micro-plate: An Analytical Approach

Bhupesh Kumar Chandrakar, N. K. Jain, and Ankur Gupta

Abstract The various orientation of crack and different length scale parameter values affects the vibrational characteristics of a isotropic cracked tapered micro-plate in the current work. Linear variation in the plate thickness is assumed in two directions. The partial crack is in the centre, and arbitrary orientations are considered. The equilibrium principle is used to develop a tapered isotropic plate's governing equation based on classical plate theory (CPT). Using the non-classical modified couple stress theory (MCST), the microstructure effect was also included in the governing equation. The line spring model (LSM) is used in in-plane forces and bending moments to account for the impact of a partial crack on plate dynamics. The Berger's formulation introduces nonlinearity to the model. Galerkin's method was chosen to transform the derived governing equation into time-dependent modal coordinates, and the nonlinear Duffing equation was solved using an approximate solution technique. The results of an isotropic bi-directional linearly varying thickness cracked micro-plate are discussed. The effects of crack angle, crack size, taper constant, and length scale parameter variations are calculated for different boundary conditions for a cracked isotropic micro-plate and found to influence vibration characteristics.

Keywords Micro-plate · Crack · Variable thickness · Vibration

1 Introduction

Recent studies suggest that the plate structures have significantly contributed to large application areas in building complicated structures. An improved design consideration always involves the structure should be of reduced weight but possess high strength. To achieve these properties, plates with non-uniform thickness are uses

B. K. Chandrakar (✉) · N. K. Jain · A. Gupta
Department of Mechanical Engineering, National Institute of Technology Raipur (C.G.), Raipur 492010, India

N. K. Jain
e-mail: nkjain.me@nitrr.ac.in

S. Pal et al. (eds.), *Processing and Characterization of Materials*, Springer Proceedings in Materials 13, https://doi.org/10.1007/978-981-16-3937-1_33

significantly; further, the properties can be optimised by selecting desired material like isotropic, FGM, and orthotropic. A precise review on cracked structures vibration is presented by Dimarogonas [1]. Rice and Levy [2] developed the LSM using CPT. The LSM model for a centrally located continuous line cracked isotropic plate to develop an analytical model for the vibrational analysis have used by Israr et al. [3]. To understand the crack orientation behavior on isotropic plate's, Ismail and Cartmell [4] have proposed an analytical method to determine the fundamental frequencies. Joshi et al. [4–6] have used CPT and LSM for the vibration study of isotropic internally cracked plate [4], internally cracked orthotropic/FGM plate [5], and partially cracked orthotropic rectangular plate [6] using classical plate theory (CPT) and the LSM. Yang et al. [7] introduced the MCST, and the couple stress tensor is taken into account symmetric. Gupta et al. [8] have used CPT in the combination of MCST to developed partially cracked analytical models of isotropic, FGM, and micro-plate for vibration analysis. They also demonstrated how fibre orientation affects fundamental frequency in orthotropic micro-plates [9]. By shifting the crack centre to the left and right sides of the plate's centre line, Gupta et al. [10] investigated the crack position influences on vibration of Isotropic and FGM tapered micro-plates. It is worth saying that no such work has been published to date on vibration analysis checking the vibrational characteristics of a cracked isotropic micro-plate of bi-directional linearly varying thicknesses and crack orientations.

1.1 Governing Equation

According to numerous works of literature, the equation that governs varying thickness isotropic plate is:

$$\begin{aligned}&\frac{\partial^2}{\partial x^2}\left\{D(x,y)\left(\frac{\partial^2 w}{\partial x^2}+\frac{\partial^2 w}{\partial y^2}\right)\right\}+\frac{\partial^2}{\partial y^2}\left\{D(x,y)\left(\frac{\partial^2 w}{\partial x^2}+\frac{\partial^2 w}{\partial y^2}\right)\right\}\\&-(1-\nu)\left(\frac{\partial^2 D(x,y)}{\partial y^2}\frac{\partial^2 w}{\partial x^2}-2\frac{\partial^2 D(x,y)}{\partial x\partial y}\frac{\partial^2 w}{\partial x\partial y}+\frac{\partial^2 D(x,y)}{\partial x^2}\frac{\partial^2 w}{\partial y^2}\right)\\&=-\rho h\frac{\partial^2 w}{\partial t^2}+N_x\frac{\partial^2 w}{\partial x^2}+N_y\frac{\partial^2 w}{\partial y^2}+2N_{xy}\frac{\partial^2 w}{\partial x\partial y}+P_z\end{aligned}$$

A new governing equation for isotropic tapered plate with crack orientation is derived using a length scale parameter with crack orientation and using the same method as [4], which is described here.

$$\begin{aligned}&\frac{\partial^2}{\partial x^2}\left\{D^*(x,y)\left(\frac{\partial^2 w}{\partial x^2}+\frac{\partial^2 w}{\partial y^2}\right)\right\}+\frac{\partial^2}{\partial y^2}\left\{D^*(x,y)\left(\frac{\partial^2 w}{\partial x^2}+\frac{\partial^2 w}{\partial y^2}\right)\right\}\\&-(1-\nu)\left(\frac{\partial^2 D^*(x,y)}{\partial y^2}\frac{\partial^2 w}{\partial x^2}-2\frac{\partial^2 D^*(x,y)}{\partial x\partial y}\frac{\partial^2 w}{\partial x\partial y}+\frac{\partial^2 D^*(x,y)}{\partial x^2}\frac{\partial^2 w}{\partial y^2}\right)\end{aligned}$$

$$= -\rho h \frac{\partial^2 w}{\partial t^2} + N_x^* \frac{\partial^2 w}{\partial x^2} + N_y^* \frac{\partial^2 w}{\partial y^2} + 2N_{xy}^* \frac{\partial^2 w}{\partial x \partial y} + 2\frac{\partial^2 M_{xy}^*}{\partial x \partial y} + \frac{\partial^2 M_y^*}{\partial y^2} + P_z$$

Here $D^*(x, y) = D(x, y) + D_l(x, y)$ where flexural rigidity $D(x, y) = \frac{Eh^3(x,y)}{12(1-\nu^2)}$ and additional flexural rigidity $D_l(x, y) = \frac{El^2 h(x,y)}{2(1+\nu)}$.

$$N_x^* = \frac{a(1-\cos 2\beta)}{(6\varepsilon_{bt} + \varepsilon_{tt})(1-\nu^2)h_c + 2a} N_x,\ N_y^* = \frac{a(1+\cos 2\beta)}{(6\varepsilon_{bt} + \varepsilon_{tt})(1-\nu^2)h_c + 2a} N_y$$

$$M_y^* = \frac{a(1+\cos 2\beta)}{3\left(\frac{\varepsilon_{tb}}{6} + \varepsilon_{bb}\right)(3+\nu)(1+\nu)h_c + 2a} M_y$$

$$M_{xy}^* = \frac{a(\sin 2\beta)}{3\left(\frac{\varepsilon_{tb}}{6} + \varepsilon_{bb}\right)(3+\nu)(1+\nu)h_c + 2a} M_y,\ N_{xy}^* = \frac{a(\sin 2\beta)}{(6\varepsilon_{bt} + \varepsilon_{tt})(1+\nu)h_c + 2a} N_y$$

where N_x^*,N_y^*, M_y^*, N_{xy}^* and M_{xy}^* are the crack terms as given in the literature [4].

1.2 The Solution of Governing Equation

The plate under transverse load consideration's transverse deflection is calculated by introducing the characteristic modal functions in the final governing equation for variable thickness isotropic cracked micro-plate. The most general form of the deflection equation based on the plate's boundary condition is as follows:

$$w(x, y, t) = \sum_{p=1}^{\infty} \sum_{q=1}^{\infty} A_{pq} X_p Y_q \phi_{pq}(t)$$

Here X_p, Y_q, A_{pq} and $\phi_{pq}(t)$ are well expressed in Ref. [3].

$$M_{pq} \frac{\partial^2 f_{pq}(t)}{\partial t^2} + K_{pq} f_{pq}(t) + G_{pq} f_{pq}(t)^3 = 0$$

Comparing the final solution to the above Duffing equation, the final equation for natural frequency (ω_{pq}) can be found.

$$\omega_{pq} = \sqrt{\frac{K_{pq}}{M_{pq}}}$$

$$M_{pq} = \rho h \sum_{p=1}^{\infty} \sum_{q=1}^{\infty} A_{pq} \int_0^{L_1} \int_0^{L_2} X_p^2 Y_q^2 dx dy$$

$$K_{pq} = \sum_{q=1}^{\infty}\sum_{p=1}^{\infty} A_{pq} \int_0^{L_1}\int_0^{L_2} D^*(x,y)\left(X_p^{iv}Y_q + 2X_p^{ii}Y_q^{ii} + X_pY_q^{iv}\right)X_pY_q\,dxdy$$

$$+ \sum_{q=1}^{\infty}\sum_{p=1}^{\infty} A_{pq} \int_0^{L_1}\int_0^{L_2} 2\frac{\partial}{\partial x}D^*(x,y)\left(X_p^{iii}Y_q + X_p^{i}Y_q^{ii}\right)X_pY_q\,dxdy$$

$$+ \sum_{q=1}^{\infty}\sum_{p=1}^{\infty} A_{pq} \int_0^{L_1}\int_0^{L_2} 2\frac{\partial}{\partial y}D^*(x,y)\left(X_pY_q^{iii} + X_p^{ii}Y_q^{i}\right)X_pY_q\,dxdy$$

$$+ \sum_{q=1}^{\infty}\sum_{p=1}^{\infty} A_{pq} \int_0^{L_1}\int_0^{L_2} \frac{\partial^2}{\partial x^2}D^*(x,y)\left(X_p^{ii}Y_q + \nu X_pY_q^{ii}\right)X_pY_q\,dxdy$$

$$+ \sum_{q=1}^{\infty}\sum_{p=1}^{\infty} A_{pq} \int_0^{L_1}\int_0^{L_2} \frac{\partial^2}{\partial y^2}D^*(x,y)\left(X_pY_q^{ii} + \nu X_p^{ii}Y_q\right)X_pY_q\,dxdy$$

$$+ \sum_{q=1}^{\infty}\sum_{p=1}^{\infty} A_{pq} \int_0^{L_1}\int_0^{L_2} 2\frac{\partial^2 D^*(x,y)}{\partial x\partial y}(1-\nu)X_p^{i}Y_q^{i}X_pY_q\,dxdy$$

$$+ \sum_{q=1}^{\infty}\sum_{p=1}^{\infty} A_{pq} \int_0^{L_1}\int_0^{L_2} \frac{\partial^2}{\partial y^2}\left(\frac{-a(1+\cos 2\beta)D^*(x,y)\left(X_pY_q^{ii} + \nu X_p^{ii}Y_q\right)}{3\left(\frac{\varepsilon_{tb}}{6}+\varepsilon_{bb}\right)(3+\nu)(1+\nu)h_c + 2a}\right)X_pY_q\,dxdy$$

$$+ \sum_{q=1}^{\infty}\sum_{p=1}^{\infty} A_{pq} \int_0^{L_1}\int_0^{L_2} \frac{\partial^2}{\partial x\partial y}\left(\frac{-2a(\sin 2\beta)D^*(x,y)\left(X_pY_q^{ii} + \nu X_p^{ii}Y_q\right)}{3\left(\frac{\varepsilon_{tb}}{6}+\varepsilon_{bb}\right)(3+\nu)(1+\nu)h_c + 2a}\right)X_pY_q\,dxdy$$

$$G_{pq} = \sum_{q=1}^{\infty}\sum_{p=1}^{\infty} A_{pq}^3 \int_0^{L_1}\int_0^{L_2} \left\{\frac{a(1+\cos 2\beta)B_{2pq}Y_q^{ii}Y_qX_p^2}{(6\alpha_{bt}+\alpha_{tt})(1-\nu^2)h_c + 2a}\right.$$

$$\left. - B_{1pq}X_p^{ii}X_pY_q^2 + \frac{2a\sin 2\beta B_{2pq}X_p^{i}Y_q^{i}X_pY_q}{(6\alpha_{bt}+\alpha_{tt})(1+\nu)h_c + 2a}\right\}dxdy$$

$$B_{1pq} = \frac{6D^*(x,y)}{h^2L_1L_2}\sum_{q=1}^{\infty}\sum_{p=1}^{\infty}\int_0^{L_1}\int_0^{L_2}\left\{\left(\frac{\partial X_p}{\partial x}\right)^2Y_q^2 + \nu\left(\frac{\partial Y_q}{\partial y}\right)^2X_p^2\right\}dxdy$$

$$- \frac{6}{L_1L_2}\int_0^{L_1}\int_0^{L_2}\left\{\frac{\partial}{\partial x\partial y}\left[\frac{12D^*(x,y)}{h^2(x,y)}\right]\right.$$

$$\left.\int_0^{L_1}\int_0^{L_2}\left(\left(\frac{\partial X_p}{\partial x}\right)^2Y_q^2 + \nu\left(\frac{\partial Y_q}{\partial y}\right)^2X_p^2\right)dxdy\right\}dxdy$$

$$B_{2pq} = \frac{6D^*(x,y)}{h^2 L_1 L_2} \sum_{q=1}^{\infty}\sum_{p=1}^{\infty} \int_0^{L_1}\int_0^{L_2} \left\{ \left(\frac{\partial Y_q}{\partial y}\right)^2 X_p^2 + \nu \left(\frac{\partial X_p}{\partial x}\right)^2 Y_q^2 \right\} dxdy$$
$$- \frac{6}{L_1 L_2} \int_0^{L_1}\int_0^{L_2} \left\{ \frac{\partial}{\partial x \partial y}\left[\frac{12D^*(x,y)}{h^2(x,y)}\right] \right.$$
$$\left. \int_0^{L_1}\int_0^{L_2} \left(\left(\frac{\partial Y_q}{\partial y}\right)^2 X_p^2 + \nu \left(\frac{\partial X_p}{\partial x}\right)^2 Y_q^2 \right) dxdy \right\} dxdy$$

1.3 Bi-directional Linearly Varying Thickness Isotropic Micro-plate

Bi-axial linearly variable thickness 'h' is given by

$$h = h_m \left(1 + \frac{\zeta x}{L_1} + \frac{\eta y}{L_2}\right)$$

The minimum plate thickness is h_m, h_c is the thickness at the crack centre and ζ and η are the taper parameters in X and Y-directions, respectively. Thus, h_m and h_c can be defined as;

$$h_m = \frac{0.01}{1 + \frac{\zeta}{2} + \frac{\eta}{2}}, h_c = h_m \left(1 + \frac{\zeta}{2} + \frac{\eta}{2}\right), D_0 = \frac{E h_m^3}{12(1-\nu^2)}, D_{l0} = \frac{E l^2 h_m}{2(1+\nu)}.$$

The flexural stiffness corresponding to minimum thickness is $D_0.D_{l0}$ is the additional flexible stiffness due to the micro-plate theory's.

$$K_{pq}$$
$$= \sum_{q=1}^{\infty}\sum_{p=1}^{\infty} A_{pq} \int_0^{L_1}\int_0^{L_2} \left(D_0 \left(1 + \frac{\zeta x}{L_1} + \frac{\eta y}{L_2}\right)^3 \right.$$
$$\left. + D_{l0}\left(1 + \frac{\zeta x}{L_1} + \frac{\eta y}{L_2}\right)\right)\left(X_p^{iv} Y_q + 2X_p^{ii} Y_q^{ii} + X_p Y_q^{iv}\right) X_p Y_q dxdy$$
$$+ \sum_{q=1}^{\infty}\sum_{p=1}^{\infty} A_{pq} \int_0^{L_1}\int_0^{L_2} \left(6D_0 \frac{\zeta}{L_1}\left(1 + \frac{\zeta x}{L_1} + \frac{\eta y}{L_2}\right)^2 + 2D_{l\,0} \frac{\zeta}{L_1}\right)$$
$$\left(X_p^{iii} Y_q + X_p^{i} Y_q^{ii}\right) X_p Y_q dxdy$$
$$+ \sum_{q=1}^{\infty}\sum_{p=1}^{\infty} A_{pq} \int_0^{L_1}\int_0^{L_2} \left(6D_0 \frac{\eta}{L_2}\left(1 + \frac{\zeta x}{L_1} + \frac{\eta y}{L_2}\right)^2 + 2D_{l\,0} \frac{\eta}{L_2}\right)$$

$$\left(X_q\, Y_q^{iii} + X_p^{ii}\, Y_q^{i}\right) X_p Y_q dxdy$$

$$+\sum_{q=1}^{\infty}\sum_{p=1}^{\infty} A_{pq} \int_0^{L_1}\int_0^{L_2} 6D_0 \frac{\zeta^2}{L_1^2}\left(1+\frac{\zeta x}{L_1}+\frac{\eta y}{L_2}\right)$$

$$\left(X_p^{ii} Y_q + \nu X_p Y_q^{ii}\right) X_p Y_q dxdy$$

$$+\sum_{q=1}^{\infty}\sum_{p=1}^{\infty} A_{pq} \int_0^{L_1}\int_0^{L_2} 6D_0 \frac{\eta^2}{L_2^2}\left(1+\frac{\zeta x}{L_1}+\frac{\eta y}{L_2}\right)$$

$$\left(X_p^{ii} Y_q + \nu X_p Y_q^{ii}\right) X_p Y_q dxdy$$

$$+\sum_{q=1}^{\infty}\sum_{p=1}^{\infty} A_{pq} \int_0^{L_1}\int_0^{L_2} 6D_0 \frac{\zeta\eta}{L_1 L_2}\left(1+\frac{\zeta x}{L_1}+\frac{\eta y}{L_2}\right)$$

$$(1-\nu) X_p^i Y_q^i X_p Y_q dxdy$$

$$+\sum_{q=1}^{\infty}\sum_{p=1}^{\infty} A_{pq} \int_0^{L_1}$$

$$\int_0^{L_2}\left(\frac{-a(1+\cos 2\beta)\left(D_0\left(1+\frac{\zeta x}{L_1}+\frac{\eta y}{L_2}\right)^3 + D_{l0}\left(1+\frac{\zeta x}{L_1}+\frac{\eta y}{L_2}\right)\right)\left(X_p Y_q^{iv} + \nu X_p^{ii} Y_q^{ii}\right)}{3\left(\frac{\varepsilon_{tb}}{6}+\varepsilon_{bb}\right)(3+\nu)(1+\nu)h_c + 2a}\right) X_p Y_q dxdy$$

$$+\sum_{q=1}^{\infty}\sum_{p=1}^{\infty} A_{pq} \int_0^{L_1}$$

$$\int_0^{L_2}\left(\frac{-2a(\sin 2\beta)\left(D_0\left(1+\frac{\zeta x}{L_1}+\frac{\eta y}{L_2}\right)^3 + D_{l0}\left(1+\frac{\zeta x}{L_1}+\frac{\eta y}{L_2}\right)\right)\left(X_p X_p^i Y_q^{iii} + \nu X_p^{iii} Y_q Y_q^i\right)}{3\left(\frac{\varepsilon_{tb}}{6}+\varepsilon_{bb}\right)(3+\nu)(1+\nu)h_c + 2a}\right) X_p Y_q dxdy$$

2 Results and Discussions

Young's modulus = 70.3GPa, Poisson's ratio = 0.33, and plate density = 2660 kg/m^3 are the mechanical properties of the chosen isotropic material [4, 9]. The present study employs two boundary conditions: SSSS (all edges of the plate are simply supported) and CCSS (two adjacent edges are clamped, and another two are simply supported). With the work of Refs. [4] and [9], the free vibration of uniform thickness isotropic plate with different crack angles (Table 1) and length scale parameters (Table 2) is validated. When the taper parameter values are taken ($\zeta = \eta = 0$), the current non-uniform thickness model reduces to a plate of uniform thickness. Tables 1 and 2 demonstrate that the SSSS and CCSS boundary conditions are in good agreement. As a result, the authors' decision to extend the current research to isotropic tapered plates appears justified.

Furthermore, the fundamental frequency rises as the crack angle's value increase from 0^0 to 90^0 in Table 3. A similar response is seen in the work of Ref. [4] for

Table 1 For various boundary conditions and crack orientation angles, fundamental frequencies of the uniform thickness ($\zeta = \eta = 0$) plate models

B.C	Crack orientation angle	Fundamental frequency, $\omega_{m\,n}$(rad/s),			
		Intact plate (a = 0.0 m)		Cracked plate (a = 0.003 m)	
	β(deg.)	Plate dimensions			
		l1 = 0.3			
		l2 = 0.3			
		Present analysis	Ref. [4]	Present analysis	Ref. [4]
SSSS		258.6	258.6	–	–
	0			250.93	251.81
	20			251.84	252.61
	40			254.13	254.64
	60			256.70	256.92
	80			258.37	258.40
	90			258.60	258.60
CCSS		1485.6	1485.6	–	–
	0			1436.0	1441.70
	20			1442.0	1446.84
	40			1456.7	1459.88
	60			1473.3	1474.63
	80			1484.1	1484.22
	90			1485.6	1485.55

Table 2 Fundamental frequency parameters of the uniform thickness ($\zeta = \eta = 0$) cracked micro-plate models

Fundamental frequency parameter, $\delta_1 = \omega L^2\sqrt{(\rho\, h_m\, /D_o)}, \left(\frac{L_1}{L_2} = 1\right)$

B.C	Crack length ('a')	Modified couple stress theory					
		Length scale parameter, ('l')					
		0.0005		0.001		0.003	
		Present analysis	Ref. [9]	Present analysis	Ref. [9]	Present analysis	Ref. [9]
SSSS	0	19.838	19.835	20.132	20.129	23.049	23.032
	0.01	19.249	19.247	19.543	19.532	22.351	22.348
	0.05	18.055	18.053	18.323	18.321	20.965	20.962
	0.1	17.448	17.446	17.707	17.705	20.26	20.257
CCSS	0	28.490	28.486	28.912	28.908	33.081	33.077
	0.01	27.439	27.536	27.947	27.944	31.977	31.973
	0.05	25.600	25.597	25.979	25.976	29.725	29.721
	0.1	24.606	24.603	24.971	24.968	28.571	28.568

Table 3 For various boundary conditions and crack orientation angles, fundamental frequencies of the linearly varying thickness isotropic cracked micro-plate models

B.C	Crack angle	Fundamental frequency, ω_{mn}(rad/s),					
		Uniform thickness ($\zeta = \eta = 0$)			Varying thickness ($\zeta = \eta = 1$)		
	β(deg.)	Plate dimensions					
		l1 = 0.3					
		l2 = 0.3					
		l = 0.0001	l = 0.0002	l = 0.0003	l = 0.0001	l = 0.0002	l = 0.0003
SSSS	0	251.49	253.16	255.92	264.08	265.67	268.30
	20	252.40	254.08	256.85	265.89	267.48	270.11
	40	254.69	256.39	259.18	268.64	270.25	272.91
	60	257.28	258.99	261.81	271.05	272.68	275.36
	80	258.95	260.67	263.51	272.00	273.64	276.35
	90	259.18	260.90	263.75	272.36	273.81	276.72
CCSS	0	1439.2	1448.8	1464.6	1640	1648.4	1662.4
	20	1445.1	1454.7	1470.6	1653.8	1662.3	1676.3
	40	1459.9	1469.6	1485.7	1673.4	1681.9	1696.1
	60	1476.6	1486.4	1502.6	1689.4	1698.1	1712.3
	80	1487.4	1497.3	1513.6	1694.6	1703.3	1717.8
	90	1488.9	1498.8	1515.1	1695.2	1703.9	1718.4

an isotropic cracked plate of uniform thickness ($\zeta = \eta = 0$). As the length scale parameters and taper constant for bi-directional varying thickness are increased, the fundamental frequency parameter rises. A similar response is seen shown in the work of Ref. ([9, 11]). Table 3 shows that increasing the value of the length scale parameter, and taper parameters will also increase the natural frequency of Bi-directional linearly varying thickness isotropic micro- plate.

3 Conclusions

The current work analyses the vibration characteristics of an bi-directional linearly varying thickness isotropic cracked micro-plate based on CPT and MCST. New results of the cracked isotropic micro-plate's fundamental frequencies are obtained for the CCSS and SSSS boundary conditions, various internal length scale parameters, various crack angle, and taper parameters.

According to the findings, fundamental frequencies are influenced by taper parameters, crack lengths and crack orientation. Cracks reduce the natural frequency of

varying thickness plates, just as they do for uniform thickness plates. The fundamental frequencies are also found to increased as the crack angle, taper parameter, and length scale parameter are increased.

References

1. Dimarogonas AD (1996) Vibration of cracked structures: a state of the art review. Eng Fract Mech 55:831–857. https://doi.org/10.1016/0013-7944(94)00175-8
2. Rice JR, Levy N (1972) The part-through surface crack in an elastic plates 185–194
3. Israr A et al. Analytical modelling and vibration analysis of partially cracked rectangular. J App Mech. 76:011005-1–011005-9
4. Ismail R, Cartmell MPP (2012) An investigation into the vibration analysis of a plate with a surface crack of variable angular orientation. J Sound Vib 331:2929–2948. https://doi.org/10.1016/j.jsv.2012.02.011
5. Joshi PV, Jain NK, Ramtekkar GD (2014) Analytical modelling and vibration analysis of internally cracked rectangular plates. J Sound Vib 333:5851–5864. https://doi.org/10.1016/j.jsv.2014.06.028
6. Joshi PV, Jain NK, Ramtekkar GD (2015) Analytical modelling for vibration analysis of thin rectangular orthotropic/functionally graded plates with an internal crack. J Sound Vib 344:377–398. https://doi.org/10.1016/j.jsv.2015.01.026
7. Joshi PV, Jain NK, Ramtekkar GD (2015) Analytical modelling for vibration analysis of partially cracked orthotropic rectangular plates. Eur J Mech A/Solids 50:100–111. https://doi.org/10.1016/j.euromechsol.2014.11.007
8. Yang F, Tong P (2002) Couple stress based strain gradient theory for elasticity 39:2731–2743
9. Gupta A, Jain NK, Salhotra R, Joshi PV (2015) Effect of microstructure on vibration characteristics of partially cracked rectangular plates based on a modified couple stress theory. Int J Mech Sci 100:269–282. https://doi.org/10.1016/j.ijmecsci.2015.07.004
10. Gupta A, Jain NK, Salhotra R, Rawani AM, Joshi PV (2016) Effect of fibre orientation on nonlinear vibration of partially cracked thin rectangular orthotropic microplate: an analytical approach. Int J Mech Sci 105:378–397. https://doi.org/10.1016/j.ijmecsci.2015.11.020
11. Gupta A, Jain NK, Salhotra R, Joshi PV (2018) Effect of crack location on vibration analysis of partially cracked isotropic and FGM micro-plate with non-uniform thickness: an analytical approach. Int J Mech Sci 145:410–429. https://doi.org/10.1016/j.ijmecsci.2018.07.015

A Comparative Nanoindentation Study on HEA Coated FCC Metals and Stacking Fault Tetrahedra Evolution in HEA Coated Single Crystal Al: A MD Simulation Study

Dinesh Kumar Mishra, S. K. BadJena, and Snehanshu Pal

Abstract In the present study, the nanoindentation test has done on $Mo_{20}W_{20}Co_{20}Ta_{20}Zr_{20}$ (HEA) film-coated single crystal (SC) Cu and Al by replacing the substrate SC Ni in the earlier reported study to compare the underlying deformation activities and mechanical properties using molecular dynamics (MD) simulation. The development mechanism of stacking fault tetrahedra (SFT) in $Mo_{20}W_{20}Co_{20}Ta_{20}Zr_{20}$ coated SC Al has also been investigated. The comparative study suggests the appearance of different dislocation structures at higher indentation depth are effectively influence the plastic deformation in HEA-SC FCC specimens. The deformed structures seen in HEA-SC Ni are prismatic loops and interface distorted dislocations. The deformed structures seen in HEA-SC Cu are long lengthed Hirth partials, Lomer-Cottrell (LC) barriers, closed stair-rod partial dislocation steps, multi-dislocation loops, and complex distorted interface structures. The deformed structures seen in HEA-SC Al are SFT, LC barriers, closed stair-rod partial dislocation steps and loops. The SFT development in $Mo_{20}W_{20}Co_{20}Ta_{20}Zr_{20}$ coated SC Al is dislocation-based mechanism. The dislocation-based mechanism is primarily governed by stacking fault (SF) planes' interaction and dislocation gliding. The shear strain and displacement vector plots confirm the growth of distorted dislocation structure below the indenter tip in HEA coated SC Ni is relatively more symmetric and significant than others due to its high stiffness. In HEA coated SC Cu; the appearance of complex distorted dislocation structures at the interface restricts the plastic deformation to a greater extent in the interface layer.

Keywords HEA · MD Simulation · Nanoindentation · Stacking Fault Tetrahedra · Lomer-Cottrell Barrier

D. K. Mishra (✉) · S. K. BadJena
Department of Metallurgical & Materials Engineering, Veer Surendra Sai University of Technology, Burla 768018, India

S. Pal
Department of Metallurgical & Materials Engineering, National Institute of Technology, Rourkela 769008, India

S. Pal et al. (eds.), *Processing and Characterization of Materials*, Springer Proceedings in Materials 13, https://doi.org/10.1007/978-981-16-3937-1_34

1 Introduction

Face-centered cubic (FCC) metals and their alloys are widely used in aircraft components, automotive parts, electrical appliances, heat-exchangers, utensils, furniture, and many other domestic and industrial applications because of their better ductility, higher strength to weight ratio, excellent electrical and thermal conductivity behavior [1–3]. In the meanwhile, they encounter several challenges like heavy wear and load, high-temperature corrosion, and oxidation [4–7]. So, to enhance its durability and performance, high entropy alloy (HEA) coating is proven as the most appropriate one [7–11]. There so far, numerous studies have been reported on HEA coated metals and alloys. The past studies confirm the variation in chemical composition, temperature, and coating techniques have controlled the uniform phase formation, phase transformation, and formation of new intermetallic phases. Due to this the overall enhancement in resistance to corrosion, wear, oxidation, diffusion, and temperature, which will contribute to their outstanding thermal stability and superior mechanical properties [7–16]. On the other hand, nanoindentation is the most reliable, efficient, and accurate technique in the determination of mechanical properties of thin film coated bulk materials in the nanoscale range. The major characteristics of nanoindentation analysis include the use of a projected contact area instead of a residual contact area to interpret the load-depth curve more precisely in a continuous manner and further determine the mechanical properties within a much-specified small volume space under a small localized load [17–21]. Nair et al. [21] have performed nanoindentation on a 20 nm thin single crystal (SC) Ni film by using both experiment and simulation and observed that the deformation during indentation is primarily influenced and controlled by dislocation evolution, movement, and subsequent interactions with each other. Henceforth, an efficient simulation tool is very much needed to capture all the underlying deformation phenomena more precisely to provide considerable details on dynamic deformation behavior. To date, most of the reported studies [21–27] recommend the use of molecular dynamics (MD) simulation to conduct a nanoindentation test that produces a clear insight on underlying deformation phenomena. Several pioneering MD simulation-based studies on deformation motivate the researchers to work on further. Ma and Yang [26] have studied on nanocrystalline Cu during nanoindentation using MD simulation. It has been found the deformation mechanism mainly governs by frequently observed stacking fault (SF) burst and their subsequent arrest at grain boundaries (GBs). Kim et al. [27] have performed nanoindentation on both SC and bicrystal Ni using MD simulation. The result has shown the evolution and propagation of prismatic loops in SC Ni, whereas, in case of Ni bicrystal, a series of atom shifting near GB are observed due to lattice dislocations' interaction with $\sum = 5(210)$ GB to cause GB migration. But, in another study on Ni bicrystal by Jang and Farkas [28] have reported the new step development at GB that guides the GB movement and SF expansion. The nanoindentation test by Lee et al. [29] on Al (111) interface has observed the nucleation of homogeneous embryonic dislocation at the beginning of deformation. Later on, tetrahedral dislocation locks have formed subsequently. Finally, it has ended up with

prismatic dislocation loop (PDL) formation. Jiao et al. [30] have reported the transition from embryonic prismatic loop to PDL by "lasso"-like mechanism [31] during the nanoindentation on Al (100) interface using MD simulation. Liu et al. [32] have revealed the development of parallelogram Frank sessile loop and twinning dislocation due to PDL interaction with coherent twin boundary (CTB). Further, the repeated interactions multiply the twinning dislocation evolution during the nanoindentation test on SC Cu with CTB. Stacking fault tetrahedra (SFT) defective structure is one of the most stabled pyramidal structures that are usually found in low stacking fault energy (SFE) based FCC metals such as Ag, Au, Cu, etc. In this structure, the four faces of the tetrahedron represents the {111} planes with triangular intrinsic stacking faults and the interconnected [110] edges are the set of stair-rod partial dislocations [33]. Silcox and Hirsch [34] have proposed the mechanism of SFT evolution that is well-known as the Silcox-Hirsch mechanism. Under this mechanism, initially, the Frank dislocation loop has developed due to the coalescence vacancies that later on dissociate along three ⟨110⟩ directions of {111} plane to form SFT. In a recent study, Liu et al. [35] have reported on SFT development without the involvement of any vacancy or Frank loop during the plastic deformation of SC Cu with pre-existing CTBs.

Apart from deformation studies concerning on nanoindentation test on HEA coated SC metals using MD simulation, few pieces of literature have reported so far as per the authors' knowledge. The deformation of $Cu_{20}Ni_{20}Al_{20}Co_{20}Fe_{20}$ (HEA)-SC Cu specimen has reported unveiling the V-shaped distorted structure growth during nanoindentation [36]. In another study, the structural deformation of $Mo_{20}W_{20}Co_{20}Ta_{20}Zr_{20}$ (HEA) film-SC Ni has studied to reveal the detailed underlying deformation during the nanoindentation test [37]. The present study has based on the previously reported nanoindentation deformation study on $Mo_{20}W_{20}Co_{20}Ta_{20}Zr_{20}$ (HEA) film-coated SC Ni [37] by replacing the substrate with SC Al and SC Cu; then it is compared. Furthermore, the development of SFT in $Mo_{20}W_{20}Co_{20}Ta_{20}Zr_{20}$ (HEA) film-coated SC Al and its effect on nanoindentation deformation have been investigated in a detailed manner.

2 Simulation Details

A three-dimensional specimen consists of (200 × 200 × 180 Å) SC FCC metal substrate coated with $Mo_{20}W_{20}Co_{20}Ta_{20}Zr_{20}$ HEA film having a thickness of 20 Å along Z-axis is shown in Fig. 1. In this paper, SC FCC metals such as Cu, Ni, and Al have been used as substrates. Further, the MD simulation has been employed to conduct the nanoindentation test on HEA-coated specimens at low temperature (1 K) to minimize the thermal fluctuation effects. At the beginning of the test, a spherical diamond indenter with 50 Å tip radius has kept 2.8 Å height above the specimen interface, and, afterward, it has moved with 40 m/s velocity towards the specimen along the downward Z-direction. The indentation velocity in most of the reported MD simulation based nanoindentation studies are kept in the range of 1–100 m/s

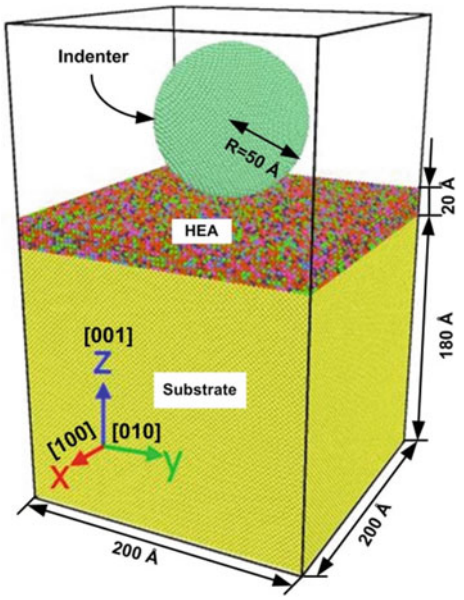

Fig. 1 Three dimensional HEA coated SC FCC metal specimen with spherical diamond indenter

due to the limitations in computational power [29, 38, 39]. The indenter velocity in real experiments is usually kept below 50 m/s [40]. The film thickness concern, the thickness of the coated layer is 1.5–4 times smaller in comparison to indenter size during low and room temperature simulation studies [41]. In the present study, the authors have chosen the indentation velocity as 40 m/s and the HEA film coating thickness as 20 Å to get a more realistic material behavior. The crystal orientation has been chosen as ⟨110⟩ directions. Periodic boundary conditions (PBCs) have applied along both the X and Y-axis, and free boundary condition has employed along Z-axis. The time step has used 2 fs for MD simulation.

The energy minimization has done using the conjugate gradient (CG) algorithm. *Canonical* or *NVT* ensemble has been used to perform MD simulation by employing the Nose–Hoover thermostat [42, 43] for temperature control. The bottom region of the specimen with dimension (200 × 200 × 10 Å) has kept frozen during nanoindentation to prevent the movement of HEA coated specimen and, further, the velocity-Verlet algorithm is employed to integrate the atomic motion. The number of atoms involved during the nanoindentation process of HEA film coated Cu, Ni and Al are 677398, 721780 [37], and 483932, respectively. The exerted repulsive force by the spherical indenter on each atom can be computed as [44]

$$F(r) = \begin{cases} k(R-r)^2, & r < R, \\ 0, & r \geq R. \end{cases} \tag{1}$$

where $k = 1000\left(eV/\text{Å}^3\right)$ is the specified force constant, r is the distance from the indenter center to the atom under consideration, and R is the indenter radius. The MD simulation has performed with the help of LAMMPS open-source software package [44] for specimen preparation and nanoindentation simulation. Moreover, the Ovito software is employed to visualize and analyze the nucleation and growth of the underlying structural defects [45]. Furthermore, the developed embedded-atom method (EAM) potential by Zhou et al. [46] is employed to elucidate the interatomic forces between the atoms in the $Mo_{20}W_{20}Co_{20}Ta_{20}Zr_{20}$ HEA coating system and their subsequent interactions with the substrate atoms. The total energy in EAM can be calculated as [46]

$$E = \frac{1}{2}\sum_{i,j,\ j\neq i} \emptyset_{ij}\left(r_{ij}\right) + \left(\sum_{i} F_i(\rho_i)\right) \tag{2}$$

where $\emptyset_{ij}\left(r_{ij}\right)$ is the pair energy between i and j atoms with a distance of separation r_{ij}, and $F_i(\rho_i)$ represents the embedding energy in associate with embedding atom i within the local site with an electron density (ρ_i) that can be expressed as

$$\rho_i = \sum_{j,j\neq i} f_j\left(r_{ij}\right) \tag{3}$$

where $f_j\left(r_{ij}\right)$ is the electron density emerged at atom i from atom j with separation distance r_{ij}.

3 Results and Discussion

3.1 Indentation Load-Depth and Hardness-Depth Curves

The nanoindentation test on $Mo_{20}W_{20}Co_{20}Ta_{20}Zr_{20}$ (HEA) film-SC Ni [37], SC Cu, and SC Al using the MD simulation model have validated by comparing the obtained P–h curves from MD simulation with Hertz solution [47] as presented in Fig. 2a. The Hertz theory-based relationship between indentation load (P) and indentation depth (h) can be expressed as,

$$P = \frac{4}{3}E^* R^{1/2} h^{3/2} \tag{4}$$

where E^* is the reduced elastic modulus and mathematically it can be expressed as

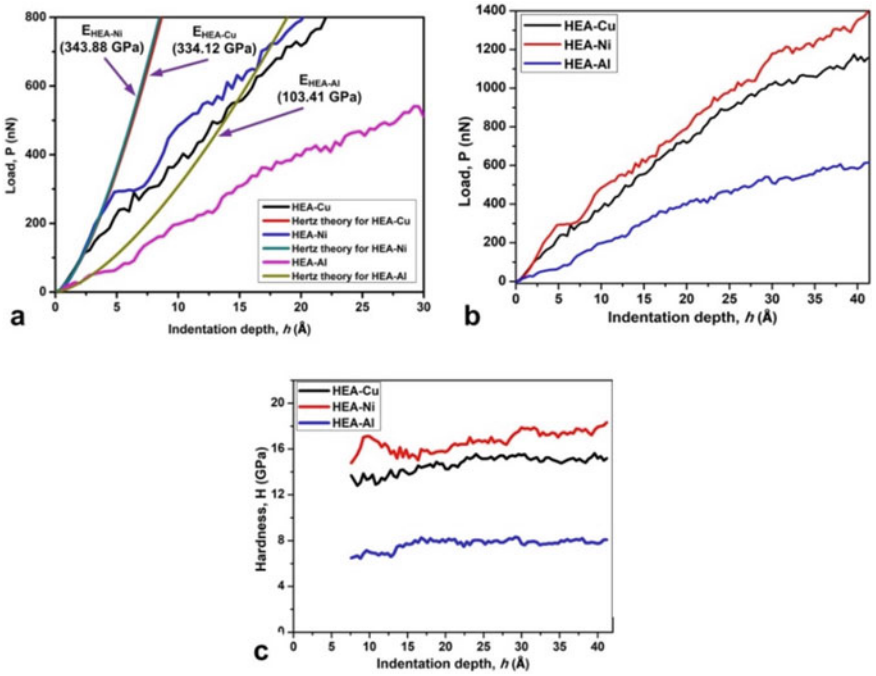

Fig. 2 Plot of (a) *P–h* curves based on MD simulation with Hertz theory (b) *P–h* curves (c) *H–h* curves for $Mo_{20}W_{20}Co_{20}Ta_{20}Zr_{20}$ HEA film-coated SC Ni [37], SC Cu, and SC Al specimens

$$\frac{1}{E^*} = \frac{1 - v_1^2}{E_1} + \frac{1 - v_2^2}{E_2} \tag{5}$$

where (v_1, v_2) represents the Poisson's ratios and (E_1, E_2) indicates the elastic modulus values for the specimen sample and spherical diamond indenter, respectively. The values of E^* for $Mo_{20}W_{20}Co_{20}Ta_{20}Zr_{20}$ (HEA) film-SC Ni [37], SC Cu, and SC Al have computed as 343.88 [37], 334.12, and 103.41 GPa, respectively, by fitting the MD simulation-based *P–h* curve with the Hertz equation-based *P–h* curve.

The computed reduced elastic modulus of a specimen has depicted its stiffness. So, the relatively higher E^* value of HEA film-coated SC Ni [37] in comparison to HEA-SC Cu and HEA-SC Al attributes to the higher stiffness that is higher energy has accumulated before it crosses the elastic to plastic transition point. Similarly, the lowest reduced elastic modulus for HEA coated SC Al has attributed to the lowest stiffness value that is relatively lower energy has accumulated before the elastic–plastic transition. The storage of energy before the elastic to plastic transition point acts as a driving force for the sudden deviation in the *P–h* curve just after the evolution in the very first dislocation. In the comparative MD simulated *P–h* curve analysis, the highest stiffness of HEA coated SC Ni has produced a relatively larger deviation in load in comparison to the indentation depth just after the evolution in the first

dislocation. Whereas in HEA coated SC Al, a relatively smaller deviation occurs. The nearby E^* values for HEA coated SC Ni and SC Cu attribute to very nearby stiffness values. In Fig. 2a, it can observe that the MD simulated P–h curves have reproduced the similar elastic response as Hertz solution up to a specific point, then, it starts deviating to cause the onset inelastic response. The point of deviation usually refers to the elastic–plastic transition point or yielding point at which the pop-in event has materialized through dislocation nucleation. The elastic–plastic transition point for HEA coated SC Ni, SC Cu, and SC Al are appeared at the indentation depth of around 3.6, 2.3, and 3.2 Å, respectively.

The comparative P–h and H–h curves for the nanoindentation test on $Mo_{20}W_{20}Co_{20}Ta_{20}Zr_{20}$ (HEA) film-SC Ni [37], SC Cu, and SC Al have shown in Fig. 2b, and 2c, respectively. The trends of both P–h and H–h curves for HEA-SC Ni and HEA-SC Cu are very similar up to indentation depth around $h \sim 27.5$ Å, but, after that, at higher indentation depth, the uncertainty in plastic deformation makes a significant difference in the final result. On the other hand, the P–h curve for the HEA-SC Al specimen has considerably decreased to a lower level in comparison to HEA-SC Ni and HEA-SC Cu. So it is proven that HEA-SC Al is deformed more readily than the other two specimens. The hardness (H) is usually expressed as the applied load per unit projected contact area. The projected contact area (S) is used as $\pi(2R - h)h$ to eradicate the difficulties in the roughness of the indenter interface and contact depth calculation during plastic deformation [23–25]. The H–h curve for the HEA-SC Al specimen observe at a much lower level (refer to Fig. 2c) that indicates the HEA-SC Al specimen relatively softer and easily deformed than HEA-SC Ni and HEA-SC Cu.

Figure 3 depicts the comparative ρ-h curves for the nanoindentation test on HEA coated SC Cu, SC Ni [37], and SC Al specimen, where Fig. 3a is for whole specimen volume (200 × 200 × 200 Å) and Fig. 3b is for the nearby region with dimension (110 × 110 × 70 Å) around the indenter tip. The analysis of ρ-h curves for all three specimens has been done by dividing it into three regions, such as I, II, and III. In the region-I, the ρ-h curves for all three specimens are showing almost the same trend up

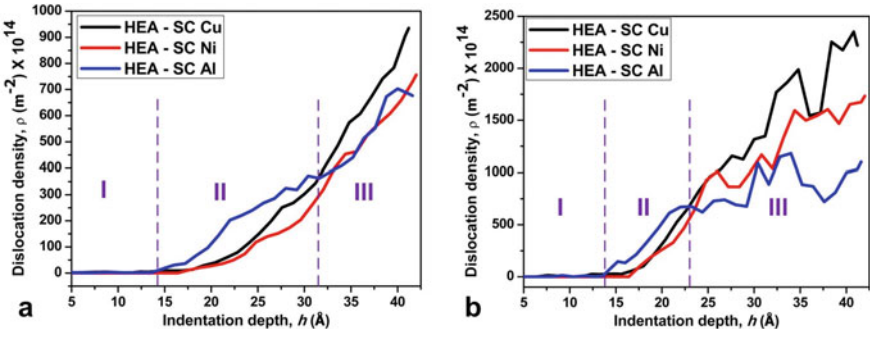

Fig. 3 Plot of (a) ρ-h curves (b) ρ-h curves near indenter region for $Mo_{20}W_{20}Co_{20}Ta_{20}Zr_{20}$ (HEA) film-coated SC Cu, SC Ni [37] and SC Al specimens

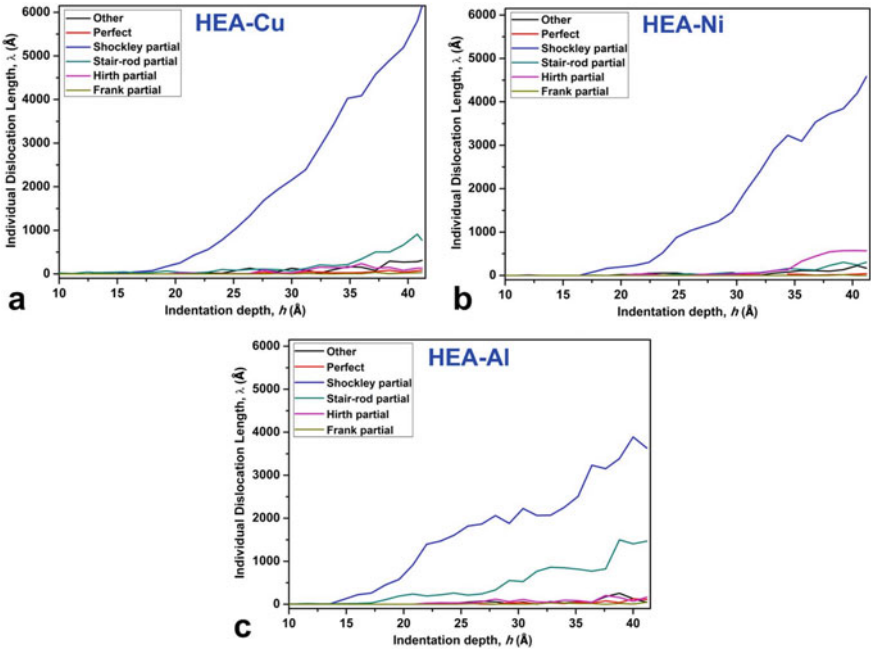

Fig. 4 Plots of λ-h curves for different types of dislocation for (a) $Mo_{20}W_{20}Co_{20}Ta_{20}Zr_{20}$ (HEA)-SC Cu (b) $Mo_{20}W_{20}Co_{20}Ta_{20}Zr_{20}$ (HEA)-SC Ni [37] (c) $Mo_{20}W_{20}Co_{20}Ta_{20}Zr_{20}$ (HEA)-SC Al specimen

to $h \sim 13.6$ Å, but afterward in region-II, they start deviating from each other due to the significant rise in dislocation evolutions. In region-II, the ρ-h curve for the HEA-Al specimen remains higher than the other two specimens. As move on to higher indentation depth as in region-III, the ρ-h curve for the HEA-Ni specimen remains higher than the other two specimens. Figure 4 depicts the comparative λ-h curves for the nanoindentation test on HEA film coated SC Cu, SC Ni [37], and SC Al specimen. So, it can observe that the evolution in Shockley partials is comparatively showing greater increasing trend for HEA film coated SC Cu helps in easy dislocation gliding than other specimens. But, it is interesting to observe, there is a dramatic increase in stair-rod partials that occur in the case of HEA film coated SC Al. So, the decreasing trend in the ρ-h curve for HEA-SC Al in region III (refer to Fig. 3a, b) can explain by considering the significant rise in stair-rod partials. Because since stair-rod partials are sessile in nature hence acts as a barrier to the usual plastic flow. Moreover, the significant rise in dislocations nearer to the indentation tip region is accountable for the early appearance of region-III and the more random nature of ρ-h curves in the case of Fig. 3b than Fig. 3a.

3.2 Comparison of Defect Evolution and Propagation Between HEA Coated FCC Metals

Nanoindentation on (001) interface of $Mo_{20}W_{20}Co_{20}Ta_{20}Zr_{20}$ HEA film-coated SC Cu, SC Ni [37], and SC Al has done along the Z-axis. As the indenter touches the specimen surface, massive compressive stress has developed around the indenter tip, which gradually increases with an increase in indentation depth. When the increased stress overcomes the critical stress value, it emancipates in the form of fresh and energetic dislocations evolution along the preferred active slip systems [48]. Moreover, the newly developed unsteady dislocations undergo splitting into partial dislocations by leaving the SF ribbon behind them [32] to release the surplus energy, and their subsequent interactions cause difficulties in further dislocation movement.

3.2.1 Dislocation Extraction Algorithm (DXA) and Common Neighbor Analysis (CNA)

CNA method is proposed by Honeycutt and Andersen [49] that employ complex and multi-dimensional characteristic signatures [50] to determine the local structures around the central atom. On the other hand, adaptive common neighbor analysis (A-CNA) is an extension of the original CNA method that has frequently used to describe the evolution of multi-phase structures by considering the individual particle's cut-off radius [51, 52]. DXA method is proposed by Stukowski and Albe [53] to characterize the topological structural changes in the dislocation network by identifying the individual dislocation and subsequently determining their burger vectors. In this study, both A-CNA and DXA methods have been employed to describe the local defect structures evolution during the indentation of $Mo_{20}W_{20}Co_{20}Ta_{20}Zr_{20}$ HEA film-coated SC Cu, SC Ni [37], and SC Al. Figure 5 shows CNA and DXA analysis of SF and dislocation evolution during nanoindentation test of $Mo_{20}W_{20}Co_{20}Ta_{20}Zr_{20}$-SC Cu specimen with the variation in indentation depths from $h = 20.8$ to $41.2\,\mathring{A}$. At the initial stage of deformation, at $h = 20.8\,\mathring{A}$, a V-shaped distorted SF structure is grown around the indenter tip along two planes (111) and $\left(1\,\bar{1}\,1\right)$ with an interplanar angle of 70.53^0 (refer Fig. 5a) to release the excess stress near the indenter tip region. With further increase in indentation depth, there is a significant rise in the interface distorted structures i.e. deformed dislocation structures. The interface deformed dislocations structures have accompanied with V-shaped defect structures, discrete dislocations, multi-dislocation nodes, perfect dislocations, and few dislocation loops.

On the other hand, the appearance of long lengthed Hirth partial dislocations, closed stair-rod steps, dislocation tangles, Frank partials, interface Lomer-Cottrell (LC) barriers, and multi-dislocation loops at higher indentation depth (refer to Fig. 5c, d) slows down the distorted structure propagation and henceforth, resulting in strain

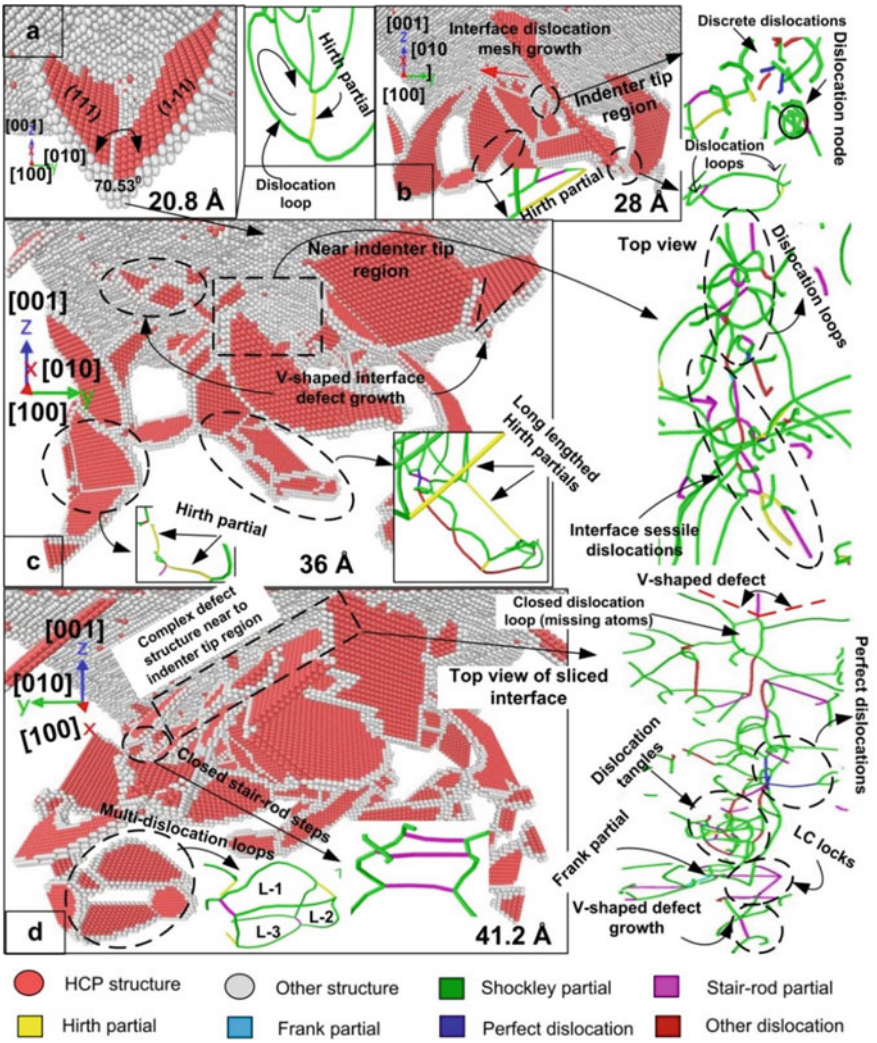

Fig. 5 CNA and DXA analysis of stacking fault and dislocation evolution at (a) $h = 20.8$ Å (b) $h = 28$ Å (c) $h = 36$ Å (d) $h = 41.2$ Å for $Mo_{20}W_{20}Co_{20}Ta_{20}Zr_{20}$ (HEA) film-SC Cu specimen

hardening [32, 54]. Figure 6 depicts the CNA and DXA analysis of SF and dislocation evolution, during nanoindentation of $Mo_{20}W_{20}Co_{20}Ta_{20}Zr_{20}$ (HEA) coated SC Ni at different indentation depths varies from $h = 20.8$ to 41.2 Å. At the beginning of deformation, at $h = 20.8$ Å, just beneath the indenter tip, a triangular distorted interface mesh is observed that has grown along three planes, such as $\left(\bar{1}\ 11\right)$, $\left(\bar{1}\bar{1}\bar{1}\right)$,

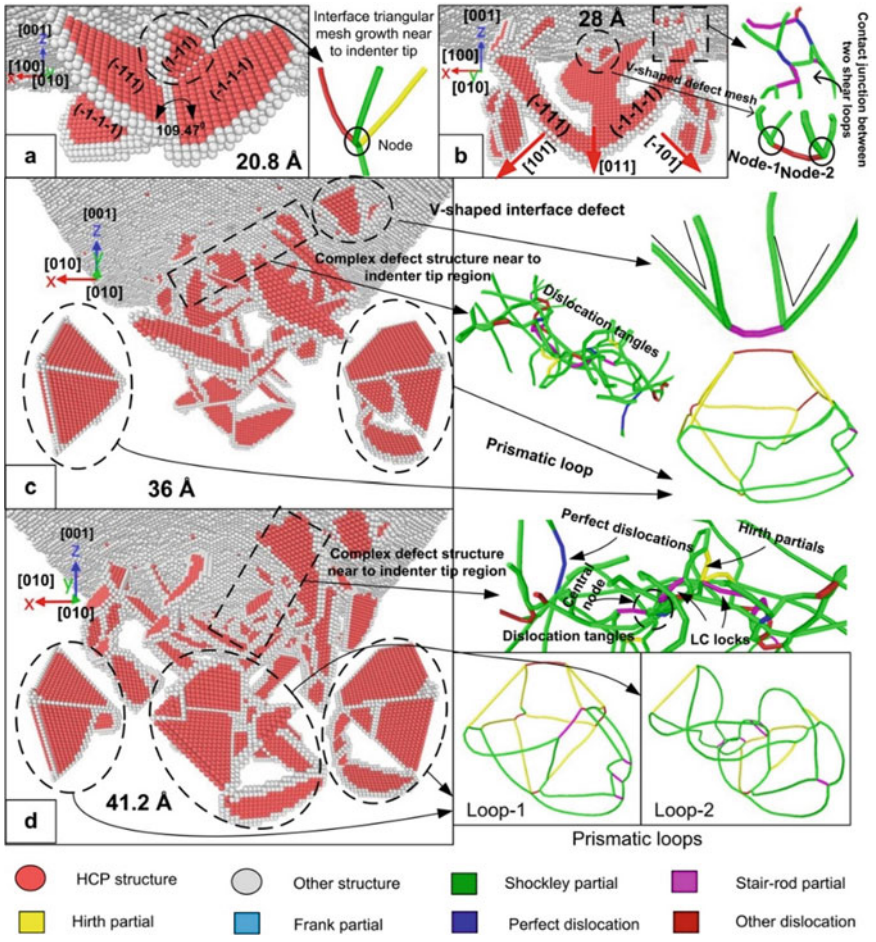

Fig. 6 CNA and DXA analysis of stacking fault and dislocation evolution at (a) $h = 20.8$ Å (b) $h = 28$ Å (c) $h = 36$ Å (d) $h = 41.2$ Å for $Mo_{20}W_{20}Co_{20}Ta_{20}Zr_{20}$ (HEA) film-SC Ni specimen

and $\left(1\,\bar{1}\,1\right)$ as shown in Fig. 6a. Later on, at $h = 28\,\mathring{\text{A}}$ with the evolution of perfect dislocations and increase in accumulation shear stress near the indenter tip are governed the extension of planar SF structures into shear loops along [101], [011], and $\left[\bar{1}\,01\right]$ slip directions as reported earlier [37]. At higher indentation depth, the excess stress around the indenter tip has preferably released in terms of evolution in prismatic loops and interface V-shaped distorted structures. In the meanwhile, the involvement of sessile dislocations (Hirth and stair-rod partials) and complex dislocation structure around the indenter tip region restrict the easy gliding of dislocation structures to cause strain hardening (refer to Fig. 6c, d).

The CNA and DXA analysis of SF and dislocation evolution of $Mo_{20}W_{20}Co_{20}Ta_{20}Zr_{20}$ (HEA) film-SC Al specimen during nanoindentation at different indentation depths varies from $h = 20.8$ to 41.2 Å have shown in Fig. 7. The specimen has initially deformed due to the extension of planar defect structure along $\left(\bar{1}\ 11\right), \left(\bar{1}\ 1\ \bar{1}\right)$ and $\left(11\ \bar{1}\right)$ planes around the indenter tip. Apart from this, closed stair-rod steps also observe along with the extended SF structures that, in turn, amplify the deformation proportionally (refer to Fig. 7a). The appearance of extended dislocations and SF structures denotes the low SFE [55, 56] of $Mo_{20}W_{20}Co_{20}Ta_{20}Zr_{20}$ film coated SC Al specimen. However, the subsequent development in few cross-slip

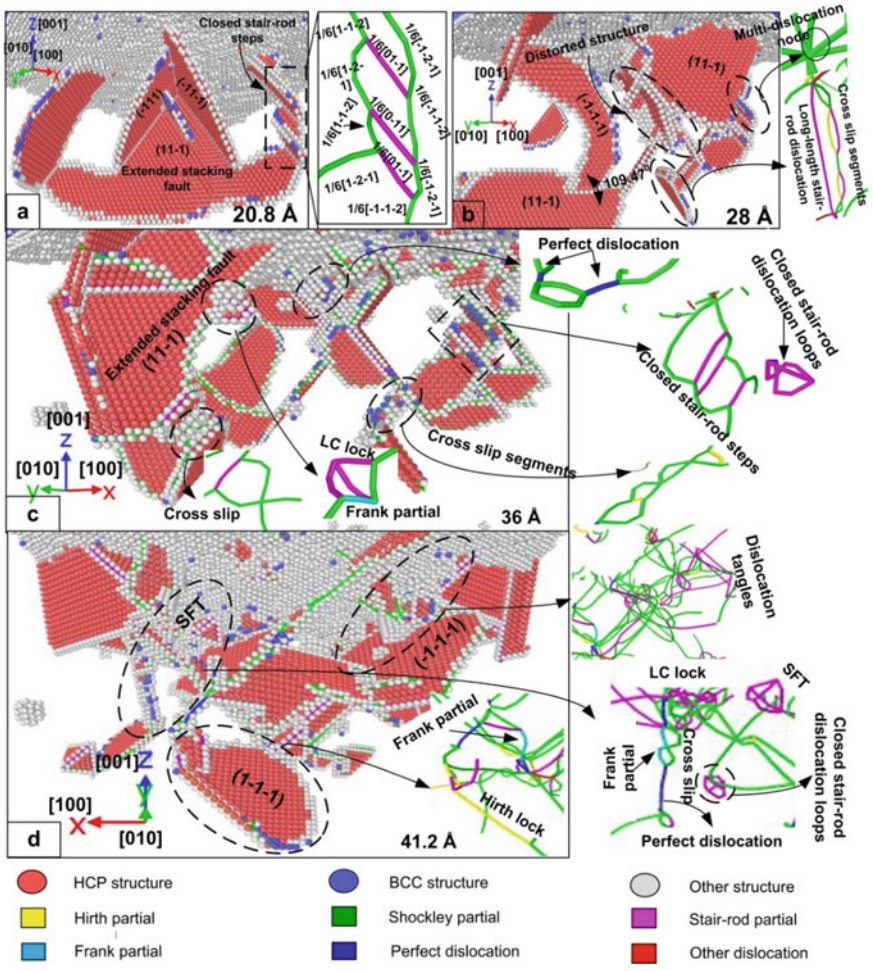

Fig. 7 CNA and DXA analysis of stacking fault and dislocation evolution at (a) $h = 20.8$ Å (b) $h = 28$ Å (c) $h = 36$ Å (d) $h = 41.2$ Å for $Mo_{20}W_{20}Co_{20}Ta_{20}Zr_{20}$ (HEA) film-SC Al specimen

segments and multi-dislocation nodes helps to release out the accumulated stress around the indentation region, which significantly slows down the strain rate. At higher indentation depth (refer to Fig. 7c, d), the increase in stair-rod partials (refer to Fig. 4c), Hirth partials, Frank partials, closed stair-rod loops, SFT, and dislocation tangles restrict the dislocation movement to counter-strike the easy gliding to cause strain hardening.

The CNA and DXA analysis relatively at lower indentation depths for HEA-SC Cu (refer to Fig. 5a, b), HEA-SC Ni (refer to Fig. 6a, b) and HEA-SC Al (refer to Fig. 7a, b) can use to explain the nature of *P–h* and *H–h* curve (refer to Fig. 2) just after the yield point. Further, at higher indentation depths, the CNA and DXA analysis for HEA-SC Cu (refer to Fig. 5c, d), HEA-SC Ni (refer to Fig. 6c, d) and HEA-SC Al (refer to Fig. 7c, d) infer the overall increase in strain hardening behavior due to the evolution and growth in different types of distorted structures suitably retaliate the plastic flow to preserve the improved mechanical properties like hardness, strength, and stiffness, etc.

3.2.2 SFT Evolution Analysis in HEA-Al Specimen

SFT is a three-dimensional volume defect, which is surrounded by four distorted {111} SF planes with six stair-rod partials along six edges [33]. In general, SFT has considered the most stable low energy-based-defect structure for small clusters [57]. But, still, the mechanism of SFT development is a challenge. Past studies have mostly prioritized on the SFT inception through the subsidence of vacancy cluster followed by dislocation reaction to minimize the dislocation energy [33, 34].

Figure 8 represents the schematic of SF evolutions at $h = 38.4$ Å to $h = 40.4$ Å for $Mo_{20}W_{20}Co_{20}Ta_{20}Zr_{20}$ (HEA) film-SC Al to unveil the exact mechanism SFT development. In the beginning, two sets of atomic planes as $\left(1\ \bar{1}\ 1\right)$ and $\left(1\ \bar{1}\bar{1}\right)$ are slipped away along [110] direction from a common stair-rod partial dislocation based constriction point with an interplanar angle of 70.53^0 in between them. Afterward, as the indentation depth has increased, the evolution of Hirth partials are observed just below the constriction point around the necking portion that restrict the atomic slipping leads to unsymmetrical growth in atomic clusters and missing of atoms (refer to Fig. 8c, d). Further deformation in progress, the accumulation of compressive stress around the necking portion has gradually increased. The excess built-up in compressive stress has eventually emancipated to mitigate the strain around the constriction points and hence develops a more confined central node (refer to Fig. 8e). On the other hand, the nucleation of vacancies due to the missing of atoms and unsymmetrical atomic cluster growth leads to dislocation climb to preserve the local equilibrium structure. The further increase in indentation depth, the distorted structure below the central node is get detached and slips away along the active slip system with an increase in stress and hence leaving behind the SFT structure, as shown in Fig. 8f.

Figure 9 has shown the DXA snapshots of dislocation evolutions from $h = 39.2$ to 40.4 Å for HEA-SC Al specimen. The DXA analysis has done to analyze and

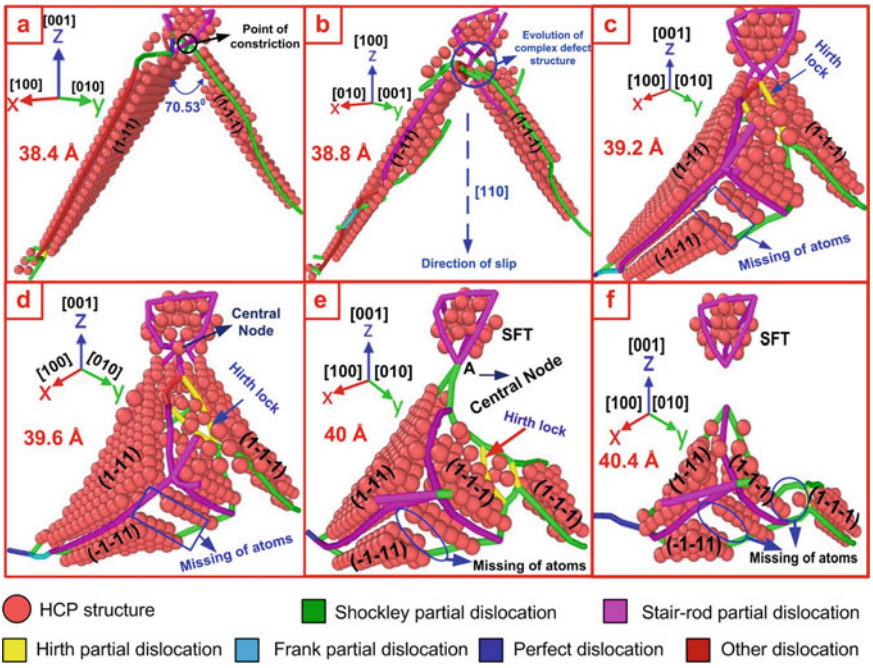

Fig. 8 Schematic of SF evolutions at (a) $h = 38.4$ Å (b) $h = 38.8$ Å (c) $h = 39.2$ Å (d) $h = 39.6$ Å (e) $h = 40$ Å (f) $h = 40.4$ Å for $Mo_{20}W_{20}Co_{20}Ta_{20}Zr_{20}$-SC Al specimen

understand the SFT development in a more detailed manner. At $h = 39.2$ Å, three triangular dislocation loops such as ABC, BCD, and DEF have developed (refer to Fig. 9a). Further, at higher indentation depth, $h = 39.6$ Å, the lower triangular loop as DEF slips away due to the increase in stress. Moreover, the increase in stress at the lower points of dislocation loops ABC and BCD, such as A and D, respectively, is get concentrated to develop the central node O, where the increase in stress has accumulated. During this process, two hexangular loops such as OPQRST and OJKLMN have developed across the central node O, which are connected by the dislocation junction RL at the other end (refer to Fig. 9b). As the nanoindentation further proceeds to $h = 40$ Å, cause the shifting of the central node to new position A along the slip direction, and hence closed SFT structure has observed above the central node (refer to Fig. 9c). The dislocation reaction across the central node A can write as

$$1/6[\,21\bar{1}\,] + 1/6[\,011\,] + 1/6[\,\bar{1}0\bar{1}\,] = 1/6[\,21\bar{1}\,] + 1/6[\,\bar{1}10\,]$$

(Shockley Partial) (Stair-rod Partial) (Stair-rod Partial) (Shockley Partial) (Stair-rod Partial).

Further, increase the stress to $h = 40.4$ Å eventually cause the detachment of Shockley partials from the central node A and slipping away along the active slip

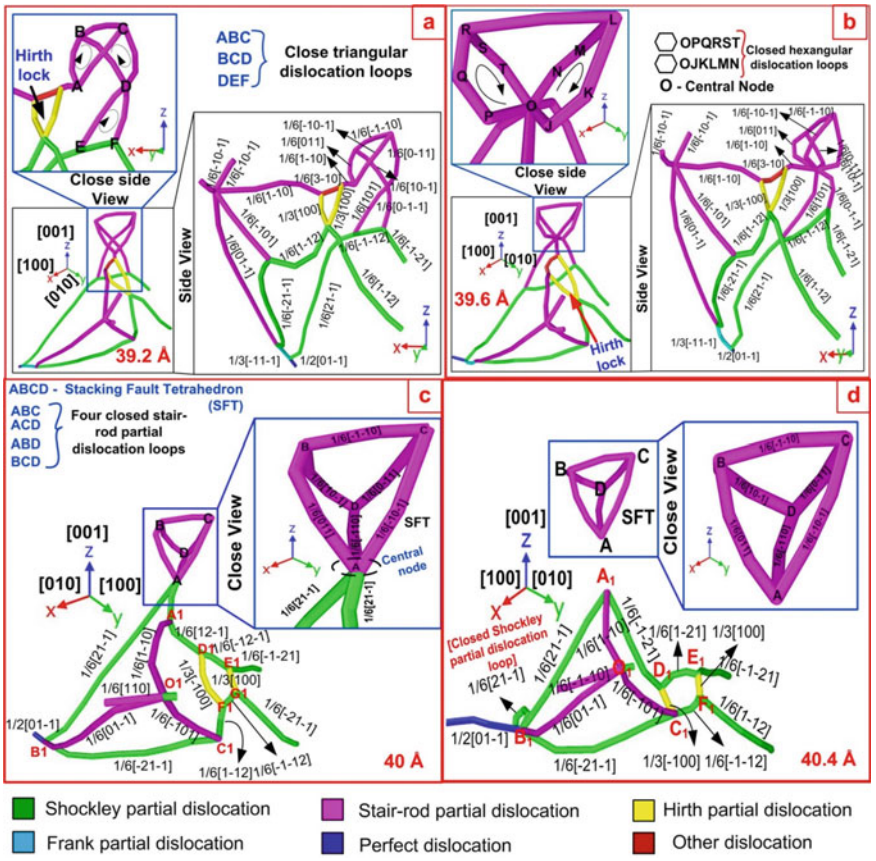

Fig. 9 DXA snapshots of dislocation evolutions at (a) $h = 39.2$ Å (b) $h = 39.6$ Å (c) $h = 40$ Å (d) $h = 40.4$ Å for $Mo_{20}W_{20}Co_{20}Ta_{20}Zr_{20}$-SC Al specimen

system by leaving behind the SFT as ABCD (refer to Fig. 9d). This finding has well supported by the evidence that has obtained in Fig. 8. After the detachment of distorted structure at central node A, the dislocation reaction at A can express as

$$1/6[\,011\,] + 1/6[\,\bar{1}\,0\bar{1}\,] = 1/6[\,\bar{1}10\,]$$

(Stair-rod Partial) (Stair-rod Partial) (Stair-rod Partial)

The active involvement of stair-rod partials in the development of the SFT structure makes it sessile. Hence the evolution in SFT structure causes difficulties in dislocation gliding that result in strain hardening. The high SFT concentration can localize the plastic deformation in narrow slip bands to strengthen the material [58–60]. So, the observation of narrow slip band structures, as shown in Fig. 7c, d, can be explained due to the development in SFT and other kinds of closed stair-rod dislocation loops. Further, the present study confirms the SFT development in HEA-SC

Al specimen during nanoindentation deformation is a dislocation based mechanism that is principally governed by the interaction of different SF planes and dislocation gliding. Moreover, the current mechanism of SFT development is different from the Silcox-Hirsch mechanism [34]. The present SFT development mechanism is well supported and agreed with the earlier discussed and reported dislocation based SFT development mechanism [35, 61–63].

3.2.3 Shear Based Deformation Analysis

At the beginning of nanoindentation, the HEA film-coated SC Ni, SC Cu, and SC Al oppose the applied load up to a definite limit and henceforth, restore the localized stress around the indenter tip region. The extent of specimen resistance against the applied load to restore the localized stress is directly dependent on its stiffness value. Since HEA coated SC Ni has higher stiffness than the other two specimens (refer to Fig. 2a), so have a higher resistance to the applied load, and, in consequence, higher stress has accumulated before the plastic deformation. Similarly, since HEA coated SC Al has a relatively lower stiffness value than the other two specimens (refer to Fig. 2a) so comparatively has lower resistance to the applied load, and, hence lower stress has accumulated before plastic deformation. On the other hand, since HEA-SC Cu has a stiffness value very close to the HEA-SC Ni, so it resists the applied stress in a very similar way as in HEA-SC Ni. Hence, it restores the stress around the same as in the HEA-SC Ni specimen before undergoing plastic deformation. Later on, when the accumulative stress overcomes the critical stress limit, it liberates by causing the deformation in the HEA coated specimens.

Figure 10 represents the atomic shear strain snapshots for indentation depth varying from $h = 16.4$ to $h = 41.2$ Å for $Mo_{20}W_{20}Co_{20}Ta_{20}Zr_{20}$ (HEA) film-SC Cu, SC Ni, and SC Al specimens. The observation of the shear strain color band for all HEA film-coated specimens infers to the equiproportional growth in shear strain intensity at the center of the specimen surface all around the indenter tip with the rise in indentation depth. Moreover, the developed shear strain in HEA-SC Al is not much significant in contrast to HEA-SC Ni and HEA-SC Cu due to its low stiffness value that accounts for the low-stress accumulation before undergoing the deformation process. In the meanwhile, comparing the spreading of shear strain for all the three specimens, it can observe that the spreading of shear strain in HEA-SC Cu has comparatively restricted in the interface layer to a greater extent instead of spreading to the interior part of the specimen. The reason for significant interface deformation in HEA-SC Cu may infer to the appearance of complex distorted dislocation structures that includes discrete dislocations, V-shaped defect structures, dislocation tangles, LC locks, etc. as shown in Fig. 5. That implies the $Mo_{20}W_{20}Co_{20}Ta_{20}Zr_{20}$ (HEA) coating can effectively use to restrict the deformation within the interface layer to a large extent without deforming the Cu substrate. However, the overall deformation can be observed minimum for HEA-SC Ni in comparison to other specimens (refer to Fig. 10) due to its high stiffness value, as discussed earlier.

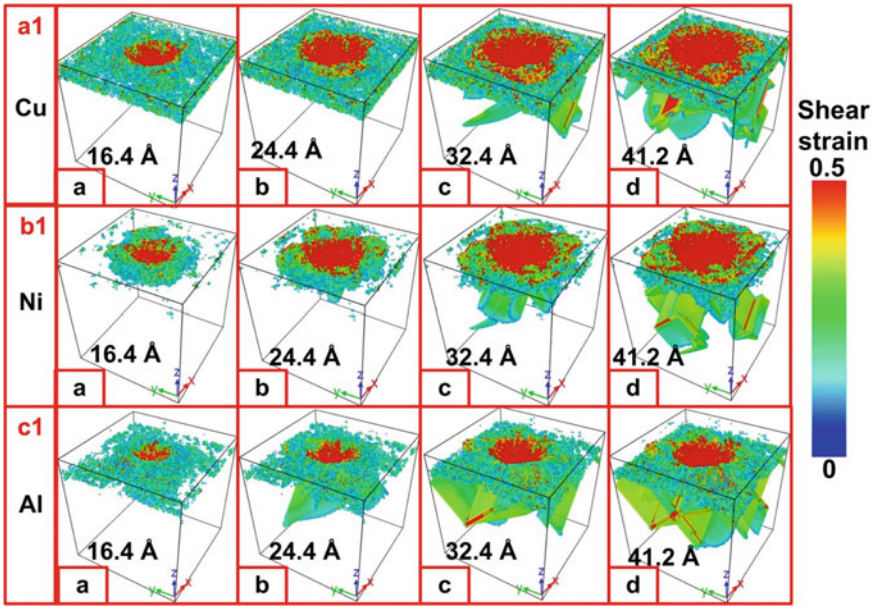

Fig. 10 Atomic shear strain snapshots for indentation depth (h) varying from (a) 16.4 Å to (d) 41.2 Å from top view for (a1) $Mo_{20}W_{20}Co_{20}Ta_{20}Zr_{20}$-SC Cu (b1) $Mo_{20}W_{20}Co_{20}Ta_{20}Zr_{20}$-SC Ni (c1) $Mo_{20}W_{20}Co_{20}Ta_{20}Zr_{20}$-SC Al specimen

Figure 11 shows the atomic displacement vector plots for different indentation depth values varying from $h = 16.4$ to 41.2 Å of the cross-section of all the three HEA coated specimens. The significant rise in strain rate near to indentation center all around the indenter tip with the increase in indentation depth is accountable for the diverse atomic displacement along with the convective atomic trajectory [64]. The observation and analysis of comparative displacement plots for all HEA coated specimens infer, the atomic displacement in HEA-SC Ni is more symmetrical from the indentation center to both sides of the specimen (refer to Fig. 11b1) due to the stable and symmetric growth in shear dislocation loops below the bottom of the indenter tip as reported earlier [37]. In meanwhile, the atomic displacement vectors in HEA-SC Cu are preferably appeared over the interface region to a greater extent in contrast to the other two HEA coated specimens, and this finding is well supported by the evidence as found in atomic shear strain snapshots (refer to Fig. 10a1). In HEA-SC Al, the densities of atomic displacement vectors are comparatively found lesser than in HEA-SC Cu and HEA-SC Ni due to its small stiffness value that accounts for the storage of relatively lower localized stress before undergoing for plastic deformation. In the meanwhile, the appearance of Hirth partials, LC barriers, SFT, dislocation tangles, closed stair-rod partial dislocation steps and loops, etc. (refer to Fig. 7c, d) in HEA-SC Al strongly affect the symmetry of atomic displacement from the indentation center, whereas in case of HEA-SC Cu, the appearance of long lengthed Hirth partial dislocations, dislocation tangles, multi-dislocations loops, LC

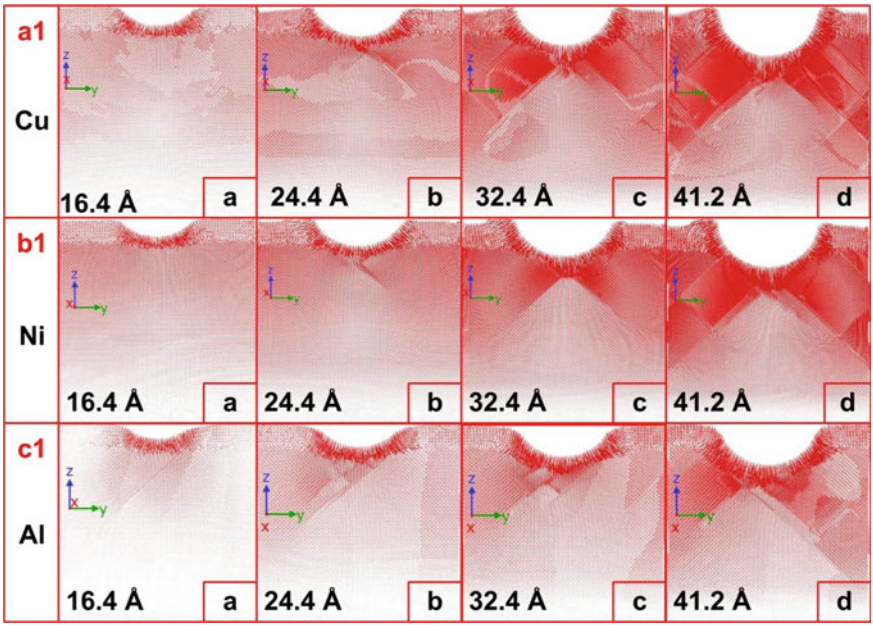

Fig. 11 Schematic of atomic displacement vector plots for the indentation depth (h) varies from (a) 16.4 Å to (d) 41.2 Å from top view for (a1) $Mo_{20}W_{20}Co_{20}Ta_{20}Zr_{20}$-SC Cu (b1) $Mo_{20}W_{20}Co_{20}Ta_{20}Zr_{20}$-SC Ni (c1) $Mo_{20}W_{20}Co_{20}Ta_{20}Zr_{20}$-SC Al specimen

locks, and closed stair-rod steps, etc. (refer to Fig. 5c, d) moderately affects the atomic displacement symmetry below the indenter tip.

Figure 12 has shown the combined radial distribution function ($g(r)$) plots of the near indenter region with indentation depth (h) varies from 0 to 41.2 Å for $Mo_{20}W_{20}Co_{20}Ta_{20}Zr_{20}$-SC Cu, SC Ni, and SC Al. Figure 12a shows, at $h = 0$ Å, the occurrence of needle-like peaks at some definite radius values denotes the higher probability of finding particles. Further, at $h = 0$ Å, the peak height for HEA-SC Ni at almost all radius values are relatively higher than that for HEA-SC Cu and HEA-SC Al, which infer the probability of finding particles in HEA-SC Ni at those radius values is much higher than others. Moreover, the higher peak height in HEA-SC Ni also attribute to its high stiffness value, which resists the applied load to a much greater extent than for other specimens, and it has well agreed with the findings in Fig. 2a. Later on, the significant reduction in peak height for all specimens with the increase in indentation depth indicates the notable lowering in particle finding probability due to the equiproportional growth in shear strain intensity all around the indenter tip region (refer to Fig. 10). On the other hand, the peak broadening with the increment in indentation depth represents the crystalline to amorphous transition due to considerable growth in plastic deformation.

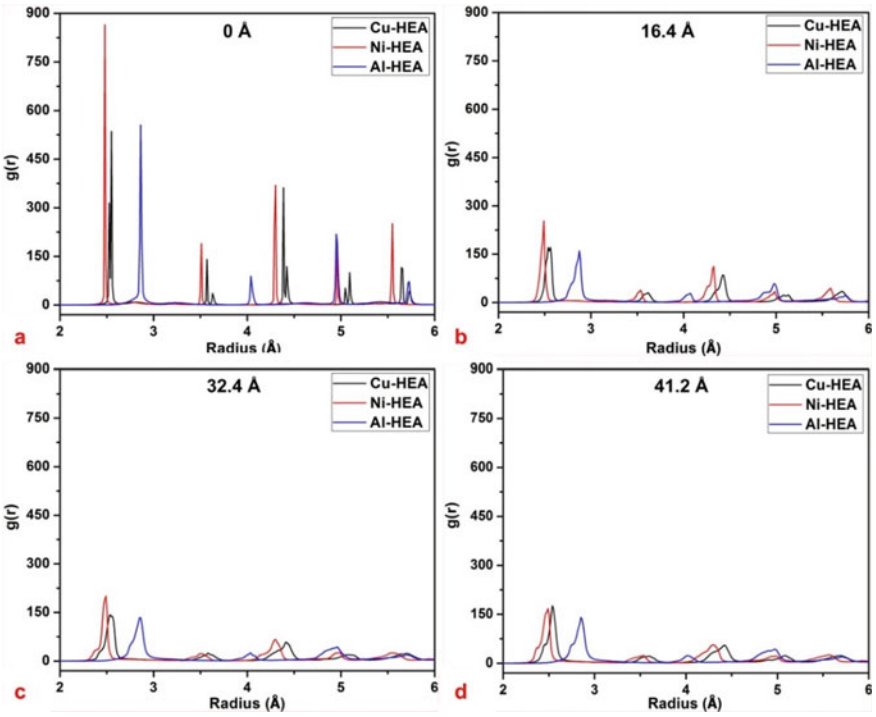

Fig. 12 Combined radial distribution function plots of near indenter region for different indentation depth (*h*) (a) 0 Å (b) 16.4 Å (c) 32.4 Å (d) 41.2 Å for $Mo_{20}W_{20}Co_{20}Ta_{20}Zr_{20}$-SC Cu, SC Ni and SC Al specimens

4 Conclusions

In the present study, the nanoindentation test has done on $Mo_{20}W_{20}Co_{20}Ta_{20}Zr_{20}$ (HEA) film-SC Cu and SC Al by replacing the substrate SC Ni in the earlier reported study at 1 K temperature. Then, the comparison of mechanical properties and nanoindentation deformation behavior between the $Mo_{20}W_{20}Co_{20}Ta_{20}Zr_{20}$ (HEA) coated SC Ni, SC Cu, and SC Al has been carried out. In addition, the development of SFT structure in $Mo_{20}W_{20}Co_{20}Ta_{20}Zr_{20}$ (HEA) film-coated SC Al and its effect on nanoindentation deformation also have been analysed precisely. HEA ($Mo_{20}W_{20}Co_{20}Ta_{20}Zr_{20}$) coated SC Ni has higher stiffness (reduced elastic modulus) and hardness than HEA ($Mo_{20}W_{20}Co_{20}Ta_{20}Zr_{20}$) coated SC Cu and HEA ($Mo_{20}W_{20}Co_{20}Ta_{20}Zr_{20}$) coated SC Al. The CNA and DXA analysis suggests the appearance of different deformed structures in HEA coated specimens affects the plastic deformation at higher indentation depth. The deformed structures seen in HEA-SC Ni are prismatic loops and interface distorted dislocations. The deformed structures seen in HEA-SC Cu are long lengthed Hirth partials, Lomer-Cottrell (LC) barriers, closed stair-rod partial dislocation steps, multi-dislocation loops, and

complex distorted interface structures. The deformed structures seen in HEA-SC Al are SFT, LC barriers, closed stair-rod partial dislocation steps and loops. The critical analysis of SFT development in HEA-SC Al has found the SFT development mechanism is dislocation-based, which is predominately governed by different SF planes' interaction and dislocation gliding. The observed SFT development mechanism is well supported and agreed with the earlier reported studies on SFT development. Eventually, the comparative plots of shear strain, displacement vector, and radial distribution function confirms the growth of the dislocation structure for $Mo_{20}W_{20}Co_{20}Ta_{20}Zr_{20}$-SC Ni is much more significant and symmetric from the indentation center towards the all-around in contrast to others due to its high stiffness. Moreover, in $Mo_{20}W_{20}Co_{20}Ta_{20}Zr_{20}$-SC Cu, the observation of plastic deformation is restricted in the surface layer to a greater extent due to the appearance in complex distorted dislocation structures, which suggests the $Mo_{20}W_{20}Co_{20}Ta_{20}Zr_{20}$ (HEA) film coating can effectively use as a surface coating to protect the bulk Cu substrate.

Acknowledgements The authors want to thank the computer centre of National Institute of Technology Rourkela for providing high-performance computing facility (HPCF) required for performing this study and TEQIP for financial assistance.

References

1. Rosenberg SJ (1968) Nickel and its alloys. US Department of Commerce, National Bureau of Standards, Washington, DC
2. Francis R (2010) The corrosion of copper and its alloys: a practical guide for Engineers. NACE International, Houston, Texas
3. Lumley R (ed) (2010) Fundamentals of aluminium metallurgy: production, processing and applications. Woodhead Publishing Limited Elsevier
4. Buckley DH (1981) Surface effects in adhesion, friction, wear, and lubrication. Elsevier Scientific Publishing Company, Amsterdam
5. Brenneman J, Wei J, Sun Z, Liu L, Zou G, Zhou Y (2015) Oxidation behavior of GTD111 Ni-based superalloy at 900° C in air. Corros Sci 100:267–274
6. Singh H, Puri D, Prakash S (2007) An overview of Na 2 SO 4 and/or V 2 O 5 induced hot corrosion of Fe-and Ni-based superalloys. Rev Adv Mater Sci 16(1–2):27–50
7. Gao MC, Yeh JW, Liaw PK, Zhang Y (2016) High-entropy alloys. Springer International Publishing, Cham
8. Tsai MH, Wang CW, Lai, CH, Yeh JW, Gan JY (2008) Thermally stable amorphous (Al Mo Nb Si Ta Ti V Zr) 50 N 50 nitride film as diffusion barrier in copper metallization. Appl. Phys. Lett. 92(5):052109
9. Argade GR, Joshi SS, Ayyagari AV, Mukherjee S, Mishra RS, Dahotre NB (2019) Tribocorrosion performance of laser additively processed high-entropy alloy coatings on aluminum. Appl Phys A 125(4):272
10. Gleeson B (2006) Thermal barrier coatings for aeroengine applications. J Propul Power 22(2):375–383
11. Chou YL, Yeh JW, Shih HC (2010) The effect of molybdenum on the corrosion behaviour of the high-entropy alloys Co1. 5CrFeNi1. 5Ti0. 5Mox in aqueous environments. Corros. Sci. 52(8):2571–2581
12. Shon Y, Joshi SS, Katakam S, Rajamure RS, Dahotre NB (2015) Laser additive synthesis of high entropy alloy coating on aluminum: corrosion behavior. Mater Lett 142:122–125

13. Chao Q, Guo T, Jarvis T, Wu X, Hodgson P, Fabijanic D (2017) Direct laser deposition cladding of AlxCoCrFeNi high entropy alloys on a high-temperature stainless steel. Surf Coat Technol 332:440–451
14. Wu CL, Zhang S, Zhang CH, Zhang H, Dong SY (2017) Phase evolution and cavitation erosion-corrosion behavior of FeCoCrAlNiTix high entropy alloy coatings on 304 stainless steel by laser surface alloying. J Alloys Compd 698:761–770
15. Wu CL, Zhang S, Zhang CH, Chen J, Dong SY (2017) Phase evolution characteristics and corrosion behavior of FeCoCrAlCu-X0. 5 coatings on cp Cu by laser high-entropy alloying. Opt Laser Technol 94:68–71
16. Wu CL, Zhang S, Zhang CH, Zhang H, Dong SY (2017) Phase evolution and properties in laser surface alloying of FeCoCrAlCuNix high-entropy alloy on copper substrate. Surf Coat Technol 315:368–376
17. Qian L, Li M, Zhou Z, Yang H, Shi X (2005) Comparison of nano-indentation hardness to microhardness. Surf Coat Technol 195(2–3):264–271
18. Broitman E (2017) Indentation hardness measurements at macro-, micro-, and nanoscale: a critical overview. Tribol Lett 65(1):23
19. Elmustafa AA, Stone DS (2003) Nanoindentation and the indentation size effect: Kinetics of deformation and strain gradient plasticity. J Mech Phys Solids 51(2):357–381
20. Zhu C, Lu ZP, Nieh TG (2013) Incipient plasticity and dislocation nucleation of FeCoCrNiMn high-entropy alloy. Acta Mater 61(8):2993–3001
21. Nair AK, Cordill MJ, Farkas D, Gerberich WW (2009) Nanoindentation of thin films: simulations and experiments. J Mater Res 24(3):1135–1141
22. Liu CL, Fang TH, Lin JF (2007) Atomistic simulations of hard and soft films under nanoindentation. Mater Sci Eng A 452:135–141
23. Li Y, Goyal A, Chernatynskiy A, Jayashankar JS, Kautzky MC, Sinnott SB, Phillpot SR (2016) Nanoindentation of gold and gold alloys by molecular dynamics simulation. Mater Sci Eng A 651:346–357
24. Zhu PZ, Fang FZ (2012) Molecular dynamics simulations of nanoindentation of monocrystalline germanium. Appl Phys A 108(2):415–421
25. Fu T, Peng X, Chen X, Weng S, Hu N, Li Q, Wang Z (2016) Molecular dynamics simulation of nanoindentation on Cu/Ni nanotwinned multilayer films using a spherical indenter. Sci Rep 6:35665
26. Ma XL, Yang W (2003) Molecular dynamics simulation on burst and arrest of stacking faults in nanocrystalline Cu under nanoindentation. Nanotechnology 14(11):1208
27. Kim KJ, Yoon JH, Cho MH, Jang H (2006) Molecular dynamics simulation of dislocation behavior during nanoindentation on a bicrystal with a $\Sigma = 5$ (210) grain boundary. Mater Lett 60(28):3367–3372
28. Jang H, Farkas D (2007) Interaction of lattice dislocations with a grain boundary during nanoindentation simulation. Mater Lett 61(3):868–871
29. Lee Y, Park JY, Kim SY, Jun S, Im S (2005) Atomistic simulations of incipient plasticity under Al (1 1 1) nanoindentation. Mech Mater 37(10):1035–1048
30. Jiao S, Tu W, Zhang P, Zhang W, Qin L, Sun Z, Chen J (2018) Atomistic insights into the prismatic dislocation loop on Al (1 0 0) during nanoindentation investigated by molecular dynamics. Comput Mater Sci 143:384–390
31. Remington TP, Ruestes CJ, Bringa EM, Remington BA, Lu CH, Kad B, Meyers MA (2014) Plastic deformation in nanoindentation of tantalum: a new mechanism for prismatic loop formation. Acta Mater 78:378–393
32. Liu Q, Deng L, Wang X (2016) Interactions between prismatic dislocation loop and coherent twin boundary under nanoindentation investigated by molecular dynamics. Mater Sci Eng A 676:182–190
33. Kiritani M (1997) Story of stacking fault tetrahedra. Mater Chem Phys 50(2):133–138
34. Silcox J, Hirsch PB (1959) Direct observations of defects in quenched gold. Philos Mag 4(37):72–89

35. Liu Q, Deng L, Wang X, Li J (2017) Formation of stacking fault tetrahedron in single-crystal Cu during nanoindentation investigated by molecular dynamics. Comput Mater Sci 131:44–47
36. Mishra DK, Meraj M, BadJena SK, Pal S (2019) Dislocation interaction and V-shaped growth of the distorted structure during nanoindentation of Cu 20 Ni 20 Al 20 Co 20 Fe 20 (high-entropy alloy)-coated copper: a molecular dynamics simulation-based study. Trans Indian Inst Met 72(1):167–180
37. Mishra DK, Meraj M, BadJena SK, Pal S (2019) Structural evolution and dislocation behaviour study during nanoindentation of Mo20W20Co20Ta20Zr20 high entropy alloy coated Ni single crystal using molecular dynamic simulation. Mol Simul 45(7):572–584
38. Jian SR, Fang TH, Chuu DS, Ji LW (2006) Atomistic modeling of dislocation activity in nanoindented GaAs. Appl Surf Sci 253(2):833–840
39. Sushko GB, Verkhovtsev AV, Yakubovich AV, Solov'yov AV (2013) Molecular dynamics simulation of nanoindentation of nickel-titanium crystal. J Phys Conf Ser 438:012021
40. Peng P, Liao G, Shi T, Tang Z, Gao Y (2010) Molecular dynamic simulations of nanoindentation in aluminum thin film on silicon substrate. Appl Surf Sci 256(21):6284–6290
41. Saraev D, Miller RE (2006) Atomic-scale simulations of nanoindentation-induced plasticity in copper crystals with nanometer-sized nickel coatings. Acta Mater 54(1):33–45
42. Nosé S (1984) A unified formulation of the constant temperature molecular dynamics methods. J Chem Phys 81(1):511–519
43. Hoover WG (1985) Canonical dynamics: equilibrium phase-space distributions. Phys Rev A 31(3):1695
44. Plimpton S (1995) Fast parallel algorithms for short-range molecular dynamics. J Comput Phys 117(1):1–19
45. Stukowski A (2009) Visualization and analysis of atomistic simulation data with OVITO–the open visualization tool. Modell Simul Mater Sci 18(1):015012
46. Zhou XW, Johnson RA, Wadley HNG (2004) Misfit-energy-increasing dislocations in vapor-deposited CoFe/NiFe multilayers. Phys Rev B 69(14):144113
47. Hertz H (1882) Ueber die Beruhrung fester elastischer Korper. J Fur Die Rein Und Angew Math 92:156–171
48. Juday RM, Silva EY, Huang JG, Caldas P, Prioli R, Ponce FA (2013) Strain-related optical properties of ZnO crystals due to nanoindentation on various surface orientations. J Appl Phys 113(18):183511
49. Honeycutt JD, Andersen HC (1987) Molecular dynamics study of melting and freezing of small Lennard-Jones clusters. J Phys Chem 91(19):4950–4963
50. Faken D, Jónsson H (1994) Systematic analysis of local atomic structure combined with 3D computer graphics. Comput Mater Sci 2(2):279–286
51. Stukowski A (2012) Structure identification methods for atomistic simulations of crystalline materials. Modell Simul Mater Sci Eng 20(4):045021
52. Li D, Wang F, Yang Z, Zhao Y (2014) How to identify dislocations in molecular dynamics simulations? Sci China Phys Mech Astron 57(12):2177–2187
53. Stukowski A, Albe K (2010) Extracting dislocations and non-dislocation crystal defects from atomistic simulation data. Modell Simul Mater Sci Eng 18(8):085001
54. Wang Z, Li J, Fang Q, Liu B, Zhang L (2017) Investigation into nanoscratching mechanical response of AlCrCuFeNi high-entropy alloys using atomic simulations. Appl Surf Sci 416:470–481
55. Hirsch PB, Horne RW, Whelan MJ (1956) LXVIII. Direct observations of the arrangement and motion of dislocations in aluminium. Philos Mag 1(7):677–684
56. Whelan MJ, Hirsch PB, Horne RW, Bollmann W (1957) Dislocations and stacking faults in stainless steel. Proc Math Phys Sci 240(1223):524–538
57. Zinkle SJ, Seitzman LE, Wolfer WG (1987) I. Energy calculations for pure metals. Philos Mag A 55(1):111–125
58. Osetsky YN, Matsukawa Y, Stoller RE, Zinkle SJ (2006) On the features of dislocation–obstacle interaction in thin films: large-scale atomistic simulation. Philos Mag Lett 86(8):511–519

59. Howe LM (1974) Irradiation hardening and annealing in copper at high neutron fluences. Radiat Eff 23(3):181–195
60. Singh BN, Zinkle SJ (1993) Defect accumulation in pure fcc metals in the transient regime: a review. J Nucl Mater 206(2–3):212–229
61. Li R, Chew HB (2015) Closed and open-ended stacking fault tetrahedra formation along the interfaces of Cu–Al nanolayered metals. Philos Mag 95(25):2747–2763
62. Liu HT, Zhu XF, Sun YZ, Xie WK (2017) Evolution of stacking fault tetrahedral and work hardening effect in copper single crystals. Appl Surf Sci 422:413–419
63. Panda AK, Divakar R, Singh A, Thirumurugesan R, Parameswaran P (2021) Molecular dynamics studies on formation of stacking fault tetrahedra in FCC metals. Comput Mater Sci 186:110017
64. Yedla N, Ghosh S (2017) Nature of atomic trajectories and convective flow during plastic deformation of amorphous Cu50Zr50 alloy at room temperature-classical molecular dynamics studies. Intermetallics 80:40–47

Performance Evaluation of Uncoated and Coated Carbide Tools During Hard Machining of AISI 4340 Steel

Anshuman Das, Pawan Kumar, Ashish Agarawal, and Akhtar Khan

Abstract The present paper highlights a comparative assessment of the influence of cutting velocity on the tool performance in machining of hardened AISI 4340 steel using uncoated and coated inserts. For hard machining of the workpiece, one uncoated and two multi-layer coated inserts were utilized. A series of experiments were conducted at four different levels whereas the cutting depth and tool advancement in mm per revolution were kept constant. Two important machining characteristics are studied tool life and surface roughness by varying machining parameters. The outcomes of the investigation revealed that both the aforementioned machining characteristics were potentially influenced by the cutting speed. It was found that the high cutting speed was responsible for curtailing tool performance as well as the surface quality of the machined part. Besides, in contrast to its coated equivalent, uncoated instruments struggled to perform effectively at higher cutting velocity. Whereas, in the context of declining wear in the flank surface of the inserts at preeminent cutting speeds, the difference in the efficiencies of both the selected coated tools was not significant.

Keywords Flank wear · Surface roughness · Hard machining · Tool coating · Carbide inserts

1 Introduction

Achieving promising surface quality for a long time with little tool damage is of utmost importance in today's real-time manufacturing systems. These are the only factors that significantly govern the rate of production along with the profit, as they

A. Das (✉)
Department of Mechanical Engg, DIT University, Dehradun, Uttarakhand 248001, India

P. Kumar · A. Agarawal
Department of Mechanical Engg, MITS, Madanapalle, Andhra Pradesh 517325, India

A. Khan
Department of Mechanical Engg, Indian Institute of Information Technology, Design and Manufacturing, Kurnool, Andhra Pradesh 518007, India

S. Pal et al. (eds.), *Processing and Characterization of Materials*, Springer Proceedings in Materials 13, https://doi.org/10.1007/978-981-16-3937-1_35

are recognized as the key indicators of machining performance [1–3]. Generally, it is difficult to achieve superior surface quality without significant tool damage, since abundant newer materials are entering the manufacturing industry. AISI 4340 hardened steel alloy (48 HRC) is regarded as a high production industrial application material for diverse purposes viz., sintering, forming, casting, and machining, etc. [4]. Machining these alloys causes elevated temperatures in the machining zone, which in turn contributes to rough machined surface and premature tool failure. The performance of tool material is generally measured by both flank and crater wear, respectively. If the size or amount of wear on any of the surfaces mentioned above is high, the chosen tool must be replaced by a new age. This leads to both increased costs as well as the time of production [5, 6]. This condition imposes to select an appropriate tool material for machining of such alloys. Promising tool materials such as Ceramics, Cermet, Cubic Boron Nitride (CBN), Polycrystalline Cubic Boron Nitride (PCBN), and Polycrystalline diamond (PCD), etc. have the capability to address this problem due to their inherent characteristics viz. high toughness and good hardness. On the other hand, these tool materials are costlier than carbide tools and thus not so much traditionally used for the machining of hardened steel alloys. Because of the aforesaid reason, the carbide inserts were adopted in the present experimental investigation. New tool coating exercises have resulted in highly potential carbide tools portraying dramatically enhanced qualities such as improved wear resistance, thermal shock resistance, toughness, fracture strength, and so on. Coatings are normally provided on the top surfaces of uncoated carbide inserts by adding one or more layers of wear-resistant materials. [7]. Earlier research studies reported a tremendous improvement in the performance of uncoated carbide tools by adding thin and hard coatings of the magnitudes 0.1to 30 μm and >2500 VHN respectively which in turn helped in enhancing tool life and therefore the production rate [8].

Over the last few decades, numerous studies have been reported evaluating the performance of carbide, ceramic, PCD, CBN, and PCBN cutting materials while machining hard materials and heat resistant alloys. Aslan [9] highlighted the performance assessment of various cutting tool inserts during high-speed machining of AISI D3 cold work steel. During this investigation, a total of five cutting inserts were used. Results of the investigation revealed that in contrast to the other counterparts, CBN tools performed better in achieving high material removal rate, high tool life and low surface roughness. Yallase et al. [10] examined the performance of CBN inserts in machining of hardened steel and compared with grinding. In comparison to the grinding operation, the superior surface finish was noted during the turning of work material using CBN tools. Lima et al. [8] examined the machining characteristics of two Steel alloys with two different inserts. During the study, CBN outperformed carbide. Aneiro et al. [11] in their experimental investigation, explained a comparative study between PCBN and TiCN/Al_2O_3/TiN coated carbide inserts to achieve greater tool life. In the current investigation, when compared to their counterparts, PCBN tools were found to be more capable of achieving enhanced tool life. Luo et al. [12] investigated the tool life of two cutting inserts during hard turning of alloy steel. The major tool wear mechanism was noticed as abrasion with CBN inserts whereas abrasion and adhesion were spotted with ceramic inserts. In terms of tool

life, improved tool performance was also perceived for both inserts in higher cutting velocity. This might be contributed to the formation of coating layers at the tool-chip mating region. Tamisharasan et al. [13] exploited three distinct grades of CBN inserts to investigate the economy, material removal rate, flank wear and tool life during hard machining of hardened petrol engine crank pin material. In a different study conducted by Yigit et al. [14]exhibited that, a multilayer coating along with an additional TiN layer performed effectively in diminishing wear at the flank face and improving machined surface characteristics during hard machining operation. Similarly, Oliviera et al. [15] in their study, demonstrated that greater tool life could be possible during machining of hardened steel using PCBN inserts. In a different study, Jiang et al. [16] also used CBN based inserts during turning of the same material. They examined and reported better surface morphology on the machined part. In the same way, Knutsson et al. [17] showed greater resistance against wear by using TiAlN/TiN multilayer coated tool inserts.

It is evident from the above-discussed literature that important research works have already been reported that have highly lightened the advantages of coated instruments in hard turning operations. But the cutting characteristics of AISI 4340 (48 HRC) have so far not been adequately addressed. Besides, very few pieces of literature have focused on comparing the performance of coated carbide inserts with an uncoated insert by varying cutting speeds during the hard machining of AISI 4340. Therefore, in the current investigation, an attempt was made to explore the effects of varying cutting speeds on the cut quality of the selected part of the work. To highlight the importance of the use of multilayer coated carbide inserts in machining hard materials, extensive comparative analysis has been carried out.

2 Experimental Details

The cylindrical bar of AISI 4340 having a diameter and length of 50 and 120 mm, respectively was selected as the workpiece for the present investigation. For hard turning operations, these test specimens were undergone heat treatment process to achieve a hardness value of 48 HRC. The percentage involvement of different materials in the test specimen is portrayed in Table 1, whereas Fig. 1 shows the actual photograph of it.

The selected work part was machined using three different carbide inserts, one uncoated and two multi-layer coated inserts. The inserts of the cutting tool were ISO designated as CNMG 120,408. These cutting inserts were clamped on the tool holder designated by ISO (PCLNR 2525M12). A series of experimental runs were carried

Table 1 Percentage involvement of different materials in test specimen

Elements	Ni	Cr	Mn	C	Si	Mo
Percentage (%)	1.55	1.10	0.77	0.397	0.389	0.175

Fig. 1 AISI 4340 alloy steel

out in dry cutting regime at four distinct cutting speeds whereas the cutting depth and tool advancement in mm per revolution were kept constant. The work material was turned on a CNC lathe machine (Jobber XL, AMS India). A portable roughness testing device (Taylor Hobson, Surtronic25) was used to measure the roughness parameter Ra. Tool wear on the flank and rake surfaces was examined under a stereo zoon optical microscope (Carl Zeiss 5ERc). Taking into account the accuracy of the measurement, the measured values were recorded at five random positions on the machined portion, and the mean value was computed and furnished. Figure 2 shows the experimental setup of the present experimental work.

Fig. 2 Experimental setup of the investigation

3 Results and Discussion

3.1 Analysis of Flank Wear

Figure 3 depicts the progression of wear at the flank surface corresponds to each cutting velocity for all three tools (Tool 1: Uncoated Carbide insert, Tool 2: TiC/TiCN/TiN coated carbide insert, and Tool 3: TiCN/TiC/Al_2O_3 coated carbide insert).It is evident from the above figure that uncoated carbide inserts exhibited inferior performance for the entire range of selected cutting speeds than that of the coated counterparts. When compared to the coated tools, this may lead to the lower hardness of the uncoated tool, which in turn failed to provide adequate wear resistance as the coated tool was offered. Besides, both coated tools were found to show analogous wear behavior in the specific cutting range from 150 to 250 m/min. However, within all the selected range of cutting speeds, Tool 3 exhibited marginally better than Tool 2.

Moreover, the effect of varying cutting speed son flank wear is also apparent from Fig. 3. For all of the selected tool inserts, wear on the flank surface increased with the increment in cutting speed. The wear rate of Tool 1 increases exponentially with cutting speed, while in the case of coated one, a different pattern has been observed. The graph shows the flank wear for second and third Tool tends to be parallel to each other, taking advantage of identical wear properties. No major difference was found between the two coated inserts in the amount of flank wear. However, relative to the other two inserts, Tool 3was found to be more effective in curtailing flank wear.

The microscopic flank wear snaps of all three tools are delimited in Fig. 4. In case of uncoated tools, significant degradation of the tool is exposed from the figure, although less flank wear is also noticeable when using coated tools. The damage to the tool leads to increased pressure and temperature at higher cutting speeds in the tool chip interface area. Besides, it was also noticed that tool wear was mainly concentrated on areas of the tool nose. This could lead to thermal softening and increased stress in the tool-chip mating zone induced by extreme temperatures. The chipping phenomenon was also witnessed at higher cutting speed (250 m/min), particularly while using uncoated carbide inserts whereas negligible chipping was observed with coated tools.

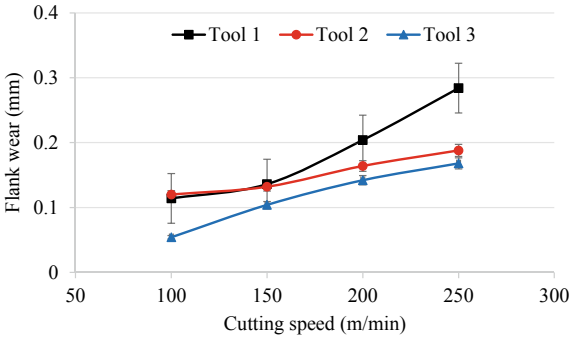

Fig. 3 The trends of Flank wear w.r.t. cutting speed

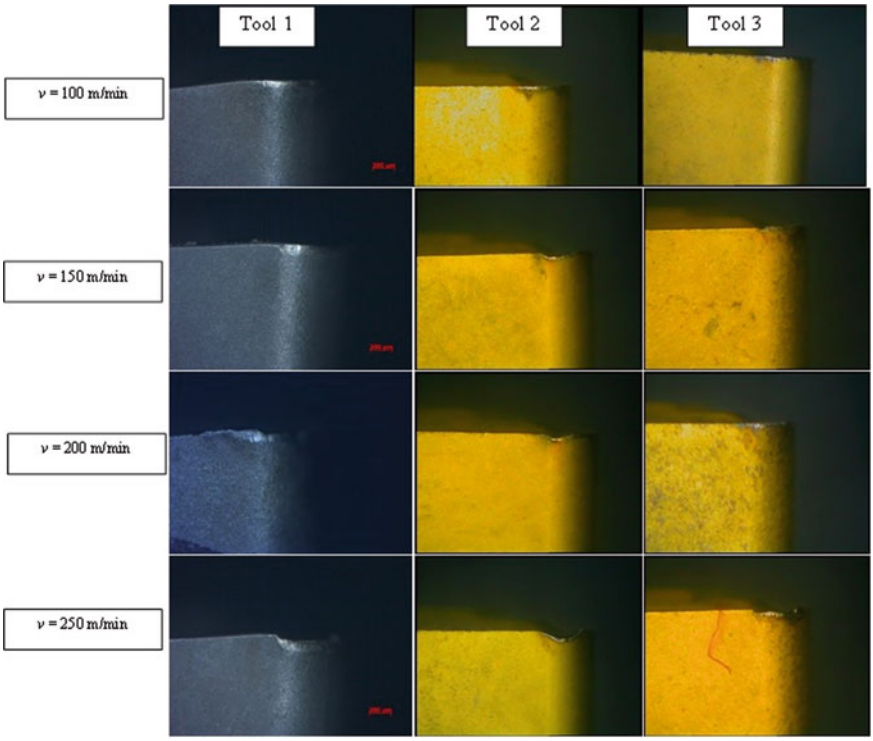

Fig. 4 Microscopic views of Flank wear

3.2 Surface Roughness Analysis

The roughness profiles for all three cutting inserts corresponds to their cutting velocity are illustrated in Fig. 5. It is observed from the above figure that roughness values

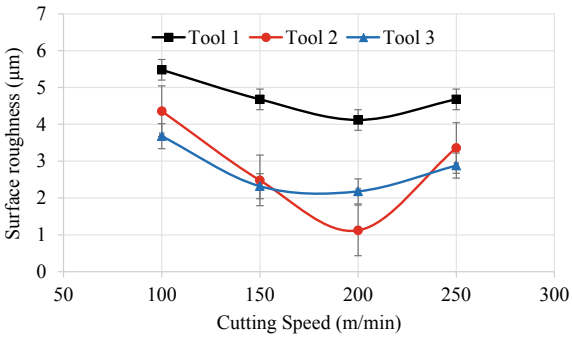

Fig. 5 Variation in surface roughness with respect to cutting speed

increased remarkably in the case of uncoated tools relative to their coated counterparts. This might contribute to the highly ductile behavior of the chosen work part, which could lead to a notable formation of built-up edges (BUEs) and thus to poor surface finish. Moreover, during this analysis, the effect of various cutting speeds was also illustrated. It is observed from the graph that the minimum cutting speed provided the maximum roughness among all the three tool inserts. The pattern of variation of surface roughness disclosed that surface roughness diminishes at higher cutting speed. However, the same reduced until the lowest value achieved after which roughness increased again. This could be clarified and justified by noticing the weakened built-up edges due to high cutting speed. As a result, in the present investigation, the value of surface roughness increased again with an increment in cutting velocity beyond 200 m/min.

4 Conclusions

Using three distinct cutting tool inserts, an extensive experimental work was conducted on AISI 4340 hardened steel. The effectiveness of the coating layer and cutting speed was tested and furnished. It is possible to draw the following conclusions based on the observations made during the current investigation:

1. The cutting speed was identified as having a potential impact on both tool life and surface finish.
2. The highest surface roughness was reported at the lowest cutting speed. However, it may be limited to the specific range of cutting speeds.
3. Initially, surface roughness declined with higher speed level and reaches minimum value. It again increases with an increment in cutting speed and therefore a moderate value of cutting speed is to be chosen properly to confirm better surface quality.
4. TiCN/TiC/Al_2O_3 coated carbide inserts offered lesser tool damage compared to TiC/TiCN/TiN coated and uncoated carbide inserts.

References

1. Wu D, Matsumoto Y (1990) The effect of hardness on residual stresses in orthogonal machining of AISI 4340 steel
2. Reddy NSK, Rao PV (2005) Selection of optimum tool geometry and cutting conditions using a surface roughness prediction model for end milling. Int J Adv Manuf Technol 26(11–12):1202–1210
3. Khan A, Maity K (2018) Influence of cutting speed and cooling method on the machinability of commercially pure titanium (CP-Ti) grade II. J Manuf Process 31:650–661
4. Gupta MK, Sood PK (2016) Optimizing multi characterstics in machining of AISI 4340 steel using Taguchi's approach and utility concept. J Inst Eng Ser C 97(1): 63–69

5. Singh J (2008) Experimental investigation for tool life enhancement of single point cutting tool with cryogenic treatment. M. Tech dissertation, Punjab Technical University, Jalandhar
6. Aujla H, Singh R (2008) Applications of cryogenic treatment for enhancing the machining properties of titanium alloy (Ti-6Al-4V). Manuf Technol Today 7(10):22–26
7. Sahin Y, Motorcu AR (2005) Surface roughness model for machining mild steel with coated carbide tool. Mater Des 26(4):321–326
8. Lima J et al (2005) Hard turning: AISI 4340 high strength low alloy steel and AISI D2 cold work tool steel. J Mater Process Technol 169(3):388–395
9. Aslan E (2005) Experimental investigation of cutting tool performance in high speed cutting of hardened X210 Cr12 cold-work tool steel (62 HRC). Mater Des 26(1):21–27
10. Yallese MA et al (2009) Hard machining of hardened bearing steel using cubic boron nitride tool. J Mater Process Technol 209(2):1092–1104
11. Aneiro FM, Coelho RT, Brandao LC (2008) Turning hardened steel using coated carbide at high cutting speeds. J Braz Soc Mech Sci Eng 30(2):104–109
12. Luo S, Liao Y, Tsai Y (1999) Wear characteristics in turning high hardness alloy steel by ceramic and CBN tools. J Mater Process Technol 88(1–3):114–121
13. Tamizharasan T, Selvaraj T, Haq AN (2006) Analysis of tool wear and surface finish in hard turning. Int J Adv Manuf Technol 28(7–8):671–679
14. Yigit R et al (2008) Tool life performance of multilayer hard coatings produced by HTCVD for machining of nodular cast iron. Int J Refract Metal Hard Mater 26(6):514–524
15. De Oliveira AJ, Diniz AE, Ursolino DJ (2009) Hard turning in continuous and interrupted cut with PCBN and whisker-reinforced cutting tools. J Mater Process Technol 209(12–13):5262–5270
16. Jiang W et al (2006) A cBN-TiN composite coating for carbide inserts: coating characterization and its applications for finish hard turning. Surf Coat Technol 201(6):2443–2449
17. Knutsson A et al (2011) Machining performance and decomposition of TiAlN/TiN multilayer coated metal cutting inserts. Surf Coat Technol 205(16):4005–4010

Utilization and Geopolymerization of Fly ash for Concrete Preparation and Soil Stabilization: A Short Review

Nikita Barik and Jyotirmoy Mishra

Abstract Geopolymers are green composite materials developed by the alkali treatment of aluminosilicate wastes such as fly ash. Over the last 30 years, different applications of geopolymer binders, which include the production of green concrete, coating material, bricks, and as a method of stabilization of soil have been studied. This review paper primarily concentrates on the employment of fly ash for concrete preparation and soil stabilization through this novel geopolymer technology. Therefore, the first part of the paper highlights the advantages and properties of fly ash-based geopolymer while the second part describes its utilization as a method of soil stabilization for geotechnical applications. The fly ash is mixed with an alkaline solution to form a paste that binds the coarse and fine aggregates together to produce concrete. The findings of the past research studies have been highlighted in this paper, which shows that fly ash derived geopolymer exhibits higher compressive strength, better durability properties, when matched with traditional cement-based concrete. Further, in the context of geotechnical engineering, soil stabilization is the moderation of soil properties to obtain a type of soil that remains in an unchanged condition throughout its serviceable life. Use of geopolymerized fly ash as a method of soil stabilization includes developing a geopolymer paste i.e. fly ash added to alkaline activator, then adding it with varying percent to the soil. As a result of geopolymeric reactions, the soil becomes chemically stable, which increases the coherence of the soil particles. Past literature demonstrates that soils may be stabilized to enhance their strength and to reduce plasticity. The finding of this paper suggests that fly ash, through geopolymerization, could be successfully used for concrete preparation and soil stabilization.

Keywords Fly ash · Geopolymerization · Geopolymer concrete · Soil stabilization · Waste utilization

N. Barik
College of Engineering and Technology, Bhubaneswar, Odisha, India

J. Mishra (✉)
Veer Surendra Sai University of Technology, Burla, Odisha, India

S. Pal et al. (eds.), *Processing and Characterization of Materials*, Springer Proceedings in Materials 13, https://doi.org/10.1007/978-981-16-3937-1_36

1 Introduction

At present, the demand of concrete is growing along with the rate of urbanization. Cement, a key component of concrete, is a source of carbon emissions and is responsible for greenhouse gas emissions (CO_2). It is reported that 0.82 kg of carbon dioxide gas is released for every kg of cement produced [1]. Therefore, in the current scenario, it becomes imperative to use alternative green technologies to scale down the use of cement for the production of concrete. Geopolymer technology is one such alternative, which utilizes geopolymer binders for the production of low-carbon concrete with enhanced properties.

Geopolymer technology is relatively new and its implementation is a step forward in the direction of sustainable development. The raw materials used in this technology are the industrial wastes (known as source materials) that are abundant in silicon and aluminum and an alkaline solution; generally composed of sodium hydroxide and sodium silicate. These source materials when combined with the alkaline solution undergo the process of geopolymerization to form novel geopolymer materials that are eco-friendly in nature. The geopolymerization is the reaction process that is characterized by the formation of a three-dimensional network structure comprising of chains of –Si–O–Al–O– bonds, generated from the mixture of source materials and the alkaline solution [2]. However, the rate of geopolymerization depends upon temperature conditions and chemical compositions of source materials and alkaline solutions.

Fly ash, the most extensively available industrial waste, is produced from the combustion of coal in power plants having very fine-sized particles [3]. It is easily available and is rich in silicon and aluminum oxides, which makes it an ideal choice to be re-used as source materials for geopolymerization.

On the other hand, problematic soils have been a major issue for geotechnical engineers, and therefore requires improvement before its use. In the past, improvement of soil has been usually achieved through mechanical or chemical solution treatment [4]. Currently, the geopolymer binders are employed for soil stabilization and are considered to be a worthy technique that will lead to smart infrastructures. The stabilization of soil through the technique of geopolymerization generally includes the process of dissolution of aluminosilicates from the source materials such as fly ash using an alkaline solution and then treating the soil with the resulting geopolymer paste, that ultimately leads to the enhancement of the soil properties [5].

Over the last 30 years, different applications of geopolymer binders made out of fly include the production of green concrete, coating material, bricks, and as a method of stabilization of soil. However, this paper primarily focuses upon the utilization and geopolymerization of fly ash for concrete preparation and soil stabilization; to encourage its large-scale implementations.

Table 1 Chemical compositions of fly ash [8]

Wt.%	SiO_2	Al_2O_3	Fe_2O_3	CaO	MgO	SO_3	K_2O
FA	59.0	21.00	3.70	6.90	1.40	1.00	0.90

Table 2 Chemical compositions of fly ash [9]

Wt.%	SiO_2	Al_2O_3	Fe_2O_3	CaO	MgO	SO_3	K_2O
FA	52.06	20.54	5.5	14.07	3.29	0.57	0.69

2 Significance of this Study

Geopolymers exhibit a unique set of properties; particularly based on their source material composition. Hence, categorical understanding of each source material-based geopolymer composite becomes imperative and, in this paper, the authors have endeavored to review the characteristics of geopolymer binder derived from fly ash for manufacturing of concrete, together with its properties as a soil stabilizer. Till now, this kind of review has not been explored even if fly ash is available in plenty and whose disposal is a great concern, at present. Hence, this paper also aids in sustainable waste management of fly ash because the application of fly ash covers structural as well as geotechnical applications. This paper tries to integrate these two areas for achieving a high degree of sustainable development through this geopolymer technology.

2.1 Fly ash and its Properties

Fly ash is a waste obtained from the ignition of coal and contains particle size in the range of (10–100 micron) [6]. It usually carries a color ranging from light tan to buff, representing a low quantity of carbon emission along with a little quantity of lime [7]. The chemical constituents of fly ash alter according to the class of coal and the various practices used for the combustion of coal. Below are the Table 1 and Table 2 that represent the chemical compositions found in fly ash; as reported in [8, 9].

2.2 Reaction Mechanisms of Geopolymer

The reaction mechanism of geopolymer varies across the different source material combinations used, while the core reaction mechanism yielding a solid framework of the Si–O–Al–O series remains the same. Figure 1 shows a reaction model from the study by [10]. Davidovits, a renowned French scientist, in a study [11], coined the term "geopolymer" to the inorganic mineral polymer having the "polysialate"

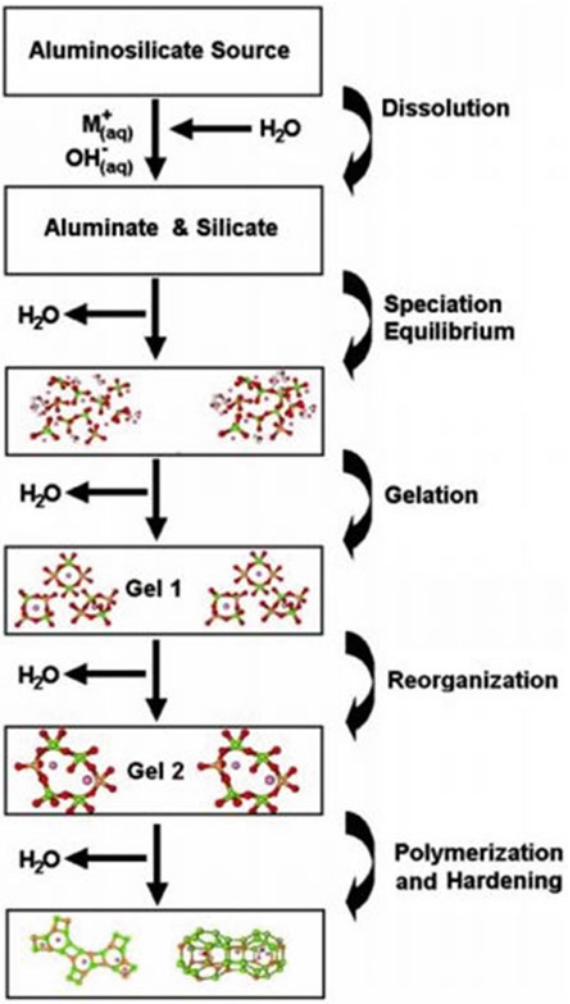

Fig. 1 Reaction model of geopolymerization [10]

series. He further stated that it because of the polycondensation reaction mechanism between source materials and alkali solution which finally resulted in Si–O–Al bonds and expulsion of free water at the end of the process. Geopolymers are often referred to as alkali-activated materials, though the end products are fundamentally different, yet, the results are very similar, and therefore, the practitioners' term them as geopolymers, for generalized research understanding and outcomes. In 1940, the alkali-activation process of GGBFS had been studied by Purdon in [12] where he explained that reaction broadly takes place in two steps i.e. dissolution of silicon and aluminum atoms by the alkaline solution and generation of calcium silicate aluminate hydrate (C–A–S–H) gels. Likewise, Glukhovsky in a study [13], proposed a reaction model that occurred in three fundamental steps. Initially, the bonds of Si–O–Si gets

fragmented then convert into colloid phase. Soon after, these units interact among themselves giving rise to a stable matrix leading to a more condensed solid structure/products namely C-A-S–H/ (N-A-S–H) sodium aluminate silicate hydrate gels in the final step. It is understood that over the past years, different researchers have attempted to study this complex multiphase reaction process—geopolymerization. However, to date, the accurate mechanism is still under investigation or yet to be comprehended because geopolymer chemistry for each source material is different.

3 Geopolymerization of Fly ash for Preparation of Concrete

3.1 Preparation of Fly ash-Based Geopolymer Concrete

The authors aim to promote the geopolymer derived from fly ash as a pathway to sustainable manufacturing of concrete. Therefore, this section provides a synopsis of the preparation of geopolymer concrete along with a simplified flowchart; presented in Fig. 2.

Fly ash: It is one of the constituents used in the synthesis of geopolymer concrete and is regarded as a source material. It contains a high amount of silicon and aluminum oxides which, after reacting with the alkaline solution results in the creation of -Si–O–Al-O- framework. More often, the fly ash with low calcium is preferred instead of

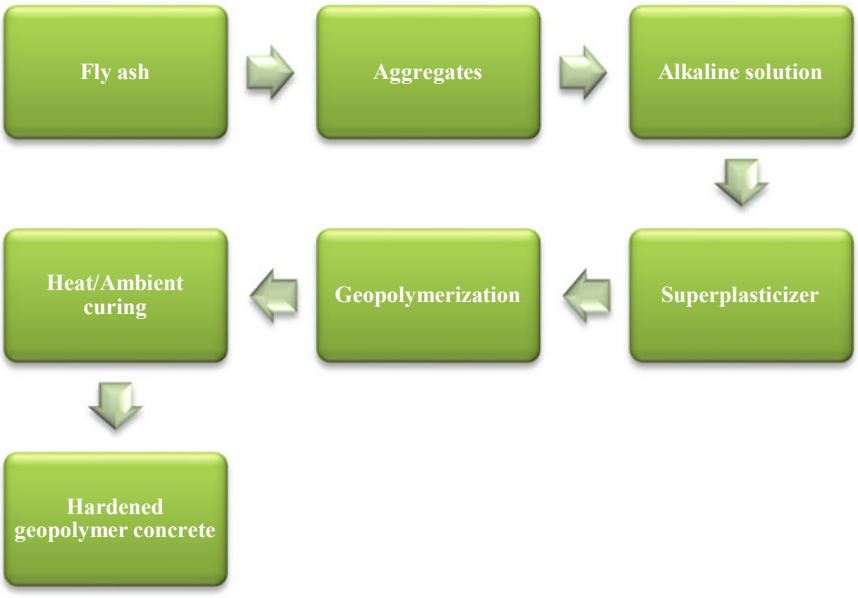

Fig. 2 A flow chart representing the preparation of geopolymer concrete with fly ash

fly ash having excessive calcium because excessive amount of calcium could inhibit the geopolymerization process, resulting in low strength properties [14].

Alkaline solution: The alkaline solution acts as an essential component of the geopolymerization process [15]. Usually, the sodium-based hydroxides/silicates are employed in the preparation of fly ash-based geopolymerization [16, 17]. Due to low cost, sodium-based hydroxides/silicates are generally used instead of potassium-based hydroxides/silicates.

Aggregate: For the preparation of geopolymer concrete with fly ash, different sizes of coarse aggregates acquired in crushed rock form and fine aggregate in uncrushed form, have been used [18].

Super-plasticizer (If required): To achieve the desired workability, a super-plasticizer can be used while preparing fly ash-based geopolymer concrete [19].

4 Properties of Geopolymer Concrete Derived from Fly ash

4.1 Compressive Strength

In a study [20], the compressive strength of the geopolymer concrete made with fly ash was assessed under elevated temperature curing conditions. It was found that the geopolymerization reaction was enhanced and the strength increased once the curing temperature was raised from 60 to 100 °C. A similar observation was noticed in a study [21], where at 100 °C, the increment in compressive strength was found to be 96.4% more after 28 days when compared to the samples cured below 100 °C. The impact of NaOH concentration and ratio of Na_2SiO_3 and NaOH on compressive strength of geopolymer concrete prepared with fly ash was studied in [22]. It was found that the compressive strength enhanced with the rise in the concentration of NaOH. And from the perspective of the effect of the ratio of Na_2SiO_3 and NaOH, it was revealed the compressive strength improved up to 2.5 (Na_2SiO_3/NaOH), and beyond this, it eventually decreased.

4.2 Flexural Strength

In a study [23], it was noticed that the replacement of source material by 50% fly ash led to the rise in the flexural strength. The cracks caused by flexure occurred at the mid-span and better crack resistance was shown by the samples containing a high amount of fly ash. Similar observations are also noticed in a study [24]. In another study [25], the geopolymer concrete comprising 50–100% fly ash exhibited improved flexural strength in the scope of 5–7 MPa under ambient curing conditions. Thus, it can be stated that with the rise in the content of fly ash in the mix, the flexural strength is found to be improved; irrespective of curing conditions.

4.3 Durability

In a study [26], the samples made with fly ash were immersed in a 10% sulfuric acid solution for 45 days, after 7 days of curing. It was found that there was no change in the shape of the samples and exhibiting no visible cracks. In another study [27], following the immersion of high temperature cured geopolymer samples containing fly ash, under sulfate solution, the compressive strength was found to be increased by 4–12%. Improved resistance under 5% sulfate solution was also observed in a study [28], where the geopolymer concrete samples made with fly ash, showed no significant damage on their surfaces even after one year of the observation period.

5 Geopolymerization of Fly ash for Soil Stabilization

5.1 Soil Stabilization and its Advantages

Soil stabilization is a practice wherein the properties (physical or chemical) of the soil are modified so as to make it suitable for construction or design [29]. Some of the improvements in the soil achieved through this technique include the enhancement in weight-bearing abilities and tensile strength along with control of erosion. Currently, geopolymer binders are utilized to stabilize the soil to achieve improvements in its properties—from the economical viewpoint. The desired soil is treated with the geopolymer binder pastes formed out of the industrial wastes such as fly ash, which rapidly enhances the soil properties [30].

Advantages of Soil Stabilization

- Strength improvement
- Mitigation of volume instability, swelling potential, and shrinkage
- Reduction in plasticity
- Reduction in permeability
- Reduction in soil deformation, compressibility, and settlement.

5.2 Preparation of Fly ash Derived Geopolymer Binder for Stabilization of Soil

This section aims to provide a simplified approach to stabilize soil through treatment with geopolymer binder derived from fly ash. Figure 3 exhibits the flowchart for the method of preparation of geopolymer made out of fly ash for soil stabilization. When fly ash is fused with an alkaline solution (composed of alkali hydroxides/silicates) and then finally mixed with the soil, the geopolymerization reaction occurs which ultimately leads to the improvement in the soil properties.

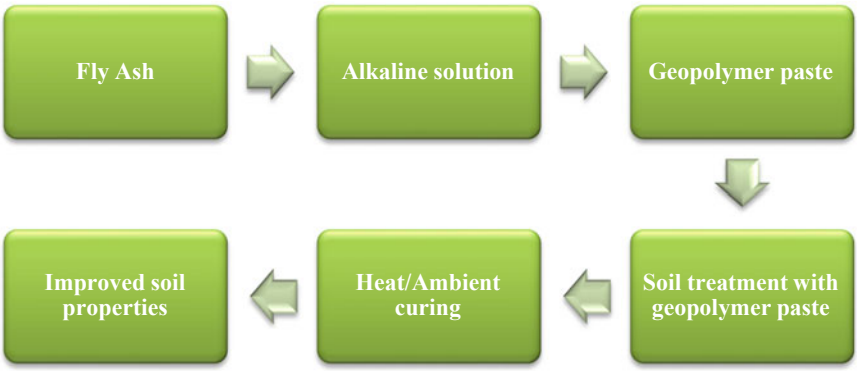

Fig. 3 A flowchart representing the method of soil stabilization by treatment with fly ash-based geopolymer

6 Properties of Soil Stabilization Through Geopolymerization of Fly ash

6.1 Compressive Strength

In a study [31], the soil was mixed with geopolymer binder utilizing fly ash to evaluate the unconfined compressive strength (UCS) test results. It was revealed that the strength increased with the rise in alkaline solution/fly ash ratio at different ages of curing. In another study [32], the amount of fly ash content was augmented from 0 to 25% to prepare a geopolymer binder and after soil treatment, it was revealed that the failure stress and strain were found to be augmented by 106 and 50% respectively. In the same way, the variation in the UCS values of the black cotton soil specimens was observed, which were treated with geopolymer binder containing 5, 10, 15, and 20% of fly ash, and it was found that strength gained was more than 1500 kPa for each of the samples, after the age of 7 days [33].

6.2 Compressibility and Settlement

In a study [34], the california bearing ratio (CBR) values were evaluated for the soil stabilized by geopolymer paste based on fly ash and having an alkaline solution/fly ash ratio of 0.4. The geopolymer concentration for each soil sample was considered to be 10, 20, and 30% (by wt.). From the experimental results, it was found that the CBR index improved with rise in geopolymer concentration; 9.89, 16.24, and 34.32% respectively. The reason for this increment in CBR index was attributed to the generation of aluminosilicate gels which helped in binding the fly ash and

soil particles together. In a study [35], the settlement of fly ash-based geopolymer-stabilized soil was evaluated. The degree of consolidation was found to be 90% after 7 days. The CBR values of black cotton soil treated with fly ash-based geopolymer binder were studied in [36]. Two batches of mix samples were manufactured for the purpose; one was mixed with alkaline solution (treated) and the other with water (untreated). The CBR tests on the samples revealed that there was a significant rise in the CBR values of treated samples in contrast to the untreated samples. In addition, CBR values of samples (treated and untreated) were determined under soaked and unsoaked conditions. It was observed that soaked CBR values of treated specimens exhibited a higher degree of increment in CBR values. In the case of treated soaked samples, when the fly ash was added—5, 10, and 20% by wt. of the binder, the CBR values were found to increase by 939, 1013, 1147, and 1178% respectively. The reason for this increment in CBR values was attributed to geopolymer gel formation which enhanced as the quantity of fly ash in the binder raised. This led to the development of dense microstructure that ultimately resulted in the enhancement of CBR values.

6.3 Plasticity Index

In general, the fly ash does not carry any plasticity, therefore, when geopolymer binder made out of fly ash was mixed with the clay soil, a reduction in plasticity index was noted with rising content of fly ash [37]. Likewise, in a study [38], the geopolymer mix carrying varying percentages of fly ash (0–20%) was treated with the soil and it was revealed that the plasticity index significantly diminished by 7%. It is required to mention that the high plasticity value influences the workability in the course of its mixing with the fly ash-based geopolymer binder. This eventually affects the overall homogeneity of the soil sample and the degree of dissemination of the geopolymer binder within the soil sample [39]. In another study [40], it was revealed that the plasticity index values were significantly reduced and ultimately there was a change in the characteristics of the clay soil from high plasticity to low plasticity; when fly ash content was increased in the binder mix. This could be due to the effect of fly ash and also because of chemical activator solution which helped to aid in the sliding of the soil particles between themselves.

7 Conclusions

The foremost objective of this paper was to describe the utilization and geopolymerization potential of fly ash for concrete preparation and soil stabilization. The studies, discussed here, suggest that the geopolymer concrete manufactured with fly ash, can be employed as a substitute to the cement-based concrete. Likewise, to

improve the soil properties, concerning soil stabilization for geotechnical applications, fly ash-based geopolymer binder seems to be a worthy choice. The paper thus aimed to promote higher utilization of fly ash for efficient solid waste management, which will lead to a more sustainable society.

Acknowledgements The authors convey their gratitude to the College of Engineering and Technology, Bhubaneswar, and Veer Surendra Sai University of Technology, Burla, for providing the needful resources, during the conduct of this research paper. The authors also acknowledge Prof. Sanjaya Ku. Patro, Dr. Bharadwaj Nanda, Dr. Syed M. Mustakim, Mr. Shaswat Ku. Das, Mr. R.S. Krishna, for their continuous encouragement.

References

1. Turner LK, Collins FG (2013) Carbon dioxide equivalent (CO2-e) emissions: a comparison between geopolymer and OPC cement concrete. Constr Build Mater 43:125–130
2. Rao G, Kumar G, Ganesh S (2016) Comparison of compressive strength of M25, M30 grades of concrete by partially replacement of fly ash with normal and accelerated curing. Int J Innov Res Technol 3(1):164–172
3. Singh B, Ishwarya G, Gupta M, Bhattacharyya S (2015) Geopolymer concrete: a review of some recent developments. Constr Build Mater 85:78–90
4. Han J (2015) Principles and practice of ground improvement. John Wiley & Sons, Hoboken, NJ
5. Sargent P (2015) The development of alkali-activated mixtures for soil stabilization. In: Handbook of alkali-activated cements, mortars, and concretes. Elsevier BV, Amsterdam, pp 555–604
6. Nizar K, Kamarudin H, Idris M (2007) Physical, chemical & mineralogical properties of fly-ash. J Nucl Relat Technol 4:47–51
7. Mishra S, Naval A, Gajre G, Dixit A (2014) Fly ash: a suitable material for solid waste management through vermicomposting. Indian Inst Environ Manag 125–136
8. Ismail K, Hussin K, Idris M (2007) Physical, Chemical & Mineralogical properties of Fly Ash. J Nucl Relat Technol 4:47–51
9. Liu Z, Cai C, Liu F, Fan F (2016) Feasibility study of loess stabilization with fly ash–based geopolymer. J Mater Civil Eng 28(5)
10. Duxson P, Jiménez A, Provis JL, Lukey GC, Palomo A, Deventer J (2007) Geopolymer technology: the current state of the art. J Mater Sci 42(9):2917–2933
11. Davidovits J, Sawyer JL (1985) Early high-strength mineral polymer. US Patent No. 4509985
12. Purdon A (1940) The action of alkalis on blast furnace slag. J Soc Chem Ind 59:191–202
13. Glukhovsky VD, Rostovskaja GS, Rumyna GV (1980) High strength slag alkaline cements. Proc Seventh Int Congr Chem Cem 3:164–168
14. Nanavati S, Avtar S, Singh R, Mehta D, Patel A, Lade A (2017) A review on fly ash based geopolymer concrete. IOSR J Mech Civ Eng (IOSR-JMCE) 14(4):12–16
15. García-Lodeiro I, Palomo A, Fernández-Jiménez A (2007) Alkali–aggregate reaction in activated fly ash systems. Cem Concr Res 37:175–183
16. Hardjito D, Rangan BV (2005) Development and properties of low-calcium fly ash-based geopolymer concrete, vol 14. Curtin University of Technology, Perth, Australia, 12–16
17. Khale D, Chaudhary R (2007) Mechanism of geopolymerization and factors influencing its development: a review. J Mater Sci 42(3):729–746
18. Ferdous M, Kayali O, Khennane A (2013) A detailed procedure of mix design for fly ash based geopolymer concrete. In: International institute for FRP in construction. pp 1619–1634

19. Gurlhosur S, Samad A, Kamdod M, Pati M, Sreekanth B (2014) A comparative study of green geopolymer concrete using fly ash. Int J Electronics Commun Soft Comput Sci Eng 3(5)
20. Hardjito D, Wallah S, Sumajouw M, Rangan B (2004) On the development of fly ash-based geopolymer concrete. ACI Mater J 101(6):467–472
21. Joseph B, Mathew G (2012) Influence of aggregate content on the behavior of fly ash based geopolymer concrete. Sci Irani Trans A Civ Eng 19(5):1188–1194
22. Sofi Y, Gull I (2015) Study of properties of fly ash based geo polymer concrete. Int J Eng Res 3:73–79
23. Shehab H, Ahmed M, Eisa S (2016) Mechanical properties of fly ash based geopolymer concrete with full and partial cement replacement. Constr Build Mater 126(2016):560–565
24. Nguyen K, Ahn N, Le T, Lee K (2016) Theoretical and experimental study on mechanical properties and flexural strength of fly ash-geopolymer concrete. Constr Build Mater 106(2016):65–77
25. Jawahar J, Mounika G (2016) Strength properties of fly ash and GGBS based geopolymer concrete. Asian J Civ Eng (BHRC) 17(1):127–135
26. Shankar S, Khadiranaikar B (2012) Performance of geopolymer concrete under severe environmental conditions. Int J Civ Struct Eng 3:396–407
27. Wallah S, Rangan B (2006) Low-calcium Fly ash-based Geopolymer concrete: long-term properties. Faculty of Engineering, Curtin University of Technology Research report, Australia
28. Bakharev T (2005) Durability of geopolymer materials in sodium and magnesium sulfate solutions. Cem Concr Res 35(6):1233–1246
29. Sargent P (2015) The development of alkali-activated mixtures for soil stabilization. In: Handbook of alkali-activated cements, mortars and concretes. pp 555–604
30. Winterkorn HF, Pamukcu S (1991) Soil stabilization and grouting. In: Hsai F (ed) Foundation engineering handbook, 2nd edn. VanNostrand Reinhold, New York, NY, p 371
31. Parikshith V, Shekhar D (2019) Feasibility of Flyash based Geopolymer for Soil Stabilization. Int J Innov Technol Explor Eng (IJITEE) 9(1):2319–7064
32. Dhakar S, Jain S (2020) Stabilization of soil: a review. Int J Geosynth Ground Eng 5(6):2016
33. Patel A (2020) Studies on the properties of fly ash-rice husk ash-based geopolymer for use in black cotton soils. Int J Geosynth Ground Eng 6:38
34. Dungca JR, Codilla T (2018) Fly-ash based geopolymer as stabilizer for silty sand embankment materials. Int J GEOMATE 14(46):143–149
35. Yaghoubia M, Arulrajaha A, Horpibulsuka C, Leong M (2020) Compressibility and strength development of geopolymer stabilized columns cured under stress. Soils and Found 60(5)
36. Murmu A, Dhole N, Patel A (2018) Stabilization of black cotton soil for subgrade application using fly ash geopolymer. Road Mater Pavement Des 21(3):867–885
37. Bose B (2012) Geo engineering properties of expansive soil stabilized with fly ash. Electron J Geotech Eng 17:1339–1353
38. Raveendran H, Anjana R (2017) Effect of fly ash geopolymer on geotechnical properties of soil. Int J Adv Res Eng Manag 3(5):17–22
39. Abdullah HH, Shahin MA, Sarker P (2020) Stabilization of clay with fly-ash geopolymer incorporating GGBFS. Geosciences 10:249
40. Abdullah HH, Shahin MA, Sarker P (2017) Stabilization of clay with fly-ash geopolymer incorporating GGBFS. In: Proceedings of the 2nd world congress on civil, structural, and environmental engineering (CSEE'17). Barcelona, Spain, pp 1–8

Epilogue

The book successfully covers the dynamic and novel research works presented for the Conference on Processing and Characterisation of Materials (CPCM-2020). We witnessed the authors with their distinguished investigations over the sea of topics in the materials world, broadly inclining on materials processing, advanced materials, composites, materials characterization, composites, defence materials and surface engineering. The book aims to integrate the notable work of the material users, manufacturers, experimentalists and theoretical researchers and nevertheless share their field of expertise. Our goal and the primary purpose in this book are to bring together the attempts made by material researchers and to consider the various methodologies employed in the complex problem solving as well as to understand the structural and morphological aspects. The immense approaches made by all the authors gave us an opportunity to exchange knowledge and future insights towards the direction of research, development, experimental analysis, fabrication methodologies and several theoretical modelling of the materials. Considering some of the studies in this book, likewise the electronic structure of material studied using an open-source ab initio quantum chemistry software, Quantum Espresso. It can clearly serve huge platform to carry DFT (Density Functional Theory) calculations or study quantum energy states in materials like semiconducting materials for the theoretical researchers. Also, the advance fibre-reinforced composites developed from natural fibres like hemp when mixed along brick powder show enhanced ultimate tensile strength and flexural properties. The low cost and renewable properties of these natural fibres can clearly attract the manufacturers as well as the users. We witnessed the study of the dual phase steel used as advanced high strength steel grades in automotive industries, this clearly helps the researchers and manufacturers to improve fuel efficacy and minimize CO_2 emissions. Readers can witness the spectrum of topics covered from the atomistic scale to continuum scale of materials. All the manuscripts under this book serves to demonstrate the meaningful step towards systematic definition and organization of the technical skills, concepts and so far, the applications of composite materials. It's truly said by Sir Edwin Hubble that "Science is the one human activity

S. Pal et al. (eds.), *Processing and Characterization of Materials*, Springer Proceedings in Materials 13, https://doi.org/10.1007/978-981-16-3937-1

that is truly progressive. The body of positive knowledge is transmitted from generation to generation." We hope the patient reader has been through the chapters of this book and came across the vast dimensions of research and developments made in the materials world. Finally, we could conclude the wealth of applications arising from the novel approaches made. We owe to science and technology and as researchers thrive more knowledge and make better problem-solving approaches with the aim to build a better world. At last, we would like to conclude with Sir Albert Einstein's quote, "The important thing is to never stop questioning".